DOE/ER-0313/23

Fusion Materials

Semiannual Progress Report for Period Ending December 31, 1997

U. S. Department of Energy
Office of Fusion Energy Sciences

DOE/ER-0313/23
Distribution
Categories
UC-423, -424

FUSION MATERIALS
SEMIANNUAL PROGRESS REPORT
FOR THE PERIOD ENDING
December 31, 1997

Prepared for
DOE Office of Fusion Energy Sciences
(AT 60 20 00 0)

DATE PUBLISHED: MARCH 1998

Prepared for
OAK RIDGE NATIONAL LABORATORY
Oak Ridge, Tennessee 37831
Managed by
Lockheed Martin Energy Research Corp.
for the
U.S. DEPARTMENT OF ENERGY
under Contract DE-AC05-96OR22464

FOREWORD

This is the tweny-third in a series of semiannual technical progress reports on fusion materials. This report combines the full spectrum of research and development activities on both metallic and non-metallic materials with primary emphasis on the effects of the neutronic and chemical environment on the properties and performance of materials for in-vessel components. This effort forms one element of the materials program being conducted in support of the Fusion Energy Sciences Program of the U.S. Department of Energy. The other major element of the program is concerned with the interactions between reactor materials and the plasma and is reported separately.

The Fusion Materials Program is a national effort involving several national laboratories, universities, and industries. A large fraction of this work, particularly in relation to fission reactor experiments, is carried out collaboratively with our partners in Japan, Russia, and the European Union. The purpose of this series of reports is to provide a working technical record for the use of the program participants, and to provide a means of communicating the efforts of materials scientists to the rest of the fusion community, both nationally and worldwide.

This report has been compiled and edited under the guidance of A. F. Rowcliffe by Gabrielle Burn, Oak Ridge National Laboratory. Their efforts, and the efforts of the many persons who made technical contributions, are gratefully acknowledged.

F. W. Wiffen
International and Technology Division

CONTENTS

T87, plus 44 from General Atomics) are being evaluated. Other variables of interest are the effect of initial grain size on hydrogen uptake and tensile properties, and the synergistic effects of oxygen and hydrogen on the tensile behavior of the alloys. Experiments conducted thus far on specimens of various V-Cr-Ti alloys exposed to pH_2 levels of 0.01 and 3×10^{-6} torr showed negligible effect of H_2 on either maximum engineering stress or uniform/total elongation. Further, preliminary tests on specimens annealed at different temperatures showed that grain size variation by a factor of ≈2 had a negligible effect on tensile properties.

A systematic study was conducted to evaluate the oxidation kinetics of V-4Cr-4Ti ("44 alloy") and V-5Cr-5Ti alloys ("55 alloy") and to establish the role of oxygen ingress on the tensile behavior of the alloys at room temperature and at 500°C. The oxidation rate of the 44 alloy is slightly higher than that of the 55 alloy. The oxidation process followed parabolic kinetics. Maximum engineering stress for 55 alloy increased with an increase in oxidation time at 500°C. The maximum stress values for 55 alloy were higher at room temperature than at 500°C for the same oxidation treatment. Maximum engineering stresses for 44 alloy were substantially lower than those for 55 alloy in the same oxidation treatment. Uniform and total elongation values for 55 alloy were almost zero at room temperature after ≈500 h exposure in air at 500°C; the same values were 4.8 and 6.1%, respectively, at 500°C after ≈2060 h oxidation in air at 500°C. Uniform and total elongation values for 44 alloy were 1.6 and 3.6% at 500°C after 2060 h oxidation in air at 500°C.

Maximum engineering stress for 44 alloy at room temperature was 421.6-440.6 MPa after ≈250 h exposure at 500°C in environments with a pO_2 range of 1×10^{-6} to 760 torr. The corresponding uniform and total elongation values were 11-14.4% and 14.5-21.7%, respectively. Measurements of crack depths in various specimens showed that depth is independent of pO_2 in the preexposure environment and was of 70-95 μm after 250-275 h exposure at 500°C.

A systematic study has been initiated to examine the use of lasers to weld sheet materials of V-Cr-Ti alloys and to characterize the microstructural and mechanical properties of the laser-welded materials. In addition, several post-welding heat treatments are being applied to the welded samples to evaluate their benefits, if any, to the structure and properties of the weldments. Hardness measurements are made across the welded regions of different samples to evaluate differences in the characteristics of various weldments.

A series of tests is being conducted in the DIII-D tokamak to determine the effects of environmental exposure on a V-4Cr-4Ti vanadium alloy. These tests are part of the effort to build and install a water-cooled vanadium V alloy structure in the upgrade of the DIII-D radiative divertor. Data from the test series indicate that the performance

1.0 VANADIUM ALLOYS

Revised ANL-Reported Tensile Data for Unirradiated and Irradiated (FFTF, HFIR) V-Ti and V-Cr-Ti Alloys* -- M. C. Billone (Argonne National Laboratory)

SUMMARY

The tensile data for all unirradiated and irradiated vanadium alloys samples tested at Argonne National Laboratory (ANL) have been critically reviewed and, when necessary, revised. The review and revision are based on reanalyzing the original load-displacement strip chart recordings by a methodology consistent with current ASTM standards. For unirradiated alloys (162 samples), the revised values differ from the previous values as follows: -11±19 MPa (-4±6%) for yield strength (YS), -3±15 MPa (-1±3%) for ultimate tensile strength (UTS), -5±2% strain for uniform elongation (UE), and -4±2% strain for total elongation (TE). For irradiated alloys (91 samples), the differences between revised and previous values are: 30±37 MPa (6±7%) for YS, -1±6 MPa (0±1%) for UTS, -5±2% for UE, and -4±2% for TE. Of these changes, the decrease in UE values for alloys irradiated and tested at 400-435°C is the most significant. This decrease results from the proper subtraction of nongauge-length deformation from measured crosshead deformation. In previous analysis of the tensile curves, the nongauge-length deformation was not correctly determined and subtracted from the crosshead displacement. The previously reported and revised tensile values for unirradiated alloys (20-700°C) are tabulated in Appendix A. The revised tensile values for the FFTF-irradiated (400-600°C) and HFIR-irradiated (400°C) alloys are tabulated in Appendix B, along with the neutron damage and helium levels. Appendix C compares the revised values to the previously reported values for irradiated alloys. Appendix D contains previous and revised values for the tensile properties of unirradiated V-5Cr-5Ti (BL-63) alloy exposed to oxygen.

PROGRESS AND STATUS

Introduction

The V-Ti and V-Cr-Ti tensile data reported by Argonne National Laboratory (ANL) have been reviewed and revised as necessary in this effort. The tensile properties of interest are yield strength (YS), ultimate tensile strength (UTS), uniform elongation (UE), total elongation (TE) and reduction in area (RA) at the failure site. The data have been reported in tabular and/or graphical form in the Fusion Reactor Materials Semiannual Progress Reports from the periods ending March 31, 1987 (DOE/ER-0313/2) to June 30, 1996 (DOE/ER-0313/20), as well as at workshop meetings and in open literature publications. In this report, the original force-displacement strip chart recordings for these tests have been reanalyzed according to a standardized and consistent methodology (see Ref. 1 for ASTM definitions of YS, UTS, UE and TE, along with methods for determining these parameters from strip chart recordings).

Loomis et al. describe the tensile machine and sample parameters in Refs. 2 and 3. The tensile specimens (SS3) used in most ANL tensile tests have a gauge length of 7.62 mm and a cross-sectional area of ≈1 mm^2 (0.9-1.4 mm^2), as shown in Ref. 3. The Instron testing machine is equipped with a 500 kgf (4900 N) load cell. A uniform crosshead speed of 0.5 mm/min was used for all but the oxidation study tests, giving a gauge-length strain rate of 0.11%/s. Based on information recorded on the load-displacement curves, in laboratory notebooks [4, 5] and on data sheets [6], the load cell was varied from a full vertical scale value of 2 to 250 kgf. Useful data for most tests were recorded with a full scale of 50 kgf for unirradiated alloys and 100 kgf for irradiated

* Work supported by U.S. Department of Energy, Office of Fusion Energy Sciences, under Contract W-31-109-Eng-38.

alloys. The strip chart recording speed was generally 50 mm/min, although 100 mm/min was used in several cases. At 50 mm/min, each horizontal grid mark corresponds to 0.02 mm crosshead displacement and 0.262% gauge-length strain.

Reference 2 contains load-strain curves, along with tables of tensile properties, for several of the older V-Ti and V-Cr-Ti alloys tested at room temperature. It is readily apparent from a comparison of the tabular values to those determined directly from the curves that the initial "elastic" portion of the curve is included in the calculation of UE and TE, whereas standard procedures require that the effective "elastic" strain be subtracted from the total strain at any point along the curve to determine the permanent plastic strain. It is also apparent that the slope of the initial linear portion of the load-strain curve is at least one order of magnitude lower than what would be derived from the Young's modulus for vanadium alloys. Based on an analysis of all of the original strip chart recordings, the initial linear portion of the force-displacement curves corresponds to an effective stiffness of about 1.2 kN/mm for unirradiated alloys and 1.8 kN/mm for irradiated alloys. If these are converted to "effective" Young's moduli (E') based on a gauge length of 7.62 mm and the particular gauge cross-sectional area for each sample, then E' ≈ 8.2 GPa for unirradiated alloys and E' ≈ 12 GPa for irradiated alloys (vs. 126 GPa for vanadium alloys [7]). Clearly, the nongauge displacement must be subtracted from the crosshead displacement in order to determine the permanent or plastic deformation and strain of the sample at a particular stress (load/initial-cross-sectional-area).

The purpose of the current work is to revise the tensile data to be consistent with a proper interpretation of the original load-displacement data curves. The reduction in area values reported in Refs. 8 and 10 are determined directly from the failed samples, so no corrections to the RA data base are necessary. Specific references for the data to be reanalyzed and reinterpreted include Ref. 9 for tabular listing of the tensile properties of most of the unirradiated alloys, Ref. 10 for graphical representation of the tensile properties of the newer heats of unirradiated V-(4-5)Cr-(4-5)Ti (i.e., BL-71 and BL-72), Refs. 12-14 for graphical representation of the tensile properties of FFTF-irradiated alloys, Ref. 15 for the graphical representation of the tensile properties of HFIR-irradiated alloys at 400°C, and Ref. 18 for the tensile data on the effects of oxygen on unirradiated V-5Cr-5Ti (BL-63).

Methodology

Determination of YS, UTS, UE and TE

The terminology and methodology for analyzing tensile data from strip chart recordings are established in ASTM Designations E 6 and E 8, respectively [1]. It is worthwhile to review these terms and methods. For monotonically increasing load vs. displacement curves up to the maximum load, YS is the load (divided by the initial gauge cross-sectional area) corresponding to an offset strain of 0.2%. The offset value of 0.2% has no intrinsic significance, but is based on practicality and experience in analyzing tensile curves. The option to use an offset strain of 0.5% is also allowed by E 8. Offset strain is determined by "analytically" or "graphically" unloading the specimen at a linear load-displacement slope corresponding to the effective linear portion of the load-displacement curve. The intersection of this line with the horizontal axis determines the offset displacement and strain. Some of the analyzed load-displacement curves exhibit discontinuous yielding, which consists of a rise to a high load (upper yield point, UYP) followed by a drop in load to a minimum value (lower yield point, LYP) followed by a rise in load with displacement up to the maximum load. For these cases, the 0.2% offset stress may not be a good

measure for YS. For consistency, the stress corresponding to the minimum yield point is designated as YS in the current work for samples that exhibit discontinuous yielding. In the event that 0.2% offset is reached on the rise in load and corresponds to a lower value than determined by LYP, then the stress corresponding to 0.2% offset is used to define YS. Thus, YS is defined as the minimum of the stress corresponding to 0.2% offset and the stress corresponding to LYP. For several of the older alloys irradiated at 400-435°C, the load curve bends to an offset strain of >0.2%, then straightens and bends again at about double the load. These cases generally corresponded to plastic deformation of the support pins used prior to 1992. For these cases, YS, as well as UE, of the gauge section was deemed to be indeterminate. Tabulated values of TE for these tests are based on direct post-test measurement of the change in sample length. After 1991, stiffer pins with near-zero bending span were used to eliminate this problem.

Determination of UTS is relatively straightforward. For monotonically increasing load with displacement up to the maximum load, the UTS is simply the maximum load divided by the initial gauge cross-sectional area. In the case of discontinuous yielding, the UYP may represent a higher load than for the continuous part of the curve after the discontinuous yielding. In such cases, the UYP is not to be used in determining UTS. The offset displacement (or strain) corresponding to the peak load (or UTS) is called the uniform elongation (UE). While UTS can be uniquely determined, more uncertainty is involved in determining UE, particularly for cases for which the maximum load is nearly constant over a displacement (or strain) range. Although the ASTM standards imply that the midpoint of this flat region should be used to determine UE, the maximum offset strain corresponding to the maximum load is used in the current work. This decision is based on detailed analyses of stainless steel stress-strain curves and the criteria for necking. The maximum strain at peak load is more characteristic of the uniform elongation of the gauge section prior to necking. Total elongation (TE) corresponds to the offset strain just prior to failure. The same slope used to determine YS and UE is used to determine TE.

Some of the load-displacement curves exhibit serrations, particularly in the region of the peak load to the failure load. The treatment of these serrations is described in the following. If the serrations are characterized by an instantaneous drop in load followed by a more gradual rise in load, then the maximum of the serrated portion is used. If the serrations are characterized by a more sinusoidal variation with displacement, then the average of the serrated portion is used. If the serrations are characterized by an instantaneous rise in load followed by a more gradual decrease in load, then the minimum of the serrated portion is used. Thus, the choice of maximum, average or minimum is based on the generation of a continuous and smooth curve through serrated and non-serrated regions of the load-displacement trace.

Determination of Effective Modulus

While various methods (e.g., initial tangent modulus, tangent modulus, secant modulus and chord modulus) are given in the ASTM standards to determine the effective modulus, the methodology used in the current work corresponds most closely to the tangent modulus approach. With most of the load-displacement curves for vanadium alloys tested in the ANL Instron machines exhibiting an elongated "S" shape during the initial rise in load, the modulus is determined by the tangent line coinciding with the greatest number of points in the elongated part of the S-shape.

The strip chart recordings from the tensile tests give measured load vs. calculated crosshead displacement. The crosshead displacement is a combination of the axial deformation of the

gauge section, the nongauge section, the local deformation of the sample near the pin supports, the pins themselves, the grips supporting the pins and the load train compliance. It has already been established in the Introduction of this report that the initial rise in load for the SS3 samples is not governed by the gauge section. Figure 1 shows the linearized load vs. displacement slope (k) for all of the samples analyzed in the current work. For unirradiated material, k = 1.20±0.20 kN/mm, where the ± values indicate one standard deviation. For irradiated material, k = 1.76±0.34 kN/mm. There is also a decrease in k with temperature for both cases (see best-fit lines in Fig. 1). Because most of the load train is outside the heated region of the sample and does not change with the unirradiated/irradiated condition of the sample, it appears that the nongauge section of the sample, the support pins and the grips play a major role in determining the effective stiffness used to analyze the force-displacement curves.

The effective modulus (E') is determined from the effective stiffness (k) according to

$$E' = k\,(L_o/A_o), \qquad (1)$$

where L_o is the initial gauge length and A_o is the initial gauge cross-sectional area. The results for E' are shown in Fig. 2, where the units have been converted to MPa/% rather than to the traditional units of GPa. For unirradiated material, E' = 82±15 MPa/%; for irradiated material, E' = 120±28 MPa/%. The solid lines show the best linear fit of E' with test temperature for the two cases.

Tensile Properties of Unirradiated V-Ti and V-Cr-Ti Alloys

Comparison of YS, UTS, UE and TE

Appendix A contains tables listing both the revised and previously reported values for the tensile properties for unirradiated V-Ti and V-Cr-Ti alloys (Tables A.1-A.12). The revised values have been determined from the original load-displacement strip chart recordings according to the methodology described. Also tabulated are the effective stiffness (k) values used to analyze the data.

The difference between revised and previously reported values for UTS is insignificant for the majority of the cases analyzed. On the average, the new values are 3 MPa lower than the old values with a standard deviation of ±15 MPa. These values correspond to -1±3%. Differences as high as ±20 MPa can be attributed to the methodology used for the cases in which serrations occur at the maximum load. Larger differences in interpretation can occur if the zero-load line does not correspond to the bottom horizontal axis of the chart (see 100°C value for BL-71 in Table A.7). For the majority of the cases analyzed, the difference between new and previously reported values of UTS is less than a few MPa. Overall, the deviation in UTS due to methodology changes is much less than the ±10% expected from heat-to-heat variation for the same nominal composition alloy.

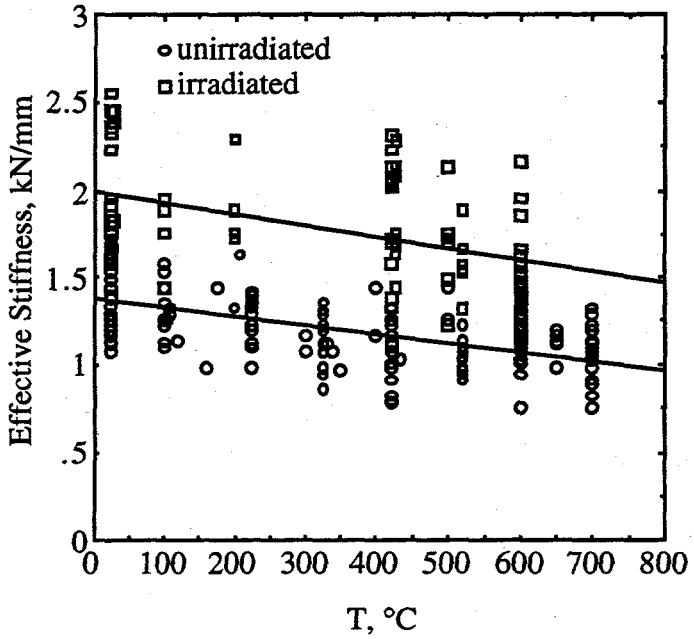

Fig. 1. Effective stiffness vs. temperature determined from the linearized increase of load with crosshead displacement for SS3 vanadium alloy tensile samples. Lower and upper lines are best fits, respectively, to stiffness values for unirradiated and irradiated samples.

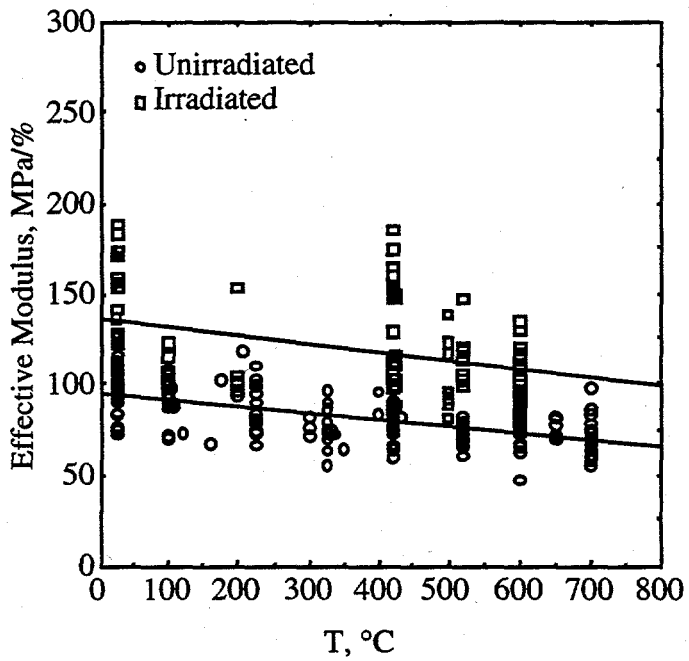

Fig. 2. Effective modulus vs. temperature for SS3 vanadium alloy tensile samples. Lower and upper lines are best fits, respectively, to moduli for unirradiated and irradiated samples.

The new values for YS are generally lower than the previous values because of the change in methodology from the 0.5% offset (previously used) to the 0.2% offset (currently used). For cases in which the material exhibits elastic/perfectly-plastic behavior to plastic strains > 0.5%, the two definitions for YS result in the same value. Larger differences are encountered for samples which reach 0.2% offset before the upper yield point (UYP) and where the ensuing lower yield point (LYP) results in a higher value for YS than does the 0.2% offset stress. These comments apply to all unirradiated cases except for the newer heats presented in Table A.7. For these cases, the previously reported values are either the proportional elastic limit or the 0.2% offset stress. Even with the methodology differences, the new values differ from the old values by only -11±19 MPa (-4±6%), well within the heat-to-heat variation in YS for structural materials.

By properly determining the offset (i.e., plastic) strains from the force-displacement tensile curves, UE decreases by 5±2% from previously reported values. Figure 3 shows the previously reported and revised values. While this correction is significant with regard to showing trends in alloy behavior (e.g., change in uniform ductility with increased ultimate tensile strength), the unirradiated vanadium alloys remain ductile for the full temperature range tested (20-700°C). For higher-strength alloys, the decrease in UE may be as high as 10%.

With regard to the total elongation (TE), this property decreases by 4±2% with proper determination of the plastic strain. The corrected values remain relatively high for most of the alloys tested.

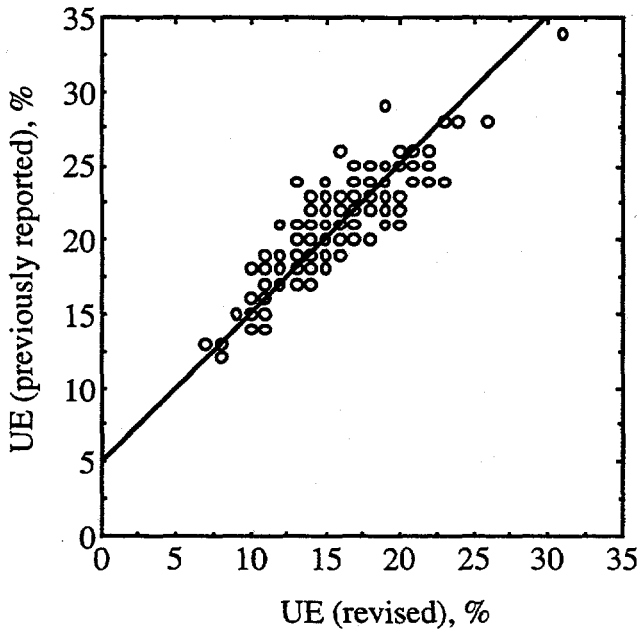

Fig. 3. Previously reported and revised values for uniform elongation (UE) of unirradiated V-Ti and V-Cr-Ti alloys tested at ANL. Total number of data points is 162, many of which overlap.

Stress-Strain Curves

While tables of tensile properties are important, it is instructive to examine a few stress-strain curves in more detail. The engineering stress-strain curves for unirradiated V-3.8Cr-3.9Ti (BL-71) are shown in Figs. 4-6 for test temperatures of 400, 500 and 600°C, which are close to the irradiation/test temperatures for irradiated alloys. In constructing these curves from the original load-displacement curves, an effective linear rise to the curve is used instead of the more S-shaped curve on the strip chart recording. Also, the zero strain point is redefined by the intersection of the effective linear portion with the displacement axis. Finally, the serrations are smoothed by the methods described in a previous section. The change in work-hardening rate in the neighborhood of the yield point has been preserved in the stress-strain plots.

The strip chart recording for Fig. 4 exhibits a 0.2% offset YS prior to the leveling off and dip in the curve. Because this value is lower than that corresponding to the lower yield point (LYP), it is used to determine YS. Serrations are initiated at the 0.2% offset stress and continue until failure. The peak-to-peak amplitude of the serrations is ≤1.5 kgf (15 N) corresponding to 14 MPa. The peaks of the serrations are used in constructing Fig. 4. For Fig. 5, the serrations occur closer to the maximum load and have a peak-to-peak value of ≤2.5 kgf (25 N), corresponding to 21 MPa. Again, the peak values are used in constructing Fig. 5. For Fig. 6, the serrations occur after the peak load has been reached. They have a peak-to-peak amplitude ≤ 4 kgf (39 N), which corresponds to 34 MPa. As before, the peaks are used to construct Fig. 6. Because of the location of these serrations, they have no influence on the determination of YS, UTS and UE; however, they have a small influence on the determination of TE.

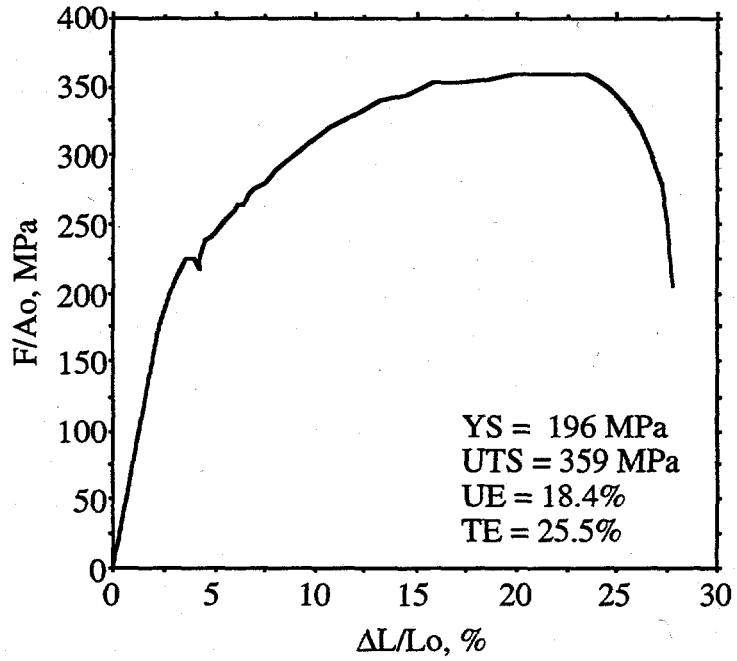

Fig. 4. Engineering stress (F/Ao)-strain (ΔL/Lo) curve for unirradiated V-3.8Cr-3.9Ti (BL-71) tested at 400°C. Gauge strain rate is 0.11%/s. Gauge length (Lo) and cross-sectional area (Ao) are 7.62 mm and 1.078 mm^2, respectively.

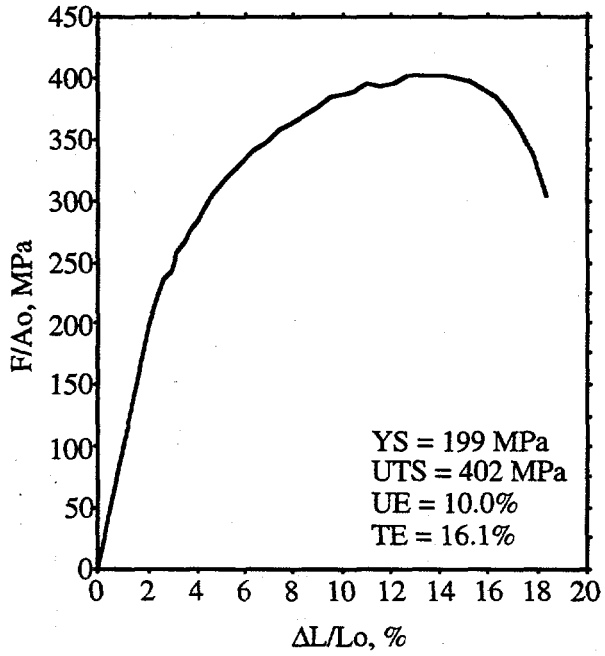

Fig. 5. Engineering stress (F/Ao)-strain (ΔL/Lo) curve for unirradiated V-3.8Cr-3.9Ti (BL-71) tested at 500°C. Gauge strain rate is 0.11%/s. Gauge length (Lo) and cross-sectional area (Ao) are 7.62 mm and 1.147 mm^2, respectively.

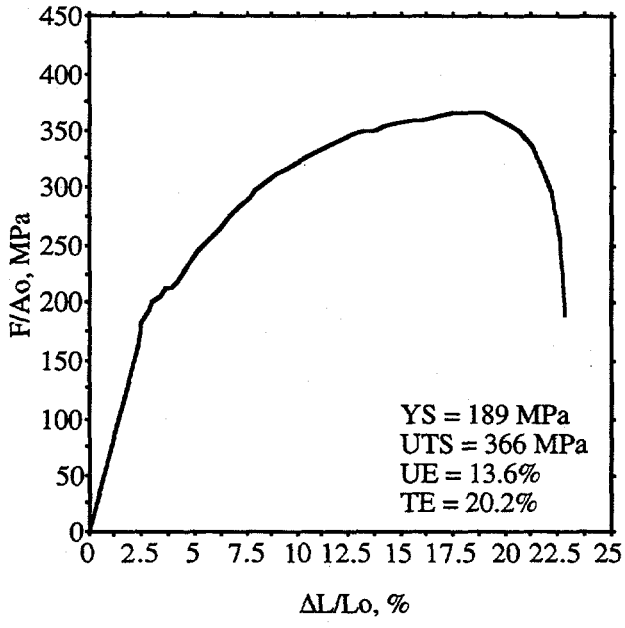

Fig. 6. Engineering stress (F/Ao)-strain (ΔL/Lo) curve for unirradiated V-3.8Cr-3.9Ti (BL-71) tested at 600°C. Gauge strain rate is 0.11%/s. Gauge length (Lo) and cross-sectional area (Ao) are 7.62 mm and 1.1396 mm^2, respectively.

Tensile behavior of V-(4-5)Cr-(4-5)Ti

Because of the interest in the V-(4-5)Cr-(4-5)Ti alloys, it is worthwhile to establish baseline tensile properties for these alloys as a function of temperature. The particular compositions and heats of interest are V-3.8Cr-3.9Ti-0.078Si (BL-71, #832665), V-4.1Cr-4.3Ti-0.087Si (BL-47, #9144), V-4.6Cr-5.1Ti-0.031Si (BL-63, #832394) and V-4.9Cr-5.1Ti-0.055Si (BL-72 or T87). Figures 7-10 show the variations of YS, UTS, UE and TE, respectively, with temperature. The solid lines represent best-fit cubic equations to these parameters.

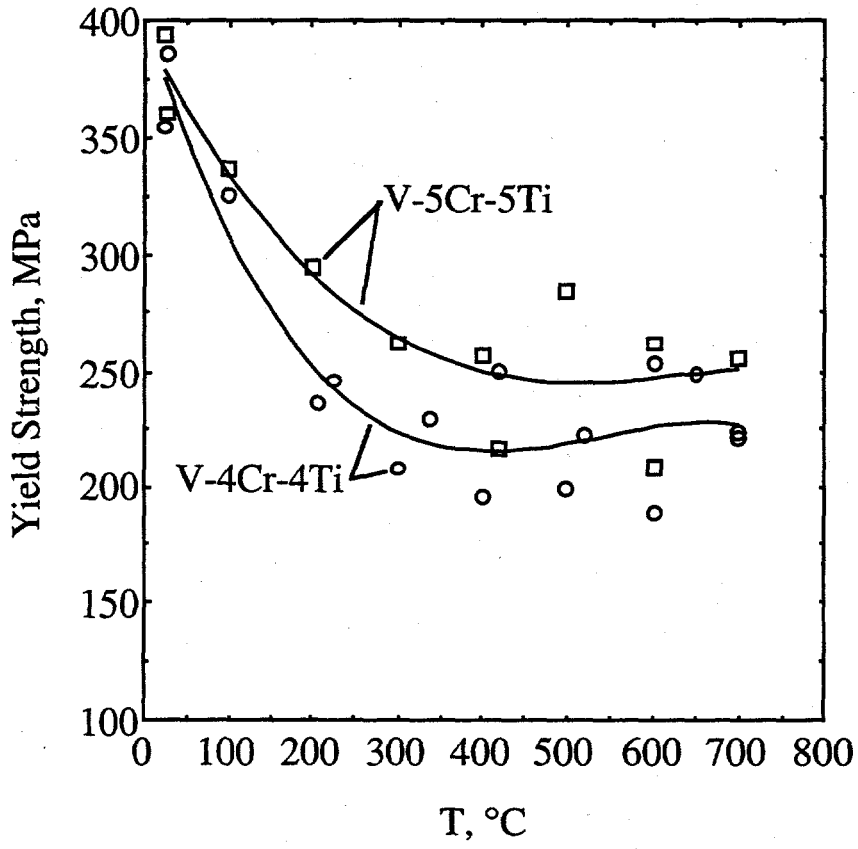

Fig. 7. Yield strength vs. temperature for unirradiated V-4Cr-4Ti (BL-47 and BL-71) and V-5Cr-5Ti (BL-63 and BL-72).

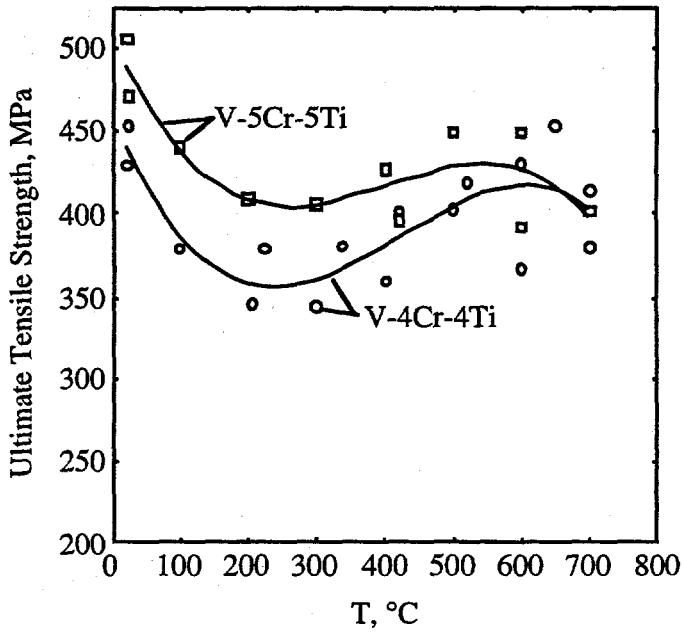

Fig. 8. Ultimate tensile strength vs. temperature for unirradiated V-4Cr-4Ti (BL-47 and BL-71) and V-5Cr-5Ti (BL-63 and BL-72).

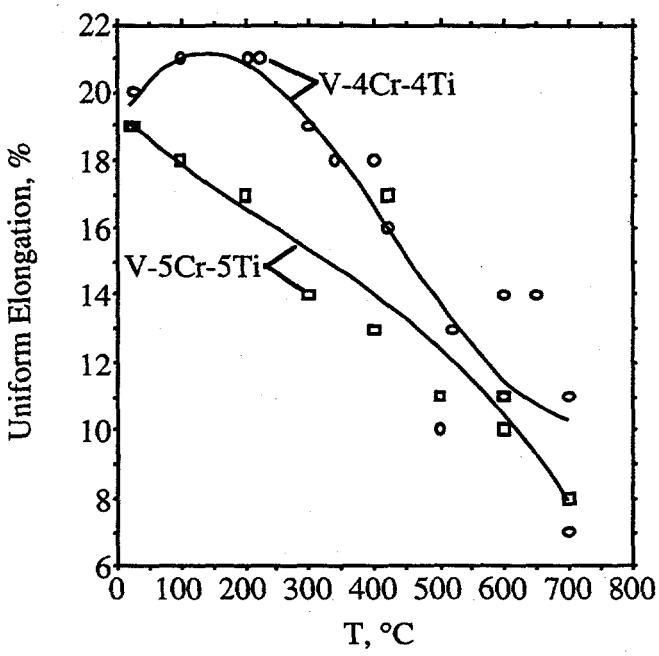

Fig. 9. Uniform elongation vs. temperature for unirradiated V-4Cr-4Ti (BL-47 and BL-71) and V-5Cr-5Ti (BL-63 and BL-72).

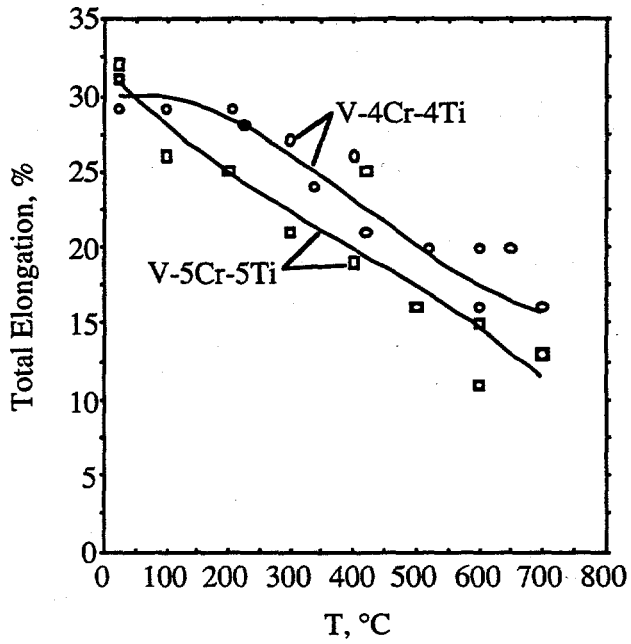

Fig. 10. Total elongation vs. temperature for unirradiated V-4Cr-4Ti (BL-47 and BL-71) and V-5Cr-5Ti (BL-63 and BL-72).

Tensile Properties of Irradiated V-Ti and V-Cr-Ti Alloys

Comparison of YS, UTS, UE and TE

Appendix B contains the irradiation conditions (Tables B.1-B.6) for vanadium alloys irradiated in FFTF MOTA positions. Sample ID numbers are taken from data sheets and lab notebooks [5]. Operating conditions are taken from Ref. 11 for temperature and neutron damage (in dpa) in stainless steel. A factor of 1.31 has been used to convert the Ref. 11 stainless-steel damage values to those for the vanadium alloys [16]. Previously reported values differ somewhat from the revised values in Appendix B because some of the previous values were based on pre-test predictions and expectations rather than on the post-test values listed in Ref. 11. The He values are taken from Refs. 13 and 14 and are based on post-test measurements for a few BL-47 samples.

Tables B.7-B.11 list the revised tensile properties for vanadium alloys irradiated in FFTF. The original load-displacement strip chart recordings have been used to determine these values. Because of the subjective nature of interpreting the strip chart plots, each plot was analyzed twice (on different days) to test the consistency of the methodology and to double-check for clerical and interpretive errors. Table B.12 summarizes the revised values for the tensile properties of vanadium alloys tested at 400°C after irradiation in HFIR at 400°C. No attempt has been made to double-check the reported operating conditions and damage levels for this irradiation.

The revised tensile properties have been compared to the previously published values for FFTF-irradiated alloys [12-14] and HFIR-irradiated alloys [15]. The major changes are in the uniform and total elongation values. Appendix C shows the comparison in tabular form for some of these alloys. The difference between the revised and previously-reported values of UTS for irradiated alloys is -1±6 MPa, which is insignificant. The revised values for YS are higher than previous values by 30±37 MPa (6±7%). While this difference is within the scatter for YS determined from different heats of the same nominal material, it arises primarily because several different methodologies (e.g., proportional elastic limit, 0.2% offset load, 0.5% offset load, etc.) were used to determine the previous values. The decrease in UE is 5±2% (see Fig. 11) and the decrease in TE is 4±2%. The consequences of these elongation decreases are described in the Discussion Section.

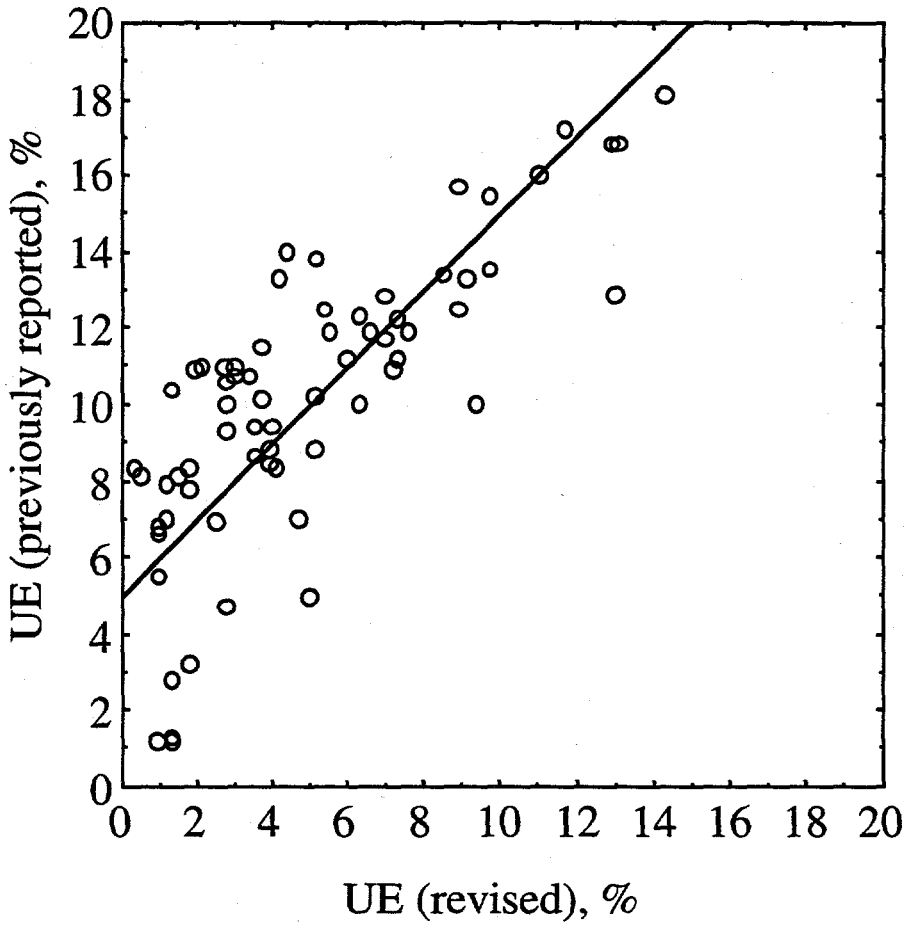

Fig. 11. Previously reported and revised values for uniform elongation (UE) of FFTF- and HFIR-irradiated V-Ti and V-Cr-Ti alloys tested at ANL. Total number of data points is 69, many of which overlap.

Stress-Strain Curves

Figure 12 shows the load-displacement curve for a V-4.1Cr-4.3Ti alloy (BL-47) sample irradiated at 430°C in FFTF to 27 dpa with 23 appm He and tensile-tested at 425°C. The curve shows the initial change in slope, along with the slight discontinuities with load-cell recording scale change, and the serrations in the region of the UTS. Figure 13 shows the simplifications made in deriving the engineering stress-strain curve from the load-displacement data in Fig. 12. The effective elastic modulus has been used to draw the initial linear portion of the curve, and the serrations have been smoothed by taking the minimum values to generate a smooth, continuous curve. The results of graphical analysis for YS, UTS, UE and TE are also shown in Fig. 13. The same simplifications have been used in constructing the engineering stress-strain curves for alloy BL-47 shown in Figs. 14-21.

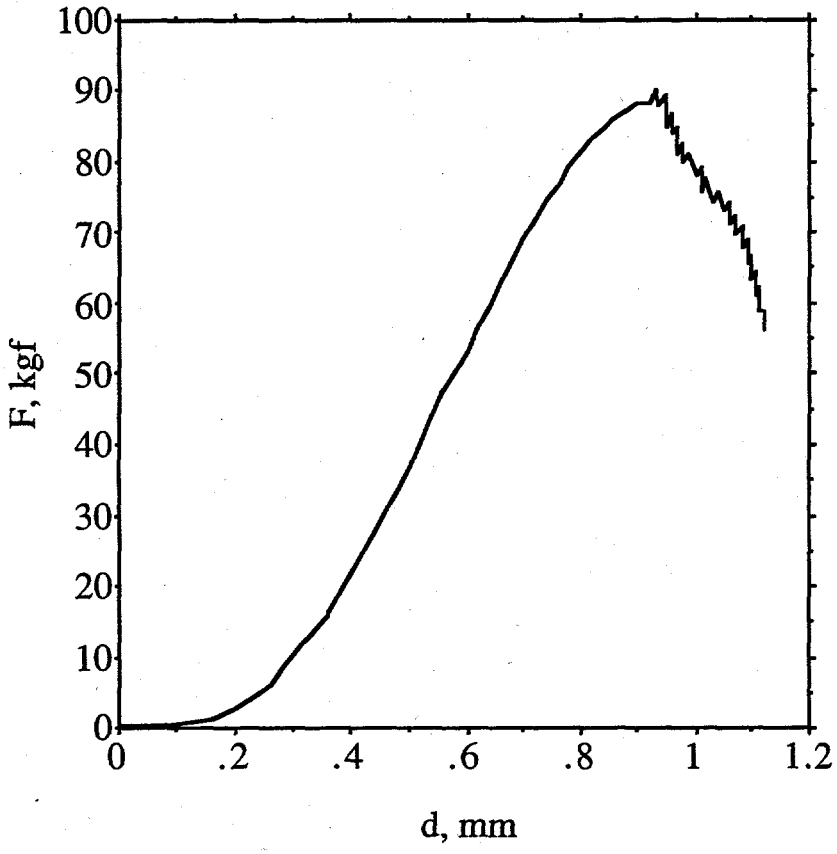

Fig. 12. Load (F)/displacement (d) curve for V-4.1Cr-4.3Ti alloy BL-47 (FFTF Cycle 12, MOTA 2B position 4D2) at 425°C after irradiation at 430°C to 27 dpa with 23 appm He. Tensile specimen gauge length (Lo) and cross-sectional area (Ao) are 7.62 mm and 1.26 mm^2, respectively. Scale changes occurred at d = 0.36 mm (20 to 50 kgf) and at d = 0.56 mm (50 to 100 kgf). Spring constant for the nongauge part of the specimen, grips and tensile machine is ≈1.5 kN/mm, where 1 kgf = 9.806 N. Crosshead speed is 0.5 mm/min and strip chart recording speed is 50 mm/min.

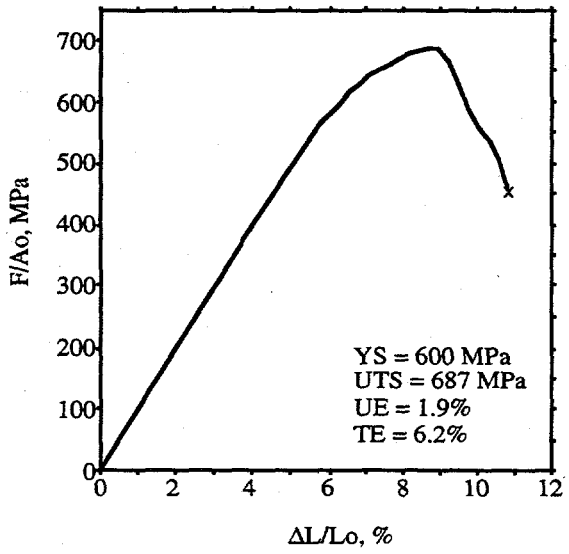

Fig. 13. Engineering stress-strain curve for V-4.1Cr-4.3Ti alloy BL-47 (FFTF Cycle 12, MOTA 2B position 4D2) at 425°C after irradiation at 430°C to 27 dpa with 23 appm He. Lo = 7.62 mm, Ao = 1.26 mm^2 and gauge strain rate = 0.11%/s.

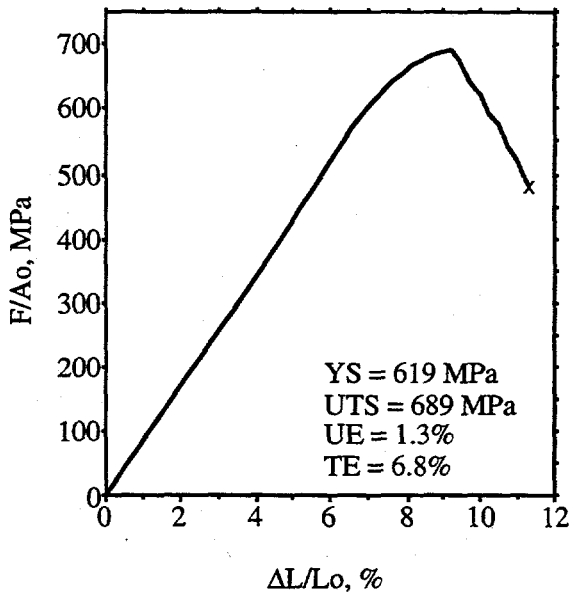

Fig. 14. Engineering stress-strain curve for V-4.1Cr-4.3Ti alloy BL-47 (FFTF Cycle 12, MOTA 2B position 4D1) at 425°C after irradiation at 430°C to 25 dpa with 12 appm He. Lo = 7.62 mm, Ao = 1.42 mm^2 and gauge strain rate = 0.11%/s.

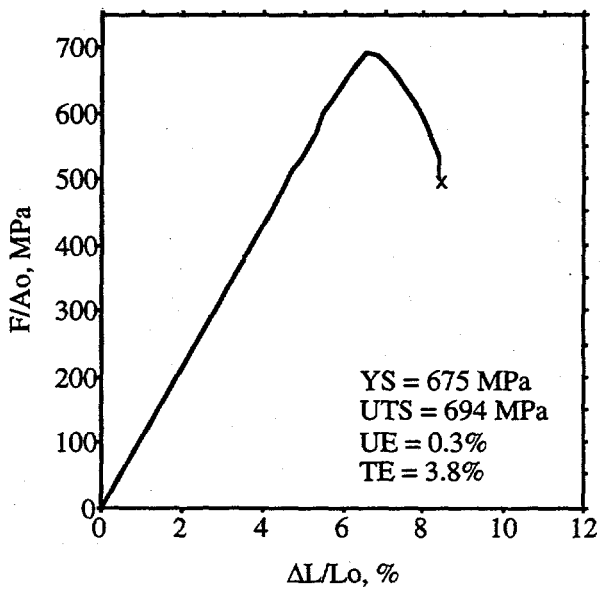

Fig. 15. Engineering stress-strain curve for V-4.1Cr-4.3Ti alloy BL-47 (FFTF Cycle 12, MOTA 2B position 3D6, sample ID #47-484-2) at 420°C after irradiation at 427°C to 33 dpa and ≈0 appm He. Lo = 7.62 mm, Ao = 1.16 mm^2 and gauge strain rate = 0.11%/s.

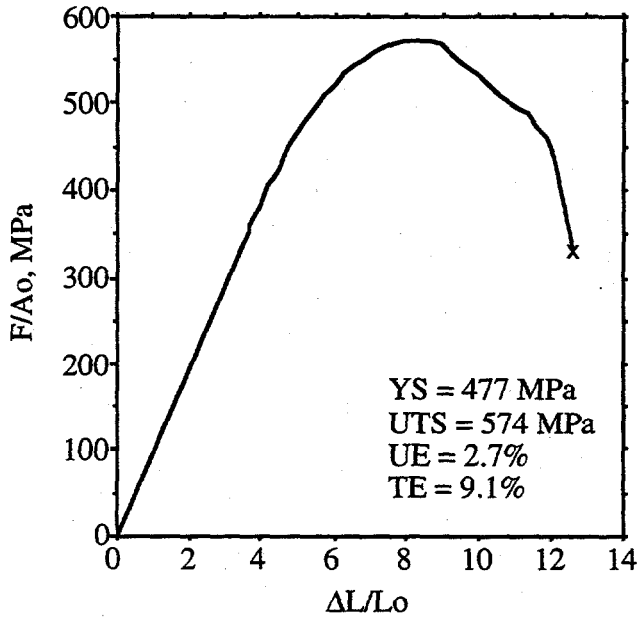

Fig. 16. Engineering stress-strain curve for V-4.1Cr-4.3Ti alloy BL-47 (FFTF Cycle 12, MOTA 2B position 5D2) at 500°C after irradiation at 500°C to 18 dpa with 7 appm He. Lo = 7.62 mm, Ao = 1.38 mm^2 and gauge strain rate = 0.11%/s.

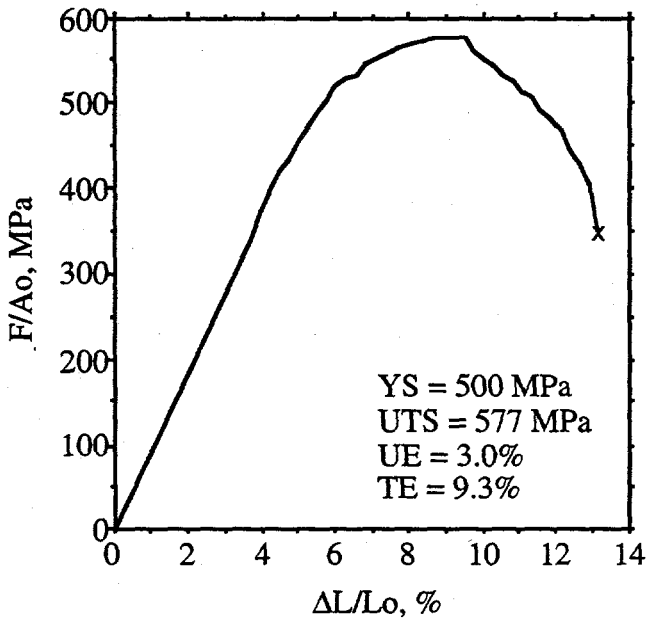

Fig. 17. Engineering stress-strain curve for V-4.1Cr-4.3Ti alloy BL-47 (FFTF Cycle 12, MOTA 2B position 5D1) at 500°C after irradiation at 500°C to 14 dpa with 12 appm He. Lo = 7.62 mm, Ao = 1.40 mm^2 and gauge strain rate = 0.11%/s.

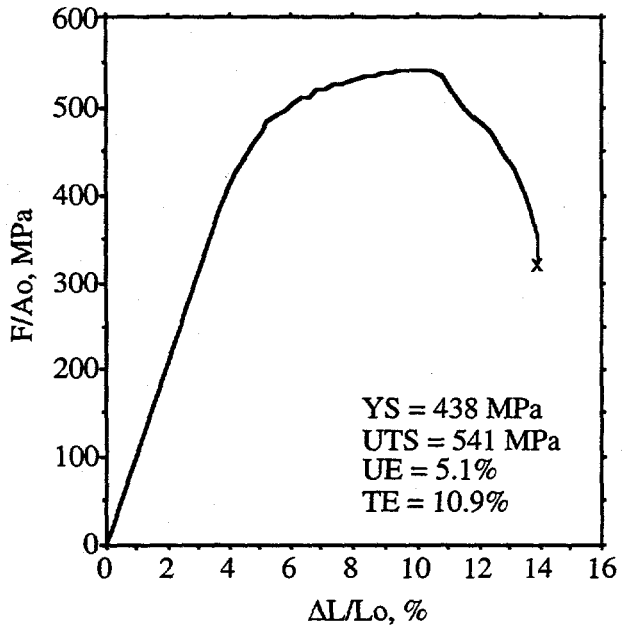

Fig. 18. Engineering stress-strain curve for V-4.1Cr-4.3Ti alloy BL-47 (FFTF Cycle 12, MOTA 2B position 1D3, sample ID #47-562-1) at 520°C after irradiation at 519°C to 14 dpa and ≈0 appm He. Lo = 7.62 mm, Ao = 1.16 mm^2 and strain rate is 0.11%/s.

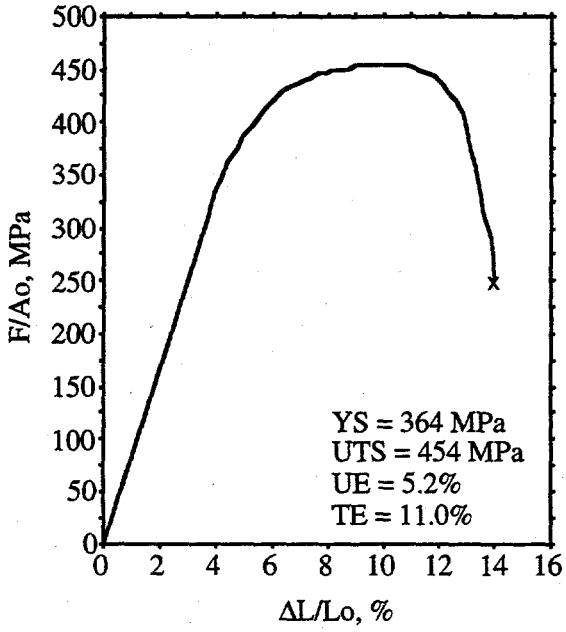

Fig. 19. Engineering stress-strain curve for V-4.1Cr-4.3Ti alloy BL-47 (FFTF Cycle 12, MOTA 2B position 5C1) at 600°C after irradiation at 599°C to 14 dpa with 10 appm He. Lo = 7.62 mm, Ao = 1.05 mm^2 and gauge strain rate = 0.11%/s.

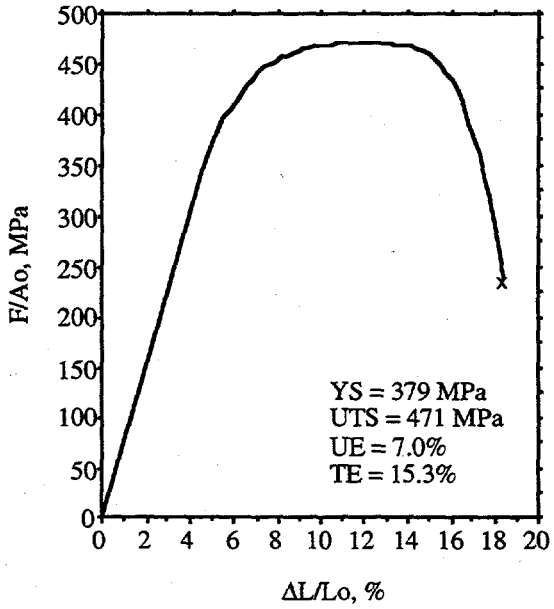

Fig. 20. Engineering stress-strain curve for V-4.1Cr-4.3Ti alloy BL-47 (FFTF Cycle 12, MOTA 2B position 5C2) at 600°C after irradiation at 599°C to 18 dpa with 75 appm He. Lo = 7.62 mm, Ao = 1.40 mm^2 and gauge strain rate = 0.11%/s.

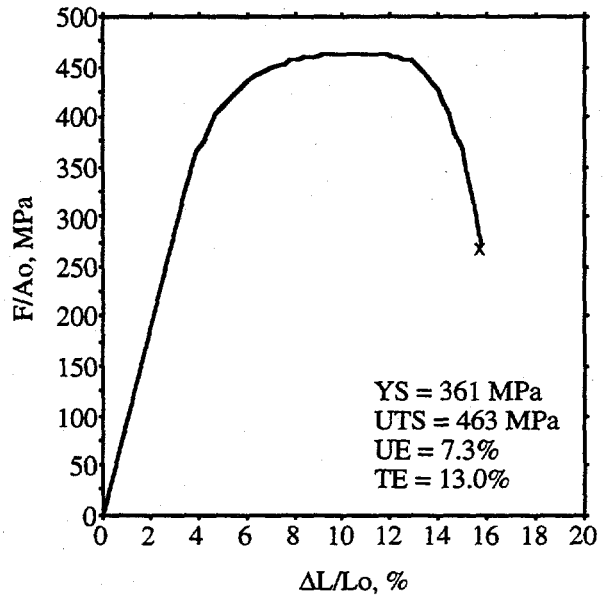

Fig. 21. Engineering stress-strain curve for V-4.1Cr-4.3Ti alloy BL-47 (FFTF Cycle 12, MOTA 2B position 1E2, sample ID # 47-672-1) at 600°C after irradiation at 599°C to 17 dpa and ≈0 appm He. Lo = 7.62 mm, Ao = 1.17 mm^2 and gauge strain rate = 0.11%/s.

The serrations for the curves in Figs. 14-18 (420-430°C and 500-520°C irradiation/test temperatures) all begin at or near the peak load and continue until failure. The peak values are used for Figs. 14-18. For samples irradiated/tested at 600°C, the serrations begin well after the peak load has been achieved. The serrations disappear when sibling samples are tested at lower temperatures (25-200°C).

The engineering stress-strain curves are compared in Fig. 22 for V-4.1Cr-4.3Ti alloy BL-47 irradiated and tested at 400-430°C. In comparing these curves to the curve for unirradiated V-4Cr-4Ti (BL-71), it is clear that there is significant increase in strength and decrease in ductility. This is particularly true for the non-DHCE sample irradiation to 33 dpa where the uniform elongation drops to ≈0.3% – too low a value to be determined accurately. For the DHCE samples with He, the uniform elongation remains at 2-3% at about 26 dpa. It is not clear whether the He actually modifies the microstructure of V-4Cr-4Ti to produce a more ductile alloy under irradiation or that the higher dpa value of the non-DHCE sample causes more hardening. It is likely that the presence of the He in these samples actually improves the irradiation performance of V-4Cr-4Ti, although more data would be needed, along with microstructural studies, to support this view.

Figure 23 shows the stress-strain curves for V-4Cr-4Ti irradiated/tested at 500-520°C. The two DHCE samples and the one non-DHCE sample all have adequate ductility. Again, without more data, it is not clear whether the irradiation damage partially anneals out at ≈ 500°C or the lower neutron damage level (about 15 dpa) results in less damage. Figure 24 compares the results at an irradiation/test temperature of ≈600°C. At this temperature, the irradiated alloy still has adequate ductility.

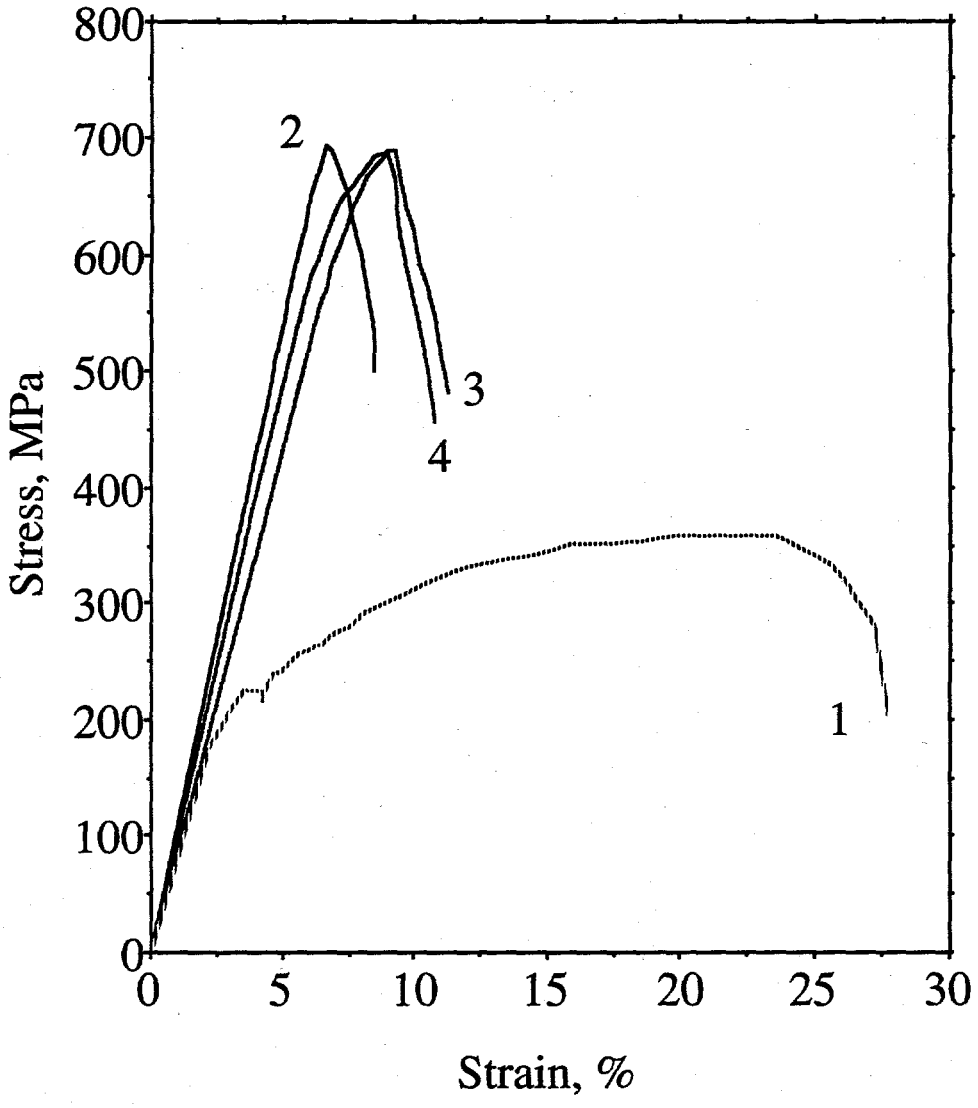

Fig. 22. Unirradiated (Fig. 4), non-DHCE (Fig. 15) and DHCE (Figs. 13 and 14) engineering stress-strain curves for V-4Cr-4Ti irradiated in FFTF (cycle 12) MOTA 2B. Gauge strain rate = 0.11%/s, gauge length = 7.62 mm and cross-sectional area is 1.08 to 1.42 mm^2. ANL heat, irradiation/test temperatures, neutron damage level and He concentration in appm for each curve are: 1) BL-71, ---/400°C, 0 dpa, 0 appm; 2) BL-47, 427/420°C, 33 dpa, ≈0 appm; 3) BL-47, 430/425°C, 25 dpa, 12 appm; and 4) BL-47, 430/425°C, 27 dpa, 23 appm.

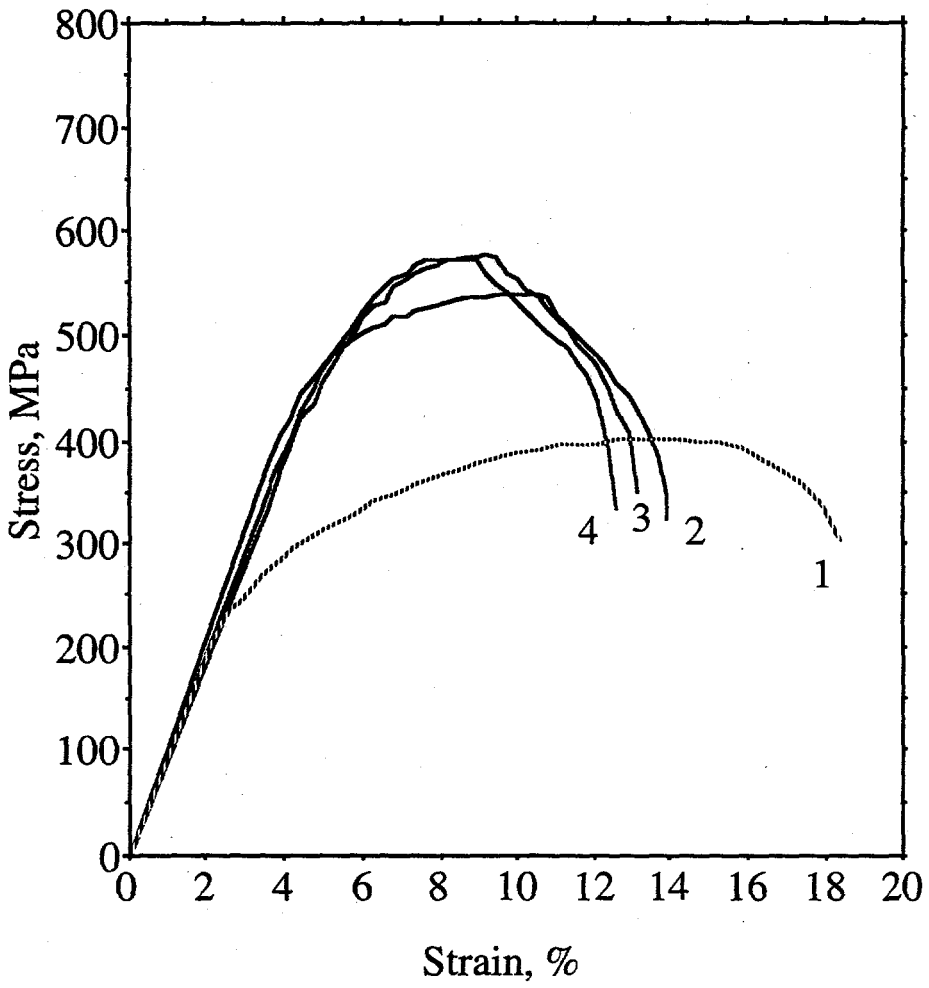

Fig. 23. Unirradiated (Fig. 5), non-DHCE (Fig. 18) and DHCE (Figs. 16 and 17) engineering stress-strain curves for V-4Cr-4Ti irradiated in FFTF (cycle 12) MOTA 2B. Gauge strain rate = 0.11%/s, gauge length = 7.62 mm and cross-sectional area is 1.15 to 1.40 mm^2. ANL heat, irradiation/test temperatures, neutron damage level and He concentration in appm for each curve are: 1) BL-71, ---/500°C, 0 dpa, 0 appm; 2) BL-47, 519/520°C, 14 dpa, ≈0 appm; 3) BL-47, 500/500°C, 14 dpa, 12 appm; and 4) BL-47, 500/500°C, 18 dpa, 7 appm.

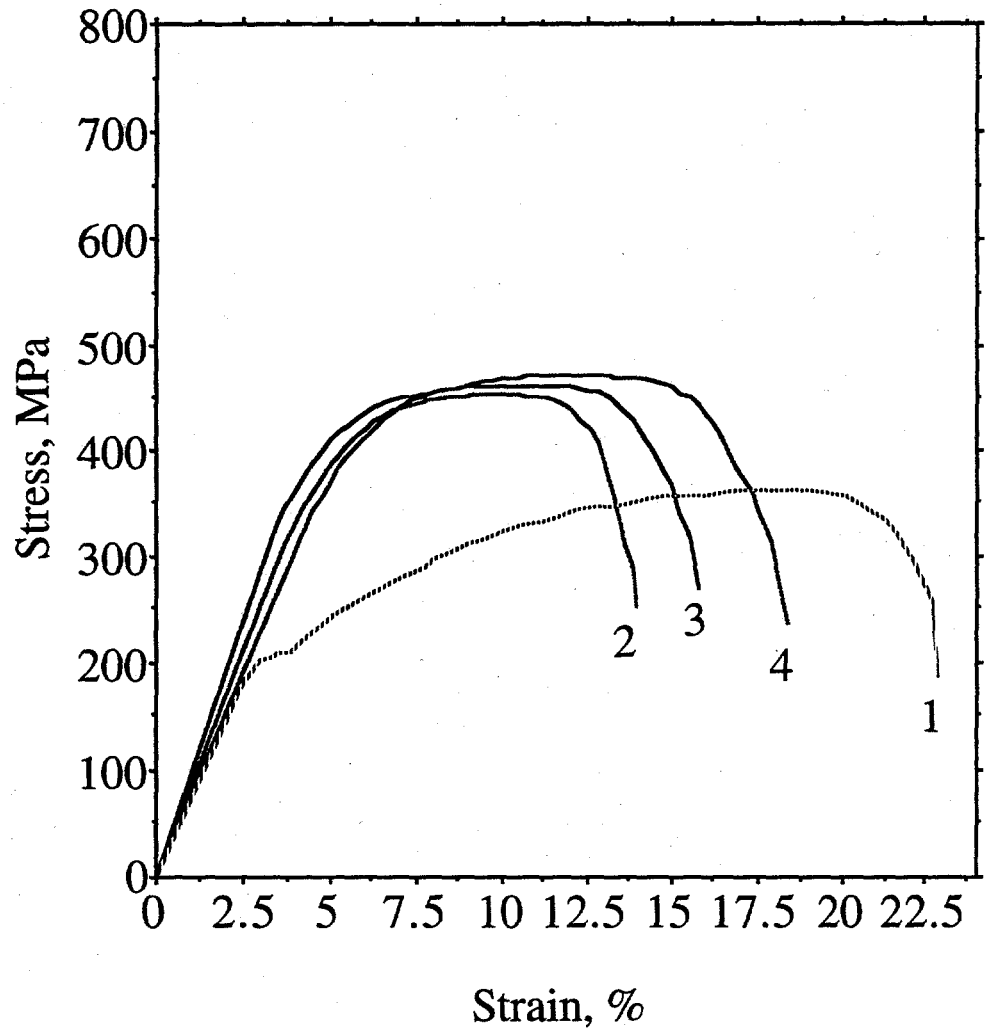

Fig. 24. Unirradiated (Fig. 6), non-DHCE (Fig. 21) and DHCE (Figs. 19 and 20) engineering stress-strain curves for V-4Cr-4Ti irradiated in FFTF (cycle 12) MOTA 2B. Gauge strain rate = 0.11%/s, gauge length = 7.62 mm and cross-sectional area is 1.14 to 1.40 mm^2. ANL heat, irradiation/test temperatures, neutron damage level and He concentration in appm for each curve are: 1) BL-71, ---/600°C, 0 dpa, 0 appm; 2) BL-47, 599/600°C, 14 dpa, 10 appm; 3) BL-47, 599/600°C, 17 dpa, ≈0 appm; and 4) BL-47, 599/600°C, 18 dpa, 75 appm.

Tensile behavior of irradiated V-4Cr-4Ti alloy BL-47

Based on the data presented in this report, V-4Cr-4Ti exhibits both an increase in strength and a decrease in ductility with irradiation. The degree of hardening and embrittlement decreases with increasing irradiation/test temperature. Based on results for samples irradiated and tested at about the same temperature, the increase in UTS is: 79% for 400-430°C, 35% for 500-520°C, and 8% for 600°C. The same pattern holds true for YS but the increases are larger: 162% for 400-430°C, 112% for 500-520°C, and 45% for 600°C. UE decreases with irradiation to strain values of 1.6±1.0% for 400-430°C, 3.6±1.3% for 500-520°C and 6.5±1.1% for 600°C. Similarly, TE decreases to strain values of 5.5±1.3% for 400-430°C, 10±1% for 500-520°C, and 13±2% for 600°C.

Discussion

The tensile data for unirradiated and irradiated vanadium alloys tested at ANL have been reviewed and reanalyzed in accordance with ASTM procedures. The resulting values for ultimate tensile strength are in good agreement with values reported previously. On the average, the changes in yield strength are small and well within the heat-to-heat scatter for this parameter. The differences between the new and old values for YS are due primarily to different methodologies used in determining YS. In the current work, YS is determined to be the minimum of the 0.2% offset stress and the stress corresponding to the lower yield point. The previous YS values for unirradiated materials were determined mainly from the 0.5% offset stress criterion. For irradiated materials, several different methodologies (proportional elastic limit, upper yield point, 0.2% offset stress, etc.) were used previously. The main contribution of the current set of values is that they have been determined by a consistent methodology.

Consistency in methodology does not necessarily ensure that the best results are obtained, particularly for the yield strength of the unirradiated alloys. It has been established that the initial rise in load with crosshead displacement is dominated by the nongauge sections of the sample, the support pin, the grips, and the compliance of the load train. A transition occurs as the gauge section deforms plastically. If the nonlinear load vs. displacement response is due solely to plastic deformation of the gauge, then the 0.2% offset method of determining YS should lead to reasonably good values for YS. If the initial nonlinearity is a combination of gauge displacement, plastic deformation in the transition region of the dog-boned specimen, plastic deformation around the support hole, plastic deformation of the support pin, and geometrical factors such as the untwisting of an improperly aligned specimen, then 0.2% offset may not be large enough to be in the region of the load-displacement curve dominated by the gauge length. Referring to Figs. 4-6, the analyst could use a case-by-case method to decide that the flattening off and/or inflection point of the nonlinear portion of the curve is more representative of YS than the stress determined from the 0.2% offset strain. However, this would lead to too much freedom and inconsistency in data interpretation from experimenter to experimenter and laboratory to laboratory within the fusion materials program.

The current values for uniform and total elongation are smaller than those reported previously. This arises from properly subtracting nongauge-length deformation from the total crosshead deformation. For unirradiated and irradiated alloys, the decreases in UE and TE are 5±2% and 4±2%, respectively, where the ± value refers to one standard deviation. There is a significant impact on the ductility of the alloys irradiated and tested at 400-430°C. For unirradiated alloys and alloys irradiated/tested at ≥500°C, the revised values for UE are still within the ductile range.

FUTURE WORK

The tensile data set presented in the current work should be combined with tensile data for vanadium alloys irradiated in other reactors (e.g., EBR-II, HFIR, ATR, BOR-60, HFBR, etc.) at a range of temperatures and neutron damage levels to form a more complete picture of the temperatures, neutron damage levels and helium levels for which the uniform elongation decreases to a low value (e.g. <1%). Currently, the number of data points for any one alloy is insufficient to determine uniform elongation transition temperatures. The case of V-4.1Cr-4.3Ti (BL-47) is a good example. Based on irradiation/test temperatures of 420-435°C and neutron damage levels of 10-33 dpa, three samples give UE values in the range of 1.3-2.8% and one sample indicates a UE value of 0.3%.

To support the point that more data are needed to characterize the transition of UE to <1%, the case of 316L(N) is reviewed [19]. Twenty-three UE data points are available in the irradiation/test temperature range of 227-400°C and the neutron damage range of 3-11 dpa. An additional 31 data points are available for 316-type stainless steels (e.g., Japanese PCA and 316) which exhibit the same behavior as 316L(N). As each data point was added to the plot, the pattern evolved to show that UE decreased from ≈10% at 5 dpa to ≈0.3% at 7 dpa for 227-340°C.

REFERENCES

1. 1996 Annual Book of ASTM Standards, Section 3: Metals Test Methods and Analytical Procedures, Volume 03.01: Metals -- Mechanical Testing; Elevated and Low-Temperature Tests; Metallography; Designation E 6 (Standard Terminology Relating to Methods of Mechanical Testing, pp. 17-26) and Designation E 8 (Standard Test Methods for Tension Testing of Metallic Materials, pp. 55-96), ASTM, West Conshohocken, PA.

2. B. A. Loomis, R. H. Lee and D. L. Smith, "Effect of Heat Treatment and Impurity Concentration on the Tensile Deformation of Unirradiated and Irradiated Vanadium Alloys," Fusion Reactor Materials Semiannual Progress Report for Period Ending March 31, 1987, DOE/ER-0313/2, Sept. 1987, pp. 250-258.

3. B. A. Loomis, R. H. Lee and D. L. Smith, "Strength, Ductility and Ductile-Brittle Transition Temperature for MFR Candidate Vanadium Alloys," Fusion Reactor Materials Semiannual Progress Report for Period Ending September 30, 1987, DOE/ER-0313/3, March 1988, pp. 246-253.

4. B. A. Loomis, H. M Chung and K. Natesan, unpublished work: original load-displacement strip chart recordings for unirradiated, oxidized and irradiated vanadium alloys.

5. B. A. Loomis , unpublished laboratory notebooks from Oct. 27, 1986 to Aug. 27, 1992, Argonne National Laboratory.

6. H. M. Chung, unpublished data sheets for tensile properties of vanadium alloys, Argonne National Laboratory, Feb. 22, 1996.

7. W. A. Simpson, "Room Temperature Elastic Properties of V-5Cr-5Ti," Fusion Reactor Materials Semiannual Progress Report for Period Ending March 31, 1994, DOE/ER-0313/16, Sept. 1994, pp. 258-259.

8. B. A. Loomis, R. H. Lee, D. L. Smith and J. R. Peterson, "Strength, Ductility and Ductile-Brittle Transition Temperature for MFR Candidate Vanadium Alloys," J. Nucl. Mater. 155-157 (1988) 631-638.

9. B. A. Loomis, L. J. Nowicki and D. L. Smith, "Tensile Properties of Unirradiated V-Cr-Ti Alloys and Alternative Approaches for Strengthening the V-4Cr-4Ti Alloy," Fusion Reactor Materials Semiannual Progress Report for Period Ending March 31, 1995, DOE/ER-0313/18, July 1995, pp. 265-272.

10. H. M. Chung, L. Nowicki, D. Busch and D. L. Smith, "Tensile Properties of V-(4-5)Cr-(4-5)Ti Alloys," Fusion Reactor Materials Semiannual Progress Report for Period Ending December 31, 1995, DOE/ER-0313/19, April 1996, pp. 17-21.

11. A. M. Ermi, L. R. Greenwood and H. L. Heinisch, "Irradiation Parameters for the FFTF Materials Open Test Assemblies from 1983 to 1992," Westinghouse Hanford Report WHC-SD-FF-TD-010, Aug. 1994.

12. B. A. Loomis, L. J. Nowicki, and D. L. Smith, "Effect of Irradiation on Tensile Properties of V-Cr-Ti Alloys," Fusion Reactor Materials Semiannual Progress Report for Period Ending September 30, 1993, DOE/ER-0313/15, Feb. 1994, pp. 219-221.

13. H. M. Chung, B. A. Loomis, L. Nowicki and D. L. Smith, "Effects of Dynamically Charged Helium on the Tensile Properties of V-5Ti, V-4Cr-4Ti, and V-3Ti-1Si," Fusion Reactor Materials Semiannual Progress Report for Period Ending December 31, 1995, DOE/ER-0313/19, April 1996, pp. 77-82.

14. H. M. Chung, L. Nowicki and D. L. Smith, "Properties of V-(8-9)Cr-(5-6)Ti Alloys Irradiated in the Dynamic Helium Charging Experiment," Fusion Reactor Materials Semiannual Progress Report for Period Ending June 30, 1996, DOE/ER-0313/20, Oct. 1996, pp. 78-83.

15. H. M. Chung, L. Nowicki and D. L. Smith, "Tensile Properties of V-(4-15)Cr-5Ti Alloys Irradiated at 400°C in the HFIR," Fusion Reactor Materials Semiannual Progress Report for Period Ending June 30, 1996, DOE/ER-0313/20, Oct. 1996, pp. 84-86.

16. I. Gomes, unpublished data, Argonne National Laboratory, 1997.

17. H. Matsui, "On the Actual Loading of Tritium to DHCE Subcapsules," ANL internal memo to D. L. Smith, Nov. 22, 1993.

18. K. Natesan and W. K. Soppet, "Effect of Oxygen and Oxidation on the Tensile Behavior of V-5Cr-5Ti," Fusion Reactor Materials Semiannual Progress Report for Period Ending December 31, 1995, DOE/ER-0313/19, April 1996, pp. 50-53.

19. M. C. Billone and J. E. Pawel, "Summary of Recommended Correlations for ITER-Grade Type 316L(N) for the ITER Material Properties Handbook," Fusion Reactor Materials Semiannual Progress Report for Period Ending December 31, 1995, DOE/ER-0313/19, April 1996, pp. 295-304.

Appendix A:

Baseline Tensile Properties for Unirradiated V-Ti and V-Cr-Ti Alloys

The baseline tensile properties for V-Ti and V-Cr-Ti alloys are listed in Tables A.1-A.12. Cr and Ti values refer to weight %. The properties of interest are yield strength (YS), ultimate tensile strength (UTS), uniform elongation (UE), total elongation (TE) and reduction in area (RA). The tests were performed in an Instron tensile machine with a 500 kgf load cell. A uniform crosshead speed of 0.5 mm/min and a specimen gauge length of 7.62 mm were used for all tests. The gauge cross-sectional area varied from sample to sample, but was ≈1 mm^2. Gauge-length strain rate was 0.11%/s based on crosshead displacement rate and gauge length. The strip chart recordings give load vs. time. The speed of the recorder (50-100 mm/min) and the crosshead speed allow the horizontal time axis to be converted to displacement and engineering strain. The final extensometer reading provides a cross-check for this methodology. Direct measurement of the change in total specimen length after failure provides an additional check on the results. The initial cross-sectional area of the gauge allows conversion of the load to engineering stress.

The references in the tables refer to the previously reported tensile properties listed in parentheses. Fabrication, polishing and annealing of the tensile specimens are described in Refs. 9 and 10. In general, samples were polished and then annealed for 1 h in vacuum at temperatures ranging from 1000 to 1125°C. The tensile values just above those in parentheses are the revised values based on reanalyses of the original strip chart recordings of load vs. displacement [4]. Revisions are based primarily on the proper accounting for the tensile machine and sample springback if unloading were to occur at the load of interest. The new values for yield strength are based on the engineering stress corresponding to an offset (i.e., plastic) strain of 0.2% except for cases that exhibit upper and lower yield points and/or discontinuous yielding (see Ref. 1 for definitions of terms). For these cases, the stress corresponding to the minimum of the 0.2% offset strain and the lower yield point is defined as YS. Most of the previously reported values for YS correspond to an offset strain of 0.5% and are higher than the new values. Reduction in area (RA) at the failure site is used to determine the true strain at rupture. The RA values listed in the tables are those that were published [8,10]. These values are determined directly from post-test analysis of the failed samples and require no correction .

For several samples, the original force-displacement curves could not be located. Because significant changes in YS and UTS are not anticipated, the previously reported values are recommended for these cases. Algorithms for correcting previously reported values of uniform (UE') and total (TE') elongations are based on an analysis of the spring constants (k) and effective Young's moduli (E') for the known force-displacement curves. This analysis indicates that E' = 82±15 MPa/% for the SS3 unirradiated vanadium alloys tested at ANL. Thus, the recommended algorithms for correcting UE and TE are:

$$UE = UE' - UTS/(82\ MPa/\%) \qquad (A.1)$$

and

$$TE = TE' - YS/(82\ MPa/\%). \qquad (A.2)$$

Equation A.1 has a fundamental basis, while Eq. A.2 has been determined empirically.

Table A.1. Revised tensile properties for unirradiated V and V-1.0Ti alloys: yield strength (YS), ultimate tensile strength (UTS), uniform elongation (UE), total elongation (TE) and reduction in area (RA). k = force-displacement slope used to reanalyze the data [4]. UE/TE values with superscript "c" are calculated from Eqs. A.1/A.2. Previous values are in parentheses and are from the Refs. listed.

Alloy (ANL ID)	ID #	T °C	k kN/mm	YS MPa	UTS MPa	UE %	TE %	RA %	Ref.
V	1	25	1.13	259 (259)	309 (309)	23 (28)	48 (49)	—	9
(BL-51)	10	100	—	— (220)	— (290)	20[c] (24)	29[c] (32)	—	
287 wppm Si	5	225	a	a (175)	a (279)	18[c] (21)	26[c] (28)	—	
297 wppm O									
35 wppm N	9	300	1.07	181 (181)	348 (348)	20 (26)	27 (32)	—	
30 wppm C									
	4	325	0.94	144 (153)	329 (335)	22 (24)	30 (32)	—	
	8	350	0.96	133 (138)	310 (310)	19 (24)	29 (32)	—	
	2	420	1.23	167 (167)	282 (283)	22 (25)	35 (36)	—	
	7	520	0.91	133 (134)	187 (187)	31 (34)	64 (65)	—	
	3	600	0.94	124 (124)	134 (134)	26 (28)	64 (64)	—	
	6	700	0.98	124 (124)	124 (124)	1.4 (4)[b]	18 (18)[b]	—	
V-1.0Ti	1	25	1.20	268 (268)	343 (343)	19 (23)	33 (34)	—	9
(BL-50)	8	120	1.14	236 (236)	317 (317)	20 (23)	34 (34)	—	
1050 wppm Si	4	225	1.11	188 (188)	275 (275)	16 (20)	26 (28)	—	
230 wppm O									
130 wppm N	7	325	0.86	174 (174)	386 (396)	16 (23)	24 (29)	—	
235 wppm C									
	3	420	0.98	198 (198)	401 (402)	16 (22)	25 (28)	—	
	6	520	1.09	175 (181)	398 (398)	24 (28)	32 (37)	—	
	5	600	0.75	150 (174)	350 (351)	18 (24)	31 (32)	—	
	9	700	0.89	147 (157)	317 (317)	16 (21)	27 (29)	—	

[a]Recording too faint to read. [b]UE and TE values from strip chart. Ref. 9 values may be misprints.

Table A.2. Revised tensile properties for unirradiated V-3.1Ti alloys : yield strength (YS), ultimate tensile strength (UTS), uniform elongation (UE), total elongation (TE) and reduction in area (RA). k = force-displacement slope used to reanalyze the data [4]. UE/TE values with superscript "c" are calculated from Eqs. A.1/A.2. Previous values are in parentheses and are from the Refs. listed.

Alloy (ANL ID)	ID #	T °C	k kN/mm	YS MPa	UTS MPa	UE %	TE %	RA %	Ref.
V-3.1Ti	1	25	1.49	245 (295)	356 (409)	23 (24)	36 (33)	—	9
(BL-62)	—	100	—	— (210)	— (340)	18[c] (22)	24[c] (27)	—	
660 wppm Si	—	225	—	— (180)	— (298)	18[c] (22)	26[c] (28)	—	
320 wppm O									
86 wppm N	—	325	—	— (177)	— (350)	17[c] (20)	22[c] (24)	—	
109 wppm C									
	2	420	a	a (183)	a (404)	15[c] (20)	24[c] (26)	—	
	—	520	—	— (170)	— (406)	14[c] (19)	21[c] (23)	—	
	3	600	1.09	173 (177)	359 (410)	15 (21)	23 (25)	—	
	—	700	—	— (183)	— (405)	14[c] (19)	21[c] (23)	—	
V-3.1Ti	1	25	1.49	344 (367)	456 (465)	21 (24)	31 (33)	—	9
(BL-27)	14	100	1.14	343 (352)[b]	465 (464)[b]	19 (22)	23 (27)	80	8,9
2500 wppm Si	6	225	0.98	235 (235)	344 (344)	18 (22)	25 (28)	90	
210 wppm O									
310 wppm N	5	325	1.07	228 (227)	373 (386)	15 (20)	20 (24)	90	
300 wppm C									
	2	420	1.07	245 (242)	431 (431)	15 (20)	22 (26)	84	
	3	520	1.02	207 (228)	424 (428)	15 (19)	20 (23)	87	
	4	600	1.02	213 (230)	435 (435)	15 (21)	20 (25)	77	
	10	700	0.75	203 (224)	413 (413)	12 (19)	18 (23)	68	

[a]Recording too faint to read. [b]YS and UTS values from strip chart. Ref. 9 values may be misprints.

Table A.3. Revised tensile properties for unirradiated V-3Ti alloys: yield strength (YS), ultimate tensile strength (UTS), uniform elongation (UE), total elongation (TE) and reduction in area (RA). k = force-displacement slope used to reanalyze the data [4]. Previous values are in parentheses and are from the Refs. listed.

Alloy (ANL ID)	ID #	T °C	k kN/mm	YS MPa	UTS MPa	UE %	TE %	RA %	Ref.
V-2.5Ti	10	25	1.20	412 (421)	480 (480)	19 (25)	26 (34)	—	9
(BL-45)	5	105	1.26	352 (355)	431 (430)	21 (26)	28 (33)	—	
9900 wppm Si 345 wppm O	9	225	1.33	286 (286)	392 (392)	22 (26)	29 (32)	—	
125 wppm N 90 wppm C	2	325	0.98	257 (259)	405 (405)	15 (21)	22 (26)	—	
	2'	420	0.82	208 (274)	382 (447)	17 (24)	21 (29)	—	
	6	520	0.96	264 (274)	446 (447)	18 (24)	24 (29)	—	
	1	600	1.09	234 (265)	445 (446)	16 (21)	20 (26)	—	
	3	700	0.98	233 (260)	436 (437)	11 (17)	17 (21)	—	
V-3.1Ti	L1[a]	25	1.53	447 (459)	552 (552)	14 (18)	21 (24)	—	4
(BL-42)	1	25	1.17	436 (473)	545 (545)	14 (20)	22 (26)	88	8,9
5400 wppm Si 580 wppm O	6	100	1.09	433 (405)	503 (519)	13 (19)	19 (22)	76	
190 wppm N 140 wppm C	2	225	1.23	299 (317)	410 (410)	13 (18)	20 (23)	75	
	3	325	1.07	259 (300)	431 (436)	15 (21)	22 (27)	79	
	4	420	1.26	302 (328)	464 (463)	10 (16)	16 (20)	63	
	5	520	1.07	296 (312)	482 (466)	11 (18)	17 (23)	—	9
	8	600	b	b (308)	b (470)	b (18)	b (21)	—	
	9	700	1.02	319 (291)	452 (452)	11 (17)	14 (20)	—	

[a]Exposed to Li at 482°C for 1001 h prior to tensile testing.
[b]Recording is too garbled to interpret with confidence.

Table A.4. Revised tensile properties for unirradiated V-4.6Ti and V-9.8Ti alloys: yield strength (YS), ultimate tensile strength (UTS), uniform elongation (UE), total elongation (TE) and reduction in area (RA). k = force-displacement slope used to reanalyze the data [4]. Previous values are in parentheses and are from the Refs. listed.

Alloy (ANL ID)	ID #	T °C	k kN/mm	YS MPa	UTS MPa	UE %	TE %	RA %	Ref.
V-4.6Ti	9	25	1.07	336 (336)	412 (412)	17 (22)	32 (35)	—	9
(BL-46)	6	108	1.29	307 (294)	336 (366)	11 (16)	21 (24)	—	
160 wppm Si	10	160	0.98	239 (259)	342 (342)	15 (20)	23 (25)	—	
305 wppm O									
53 wppm N	3	225	1.09	194 (217)	317 (317)	18 (23)	26 (28)	—	
85 wppm C									
	5	330	1.11	209 (214)	338 (342)	18 (22)	25 (28)	—	
	2	420	0.78	183 (215)	316 (334)	11 (15)	16 (19)	—	
	8	520	0.91	176 (195)	344 (350)	15 (20)	20 (24)	—	
	7	600	1.20	191 (195)	386 (388)	16 (19)	21 (25)	—	
	4	700	0.91	204 (203)	377 (376)	11 (17)	15 (19)	—	
V-9.8Ti	1	25	1.23	434 (435)	532 (532)	19 (25)	29 (33)	—	9
(BL-12)	8	100	1.26	336 (374)	477 (477)	20 (25)	30 (32)	—	
245 wppm Si	6	225	1.33	310 (326)	463 (463)	18 (23)	25 (28)	—	
1670 wppm O									
390 wppm N	5	325	1.06	310 (310)	477 (479)	17 (21)	23 (27)	—	
450 wppm C									
	2	420	1.11	300 (308)	486 (496)	16 (21)	23 (27)	—	
	7	520	0.98	299 (303)	525 (529)	14 (21)	20 (25)	—	
	3	600	1.23	299 (298)	538 (538)	17 (23)	20 (25)	—	
	4	700	1.14	247 (262)	466 (466)	14 (19)	20 (24)	—	

Table A.5. Revised tensile properties for unirradiated V-17.7Ti alloy : yield strength (YS), ultimate tensile strength (UTS), uniform elongation (UE), total elongation (TE) and reduction in area (RA). k = force-displacement slope used to reanalyze the data [4]. UE/TE values with superscript "c" are calculated from Eqs. A.1/A.2. Previous values are in parentheses and are from the Refs. listed.

Alloy (ANL ID)	ID #	T °C	k kN/m m	YS MPa	UTS MPa	UE %	TE %	RA %	Ref.
V-17.7Ti	L1[a]	25	1.44	693 (693)	731 (731)	13 (18)	20 (25)	—	4
(BL-15)	L3[a]	25	1.34	674 (681)	728 (728)	13 (19)	21 (25)	—	4
480 wppm Si 830 wppm O 160 wppm N 380 wppm C	1	25	1.61	628 (628)	692 (692)	17 (22)	27 (32)	68	8,9
	18	100	—	— (525)	— (640)	14[c] (22)	24[c] (30)	76	
	6	225	1.42	437 (437)	588 (588)	13 (20)	19 (25)	66	
	5	325	1.29	436 (436)	636 (636)	17 (24)	23 (29)	69	
	3	420	0.91	394 (443)	612 (658)	13 (24)	19 (30)	60	
	2	520	1.14	404 (445)	680 (678)	19 (29)	24 (33)	59	
	4	600	1.29	417 (417)	667 (667)	13 (20)	22 (28)	55	
	8	650	1.20	350 (400)	554 (554)	15 (20)	25 (29)	72	
	7	700	1.29	405 (393)	496 (496)	9 (15)	18 (23)	67	

[a]Exposed to Li at 482°C for 1001 h (L1) and 3377 h (L3) prior to tensile testing.

Table A.6. Revised tensile properties for unirradiated V-(4-5)Cr-(3-5)Ti alloys: yield strength (YS), ultimate tensile strength (UTS), uniform elongation (UE), total elongation (TE) and reduction in area (RA). k = force-displacement slope used to reanalyze the data [4]. UE/TE values with superscript "c" are calculated from Eqs. A.1/A.2. Previous values are in parentheses and are from the Refs. listed.

Alloy (ANL ID)	ID #	T °C	k kN/mm	YS MPa	UTS MPa	UE %	TE %	RA %	Ref.
V-5.1Cr-3.0Ti	1	25	1.53	327 (337)	430 (430)	14 (18)	24 (25)	—	9
(BL-54, #9928)	2	420	0.79	205 (208)	349 (349)	12 (17)	21 (23)	—	
655 wppm Si 480 wppm O 82 wppm N 133 wppm C	3	600	1.09	182 (204)	346 (346)	10 (14)	16 (21)	—	
V-4.1Cr-4.3Ti	9	25	1.53	404 (386)	461 (454)	20 (25)	31 (34)	—	9
(BL-47, #9144)	10	100	—	— (325)	— (420)	20^c (25)	29^c (33)	—	
870 wppm Si 350 wppm O 220 wppm N 200 wppm C	5	225	1.20	246 (272)	379 (379)	21 (26)	28 (31)	—	
	3	337	1.07	229 (254)	381 (388)	18 (20)	24 (28)	—	
	11	420	1.25	250 (250)	401 (405)	16 (21)	21 (25)	—	
	8	520	1.02	222 (244)	419 (423)	13 (19)	20 (24)	—	
	4	600	1.17	253 (256)	430 (434)	11 (16)	16 (21)	—	
	7	650	1.17	249 (264)	453 (453)	14 (19)	20 (23)	—	
	6	700	1.04	223 (266)	414 (414)	11 (17)	16 (20)	—	
V-4.6Cr-5.1Ti	4	25	1.49	360 (386)	470 (465)	19 (22)	32 (34)	—	9
(BL-63, #832394)	5	420	1.00	216 (238)	396 (396)	17 (21)	25 (28)	—	
310 wppm Si 440 wppm O 28 wppm N 73 wppm C	5'	600	1.07	209 (225)	382 (382)	10 (15)	11 (20)	—	

Table A.7. Revised tensile properties for unirradiated V-(4-5)Cr-(4-5)Ti alloys : yield strength (YS), ultimate tensile strength (UTS), uniform elongation (UE), total elongation (TE) and reduction in area (RA). k = force-displacement slope used to reanalyze the data [4]. Previous values are in parentheses and are from the Refs. listed.

Alloy (ANL ID)	ID #	T °C	k kN/mm	YS MPa	UTS MPa	UE %	TE %	RA %	Ref.
V-3.8Cr-3.9Ti		23	1.63	355 (457)	429 (528)	19 (24)	29 (32)	94	6,10
(BL-71, #832665)		100	1.36	325[a] (337)	379[a] (435)	21 (24)	29 (30)	—	
783 wppm Si		206	1.63	236 (230)	345 (346)	21 (24)	29 (30)	92	
310 wppm O									
85 wppm N		300	1.07	208 (216)	343 (343)	19 (23)	27 (30)	93	
80 appm C									
		400	1.17	196 (205)	359 (359)	18 (23)	26 (28)	—	
		500	1.44	199 (232)	402 (402)	10 (18)	16 (22)	84	
		600	1.11	189 (245)	366 (409)	14 (19)	20 (24)	—	
		700	1.23	221 (212)	380 (380)	7 (13)	13 (17)	48	
V-4.9Cr-5.1Ti		23	1.58	394 (397)	503 (503)	19 (23)	31 (33)	88	6,10
(BL-72, T87)		100	1.44	337 (317)	439 (439)	18 (22)	26 (29)	83	
545 wppm Si		200	1.33	294 (280)	408 (408)	17 (22)	25 (28)	88	
380 wppm O									
89 wppm N		300	1.17	262 (249)	405 (405)	14 (21)	21 (25)	91	
109 wppm C									
		400	1.44	256 (256)	427 (427)	13 (18)	19 (23)	82	
		500	1.26	285 (265)	449 (453)	11 (14)	16 (19)	81	
		600	1.44	262 (254)	449 (449)	11 (17)	15 (20)	73	
		700	1.33	255 (241)	401 (401)	8 (13)	13 (16)	36	

[a]Uncertainty of ±47 MPa due to uncertainty in load baseline.

Table A.8. Revised tensile properties for unirradiated V-(8-9)Cr-(5-6)Ti alloys : yield strength (YS), ultimate tensile strength (UTS), uniform elongation (UE), total elongation (TE) and reduction in area (RA). k = force-displacement slope used to reanalyze the data [4]. Previous values are in parentheses and are from the Refs. listed.

Alloy (ANL ID)	ID #	T °C	k kN/mm	YS MPa	UTS MPa	UE %	TE %	RA %	Ref.
V-7.9Cr-5.7Ti	3	25	1.11	404 (440)	512 (541)	20 (23)	33 (33)	—	9
(BL-49)	9	108	1.33	394 (393)	489 (489)	18 (23)	28 (30)	—	
36 wppm Si	10	175	1.44	313 (318)	404 (404)	8 (12)	9 (13)	—	
400 wppm O									
150 wppm N	8[a]	225	1.36	228 (236)	347 (347)	13 (17)	21 (23)	—	
127 wppm C	6	325	1.07	250 (261)	424 (429)	15 (18)	23 (26)	—	
	4	420	1.26	289 (287)	461 (470)	15 (20)	22 (25)	—	
	5	600	1.33	261 (285)	486 (486)	14 (19)	20 (22)	—	
	7	700	1.11	270 (271)	487 (487)	16 (21)	21 (26)	—	
V-9.2Cr-4.9Ti	L1[b]	25	1.26	498 (504)	599 (599)	15 (21)	26 (30)	—	4
(BL-43)	L3[b]	25	1.63	511 (511)	617 (617)	16 (21)	24 (29)	—	4
340 wppm Si	9	25	1.29	430 (440)	541 (541)	19 (23)	30 (33)	91	8,9
230 wppm O									
31 wppm N	8	100	1.12	423 (387)	533 (482)	17 (20)	29 (32)	91	
100 wppm C	3	225	1.29	318 (334)	448 (448)	17 (22)	25 (29)	82	
	6	325	1.23	300 (312)	452 (452)	19 (21)	27 (30)	86	
	1	420	1.17	291 (300)	460 (467)	14 (20)	21 (25)	83	
	4	520	1.07	275 (297)	459 (463)	12 (18)	19 (23)	84	
	5	600	1.02	273 (297)	502 (512)	14 (21)	19 (25)	78	
	7	700	1.07	259 (277)	488 (488)	15 (21)	23 (27)	62	

[a]Sample may have been prematurely loaded. [b]Exposed to Li at 482°C for 1001 h (L1) and 3377 h (L3) prior to tensile testing.

Table A.9. Revised tensile properties for unirradiated V-(11-13)Cr-(5-6)Ti alloys: yield strength (YS), ultimate tensile strength (UTS), uniform elongation (UE), total elongation (TE) and reduction in area (RA). k = force-displacement slope used to reanalyze the data [4]. Previous values are in parentheses and are from the Refs. listed.

Alloy (ANL ID)	ID #	T °C	k kN/mm	YS MPa	UTS MPa	UE %	TE %	RA %	Ref.
V-10.9Cr-5.0Ti	12	25	1.11	471 (491)	575 (573)	19 (23)	28 (31)	85	8,9
(BL-40)	T3	100	1.23	434 (402)	539 (500)	20 (21)	26 (27)	91	
270 wppm Si	6	225	1.23	332 (347)	464 (464)	17 (21)	23 (26)	80	
470 wppm O									
80 wppm N	5	325	1.11	287 (304)	446 (448)	14 (17)	20 (24)	82	
90 wppm C									
	2	433	1.02	308 (321)	496 (501)	14 (18)	20 (24)	78	
	3	520	0.94	277 (303)	485 (488)	12 (17)	17 (22)	72	
	4	600	1.11	293 (299)	520 (519)	16 (22)	22 (26)	72	
	T2	650	0.98	286 (310)	529 (529)	14 (20)	20 (25)	66	
	T1	700	0.82	297 (299)	513 (513)	14 (21)	20 (26)	64	
V-12.9Cr-5.9Ti	15	25	1.29	526 (533)	627 (627)	21 (25)	33 (37)	85	8,9
BL-23	14	100	1.36	474 (483)	589 (589)	22 (25)	32 (37)	59	
1230 wppm Si	6	225	1.40	386 (407)	548 (548)	17 (23)	26 (29)	82	
400 wppm O									
490 wppm N	5	325	1.20	341 (368)	518 (522)	17 (23)	25 (30)	85	
280 wppm C									
	12	420	1.33	370 (379)	554 (571)	15 (21)	22 (27)	78	
	3	520	1.23	337 (360)	562 (567)	15 (21)	22 (27)	72	
	4	600	1.23	346 (384)	611 (610)	18 (25)	25 (31)	71	
	10	650	1.11	332 (373)	573 (573)	17 (22)	26 (30)	70	
	13	700	1.09	346 (355)	541 (519)	15 (21)	30 (32)	73	

Table A.10. Revised tensile properties for unirradiated V-13.5Cr-5.2Ti alloy: yield strength (YS), ultimate tensile strength (UTS), uniform elongation (UE), total elongation (TE) and reduction in area (RA). k = force-displacement slope used to reanalyze the data [4]. Previous values are in parentheses and are from the Refs. listed.

Alloy (ANL ID)	ID #	T °C	k kN/mm	YS MPa	UTS MPa	UE %	TE %	RA %	Ref.
V-13.5Cr-5.2Ti	L1[a]	25	1.44	551 (571)	652 (652)	16 (—)	20 (28)	—	4
(BL-24)	L3[a]	25	1.72	589 (592)	685 (685)	18 (28)	25 (34)	—	4
390 wppm Si	18	25	1.29	532	633	18	28	80	8,9
1190 wppm O				(545)	(634)	(23)	(32)		
360 wppm N	27	100	1.58	482	593	20	27	86	
500 wppm C				(439)	(545)	(22)	(31)		
	12	225	1.40	347	478	14	22	86	
				(370)	(478)	(17)	(25)		
	2	325	1.36	303	448	14	20	81	
				(317)	(449)	(17)	(23)		
	11	420	1.26	327	512	16	23	83	
				(341)	(518)	(21)	(27)		
	15	520	1.04	317	500	11	18	75	
				(326)	(502)	(17)	(23)		
	13	600	0.94	305	555	14	19	72	
				(342)	(555)	(21)	(26)		
	26	650	1.17	305	559	17	24	61	
				(342)	(559)	(25)	(30)		
	25	700	1.20	340	544	13	20	60	
				(337)	(544)	(21)	(26)		

[a]Exposed to Li at 482°C for 1001 h (L1) and 3377 h (L3) prior to tensile testing.

Table A.11. Revised tensile properties for unirradiated V-14.5Cr-5.0Ti and V-9.9Cr-9.2Ti alloys: yield strength (YS), ultimate tensile strength (UTS), uniform elongation (UE), total elongation (TE) and reduction in area (RA). k = force-displacement slope used to reanalyze the data [4]. Previous values are in parentheses and are from the Refs. listed.

Alloy (ANL ID)	ID #	T °C	k kN/mm	YS MPa	UTS MPa	UE %	TE %	RA %	Ref.
V-14.5Cr-5.0Ti	1	25	1.63	570 (570)	674 (674)	20 (26)	26 (33)	83	8,9
(BL-41)	13	100	1.36	492 (494)	599 (579)	17 (23)	23 (29)	82	
400 wppm Si 330 wppm O 96 wppm N 120 wppm C	T1	225	1.23	387 (399)	525 (525)	16 (22)	24 (27)	82	
	5	325	1.11	346 (348)	500 (500)	14 (19)	22 (26)	81	
	2	420	1.23	326 (346)	514 (524)	14 (20)	21 (26)	80	
	3	520	0.94	344 (350)	542 (538)	11 (19)	19 (25)	70	
	4	600	1.00	327 (335)	560 (560)	12 (21)	18 (25)	66	
	T3	650	1.14	307 (356)	575 (575)	14 (22)	21 (27)	63	
	T2	700	1.09	337 (339)	563 (564)	15 (22)	22 (28)	62	
V-9.9Cr-9.2Ti	7	25	1.58	506 (534)	628 (628)	19 (24)	30 (34)	—	9
(BL-44)	12	100	1.58	457 (469)	571 (571)	19 (24)	34 (36)	—	
270 wppm Si 300 wppm O 87 wppm N 150 wppm C	8	225	1.40	382 (387)	516 (516)	16 (21)	26 (29)	—	
	5	325	1.31	352 (367)	528 (532)	16 (23)	25 (30)	—	
	9	420	1.17	364 (364)	567 (570)	15 (23)	24 (30)	—	
	10	520	1.23	347 (349)	558 (560)	14 (23)	23 (29)	—	
	11	600	1.29	351 (352)	565 (565)	17 (23)	24 (30)	—	
	3	700	0.98	312 (328)	492 (492)	16 (20)	21 (28)	—	

Table A.12. Revised tensile properties for unirradiated V-7.2Cr-14.5Ti alloy: yield strength (YS), ultimate tensile strength (UTS), uniform elongation (UE), total elongation (TE) and reduction in area (RA). k = force-displacement slope used to reanalyze the data [4]. Previous values are in parentheses and are from the Refs. listed.

Alloy (ANL ID)	ID #	T °C	k kN/mm	YS MPa	UTS MPa	UE %	TE %	RA %	Ref.
V-7.2Cr-14.5Ti	L1[a]	25	1.38	738 (738)	835 (835)	16 (23)	25 (31)	—	4
(BL-10)	L3[a]	25	1.69	790 (788)	884 (884)	14 (22)	21 (28)	—	4
400 wppm Si 1100 wppm O 250 wppm N 400 wppm C	12	25	1.58	634 (636)	717 (717)	15 (20)	24 (28)	75	8,9
	13	100	1.53	537 (556)	647 (647)	14 (21)	23 (28)	77	
	6	225	1.33	479 (490)	618 (618)	13 (20)	20 (25)	74	
	5	325	1.29	485 (487)	673 (682)	13 (21)	19 (25)	69	
	T1	420	1.26	469 (471)	695 (695)	17 (22)	23 (29)	67	
	2	520	1.02	465 (468)	727 (730)	15 (24)	20 (28)	62	
	3	600	1.11	465 (469)	738 (738)	16 (26)	18 (27)	51	
	10	650	b	b (441)	b (661)	b (23)	b (28)	53	
	T2	700	1.23	359 (404)	584 (584)	12 (18)	24 (30)	53	

[a]Exposed to Li at 482°C for 1001 h (L1) and 3377 h (L3) prior to tensile testing.
[b]Poor chart performance (i.e., stops and starts) renders data difficult to interpret.

Appendix B:

Revised Tensile Properties for FFTF- and HFIR-Irradiated V-Ti and V-Cr-Ti Alloys

The revised tensile properties for V-Ti and V-Cr-Ti alloys are listed in Tables B.7-B.11 for alloys irradiated in FFTF and in Table B.12 for alloys irradiated in HFIR. Alloy composition, specimen identification number, MOTA positions and operating conditions for FFTF-irradiated ANL alloys are taken from Ref. 11 and are listed in Tables B.1-B.6. The subcapsule and specimen identification numbers in these tables are consistent with those specified on the loading charts. The properties listed are yield strength (YS), ultimate tensile strength (UTS), uniform elongation (UE), and total elongation (TE). These have been determined from the original load-displacement strip chart recordings [4]. The tests were performed in an Instron tensile machine with a 500 kgf load cell. A uniform crosshead speed of 0.5 mm/min and a specimen gauge length of 7.62 mm were used for all tests. The gauge cross-sectional area varied from sample to sample, but was ≈ 1 mm^2. The gauge-length strain rate was 0.11%/s, based on crosshead displacement rate and gauge length. The strip chart recordings give load vs. time. The speed of the recorder (50-100 mm/min) and the crosshead speed allow the horizontal time axis to be converted to engineering strain. The final extensometer reading provides a cross-check for this methodology. Direct measurement of the change in total specimen length after failure provides an additional check on the results. The specimen gauge initial cross-sectional area allows conversion of the load to engineering stress. In some cases (e.g., plastic deformation of support pins for irradiated, high strength alloys tested before 1992), the direct measurement of sample elongation is much smaller than the extensometer reading and the reanalyzed values. For these cases, this direct measurement is used to determine TE. It is also assumed that the UTS values determined from the recording are reasonably accurate, but that YS and UE cannot be determined accurately.

The values in Tables B.7-B.12 have been determined by a standard and consistent methodology that properly accounts for tensile-machine and sample springback in order to determine permanent plastic values for UE and TE. In general, YS values have been determined to correspond to the load giving an offset (i.e., plastic) strain of 0.2%. In cases that exhibit upper and lower yield points and/or discontinuous yielding (see Ref. 1 for definitions), the minimum of the 0.2% offset load and the lower yield point load has been used to determine YS.

The irradiation test temperatures and dpa levels in Tables B.7 to B.12 are consistent with those listed in Tables B.1 to B.6. The Specimen ID numbers are consistent with those listed on the strip chart recordings. In general, the loading chart ID numbers and the strip chart ID numbers are consistent. For some cases involving samples of the same composition and the same subcapsule (e.g., 45-485), they are distinguished on the strip charts by adding an extra number (e.g., 45-485-1 and 45-485-2). In these examples, the 45 refers to the ANL heat identification (BL-45 , V-2.5Ti-1.0Si) and the 485 refers to the subcapsule ID (V485). The helium contents listed in Tables B.7-B.11 are based on direct measurements of the BL-47 samples. It is assumed that vanadium alloys in the same subcapsule have the same helium content as the BL-47 alloy. Unusual behavior exhibited in these strip chart recordings and uncertainties in their interpretation are mentioned in footnotes to the tables. Also noted in the tables are the force-displacement slope (k in kN/mm) values used to reanalyze the strip chart recordings.

Table B.1. Vanadium-alloy tensile specimens and FFTF operating conditions for MOTA 1D in Cycle 8 (185.8 EFPD at 400 MWth). Damage values are listed for Cycle 8. Total accumulated damage values are included in parentheses; they were obtained from the stainless steel values listed in Ref. 11 by multiplying by 1.31. Under "Tensile Curve," Y means the strip chart recording has been located and analyzed, B means the specimen was damaged during irradiation/handling, and N means no tensile curve was found, which may indicate that the sample was not tensile-tested.

Alloy (ANL ID)	Specimen ID	Subcapsule ID	MOTA Position	T °C	Damage dpa	Tensile Curve
V-3.1Ti-0.25Si (BL-27)	MK01	V424	2E-3	404	38	Y
	MK02*	V519	1B-3	520	21	N
	MK03*	V624	5D-3	601	15	Y
V-17.7Ti (BL-15)	ML01	V425	2E-3	404	38	B
	ML02*	V519	1B-1	520	27	N
	ML03	V624	5D-3	601	15	N
V-7.2Cr-14.5Ti (BL-10)	MH01	V424	2E-3	404	38	N
	MH02*	V519	1B-1	520	27	N
	MH03*	V623	5D-3	601	15	B
V-13.5Cr-5.2Ti (BL-24)	MF01	V423	2E-3	404	38	B
	MF02*	V521	1B-3	520	21	B
	MF03	V627	5D-2	601	12	B

*These samples experienced temperature excursions during irradiation in FFTF.

Table B.2. Vanadium-alloy tensile specimens and FFTF operating conditions for MOTA 1E in Cycle 9 (341.8 EFPD at 291 MWth). Damage values are listed for Cycle 9. Total accumulated damage values are included in parentheses; they were obtained from the stainless steel values listed in Ref. 11 by multiplying by 1.31. Under "Tensile Curve," Y means the strip chart recording has been located and analyzed, B means the specimen was damaged during irradiation/handling, C means the irradiated sample was reloaded into the next MOTA, and N means no tensile curve was found, which may indicate that the sample was not tensile-tested.

Alloy (ANL ID)	Specimen ID	Subcapsule ID	MOTA Position	T °C	Damage dpa	Tensile Curve
V-3.1Ti-0.25Si (BL-27)	MK04	V441	2E-3	396	53	Y
	MK06	V441	2E-3	396	53	B
	MK08	V441	2E-3	396	53	Y
	MK05	V531	1B-3	520	24	B
	MK07	V530	1B-3	520	24	Y
	MK09	V530	1B-3	520	24	Y
	MK10	V637	2B-3	599	50	C
V-17.7Ti (BL-15)	ML04	V440	2E-3	396	53	Y
	ML06	V440	2E-3	396	53	Y
	ML08	V440	2E-3	396	53	N
	ML10	V637	2B-3	599	50	C
V-7.2Cr-14.5Ti (BL-10)	MH04	V439	2E-3	396	53	Y
	MH06	V439	2E-3	396	53	Y
	MH10	V439	2E-3	396	53	Y
	MH14	V439	2E-3	396	53	Y
	MH07	V440	2E-3	396	53	B
	MH11	V440	2E-3	396	53	N
	MH12	V441	2E-3	396	53	N
	MH05	V530	1B-3	520	24	B
	MH08	V530	1B-3	520	24	B
	MH13	V530	1B-3	520	24	B
	MH16	V530	1B-3	520	24	N
	MH09	V637	2B-3	599	50	C
	MH17	V637	2B-3	599	50	C
V-13.5Cr-5.2Ti (BL-24)	MF04	V439	2E-3	396	53	Y
	MF07	V439	2E-3	396	53	Y
	MF11	V439	2E-3	396	53	Y
	MF14	V439	2E-3	396	53	Y
	MF05	V441	2E-3	396	53	Y
	MF08	V441	2E-3	396	53	Y
	MF12	V441	2E-3	396	53	B
	MF15	V441	2E-3	396	53	B
	MF06	V530	1B-3	520	24	B
	MF09	V530	1B-3	520	24	B
	MF13	V530	1B-3	520	24	B
	MF16	V530	1B-3	520	24	N
	MF10	V637	2B-3	599	50	C
	MF17	V637	2B-3	599	50	C

Table B.5. Vanadium-alloy non-DHCE tensile specimens and FFTF operating conditions for MOTA 2B in Cycle 12 (203.3 EFPD at 291 MWth). The damage values listed are those accumulated during Cycle 12; they were obtained from the stainless steel values listed in Ref. 11 by multiplying by 1.31. Under "Tensile Curve," Y means the strip chart recording has been located and analyzed, C means the irradiated sample was reloaded into the next MOTA, and N means no tensile curve was found, which may indicate that the sample was not tensile-tested.

Alloy (ANL ID)	Specimen ID (number)	Subcapsule ID	MOTA Position	T °C	Damage dpa	Tensile Curve
V-2.5Ti-1Si (BL-45)	45-485-1, 2 45-563-1, 2 45(2)	V485 V563 V676	3D-6 1D-3 1E-3	427 519 599	33 14 14	Y, Y Y, N C
V-4.6Ti (BL-46)	46(2) 46-561-1, 2 46-678-1, 2	V483 V561 V678	3D-6 1D-2 1E-2	427 519 599	33 17 17	N, N Y, Y Y, N
V-9.8Ti (BL-12)	12(1) 12(1) 12(1)	V486 V564 V674	3D-6 1D-3 1E-3	427 519 599	33 14 14	C C C
V-17.7Ti (BL-15)	15(1)	V675	1E-3	599	14	C
V-4.1Cr-4.3Ti (BL-47)	47-484-1, 2 47-562-1, 2 47-672-1, 2	V484 V562 V672	3D-6 1D-3 1E-2	427 519 599	33 14 17	Y, Y Y, N Y, N
V-7.9Cr-5.7Ti (BL-49)	49-486 49-564 49-673	V486 V564 V673	3D-6 1D-3 1E-2	427 519 599	33 14 17	Y C Y
V-9.2Cr-4.9Ti (BL-43)	43-673	V673	1E-2	599	17	Y
V-13.5Cr-5.2Cr (BL-24)	24-674	V674	1E-3	599	14	Y

Table B.3. Vanadium-alloy tensile specimens and FFTF operating conditions for MOTA 1F in Cycle 10 (335.4 EFPD at 291 MWth). Damage values are listed for Cycle 10. Total accumulated damage values are included in parentheses; they were obtained from the stainless steel values listed in Ref. 11 by multiplying by 1.31. Under "Tensile Curve," Y means the strip chart recording has been located and analyzed, B means the specimen was damaged during irradiation/handling, C means the irradiated sample was reloaded into the next MOTA, and N means no tensile curve was found, which may indicate that the sample was not tensile-tested.

Alloy (ANL ID)	Specimen ID	Subcapsule ID	MOTA Position	T °C	Damage dpa	Tensile Curve
V-3.1Ti-0.25Si (BL-27)	MK10	V637	2B-3	600	46 (96)	Y
V-17.7Ti (BL-15)	ML11	V448	2D-5	404	46	Y
	ML12	V537	1E-3	520	26	Y
	ML10	V637	2B-3	600	46 (96)	Y
	ML13	V642	2B-2	600	49	Y
	ML14	V643	2B-3	600	46	C
V-7.2Cr-14.5Ti (BL-10)	MH18	V447	2D-5	404	46	Y
	MH19	V536	1E-3	520	26	Y
	MH21	V538	1E-3	520	26	C
	MH22	V539	2A-4	520	46	C
	MH09	V637	2B-3	600	46 (96)	N
	MH20	V641	2B-2	600	49	Y
	MH17	V637	2B-3	600	46 (96)	Y
V-9.2Cr-4.9Ti (BL-43)	MV01	V448	2D-5	404	46	Y
	MV02	V537	1E-3	520	26	Y
	MV03	V642	2B-2	600	49	Y
	MV04	V643	2B-3	600	46	C
V-13.5Cr-5.2Cr (BL-24)	MF18	V447	2D-5	404	46	Y
	MF19	V536	1E-3	520	26	Y
	MF21	V538	1E-3	520	26	C
	MF22	V539	2A-4	520	46	C
	MF10	V637	2B-3	600	46 (96)	N
	MF20	V641	2B-2	600	49	Y
	MF17	V637	2B-3	600	46 (96)	Y

Table B.4. Vanadium-alloy tensile specimens and FFTF operating conditions for MOTAs 1G and 2A in Cycle 11 (299.7 EFPD at 291 MWth). Damage values are listed for Cycle 11. Total accumulated damage values are included in parentheses; they were obtained from the stainless steel values listed in Ref. 11 by multiplying by 1.31. Under "Tensile Curve," N means no tensile curve was found, which may indicate that the sample was not tensile-tested. Only ANL samples are listed.

Alloy (ANL ID)	Specimen ID (number)	Subcapsule ID	MOTA/ Position	T °C	Damage dpa	Tensile Curve
V-3.1Ti-0.5Si (BL-42)	42	V548	1G/2F-3	520	41	N
	42	V549	1G/2F-3	520	41	N
	42/42L	V552	1G/2A-4	520	46	N
	42/42L (2)	V653	2A/4C-2	600	47	N
	42 (2)	V656	2A/4C-3	600	51	N
	42 (2)	V657	2A/4C-3	600	51	N
V-17.7Ti (BL-15)	15	V548	1G/2F-3	520	41	N
	15	V550	1G/2A-4	520	46	N
	15	V551	1G/2A-4	520	46	N
	ML14	V643	1G/4A-4	600	46 (92)	N
V-7.2Cr-14.5Ti (BL-10)	MH21	V538	1G/2F-3	520	41	N
	MH22	V539	1G/2A-4	520	46	N
	10/10L	V548	1G/2F-3	520	41	N
	10/10L (2)	V658	2A/4C-3	600	51	N
V-9.2Cr-4.9Ti (BL-43)	43 (2)	V548	1G/2F-3	520	41	N
	43	V552	1G/2A-4	520	46	N
	MV04	V643	1G/4A-4	600	46 (92)	N
	43	V655	2A/4C-2	600	47	N
	43 (2)	V658	2A/4C-3	600	51	N
V-9.9Cr-9.2Ti (BL-44)	44	V548	1G/2F-3	520	41	N
	44	V549	1G/2F-3	520	41	N
	44	V550	1G/2A-4	520	46	N
	44	V551	1G/2A-4	520	46	N
	44 (2)	V654	2A/4C-2	600	47	N
	44	V655	2A/4C-2	600	47	N
	44 (2)	V658	2A/4C-3	600	51	N
V-13.5Cr-5.2Cr (BL-24)	MF21	V538	1G/2F-3	520	41 (67)	N
	MF22	V539	1G/2A-4	520	46 (92)	N
	24 (2)	V548	1G/2F-3	520	41	N
	24 (2)	V658	2A/4C-3	600	51	N

Table B.6. Vanadium-alloy DHCE tensile specimens and FFTF operating conditions for MOTA 2B in Cycle 12 (203.3 EFPD at 291 MWth). The damage values refer to damage accumulated during Cycle 12; they have been obtained from the stainless steel values listed in Ref. 11 by multiplying by 1.31. Under "Tensile Curve," Y means the strip chart recording has been located and reanalyzed and N means that no tensile curve was found, which may indicate that the sample was not tensile-tested.

Alloy (ANL ID)	Specimen ID #	Subcapsule ID	MOTA Position	T °C	Damage dpa	Tensile Curve
V-2.5Ti-1Si (BL-45)	453	4D-1	4D-1	430	25	Y
	456	4D-2	4D-2	430	27	Y
	45	5E-2	5E-2	435	13	Y
	458	5D-1	5D-1	500	14	Y
	455	5D-2	5D-2	500	18	N
	45(5E1)	5E-1*	5D-2*	500	18	Y
	457	5C-1	5C-1	599	14	Y
	454	5C-2	5C-2	599	18	Y
V-4.6Ti (BL-46)	46, 46	4D-1	4D-1	430	25	Y, Y
	46, 46	4D-2	4D-2	430	27	Y, Y
	46, 46	5E-2	5E-2	435	13	Y, Y
	46, 46	5D-1	5D-1	500	14	Y, Y
	46, 46	5D-2	5D-2	500	18	Y, Y
	46(5E1),	5E-1*	5D-2*	500	18	Y, Y
	46(5E1)	5C-1	5C-1	599	14	Y, Y
	46, 46	5C-2	5C-2	599	18	Y, Y
	46, 46					
V-9.8Ti (BL-12)	12	4D-1	4D-1	430	25	N
	12	4D-2	4D-2	430	27	N
	12	5E-2	5E-2	435	13	N
	12	5D-1	5D-1	500	14	N
	12	5D-2	5D-2	500	18	N
	12(5E1)	5E-1*	5D-2*	500	18	N
	12	5C-1	5C-1	599	14	N
	12	5C-2	5C-2	599	18	N

*Subcapsule and/or specimen ID has been referred to as 5E-1 in the literature because that was the planned MOTA-2B location. However, it was actually put in the 5D-2 position (see Ref. 16).

Table B.6. Vanadium-alloy DHCE tensile specimens and FFTF operating conditions for MOTA 2B in FFTF cycle 12 (203.3 EFPD at 291 MWth). The damage values refer to damage accumulated during cycle 12; they have been obtained from the stainless steel values listed in Ref. 9 by multiplying by 1.31. Under "Tensile Curve," Y means the strip chart recording has been located and analyzed and N means no tensile curve was found, which may indicate that the sample was not tensile-tested. (continued)

Alloy (ANL ID)	Specimen ID #	Subcapsule ID	MOTA Position	T °C	Damage dpa	Tensile Curve
V-4.1Cr-4.3Ti (BL-47)	474, 47	4D-1	4D-1	430	25	Y,Y
	475, 47	4D-2	4D-2	430	27	Y,Y
	47, 47	5E-2	5E-2	435	13	Y,N
	476, 47	5D-1	5D-1	500	14	Y,Y
	473, 47	5D-2	5D-2	500	18	Y,Y
	47(5E1),	5E-1*	5D-2*	500	18	Y,Y
	47(5E1)	5C-1	5C-1	599	14	Y,Y
	477, 47	5C-2	5C-2	599	18	Y,Y
	478, 47					
V-7.9Cr-5.7Ti (BL-49)	49	4D-1	4D-1	430	25	Y
	49	4D-2	4D-2	430	27	Y
	49	5E-2	5E-2	435	13	Y
	49	5D-1	5D-1	500	14	Y
	49	5D-2	5D-2	500	18	N
	49(5E1)	5E-1*	5D-2*	500	18	Y
	49	5C-1	5C-1	599	14	Y
	49	5C-2	5C-2	599	18	Y
V-9.2Cr-4.9Ti (BL-43)	43	4D-1	4D-1	430	25	Y
	43	4D-2	4D-2	430	27	Y
	43	5E-2	5E-2	435	13	Y
	43	5D-1	5D-1	500	14	Y
	43	5D-2	5D-2	500	18	N
	43(5E1)	5E-1*	5D-2*	500	18	Y
	43	5C-1	5C-1	599	14	Y
	43	5C-2	5C-2	599	18	Y

*Subcapsule and/or specimen ID has been referred to as 5E-1 in the literature because that was the planned MOTA-2B location. However, it was actually put in the 5D-2 position (see Ref. 15).

Table B.7. Revised tensile properties for V-3Ti-xSi alloys irradiated in FFTF: yield strength (YS), ultimate tensile strength (UTS), uniform elongation (UE), and total elongation (TE). k = force-displacement slope used to reanalyze the data [4].

Alloy (ANL ID)	Specimen ID (Position)	T, °C Irr./Test	Dam./He dpa/appm	k kN/mm	YS MPa	UTS MPa	UE %	TE %
V-2.5Ti-1Si (BL-45)	453 (4D1)	430/425	25/12	2.09	547	649	6.3	10
	456 (4D2)	430/25	27/23	1.96	671	750	9.4	16
	45(5E2)	435/425	13/4	1.44	512	645	5.1	10
	45-485-2	427/420	33/≈0	1.58	564	691	3.7	8.0
	45-485-1	427/25	33/≈0	1.58	783	823	4.1	6.8
	458 (5D1)	500/500	14/15	1.69	407	554	7.6	13
	45(5E1)	500/26	18/7	1.92	529	626	9.4	15
	45-563-1	519/520	14/≈0	1.32	341	491	8.5	14
	457 (5C1)	599/600	14/10	1.66	381	439	11	19
	454 (5C2)	599/25	18/75	1.75	403	545	15	21
V-3.1Ti-0.25Si (BL-27)	V424/MK01	404/420	38/≈0	2.23	817	930	1.8	3.4
	V441/MK08	[b]	53/≈0	2.04	912	1003	1.5	2.3
	V441/MK04	396/420 [b]	53/≈0	2.33	896	1020	4.0	8.9
	V531/MK09	396/25[b]	24/≈0	1.57	571	678	1.0	1.7
	V531/MK07		24/≈0	1.63	634	712	3.9	6.6
		520/520						
	V624/MK03	520/25	15/≈0	1.26	422	520	6.6	14
	V627/MK10		96/≈0	1.21	441	574	5.4	12
		601/600						
		600/600						

[a]Sample annealed at 7°C/min to 510°C for H_2 removal prior to tensile testing; test temperature may be as low as 340°C for this case due to a broken thermocouple.

[b]Sample annealed at 7°C/min to 510°C for H_2 removal prior to tensile testing.

Table B.8. Revised tensile properties for V-4.6Ti and V-17.7Ti alloys irradiated in FFTF: yield strength (YS), ultimate tensile strength (UTS), uniform elongation (UE), and total elongation (TE). k = force-displacement slope used to reanalyze the data [4].

Alloy (ANL ID)	Specimen ID (Position)	T, °C Irr./Test	Dam./He dpa/appm	k kN/mm	YS MPa	UTS MPa	UE %	TE %
V-4.6Ti (BL-46)	46(5E2)	435/425	13/4	1.75	499	587	1.8	7.5
	46(5E2)	435/200	13/4	1.72	547	614	3.0	9.1
	46(4D2)	430/425	27/23	1.69	561	645	1.4	6.3
	46(4D2)	430/100	27/23	1.75	624	705	2.4	5.9
	46(4D1)	430/425	25/12	1.69	582	648	1.4	4.5
	46(4D1)	430/27	25/12	1.82	680	797	4.5	8.4
	46(5E1)	500/500	18/7	1.49	337	437	4.5	12
	46(5E1)	500/200	18/7	1.75	330	439	6.2	13
	46(5D1)	500/500	14/15	1.23	342	450	5.5	11
	46(5D1)	500/25	14/15	1.82	422	520	9.0	20
	46-561-2	519/520	17/≈0	1.57	343	430	5.1	9.4
	46-561-1	519/420	17/≈0	1.38	324	406	4.3	10
	46(5C2)	599/600	18/75	1.56	190	377	6.7	15
	46(5C2)	599/100	18/75	1.44	281	402	12	20
	46(5C1)	599/600	14/10	1.29	215	349	7.3	13
	46(5C1)	599/26	14/10	1.40	305	439	15	26
	46-678-1	599/600	17/≈0	1.58	326	384	9.1	14
V-17.7Ti (BL-15)	V448/ML11	404/420[a]	46/≈0	1.33	694	982	3.7	8.9
	V440/ML06	396/420	53/≈0	2.23	1001	1212	4.1	7.3
	V440/ML04	396/25 [a]	53/≈0	2.36	973	1049	2.8	8.5
	V537/ML12	520/520	26/≈0	1.53	533	743	12	17
	V642/ML13	600/600	49/≈0	1.56	415	587	13	20
	V637/ML10	600/600	96/≈0	1.07	396	535	13	20

[a]Sample annealed at 7°C/min to 510°C for H_2 removal prior to tensile testing.

Table B.9. Revised tensile properties for V-4.1Cr-4.3Ti alloy irradiated in FFTF: yield strength (YS), ultimate tensile strength (UTS), uniform elongation (UE), and total elongation (TE). k = force-displacement slope used to reanalyze the data [4].

Alloy (ANL ID)	Specimen ID (Position)	T, °C Irr./Test	Dam./He dpa/appm	k kN/mm	YS MPa	UTS MPa	UE %	TE %
V-4.1Cr-4.3Ti (BL-47)	475 (4D2)	430/425	27/23	1.63	600	687	1.9	6.2
	47 (4D2)	430/100	27/23	1.89	650	748[a]	2.1[a]	9.8
	474 (4D1)	430/425	25/12	1.63	619	689	1.3	6.8
	47 (4D1)	430/24	25/12	1.66	698	783	4.4	11
	47 (5E2)	435/200	13/4	1.89	606	681	3.0	11
	47-484-2	427/420	33/≈0	1.69	675	694	0.3	3.8
	47-484-1	427/25	33/≈0	1.85	824	841	0.5	5.8
	47 (5E1)	500/500	18/7	1.72	477	574	2.7	9.1
	47 (5E1)	500/200	18/7	1.75	519	599	2.8	12
	476 (5D1)	500/500	14/12	1.69	500	577	3.0	9.3
	47 (5D1)	500/24	14/12	1.58	525	604	b	b
	47-562-1	519/520	14/≈0	1.54	438	541	5.1	11
	477 (5C1)	599/600	14/10	1.17	364	454	5.2	11
	47 (5C1)	599/24	14/10	1.75	424	575	13	20
	478 (5C2)	599/600	18/75	1.44	379	471	7.0	15
	47 (5C2)	599/100	18/75	1.44	403	518	9.7	16
	47-672-1	599/600	17/≈0	1.46	361	463	7.3	13

[a]Values obtained by extrapolation as load recording was off scale near peak.

[b]Stoppages of chart recorder render these parameters very difficult to determine with any degree of certainty.

Table B.10. Revised tensile properties for V-7.9Cr-5.7Ti and V-9.2Cr-4.9Ti alloys irradiated in FFTF: yield strength (YS), ultimate tensile strength (UTS), uniform elongation (UE), and total elongation (TE). k = force-displacement slope used to reanalyze the data [4].

Alloy (ANL ID)	Specimen ID (Position)	T, °C Irr./Test	Dam./He dpa/appm	k kN/mm	YS MPa	UTS MPa	UE %	TE %
V-7.9Cr-5.7Ti (BL-49)	49 (5E2)	435/425	13/4	2.13	690	774	1.8	7.5
	49 (4D1)	430/425	25/12	2.13	609	656	1.0	5.9
	49 (4D2)	430/26	27/23	2.23	748	857	4.2	10
	49-486-1 (3D6)	427/420	33/≈0	2.13	772	821	1.2	6.7
	49 (5D1)	500/500	14/15	1.75	435	530	2.5	7.9
	49 (5E1)	500/25	18/7	2.45	615	750	9.7	16
	49 (5C1)	599/600	14/10	1.66	325	446	7.2	14
	49 (5C2)	599/24	18/75	1.96	450	576	14	21
	49-673 (1E2)	599/600	17/≈0	1.63	387	517	7.6	14
V-9.2Cr-4.9Ti (BL-43)	43 (4D1)	430/425	25/12	2.28	811	860	1.0	6.4
	43 (4D2)	430/27	27/23	2.45	887	967	6.3	13
	43 (5E2)	435/200	13/10	2.29	817	895	3.5	10
	V448/MV01	404/420[a]	46/≈0	1.72	788	930	1.2	6.7
	43 (5D1)	500/500	14/15	2.13	587	716	3.5	9.2
	43 (5E1)	500/27	18/7	2.38	679	829	7.0	15
	V537/MV02	520/520	26/≈0	1.53	606	738	3.9	9.7
	43 (5C2)	599/600	18/75	1.85	416	559	7.0	14
	43 (5C1)	599/100	14/10	1.96	467	605	13	23
	V642/MV03	600/600	49/≈0	1.42	430	566	7.3	14
	43-673 (1E2)	599/600	17/≈0	1.96	457	581	6.0	12

[a]Sample annealed at 7°C/min to 510°C for H_2 removal prior to tensile testing.

Table B.11. Revised tensile properties for V-7.2Cr-14.5Ti and V-13.5Cr-5.2Ti alloys irradiated in FFTF: yield strength (YS), ultimate tensile strength (UTS), uniform elongation (UE), and total elongation (TE). k = force-displacement slope used to reanalyze the data [4].

Alloy (ANL ID)	Specimen ID	T, °C Irr./Test	Dam./He dpa/appm	k kN/mm	YS MPa	UTS MPa	UE %	TE %
V-7.2Cr-14.5Ti (BL-10)	V447/MH18	404/420[a]	46/≈0	1.44	b	1120	b	10[b]
	V439/MH10	396/420	53/≈0	2.31	1009	1136	3.0	6.2
	V439/MH04	396/420	53/≈0	2.02	1075	1190	2.6	6.2
	V439/MH14	396/420	53/≈0	2.23	953	1153	4.9	7.9
	V439/MH06	396/25	53/≈0	2.33	1086	1210	2.8	8.1
	V536/MH19	520/520	26/≈0	1.66	562	855	8.9	14
	V641/MH20	600/600	49/≈0	1.53	468	685	8.9	8.9
	V637/MH17	600/600	96/≈0	1.10	432	547	3.4	3.4
V-13.5Cr-5.2Ti (BL-24)	V447/MF18	404/420[a]	46/≈0	1.10	b	1064	b	7.6[b]
	V439/MF07	396/420[a]	53/≈0	1.38	b	1130	b	8.8[b]
	V439/MF14	396/420	53/≈0	2.06	1152	1195	0.9	3.9
	V439/MF04	396/420	53/≈0	1.38	b	1124	1.8[b]	1.8[b]
	V441/MF08	396/420	53/≈0	—	c	c	c	c
	V441/MF05	396/420	53/≈0	—	d	d	d	d
	V440/MF11	396/25	53/≈0	2.55	1259	1358	1.3	1.3
	V536/MF19	520/520	26/≈0	1.89	747	930	4.7	10
	V641/MF20	600/600	49/≈0	1.36	542	713	5.1	9.3
	V637/MF17	600/600	96/≈0	1.40	566	730	5.5	10
	V674/24	599/600	14/≈0	2.16	549	725	6.4	13

[a]Sample annealed at 7°C/min to 510°C for H_2 removal prior to testing.

[b]Support pins are obviously plastically deformed; TE is measured directly; YS and UE obtained from force-displacement curve are considered unreliable.

[c]Specimen broke at pin before plastic flow of gauge length initiated.

[d]Plastic flow part of curve is off scale.

Table B.12. Revised tensile data for V-Cr-Ti alloys irradiated in HFIR: yield strength (YS), ultimate tensile strength (UTS), uniform elongation (UE), and total elongation (TE). k = force-displacement slope used to reanalyze the data [4].

Alloy (ANL ID)	Specimen ID	T, °C Irrad./Test	Dam./He dpa/appm	k kN/mm	YS MPa	UTS MPa	UE %	TE %
V-4.1Cr-4.3Ti (BL-47)	—	~400/400	~10/≈0	2.45	722	803	2.8	5.0
V-7.9Cr-5.7Ti (BL-49)	—	~400/400	~10/≈0	2.23	775	829	1.3	5.0
V-9.2Cr-4.9Ti (BL-43)	—	~400/400	~10/≈0	2.33	834	871	1.3	2.1
V-14.5Cr-5.0Ti (BL-41)	—	~400/400	~10/≈0	2.33	980	1022	0.9	3.5

Appendix C:

Comparison of Revised and Previously Reported Tensile Properties of FFTF- and HFIR-Irradiated V-Ti and V-Cr-Ti Alloys

The revised tensile properties for V-Ti and V-Cr-Ti alloys irradiated in FFTF and HFIR [Appendix B] are compared to previously reported values [12-15] in Tables C.1 to C.7. The revised values have been determined from the original strip chart recordings [4] by a standard and consistent methodology that properly accounts for tensile-machine and sample springback in order to determine permanent plastic strain values for UE and TE. Unusual behavior exhibited in these strip chart recordings and uncertainties in their interpretation are given in footnotes to the tables in Appendix B. In the case of ANL alloy BL-47, previously reported tensile values have been thoroughly traced from those printed on strip chart recordings, from those described in laboratory notebooks and from those that appear graphically in the more recent semiannual publications. For some of the older alloys, only the strip-chart-recorded and laboratory-notebook-recorded values have been examined. These values have been modified over a period of time based on interim reanalyses of the strip chart data and post-test observations (e.g., bent pins, extensometer readings, direct measurements of sample length change, etc.) The previously reported values are listed in parentheses under the revised values.

Table C.1. Revised and previously reported (in parentheses) tensile data for V-17.7Ti alloy irradiated in FFTF: yield strength (YS), ultimate tensile strength (UTS), uniform elongation (UE), and total elongation (TE).

Alloy (ANL ID)	Specimen ID (Pos.)	T, °C Irr./Test	Dam./He dpa/appm	YS MPa	UTS MPa	UE %	TE %
V-17.7Ti (BL-15)	V448/ML11	404/420	46/≈0	694 (710)	982 (982)	3.7 (12)	8.9 (14)
	V440/ML06	396/420	53/≈0	1001 (—)	1212 (—)	4.1 (—)	7.3 (—)
	V440/ML04	396/25	53/≈0	973 (947)	1049 (1049)	2.8 (10)	8.5 (11)
	V537/ML12	520/520	26/≈0	533 (543)	743 (755)	12 (15)	17 (18)
	V642/ML13	600/600	49/≈0	415 (427)	587 (592)	13 (17)	20 (23)
	V637/ML10	600/600	96/≈0	396 (419)	535 (537)	13 (18)	20 (26)

Table C.2. Revised and previously reported (in parentheses) tensile data for V-3Ti-xSi alloys irradiated in FFTF: yield strength (YS), ultimate tensile strength (UTS), uniform elongation (UE), and total elongation (TE).

Alloy (ANL ID)	Specimen ID (Pos.)	T, °C Irr./Test	Dam./He dpa/appm	YS MPa	UTS MPa	UE %	TE %
V-2.5Ti-1Si (BL-45)	453 (4D1)	430/425	25/12	547 (—)	649 (659)	6.3 (10)	10 (15)
	456 (4D2)	430/25	27/23	671 (—)	750 (750)	9.4 (10)	16 (20)
	45-485-2	427/420	33/≈0	564 (540)	691 (671)	3.7 (10)	8.0 (13)
	45-485-1	427/25	33/≈0	783 (779)	823 (823)	4.1 (8.3)	6.8 (9.6)
	458 (5D1)	500/500	14/15	407 (—)	554 (554)	7.6 (—)	13 (17)
	45(5E1)	500/26	18/7	529 (—)	626 (627)	9.4 (—)	15 (18)
	45-563-1	519/520	14/≈0	341 (360)	491 (491)	8.5 (13)	14 (17)
	457 (5C1)	599/600	14/10	381 (300)	439 (480)	11 (16)	19 (21)
	454 (5C2)	599/25	18/75	403 (—)	545 (545)	15 (—)	21 (25)
V-3.1Ti-0.25Si (BL-27)	V424/MK01	404/420	38/≈0	817 (746)	930 (930)	1.8 (8.3)	3.4 (12)
	V441/MK08	396/420	53/≈0	912 (867)	1003 (1003)	1.5 (8.1)	2.3 (8.6)
	V441/MK04	396/25	53/≈0	896 (911)	1020 (1020)	4.0 (9.4)	8.9 (13)
	V531/MK09	520/520	24/≈0	571 (522)	678 (678)	1.0 (6.6)	1.7 (7.0)
	V531/MK07	520/25	24/≈0	634 (595)	712 (712)	3.9 (8.8)	6.6 (11)
	V624/MK03	601/600	15/≈0	422 (390)	520 (520)	6.6 (12)	14 (19)
	V627/MK10	600/600	96/≈0	441 (381)	574 (574)	5.4 (13)	12 (19)

Table C.3. Revised and previously reported (in parentheses) tensile data for V-4.6Ti alloy irradiated in FFTF: yield strength (YS), ultimate tensile strength (UTS), uniform elongation (UE), .and total elongation (TE).

Alloy (ANL ID)	Specimen ID (Pos.)	T, °C Irr./Test	Dam./He dpa/appm	YS MPa	UTS MPa	UE %	TE %
V-4.6Ti (BL-46)	46(5E2)	435/425	13/4	499	587	1.8	7.5
				(—)	(587)	(—)	(13)
	46(5E2)	435/200	13/4	547	614	3.0	9.1
				(—)	(614)	(—)	(13)
	46(4D2)	430/425	27/23	561	645	1.4	6.3
				(—)	(645)	(—)	(16)
	46(4D2)	430/100	27/23	624	705	2.4	5.9
				(—)	(705)	(—)	(12)
	46(4D1)	430/425	25/12	582	648	1.4	4.5
				(—)	(648)	(—)	(15)
	46(4D1)	430/27	25/12	680	797	4.5	8.4
				(—)	(796)	(—)	(14)
	46(5E1)	500/500	18/7	337	437	4.5	12
				(—)	(437)	(—)	(15)
	46(5E1)	500/200	18/7	330	439	6.2	13
				(—)	(439)	(—)	(16)
	46(5D1)	500/500	14/15	342	450	5.5	11
				(—)	(450)	(—)	(15)
	46(5D1)	500/25	14/15	422	520	9.0	20
				(—)	(527)	(—)	(24)
	46-561-2	519/520	17/≈0	343	430	5.1	9.4
				(322)	(430)	(9.8)	(14)
	46-561-1	519/420	17/≈0	324	406	4.3	9.9
				(308)	(406)	(—)	(14)
	46(5C2)	599/600	18/75	190	377	6.7	15
				(—)	(379)	(—)	(19)
	46(5C2)	599/100	18/75	281	402	12	20
				(—)	(402)	(—)	(22)
	46(5C1)	599/600	14/10	215	349	7.3	13
				(—)	(349)	(—)	(18)
	46(5C1)	599/26	14/10	305	439	15	26
				(—)	(439)	(—)	(30)
	46-678-1	599/600	17/≈0	326	384	9.1	14
				(290)	(384)	(13)	(19)

Table C.4. Revised and previously reported (in parentheses) tensile data for V-4.1Cr-4.3Ti alloy BL-47 irradiated in FFTF: yield strength (YS), ultimate tensile strength (UTS), uniform elongation (UE), total elongation (TE).

Alloy (ANL ID)	Specimen ID (Pos.)	T, °C Irr./Test	Dam./He dpa/appm	YS MPa	UTS MPa	UE %	TE %
V-4.1Cr-4.3Ti (BL-47)	475(4D2)	430/425	27/23	600 (567)	687 (700)	1.9 (11)	6.2 (13)
	47(4D2)	430/100	27/23	650 (612)	748 (748)	2.1 (11)	9.8 (15)
	474(4D1)	430/425	25/12	619 (567)	689 (689)	1.3 (10)	6.8 (13)
	47(4D1)	430/24	25/12	698 (625)	783 (783)	4.4 (14)	11 (17)
	47(5E2)	435/200	13/4	606 (564)	681 (681)	3.0 (11)	11 (15)
	47-484-2	427/420	33/≈0	675 (594)	694 (694)	0.3 (8.3)	3.8 (10)
	47-484-1	427/25	33/≈0	824 (795)	841 (832)	0.5 (8.1)	5.8 (10)
	47(5E1)	500/500	18/7	477 (421)	574 (574)	2.7 (11)	9.1 (14)
	47(5E1)	500/200	18/7	519 (477)	599 (599)	2.8 (11)	12 (15)
	476(5D1)	500/500	14/12	500 (421)	577 (577)	3.0 (11)	9.3 (15)
	47(5D1)	500/24	14/12	525 (500)	604 (609)	— (14)	— (—)
	47-562-1	519/520	14/≈0	438 (450)	541 (541)	5.1 (10)	11 (14)
	477(5C1)	599/600	14/10	364 (318)	454 (454)	5.2 (14)	11 (18)
	47(5C1)	599/24	14/10	424 (391)	575 (575)	13.0 (13)	20.0 (20)
	478(5C2)	599/600	18/75	379 (400)	471 (471)	7.0 (13)	15 (23)
	47(5C2)	599/100	18/75	403 (455)	518 (518)	9.7 (15)	16 (20)
	47-672-1	599/600	17/≈0	361 (360)	463 (462)	7.3 (12)	13 (16)

Table C.5. Revised and previously reported (in parentheses) tensile data for V-7.9Cr-5.7Ti and V-9.2Cr-4.9Ti alloys irradiated in FFTF: yield strength (YS), ultimate tensile strength (UTS), uniform elongation (UE), and total elongation (TE).

Alloy (ANL ID)	Specimen ID (Pos.)	T, °C Irr./Test	Dam./He dpa/appm	YS MPa	UTS MPa	UE %	TE %
V-7.9Cr-5.7Ti (BL-49)	49 (5E2)	435/425	13/4	690 (624)	774 (775)	1.8 (7.8)	7.5 (10)
	49 (4D1)	430/425	25/12	609 (493)	656 (656)	1.0 (5.5)	5.9 (8.9)
	49 (4D2)	430/26	27/23	748 (660)	857 (858)	4.2 (13)	10 (9.8)
	49-486-1 (3D6)	427/420	33/≈0	772 (727)	821 (821)	1.2 (7.9)	6.7 (11)
	49 (5D1)	500/500	14/15	435 (409)	530 (531)	2.5 (6.9)	7.9 (11)
	49 (5E1)	500/25	18/7	615 (570)	750 (751)	9.7 (14)	16 (19)
	49 (5C1)	599/600	14/10	325 (280)	446 (447)	7.2 (11)	14 (16)
	49 (5C2)	599/24	18/75	450 (405)	576 (578)	14 (18)	21 (26)
	49-673 (1E2)	599/600	17/≈0	387 (332)	517 (517)	7.6 (12)	14 (17)
V-9.2Cr-4.9Ti (BL-43)	43 (4D1)	430/425	25/12	811 (728)	860 (860)	1.0 (6.8)	6.4 (10)
	43 (4D2)	430/27	27/23	887 (838)	967 (967)	6.3 (12)	13 (16)
	43 (5E2)	435/200	13/10	817 (740)	895 (894)	3.5 (9.4)	10 (14)
	V448/MV01	404/420	46/≈0	788 (712)	930 (930)	1.2 (7.0)	6.7 (8.9)
	43 (5D1)	500/500	14/15	587 (524)	716 (716)	3.5 (8.6)	9.2 (13)
	43 (5E1)	500/27	18/7	679 (674)	829 (819)	7.0 (12)	15 (17)
	V537/MV02	520/520	26/≈0	606 (568)	738 (738)	3.9 (8.4)	9.0 (9.0)
	43 (5C2)	599/600	18/75	416 (408)	559 (559)	7.0 (12)	14 (17)
	43 (5C1)	599/100	14/10	467 (451)	605 (604)	12.9 (17)	23 (25)
	V642/MV03	600/600	49/≈0	430 (447)	566 (566)	7.3 (11)	14 (15)
	43-673 (1E2)	599/600	17/≈0	457 (427)	581 (581)	6.0 (11)	12 (16)

Table C.6. Revised and previously reported (in parentheses) tensile data for V-7.2Cr-14.5Ti and V-13.5Cr-5.2Ti alloys irradiated in FFTF: yield strength (YS), ultimate tensile strength (UTS), uniform elongation (UE), total elongation (TE).

Alloy (ANL ID)	Specimen ID (pos.)	T, °C Irr./Test	Dam./He dpa/appm	YS MPa	UTS MPa	UE %	TE %
V-7.2Cr-14.5Ti (BL-10)	V447/MH18	404/420	46/≈0	— (764)	1120 (1120)	— (12)	10 (13)
	V439/MH10	396/420	53/≈0	1009 (—)	1136 (—)	3.0 (—)	6.2 (—)
	V439/MH04	396/420	53/≈0	1075 (—)	1190 (—)	2.6 (—)	6.2 (—)
	V439/MH14	396/420	53/≈0	953 (—)	1153 (—)	4.9 (—)	7.9 (—)
	V439/MH06	396/25	53/≈0	1086 (1086)	1210 (1210)	2.8 (9.3)	8.1 (13)
	V536/MH19	520/520	26/≈0	562 (608)	855 (855)	8.9 (13)	14 (15)
	V641/MH20	600/600	49/≈0	468 (492)	685 (683)	8.9 (16)	8.9 (16)
	V637/MH17	600/600	96/≈0	432 (452)	547 (547)	3.4 (11)	3.4 (11)
V-13.5Cr-5.2Ti (BL-24)	V447/MF18	404/420	46/≈0	— (866)	1064 (1064)	5.0 (5.0)	7.6 (7.6)
	V439/MF07	396/420	53/≈0	— (636)	1130 (1130)	— (6.3)	8.8 (8.8)
	V439/MF14	396/420	53/≈0	1152 (—)	1195 (—)	0.9 (—)	3.9 (—)
	V439/MF04	396/420	53/≈0	— (687)	1124 (1124)	1.8 (3.2)	1.8 (3.2)
	V441/MF08	396/420	53/≈0	— (—)	— (—)	— (—)	— (—)
	V441/MF05	396/420	53/≈0	— (—)	— (—)	— (—)	— (—)
	V440/MF11	396/25	53/≈0	1259 (1174)	1358 (1358)	1.3 (2.8)	1.3 (2.8)
	V536/MF19	520/520	26/≈0	747 (710)	930 (950)	4.7 (7.0)	10 (15)
	V641/MF20	600/600	49/≈0	542 (563)	713 (713)	5.1 (8.8)	9.3 (11)
	V637/MF17	600/600	96/≈0	566 (521)	730 (730)	5.5 (12)	10 (16)
	V674/24	599/600	14/≈0	549 (—)	725 (—)	6.4 (—)	13 (—)

Table C.7. Revised and previously reported (in parentheses) tensile data for V-Cr-Ti alloys irradiated in HFIR: yield strength (YS), ultimate tensile strength (UTS), uniform elongation (UE), total elongation (TE).

Alloy (ANL ID)	Specimen ID	T, °C Irr./Test	Damage/ He dpa/appm	YS MPa	UTS MPa	UE %	TE %
V-4.1Cr-4.3Ti (BL-47)		~400/400	~10/≈0	722 (704)	803 (803)	2.8 (4.7)	5.0 (12)
V-7.9Cr-5.7Ti (BL-49)		~400/400	~10/≈0	775 (713)	829 (829)	1.3 (1.3)	5.0 (8.8)
V-9.2Cr-4.9Ti (BL-43)		~400/400	~10/≈0	834 (784)	871 (871)	1.3 (1.2)	2.1 (8.8)
V-14.5Cr-5.0Ti (BL-41)		~400/400	~10/≈0	980 (922)	1022 (1022)	0.9 (1.2)	3.5 (10)

Appendix D:

Comparison of Revised and Previously Reported Tensile Properties of Unirradiated V-5Cr-5Ti Preoxidized in Air

Natesan and Soppet [18] have reported the effects of oxidation on the tensile properties of V-4.6Cr-5.1Ti (BL-63). Tensile specimens were prepared according to ASTM specifications. The approximate gauge dimensions were 19-mm length, 4.5-mm width and 1.0-mm thickness. The control specimens (unoxidized) were tensile-tested at crosshead speeds ranging from 0.005 to 20 mm/min, which correspond to gauge length strain rates of 0.00044 to 0.18%/s. The preoxidized samples were tested at a gauge-length strain rate of 0.018%/s. Table D.1 shows the revised values of tensile properties (determined from the original strip chart recordings) and the previously reported values. The primary difference is in determination of total elongation (TE). In the revised values, the contribution of the machine and nongauge compliance to the crosshead displacement is subtracted from the total displacement in order to determine TE.

Table D.1 Comparison between revised and previously reported (in parentheses) values for tensile properties of V-4.6Cr-5.1Ti (BL-63) preexposed to air: yield stress (YS), ultimate tensile stress (UTS), uniform elongation (UE), and total elongation (TE). Also indicated are initial cross-sectional areas (Ao) for samples and oxidation conditions. Specimens were preoxidized in air at 500°C for times indicated. Tensile tests were conducted in air.

Tensile Test Temperature °C	Preexposure Time in Air at 500°C, h	Specimen ID# Test #	Room Temp. Ao, mm^2	YS MPa	UTS, MPa	UE %	TE %
24	0	T5-28	4.78	326	406	19	31
		VNAT-26		(—)	(—)	(—)	(32)
	24	T5-21	4.90	414	510	16	24
		VNAT-23		(—)	(—)	(—)	(27)
	260	T5-22	5.03	439	511	3.5	3.5
		VNAT-24		(—)	(—)	(—)	(6.5)
	600	T5-23	4.94	455	468	0.3	0.3
		VNAT-21		(—)	(—)	(—)	(3.2)
	1050	T5-24	4.97	467	483	0.4	0.4
		VNAT-29		(—)	(—)	(—)	(3.2)
500	0	V-2	4.88	241	405	15	23
		VNAT-2		(—)	(—)	(—)	(23)
	24	V-7	4.91	243	412	14	18
		VNAT-7		(—)	(—)	(—)	(22)
	250	V-3	4.91	272	457	11	14
		VNAT-34		(—)	(—)	(—)	(17)
	600	V-6	5.02	266	454	9.5	11
		VNAT-6		(—)	(—)	(—)	(15)
	1000	V-8	4.97	313	448	7.2	10
		VNAT-8		(—)	(—)	(—)	(14)
	2060	V-9	5.05	336	392	5.6	6.2
		VNAT-9		(—)	(—)	(—)	(9.0)

IMPACT PROPERTIES OF VANADIUM–BASE ALLOYS IRRADIATED AT <430°C*

H. M. Chung and D. L. Smith (Argonne National Laboratory Argonne)

SUMMARY

Recent attention to vanadium-base alloys has focused on the effect of low-temperature (<430°C) neutron irradiation on the mechanical properties, especially the phenomena of loss of work-hardening capability under tensile loading and loss of dynamic toughness manifested by low impact energy and high ductile-brittle-transition temperature (DBTT). This paper summarizes results of an investigation of the low-temperature impact properties of V-5Ti, V-4Cr-4Ti, and V-3Ti-Si that were irradiated in several fission reactor experiments, i.e., FFTF-MOTA, EBR-II X-530, and ATR-A1. Irradiation performance of one production-scale and one laboratory heat of V-4Cr-4Ti and one laboratory heat of V-3Ti-Si was the focus of the investigation. Even among the same class of alloy, strong heat-to-heat variation was observed in low-temperature impact properties . A laboratory heat of V-4Cr-4Ti and V-3Ti-1Si exhibited good impact properties whereas a 500-kg heat of V-4Cr-4Ti exhibited unacceptably high DBTT. The strong heat-to-heat variation in impact properties of V-4Cr-4Ti indicates that fabrication procedures and minor impurities play important roles in the low-temperature irradiation performance of the alloys.

OBJECTIVE

The objective of this research is to evaluate the effects of irradiation on the impact properties of candidate vanadium-base alloys.

INTRODUCTION

Recent attention to vanadium alloys has focused on low-temperature (<430°C) irradiation performance of V-(4-5)Cr-(4-5)Ti, especially tensile and impact properties after irradiation at <430°C. From several irradiation experiments at 80-430°C, it has been reported that a large-scale (Heat ID #832665) and a laboratory (BL-47) heat of V-4Cr-4Ti[1-5] and a large-scale (BL-63) heat of V-5Cr-5Ti[6] exhibited low uniform elongation as a result of virtual loss of work-hardening capability, although significant susceptibility to loss of work-hardening capability has not been observed for irradiation temperatures ≥500°C. The large-scale heat of V-4Cr-4Ti (#832665) also exhibited severe embrittlement manifested by very low impact energy and high DBTT after irradiation either at 100-275°C in helium environment in the High Flux Beam Reactor (HFBR)[1] or at ≈390°C in lithium environment in EBR-II[6]. In contrast to this, laboratory heats of V-4Cr-4Ti (BL-47) and V-3Ti-1Si (BL-45) have been reported to exhibit excellent impact properties after a conventional irradiation (i.e., a non DHCE) at >430°C in Li environment in FFTF.[7] In this work, impact properties were evaluated on V-5Ti, V-4Cr-4Ti, and V-3Ti-1Si alloys that were irradiated at <430°C in several conventional fission reactor experiments, i.e., FFTF-MOTA, EBR-II X-530, and ATR-A1. In some of the experiments, to investigate the impact properties of the latter laboratory heats under more severe conditions, coldworked Charpy impact specimens were irradiated at ≤400°C in lithium environment.

MATERIALS AND TESTING PROCEDURES

The elemental composition of the alloys investigated in this study and other comparable alloys, determined prior to irradiation, is given in Table 1. Charpy impact specimens were machined from coldworked ≈3.8-mm-thick plates and were inserted in the irradiation capsules either in annealed or coldworked state. Annealed specimens from the laboratory heat of V-4Cr-4Ti (BL-47) were annealed at ≈1000°C or ≈1125°C for 1 h in an ion-pumped vacuum system, whereas specimens from the laboratory heats of V-5Ti and V-3Ti-1Si were annealed at ≈1050°C for 1 h. Following irradiation, the Charpy impact specimens were retrieved from the capsules and cleaned ultrasonically in alcohol. Some of the brittle Charpy impact specimens of V-4Cr-4Ti Heat #832665, irradiated at ≈390°C in EBR-II X-530 experiment, were deliberately annealed at >430°C to investigate the effect of high-temperature annealing on toughness recovery.

---

*Work supported by the U.S. Department of Energy, Office of Fusion Energy, under Contract W-31-109-Eng-38.

Table 1. Chemical composition of vanadium alloys

Heat ID	Nominal Comp. (wt.%)	Impurity Concentration (wt. ppm) O	N	C	Si
BL-50	1.0Ti	230	130	235	1050
BL-62	3.1Ti	320	86	109	660
BL-52	3.1Ti	210	310	300	500
BL-46	4.6Ti	305	53	85	160
BL-12	9.8Ti	1670	390	450	245
BL-15	17.7Ti	830	160	380	480
BL-10	7.2Cr-14.5Ti	1110	250	400	400
BL-24	13.5Cr–5.2Ti	1190	360	500	390
BL-40	10.9Cr-5.0Ti	470	80	90	270
BL-41	14.5Cr-5.0Ti	450	120	93	390
BL-43	9.2Cr-4.9Ti	230	31	100	340
BL-49	7.9Cr-5.7Ti	400	150	127	360
BL-63[a]	4.6Cr-5.1Ti	440	28	73	310
BL-27	3.1Ti–0.25Si	210	310	310	2500
BL-45	2.5Ti-1Si	345	125	90	9900
QN74[b]	4.0Cr–4.1Ti	480	79	54	350
BL-47	4.1Cr-4.3Ti	350	220	200	870
VX-8[c]	3.73Cr–3.93Ti	350	70	300	500
832665[d]	3.8Cr–3.9Ti	310	85	80	783

[a]80-kg heat fabricated with sponge Ti

[b]Contains ≈250 appm B^{10}.

[c]100-kg heat, contains (in wppm) 1120 Al, 280 Fe, 500 Co, 270 Mo, 1280 Nb, and 19 Zr.

[d]500–kg heat produced in Teledyne Wha Chang Albany.

[e]All others 15– to 30–kg laboratory heats.

IRRADIATION CONDITIONS

Details of the recent conventional irradiation experiments at <430°C (i.e., the FFTF-MOTA,[5] HFIR 200J and 400J,[8] EBR-II COBRA-1A2,[9] EBR-II X-530,[10] and ATR A1[11, 12] experiments) are summarized in Table 2. The coneventional irradiation in the FFTF is referred to as non-DHCE experiment.

Table 2. Summary of irradiation experiments

Experiment ID	Subcapsule	Environment	Temperature (°C)	dpa	He/dpa Ratio
FFTF-nonDHCE	many	Li	427-600	14-46	-
FFTF-DHCE	many	Li	430-600	14-27	0.4-4.2
HFIR	200J	He	200	10	-
	400J	He	400	10	-
COBRA-1A2	V499	Li	395	36	-
	V495	Li	379	31	-
EBR-II X530	S8	Li	394	4	-
	S9	Li	390	4	-
ATR-A1	many	Li	138-285	4.7	-

IMPACT PROPERTIES

Charpy impact specimens of the 500-kg heat (#832665) and the 30-kg heat (BL-47) of V-4Cr-4Ti and the 15-kg heats of V-3Ti-1Si (BL-45) and V-5Ti (BL-46) were irradiated at <400°C in the EBR-II X-530 and ATR-A1 experiments. Orientation of the blunt-notched specimen is illustrated in Fig. 1, annealing history and irradiation parameters are summarized in Table 3.

Table 3. Summary of Charpy impact specimen orientation, annealing history, and irradiation parameters

Heat ID	Composition (wt.%)	Irradiation Experiment	Specimen Orientation	Blunt Notch Angle	Annealing	Irradiation Temperature (°C)	Irradiation Damage (dpa)	Irradiation Environment
BL-46	4.6Ti	EBRII-X530	L-S	30	coldworked	≈390	4	Li
BL-45	2.5Ti-1Si	EBRII-X530	L-T	30	coldworked	≈390	4	Li
BL-47	4.1Cr-4.3Ti	EBRII-X530	L-S or L-T	30 or 45	coldworked	≈390	4	Li
		ATR-A1	–	30 or 45	1 h at 1000°C[a]	≈202 or ≈270	4.7	Li
832665	3.8Cr–3.9Ti	EBRII-X530	–	30 or 45	two-stage anneal[b]	≈390	4	Li
		ATR-A1	–	30	1 h at 1000°C[a]	≈200 or ≈220	4.7	Li

[a]Annealed in laboratory in ion-pumped high vacuum.

[b]Annealed in factory in diffusion-pumped vacuum for 2 h at a nominal temperature between 1050-1070°C.

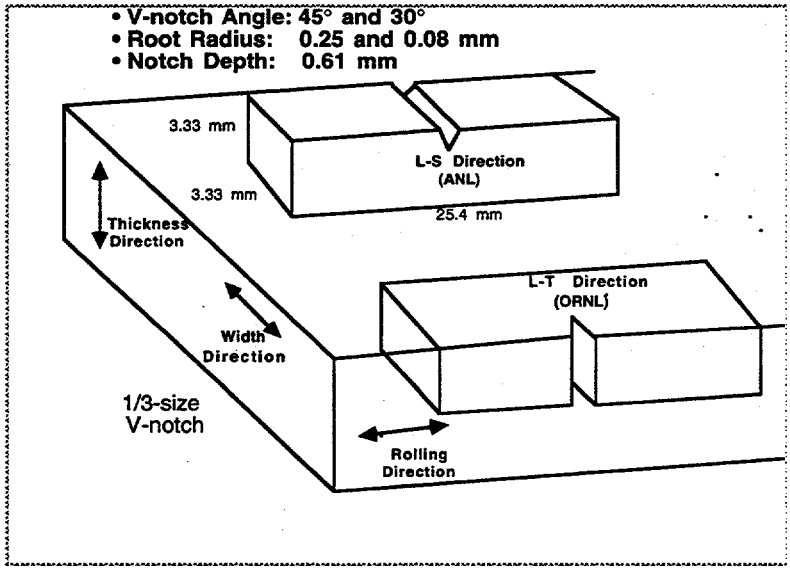

Fig. 1. Schematic illustration of the geometry and orientation of the Charpy impact specimen

Results of impact testing of the coldworked laboratory heats of V-4Cr-4Ti (BL-47), V-3Ti-1Si (BL-45), and V-5Ti (BL-46) that were irradiated to ≈4 dpa in Li in the EBR-II X-530 experiment are shown in Figs. 2, 3, and 4, respectively. Similar results obtained from the annealed specimens of the same heats that were irradiated to ≈34 dpa at ≈430°C in non-DHCE in FFTF[7] are also shown in the figures for comparison. The effect of specimen orientation of the coldworked material of V-4Cr-4Ti Heat BL-47 was very significant. Coldworked specimens of the heat machined in L-S orientation exhibited good impact properties even after irradiation at ≈390°C; in fact, the impact properties appear to be comparable to those of the annealed specimens irradiated at ≈427°C to 34 dpa in FFTF. Coldworked specimens of V-4Cr-4Ti Heat BL-47 that were machined in L-T orientation exhibited inherently inferior impact properties even before irradiation.

In contrast to the laboratory heat BL-47, the 500-kg heat (#832665) of V-4Cr-4Ti exhibited completely brittle characteristics after irradiation to ≈4 dpa at ≈390°C in the EBR-II X-530 experiment. This is shown in Fig. 5. Ductile behavior at room temperature could be restored only after post-irradiation reannealing at >650°C for ≈20 min. in high vacuum (see Fig. 6). The 3.8-mm-thick plate of Heat #832665 was inadvertently annealed in factory (nominally at ≈1050°C for 2 h in relatively poor vacuum in a diffusion-oil-pumped system), and the Charpy specimens machined out of the plate were annealed further in high vacuum in a clean ion- pumped system in laboratory.

Charpy impact specimens of the 500-kg heat (#832665) and the 30-kg heat (BL-47) of V-4Cr-4Ti were irradiated at 200-270°C in Li in the ATR-A1 experiment. Charpy specimens of both heats were machined out of coldworked plate, following annealing at 1000°C for 1 h in ion-pumped high vacuum. Results of impact testing of these specimens are shown in Fig. 7. Specimens from the laboratory heat BL-47 exhibited better impact properties than the 500-kg heat #832665, although the upper shelf energy was only ≈5 J and DBTT was as high as ≈60°C.

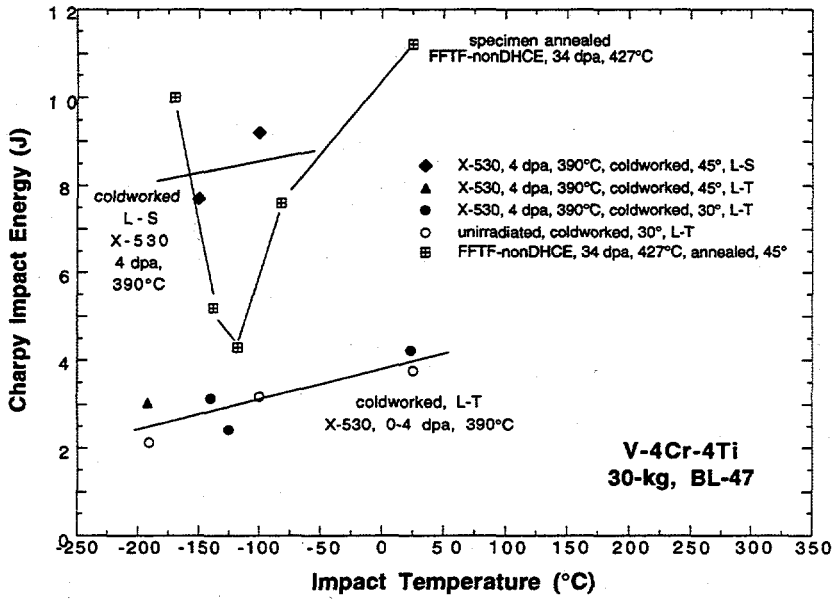

Fig. 2.

Impact properties of coldworked 30-kg heat of V-4Cr-4Ti (BL-47) irradiated to ≈4 dpa at ≈390°C in EBR-II X-530 experiment. Similar results from specimens annealed and irradiated to ≈34 dpa at ≈427°C in FFTF non-DHCE are also shown for comparison.

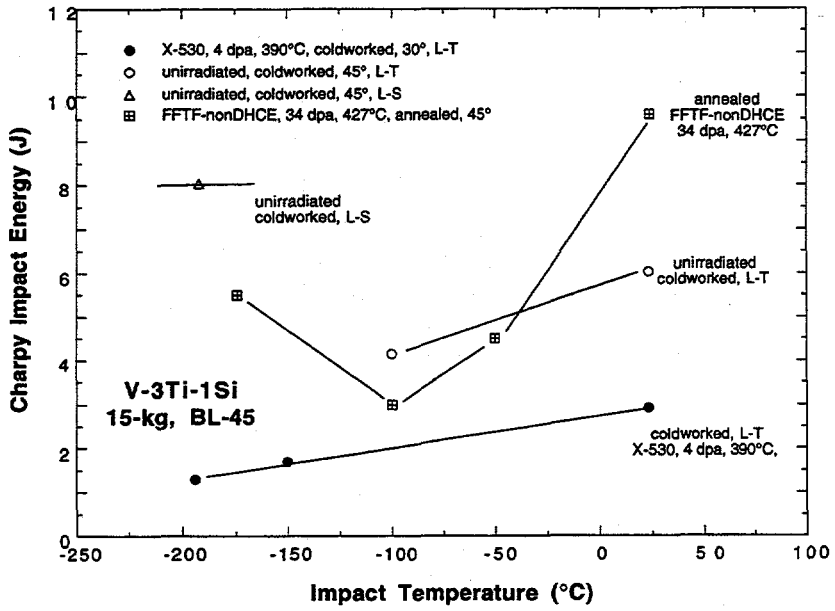

Fig. 3.

Impact properties of coldworked 15-kg heat of V-3Ti-1Si (BL-45) irradiated to ≈4 dpa at ≈390°C in EBR-II X-530 experiment. Similar results from specimens annealed and irradiated to ≈28 dpa at ≈430°C in FFTF non-DHCE are also shown for comparison.

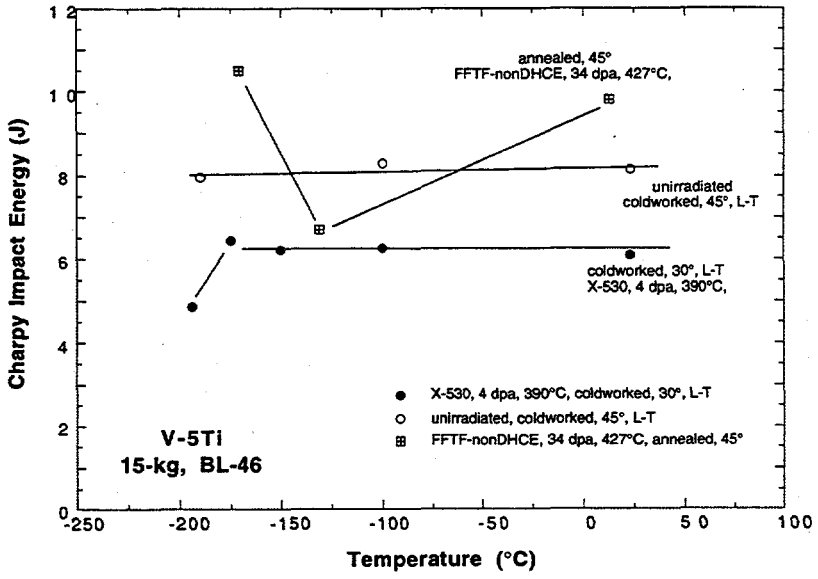

Fig. 4.

Impact properties of coldworked 15-kg heat of V-5Ti (BL-46) irradiated to ≈4 dpa at ≈390°C in EBR-II X-530 experiment. Similar results from specimens annealed and irradiated to ≈34 dpa at ≈427°C in FFTF non-DHCE are also shown for comparison.

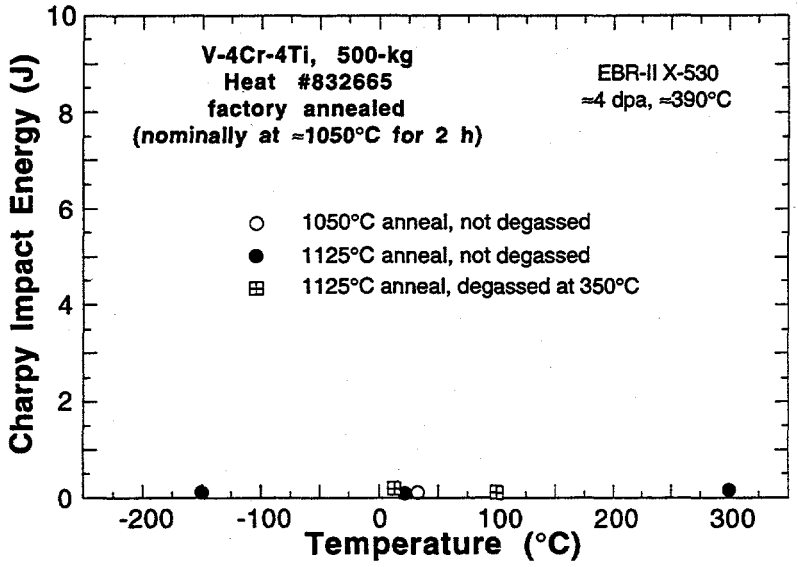

Fig. 5.

Impact properties of doubly annealed 500-kg heat of V-4Cr-4Ti (Heat #832665) irradiated to ≈4 dpa at ≈390°C in the EBR-II X-530 experiment, showing severe embrittlement.

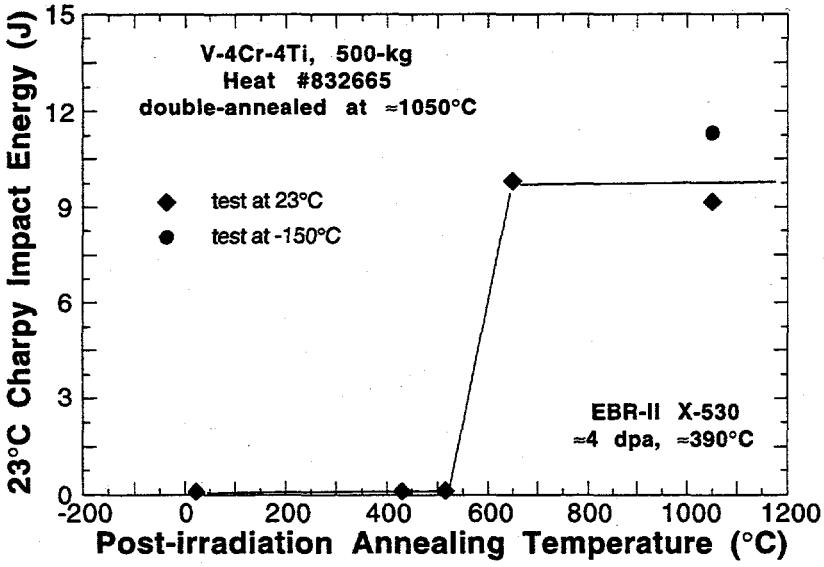

Fig. 6.

Room-temperature impact properties of 500-kg heat of V-4Cr-4Ti (Heat 832665) that were irradiated to ≈4 dpa at ≈390°C in the EBR-II X-530 experiment and reannealed for 20 min. in high vacuum.

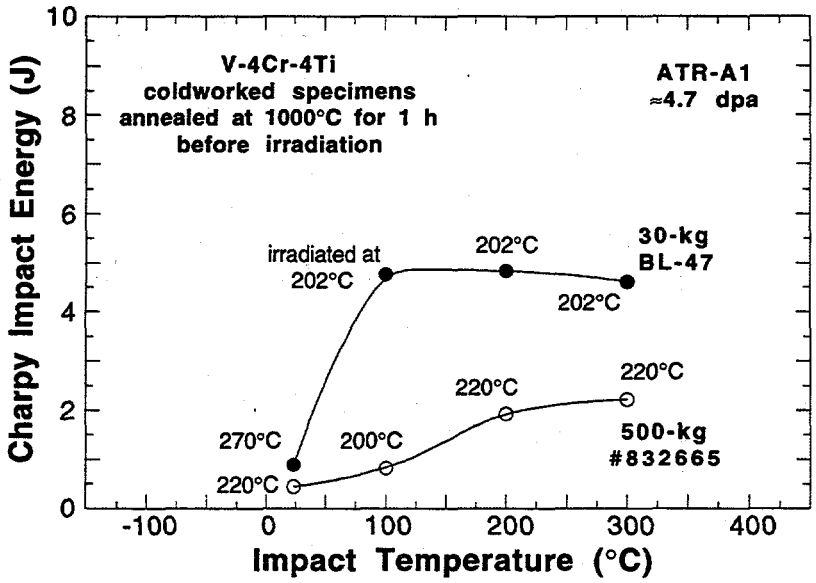

Fig. 7.

Impact properties of 500-kg and 30-kg heats of V-4Cr-4Ti irradiated to ≈4.7 dpa at ≈200-270°C in Li in the ATR-A1 experiment. All specimens were annealed at 1000°C for 1 h in an ion pump before irradiation.

CONCLUSIONS

1. The effect of specimen orientation on the impact properties of coldworked material of a 30-kg laboaratory heat of V-4Cr-4Ti (BL-47) was significant. Coldworked specimens of the heat machined in L-S orientation exhibited superior impact properties after irradiation at 390°C to ≈4 dpa. High impact energies observed at temperatures as low as -100 to -150°C are comparable to those observed for annealed specimens after irradiation at ≈427°C to ≈34 dpa. Coldworked specimens machined in L-T orientation exhibited, however, inferior impact properties even before irradiation.

2. The 500-kg heat of V-4Cr-4Ti (#832665) exhibited brittle characteristics after irradiation to ≈4 dpa at ≈390°C in the EBR-II X-530 experiment. Ductile behavior of this heat at room temperature could be restored after post-irradiation reannealing at >650°C for ≈20 min. in high vacuum.

3. Significant heat-to-heat variation in impact properties were observed for V-4Cr-4Ti after irradiation at 200-430°C. One laboratory heat exhibited consistently better impact properties than the 500-kg heat. The exact mechanism of the strong heat-to-heat variation is, however, not understood.

ACKNOWLEDGMENTS

The authors thank H.-C. Tsai and J. P. Robertson for irradiation and retrieval of the tensile and impact specimens, and L. J. Nowicki for impact testing.

REFERENCES

1. D. J. Alexander, L. L. Snead, S. J. Zinkle, A. N. Gubbi, A. F. Rowcliffe, and E. E. Bloom, "Effects of Irradiation at Low Temperature on V-4Cr-4Ti," in Fusion Reactor Materials, Semiannual Prog. Rep. DOE/ER-0313/20, Oak Ridge National Laboratory, Oak Ridge, TN (1996), pp. 87-95.

2. H. M. Chung, L. Nowicki, and D. L. Smith, "Tensile Properties of Vanadium Alloys Irradiated at 400°C in the HFIR," in Fusion Reactor Materials, Semiannual Prog. Rep. DOE/ER-0313/20, Oak Ridge National Laboratory, Oak Ridge, TN (1996), pp. 84-86.

3. H. M. Chung, L. Nowicki, and D. L. Smith, "Tensile Properties of Vanadium Alloys Irradiated at 200°C in the HFIR," in Fusion Reactor Materials, Semiannual Prog. Rep. DOE/ER-0313/22, Oak Ridge National Laboratory, Oak Ridge, TN (1997), pp. 29-32.

4. H. M. Chung, H.-C. Tsai, L. J. Nowicki, and D. L. Smith, "Tensile Properties of Vanadium Alloys Irradiated in EBR-II," ibid., pp. 18-21.

5. H. M. Chung, M. C. Billone, and D. L. Smith, "Effect of Helium on Tensile Properties of Vanadium Alloys," ibid., pp. 22-28.

6. S. J. Zinkle, D. J. Alexander, J. P. Robertson, L. L. Snead, A. F. Rowcliffe, L. T. Gibson, W. S. Eatherly, and H.-C. Tsai, "Effect of Fast Neutron Irradiation to 4 dpa at 400°C on the Properties of V-(4-5)Cr-(4-5)Ti Alloys," in Fusion Reactor Materials, Semiannual Prog. Rep. DOE/ER-0313/21, Oak Ridge National Laboratory, Oak Ridge, TN (1997), pp. 73-78.

7. B. L. Loomis, H. M. Chung, L. Nowicki, and D. L. Smith, J. Nucl. Mater. 212-215 (1994) 799-803.

8. A. W. Longest, J. E. Pawel, D. W. Heatherly, R. G. Sitterson, and R. L. Wallace, "Fabrication and Operation of HFIR–MFE RB* Spectrally Tailored Irradiation Capsules," in Fusion Reactor Materials, Semiannual Prog. Rep. DOE/ER-0313/14, Oak Ridge National Laboratory, Oak Ridge, TN (1993), pp. 14–40.

9. A. M. Ermi and M. L. Hamilton, "Preliminary Report on the Irradiation Parameters for the EBR-II COBRA-1A2 Test," in Fusion Reactor Materials, Semiannual Prog. Rep. DOE/ER-0313/18, Oak Ridge National Laboratory, Oak Ridge, TN (1995), pp. 63-78.

10. H.-C. Tsai, R. V. Strain, A. G. Hins, H. M. Chung, L. Nowicki, and D. L. Smith, "Vanadium Alloy Irradiation Experiment X530 in EBR-II," in Fusion Reactor Materials, Semiannual Prog. Rep. DOE/ER-0313/17, Oak Ridge National Laboratory, Oak Ridge, TN (1994), pp. 8-14.

11. H.-C. Tsai, R. V. Strain, I. Gomes, A. G. Hins, and D. L. Smith, "ATR-A1 Irradiation Experiment on Vanadium Alloys and Low Activation Steels," in Fusion Reactor Materials, Semiannual Prog. Rep. DOE/ER-0313/19, Oak Ridge National Laboratory, Oak Ridge, TN (1996), pp. 314-320.

12. H.-C. Tsai, R. V. Strain, I. Gomes, and D. L. Smith, "Status of ATR-A1 Irradiation Experiment on Vanadium Alloys and Low Activation Steels," in Fusion Reactor Materials, Semiannual Prog. Rep. DOE/ER-0313/22, Oak Ridge National Laboratory, Oak Ridge, TN (1997), pp. 303-326.

13. M. Satou, H. Koide, A. Hasegawa, K. Abe, H. Kayano, and H. Matsui, J. Nucl. Mater. 233-237 (1996) 447-451.

Tensile and Impact Properties of Vanadium-Base Alloys Irradiated at Low Temperatures in the ATR-A1 Experiment* H. Tsai, L. J. Nowicki, M. C. Billone, H. M. Chung, and D. L. Smith (Argonne National Laboratory)

Summary

Subsize tensile and Charpy specimens made from several V-(4-5)Cr-(4-5)Ti alloys were irradiated in the ATR-A1 experiment to study the effects of low-temperature irradiation on mechanical properties. These specimens were contained in lithium-bonded subcapsules and irradiated at temperatures between ≈200 and 300°C. Peak neutron damage was ≈4.7 dpa. Postirradiation testing of these specimens has begun. Preliminary results from a limited number of specimens indicate a significant loss of work-hardening capability and dynamic toughness due to the irradiation. These results are consistent with data from previous low-temperature neutron irradiation experiments on these alloys.

Objective

The objective of this task is to study the effects of low-temperature neutron irradiation on the mechanical properties of vanadium-base alloys. The irradiation was conducted in the ATR-A1 experiment, a collaborative effort between the U.S. Department of Energy and the Japanese Monbusho.

Background

Vanadium-base alloys [1,2] are attractive candidate structural materials for fusion reactors because of their intrinsic low activation, favorable thermal-physical properties, and good compatibility with lithium. The primary candidates are alloys in the V-(4-5)Cr-(4-5)Ti class [3]. Until a few years ago, with essentially all irradiation testing performed in fast reactors at test temperatures >400°C, these alloys also displayed significant resistance to radiation damage. However, recent irradiation studies [4,5] at lower temperatures (≈80-400°C), have shown significantly reduced resistance to radiation. From several irradiation experiments conducted at ≈80-400°C, it has been reported that both the V-4Cr-4Ti alloys (from the 500-kg Heat 832665 and Laboratory Heat BL-47) and the V-5Cr-5Ti alloy (from Laboratory Heat BL-63) exhibited low uniform elongation, i.e., loss of work-hardening ability, during tensile testing. After the low-temperature irradiations, these alloys also exhibited significant embrittlement, manifested by low impact energy and high ductile-brittle-transition temperature (DBTT). The purpose of the ATR-A1 experiment was to further explore how this temperature sensitivity affects irradiation behavior.

Experimental Procedure

ATR-A1 Irradiation History

The ATR-A1 irradiation experiment, [6,7] consisting of 15 vertically stacked, stainless steel subcapsules, was carried out in the Advanced Test Reactor (ATR). The test specimens were contained inside gadolinium thermal neutron filters (to minimize V-to-Cr transmutation) in the subcapsules and thermally bonded with lithium. The irradiation was conducted in the A10 channel of the reactor in Cycles 108A, 108B, and 109A. The total exposure was 133 effective full power days and the achieved peak neutron damage was 4.7 displacements per atom (dpa) in the test materials. The calculated temperatures and dpa values for specimens in each subcapsule are given in Table 1. Following the irradiation, the subcapsules were disassembled and the lithium bond was removed with liquid ammonia and alcohol. The U.S. specimens have been

* Work supported by U.S. Department of Energy, Office of Fusion Energy Research, under Contract W-31-109-Eng-38.

disseminated to Oak Ridge National Laboratory (ORNL), Pacific Northwest National Laboratory (PNNL), and Argonne National Laboratory (ANL).

Table 1. Calculated irradiation conditions of ATR-A1 experiment

Axial Position	Subcapsule Number	Test Materials	Specimen Temp. (°C)[a]	Dpa
15 (top)	AS1	V-alloys	139/144	0.7
14	AS3	V-alloys	186/194	1.5
13	AS4	Fe-alloys	263/277	2.2
12	AS5	V-alloys	198/212	3.0
11	AS6	V-alloys	223/234	3.5
10	AS8	V-alloys	246/259	3.9
9	AS9	V-alloys	273/286	4.3
8	AS10	V-alloys	288/302	4.6
7	AS11	V-alloys	285/300	4.7
6	AS12	V-alloys	282/295	4.5
5	AS14	V-alloys	284/300	4.1
4	AD16	Fe-alloys	337/355	3.8
3	AS7	V-alloys	287/303	3.0
2	AS13	V-alloys	245/258	2.3
1	AS17	V-alloys	204/213	1.5

[a] First value is for Cycles 108A and 109A, with a lobe power of 25 MW; second value is for Cycle 108B, with a lobe power of 27 MW. Rounded averages of the two are used in this report.

Test Materials and Specimens

The test specimens for this study were prepared from three V-(4-5)Ti-(4-5)Cr alloy heats: 832665, BL-47, and T-87. The nominal compositions of these three alloys are shown in Table 2.

Table 2. Composition of the three alloys investigated

Heat Number	Ingot Size (kg)	Nominal Composition (wt.%)	Impurity Content (wppm)			
			O	N	C	Si
832665	500	V-3.8Cr-3.9Ti	310	85	80	780
BL-47	30	V-4.1Cr-4.3Ti	350	220	200	870
T87	30	V-5.0Cr-5.0Ti	380	90	110	550

The tensile specimens for the study at ANL consisted of 15 base-metal specimens and two weldment specimens. The nominal gauge dimensions of the base-metal specimens, size SS-3, were 0.76 mm thick x 1.52 mm wide x 7.6 mm long. The specimens were machined from cold-rolled sheets with the longitudinal direction parallel to the final rolling direction of the sheets. After the machining, the base-metal tensile specimens were annealed in a vacuum that was better than 10^{-7} torr at 1000°C for 1 h before the irradiation.

The two weldment specimens were prepared by bead-on-plate welding onto a piece of annealed plate with a laser beam. The beam traveled in a direction that was perpendicular to the rolling direction of the plate. After the welding, the specimens, also of SS-3 size, were machined from the plate with the weldment at the center and across the width of the gauge section. The

weldment specimens were given only a hydrogen-outgassing at 400°C for 1 h in vacuum (i.e., without a postweld heat treatment or the nominal 1000°C anneal) prior to the irradiation.

The Charpy specimens for the study at ANL consisted of 19 base-metal specimens and eight weldment specimens. The base-metal specimens were 1/3-size, i.e., 3.3 mm thick x 3.3 mm wide x 25.4 mm long, machined from cold-rolled plates; they contained a 30°, 0.61-mm-deep notch with a root radius of 0.08 mm, except for some of the BL-47 specimens, which had a notch angle of 45° from an earlier fabrication campaign. The notch orientation (i.e., crack propagation direction) was perpendicular to the final rolling direction: L-S (crack into the thickness direction of the plate) for the 832665 and T87 specimens, and L-T (crack into the width of the plate) for the BL-47 specimens. Three of the 832665 specimens were fatigue precracked. After the machining/precracking, the base-metal specimens were annealed in vacuum at 1000°C for 1 h before the irradiation.

The weldment Charpy specimens were prepared by bead-on-plate welding with an electron-beam (EB) or tungsten-inert-gas (TIG) welder on annealed plates. The direction of weld travel was perpendicular to the rolling direction of the plate. After welding, the specimens were prepared with the V-notch in the weldment in the L-S direction. Although the EB weld specimens were 1/3-size, the TIG weld specimens were smaller, 1.5 (1.5 x 1.5 x 20.0 mm) because of the limit on the irradiation space. Similar to the tensile weldment specimens, the Charpy weldment specimens were given only a hydrogen-outgassing treatment at 400°C for 1 h in vacuum but no postweld heat treatment or annealing before the irradiation.

The list of tensile and Charpy specimens from the ATR-A1 experiment for investigation at ANL are shown in Tables 3 and 4, respectively.

Table 3. Inventory of ATR-A1 tensile specimens for the investigation at ANL

Specimen ID No.	Specimen Type[a]	Heat	Subcapsule	Irrad. Temp.(C)	dpa
71-A	SS-3	832665	AS1	139/144	0.7
71-B	SS-3	832665	AS8	246/259	3.9
71-C	SS-3	832665	AS8	246/259	3.9
71-D	SS-3	832665	AS9	273/286	4.3
71-E	SS-3	832665	AS9	273/286	4.3
71-F	SS-3	832665	AS9	273/286	4.3
47-A	SS-3	BL-47	AS1	139/144	0.7
47-B	SS-3	BL-47	AS17	204/213	1.5
47-C	SS-3	BL-47	AS17	204/213	1.5
47-D	SS-3	BL-47	AS10	288/302	4.6
47-E	SS-3	BL-47	AS10	288/302	4.6
72-A	SS-3	T87	AS1	139/144	0.7
72-B	SS-3	T87	AS17	204/213	1.5
72-C	SS-3	T87	AS14	284/300	4.1
72-D	SS-3	T87	AS14	284/300	4.1
71-LZ-A	SS-3	832665-weld	AS8	246/259	3.9
71-LZ-B	SS-3	832665-weld	AS10	288/302	4.6

[a] SS-3: 25.4 mm overall specimen length, gauge 0.76 mm thick x 1.52 mm wide x 7.6 mm long mm long.

Table 4. Inventory of ATR-A1 Charpy Specimens for the Investigation at ANL

Specimen ID No.	Heat	Configuration[a]	Weld[b]	Subcap.	Irrad. Temp(°C)	dpa
71-A	832665	1/3, M, 30, L-S	–	AS1	139/144	0.7
71-B	832665	1/3, M, 30, L-S	–	AS5	198/212	3.0
71-C	832665	1/3, M, 30, L-S	–	AS6	223/234	3.5
BL71W-39	832665	1/3, M, 30, L-S	–	AS6	223/234	3.5
BL71W-54	832665	1/3, M, 30, L-S	–	AS6	223/234	3.5
BL71W-20	832665	1/3, M, 30, L-S	–	AS9	273/286	4.3
BL71W-21	832665	1/3, M, 30, L-S	–	AS10	288/302	4.6
BL71W-22	832665	1/3, M, 30, L-S	–	AS10	288/302	4.6
BL71W-30	832665	1/3, M, 30, L-S	–	AS10	288/302	4.6
47-09	BL-47	1/3, M, 30, L-S	–	AS9	273/286	4.3
47-A	BL-47	1/3, M, 45, L-T	–	AS1	139/144	0.7
47-B	BL-47	1/3, M, 45, L-T	–	AS11	285/300	4.7
47-C	BL-47	1/3, M, 45, L-T	–	AS11	285/300	4.7
47-D	BL-47	1/3, M, 45, L-T	–	AS11	285/300	4.7
47-E	BL-47	1/3, M, 45, L-T	–	AS17	204/213	1.5
47-F	BL-47	1/3, M, 45, L-T	–	AS17	204/213	1.5
47-G	BL-47	1/3, M, 45, L-T	–	AS17	204/213	1.5
71E-A	832665	1/3, M, 30, L-S	EB	AS5	198/212	3.0
71E-B	832665	1/3, M, 30, L-S	EB	AS5	198/212	3.0
71E-C	832665	1/3, M, 30, L-S	EB	AS7	287/303	3.0
71E-D	832665	1/3, M, 30, L-S	EB	AS7	287/303	3.0
47-H	BL-47	1.5, M, 30, L-S	TIG	AS9	273/286	4.3
47-I	BL-47	1.5, M. 30, L-S	TIG	AS9	273/286	4.3
47-J	BL-47	1.5, M, 30, L-S	TIG	AS9	273/286	4.3
47-K	BL-47	1.5, M, 30, L-S	TIG	AS9	273/286	4.3
BL71W-27	832665	1/3, P, 30, L-S	–	AS14	284/300	4.1
BL71W-40	832665	1/3, P, 30, L-S	–	AS14	284/300	4.1
BL71W-45	832665	1/3, P, 30, L-S	–	AS14	284/300	4.1

[a] 1/3-size: 3.3 x 3.3 x 25.4 mm; 1.5-size: 1.5 x 1.5 x 20.0 mm;
M: machined blunt notch; P: precracked notch;
30: notch angle of 30°; 45: notch angle of 45°;
L-S or L-T: notch (crack propagation) direction.

[b] EB: electron beam welding; TIG: tungsten-inert-gas welding.

Results and Discussion

Tensile Tests

Four tensile tests, one each for the 832665, T87, and BL-47 base metal and one for the laser weldment, have been completed. All four tests were conducted in high-purity argon at 290°C, near the specimens' irradiation temperature. The tests were performed with an Instron machine without an extensometer attached to the specimen. Extensions due to the slack in the grips and the deformation of the load frame were subtracted from the crosshead displacement to obtain the correct gauge section extension. The strain rate for all of the tests was 1.09×10^{-3}/s.

In all four cases, the yield strength of the material increased significantly over the nonirradiated material because of the irradiation. At the same time, a significant loss of work-hardening ability was manifested by the small measured uniform elongation. After yielding, the base-metal

specimens failed rapidly because of plastic instability. The recorded load-crosshead displacement curve for the T87 heat specimen is shown in Fig. 1. The peak load of 108 kg corresponds to an ultimate tensile strength of 941 MPa. The load-displacement profiles for other base-metal specimens are similar. The weld specimen was extremely brittle and displayed no measurable plastic deformation before it abruptly failed at a calculated engineering stress of 607 MPa. The tensile test results are summarized in Table 5.

Table 5. Summary of tensile test results for a limited number of ATR-A1 specimens.[a]

Specimen ID No.	Material	0.2% offset Yield Strength (Mpa)	Ultimate Tensile Strength (MPa)	Uniform Elongation (%)	Total Elongation (%)
71-F	832665	945 (208)	983 (343)	0.7 (19)	2.1 (27)
47-E	BL-47	844 (229)	866 (381)	0.5 (18)	4.9 (24)
72-D	T87	880 (262)	941 (405)	1.1 (14)	4.1 (21)
71-LZ-B	832665-weld	N/A[b]	N/A	≈0	≈0

[a] All tests were conducted at 290°C at a strain rate of 1.09×10^{-3}/s. Values in parentheses are those of nonirradiated control materials at comparable temperatures (300-337°C) [8].

[b] Specimen failed at 607 MPa with no measurable plastic deformation before failure.

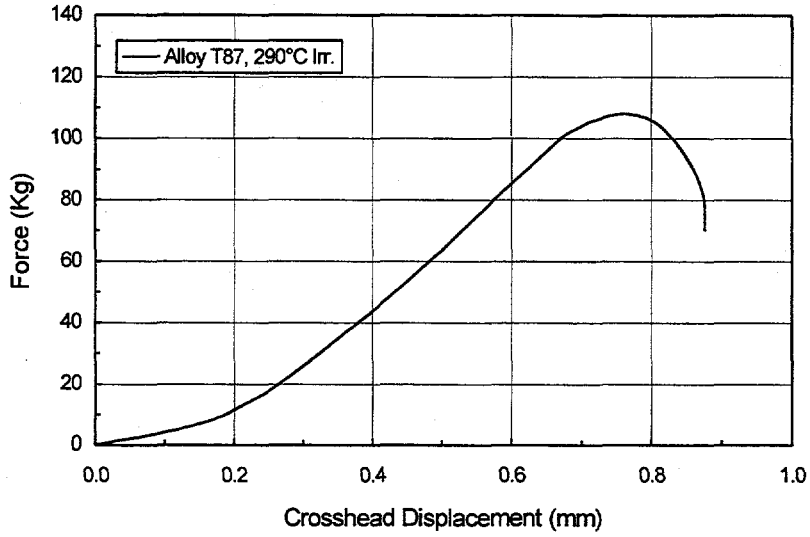

Fig. 1. Load-displacement curve for specimen 72-D (Alloy T87) after irradiation in the ATR-1.

Impact Tests

Seventeen Charpy impact tests have been completed. The tests were conducted in air with a Dynatup drop-weight tester. The specimen temperature during the impact test was measured with a thermocouple that was spot-welded to the end of the specimen. For tests in which temperatures were above ambient, a hot-air blower was used to provide the heating. None of the specimens were degassed for hydrogen before the impact tests, because that procedure has been shown to have little effect on the measured impact properties [4,9]. Furthermore, if the

established degassing procedure were to be used, it would require that the specimens be heated to 400°C, which would be substantially above the irradiation temperatures.

The test data show that the ATR-A1 irradiation caused a significant drop of the upper-shelf energy of the material and a marked increase in the DBTT. The results for the blunt-notch base-metal specimens of the 832665 and BL-47 heats are shown in Fig. 2. For the 832665 heat irradiated at either ≈230 or 300°C, the upper-shelf energy is between 2 and 3 J, which is substantially below the ≈12-15 J for the nonirradiated material [9,10]. Although the DBTT could not be accurately determined because the number of specimens was limited, within the resolution of the data, it appears that the DBTT for the irradiated 832665 material is ≈150-200°C, which is significantly higher than the approximate -190°C for the nonirradiated control specimens. Results for the irradiated BL-47 material are approximately the same. (The upper-shelf energy and DBTT of the nonirradiated BL-47 material are ≈11-14 J and -190°C, respectively [11].) The BL-47 specimens irradiated at 300°C appear to have a slightly lower upper-shelf energy (≈2-3 J) than those irradiated at ≈210°C (≈5 J). This temperature dependence was noted before by D. J. Alexander et al. [4], who, based on resistivity measurements, attributed this effect to the increased effectiveness of defect clusters as barriers to dislocation movement at temperatures >200°C due to increased oxygen and carbon migration to the clusters.

As expected, and consistent with previous findings, the precracked 832665 specimens showed even lower absorbed energy than did their blunt-notch siblings. The measured data were 0.5 J at 23°C and 0.7 J at 290°C.

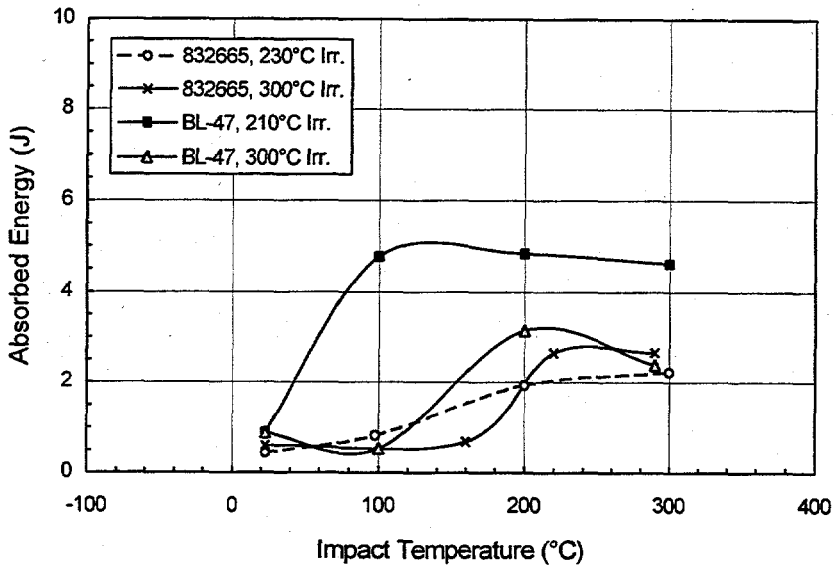

Fig. 2. Impact properties of 832665 and BL-47 specimens (1/3 size, blunt notch) after the ATR-A1 irradiation. Upper-shelf energies for the irradiated specimens, ≈2-5 J, are substantially lower than those for nonirradiated controls, ≈11-15 J.

Future Activities

The remainder of the tensile and impact tests will be completed. The fracture surfaces of selected specimens will be examined by scanning electron microscopy to delineate the fracture mode. Areal reduction of tensile specimens will be measured. Attempts will be made to prepare transmission electron microscopy specimens from the gauge section of tensile specimens near the rupture to study the interplay between dislocation channeling and hardening.

Conclusions

Results from testing three V-(4-5)Ti-(4-5)Cr alloys irradiated in the ATR-A1 experiment to ≈4-5 dpa confirmed their susceptibility to hardening and embrittlement during low-temperature neutron irradiation. Yield strength increased approximately three-fold to ≈800-900 MPa, whereas uniform elongation decreased to ≈1% or less. The impact properties of these materials were also degraded significantly.

References

1. D. L. Smith, B. A. Loomis, H. M. Chung, Plasma Devices and Operations, 3, (1994), pp. 167-179.

2. B. A. Loomis and D. L. Smith, J. Nucl. Mater., 191-194 (1992), pp. 84-91.

3. B. A. Loomis, H. M. Chung, L. J. Nowicki, and D. L. Smith, J. Nucl. Mater., 212-215 (1994), pp. 799-803.

4. D. J. Alexander, L. L. Snead, S. J. Zinkle, A. N. Gubbi, A. F. Rowcliffe, and E. E. Bloom, Fusion Materials Semiannual Progress Report, DOE/ER-0313/20, June 1996, pp. 87-95.

5. H. M. Chung, H. Tsai, L. Nowicki, and D. L. Smith, Fusion Materials Semiannual Progress Report, DOE/ER-0313/22, June 1997, pp. 18-21.

6. H. Tsai, R. V. Strain, I. Gomes, A. G. Hins, and D. L. Smith, Fusion Materials Semiannual Progress Report, DOE/ER-0313/19, Dec. 1995, pp. 314-320.

7. H. Tsai, R. V. Strain, I. Gomes, and D. L. Smith, Fusion Materials Semiannual Progress Report, DOE/ER-0313/20, June 1996, pp. 315-318.

8. M. C. Billone, "Revised ANL-Reported Tensile Data for Unirradiated and Irradiated (FFTF, HFIR) V-Ti and V-Cr-Ti Alloys," this report.

9. H. M. Chung, L. Nowicki, and D. L. Smith, Fusion Materials Semiannual Progress Report, DOE/ER-0313/18, March 1995, pp. 253-258.

10. A. N. Gubbi, A. F. Rowcliffe, D. J. Alexander, M. L. Grossbeck, and W. S. Eatherly, Fusion Materials Semiannual Progress Report, DOE/ER-0313/18, March 1995, pp. 203-213.

STRAIN RATE DEPENDENCE OF THE TENSILE PROPERTIES OF V-(4-5%)Cr-(4-5%)Ti IRRADIATED IN EBR-II AND HFBR — S. J. Zinkle, L. L. Snead, J. P. Robertson and A. F. Rowcliffe (Oak Ridge National Laboratory)

OBJECTIVE

The objective of this report is to summarize recent data on the effect of strain rate on the temperature-dependent tensile properties of neutron-irradiated V-(4-5)Cr-(4-5)Ti .

SUMMARY

Elevated temperature tensile tests performed on V-(4-5)Cr-(4-5)Ti indicate that the yield stress increases with increasing strain rate for irradiation and test temperatures near 200°C, and decreases with increasing strain rate for irradiation and test temperatures near 400°C. This observation is in qualitative agreement with the temperature-dependent strain rate effects observed on unirradiated specimens, and implies that some interstitial solute remains free to migrate in irradiated specimens. Additional strain rate data at different temperatures are needed.

PROGRESS AND STATUS

Introduction

One of the common features in the load-elongation curve of body-centered cubic tensile specimens is the appearance of serrations in the work-hardening portion of the curve at elevated test temperatures. Numerous studies have concluded that this "dynamic strain aging" effect is associated with the migration of interstitial solute atoms to dislocations during the deformation (e.g., refs. 12-18 in ref. [1]). In vanadium and vanadium alloys, dynamic strain aging is observed at temperatures above ~300°C for typical tensile test strain rates of ~10^{-4} to 10^{-3} s^{-1} [1,2]. At low test temperatures and high strain rates, where dynamic strain aging is not observed due to the limited migration of interstitial solute atoms, the yield and ultimate strength increase with increasing strain rate, i.e., the hardening strain rate exponent is positive. The appearance of dynamic strain aging at high temperatures is accompanied by a shift in hardening strain rate exponent to negative values.

Figure 1 shows the results of some recent strength measurements on unirradiated type SS-3 sheet tensile specimens of the U.S. fusion program heat of V-4Cr-4Ti (heat #832665) tested at different strain rates and temperatures [3]. At room temperature, the tensile strength (measured at 8% strain) increased monotonically with increasing strain rate between 10^{-4} and 1 s^{-1}. The value of the hardening strain rate exponent at 25°C was m = 0.024 , where m is defined by [4]

$$m = \frac{1}{\sigma}\frac{\partial \sigma}{\partial \ln \dot{\varepsilon}} \qquad (1)$$

where σ is the stress and $\dot{\varepsilon}$ is the strain rate. Conversely, at temperatures $\geq$400°C, the tensile strength *decreased* monotonically with increasing strain rate between 10^{-5} and 10^{-1} s^{-1}. The value for the strain rate exponent ranged from m = - 0.013 at 400°C to m = - 0.025 at 600°C. Tensile tests performed at 300°C clearly showed the transition from negative to positive strain rate exponents as the strain rate was increased above 10^{-3} s^{-1}. Similar temperature-dependent behavior was also observed for the lower yield point strain rate exponent. Strain rate experiments were performed on several neutron-irradiated V-(4-5)Cr-(4-5)Ti tensile specimens in order to determine the magnitude of the strain rate exponent at temperatures above and below 300°C.

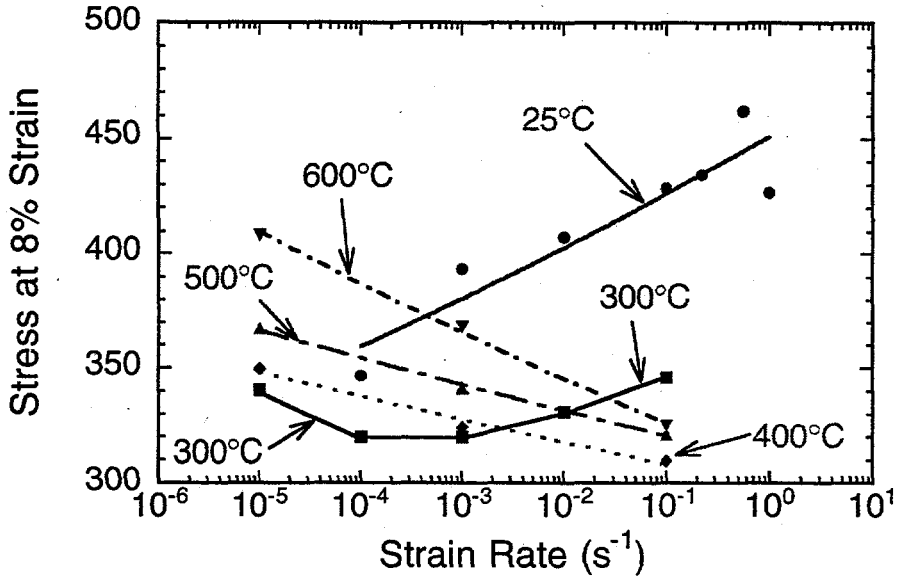

Fig. 1. Effect of strain rate on the tensile strength (measured at 8% strain) of V-4Cr-4Ti tested at temperatures between 25 and 600°C [3]. The curves for data obtained at 25°C and 400-600°C are least square fits using equation 1.

Experimental Procedure

Type SS-3 sheet tensile specimens (nominal gage dimensions 0.76 × 1.52 × 7.6 mm) from two recent neutron irradiation experiments [5,6] were selected for the strain rate study. The first set of specimens were fabricated from the 500 kg US fusion program heat of V-4Cr-4Ti (heat 832665) and were irradiated at 200°C to a dose of 0.5 dpa in the High Flux Beam Reactor [5]. The second set of specimens were fabricated from mill-annealed (1050°C) or cold-rolled and annealed (1050°C) plates of the BL-63 heat of V-5Cr-5Ti, and were irradiated at 400°C to a dose of 4 dpa in the EBR-II X530 irradiation experiment [6]. Following irradiation, the specimens were tensile tested in vacuum (<2.5×10^{-6} torr) at the irradiation temperature at constant crosshead speeds ranging from 0.025 to 12.7 mm/minute, which corresponds to initial strain rates of 5.6×10^{-5} to 0.028 s^{-1}. Further experimental details are given elsewhere [5,6].

Results and Discussion

The tensile properties of the irradiated V-(4-5)Cr-(4-5)Ti specimens tested at different strain rates are listed in Table 1. The relatively low irradiation temperatures used for this study caused considerable radiation hardening with an accompanying reduction in strain hardening capacity at all strain rates investigated. The uniform elongation in the specimens irradiated at 200 and 400°C were ~0.1 and 1% , respectively, which may be compared to the unirradiated uniform elongations in these alloys of15-20% at 200-400°C. The tensile curves in the specimens irradiated at 200°C were characterized by a yield peak at elongations <0.2%, followed by a monotonically decreasing engineering stress with increasing elongation. A significant change in the slope of the engineering stress-strain curve in these specimens occurred at elongations of ~0.2-0.4% and this Table 1. Summary of strain rate data on irradiated V-(4-5)Cr-(4-5)Ti specimens. The yield strength was determined at 0.2% plastic offset for the specimens irradiated at 400°C, whereas the lower yield point was used for the specimens irradiated at 200°C. The specimens labeled "63C" were cold-rolled and annealed at 1050°C prior to irradiation.

Specimen ID, dpa, T_{irr}	Test conditions	Yield strength	Ultimate strength	Uniform elongation	Total elongation
WH11, 0.5dpa, 203°C	200°C, 5.6×10^{-5} s^{-1}	587 MPa*	612 MPa[a]	0.1%	9.0%
WH08, 0.5dpa, 203°C	200°C, 1.1×10^{-3} s^{-1}	580 MPa*	650 MPa[a]	0.05%	9.4%
WH02, 0.5dpa, 207°C	200°C, 1.1×10^{-3} s^{-1}	603 MPa*	652 MPa[a]	0.05%	8.7%
WH10, 0.5dpa, 203°C	200°C, 0.028 s^{-1}	605 MPa*	656 MPa[a]	<0.1%	9.3%
WH03, 0.5dpa, 207°C	20°C, 1.1×10^{-4} s^{-1}	655 MPa*	672 MPa[a]	0.67%	10.3%
WH01, 0.5dpa, 207°C	20°C, 1.1×10^{-3} s^{-1}	657 MPa*	732 MPa[a]	<0.1%	9.9%
63C10/12,4dpa, 400°C	400°C, 5.6×10^{-5} s^{-1}	734 MPa	793 MPa	1.4%	7.9%
63C10/11, 4dpa, 400°C	400°C, 1.1×10^{-3} s^{-1}	723 MPa	765 MPa	0.95%	7.0%
63/4, 4dpa, 400°C	400°C, 1.1×10^{-3} s^{-1}	733 MPa	774 MPa	1.2%	7.3%
63/5, 4dpa, 400°C	400°C, 0.028 s^{-1}	734 MPa	775 MPa	1.1%	6.0%

*lower yield point
[a]upper yield point

was defined to be the location of the lower yield point, as discussed elsewhere [5]. Yield drops were not observed in the specimens irradiated to 4 dpa at 400°C.

From inspection of Table 1, the lower yield point and the ultimate strength of the specimens irradiated to 0.5 dpa at 200°C exhibited a slightly positive strain rate exponent. The magnitude of the irradiated strain rate exponent at 200°C was considerable smaller than that observed at room temperature in unirradiated specimens (Fig. 1). Conversely, the 0.2% yield strength and ultimate strength of the specimens irradiated to 4 dpa at 400°C were nearly independent of strain rate or exhibited a slightly negative strain rate exponent. This behavior at 400°C is qualitatively similar to that observed in unirradiated specimens, although the magnitude of the negative strain rate exponent appears to be considerably reduced in the irradiated specimens. The value of the irradiated strain rate exponent varied from m=0.011 at 200°C to m= -0.004 at 400°C. The irradiated ultimate tensile strength data are plotted in Figure 2 along with some recent data obtained on the 500 kg heat of V-4Cr-4Ti following neutron irradiation to ~5 dpa at 330°C [7]. The data by van Osch [7] suggest that the irradiated strain rate exponent does not become negative for temperatures at least as high as 330°C, in contrast to the unirradiated behavior where the strain rate exponent became negative at temperatures above 300°C.

The appearance of a negative strain rate exponent is an indication of a significant interstitial solute concentration in the matrix which is free to migrate to dislocations during tensile testing. This implies that some of the C, O, N solute in the irradiated V-Cr-Ti alloys remains dissolved in the matrix and is not contained in titanium oxycarbonitride precipitates or solute-point defect clusters. It is interesting to note that the apparent change in the strain rate exponent from positive values to negative values at temperatures above ~330°C in the irradiated specimens occurred even though serrated stress-strain behavior was not observed in the stress-strain curve (due to the low strain hardening capacity in the irradiated specimens). The magnitude of the irradiated strain rate exponent at 200°C is smaller than the room temperature unirradiated value, which may be due to the effect of point defect clusters on the strain rate dependence [8]. Defect clusters exhibit a positive strain rate exponent, and would be included in the experimentally measured strain rate exponent of irradiated materials. The positive defect cluster strain rate term may also be partially responsible for the small negative strain rate exponent observed in the vanadium alloys

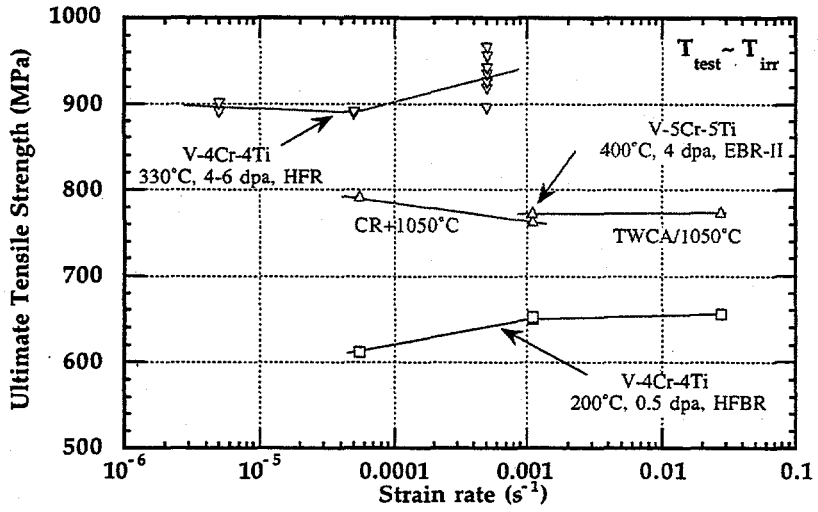

Fig. 2. Effect of temperature ($T_{test} \sim T_{irr}$) and strain rate on the tensile strength of neutron-irradiated V-(4-5)Cr-(4-5)Ti tensile specimens. Data obtained by van Osch [7] on round (4 mm diam.) tensile specimens are also included in this plot.

irradiated and tested at 400°C. Interstitial solute bound to defect clusters or small precipitates would also decrease the magnitude of the strain rate exponent at 400°C.

Additional strain rate data on irradiated specimens are clearly needed in order to establish the behavior of the strain rate exponent behavior as a function of irradiation temperature and dose. Such strain rate investigations (performed at different test temperatures) would provide useful information on the barrier strengths of defect clusters in irradiated vanadium alloys [8].

REFERENCES

1. A. N. Gubbi, A. F. Rowcliffe, W. S. Eatherly, and L. T. Gibson, in Fusion Materials Semiannual Progress Report for Period ending June 30, 1996, DOE/ER-0313/20 (Oak Ridge National Lab, 1996) p. 38.
2. H. Yoshinaga, K. Toma, K. Abe, and S. Morozumi, Philos. Mag. 23 (1971) 1387.
3. A.N. Gubbi and A.F. Rowcliffe, presented at 8th Int. Conf. on Fusion Reactor Materials, Sendai, J. Nucl. Mater. (1997).
4. P. Haasen, Physical Metallurgy (Cambridge Univ. Press, New York, 1978) p. 26.
5. L. L. Snead et al., presented at 8th Int. Conf. on Fusion Reactor Materials, Sendai, Japan; Fusion Materials Semiann. Prog. Report for period ending Dec. 31 1997, DOE/ER-0313/23 (1997) in press.
6. S. J. Zinkle et al., in Fusion Materials Semiannual Progress Report for Period ending December 31, 1996, DOE/ER-0313/21 (Oak Ridge National Lab, 1996) p. 73.
7. E. V. van Osch, 8th Int. Conf. on Fusion Reactor Materials, Sendai, J. Nucl. Mater. (1997) submitted.
8. T. J. Koppenaal and R. J. Arsenault, Metall. Reviews 16 (1971) 175.

SUMMARY OF THE INVESTIGATION OF LOW TEMPERATURE, LOW DOSE RADIATION EFFECTS ON THE V-4Cr-4Ti ALLOY — L. L. Snead, S. J. Zinkle, D. J. Alexander, A. F. Rowcliffe, J. P. Robertson, and W. S. Eatherly (Oak Ridge National Laboratory)

OBJECTIVE

This paper presents a summary of the results obtained from the HFBR-V1 through -V4 capsules which investigated the effects of low-dose, low-temperature neutron irradiation on the mechanical behavior of V-4Cr-4Ti alloys.

SUMMARY

Experimental details, raw data, method of analysis and results are presented for the low-temperature, low-dose HFBR-V1 through V4 irradiation experiments conducted at ORNL on V-4Cr-4Ti specimens (U.S. Fusion Program Heat #832665). Four separate capsules were irradiated in the V-15 and V16 In-Core Thimbles of the High Flux Beam Reactor at the Brookhaven National Laboratory to doses of 0.1 or 0.5 dpa at temperatures between 100 and 505°C. Testing included microhardness, electrical resistivity, tensile properties, and Charpy impact properties.

PROGRESS AND STATUS

Experimental Details

The V-4Cr-4Ti alloy used in this study was procured from Teledyne Wah Chang Albany (TWCA) and designated the U.S. Fusion Program Heat #832665. The interstitial impurity concentrations in this alloy were approximately 300 wppm O, 85 wppm N, and 80 wppm C [1,2]. All materials were annealed by TWCA at 1050°C for 1 or 2 hours with some receiving 50% cold work [2]. All materials used in the four irradiation capsules were nominally the same chemistry, although the specimens were machined from different plate stock provided by Argonne National Laboratory to ORNL (cf. Table 1). Specimens were electro-discharge machined (EDM) by the same machine shop into miniature Charpy vee-notch (CVN) impact specimens, type SS-3 miniature sheet tensile specimens, and transmission electron microscopy (TEM) disks. Following machining, all samples were ultrasonically cleaned in acetone and isopropyl alcohol and given a final heat treatment in vacuum (pressure $<10^{-7}$ Torr) at the conditions listed in Table 1. The CVN specimen dimensions were $3.3 \times 3.3 \times 25.4$ mm with a 30° notch, 0.67 mm deep with a 0.08 mm root radius. The notch was oriented for crack growth perpendicular to the rolling direction (L-T orientation). Following the final heat treatment, some Charpy specimens were fatigue pre-cracked (PCVN's) by cyclic loading in 3-point bending in stroke control, so the load would shed automatically as the crack extended. The final load was approximately 130 N, and the final crack length to specimen width ratio (a/W) was nominally 0.5. The SS-3 miniature sheet tensile specimens ($0.76 \times 1.52 \times 7.6$ mm gage section) were oriented in the longitudinal orientation (parallel to the rolling direction). The final grain size in both the CVN and SS-3 specimens was approximately 16 μm. TEM disks (3 mm diameter by 0.25 mm thick) were included in the HFBR-V3 and V4 capsules only. TEM disks for samples irradiated in the V1 and V2 capsules were obtained by cutting slices from irradiated CVN specimens following impact testing. Details regarding the specimen series number, initial and final thermomechanical treatment of the alloy and other information on the materials used in this study are given in Table 1. Note that the majority of materials irradiated, and all those for which postirradiation mechanical property results are presented in this summary, are for the 2 h, 1000°C heat treatment.

Table 1. Identification of materials and annealing condition.

Capsule	SS-3 Tensile Series ID & Specimen HT	1/3 PCVN Series ID & Specimen HT	1/3 MCVN Series ID & Specimen HT	TEM Disks Series ID & Specimen HT
V 1	WH (2h @ 1000°C)	WB (2h @ 1000°C)	WB (2h @ 1000°C)	
V 2	WH (2h @ 1000°C)	WB (2h @ 1000°C)	WB (2h @ 1000°C)	
V 3	WH (2h @ 1000°C) ST (2h @ 1000°C) ST (2h @ 900°C)	QC (2h @ 1000°C) QC (2h @ 900°C)	QC (2h @ 1000°C)	ND (1h @900°C) ND (1h @1000°C)
V 4	ST (2h @ 1000°C) ST (2h @ 900°C)	QC (2h @ 1000°C)		ND (1h @900°C) ND (1h @1000°C)

Specimen Series ID	ORNL ID Plate/Sheet	ANL ID Plate/Sheet	Prior Conditioning	Plate Thickness
WH	N40	Plate D	1050°C (1 h) + 50% CR (TWCA)	0.040"
ST	S40	2/96	1050°C (1 h) + 50% CR (TWCA)	0.040"
WB	M150	Plate A	1050°C (2 h) (TWCA)	0.150"
QC	Q250	Plate A (annealed)	1050°C (2 h) (TWCA)	0.250"
ND	N40-10		1000°C(1 h) + 40% CR (ORNL)	0.010"

The irradiation capsules were designed for insertion into the core thimble position in the High Flux Beam Reactor at the Brookhaven National Laboratory. Each capsule consisted of several gas-gapped subcapsules containing the samples. Variations in the sample temperature in the different subcapsules was achieved by varying the gas gap between the subcapsules and the inside of the external capsule, which was in contact with the core coolant water. A cross sectional schematic of a subcapsule is shown in Fig. 1. The subcapsule bodies were electro-discharge machined from either Type 6061-T6 aluminum or remelted V-4Cr-4Ti. Each subcapsule typically contained 8 machined or pre-cracked CVN and 4 SS-3 tensile specimens. After the samples were loaded, a Type 304 stainless steel roll pin (a spring) was lightly hammered into place to ensure that the CVN specimens were in good thermal contact with the subcapsule wall. Each subcapsule used one type-K thermocouple embedded into a Charpy specimen which monitored temperature throughout the irradiation. This thermocouple was located in Charpy #1 (see Fig. 1). In subcapsule 2 of the HFBR-V1 capsule, a second thermocouple was inserted into Charpy #3 to detect any asymmetry in heat flow distribution. As described later, the temperatures for the two thermocouples agreed within 8°C. For the case of subcapsule 1 of HFBR-V3, 21 tensile specimens filled the subcapsule and the thermocouple was placed into the body of the aluminum holder. Due to the numerous heat flow interfaces, it is likely that the differences between the thermocouple reading and the actual sample temperatures were greater in this case than for the subcapsules containing the Charpy specimens. It could also be argued that there would be a larger sample-to-sample difference for the tensile specimens in subcapsule 1, although the measured hardness values were nearly identical for the SS-3's indicating that temperature differences were not significant.

All samples and capsule components were ultrasonically cleaned in isopropyl alcohol and acetone prior to capsule assembly. After the capsule was assembled and the ~33 meter umbilical Type 8000 aluminum tubing was welded in place, the capsule was helium leak checked using a helium

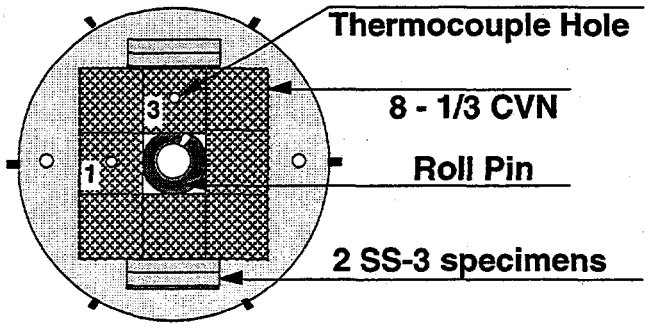

Fig. 1. Cross section of subcapsule for HFBR-V1 through V4 experiments. The numbers 1 and 3 refer to Charpy specimen positions which contained thermocouples.

mass spectrometer. The capsule was then evacuated using an oil-free turbomolecular pump and back-filled with ultra high purity helium to 15 psig. This procedure was repeated three times. Between the first and second evacuation cycles the capsule was baked out to 400°C under vacuum. After the final backfill to 15 psig the pressure was monitored continuously from time of assembly until the end of the irradiation. At no time did the capsule pressure reach atmospheric pressure during the irradiation. However, for the V1 and V2 capsules a small helium leak caused the capsule pressure to decrease during irradiation. This was corrected during irradiation by valving off the irradiation capsules, and then evacuating and back-filling with helium the gas handling manifolds (which were not removed after capsule construction.) Once the manifold was purged and backfilled with UHP helium, the capsule was repressurized with helium to 15 psig.

The four separate irradiation capsules of this study, HFBR-V1 through V4, were irradiated in the High Flux Beam Reactor between May 1995 and October 1996. Experiments HFBR-V1 and V2 were irradiated in the in-core thimble V15 while HFBR-V3 and V4 were irradiated in the symmetric V16 thimble. The HFBR-V1 and V2 capsules were first inserted near the bottom of the core (prior to startup) and began irradiation in this position. These two capsules were approximately 18 cm in length and held 4 and 5 subcapsules, respectively (cf. Table 2). HFBR-V1 was raised to the center of the core after 76 h of the 544 h irradiation. HFBR-V2 was raised to the center of the core after 94 h of the 507 h irradiation. HFBR-V3 received 510 h irradiation in the center of the V-16 thimble, and HFBR-V4 was irradiated for 100 h in the center of the V-16 thimble. The HFBR-V3 and V4 capsules were approximately 23 cm in length, and were held in the center of the core during their entire irradiation period. Each of the V3 and V4 capsules contained 6 subcapsules operating at different temperatures.

At the time of these irradiations the HFBR was operating at 30 MW_{th} power. In our earlier reports on the HFBR V1 and V2 capsules [3,4], the results from a 1976 dosimetry campaign were used to obtain estimates of the fast and thermal neutron fluences, and the nominal damage level for the V1-V2 capsules was reported to be 0.4 dpa. Greenwood and Ratner have recently compiled flux values from three separate dosimetry experiments of the HFBR V-15 In Core thimble that were conducted between 1976 and 1996 using bare and cadmium-covered flux monitors [5]. From the data analysis (scaled to a reactor power of 30 MW_{th}), it was concluded that the most reliable value for the thermal flux (E<0.5 eV) was $1.23\pm0.10 \times 10^{18}$ n/m^2-s and the fast flux (E>0.11 MeV) was $2.64\pm0.26 \times 10^{18}$ n/m^2-s. It is noted that no dosimetry has been conducted on the V-16 thimble in which the HFBR V3-V4 capsules were irradiated. It is assumed that the fast flux is essentially the same as V-15 due to its symmetric position. Also, based on Monte Carlo calculations it is assumed that the center 40 cm of 55 cm core is flux-invariant. Each of the capsules V1-V3 were irradiated to estimated fast (E>0.1 MeV) and thermal fluences of $\sim 5.0\pm0.2 \times 10^{24}$ n/m^2 and 2.3×10^{24} n/m^2,

Table 2. Variation in subcapsule temperatures during irradiation.

Capsule ID (Subcapsule)	Temperature Range, °C (average)	Comment
HFBR V1 (1)	107-108 (108)	+
HFBR V1 (2)	195-201 (198) 203-209 (206)	Position #1 CVN(fig 1)* Position #3 CVN(fig 1)*
HFBR V1 (3)	272-278 (275)	*,+
HFBR V1 (4)	204-210 (207)	*,+
HFBR V2 (1)	227-236 (232)	+
HFBR V2 (2)	232-242 (237)	+
HFBR V2 (3)	194-206 (200)	+
HFBR V2 (4)	197-208 (203)	+
HFBR V2 (5)	107-115 (111)	+
HFBR V3 (1)	159-161 (160)	+
HFBR V3 (2)	267-268 (268)	+
HFBR V3 (3)	259-262 (260)	+
HFBR V3 (4)	322-325 (324)	+
HFBR V3 (5)	305-309 (307)	+
HFBR V3 (6)	410-417 (414)	+
HFBR V4 (1)	105	+
HFBR V4 (2)	160	+
HFBR V4 (3)	256	+
HFBR V4 (4)	294	+
HFBR V4 (5)	391	+
HFBR V4 (6)	504	+

*Temperature increased monotonically throughout irradiation
+Thermocouple in CVN Position 1 (see Fig. 1)

respectively, which produced a calculated [5] damage level in vanadium of 0.5 dpa. Because of the movement of the V1 and V2 capsules from a point near the bottom of the core to the core centerline it can be assumed that these capsules received somewhat (<10%) lower fluence than did the V3 subcapsule which was irradiated at the core centerline throughout the irradiation. The thermal neutron fluence in the V1-V3 capsules would have produced a calculated chromium concentration of 0.1% Cr. The V4 experiment was irradiated for 100 h at the center of the core for an estimated fast and thermal fluence of $0.95\pm0.1 \times 10^{24}$ and $0.44\pm0.04 \times 10^{24}$ n/m^2, respectively, corresponding to a dose of about 0.1 dpa.

During irradiation, the temperatures of the samples were recorded continuously. Table 2 gives the range in temperature recorded by the thermocouples for each experiment. The temperature variations for the V1-V3 subcapsules were always less than 12°C, most of which is accounted for by movement of the V1 and V2 capsules to the center of the core during the irradiation. The V4 capsule had essentially no temperature variation (due to the shorter period of irradiation). The temperature for the V1 capsule slowly increased throughout the irradiation. The reason for this increase in unknown. Because a monotonic temperature increase did not occur in the subsequent capsules (V2-V4), thermocouple decalibration due to transmutation appears unlikely. Also of note in Table 2 is the slight difference in measured temperature between the CVN position 1 and 3 thermocouples in the second subcapsule of V1. Both thermocouples were embedded in Charpy samples to essentially the same depth and yielded about an 8°C difference in measured temperature which tracked each other during the irradiation. From inspection of

Fig.1, this may be explained by the added thermal interfaces sample #3 has between the sample and the subcapsule housing tube. The heat generated in sample #3 would have flowed through the adjacent Charpy samples or through two stacked SS-3's prior to reaching the subcapsule housing.

Results and Discussion

Hardness

Microhardness was measured using a Buehler microhardness tester with a Vickers pyramidal indenter. Data were taken at 500 g, 1 kg and 2 kg loads. Similar hardness values were obtained at all three loads. The data presented here are from the 500 g loads and represent mean values of between 8 and 20 indents each. Samples were prepared by dry sanding the surface of the vanadium specimen. To insure hydrogen pick-up did not affect the hardness results, a full series of hardness tests at 0.5 to 2 kg loads were performed on both sanded and non-sanded, unirradiated vanadium. No difference in hardness was observed. The indents were placed either in the end tab region of the SS-3 sheet tensile specimen or on the side of Charpy specimen. The hardness measurements on the Charpy specimens were taken following impact testing. Sample edges were avoided in all cases.

Figure 2 gives the results of all hardness data taken on the irradiated vanadium specimens at a load of 500 g. The unirradiated hardness values are also listed in Fig. 2. It was observed that the subtle differences in the materials processing used in this study (Table 1) had a measurable effect on the unirradiated hardness. For example, the ST and WH series tensile specimens had unirradiated hardness values of 144.8±0.9 and 134.2±0.9 VHN while the WB and QC series Charpy samples had 150.9±2.1 and 139.9±0.4 VHN, respectively. The hardness errors quoted here and plotted in Fig. 2 refer to one standard error. The temperature error given in Fig. 2 is a combination of the temperature variation during the irradiation and an assumed discrepancy between the sample temperature and the recorded thermocouple temperature of 5°C.

From Fig. 2 it is seen that hardening occurs as the irradiation temperature is increased from ~100°C to 200-300°C, particularly for the 0.5 dpa irradiation. While there is significant scatter for the compiled V1-V3 data, the point at which the room temperature hardness is maximized appears to occur at a higher irradiation temperature for the 0.5 dpa irradiation (~300°C) compared to the 0.1 dpa irradiation (~150°C).

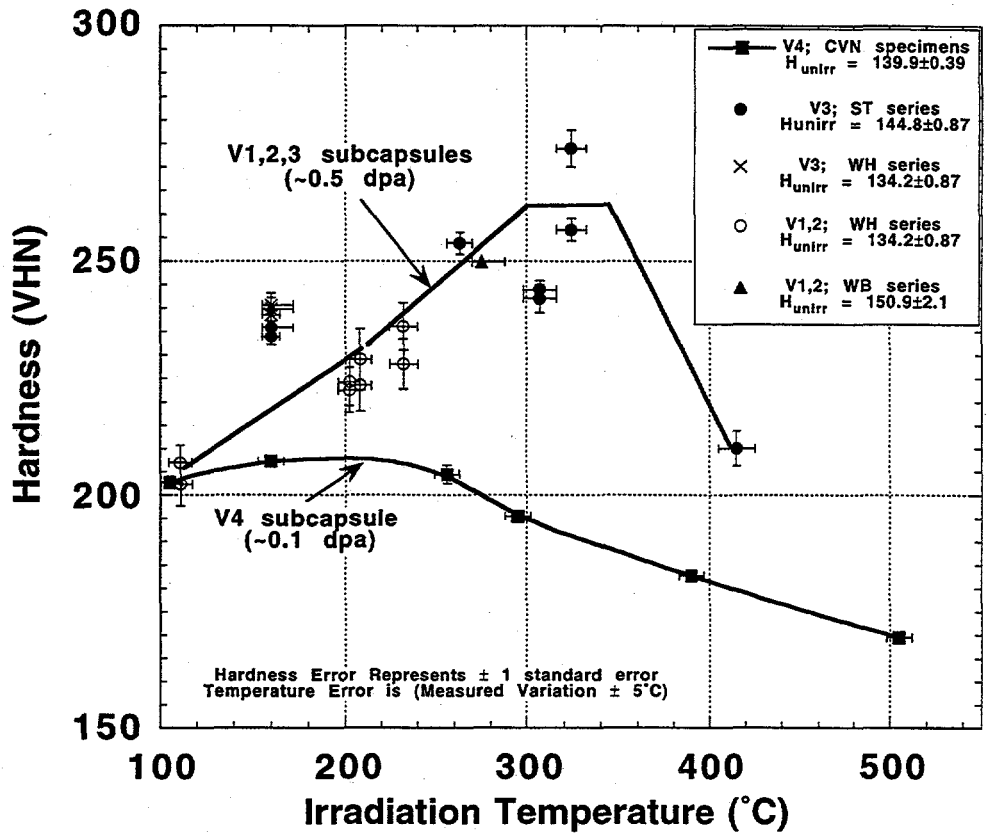

Fig. 2. Microindentation hardness of V-4Cr-4Ti irradiated in the HFBR.

Electrical Resistivity

The room temperature resistivity of the unirradiated control and irradiated tensile specimens was measured prior to tensile testing, using standard 4-point probe techniques (ASTM B 193-87, Standard Test Method for Resistivity of Electrical Conductor Materials, reapproved 1992). An electrical current of 100 mA was supplied by a Keithley Model 237 Source Measure Unit through spring-loaded electrical contacts located in the end tab regions of the tensile specimens. The potential drop in the gage region of the specimen was measured between two spring-load electrical contacts that were separated by a distance of 7.1 mm with a Keithley Model 182 Sensitive Digital Voltmeter with a low thermal connector (resolution limit of 1 nV). Potentials associated with thermal emfs in the electrical leads were subtracted using the "relative" reading function of the model 182 voltmeter. A minimum of three different tensile specimens were measured for each irradiation temperature. The typical measured resistances were ~1.5-1.8 mΩ. For capsules V2-V4, resistivity measurements were performed on the same specimens before and after irradiation in order to minimize errors associated with nonuniformities in the gage dimensions. The postirradiation measurements performed on specimens in the V1 capsule were compared with unirradiated measurements performed on sibling control specimens. The gage dimensions were measured to an accuracy of ±2 μm in two different locations using a Mitotoyo digital micrometer in order to convert the resistance measurements to resistivity values. The

experimental error in the resistivity measurements was mainly due to uncertainties in the gage cross-sectional area; the typical measured standard error was ±0.7 nΩ-m. The temperature was recorded for each measurement (20-26°C), and the data were corrected to a reference temperature of 20°C using the V-Cr-Ti alloy resistivity temperature coefficient [6] of 0.75 nΩ-m/K.

From Fig. 3 it is seen that the room-temperature resistivity increased by about 9 nΩ-m for irradiation at 108°C as compared to the unirradiated value of 280 nΩ-m. The increase in resistivity at this temperature is solely due to generation of point defect clusters in the lattice, since 108°C is too low for O, C, or N migration in vanadium [6-9]. As the irradiation temperature is increased for both the 0.1 and 0.5 dpa irradiated specimens, the change in resistivity decreases to zero (no change) at approximately 200°C and appears to reaches a relative minimum of approximately -5 nΩ-m for irradiation temperatures near 300°C. Electron microscopy performed on the irradiated vanadium specimens found no change in the defect cluster size or density in the 110 to ~275°C range [3,10], indicating that the decrease in resistivity in this temperature interval is not due to decreased defect cluster density. Using the measured migration enthalpies of C, O, and N in vanadium and V-4Cr-4Ti of ~1.18 eV, ~1.26 eV and ~1.48 eV, respectively [7-9], and the low-temperature defect cluster densities of ~0.3 to $1x10^{23}/m^3$ [3,10], migration of C and O solute to defect clusters would be predicted to become significant at temperatures above ~150°C during the one to four week HFBR irradiation and N solute migration to defect clusters would be expected at temperatures above ~250°C. Therefore, the decrease in resistivity with increasing irradiation temperature between 100 and 300°C may be due to the formation of interstitial solute-point defect clusters (the resistivity associated with a solute-defect cluster complex would be less than the resistivity of isolated solute and defect clusters). The formation of the solute-point defect complexes would produce an increase in the dislocation barrier strength compared to point defect clusters without solute atoms, as is well-known from radiation anneal hardening studies [7,11]. Increased room temperature hardness and tensile strength was observed in the present study for specimens irradiated to 0.5 dpa at ~160-300°C compared to 110°C (cf. Fig. 2 and Table 3). Therefore, both the resistivity and hardness data suggest that interstitial solute strengthening of defect clusters may be occurring in V-4Cr-4Ti specimens irradiated at temperatures between ~160 and 300°C. At irradiation temperatures above ~300°C, the resistivity change begins to increase for both the 0.1 and 0.5 dpa irradiated specimens. This may be due to the decrease in defect cluster density (i.e., lower sink strength for interstitial solutes) as the irradiation temperature is raised above 300°C [10]. For the case of the 0.1 dpa irradiated material, the change in resistivity is seen to become slightly positive for an irradiation temperature of 504°C.

The observation that the resistivity did not increase dramatically at irradiation temperatures up to 504°C indicates that the measured low-temperature radiation hardening was not due to solution hardening from pickup of O or C interstitial solutes from the surrounding environment. The specific resistivities for O, C, and N solutes in vanadium are ~50 to 90 nΩ-m/at.% solute [6]. Therefore, the incorporation of a significant (>1000 appm; >300 wppm) amount of O or C in the matrix as solid solution impurities would have caused an easily detected (>5 nΩ-m) increase in the resistivity, which according to Fig. 3 did not occur in the irradiated specimens at temperatures where interstitial solutes are mobile in vanadium (>150°C). For irradiation temperatures above 300°C, the microstructure gradually evolved from small defect clusters to larger, lower density titanium rich clusters [10]. These larger defects would be less efficient sinks for migrating solutes and would therefore have less of an effect on reducing the resistivity. This TEM observation is in agreement with the trends towards higher resistivity seen in Fig. 3 and the reduced hardening seen in Fig. 2.

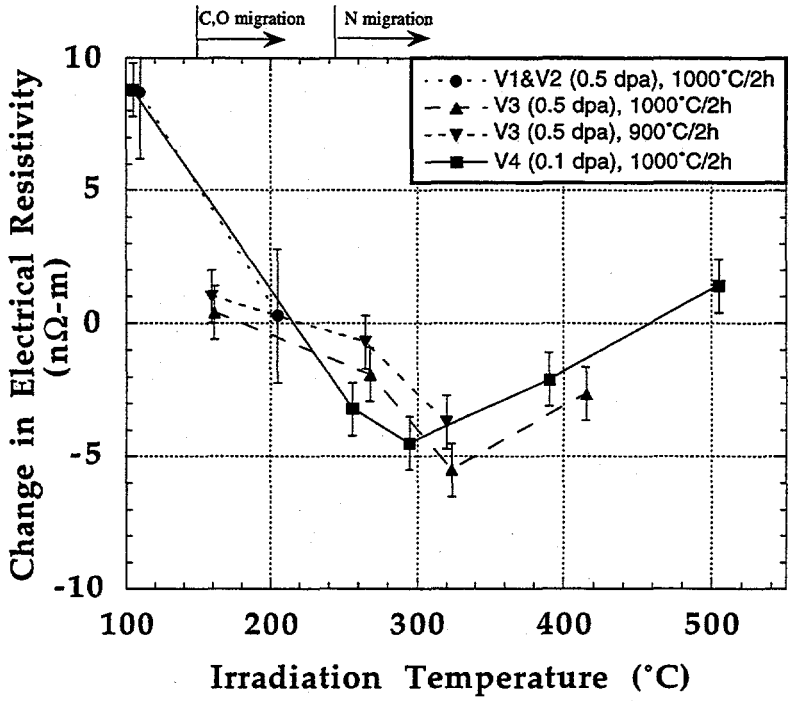

Fig. 3. Change in electrical resistivity of V-4Cr-4Ti irradiated in the HFBR.

Tensile Properties

The tensile specimens from the HFBR V1-V4 experiments were tested at ambient temperature in air or in vacuum at the irradiation temperatures. The majority of the samples were tested at a cross head speed of 0.02 or 0.05 inch/minute, corresponding to a strain rate of 10^{-3} s^{-1}. Three of the 0.1 dpa tensile specimens (capsule V4) were tested at 20°C with a shoulder-loaded specimen grip system, whereas all of the other specimens were tested using a standard pin-loading grip system. Slight deformation in the shoulder regions of the shoulder-gripped tensile specimens caused a change in the slope of the stress-strain curve prior to yielding in the gage region, and introduced a ~1% absolute error in the tensile elongation measurements for these three specimens.

Figure 4 shows examples of the stress-strain curves generated for the 0.5 dpa irradiated specimens tested at the irradiation temperature (T_{test}~T_{irr}). The offset in crosshead displacement is added for clarity. From the figure it is seen that a complete loss in strain hardening capacity has occurred for the specimens irradiated at 110-325°C. Similar behavior was also observed for the room temperature tests of specimens irradiated at 110-325°C.

The data for all tensile specimens included in the HFBR V1-V4 irradiation program are given in Table 3. Because low-temperature neutron irradiation produced a pronounced decrease in strain hardening capacity, the criterion for yielding used for these specimens is given in Fig. 5. For irradiation temperatures less than ~300°C, there is essentially no uniform elongation and therefore the 0.2% plastic deformation convention is inappropriate. For the cases, as indicated in Fig. 5, where there is <0.2% offset prior to a load drop, the yield strength is assigned to be the lower yield point which is given by the intersection of the lines drawn through the yield drop and the subsequent necking. This is given by the symbol σ_{ly} in the figure. The ultimate stress (σ_u) in

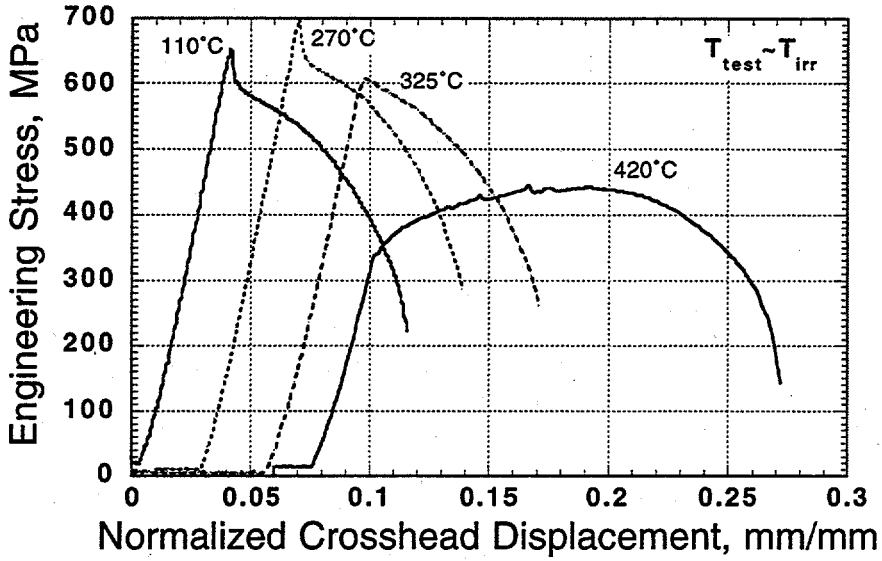

Fig. 4. Typical load vs. normalized crosshead displacement curves for V-4Cr-4Ti tensile specimens irradiated in the HFBR to 0.5 dpa.

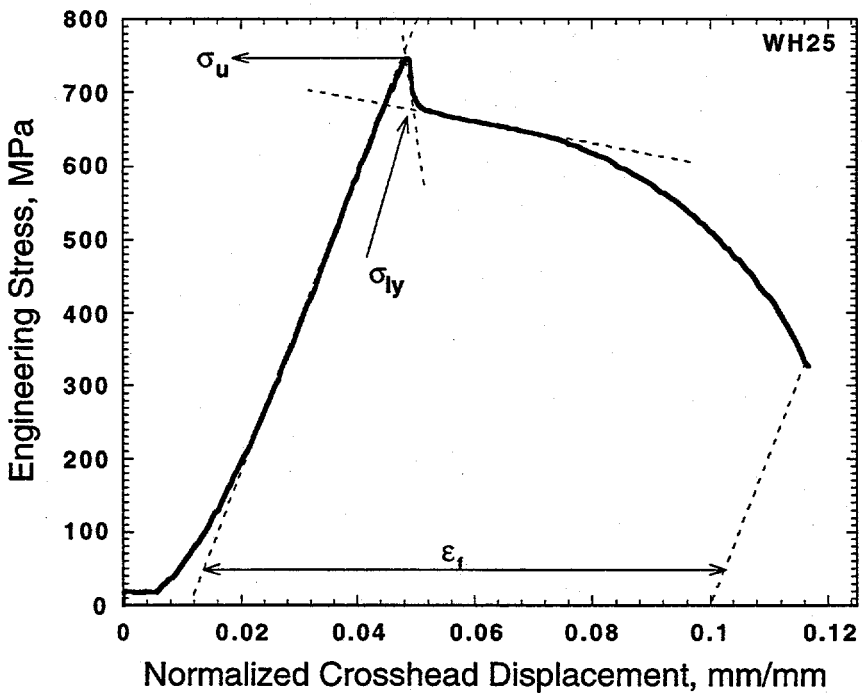

Fig. 5. Schematic illustrating how data were interpreted from the engineering tensile curves.

Table 3. Tensile data for the V-4Cr-4Ti specimens in HFBR V1-V4 capsules. All of the specimens were annealed for 2 h at 1000°C unless otherwise noted.

Sample ID	Capsule (sub-capsule)	Irrad. Temp. (°C)	Test Temp. (°C)	Strain Rate (inch/min)	Lower Yield Pt. (MPa)	Ultimate Stress (MPa)	Unif. Elong. (%)	Total Elong. (%)	Red. in Area (%)
WH01	V1 (4)	207	20	0.02	657	732	0	9.9	83
WH02	V1 (4)	207	200	0.02	603	652	0.05	8.7	
WH03	V1 (4)	207	20	0.002	655	672	0.67	10.3	
WH04	V2 (1)	232	240	0.02	591	657	0.05	9	
WH05	V2 (1)	232	20	0.02	705	769	0	9.7	
WH06	V2 (1)	232	240	0.02	589	623	0.1	8.8	
WH07	V2 (1)	232	240	0.05	635	676	0.1	9.4	
WH08	V2 (4)	203	200	0.02	580	650	0.05	9	
WH09	V2 (4)	203	20	0.02	661	695	0	9.3	80
WH10	V2 (4)	203	200	0.5	605	656	0.1	9.3	
WH11	V2 (4)	203	200	0.001	586	615	0.1	9	
WH13	V2 (5)	111	110	0.02	594	652	0.1	9.7	
WH14	V2 (5)	111	20	0.02	590	633	0	9	
WH15	V2 (5)	111	20	0.02	590	623	0.89	10.9	
WH23	V3 (1)	160	20	0.02	781	800	0.3	9	
WH25	V3 (1)	160	157	0.02	677	749	0.08	8.9	87
WH26-31	V3 (1)	160	untested						
WH32	V3 (1)	160	20	0.05	766	786	0.05	9	82
WH33-35	V3 (1)	160	untested						
ST12	V3 (1)	160	20	0.05	758	800	0	9.3	82
ST13-18	V3 (1)	160	untested						
ST45-48†	V3 (1)	160	untested						
ST19	V3 (2)	268	20	0.05	795	859	0	8.8	85
ST20	V3 (2)	268	270	0.05	635	700	0	9.1	
ST21	V3 (2)	268	untested						
ST41 †	V3 (2)	268	untested						
ST22	V3 (3)	260	*						
ST23	V3 (3)	260	untested						
ST24	V3 (3)	260	*						
ST42 †	V3 (3)	260	untested						
ST25	V3 (4)	324	20	0.05	758**	761	0.05	9.3	87
ST26	V3 (4)	324	320	0.05	608**	608	0.1	9.5	
ST27	V3 (4)	324	untested						
ST43 †	V3 (4)	324	untested						
ST28	V3 (5)	307	20	0.05	733**	733	0	9	85
ST29	V3 (5)	307	untested						
ST30	V3 (5)	307	untested						
ST44 †	V3 (5)	307	untested						
ST31	V3 (6)	414	20	0.05	446**	530	11.8	21.7	73
ST32	V3 (6)	414	420	0.05	342**	445	5.9	19.6	
ST33-34	V3 (6)	414	untested						

Table 3 (continued): Summary of data for 0.1 dpa specimens.

Sample ID	Capsule (Sub-capsule)	Irrad. Temp. (°C)	Test Temp. (°C)	Strain Rate (inch/min)	Lower Yield Pt. (MPa)	Ultimate Stress (MPa)	Unif. Elong. (%)	Total Elong. (%)	Red. in Area (%)
ST53	V4 (1)	105	108	0.02	446**	515	1.4	11.9	
ST54	V4 (1)	105	20	0.02	578	593	<1.2§	10	
ST55	V4 (1)	105	untested						
ST49 †	V4 (1)	105	untested						
ST59	V4 (3)	256	286	0.02	449	465	0.1	13	
ST60	V4 (3)	256	20	0.02	584	604	<1.2§	12	
ST61	V4 (3)	256	untested						
ST51 †	V4 (3)	256	untested						
ST62	V4 (4)	294	340	0.02	393**	402	0.4	15.2	
ST63	V4 (4)	294	20	0.02	531	538	<1§	14.3	
ST64	V4 (4)	294	290	0.02	422	437	0.1	13.6	
ST65	V4 (4)	294	untested						
ST66	V4 (5)	391	395	0.02	348	426	9	20.5	
ST67	V4 (5)	391	20	0.02	446	514	13.7	27.8	
ST68-69	V4 (5)	391							
ST57	V4 (6)	504	20	0.02	371**	503	19.2	24.4	
ST58	V4 (6)	504	untested						
ST71	V4 (6)	504	510	0.02	258**	420	11.2	22.7	
ST75	V4 (6)	504	untested						

*Sample damaged during capsule disassembly
**No load drop; table value represents 0.2% yield stress
§Shoulder loaded specimen; unreliable low-strain (<1%) elongation data
†2 h anneal at 900°C prior to irradiation

this case is by definition the stress at which the load drop occurs (i.e., upper yield point). For the cases where work hardening was present the same method was used to calculate σ_{ly}, though the line through the "necking" region has either a near-zero or positive slope depending on the extent of the Luders band region. In the few cases where a yield drop was not observed (e.g. specimens irradiated to 0.5 dpa at 307-414°C), 0.2% plastic deformation was used for the yield strength as noted in Table 3.

Figure 5 also indicates the method used for determining the total (plastic) elongation, listed as ε_t in the figure. A note of caution regarding the uniform elongation for the low-temperature irradiated materials should be mentioned. For tensile curves exhibiting load-drop behavior with no subsequent work hardening (the majority of the data in Table 3), the uniform elongation was taken to be the elongation at maximum load. As this value is inherently low (<0.2%), the absolute error (≤0.01%) is comparable to the measured value. In general, no significance should be placed on variations in the tabulated uniform elongations when the values are less than 0.2%.

Figure 6 shows the temperature-dependent strength at yielding for the unirradiated and irradiated specimens of this study. From the figure a substantial increase in the yield strength occurs at 0.1 dpa and increases further for the 0.5 dpa irradiation. Recent studies on V-4Cr-4Ti irradiated at temperatures of ~100-330°C indicate that the yield strength continues to increase up to doses of ~5 dpa [12-14], although additional data are needed at doses between 1 and 10 dpa to fully determine the dose dependence of the radiation hardening at low temperatures.

Figure 7 gives the uniform elongation for the 0.1 and 0.5 dpa irradiated V-4Cr-4Ti alloy tested at the irradiation temperature. It is clear from this figure that there is essentially no strain hardening capacity for this alloy for irradiation temperatures ≤ 324°C at 0.5 dpa. For the 0.1 dpa irradiated

material there is a limited amount of uniform elongation (1.4%) for the 108°C irradiated specimen. However, as the irradiation temperature is increased, and C and O solutes can move to defect clusters, the material loses its strain hardening capacity and only ~0.1% uniform elongations were observed in specimens irradiated to 0.1 dpa at 256 and 294°C. After irradiation to 0.1 dpa at 391°C, the material exhibits high (9%) uniform elongation. It is clear from this plot that there is a lack of data in the very important irradiation temperature regime from ~300-500°C. Another significant aspect is that at irradiation temperatures up to at least 330°C this material has lost its strain hardening capacity at extremely low doses. This would seem to rule out the suggested [15] mitigating effects that fusion neutron-produced helium may have on the tensile elongations of vanadium alloys, at least for irradiation temperatures up to 330°C. Simply put, the amount of helium generated in a fusion reactor after a dose of ~0.5 dpa (~2 appm He) would be insufficient to have an impact (positive or negative) on the severe reduction in strain hardening capacity which occurs for fission reactor irradiation temperatures up to at least 330°C.

The reduction in area for a selected group of fractured tensile specimens was measured using scanning electron microscopy (SEM). The data from these specimens are summarized in Table 3 and indicate that the reduction in area was approximately 80% for all specimens regardless of whether they exhibited a severe reduction in strain hardening capacity (e.g.,WH09), possessed limited uniform elongation (e.g., WH25), or had significant strain hardening capacity (e.g.,ST31). An SEM micrograph of the fracture surface of a tensile specimen (WH01) irradiated to 0.5 dpa at 207°C is shown in Fig. 8. A higher magnification image of a tensile fracture surface is shown in Fig. 9, exhibiting ductile tearing in a sample which had essentially no uniform elongation.

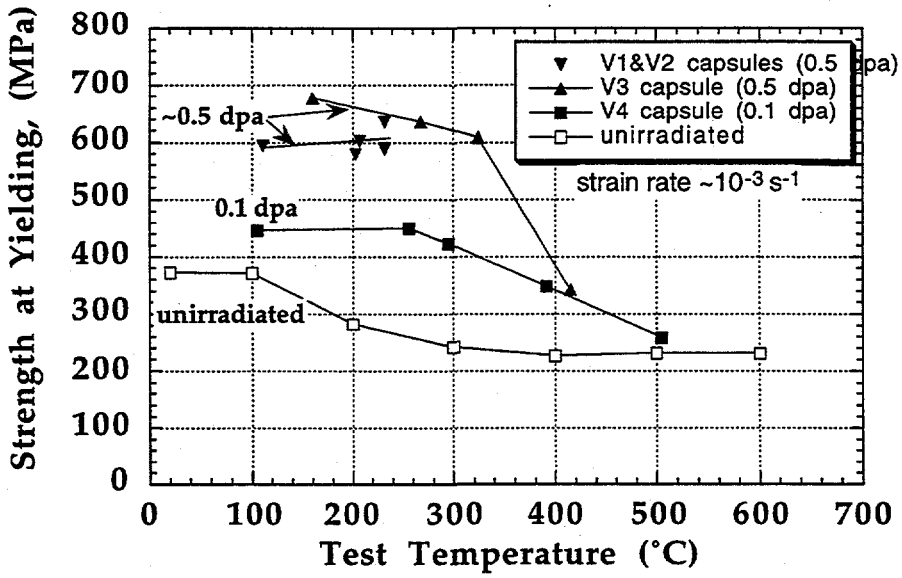

Fig. 6. Strength at yielding of V-4Cr-4Ti irradiated at low dose and low temperature in the HFBR (Testing temperature = Irradiation temperature).

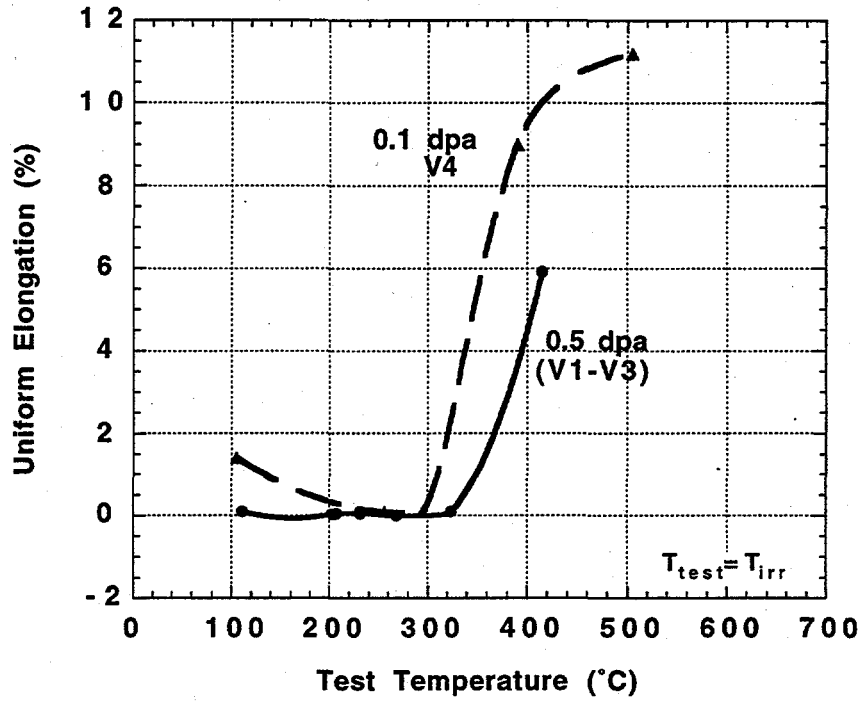

Fig. 7. Uniform elongations of V-4Cr-4Ti irradiated at low dose and low temperature in the HFBR. The tensile specimens were tested at the irradiation temperature.

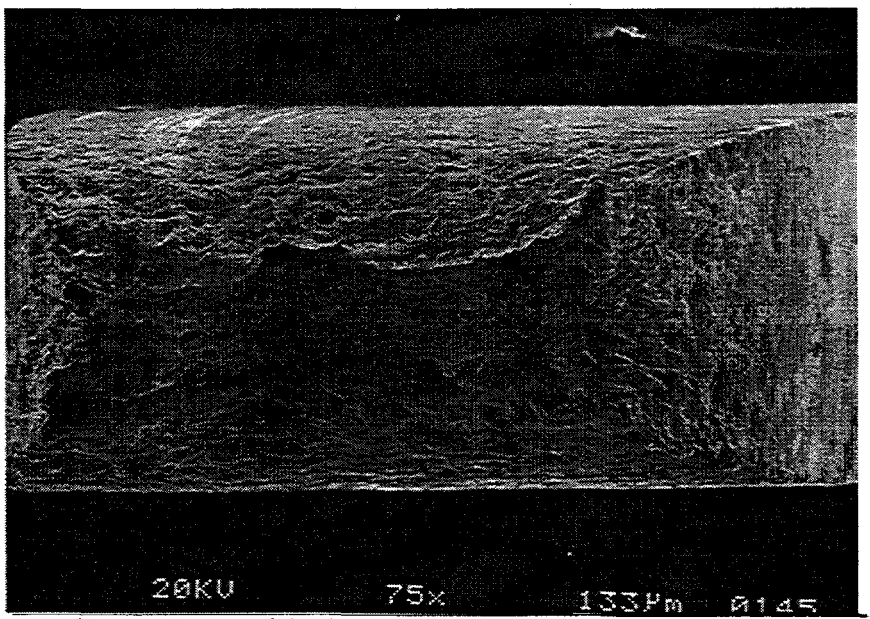

Fig. 8. Low magnification image of the fracture surface of a SS-3 sheet tensile specimen. Sample WH05 irradiated in HFBR-V2 to 0.5 dpa at 232°C and tested at room temperature.

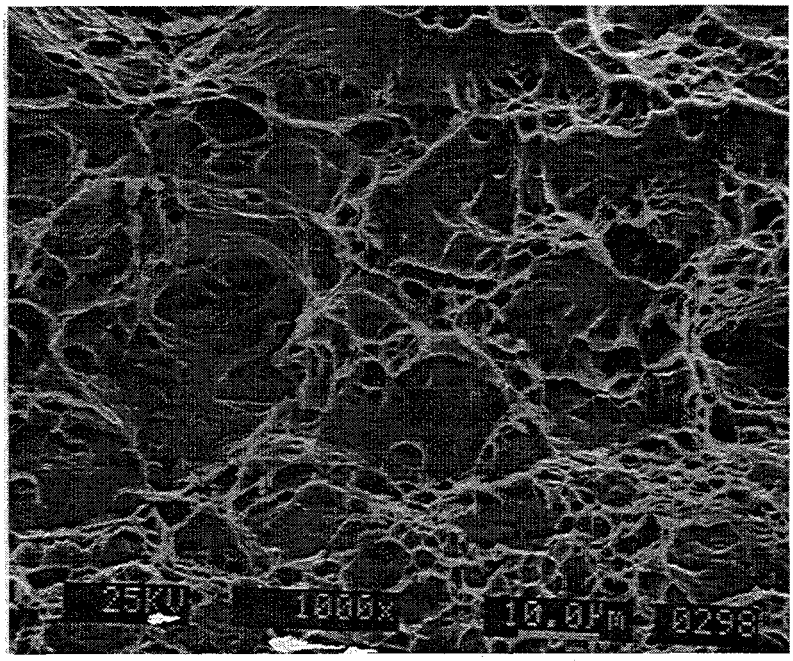

Fig. 9. High magnification image of the center of the fracture surface of a SS-3 sheet tensile specimen (Sample WH01, irradiated in HFBR-V1 to 0.5 dpa at 207°C and tested at 20°C).

Impact Testing

The subsize Charpy specimens (both machine-notched and pre-cracked) were tested in air on a pendulum machine modified for small specimens. Figures 10 and 11 give the absorbed energy data from these tests for the machined-notch (MCVN) and pre-cracked (PCVN) Charpy specimens, respectively. The unirradiated ductile to brittle transition temperature (DBTT) is seen from these figures to be ~-200°C for the machined-notched specimens and ~-150°C for the precracked specimens, indicating a notch acuity effect which has been previously seen in unirradiated vanadium alloys [1,12,16-18].

Figure 12 gives a summary of the DBTT for both the MCVN and PCVN specimens, indicating that the PCVN specimens exhibited DBTT values that were ~50 to 120°C higher than the corresponding MCVN specimens, with the largest deviations occurring when the measured DBTT's were relatively high. The largest shift in the DBTT for both types of Charpy samples correspond to the samples with near zero uniform elongation (Fig. 7 and Table 3). Other factors could contribute to the observed embrittlement such as (a) the inadvertent introduction of hydrogen during pre- or post-irradiation handling, and (b) the pick-up of oxygen and nitrogen from the capsule atmosphere during irradiation. As indicated from the section on electrical resistivity, mechanism (b) can be ruled out. Several of the irradiated CVN specimens were annealed in vacuum for 1 h at 400°C to remove hydrogen which may have been picked up by the specimens. Similar impact behavior was observed in the as-irradiated and annealed specimens, indicating that significant hydrogen pickup had not occurred [4].

Figures 13 and 14 give high magnification SEM images of fracture surfaces from the lower shelf and upper shelf samples. In both the PCVN and MCVN specimens, the upper shelf fracture surface showed ductile tearing. By stereoscopic imaging of the fracture surface of lower shelf specimens, the failure mode was seen to be cleavage, with some evidence of mixed-mode failure in the transition region from lower to upper shelf behavior.

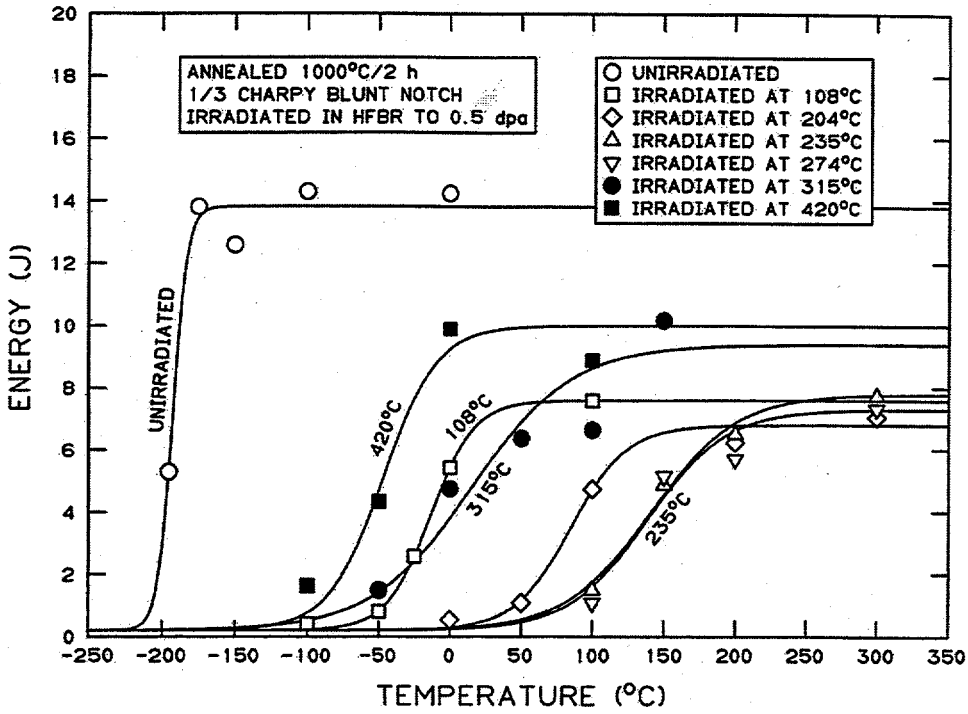

Fig. 10. Plot of the unirradiated and 0.5 dpa absorbed energy data for the impact testing of the machined-notch Charpy impact specimens (MCVN)

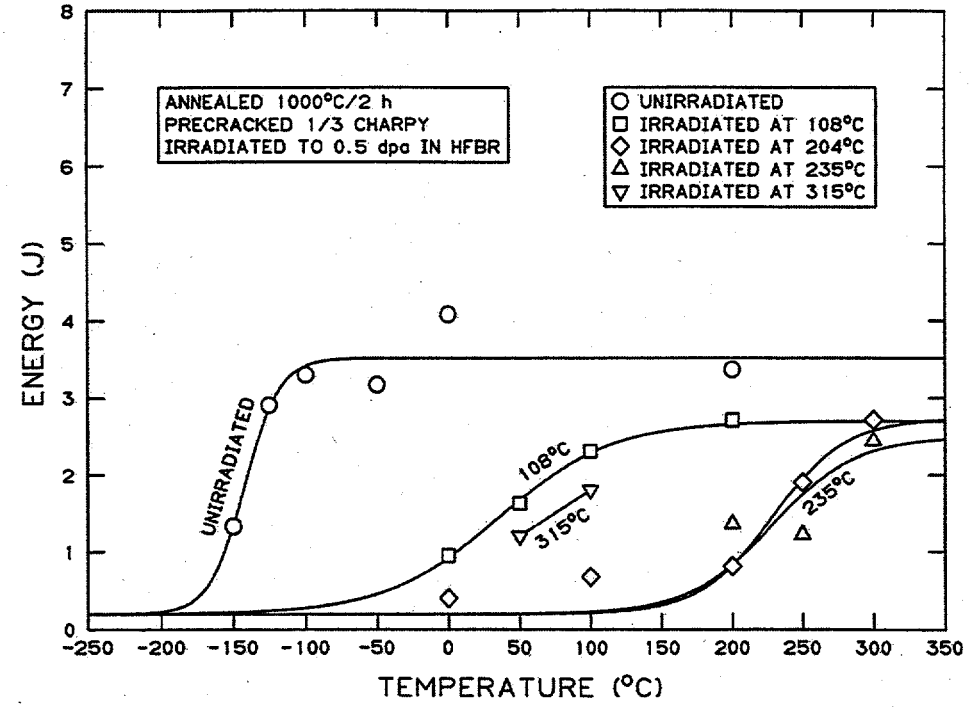

Fig. 11. Plot of the unirradiated and 0.5 dpa absorbed energy data for the impact testing of the pre-cracked Charpy impact specimens (PCVN).

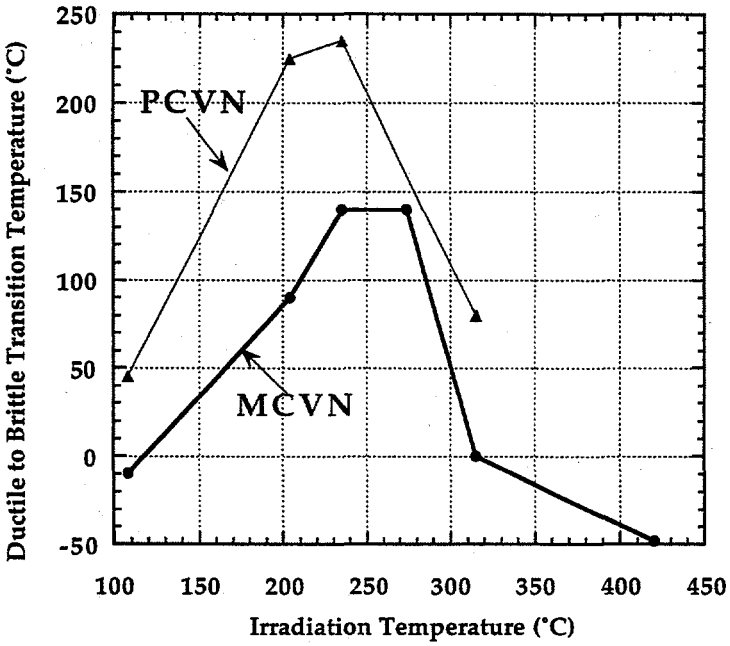

Fig. 12. Ductile to Brittle Transition Temperature for the machined-notch and pre-cracked Charpy specimens irradiated to 0.5 dpa.

Fig. 13. SEM of the fracture surface from a 0.5 dpa PCVN specimen exhibiting lower shelf behavior (sample WB81, irradiated at 110°C and tested at 0°C).

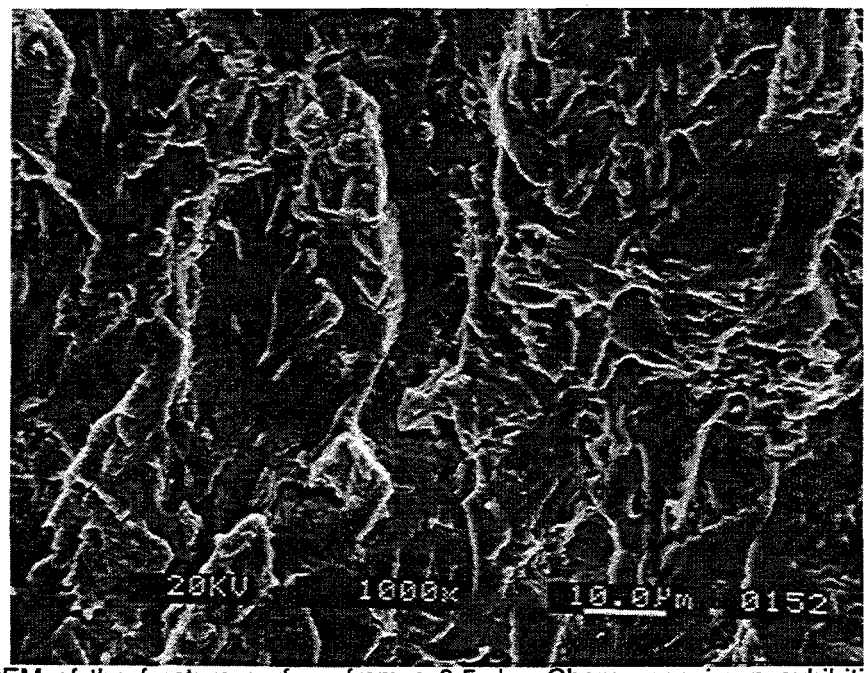

Fig. 14. SEM of the fracture surface from a 0.5 dpa Charpy specimen exhibiting behavior intermediate between upper and lower shelf. (Sample WB100, irradiated at 235°C and tested at 250°C).

CONCLUSIONS

Significant hardening of V-4Cr-4Ti with a corresponding increase in tensile strength, complete loss of strain hardening capacity, and a large increase in the DBTT has occurred for irradiation temperatures at or below 324 °C at 0.5 dpa. This embrittlement is due to the high density of radiation produced defect clusters which are further strengthened by migrating C, O and N interstitial solutes for fission reactor irradiation temperatures greater than ~150°C (C,O) and ~250°C (N), respectively. Irradiation at temperatures of 391-414°C to doses of 0.1-0.5 dpa produced reduced amounts of hardening and improved ductility compared to the low-temperature irradiations uniform elongation. A significant sensitivity of the ductile to brittle transition temperature on notch acuity has been observed in the irradiated Charpy specimens. Additional mechanical properties data on specimens irradiated at 300-500°C to higher fluences are required in order to establish the minimum operating temperature for this alloy.

FUTURE WORK

The majority of the post-irradiation testing of specimens from the HFBR V1-V4 irradiation experiment has been completed. Additional tasks which are planned include (a) the effect of strain rate on the tensile properties of the specimens irradiated at 160°C to 0.5 dpa, (b) isochronal annealing of low temperature irradiated specimens from HFBR-V1 to measure the recovery of microindentation hardness, (c) measurement of the electrical resistivity change for control specimens annealed in helium at 504°C for 1 to 4 weeks to investigate the extent of oxygen pickup, and (d) static fracture toughness testing on precracked HFBR V3 and V4 bend bars at temperatures up to 505°C. Some mechanical testing of the 900°C heat treated tensile and impact specimens (Table 3) will also be performed. Fracture mechanics testing of irradiated PCVN specimens is in progress at UC-Santa Barbara.

ACKNOWLEDGMENTS

The authors would like to give their sincere thanks to Joe O'Conor, Joel Errante, Guy Hartsough, Norman Holden, and Tim Powers of the Research Coordination Group of the Brookhaven National Laboratory for their cooperation and assisting in using the High Flux Beam Reactor. We would also like to thank Marie Williams and Jeff Bailey for assistance with the post irradiation evaluation of these samples.

REFERENCES

1. M.L. Grossbeck, A.F. Rowcliffe, and D.J. Alexander, in Fusion Materials Semiann. Prog. Report for Period ending March 31, 1994, DOE/ER-0313/16 (Oak Ridge National Lab, 1994) p. 244.
2. H.M. Chung et al., in Fusion Materials Semiann. Prog. Report for Period ending Sept. 30, 1994, DOE/ER-0313/17 (Oak Ridge National Lab, 1994) p. 178.
3. P.M. Rice, L.L. Snead, D.J. Alexander, and S.J. Zinkle, in Microstructure Evolution During Irradiation, MRS Symposium Proceedings vol. 439, eds. I.M. Robertson et al. (Materials Research Society, Pittsburgh, 1997) p. 343.
4. D.J. Alexander et al., in 18th ASTM Symp. on Effects of Radiation on Materials, Hyannis, MA, 1996, in press; also Fusion Materials Semiann. Prog. Report for Period ending June 30, 1996, DOE/ER-0313/20 (Oak Ridge National Lab, 1996) p. 87.
5. L.R. Greenwood and R.T. Ratner, in Fusion Materials Semiann. Prog Rep. for period ending Dec. 31 1997, DOE/ER-0313/23, in press.
6. S.J. Zinkle, A.N. Gubbi, and W.S. Eatherly, in Fusion Materials Semiann. Prog. Report for Period ending December 31, 1996, DOE/ER-0313/21 (Oak Ridge National Lab, 1996) p. 15.
7. J.T. Stanley, J.M. Williams, W.E. Brundage, and M.S. Wechsler, Acta Metall. 20 (1972) 191.
8. H. Nakajima, S. Nagata, H. Matsui, and S. Yamaguchi, Philos. Mag. A 67 (1993) 557.
9. M. Uz, K. Natesan and V.B. Hang, J. Nucl. Mater. 245 (1997) 191.
10. P.M. Rice and S.J. Zinkle, 8th Int. Conf. on Fusion Reactor Materials, Sendai, J. Nucl. Mater. (1998) submitted.
11. R.E. Gold and D.L. Harrod, Intern. Metals Rev. 25, no. 5-6 (1980) 232.
12. S.J. Zinkle et al., 8th Int. Conf. on Fusion Reactor Materials, Sendai, J. Nucl. Mater. (1997) submitted.
13. E.V. van Osch, 8th Int. Conf. on Fusion Reactor Materials, Sendai, J. Nucl. Mater. (1997) submitted.
14. V.A. Kazakov, V.P. Chakin, Y.D. Goncharenko, and Z.E. Ostrovsky, 8th Int. Conf. on Fusion Reactor Materials, Sendai, J. Nucl. Mater. (1997) submitted.
15. H.M. Chung, M.C. Billone, and D.L. Smith, in Fusion Materials Semiann. Prog. Report for Period ending June 30, 1996, DOE/ER-0313/22 (Oak Ridge National Lab, 1997) p. 22.
16. H. Li, R.H. Jones, and J.P. Hirth, in Fusion Materials Semiann. Prog. Report for Period ending March 31, 1994, DOE/ER-0313/16 (Oak Ridge National Lab, 1994) p. 279.
17. G.R. Odette, E. Donahue, G.E. Lucas, and J.W. Sheckherd, in Fusion Materials Semiann. Prog. Report for Period ending June 30, 1996, DOE/ER-0313/20 (Oak Ridge National Lab, 1996) p. 11.
18. G.R. Odette, G.E. Lucas, E. Donahue, and J.W. Sheckherd, J. Nucl. Mater. 233-237 (1996) 502.

THERMOPHYSICAL AND MECHANICAL PROPERTIES OF V-(4-5)%Cr-(4-5)%Ti ALLOYS — S.J. Zinkle (Oak Ridge National Laboratory)

OBJECTIVE

The objective of this report is to summarize available data on the thermophysical and mechanical properties of V-(4-5)Cr-(4-5)Ti alloys in order to provide a reference design basis for the Advanced Power EXtraction (APEX) project.

SUMMARY

Solid solution V-Cr-Ti alloys exhibit a good combination of high thermal conductivity, adequate tensile strength, and low thermal expansion. The key thermophysical and mechanical properties for V-(4-5)%Cr-(4-5)%Ti alloys are summarized in this report. Some of these data are available in the ITER Materials Properties Handbook (IMPH), whereas other data have been collected from recent studies. The IMPH is updated regularly, and should be used as the reference point for design calculations whenever possible.

PROGRESS AND STATUS

1. Ultimate tensile strength (unirradiated)

The ultimate tensile strength for the BL47 (30 kg) [1] and Teledyne Wah Chang #832665 (500 kg) [1-3] heats of V-4Cr-4Ti has been measured by several researchers. Figure 1 summarizes ultimate tensile strength (UTS) data obtained in tensile tests at strain rates near 1×10^{-3} s^{-1} on annealed (1000-1100°C for 1 to 2 h) specimens in the longitudinal orientation. The data in refs. [1,2] were obtained on "type SS3" miniature sheet tensile specimens with gage dimensions of 0.76 x 1.52 x 7.6 mm, whereas the data in ref. [3] were obtained on round tensile specimens with gage dimensions of 4 mm diam x 20 mm. Good agreement was obtained for both types of specimen geometries over the investigated temperature range. The least squares fitted equation for the ultimate tensile strength over the temperature range of 20-700°C is

$$\sigma_{UTS}(MPa)= 445.7 -0.80616*T +0.002211*T^2 -1.7943e-06*T^3 +1.8176e-10*T^4$$

where the temperature (T) is in °C. The correlation coefficient for the plotted data using this equation is R=0.76505. The relatively low value for the correlation coefficient is due to the limited number of tensile tests which have been performed on V-4Cr-4Ti.

2. Ultimate tensile strength (irradiated)

Neutron irradiation causes a large increase in the tensile strength of V-Cr-Ti alloys, particularly at temperatures below ~400°C. Figure 2 summarizes the tensile strength data for V-4Cr-4Ti irradiated to doses above 4 displacements per atom (dpa) [1,3-8]. It can be seen that the ultimate strength in the irradiated specimens is higher than that of unirradiated specimens (Fig. 1) over the investigated temperature range of 80-600°C. Generation of fusion-relevant amounts of helium (~4 appm He/dpa) appears to have a relatively minor effect on the ultimate tensile strength of vanadium alloys at temperatures between 420 and 600°C and doses up to 80 dpa [1,9-11].

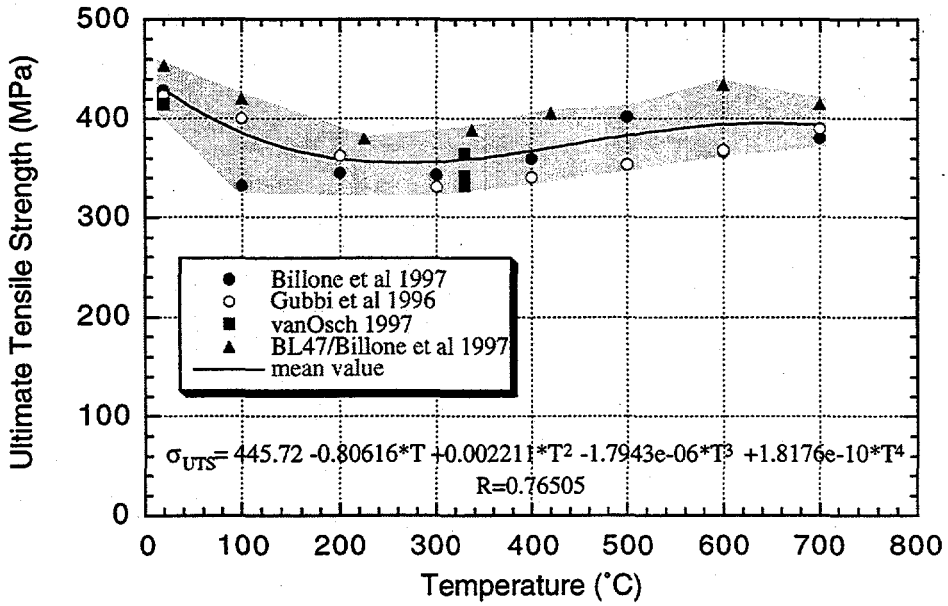

Fig. 1. Ultimate tensile strength of unirradiated V-4Cr-4Ti [1-3].

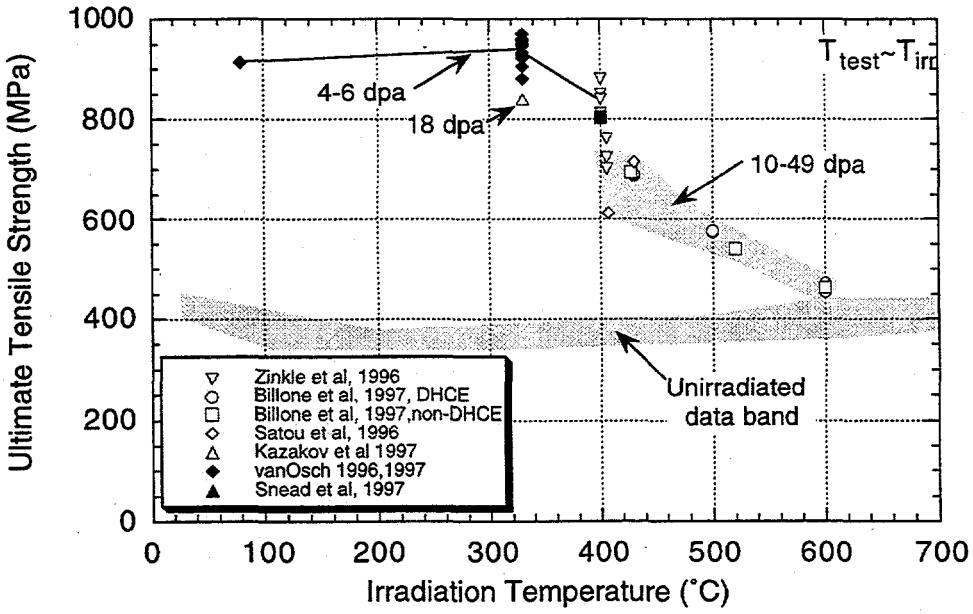

Fig. 2. Ultimate tensile strength of irradiated V-(4-5)%Cr-(4-5)%Ti alloys [1,3-8].

3. Yield strength (unirradiated)

Figure 3 summarizes the yield strength and uniform elongation data obtained in tensile tests at strain rates near 1×10^{-3} s^{-1} on annealed (1000-1100°C for 1 to 2 h) specimens in the longitudinal orientation for two different heats of V-4Cr-4Ti. The data in refs. [1,2] were obtained on "type SS3" miniature sheet tensile specimens with gage dimensions of 0.76 × 1.52 × 7.6 mm, whereas the data in ref. [3] was obtained on round tensile specimens with gage dimensions of 4 mm diam × 20 mm. Good agreement was obtained for both types of specimen geometries over the investigated temperature range. The least squares fitted equation for the yield strength over the temperature range of 20-700°C is

$$\sigma_Y(\text{MPa}) = 377.2 - 0.70384*T + 0.00089973*T^2 - 1.2279e\text{-}07*T^3 - 1.9824e\text{-}10*T^4$$

where the temperature (T) is in °C. The correlation coefficient for the plotted data using this equation is R=0.9461.

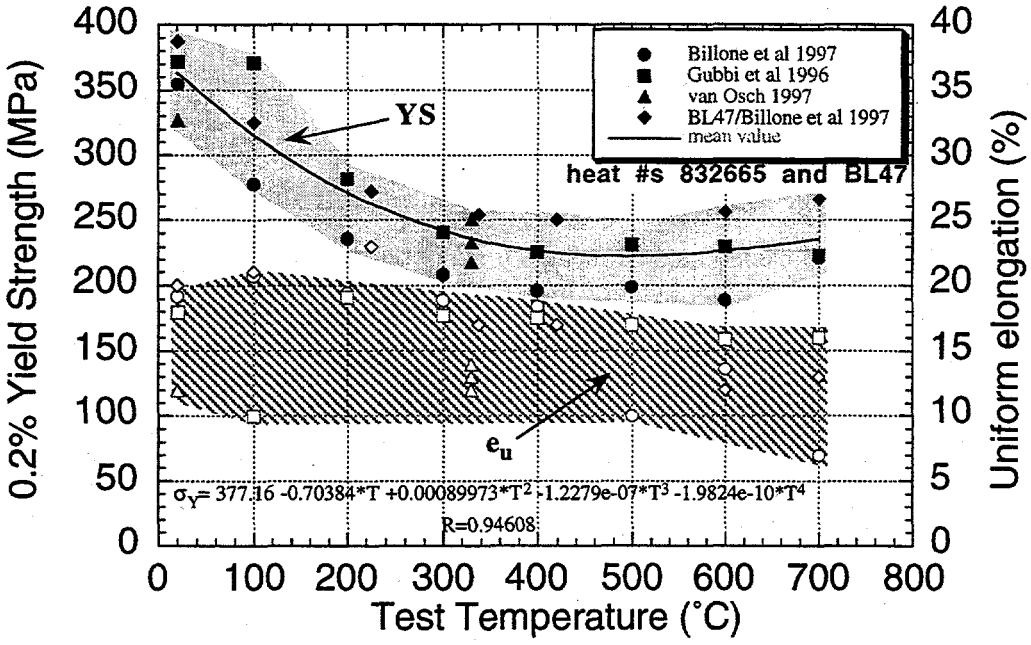

Fig. 3. Yield strength and uniform elongation of unirradiated V-4Cr-4Ti [1-3].

4. Yield strength (irradiated)

Neutron irradiation causes a pronounced increase in the yield strength of V-Cr-Ti alloys, particularly at temperatures below ~400°C. Figure 4 summarizes the yield strength and uniform elongation data for V-(4-5)%Cr-(4-5)%Ti alloys irradiated to doses above 4 dpa [1,3-8]. The yield strength in the irradiated specimens is significantly higher than that of unirradiated specimens (Fig. 3) over the investigated temperature range of 80-600°C. Fusion-relevant helium generation (~4 appm He/dpa) has a relatively minor effect on the yield strength of vanadium alloys at temperatures between 420 and 600°C and doses up to 80 dpa [1,9-11].

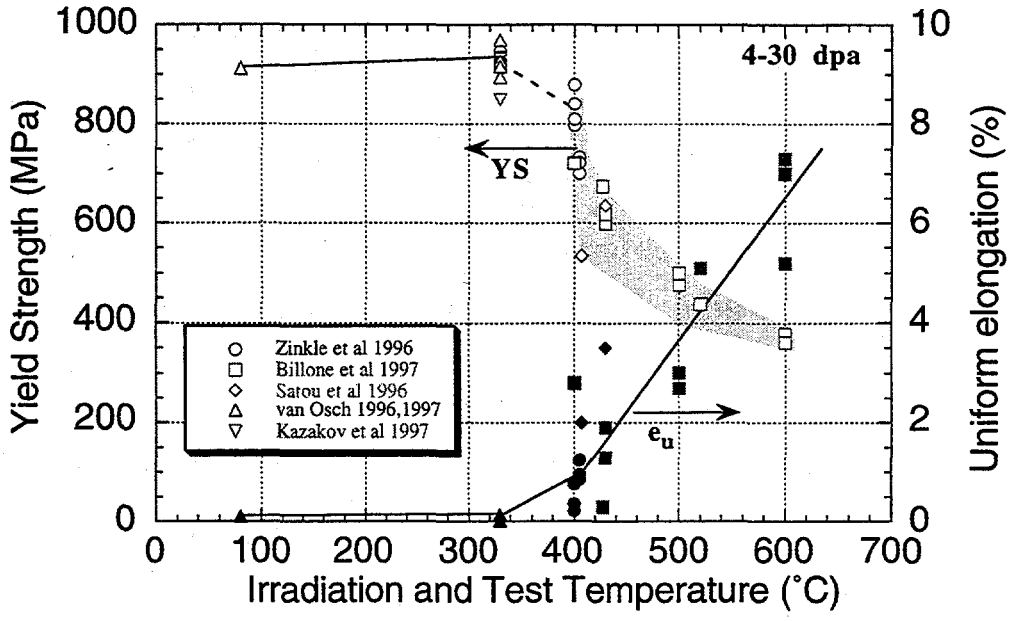

Fig. 4. Yield strength and uniform elongation of irradiated V-(4-5)%Cr-(4-5)%Ti alloys [1,3-8].

5. Elongation (unirradiated and irradiated)

The uniform and total elongation of unirradiated V-4Cr-4Ti determined from tensile testing at strain rates near 1×10^{-3} s^{-1} exhibit high values at all temperatures from 20 to 700°C [1-3]. As shown in Fig. 3, the unirradiated uniform elongation decreases slowly from ~15% to ~10% over this temperature range. The corresponding total elongation decreases from ~30% to ~20% as the temperature increases from 20 to 700°C (Fig. 5). As shown in Figs. 4 and 5, irradiation causes a decrease in the uniform and total elongations, particularly for irradiation temperatures below 400°C [1,3-8]. The total elongation remains above ~5% for all irradiation conditions investigated to date (Fig. 5). The uniform elongation decreases to <0.2% for irradiation temperatures ≤330°C and is >2% for irradiation temperatures above 400-450°C.

6. Reduction in area

The reduction in area (RA) as measured on unirradiated and irradiated V-4Cr-4Ti tensile specimens deformed at strain rates of ~1×10^{-3} s^{-1} is shown in Fig. 6. The unirradiated reduction in area is very high (~90%) at low test temperatures, and decreases to a moderate value of ~50% at 700°C. Irradiation causes a significant decrease in the RA (particularly at low irradiation and test temperatures), but the reduction in area remains acceptably high in the tensile specimens examined to date.

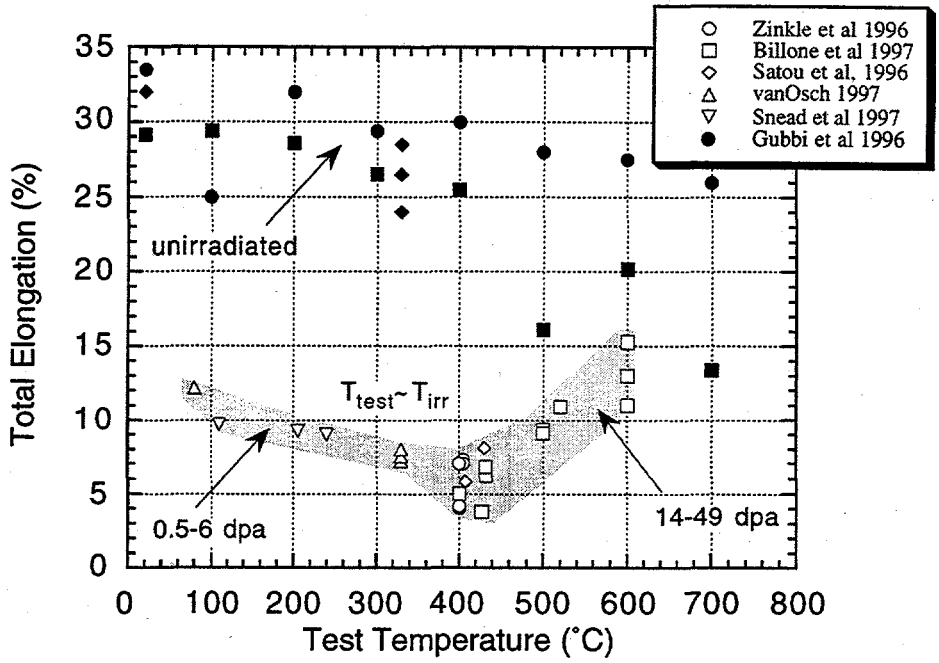

Fig. 5. Total elongation of unirradiated [1-3] and irradiated [1,3-5,7,8] V-(4-5)%Cr-(4-5)%Ti .

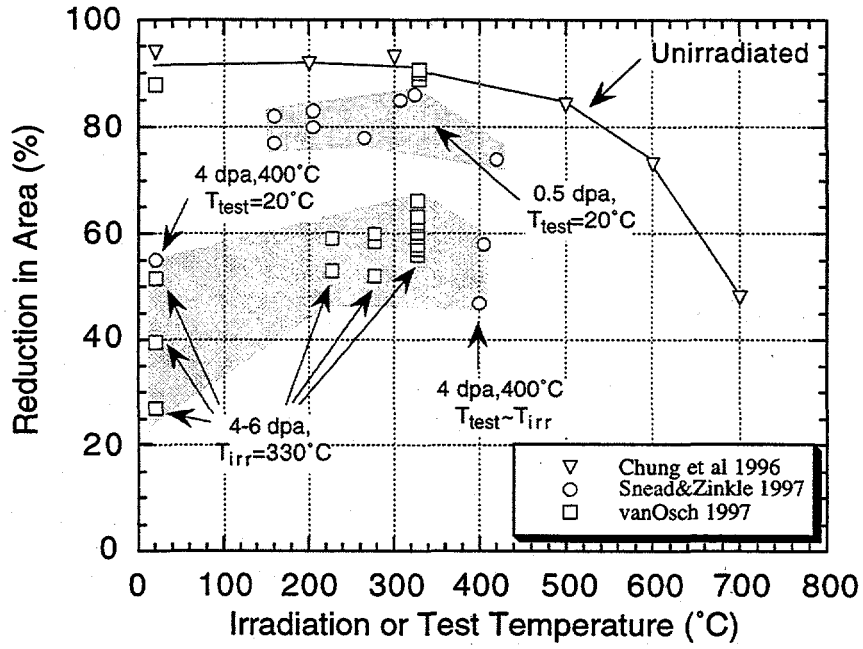

Fig. 6. Reduction in area of unirradiated [3,12] and irradiated V-4Cr-4Ti [3,8].

7. Stress-strain curves

Figure 7 shows representative stress-strain curves obtained on miniature "type SS-3" sheet tensile specimens (0.76 × 1.52 × 7.6 mm gage dimensions) for V-4Cr-4Ti tensile tested at a strain rate of 1.1×10^{-3} s^{-1} [2]. Serrations in the stress strain curve due to dislocation interactions with dissolved O, C, N interstitial solute (dynamic strain aging) become evident at test temperatures above 300°C. The strain rate exponent for the yield and ultimate tensile strength was positive at low test temperatures, and became negative at high temperatures where dynamic strain aging effects were present.

Figure 8 shows stress-strain curves obtained on miniature type SS-3 sheet tensile specimens of V-4Cr-4Ti following irradiation to a dose of 0.5 dpa at 110-420°C [8]. Pronounced flow localization is observed for irradiation temperatures up to 400°C [4,8], whereas adequate work hardenability occurs at temperatures above 425°C.

8. Elastic constants

The elastic constants for V-5Cr-5Ti (heat BL63) have been measured at room temperature, and were found to be in good agreement with published data for pure vanadium [13]. The room temperature elastic constants were: Young's modulus E_Y=125.6±0.4 GPa, shear modulus G=45.9±0.2 GPa, and Poisson's ratio 0.367±0.001. The following equations were recommended for extrapolation to temperatures above 20°C:

$$E_Y=((1.28 - 9.61 \times 10^{-5} * T) \pm 0.040) \times 10^{11} \text{ Pa}$$

$$G=((0.488 - 8.43 \times 10^{-5} * T) \pm 0.011) \times 10^{11} \text{ Pa}$$

where the temperature is given in Kelvin. Poisson's ratio at elevated temperatures can be obtained using the well-known relation $\nu=(E_Y/2G) - 1$.

9. Stress-rupture

Vanadium alloys exhibit good stress-rupture behavior at temperatures up to 600°C (0.4 T_M) [14-16]. Oxygen pickup from the surrounding atmosphere becomes a serious experimental problem for creep tests performed in vacuum at temperatures ≥600°C, due to the high affinity of vanadium for oxygen [16,17]. Thermal creep data for V-4Cr-4Ti are only available at a test temperature of 600°C and for testing times up to 4000 h [16]. Data for other vanadium alloys in the thermal creep regime ≥650°C has been summarized in review papers [14,15]. Significant thermal creep is expected in V-4Cr-4Ti at or above ~700°C (0.45 T_M).

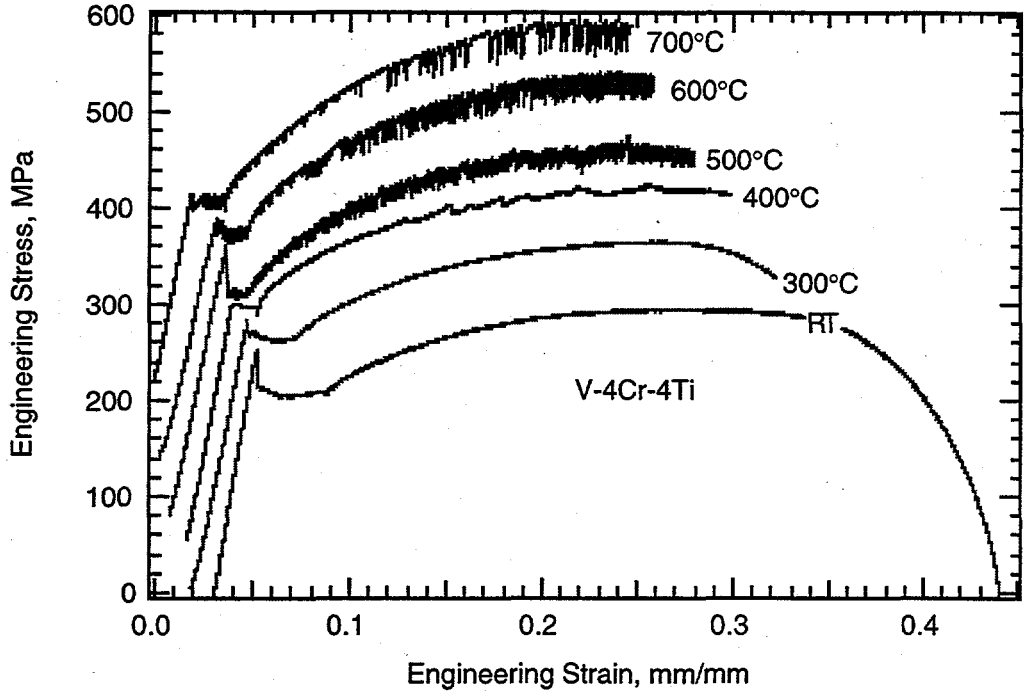

Fig. 7. Load vs. elongation tensile curves for V-4Cr-4Ti tested at temperatures between 20 and 700°C at a strain rate of 1.1×10^{-3} s^{-1} [2].

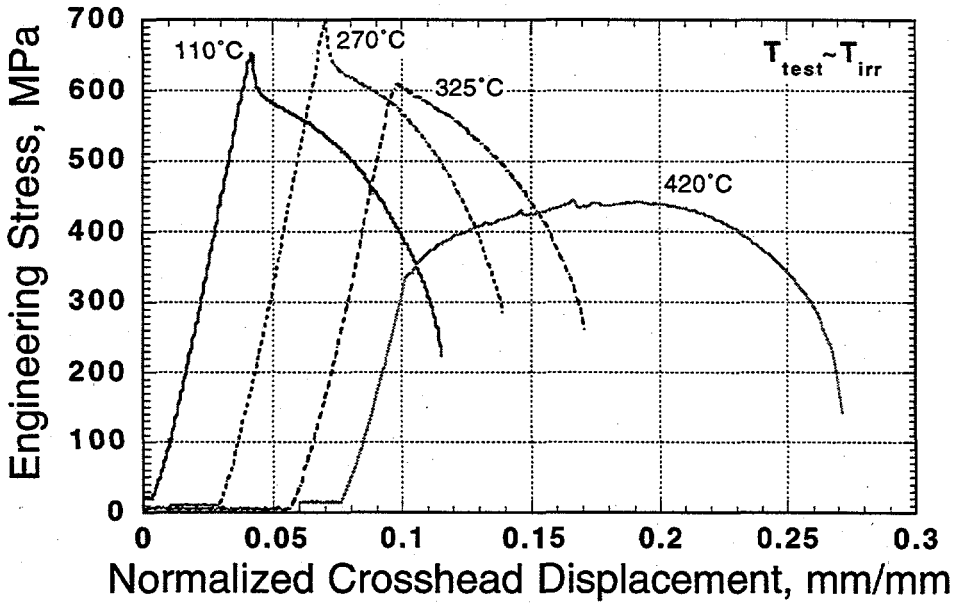

Fig. 8. Tensile load vs. elongation curves for V-4Cr-4Ti irradiated at low temperatures to a dose of 0.5 dpa [8].

10. Thermal expansion, specific heat and thermal conductivity

The thermophysical properties for V-5Cr-5Ti (heat BL63) have been measured from room temperature to 600°C, and are in agreement with published data for pure vanadium [18]. The instantaneous coefficient of thermal expansion varied from 9.1 ppm/°C at room temperature to 11.0 ppm/°C at 600°C. The fitted polynomial expressions for the linear thermal expansion ($\Delta L/L_0$) relative to the 20°C value and the instantaneous thermal expansion coefficient (α_{th}) are:

$$\Delta L/L_0 = -179.976 + 9.036385*T + 0.00154075* T^2 \text{ ppm}$$

$$\alpha_{th} = 9.03767 + 0.00301422*T + 4.95937 \times 10^{-7} * T^2 \text{ ppm/°C}$$

where the temperature (T) is given in °C.

The least squares fitted equation describing the specific heat at constant pressure over the temperature range of 100 to 600°C is

$$C_P = 0.57551 - 21.094/T \text{ J/g-K}$$

where the temperature (T) is given in Kelvin.

The thermal conductivity at 20-600°C was determined from thermal diffusivity measurements using either laser flash or xenon flash techniques with an overall accuracy of ±6%. The thermal conductivity was found to be in good agreement with literature values for pure vanadium. The least squares fitted equation for the thermal conductivity is

$$k_{th} = 27.827 + 0.008603\ T \text{ W/m-K}$$

where the temperature (T) is given in Kelvin.

11. Ductile to brittle transition temperature (unirradiated and irradiated)

The measured value of the ductile to brittle transition temperature (DBTT) in body-centered cubic materials depends on numerous experimental parameters, including the specimen geometry, strain rate, and the sharpness of the notch where the crack is initiated (notch acuity) [19,20]. The measured DBTT in miniature unirradiated V-4Cr-4Ti machined Charpy vee-notch (MCVN) specimens (25 × 3.3 × 3.3 mm) with a 30° notch depth of 0.67 mm and a notch root radius of 0.08 mm is near -200°C for L-T orientations [12,21]. Low temperature irradiation causes a sharp increase in the DBTT, even for relatively low doses of 0.5 dpa [8,21]. Figure 9 shows Charpy impact absorbed energy curves for V-4Cr-4Ti before and after neutron irradiation to doses of 0.5 and 4 dpa at temperatures near 400°C [4,8,21].

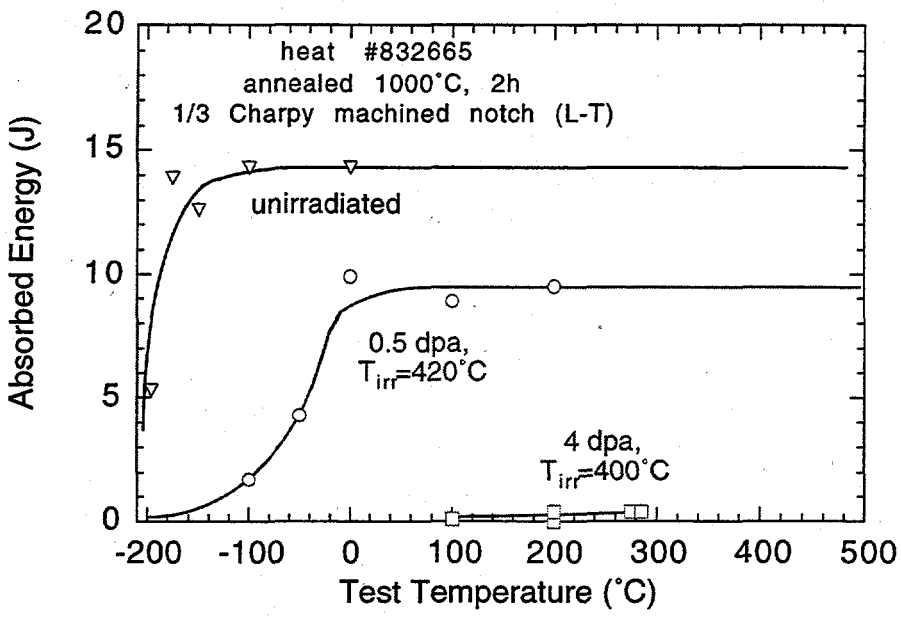

Fig. 9. Charpy impact absorbed energy curves of V-4Cr-4Ti MCVN specimens before and after low-dose neutron irradiation at ~400°C [4,8,21].

12. Recommended reference operating temperature limits

Additional work on unirradiated and irradiated specimens is needed before the maximum and minimum operating temperature limits for vanadium alloys can be established. The following reference operating temperature limits of 400 and 700°C are proposed until these data become available. The reference minimum operating temperature limit will be controlled by radiation hardening, which causes loss of ductility and an increase in the ductile to brittle transition temperature. According to analyses of the DBTT in unirradiated and irradiated V-4Cr-4Ti specimens, brittle fracture behavior in MCVN specimens occurs when the yield stress exceeds ~700 MPa [20,22,23]. From Fig. 4, this implies that the irradiation temperature must be greater than ~400°C to avoid brittle fracture behavior in structures containing undetected cracks.

The maximum operating temperature limit will likely be controlled by either thermal creep (creep rupture), helium embrittlement or chemical compatibility/corrosion effects. Significant thermal creep is expected in V-4Cr-4Ti at or above ~700°C (0.45 T_M), but experimental creep data on this alloy [16] are only available at 600°C (0.4 T_M). Slow strain rate tests to check for helium embrittlement effects have not been performed on irradiated V-(4-5)%Cr-(4-5)%Ti alloys. Tensile tests performed on some other neutron-irradiated vanadium alloys containing fusion-relevant amounts of helium have generally not observed pronounced helium embrittlement at $\geq$700°C, but creep-rupture tests on helium-containing irradiated specimens are needed to further investigate this issue [11,24-26]. Whereas vanadium alloys have good compatibility with liquid lithium at temperatures up to 600°C, interstitial solute pickup and predicted corrosion rates become significant at 650-700°C [17,27]. These corrosion and interstitial solute pickup effects might be mitigated if fully adherent self-healing insulator coatings can be successfully developed.

References

[1] M.C. Billone, 8th Int. Conf. on Fusion Reactor Materials, Sendai, J. Nucl. Mater. (1997) submitted.

[2] A.N. Gubbi, A.F. Rowcliffe, W.S. Eatherly, L.T. Gibson, Fusion Materials Semiannual Progress Report for Period ending June 30, 1996, DOE/ER-0313/20, Oak Ridge National Lab, 1996, p. 38.

[3] E.V. van Osch, 8th Int. Conf. on Fusion Reactor Materials, Sendai, J. Nucl. Mater. (1997) submitted.

[4] S.J. Zinkle et al., Fusion Materials Semiannual Progress Report for Period ending December 31, 1996, DOE/ER-0313/21, Oak Ridge National Lab, 1996, p. 73.

[5] M. Satou et al., J. Nucl. Mater. 233-237 (1996) 447.

[6] V.A. Kazakov, V.P. Chakin, Y.D. Goncharenko, Z.E. Ostrovsky, 8th Int. Conf. on Fusion Reactor Materials, Sendai, J. Nucl. Mater. (1997) submitted.

[7] E.V. van Osch, in: E.V. van Osch (Ed.) Proc. 2nd IEA Workshop on vanadium alloy development for fusion, ECN-R--96-012, Netherlands Energy Research Foundation ECN, 1996, p. 417.

[8] L.L. Snead et al., presented at 8th Int. Conf. on Fusion Reactor Materials, Sendai, (1997) to be publ. in Fusion Materials semiann. Prog Rep. for period ending Dec. 31 1997.

[9] D.N. Braski, in: F.A. Garner, C.H. Henager, Jr., N. Igata (Eds.), 13th Int. Symp. on Influence of Radiation on Material Properties (Part II), ASTM STP 956, Amer. Soc. Testing and Materials, Philadelphia, 1987, p. 271.

[10] D.N. Braski, in: R.L. Klueh et al. (Eds.), Reduced activation materials for fusion reactors, ASTM STP 1047, Amer. Soc. Testing and Materials, Philadelphia, 1990, p. 161.

[11] W. van Witzenburg, E. deVries, in: R.E. Stoller, A.S. Kumar, D.S. Gelles (Eds.), 15th Int. Symp. on Effects of Radiation on Materials, ASTM STP 1125, Amer. Soc. Testing and Materials, Philadelphia, 1992, p. 915.

[12] H.M. Chung, B.A. Loomis, D.L. Smith, J. Nucl. Mater. 239 (1996) 139.

[13] W.A. Simpson, Fusion Materials Semiannual Progress Report for Period ending March 31, 1994, DOE/ER-0313/16, Oak Ridge National Lab, 1994, p. 258.

[14] R.E. Gold, D.L. Harrod, International Metals Reviews 25 (1980) 232.

[15] B.A. Loomis, D.L. Smith, J. Nucl. Mater. 191-194 (1992) 84.

[16] H.M. Chung, B.A. Loomis, D.L. Smith, J. Nucl. Mater. 212-215 (1994) 772.

[17] D.L. Smith, B.A. Loomis, D.R. Diercks, J. Nucl. Mater. 135 (1985) 125.

[18] W.D. Porter, R.B. Dinwiddie, M.L. Grossbeck, Fusion Materials Semiann. Prog. Report for Period ending March 31, 1994, DOE/ER-0313/16, Oak Ridge National Lab, 1994, p. 260.

[19] G.E. Lucas et al., Fusion Materials Semiannual Progress Report for Period ending March 31, 1995, DOE/ER-0313/18, Oak Ridge National Lab, 1995, p. 147.

[20] G.R. Odette, E. Donahue, G.E. Lucas, J.W. Sheckherd, Fusion Materials Semiann. Prog. Report for Period ending June 30, 1996, DOE/ER-0313/20, Oak Ridge National Lab, 1996, p. 11.

[21] D.J. Alexander et al., 18th ASTM Symp. on Effects of Radiation on Materials, Hyannis, MA, 1996, in press; also Fusion Materials Semiannual Progress Report for Period ending June 30, 1996, DOE/ER-0313/20, Oak Ridge National Lab, 1996, p. 87.

[22] G.R. Odette et al., 8th Int. Conf. on Fusion Reactor Materials, Sendai, J. Nucl. Mater. (1997) submitted.

[23] S.J. Zinkle et al., 8th Int. Conf. on Fusion Reactor Materials, Sendai, J. Nucl. Mater. (1997) submitted.

[24] B. Van Der Schaaf, J. Nucl. Mater. 155-157 (1988) 156.

[25] H. Matsui et al., in: A.S. Kumar et al. (Eds.), 16th Int. Symp. on Effects of Radiation on Materials, ASTM STP 1175, Amer. Soc. Testing and Materials, Philadelphia, 1993, p. 1215.

[26] A.I. Ryazanov, V.M. Manichev, W. van Witzenburg, J. Nucl. Mater. 227 (1996) 304.

[27] V.A. Evtikhin, I.E. Lyublinski, V.Y. Pankratov, J. Nucl. Mater. 191-194 (1992) 924.

EFFECT OF THICKNESS AND LOADING MODE ON THE FRACTURE PROPERTIES OF V-4CR-4TI AT ROOM TEMPERATURE - H. Li, R. J. Kurtz and R. H. Jones (Pacific Northwest National Laboratory)*

To be published in the proceedings of the 8th International Conference on Fusion Reactor Materials held in Sendai, Japan, on October 26-31, 1997, in Journal of Nuclear Materials.

EXTENDED ABSTRACT

The effect of thickness on the room temperature (RT) mode I fracture behavior of V-4Cr-4Ti has been investigated. Mode I fracture properties were measured from J-integral tests of compact tension (CT) specimens ranging in thickness from 6.4 mm to 25.4 mm. All specimens were machined in the T-L orientation and vacuum annealed following final machining. Two heats of V-4Cr-4Ti were tested. Specimens 6.4 mm and 12.7 mm thick were taken from ANL Heat No. 832665. The 25.4 mm thick specimens were obtained from GA Heat No. 832864. J-R curves were generated by the single specimen unload-compliance test technique in accordance with ASTM E813. All tests were performed in laboratory air at 25°C.

The RT mode I fracture toughness of V-4Cr-4Ti is very high. ASTM validity criteria for J-R curve determination were not satisfied for any of the specimens tested. Ductile crack growth was observed for 6.4 mm thick specimens, but not for 12.7 mm or 25.4 mm thick specimens. It was found that V-4Cr-4Ti was prone to delaminate in planes normal to the thickness direction. More significantly, the fracture surfaces inside the delaminations indicated the fracture mode was predominantly cleavage. The severity of the delaminations increased as specimen thickness increased. The delaminations were caused, in part, by development of tensile stresses in the thickness direction due to the constraining effect of the material surrounding the crack tip plastic zone, which limits through thickness deformation. The cause of the delaminations is not known yet.

The effect of loading mode on fracture of V-4Cr-4Ti at RT was also studied. Mode I fracture behavior was compared to mixed-mode fracture properties obtained from modified CT specimens. The essential modification of the standard CT specimen is the slanted crack plane. This geometry produces a combination opening (mode I) and out-of-plane shear (mode III). Varying the crack angle varies the ratio of mode I to mode III loading. Crack angles of 0° and 25° were used.

The mixed-mode specimen behaved differently compared to the mode I specimen. During fatigue precracking the crack plane angle rotated from 25° to about 23°. However, during J-testing, the crack plane angle increased from 23° to about 30° when the crack started to grow. After crack initiation, the crack plane angle remained at about 30° until the end of the test. The mixed-mode specimen also exhibited extensive plastic deformation similar to the mode I specimen. The high J-values reached indicated that crack initiation was difficult. The reasons for this behavior are not fully understood. Crack plane rotation prior to crack initiation was one of the factors which contributed to the high J-value for initiation. While the mixed-mode crack was difficult to initiate, it propagated easily. The slope of the mixed-mode I/III J-R

*Pacific Northwest National Laboratory is operated for the U.S. Department of Energy by Battelle Memorial Institute under Contract DE-AC06-76RLO 1830.

curve beyond the exclusion line was only 140 kJ/m^2/mm, or about one-third of that for the mode I specimen.

Fracture of V-4Cr-4Ti under mixed-mode loading conditions showed the same trend observed previously for V-5Cr-5Ti and for other tough materials [1]. For materials which fail by microvoid coalescence, the addition of an out-of-plane shear loading component introduces incompatibility stresses at particle interfaces in the trajectory of the crack. These incompatibility stresses cause particle/matrix decohesion or particle fracture which leads to void formation that limits the mode I plastic flow field. The present results demonstrate that fracture of V-4Cr-4Ti is sensitive to the addition of shear loading components and that mode I fracture toughness tests may not give the most conservative measure of resistance to ductile fracture.

REFERENCES

1. H. Li, R. H. Jones, J. P. Hirth and D. S. Gelles, "Effect of Loading Mode on the Fracture Toughness of a Reduced-Activation Ferritic/Martensitic Stainless Steel," *J. of Nuc. Matls.*, 212-215, 1994, pp. 741-745.

GRAIN BOUNDARY CHEMISTRY AND HEAT TREATMENT EFFECTS ON THE DUCTILE-TO-BRITTLE TRANSITION BEHAVIOR OF VANADIUM ALLOYS -

R. J Kurtz, M. L. Hamilton, and H. Li (Pacific Northwest National Laboratory)*

OBJECTIVE

The objective of this work is to determine the effect of different heat treatments on the grain boundary chemistry and Charpy impact properties of the production-scale heat of V-4Cr-4Ti (Heat No. 832665) for comparison with results generated previously on V-5Cr-5Ti (Heat No. 832394).

SUMMARY

One-third scale Charpy impact specimens of V-4Cr-4Ti were given the same heat treatments applied to equivalent specimens of V-5Cr-5Ti. Auger specimens of V-4Cr-4Ti were also heat treated with the Charpy specimens to enable grain boundary chemistry measurements. The microstructural, microchemical and Charpy impact response of V-4Cr-4Ti displayed trends similar to those observed for V-5Cr-5Ti. The results show that grain size plays an important role in determining the ductile-to-brittle transition temperature (DBTT) of these materials and that a threshold level of grain boundary segregant appears to be required to cause grain boundary embrittlement and intergranular fracture.

PROGRESS AND STATUS

Introduction

It has been shown that the fracture toughness and Charpy impact properties of vanadium alloys being considered for fusion power system applications are sensitive to heat treatment variations [1-7]. In an earlier study, heat treatment of V-5Cr-5Ti from Heat No. 832394 at 1125°C for 1 h gave fracture toughness of about 52 kJ/m^2 when tested at room temperature (RT) and a DBTT of 80°C, Figure 1 [4]. Fracture surfaces exhibited a mixture of intergranular and cleavage fracture features. When some specimens were given an additional heat treatment at 890°C for 24 h, they became ductile at RT and fractured by microvoid coalescence [4]. The fracture toughness for material in this condition was very high (~1100 kJ/m^2) and the DBTT decreased to -145°C, Figure 1.

The reasons for this behavior are not completely understood. Based on Auger analyses sulfur concentrations on grain boundaries were higher [2,4] and precipitate densities appeared to be lower for the 1125°C/1h heat treatment relative to the 1125°C/1h + 890°C/24h treatment [4,5]. Transmission electron microscopy was performed to provide microstructural and microchemical information. Detailed microstructural comparisons showed distinct differences in precipitation behavior between the two heat treatments [6]. Following heat treatment at 1125°C, only Si was found as a minor impurity in large particles, but S could be identified at grain boundaries, which were coated with a fine distribution of precipitates. After the additional heat treatment at 890°C more precipitation consisting of (Ti,V)O and

*Pacific Northwest National Laboratory is operated for the U.S. Department of Energy by Battelle Memorial Institute under Contract DE-AC06-76RLO 1830.

containing Si, S, and P was observed. It was concluded that embrittlement of V-5Cr-5Ti was probably due to a combination of interstitial solid solution hardening and grain boundary impurity segregation since both intergranular and transgranular failure modes were found.

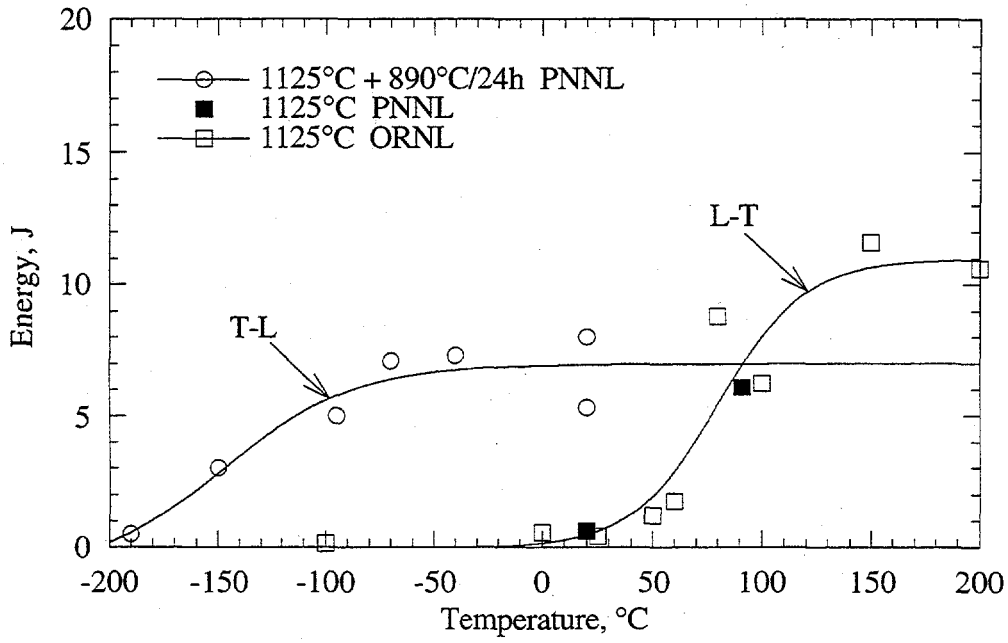

Figure 1. Unirradiated Charpy impact properties for V-5Cr-5Ti (Heat No. 832394) following heat treatments at 1125°C for 1 h [4,5,7] and 1125°C for 1 h + 890°C for 24 h [4,5].

The objective of the present study is to perform the same set of heat treatments on a production-scale heat (No. 832665) of V-4Cr-4Ti to determine if similar variations in grain boundary chemistry and Charpy impact properties are observed. Grain boundary chemistry is characterized by Auger electron spectroscopy and initial microstructural evaluation is by optical microscopy.

Experimental Procedure

The material used in this study was V-4Cr-4Ti (Heat No. 832665) produced by Wah Chang (formerly Teledyne Wah Chang) of Albany, Oregon. Material chemistry and fabrication details have been reported previously [8]. A 3.8 mm thick plate was obtained from Argonne National Laboratory in the warm rolled condition. One-third scale Charpy specimens were machined from the plate with dimensions 23.6 mm x 3.33 mm x 3.33 mm. A 30°, 0.51 mm deep notch was used with a 0.030 mm root radius. Charpy specimens were taken from the plate in the T-L orientation. After machining specimens were heat treated in a vacuum of $\leq 1.33 \times 10^{-5}$ Pa. Three different heat treatments were investigated.

1) HT1: 1000°C for 1 h, furnace cool
2) HT2: 1125°C for 1 h, furnace cool
3) HT3: HT2 + 890°C for 24 h, furnace cool

Charpy impact testing was performed at Oak Ridge National Laboratory using an instrumented system. The hammer was dropped from a low-blow position with a potential energy of 70 J at an impact velocity of ~2.3 m/s. Fracture surfaces of selected specimens were examined in a scanning electron microscope.

Grain boundary chemistry was determined by scanning Auger electron spectrometry (Perkin-Elmer Model 660). Auger specimens were hydrogen charged for 2 h prior to insertion into the Auger. Specimens were then cooled to liquid nitrogen temperature and fractured in the Auger system chamber in a vacuum of $\leq 1 \times 10^{-7}$ Pa. Auger spectra were taken at an accelerating voltage of 5 kV and an incident electron current of 200 nA.

Results

The microstructures resulting from the three heat treatments employed in this study are presented in Figure 2. Figure 2a gives the microstructure for the HT1 heat treatment. Heat treatment produces a partially recrystallized microstructure with a bimodal grain size distribution. The average grain diameter is 13 μm. In addition, there is evidence of the precipitation of secondary phases in this microstructure. The HT2 microstructure is shown in Figure 2b. The grain size in this microstructure is more equiaxed and is considerably larger (33 μm) than for the HT1 heat treatment. The precipitate volume fraction is much smaller compared to the HT1 condition. The microstructure for the HT3 heat treatment is displayed in Figure 2c. The grain shape and size (32 μm) is the same as for the HT2 microstructure but it is evident that a considerable amount of precipitation results from annealing at 890°C.

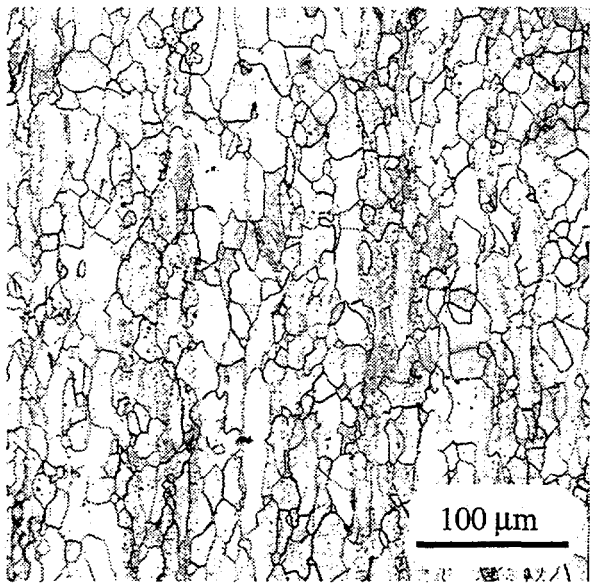

(a)

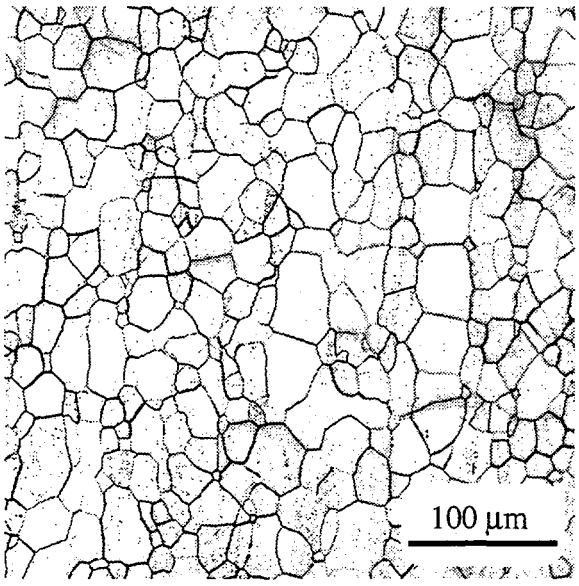

(b)

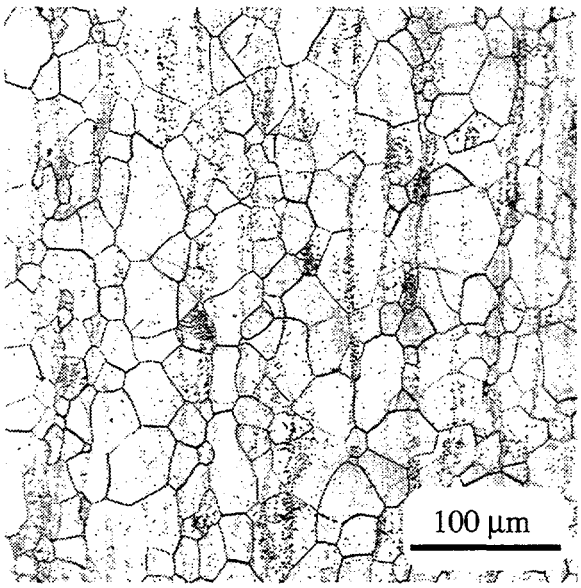

(c)

Figure 2. Optical micrographs showing microstructures of V-4Cr-4Ti resulting from various heat treatments: a) HT1, b) HT2 and c) HT3.

The Auger results for each heat treatment are collected in Table 1. Elemental measurements for intergranular facets are distinguished from cleavage facets in Table 1. Comparing the chemical information from cleavage facets to that from intergranular facets gives an indication of the degree to which various elements segregate to grain boundaries.

Comparing intergranular to cleavage facets reveals that N, S, P and to a lesser extent C tend to segregate to grain boundaries for all heat treatments. There also appears to be a slight depletion of O at grain boundaries under all conditions. Comparing results for intergranular facets shows increased concentrations of S, C and Cr, and decreased levels of P for the HT2 specimens compared to HT1 and HT3 specimens. The grain boundary chemistries of the latter two heat treatments were similar to each other and distinct from the HT2 treatment. The grain boundary O levels were the same for all three heat treatments. Little variation in grain boundary N level was found, with the highest level occurring in specimens given the HT3 heat treatment.

Table 1. Auger electron spectroscopy results (at.%) for V-4Cr-4Ti (Heat No. 832665)

Element	Heat Treatment Conditions					
	1000°C/1h		1125°C/1h		1125°C/1h + 890°C/24h	
	IF*	CF**	IF	CF	IF	CF
Cr	4.1	5.3	5.6	8.0	4.5	6.0
Ti	5.9	6.1	5.6	5.9	8.7	5.7
C	3.3	2.8	7.3	3.5	4.7	2.3
O	17	20	17	23	17	21
N	19	3.7	20	3.1	25	3.6
S	1.4	0.2	3.2	0.3	0.9	0.2
P	4.1	0.7	2.4	0.6	4.3	0.6

*IF = Intergranular Facet
**CF = Cleavage Facet

The Charpy impact results are plotted in Figure 3. The data for the HT2 and HT3 specimens were fitted to a hyperbolic tangent function to aid identification of the DBTT. The data for the HT1 heat treated material shows that no DBTT was observed down to -196°C. The trend of the data is increasing absorbed energy with decreasing test temperature, which is consistent with flow stress controlled deformation. Crack initiation and arrest was observed for HT1 specimens tested at -150°C and -196°C, but no crack initiation was seen for specimens tested at higher temperatures. The HT2 annealed material exhibited a DBTT of about-125°C. The HT3 specimens also gave a DBTT of about -125°C, but the lower shelf energies were significantly greater than the HT2 specimens demonstrating the beneficial effect of the 890°C heat treatment. Similar to the HT1 specimens crack initiation and arrest occurred for HT2 and HT3 specimens tested at the two lowest test temperatures, but not for the two highest temperatures. For HT2 and HT3 specimens, once a crack initiated it propagated almost entirely through the initial uncracked ligament.

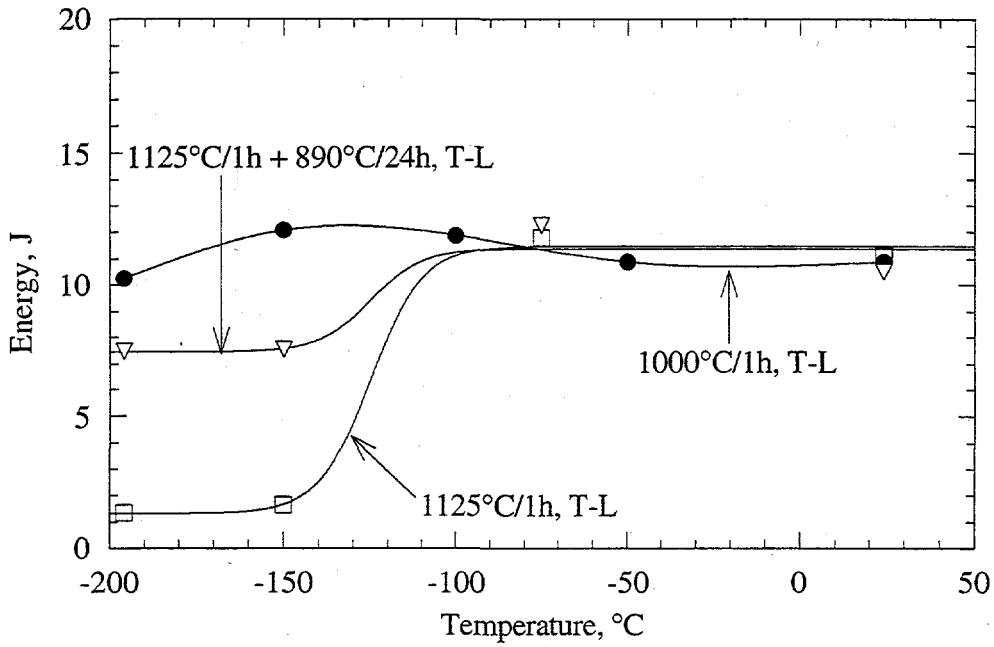

Figure 3. Unirradiated Charpy impact properties for V-4Cr-4Ti (Heat No. 832665) following heat treatments at 1000°C for 1 h, 1125°C for 1 h and 1125°C for 1 h + 890°C for 24 h.

The fracture surfaces of HT2 and HT3 specimens were examined in a scanning electron microscope to determine the fracture mechanism. For HT2 specimens the fracture surfaces displayed predominantly cleavage fracture features with a minor amount (<10%) of intergranular fracture. A small amount of microvoid coalescence was noted in the HT2 specimen tested at -150°C. For HT3 specimens a mixture of ductile and brittle fracture mechanisms was found. The fracture surface of the HT3 specimen tested at -150°C showed largely microvoid coalescence features with isolated regions of cleavage fracture. The size of the cleavage fracture areas increased near the back face of the specimen. The fracture mechanism of the HT3 specimen tested at -196°C was ductile near the notch root and along the sides of the specimen, but cleavage fracture was observed in the middle of the specimen and toward the back face. It is interesting to note that the absorbed energies of the two HT3 specimens in which crack initiation occurred were nearly the same, but the pattern of ductile versus cleavage fracture features were somewhat different.

Discussion

Table 2 summarizes the pertinent microstructural, microchemical and Charpy impact data for the different heat treatments employed on V-(4-5)Cr-(4-5)Ti. In the previous investigations [4-6] of heat treatment effects on V-5Cr-5Ti it was concluded that the improved fracture properties seen in specimens aged at 890°C was probably due to two factors 1) a reduction in the grain boundary sulfur concentration and 2) a decrease in the interstitial impurity level resulting from precipitation reactions. Low energy fractures of V-5Cr-5Ti exhibited both intergranular and transgranular cleavage features suggesting that grain boundary

embrittlement and interstitial hardening both played a role in reducing toughness. Specimens of V-5Cr-5Ti given the HT2 heat treatment yielded the highest DBTT and grain boundary S concentration. Following the HT3 heat treatment the DBTT decreased to -145°C and the grain boundary S level to 1.1 at.% with no change in grain size relative to HT2 specimens.

In the present study some of the same effects were observed. The microstructures produced by the various heat treatments were similar to those found for V-5Cr-5Ti specimens. A high density of precipitates was evident in the HT3 microstructure and to a lesser extent the HT1 microstructure relative to the HT2 condition. Measurable increases in the grain boundary S concentration (and C) were noted following the HT2 heat treatment compared to the HT1 and HT3 anneals. Although the DBTT of the HT3 material was the same as the HT2 material the lower shelf energies were significantly greater. One important difference is that intergranular fracture of low toughness specimens was observed only to a very limited extent. This result suggests that a threshold level of grain boundary segregant is needed to produce grain boundary embrittlement. It also indicates that processes which remove interstitial impurities from the matrix are an important mechanism for improving toughness. It should also be noted that aging at 890°C improved the resistance of the matrix to cleavage fracture but did not recover all of the toughness lost by annealing at 1125°C. This is caused by the much larger grain size produced at 1125°C compared to the 1000°C anneal. It is well known that the DBTT of refractory metals depends on grain size. All other factors remaining constant, the smaller the grain size, the lower the DBTT.

Table 2. Summary of microstructural, microchemical and Charpy impact data for various heat treatments of V-(4-5)Cr-(4-5)Ti.

Alloy	Heat No.	Heat Treatment, °C	Orientation	GB [S], at.%	Grain Size, μm	DBTT, °C
V-5Cr-5Ti	832394	1125/1h	L-T	6.3	45	+80
"	"	1125/1h + 890/24h	T-L	1.1	45	-145
V-4Cr-4Ti	832665	1000/1h	T-L	1.4	13	<-196
"	"	1125/1h	T-L	3.2	33	-125
"	"	1125/1h + 890/24h	T-L	0.9	32	-125

CONCLUSIONS

The effect of heat treatment on the microstructure of V-4Cr-4Ti was similar to that observed for V-5Cr-5Ti. The increase in DBTT caused by heat treatment at 1125°C for 1 h was due to a larger grain size and reduced levels of precipitation compared to heat treatment at 1000°C for 1h. Considerable toughness was recovered for V-4Cr-4Ti previously given the 1125°C/1h heat treatment by aging at 890°C for 24 h. The aging heat treatment caused precipitation of phases which reduced grain boundary S levels and lowered the concentration of interstitials in solid solution. A threshold level of grain boundary segregant appears to be required to

cause grain boundary embrittlement and intergranular fracture.

FUTURE WORK

Transmission electron microscopy will be performed on heat treated V-4Cr-4Ti specimens for comparison with the earlier work on V-5Cr-5Ti. The objective shall be to characterize the precipitates formed during heat treatment.

ACKNOWLEDGEMENTS

We are indebted to Dr. David Alexander at Oak Ridge National Laboratory for performing the Charpy impact tests.

REFERENCES

1. H. M. Chung, J. Gazda, L. J. Nowicki, J. E. Sanecki and D. L. Smith, "Effects of Fabrication Variables on Impact Properties and Microstructure of V-Cr-Ti Alloys," Fusion Materials Semiannual Progress Report, DOE/ER-0313/15, 207.

2. M. L. Grossbeck, A. F. Rowcliffe and D. J. Alexander, "The Relationship Between Recrystallization Temperature, Grain Size, and the Charpy Impact Properties of V-Cr-Ti Alloys," Fusion Materials Semiannual Progress Report, DOE/ER-0313/16, 244.

3. D. N. Braski and M. L. Grossbeck, "Analysis of Grain Boundaries in a V-5Cr-5Ti Alloy Using Auger Electron Spectroscopy," Fusion Materials Semiannual Progress Report, DOE/ER-0313/16, 272.

4. H. Li., M. L. Hamilton and R. H. Jones, "Effect of Heat Treatment on Microstructure and Fracture Toughness of a V-5Cr-5Ti Alloy," Fusion Materials Semiannual Progress Report, DOE/ER-0313/17, 165.

5. H. Li., M. L. Hamilton and R. H. Jones, "Effect of Heat Treatment and Test Method on DBTT of a V-5Cr-5Ti Alloy," Fusion Materials Semiannual Progress Report, DOE/ER-0313/18, 215.

6. D. S. Gelles and H. Li, "Effect of Heat Treatment on Precipitation in V-5Cr-5Ti Heat BL-63," Fusion Materials Semiannual Progress Report, DOE/ER-0313/19, 22.

7. A. F. Rowcliffe and S. J. Zinkle, "Assessment of the Radiation-Induced Loss of Ductility in V-Cr-Ti Alloys," Fusion Materials Semiannual Progress Report, DOE/ER-0313/21, 63.

8. H. M. Chung, H.-C. Tsai, D. L. Smith, R. Peterson, C. Curtis, C. Wojcik and R. Kinney, "Fabrication of 500-kg Heat of V-4Cr-4Ti," Fusion Materials Semiannual Progress Report, DOE/ER-0313/17, 178.

TEMPERATURE DEPENDENCE OF THE RADIATION DAMAGE MICROSTRUCTURE IN V-4Cr-4Ti NEUTRON IRRADIATED TO LOW DOSE* — P. M. Rice and S. J. Zinkle (Oak Ridge National Laboratory)

Extended Abstract

Transmission electron microscopy (TEM) was performed on the US program heat of V-4Cr-4Ti (heat #83665) irradiated to damage levels of 0.1-0.5 displacements per atom (dpa) at 110-505°C in the High Flux Beam Reactor at Brookhaven. A high density (~$1 \times 10^{23}/m^3$) of small (~3.0 nm diameter) faulted dislocation loops were observed at irradiation temperatures below 275°C. These dislocation loops became unfaulted at temperatures above ~275°C, and a high density of small Ti-rich defect clusters lying on {001} planes appeared along with the unfaulted loops at temperatures above 300°C. The density of the {001} defect clusters was much higher than that of the dislocation loops at all temperatures above ~300°C. The density of both types of defects decreased with increasing temperature above 300°C, with the most rapid decrease occurring for temperatures above 400°C. Based on the TEM and tensile measurements, the dislocation barrier strengths of the faulted dislocation loops and {001} defect clusters are ~0.4-0.5 and 0.25, respectively. This indicates that both types of defects can be easily sheared by dislocations during deformation. Cleared dislocation channels were observed following tensile deformation in a specimen irradiated at 268°C.

The microstructural investigation of V-4Cr-4Ti specimens irradiated to relatively low fission neutron doses of 0.1 to 0.5 dpa demonstrated that several complex radiation processes occur. The microstructure was independent of temperature between 110 and ~275°C, where it was composed of a high density of small faulted (b=a/2<110>) dislocation loops. The high density and low barrier strength of these dislocation loops produce significant radiation hardening with a concomitant sharp decrease in uniform elongation and an increase in the ductile to brittle transition temperature.

Loop unfaulting occurred over a rather narrow temperature range centered near 300°C, and a high density of defect clusters on {001} habit planes was observed from 315°C up to the maximum irradiation temperature in this study of 505°C. The {001} defect clusters were enriched in Ti at elevated temperatures, and their displacement vector was determined to be a/3<001> at 505°C. These {001} defect clusters may be the precursors of the Ti-rich precipitates reported in higher dose studies at temperatures $\geq$ 400°C.

It would be useful to investigate the microstructure of irradiated V-4Cr-4Ti at relatively low doses of 0.1 to 10 dpa to provide further insight into the microstructural evolution which occurs at temperatures above 400°C.

*Extended abstract of paper submitted to Journal of Nuclear Materials as part of the proceedings of the 8th International Conference on Fusion Reactor Materials, Sendai, Japan, October 27-31, 1997.

MICROSTRUCTURAL EXAMINATION OF IRRADIATED V-(4-5%)Cr-(4-5%)Ti - D. S. Gelles (Pacific Northwest National Laboratory)* P. M. Rice and S. J. Zinkle (Oak Ridge National Laboratory) and H. M. Chung (Argonne National Laboratory)

To be published in the proceedings of the 8th International Conference on Fusion Reactor Materials held in Sendai, Japan, on October 26-31, 1997, in Journal of Nuclear Materials.

EXTENDED ABSTRACT

Microstructural examination results are reported for two heats of V-(4-5%)Cr-(4-5%)Ti irradiated in the EBR-II X530 experiment to ~4 dpa at ~400°C to provide an understanding of the microstructural evolution that may be associated with degradation of mechanical properties. Fine precipitates were observed in high density intermixed with small defect clusters for all conditions examined following the irradiation. The irradiation-induced precipitation does not appear to be affected by preirradiation heat treatment at 950-1125°C. There was no evidence for a significant density of large (diameter >10 nm) dislocation loops or network dislocations. Analytical investigations successfully demonstrated that the precipitates were enriched in titanium, depleted in vanadium and contained no nitrogen.

*Pacific Northwest National Laboratory is operated for the U.S. Department of Energy by Battelle Memorial Institute under Contract DE-AC06-76RLO 1830.

MICROSTRUCTURE OF V-4Cr-4Ti ALLOY AFTER LOW-TEMPERATURE IRRADIATION BY IONS AND NEUTRONS* - J. Gazda and M. Meshii (Northwestern University), and H. M. Chung (Argonne National Laboratory)

SUMMARY

Mechanical properties of V-4Cr-4Ti alloy were investigated after low-temperature (<420°C) irradiation. The effects of fast neutrons at 390°C were investigated by irradiation to ≈4 dpa in the X530 experiment in the EBR-II reactor; these tests were complemented by irradiation with single (4.5-MeV Ni^{++}) and dual ion beams (350-keV He^{+} simultaneously with 4.5-MeV Ni^{++}). TEM observations showed the formation of a high density of point-defect clusters and dislocation loops (<30 nm diameter) distributed uniformly in the specimens. Mechanical-property testing showed embrittlement of the alloy. TEM investigations of deformed microstructures were used to determine the causes of embrittlement and yielded observation of dislocation channels propagating through the undeformed matrix. Channels are the sole slip paths and cause early onset of necking and loss of work-hardening in this alloy. Based on a review of the available literature, suggestions are made for further research of slip localization in V-base alloys .

INTRODUCTION

Interest in application of V-4 wt.% Cr - 4 wt.% Ti (V-4Cr-4Ti) alloy in the ITER prompted recent investigations of the effects of low-to-moderate temperature (200-420°C) irradiation on the alloy's mechanical properties. This irradiation temperature range is also relevant to transient situations in other fusion reactors. To address these issues, two sets of experiments were conducted within this temperature range. Effects of fast neutrons (E > 0.1 MeV) at 390°C were investigated with irradiation in the EBR-II reactor in the X530 experiment, which attained a fluence of ≈4 dpa. Due to limited space and the imminent shutdown of the EBR-II reactor, a complementary study was undertaken using single (4.5-MeV Ni^{++}) and dual ion beams (350-keV He^{+} simultaneously with 4.5-MeV Ni^{++}); details of this experiment can be found in Ref. 1.

The ion-irradiated specimens did not allow direct measurement of fracture properties of the material, but they provided a warning about the possibility of extensive hardening due to radiation-induced defects. The neutron irradiation resulted in degradation of the V-4Cr-4Ti alloy, manifested by loss of work-hardening capability in tensile specimens and an increase in ductile-to-brittle-transition temperature (DBTT) to above 300 K, as measured from instrumented Charpy tests on miniature ($^1/_3$-size) CVN specimens [2, 3]. A concurrent irradiation study in the HFBR reactor also reported dramatically increased DBTT and loss of work-hardening capability after irradiation to 0.5 dpa at temperatures of 100 to 275°C [4].

In this report, we include preliminary results of TEM work aimed at exploring the deformation mechanisms in irradiated V-4Cr-4Ti. Based on the current work and studies available in the literature, suggestions are made for further research of dislocation channeling in irradiated vanadium alloys, directed to improve postirradiation ductility.

EXPERIMENTAL PROCEDURES

Procedures used to prepare the V-4Cr-4Ti alloy (Heat 832665, ANL ID: BL71) are described in detail in Ref. 5. Specimen preparation steps for ion and neutron irradiation were provided in Ref. 1. Annealed (1 hr at 1050°C in 10^{-5} Pa UHV ion pumped vacuum) 3-mm-diameter disks were irradiated at the Argonne Tandem Accelerator facility operated by the Materials Science Division with single (4.5 MeV Ni^{++}) or dual ion beams (350 keV He^{+} simultaneously with 4.5 MeV Ni^{++}). The disks were later sectioned (surface layer of 800~1000 nm removed) and back-jet-thinned for TEM observations. The neutron irradiation was conducted during the final run of the EBR-II reactor in August/September 1994. Specimens were irradiated in Li-filled capsules, located in the core

* Work supported by the U.S. Department of Energy, Office of Fusion Energy, under Contract W-31-109-Eng-38.

position, to ≈4 dpa (2.4×10^{15} $n \cdot cm^{-2} \cdot s^{-1}$, E>0.11 MeV) at 390°C. Details of this irradiation experiment were reported in Ref. 6.

To evaluate deformation processes in the irradiated materials, three types of specimens were examined with TEM. First, specimens with ion damage were indented at room temperature (RT) with a Berkovitch nano-indentor to induce plastic deformation. TEM foils were then prepared from regions near the indentation. Second, disks were made from sections of irradiated Charpy specimens to evaluate the microstructure without and with plastic deformation. The disks were cut with a diamond saw and electropolished to remove damage due to cutting. Subsequently, some of the disks were polished for TEM examination, while others were indented at RT with a Vickers indentor to produce plastic deformation (typical indentations yielded hardness measurement of 320 VHN, as opposed to 178 VHN in annealed material). TEM foils were then prepared from regions under the indentations. For the third type, TEM foils were obtained from cross-sectional pieces of a fractured SS-3 miniature tensile sheet specimen used for determination of postirradiation mechanical properties (BL71-50 irradiated in EBR-II, X530 experiment, subcapsule S9; tensile tested to fracture at 390°C with strain rate of $1.1 \cdot 10^{-3}$ sec^{-1}: YS = 805 MPa, UTS = 808 MPa, Uniform Elong. = 0.45%, Total Elong. = 4.7%). Cross-sections were obtained from the shoulder, gauge length, and necked regions of the tensile specimen.

All TEM specimens were electropolished with a South Bay Technology Single Jet Electropolisher 550B and electrolyte consisting of (by volume) 70% H_2SO_4, 15% CH_3OH, and 15% $C_6H_{14}O_2$ Butyl Cellosolve at -10°C. Microstructure observations were conducted in Phillips CM30 transmission electron microscope.

RESULTS

The microstructure of the unirradiated V-4Cr-4Ti alloy consists of ≈20 μm grains with loosely dispersed ≈200-nm-diameter Ti(CNO) precipitates. These particles form in the ingot and are commonly found in all U.S. V-Ti-Cr alloys, as seen in Fig. 1(a). The irradiated microstructure of V-4Cr-4Ti alloy changes with fluence and temperature of irradiation; details on evolution of the irradiated microstructure are reported in Ref. 1. Ion irradiation caused formation of a high density ($\approx 2 \cdot 10^{22}$ m^{-3}) of small dislocation loops and "black dot" point-defect clusters after irradiation to 5 dpa at 350°C with 4.5 MeV Ni^{++} ions, as shown in Fig. 1(b). Similarly, neutron irradiation caused formation of uniformly distributed point-defect clusters and dislocation loops (≈5-10 nm in diameter, number density on the order of $\approx 10^{22}$ m^{-3}). Figure 1(c) provides an example of the X530 EBR-II irradiated V-4Cr-4Ti microstructure.

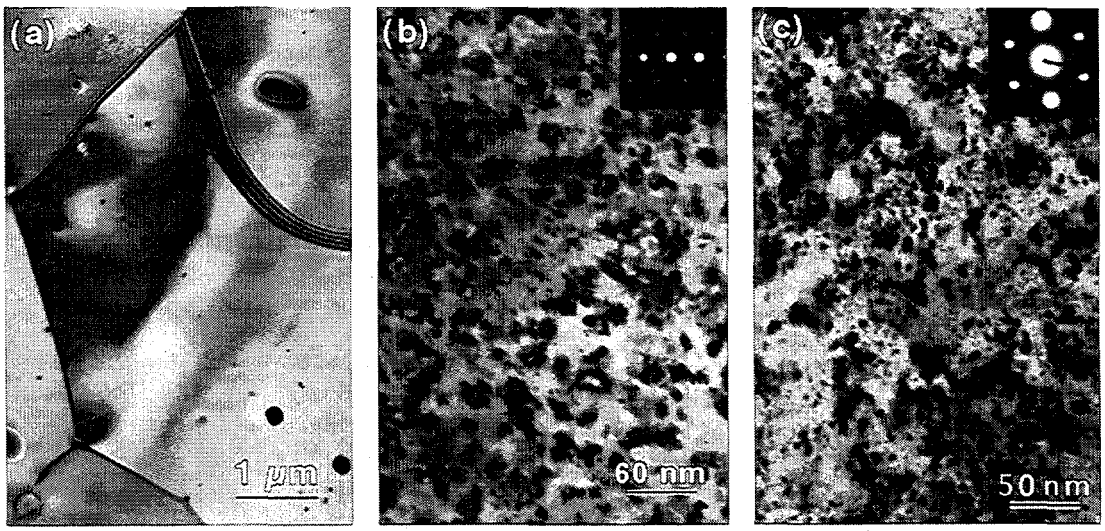

Figure 1. Typical microstructure of V-4Cr-4Ti alloy: (a) annealed for 1 hr at 1050°C in UHV furnace, (b) ion irradiated to 5 dpa at 350°C with 4.5 MeV Ni^{++}, and (c) irradiated to 4 dpa at 390°C in the X530 experiment.

Studies of the microstructure after plastic deformation were undertaken to determine the mechanisms for the radiation embrittlement of V-4Cr-4Ti irradiated below 420°C. Ion-irradiated and nano-indented specimens were used in early experiments. TEM foils prepared from areas below the indentation showed bands filled with dislocations, also known as "channels." All plastic deformation appeared to be confined to these channels, because no slip dislocations were observed elsewhere. Figure 2 shows examples of the dislocation channels in ion-irradiated and indented V-4Cr-4Ti.

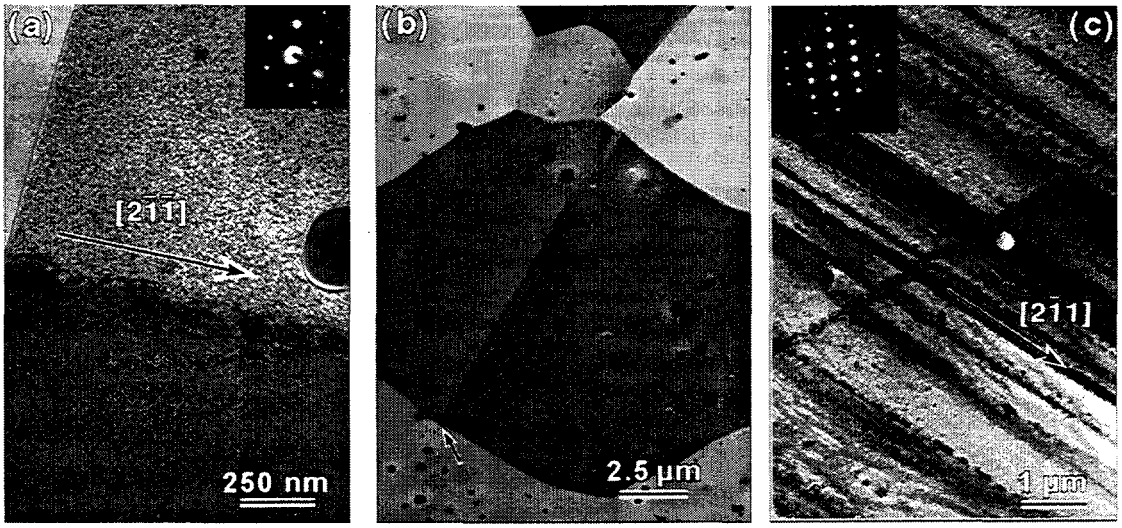

Figure 2. Dislocation channels observed in ion irradiated and indented specimens: (a) tangled dislocations forming a channel (0.5 dpa at 200°C), (b) channel arrested by grain boundary (10 dpa at 350°C), (c) channels in heavily deformed specimen (5 dpa at 420°C), two channel directions visible.

The miniature size of the limited number of the tensile specimens (gauge length dimensions: $0.6 \times 1 \times 5.6$ mm) employed in the X530 experiment and the early onset of necking made the task of TEM specimen preparation extremely difficult. Therefore, sections of X530 neutron-irradiated Charpy specimens were first indented and TEM foils were then prepared from the region near indentation in the same way as in the ion-irradiated specimens. Again, the slip activity was found to be confined exclusively to the dislocation channels; an example is given in Fig. 3(a). The crystallographic directions of the channels were determined and were consistent with the slip traces within the accuracy of the experiment, as the channels often deviated from a straight line, indicating that massive cross-slips occurred during dislocation motion.

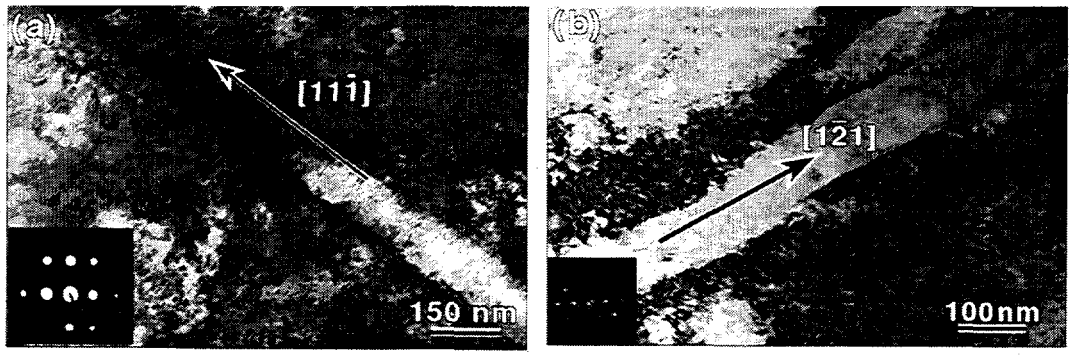

Figure 3. Dislocation channels in neutron-irradiated V-4Cr-4Ti alloy: (a) after indentation at room temperature, (b) after tensile deformation.

A limited number of TEM observations were carried out in the foils prepared from the necked regions of the tensile specimen (BL71-50). Although the fracture surface showed the ductile mode of fracture, TEM foils prepared from the necked region directly under the fracture surface exhibited dislocation channels as shown in Fig. 3(b). The channel direction was determined as <211> for the foil zone axis <111>, again consistent with the trace of {110} planes. The deviation of the channels from a straight line indicated the occurrence of cross-slip during deformation.

DISCUSSION

Dislocation channels were observed in all irradiated and deformed materials investigated in this study. Microstructural evaluation of ion-irradiated and indented specimens provided an early warning of dislocation channel formation. Channel formation was confirmed in neutron-irradiated material by TEM observation of the microstructure near a hardness indentation in Charpy specimens and parts of a tensile specimens within the necked region. In most cases, the channels contained dislocations, except for a few examples of channels nearly free of dislocations; these were found in exceptionally thin foils made from the neutron-irradiated and deformed specimen. This difference is attributed to dislocations slipping out of the foils in the vicinity of the surface, rather than a change in the character of the channels. In nearly all cases, the termination of a dislocation channel at a grain boundary triggered another channel in the adjacent grain. The crystallographic nature of the channels was the same in all three types of specimens.

Although our observations of dislocation channels are the first in the V-4Cr-4Ti alloy, dislocation channels are common in a wide variety of materials where barriers to dislocation movement are uniformly distributed throughout the specimen. Luft [7] presented a detailed overview of dislocation channeling not limited to irradiated metals; he stated that in all investigated pure BCC metals that contained visible radiation damage (Fe, Nb, V, and Mo), defect-free slip channels were observed. The localization of strain was attributed to various strain-softening mechanisms. In irradiated and deformed metals, strain softening was explained by the loss of the defects from a channel by either annihilation or "plowing" the defects to the sides of the channel. Agglomeration of defect clusters at the edges of channels characteristic of the "plowing" mechanism were not observed in this study; therefore defect annihilation is the likely mechanism responsible for channel formation.

Formation of dislocation channels was also observed by TEM in neutron-irradiated single crystals of vanadium alloys by Huang and Arsenault [8]. Dislocation channels studied in the present work bear a close resemblance to those observed by them.

Our observation of slip localization by dislocation channel formation explains the macroscopic loss of ductility found in the irradiated vanadium base alloys The following two types of observations are also well known in materials where channel formation takes place:

1. Predeformation of fully annealed material by cold working without significant rearrangement of the grain structure introduces dislocations which could be mobilized during the postirradiation deformation. In molybdenum, a critical density (6×10^8 cm^{-2} at 493 K) of obstacles is necessary for channel formation [9]. Below this density, dislocations distributed in the matrix act only as forest dislocations that provide the desired work-hardening effects. At higher dislocation densities, slip localization occurred upon redeformation. Dislocations uniformly distributed throughout the material could lead to more uniformly distributed slip in postirradiation deformation.
2. Introduction of incoherent, uncuttable particles can reduce slip localization. Dislocation channels were observed to form in Ti-base precipitation-strengthened alloys during deformation [10]. Aging studies showed that these small uniformly distributed coherent particles promote slip localization because dislocations were able to cut through them and form particle-free channels. However, when further aged, precipitates were replaced by larger semicoherent or incoherent particles that cannot be easily cut. In such cases, dislocations are forced to cross-slip around the precipitates during deformation, essentially work-hardening the alloy and leading to homogenization of macroscopic slip.

Therefore, providing uniformly distributed incoherent particles in the matrix, such as Ti(CNO), combined with a small degree of prestrain, could result in a higher macroscopic ductility in post-irradiated V-4Cr-4Ti. Limited supporting experimental evidence also exists from the recently compiled evaluations of tensile testing of vanadium-base alloys irradiated at low temperatures (<400°C). The alloy containing a high density of large uncuttable particles (V-17.7 wt.% Ti , ANL ID: BL15) and a cold-worked specimen of V-4Cr-4Ti alloy (experimental heat, ANL ID: BL47), which were used in earlier neutron irradiation studies and were replaced by the purer alloy in the current work, exhibited uniform elongation ≥2% [11]. The vanadium alloy development should be extended along this line to seek slip homogenization during deformation after low-temperature-irradiation.

CONCLUSIONS

1. The usefulness of ion irradiation as a tool in assessing the properties of fusion candidate materials should be noted. In the present case, ion irradiation was designed to provide information about both the swelling and embrittlement potential of a V-4Cr-4Ti alloy irradiated at low temperatures. In ion-irradiated specimens, voids/cavities were not observed by TEM and slip localization by dislocation channels was found near an indentation.
2. Dislocation channels were observed in V-4Cr-4Ti alloy deformed after irradiation. Slip localization resulted from the formation of defect-free, easy glide paths for slip dislocations. This is suggested to be the cause of premature necking and loss of work-hardening of the tensile specimen (BL71-50) of the V-4Cr-4Ti alloy (Heat No.: 832665, BL71) after fast neutron (E>0.1 MeV) irradiation to ≈4 dpa at 390°C in the EBR-II X530 experiment.
3. Channel formation is a common feature of the low-temperature deformation of BCC metals containing a dispersion of unstable barriers to dislocation glide. Microstructural refinement is suggested as an alloy development task to minimize post-irradiation embrittlement at low temperatures (<420°C).

REFERENCES:

1. Gazda, J., M. Meshii, and H.M Chung, in *MRS Fall '96 Meeting Proceedings Vol. 439,* Robertson, I.M., G.S. Was, L.W. Hobbs, and T. Diaz de la Rubia, eds. (1996) Boston; Materials Research Society, Pittsburgh; pp. 349-354.
2. Chung, H. M., H.-C. Tsai, L. J. Nowicki, and D. L. Smith, in Fusion Reactor Materials - Semiannual Prog. Report for Period Ending June 30, 1997; DOE/ER-0313/22, Oak Ridge Nat. Lab.: Oak Ridge, TN.; pp. 18-21
3. Zinkle, S. J., Alexander, D. J., Robertson, J. P., Snead, L. L., Rowcliffe, A. F., Gibson, L. T., Eatherly, W. S., and Tsai, H., in Fusion Reactor Materials - Semiannual Progress Report for Period Ending December 31, 1996; DOE/ER-0313/21, Oak Ridge National Laboratory: Oak Ridge, TN.; pp.73-78.
4. Alexander, D. J., Snead, L. L., Zinkle, S. J., Gubbi, A. N., Rowcliffe, A. F., and Bloom, E. E., in Fusion Reactor Materials - Semiannual Progress Report for Period Ending June 30, 1996, DOE/ER-0313/20 Oak Ridge National Laboratory: Oak Ridge, TN.; pp. 87-95.
5. Chung, H. M., Tsai, H.-C., Smith, D. L., Peterson, R., Curtis, C., Wojcik, C., and Kinney, R., in Fusion Reactor Materials - Semiannual Prog. Report, 1995, DOE/ER-0313/17, Oak Ridge National Laboratory: Oak Ridge, TN.; pp. 178-182.
6. Tsai, H.-C., Strain, R. V., Hins, A. G., Chung, H. M., Nowicki, L. J., and Smith, D. L., in Fusion Reactor Materials - Semiannual Prog. Report, 1995, DOE/ER-0313/17, Oak Ridge National Laboratory: Oak Ridge, TN.; pp. 8-14.
7. Luft, A., Prog. Mat. Sci., **35** (1991) 97-204.
8. Huang, Y. and R.J. Arsenault, Rad. Eff., **17** (1973) 3-11.
9. Ritschel, C., *Zur Stabilitat von Versetzungsstructuren in hochreinen Molybdaneikristallen bei plastischer Verformung,* 1982, Dissertation, AdW der DDR, ZFW Dresden, Germany.
10. Gysler, A., J. Lindigkeit, and G. Lutjering, Acta Met., **22** (1974) 901-909.
11. Chung, H. M. and D. L. Smith, in Fusion Reactor Materials - Semiannual Progress Report for Period Ending June 30, 1997, Oak Ridge National Laboratory: Oak Ridge, TN.; pp 33-38.

RESEARCH AND DEVELOPMENT ON VANADIUM ALLOYS FOR FUSION APPLICATIONS* — S. J. Zinkle (ORNL), H. Matsui (Tohoku Univ.), D. L. Smith (Argonne National Laboratory), A. F. Rowcliffe (ORNL), E. van Osch (NERF-Petten), K. Abe (Tohoku Univ.), and V.A. Kazakov (RIAR-Dimitrovgrad)

Extended Abstract

The current status of research and development on unirradiated and irradiated V-Cr-Ti alloys intended for fusion reactor structural applications is reviewed, with particular emphasis on the flow and fracture behavior of neutron-irradiated vanadium alloys. Recent progress on fabrication, joining, oxidation behavior, and the development of insulator coatings is also summarized. Fabrication of large (>500 kg) heats of V-4Cr-4Ti with properties similar to previous small laboratory heats has now been demonstrated. Impressive advances in the joining of thick sections of vanadium alloys using GTA and electron beam welds have been achieved in the past two years, although further improvements are still needed.

Pronounced flow localization and loss of strain hardening capacity with uniform elongations <1% generally occurs in vanadium alloys for irradiation temperatures below ~400°C (0.31 T_M). These changes in tensile properties for T_{irr}<400°C are generally accompanied by large increases in the ductile-to-brittle transition temperature measured under both dynamic and quasi-static loading conditions. The irradiated mechanical properties at temperatures between 430 and 650°C are acceptable for most structural applications. Further work is needed to determine how far the allowable lower and upper operating temperature limits can be expanded beyond the 430-650°C range. The poor work hardening behavior of vanadium alloys at irradiation temperatures below 400°C is due to small defect clusters which can be easily sheared by dislocations during deformation. The concomitant poor fracture properties of vanadium alloys at these low irradiation temperatures is attributable to matrix hardening effects. Microstructural alterations which would improve the tensile elongations of irradiated vanadium alloys (e.g., introduction of nonshearable precipitates) would not necessarily produce any improvement in the fracture properties. Tensile test ductility and toughness often provide misleading information about the temperature-dependent fracture toughness obtained from Charpy impact or compact tension specimens.

In order to build upon the present state of knowledge for vanadium alloys, additional work is needed on several different topics. Regarding unirradiated properties, additional work expanding upon the recent advances in joining technology are needed. The ultimate goal of these studies is to develop techniques for joining thick sections of vanadium alloys which do not require post-weld heat treatments. An expanded investigation of alternative alloys (controlled matrix interstitial solute contents; dispersion or precipitation hardened alloys, etc.) would be useful to see if alloys with unirradiated and irradiated properties superior to V-4Cr-4Ti are possible. Further work is also needed to develop adherent self-healing insulator coatings which are compatible with vanadium-liquid metal coolant systems. A key issue regarding radiation effects is to determine the minimum and maximum allowable operating temperatures. Further irradiation studies at 350 to 450°C to doses of 1-10 dpa are needed to evaluate the radiation hardening, ductility, and fracture toughness properties. The possible impact of fusion-relevant levels of helium on radiation hardening at higher doses should also be considered. It would also be useful to perform some fundamental studies to determine whether flow localization (dislocation channeling) modifies the relationship between fracture properties and matrix hardening. Creep rupture studies on unirradiated and irradiated specimens (with and without helium) at test temperatures $\geq$650°C are needed in order to help establish maximum allowable operating temperatures. Additional work is also needed to determine the magnitude of radiation creep in vanadium alloys.

*Extended abstract of paper submitted to Journal of Nuclear Materials as part of the proceedings of the 8th International Conference on Fusion Reactor Materials, Sendai, Japan, October 27-31, 1997.

TENSILE PROPERTIES OF V-Cr-Ti ALLOYS AFTER EXPOSURE IN HYDROGEN-CONTAINING ENVIRONMENTS*

K. Natesan and W. K. Soppet (Argonne National Laboratory)

OBJECTIVE

The objectives of this task are to (a) determine the hydrogen uptake of V-Cr-Ti alloys as a function of temperature and partial pressure of hydrogen (pH_2) in the exposure environment, (b) examine the microstructural characteristics of surfaces and cross sections of the alloys after exposure, (c) evaluate the influence of hydrogen uptake in low-pH_2 environments on the tensile properties and cracking propensity of the alloys at room and elevated temperatures, and (d) determine the effects of oxygen/hydrogen interactions on the tensile properties of the alloys.

SUMMARY

A systematic study has been initiated to evaluate the performance of several V-Cr-Ti alloys after exposure to environments containing hydrogen at various partial pressures. The goal is to correlate the chemistry of the exposure environment with the hydrogen uptake in the samples and its influence on the microstructure and tensile properties of the alloys. At present, four heats of alloys (BL-63, BL-71, and T87, plus 44 from General Atomics) are being evaluated. Other variables of interest are the effect of initial grain size on hydrogen uptake and tensile properties, and the synergistic effects of oxygen and hydrogen on the tensile behavior of the alloys. Experiments conducted thus far on specimens of various V-Cr-Ti alloys exposed to pH_2 levels of 0.01 and 3×10^{-6} torr showed negligible effect of H_2 on either maximum engineering stress or uniform/total elongation. Further, preliminary tests on specimens annealed at different temperatures showed that grain size variation by a factor of ≈2 had a negligible effect on tensile properties.

EXPERIMENTAL PROGRAM

The heats of vanadium alloy selected for the study had nominal compositions of V-5 wt.%Cr-5 wt.%Ti (designated as BL-63 and T87) and V-4 wt.%Cr-4 wt.%Ti (designated as BL-71 and 44 from GA heat). Detailed chemical analyses of these heats are given in Table 1. The tensile specimens were fabricated according to ASTM Standard E8-69 specifications and had a gauge length of ≈19 mm and a gauge width of ≈4.5 mm. Specimens were annealed for 1 h at 1050°C prior to hydrogen exposure and tensile testing. Some of the specimens of BL-63 and BL-71 heats were also annealed for 2 h at 1200°C to obtain a larger grain size before hydrogen exposure.

Tensile samples of the four alloys were exposed for 100 h at 500°C to environments containing H_2 at partial pressures of 3×10^{-6} and 0.01 torr and subsequently tensile-tested at a strain rate of 1.8×10^{-4} s^{-1} in room-temperature air. The specimens were loaded by means of pins that pass through holes in the grips and enlarged end sections of the specimen, thus minimizing misalignment. Total elongation was measured with a vernier caliper and load/elongation chart records. The fracture surfaces and longitudinal and axial cross sections of the tested specimens are being examined by scanning electron microscopy.

RESULTS AND DISCUSSION

Figure 1 shows the engineering stress/engineering strain plots at room temperature for V-4Cr-4Ti and V-5Cr-5Ti materials in as-annealed condition and after exposure to H_2 at partial pressures of 3×10^{-6} and 0.01 torr. The results indicate that in the H_2 pressure range of the present study, BL-63 exhibited negligible effect of H_2 on tensile properties. BL-71 exhibited a small decrease in uniform and total elongation after H_2 exposure. Table 2 shows the values for maximum engineering stress and uniform and total elongation for all four heats of material. The results also show that for the

Table 1. Chemical compositions of several heats of V-Cr-Ti alloys used in hydrogen studies

Element[a]	BL-63 (832394)	T87	BL-71 (832665	GA heat (832864)
Cr	4.45	4.94	3.8	3.8
Ti	5.0	5.06	3.97	4.0
V	Bal[b]	Bal[b]	Bal[b]	Bal[b]
B	<5	<5	<5	<5
C	75	110	79	45
H	3	17	-	5
N	28	90	85	135
O	410	380	320	370
P	<30	<30	<30	<30
S	25	<20	<10	15
Al	200	160	190	170
Nb	<50	<100	<50	90
Si	305	545	780	340
Fe	-	67	230	210
Cu	-	67	<50	<50
Mo	-	520	290	<50
Ta	-	<36	<20	<30
W	-	<5	25	-

[a]Concentrations for Cr, Ti, and V are in wt.%; all others are in wt ppm.
[b]Indicates balance.

Table 2. Effects of 100 h hydrogen exposure at 500°C on room-temperature tensile properties of V-Cr-Ti alloys, initially annealed for 1 h at 1050°C in vacuum

pH_2 in exposure environment (torr)	Maximum engg. stress (MPa)				Uniform elongation				Total elongation			
	BL-63	T87	BL-71	GA	BL-63	T87	BL-71	GA	BL-63	T87	BL-71	GA
-	469	-	424	-	0.165	-	0.186	-	0.303	-	0.322	-
3×10^{-6}	437	-	440	-	0.189	-	0.174	-	0.313	-	0.263	-
1×10^{-2}	445	501	459	462.5	0.194	0.178	0.169	0.151	0.313	0.296	0.263	0.224

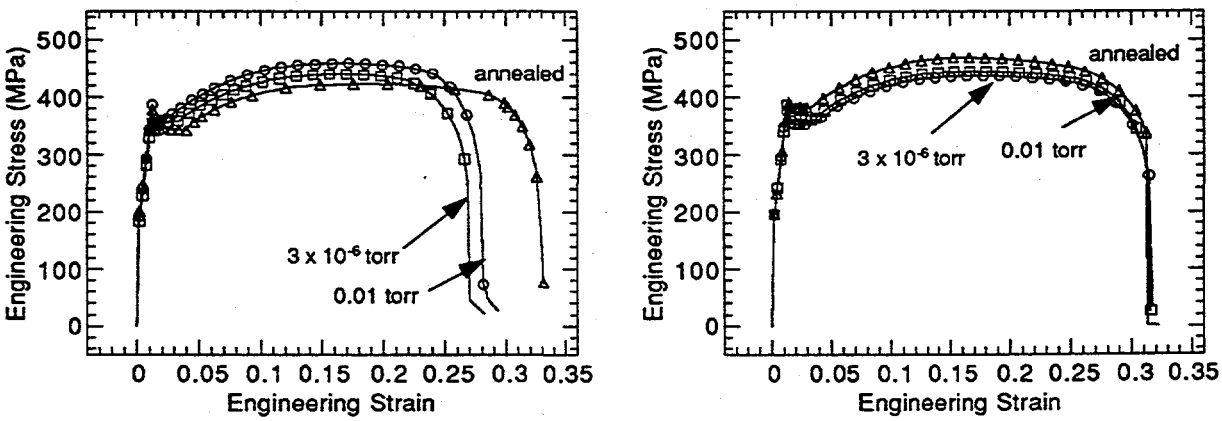

Figure 1. Engineering stress/engineering strain plots for BL-71 (left) and BL-63 (right) heats of material in as-annealed condition and after 100 h exposure at 500°C to various pH_2 levels.

same exposure condition of 0.01 torr pH_2, the BL-71 and GA heats exhibited almost similar strength properties, while the T87 heat showed somewhat higher strength than the BL-63 heat (see Figure 2). However, the total elongation values are similar for BL-63 and T87, while that for the GA heat was significantly lower than that for the BL-71 heat. Additional H_2 exposures and post-exposure tensile-testing are in progress to quantify the effects of H_2 on the tensile behavior of these alloys.

To examine the effect of initial grain size on subsequent H_2 uptake and tensile properties, specimens of BL-71 and BL-63 were annealed for 2 h at 1200°C, which increased the grain size of the alloys by at least a factor of 2 over those annealed for 1 h at 1050°C. Figure 3 shows the engineering stress/engineering strain curves for large- and small-grain materials after 100 h exposure at 500°C to a pH_2 of 0.01 torr. With the increased grain size, both alloys exhibited some increase in strength and some decrease in elongation. Similar effects were observed when the specimens were exposed for 100 h at 500°C to a pH_2 of 3×10^{-6} torr (see Table 3). Additional experiments at other pH_2 levels are in progress to quantify the grain-size effect (if any) on H_2 uptake and tensile properties.

Table 3. Effects of 100 h hydrogen exposure at 500°C on room-temperature tensile properties of enlarged-grain V-Cr-Ti alloys, initially annealed for 2 h at 1200°C in vacuum

pH_2 in exposure environment (torr)	Maximum engg. stress (MPa)		Uniform elongation		Total elongation	
	BL-63	BL-71	BL-63	BL-71	BL-63	BL-71
3×10^{-6}	515	472	0.144	0.159	0.250	0.225
1×10^{-2}	524	479	0.160	0.153	0.244	0.227

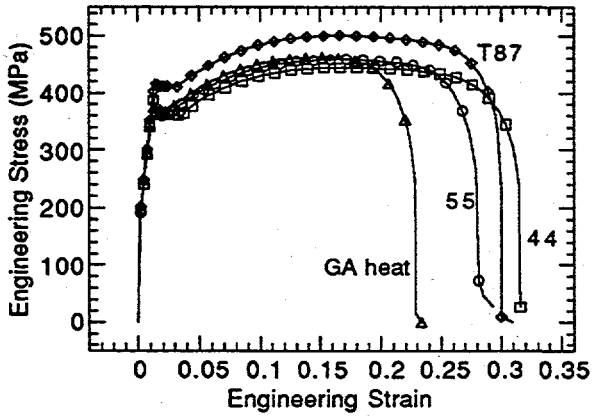

Figure 2. Engineering stress/engineering strain curves at room temperature for four heats V-Cr-Ti alloys after 100 h exposure at 500°C to 0.01 torr H_2.

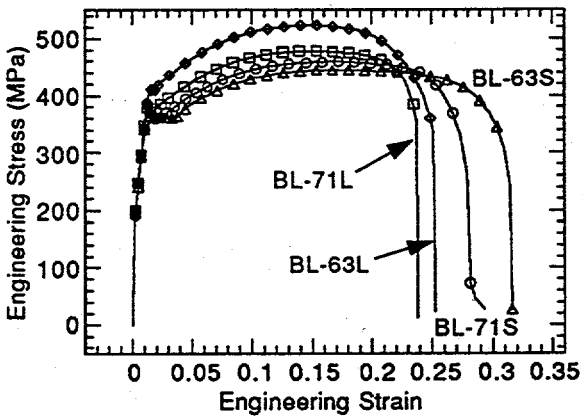

Figure 3. Engineering stress/engineering strain curves at room temperature for various grain size BL-71 and BL-63 materials after 100 h exposure at 500°C to 0.01 torr H_2. L and S indicates large- and small-grain materials, respectively.

TENSILE PROPERTIES OF V-Cr-Ti ALLOYS AFTER EXPOSURE IN OXYGEN-CONTAINING ENVIRONMENTS*

K. Natesan and W. K. Soppet (Argonne National Laboratory)

OBJECTIVE

The objectives of this task are to (a) determine the oxygen uptake of V-Cr-Ti alloys as a function of temperature and oxygen partial pressure (pO_2) in the exposure environment, (b) examine the microstructural characteristics of oxide scales and oxygen trapped at the grain boundaries in the substrate alloys, and (c) evaluate the influence of oxygen uptake in low-pO_2 environments (which include oxygen and helium of various purities) on the tensile properties and cracking propensity of the alloys at room and elevated temperatures.

SUMMARY

A systematic study was conducted to evaluate the oxidation kinetics of V-4Cr-4Ti ("44 alloy") and V-5Cr-5Ti alloys ("55 alloy") and to establish the role of oxygen ingress on the tensile behavior of the alloys at room temperature and at 500°C. The oxidation rate of the 44 alloy is slightly higher than that of the 55 alloy. The oxidation process followed parabolic kinetics. Maximum engineering stress for 55 alloy increased with an increase in oxidation time at 500°C. The maximum stress values for 55 alloy were higher at room temperature than at 500°C for the same oxidation treatment. Maximum engineering stresses for 44 alloy were substantially lower than those for 55 alloy in the same oxidation treatment. Uniform and total elongation values for 55 alloy were almost zero at room temperature after ≈500 h exposure in air at 500°C; the same values were 4.8 and 6.1%, respectively, at 500°C after ≈2060 h oxidation in air at 500°C Uniform and total elongation values for 44 alloy were 1.6 and 3.6% at 500°C after 2060 h oxidation in air at 500°C.

Maximum engineering stress for 44 alloy at room temperature was 421.6-440.6 MPa after ≈250 h exposure at 500°C in environments with a pO_2 range of 1×10^{-6} to 760 torr. The corresponding uniform and total elongation values were 11-14.4% and 14.5-21.7%, respectively. Measurements of crack depths in various specimens showed that depth is independent of pO_2 in the preexposure environment and was of 70-95 μm after 250-275 h exposure at 500°C.

EXPERIMENTAL PROGRAM

The heats of vanadium alloy selected for the study had nominal compositions of V-5 wt.%Cr-5 wt.%Ti (designated BL-63) and V-4 wt.%Cr-4 wt.%Ti (designated BL-71). Sheets of the alloys were annealed for 1 h at 1050°C prior to oxidation and tensile testing. Coupon specimens that measured ≈15 x 7.5 x 1 mm were used for the oxidation studies. Oxidation experiments were conducted in air in a thermogravimetric test apparatus at temperatures of 300 to 650°C; results were discussed in earlier publications (1,2).

Tensile specimens were fabricated according to ASTM Standard E8-69 specifications and had a gauge length of ≈19 mm and a gauge width of ≈4.5 mm. Grain sizes of the V-4Cr-4Ti and V-5Cr-5Ti specimens were ≈18 and 32 μm, respectively. Tensile samples of the two alloys were exposed to several environments with pO_2 of 1×10^{-6} to 760 torr and to 99.999% pure He for 250-275 h at 500°C; they were subsequently tensile-tested at a strain rate of 1.8×10^{-4} s^{-1} in air at room temperature or 500°C. The specimens were loaded by means of pins that pass through holes in the grips and enlarged end sections of the specimen, thus minimizing misalignment. Total elongation was measured with a vernier caliper and load/elongation chart records. The fracture surfaces and longitudinal and axial cross sections of tested specimens were examined by scanning electron microscopy (SEM). Oxide scales on the samples were identified by X-ray diffraction (XRD) analysis on the surface of several samples, as well as on the oxides scraped from their surfaces. In addition, the Vickers hardness of several tested specimens was determined.

RESULTS AND DISCUSSION

To evaluate the effect of oxide scale formation and oxygen penetration into the substrate alloy, the tensile behavior of the alloys was examined as a function of oxygen ingress and oxide scale formation after exposure. Tensile-test data were reported earlier for the 55 alloy specimens exposed to air for 24-2060 h at 500°C and then tensile-tested in air at either room temperature or 500°C [1,3]. Similar exposures to air were made for tensile specimens of 44 alloy that were tensile-tested at 500°C in air.

Figure 1 shows the engineering stress/engineering strain curves at 500°C for specimens after oxidation for several exposure times in the range of 0-2060 h. The maximum engineering stress, uniform elongation, and total elongation for specimens with various treatments are listed in Table 1. The data indicate that the stress/strain behavior of both alloys is virtually unaffected by 24 h exposure in air at 500°C. As the exposure time increases to ≈250 h, the strength of the 55 alloy (but not that of the 44 alloy) increases but with some loss in tensile ductility in both alloys. The ductility reduction continues as the exposure time increases further to 600, ≈1000, and 2060 h at 500°C. Further exposure of the alloy to air at 500°C results in loss of strength and tensile ductility, as evidenced by the stress/strain curve for both alloys preoxidized for 2060 h. Similar data were obtained for the 55 alloy specimens preoxidized at 500°C in air and tensile-tested at room temperature. The results from these tests are also listed in Table 1.

Table 1. Effects of oxidation in air on tensile properties of 44 and 55 alloys

Exposure time (h)	V-5 wt.% Cr-5 wt.% Ti alloy								V-4 wt.% Cr-4 wt.% Ti alloy							
	Maximum engg. stress (MPa)		Uniform elongation		Total elongation		Measured crack length (μm)		Maximum engg. stress (MPa)		Uniform elongation		Total elongation		Measured crack length (μm)	
	RT[a]	500°C	RT[a]	500°C	RT[a]	500°C	RT[a]	500°C	RT[a]	500°C	RT[a]	500°C	RT[a]	500°C	RT[a]	500°C
0	468.7	411.3	0.165	0.164	0.303	0.216	0	10	423.7	378.7	0.186	0.107	0.322	0.179	0	6.7
24	509.5	416.7	0.153	0.136	0.241	0.186	24	22	-	360.5	-	0.103	-	0.186	-	17
250[b]	513.9	458.5	0.035	0.113	0.035	0.145	d	50	-	367.2	-	0.099	-	0.135	-	85
600	471.4	453.3	0.003	0.095	0.003	0.114	d	90	-	362.4	-	0.082	-	0.108	-	93
1000[b]	483.9	454.4	0.001	0.085	0.001	0.104	d	110	-	340.6	-	0.059	-	0.075	-	137
2060[c]	433.6	406.4	0.002	0.048	0.002	0.061	d	160	-	329.2	-	0.016	-	0.036	-	210

[a]RT = room temperature.
[b]Exposure times were 260 and 1050 h for 55 samples tested at room temperature and for 44 samples tested at 500°C.
[c]Exposure time was 2110 h for 55 sample tested at room temperature.
[d]Specimen fully embrittled.

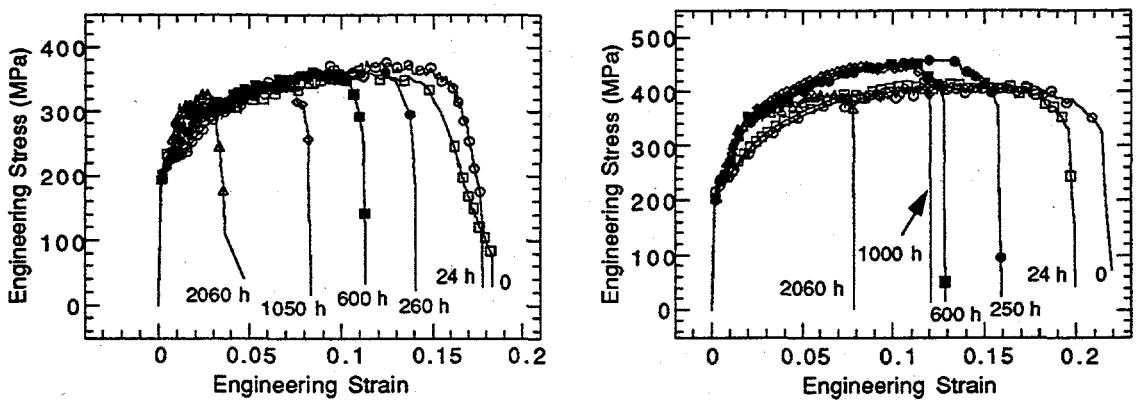

Figure 1. Effect of preoxidation at 500°C on stress-strain behavior of 44 (left) and 55 (right) alloys tested at 500°C in air at strain rate of 1.75×10^{-4} s^{-1}.

A comparison of the tensile properties of the 44 and 55 alloys shows that for the same pretreatment, the 55 alloy exhibits 10 to 25% higher ultimate tensile strength at both 500°C and at room temperature. For the same pretreatment, the uniform and total elongation values of the 44 alloys were lower than those of the 55 alloy. For example, the uniform elongation values at 500°C were 0.048 and 0.016 for 55 and 44 alloy specimens after 2060-h exposure to air at 500°C. The effect of oxidation on elongation values at room temperature for 55 alloy is even more substantial in that the specimens were fully embrittled. Even though corresponding tests were not conducted at room temperature for the 44 alloy oxidized in air, similar behavior is expected on the basis of the similarities in the oxidation characteristics of both alloys.

A test program is underway to evaluate the effect of partial pressure of oxygen in the exposure environment on oxygen ingress into the V alloys and its effect on tensile properties. Specimens of 44 alloy, initially in annealed condition, were exposed for 250-275 h at 500°C in environments with various pO_2 levels and subsequently tensile-tested at either room temperature or 500°C. Figure 2 shows the engineering stress/engineering strain curves at 500°C and at room temperature for 44 alloy specimens after oxidation for 250-275 h in environments with pO_2 of 1×10^{-6} to 760 torr. The maximum engineering stress, uniform elongation, and total elongation for specimens with various treatments are listed in Table 2. The exposure environments included pO_2 values of 760, 160, 0.15, 0.1, 7.6×10^{-4}, and 1×10^{-6} torr. Among these, 160 and 0.15 torr correspond to air and 99.999% He environments, respectively.

The stress/strain curves indicate that for a given exposure time and test temperature (500°C or room temperature), the pO_2 value in the preexposure environment has very little effect on maximum engineering stress and uniform and total elongation. The results also indicate that the alloy with identical pretreatment exhibits lower values of maximum engineering stress and uniform and total elongation at 500°C than those at room temperature. For example, the maximum engineering stress values for He-exposed specimens were 437.8 and 358.8 MPa at room temperature and 500°C, respectively. The corresponding uniform elongation values were 0.140 and 0.089 while the total elongation values were 0.191 and 0.119. A similar trend was observed in specimens exposed to pure oxygen (see Table 2).

Figure 3 shows the variations in maximum engineering stress and uniform and total elongation as a function of pO_2 value in the preexposure environment for 44 and 55 alloy specimens tested at room temperature and at 500°C. The plots indicate that the pO_2 value in the preexposure environment has virtually no effect on the any of the tensile properties reported here.

Table 2. Effects of oxygen partial pressure on tensile properties of 44 alloy

pO_2 in exposure environment (torr)	Maximum engg. stress (MPa)		Uniform elongation		Total elongation		Measured crack length (μm)	
	RT[a]	500°C	RT[a]	500°C	RT[a]	500°C	RT[a]	500°C
1×10^{-6}	426.3	-	0.127	-	0.217	-	80	-
7.6×10^{-4}	443.0	-	0.110	-	0.145	-	90	-
0.1	440.6	-	0.133	-	0.202	-	95	-
0.15 (He)	437.8	358.8	0.140	0.089	0.191	0.119	80	70
160	-	367.2	-	.099	-	0.135	-	85
760	421.6	347.4	0.148	0.097	0.208	0.135	80	80

[a]RT = room temperature.

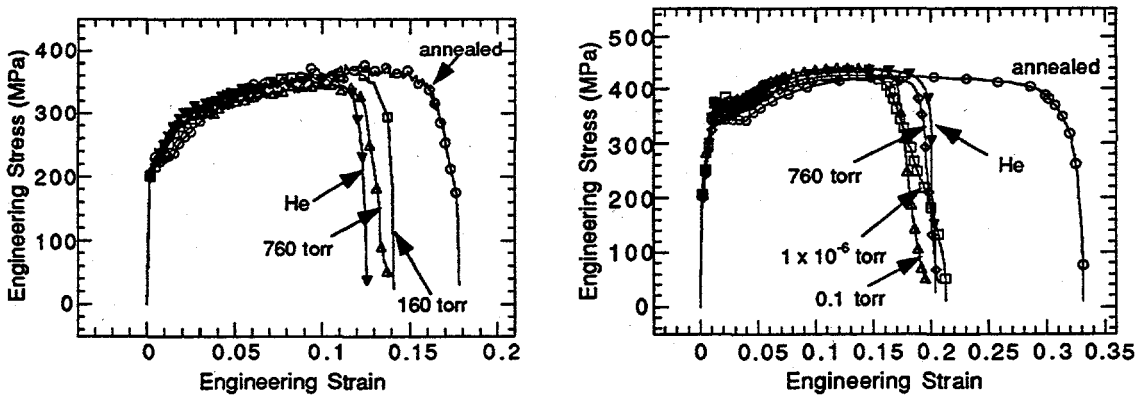

Figure 2. Effect of oxygen partial pressure in preexposure environment on stress-strain behavior of 44 alloy oxidized at 500°C for 250-275 h and tested at 500°C (left) and room temperature (right) in air at strain rate of 1.75×10^{-4} s^{-1}.

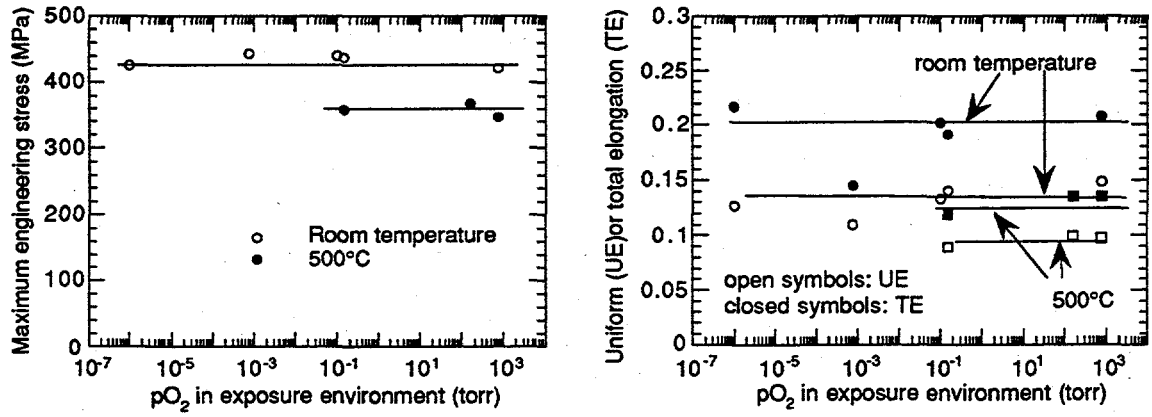

Figure 3. Effect of oxygen partial pressure in preexposure environment on maximum engineering stress (left) and uniform and total elongation (right) for 44 alloy oxidized at 500°C for 250-275 h and tested at room temperature and at 500°C at strain rate of 1.8×10^{-4} s^{-1}.

Microstructural Observations

Axial cross sections of several of the tested specimens were examined by SEM. Figure 4 shows 44 alloy specimen sections tested in as-annealed condition and after oxidation in air for 24, 260, 600, 1050, and 2060 h in air at 500°C. The photomicrographs show that as oxidation time increases, both the cracks in the transverse direction and the crack spacing in the axial direction increase. Furthermore, as the oxidation time increases, the specimen undergoes little necking of the gage section during the tensile test. It is evident, especially from specimens exposed for 1000 and 2060 h, that fracture occurred by propagation of one of the axial cracks and that because the core of the alloy was somewhat ductile, the crack-propagation direction in the core region was at an angle of ≈45°. Similar observations were reported earlier for 55 alloy specimens exposed to air for different time periods [3,4].

Figure 5 shows 44 alloy specimen sections tested in as-annealed condition and after oxidation at 500°C in environments with pO_2 values of 1×10^{-6}, 7.6×10^{-4}, 0.1, and 760 torr, and in 99.999% He at a pO_2 value of 0.15 torr. Exposure time for specimens in 760 torr O_2 and He was 275 h, while for the others it was 250 h. The photomicrographs show that transverse cracking is observed in all except the annealed specimens and that the crack spacing was almost the same except for the specimen exposed to pure oxygen (760 torr). The photomicrographs also indicate that the specimen surfaces

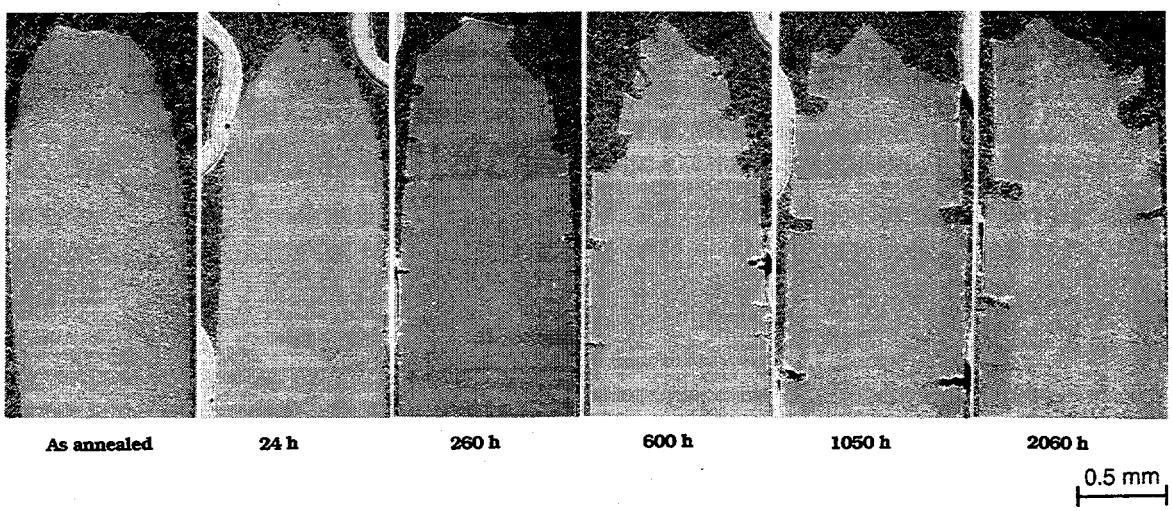

Figure 4. Scanning electron photomicrographs of axial sections of V-4Cr-4Ti specimens tensile-tested at 500°C in as-annealed condition and after oxidation in air at 500°C for several exposure times.

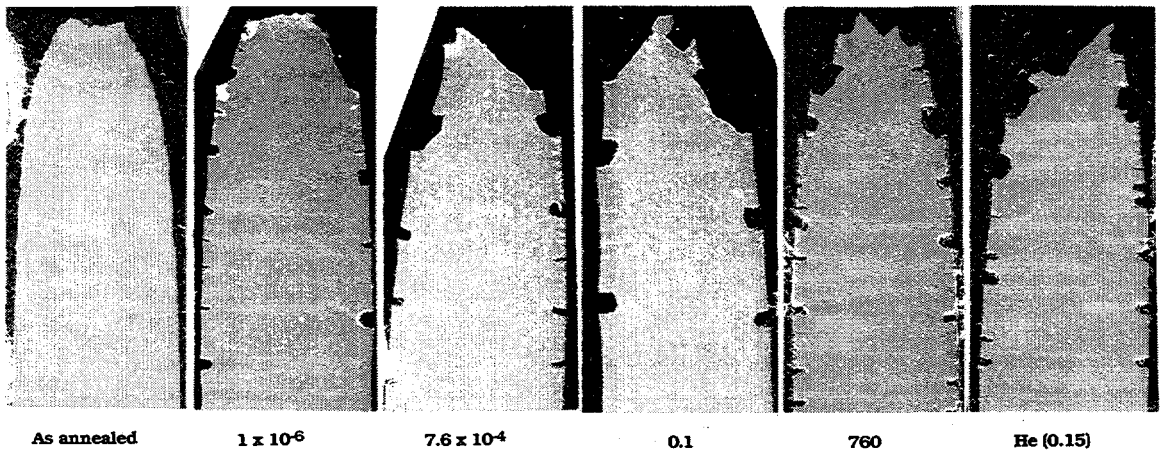

Figure 5. Scanning electron photomicrographs of axial sections of V-4Cr-4Ti specimens tensile-tested at room temperature in as-annealed condition and after oxidation at 500°C in environments with several oxygen partial pressures. Numbers in photographs are pO_2 values in torr.

equilibrate with oxygen in the environment and the increased oxygen content at the surface diffuses into the alloy with time. Even at the lowest pO_2 value of 1×10^{-6} torr, the oxygen concentration at the surface must be high enough to initiate cracks on axial loading of the specimen. The depth of the crack is determined by oxygen diffusion, which in turn is dictated by the time and temperature of preexposure.

Figure 6 shows a plot of measured crack depths for specimens exposed to environments with different pO_2 values. Over the entire range of pO_2 values used in this study, ≈250 h exposure at 500°C resulted in crack depths of 70-95 μm. These results, even though obtained from a relatively short exposure time of ≈250 h, indicate similar cracking propensity for 44 and 55 alloys at room temperature and at 500°C, and this propensity is independent of oxygen pressure in the exposure

environment. This observation, coupled with embrittlement of the alloys after ≈2000 h exposure in air (discussed earlier), makes one infer that the alloys can embrittle even in environments with low pO_2 values, if exposed for times comparable to those of the air exposures conducted in this program. The ongoing experiments will examine this issue and develop models for life prediction of alloys as functions of time, temperature, and oxygen level.

REFERENCES

1. K. Natesan and M. Uz, "Oxidation Kinetics and Microstructure of V-(4-5)wt.% Cr-(4-5)wt.% Ti Alloys Exposed to Air at 300-650°C," Fusion Reactor Materials Progress Report for the Period Ending June 30, 1996, Argonne National Laboratory, DOE/ER-0313/20, p. 105, Oct. 1996.

2. M. Uz, K. Natesan, and V. B. Hong, J. Nucl. Mater. 245, 191-200, 1997.

3. K. Natesan and W. K. Soppet, Proc. 2nd Intl. Conf. Heat Resistant Materials, eds. K. Natesan, P. Ganesan, and G. Lai, ASM International, Materials Park, OH, 375-380, 1995.

4. K. Natesan and W. K. Soppet, J. Nucl. Mater. 233-237, 482-487, 1996.

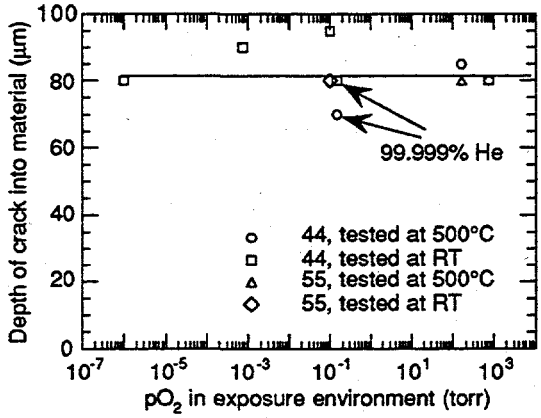

Figure 6. Measured crack depths in 44 and 55 alloy specimens after exposure for 250-275 h in various oxygen-containing environments.

LASER-WELDED V-Cr-Ti ALLOYS: MICROSTRUCTURAL AND MECHANICAL PROPERTIES*

K. Natesan, D. L. Smith, P. G. Sanders, and K. H. Leong (Argonne National Laboratory)

OBJECTIVE

The objectives of this task are to (a) determine the optimum parameters for laser beam welding of sheets of V-Cr-Ti alloys; (b) examine the microstructural characteristics of welded sections, including base metal, heat-affected-region, and core of weld; (c) evaluate the influence of different post-welding heat treatments on microstructural characteristics; and (d) evaluate the mechanical properties, such as tensile and impact, of laser-welded materials.

SUMMARY

A systematic study has been initiated to examine the use of lasers to weld sheet materials of V-Cr-Ti alloys and to characterize the microstructural and mechanical properties of the laser-welded materials. In addition, several post-welding heat treatments are being applied to the welded samples to evaluate their benefits, if any, to the structure and properties of the weldments. Hardness measurements are made across the welded regions of different samples to evaluate differences in the characteristics of various weldments.

EXPERIMENTAL PROGRAM

The heat of vanadium alloy selected for the study had a nominal composition of V-4 wt.%Cr-4 wt.%Ti (designated as BL-71). A 4-mm-thick sheet of the alloy was used for the welding study. Seven different welds were made under the same welding conditions but were subsequently given different post-welding heat treatments. Laser beam power was 1325 W and travel speed was 110 mm/s. A lens with a 125 mm focal length was used, and the focus was 1 mm into the material. The beam was 1 mm in diameter and penetration was ≈2 mm into the 4-mm-thick sheet.

Shielding gas used was argon with a flow rate of 0.25 L/s, provided by a 9.5-mm-diameter tube at 30° from horizontal. The welds were started and ended on a scrap piece of vanadium so that penetration depth could be seen at both ends of the weld. The vanadium plate was clamped to an aluminum plate, which in turn was clamped to a water-cooled copper block; this arrangement provided sufficient cooling to keep the vanadium sheet barely warm after welding. The heat treatments are listed in Table 1. Weld 3 was in as-welded condition. Welds 1 and 2 were given post-welding heat treatment of 1 and 5 passes, respectively, with a defocused beam 25 mm in diameter. Welds 4 and 5 were post-welding heat treated with ≈50% of the power level of welds 1 and 2. Welds 6 and 7 were treated with a power level of 25% of welds 1 and 2. The defocused beams were wider than the welds (≈4 mm beam, compared to 3 mm for the weld).

Table 1. Heat treatments for different laser welds

Weld No.	Beam diameter (mm)	Power (W)	Speed (mm/s)	No. of passes
1	25	1325	1	1
2	25	1325	1	5
3	untreated	-	-	-
4	25	664	0.25	1
5	25	664	0.25	5
6	25	319	0.25	1
7	25	319	0.25	5

Weld cross sections of different specimens were examined by scanning electron microscopy (SEM). In addition, Knoop hardness measurements were made at three different locations in the weld, heat-affected zone, and base metal.

RESULTS AND DISCUSSION

Figure 1 contains an SEM photomicrograph of the cross section of Weld 3 specimen in the as-welded condition. The weld has a substantial variation in grain size from the root of the weld to the free surface region of the weld. Also, the grains near the top of the weld are columnar, which is dictated by rate of cooling and solidification. Even in the root of the weld, the grains are of the order of two to five times larger than those of the base metal away from the weld. Further, the weld cross section shows definite contours evenly spaced in the root region, along which can occur preferential segregation of impurities. The dark- and light-shaded grains in the weld are due to differences in grain orientation, and virtually no compositional variations were observed between these grains.

In the Weld 3 specimen, Knoop hardness measurements were made at three different elevations and on both sides of the weld centerline. These elevations are designated by A, AA, B, BB, C, and CC, as shown in Figure 1. Knoop hardness profiles at different elevations are also shown in Figure 1 and indicate that the hardness values on either side of the weld centerline were similar at all three elevations examined. The hardness profiles at elevation A and AA indicate a peak value of ≈270 in the weld zone, while the base metal had values of 165 to 190. At weld elevations B and BB, the weld pool zone had a hardness value of ≈250 at a depth of 0.35-0.40 mm, beyond which hardness dropped monotonically to base metal values of ≈170-190. At elevations C and CC, the hardness profiles indicated a drop in the weld centerline region from 250 to 190-215, while a peak in hardness was noted at a distance of 0.8-0.9 mm from the weld centerline. Since the hardness profile of the weld specimen showed that the profiles are symmetrical on either side of the weld centerline, hardness measurements on subsequent specimens were made on only one side of the weld centerline.

Figure 2 includes an SEM photomicrograph of the cross section of a welded specimen after post-welding heat treatment, designated as Weld 1 in Table 1. As in the as-welded sample, this specimen showed a substantial variation in grain size from the root of the weld to the free surface region. Also, the grains near the top of the weld are columnar, dictated by rate of cooling and solidification. Figure 2 also shows the hardness profiles at elevations A, B, and C in the welded specimen. The effect of one pass of post-welding heat treatment with a defocused laser beam was to soften the material in the weld zone, as indicated by the monotonic decrease in hardness from the weld centerline to the base metal. Even the peak hardness value is somewhat lower and the peak is confined to the region close to the centerline. The impact of such decrease on the mechanical properties of the weld can be substantial and will probably be beneficial.

Figure 3 shows an SEM photomicrograph of the cross section of a welded specimen after post-welding heat treatment, designated as Weld 2 in Table 1. As in the previous samples, this specimen also shows that the weld has a substantial variation in grain size from the root of the weld to the free surface region. Also, the grains near the top of the weld are columnar in shape, again dictated by rate of cooling and solidification. Figure 3 also shows the hardness profiles at elevations A, B, and C in the welded specimen. The effect of five passes of post-welding heat treatment with a defocused laser beam was to soften the material in the weld zone, especially at the root region of weld. The erratic hardness variation in the weld region of this specimen at elevations B and C indicate that grain growth may have occurred in the upper portions of weld as a result of the multiple passes.

Analysis is in progress on additional specimens with the various post-welding heat treatments listed in Table 1. Subsequently, several of these welded specimens will be evaluated for their impact properties in order to establish the role of post-welding heat treatments on mechanical properties.

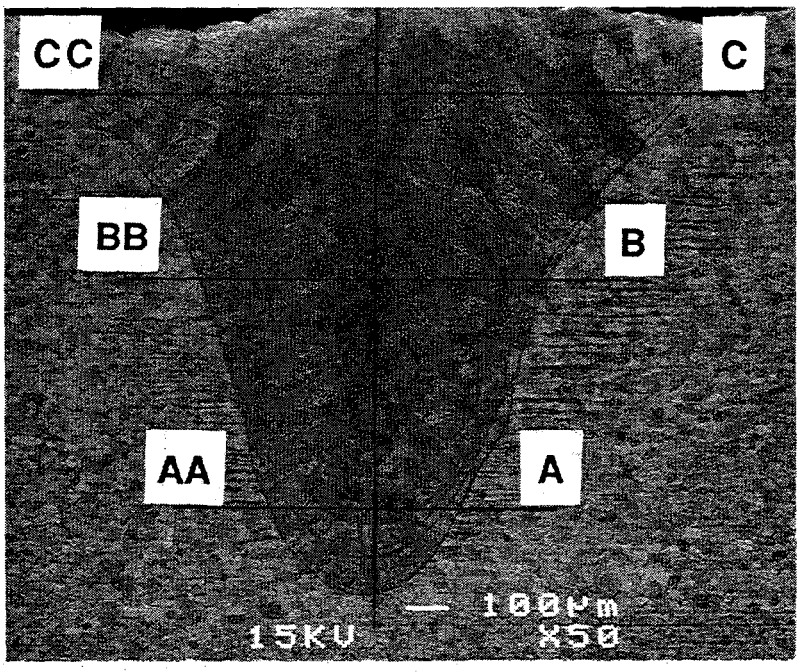

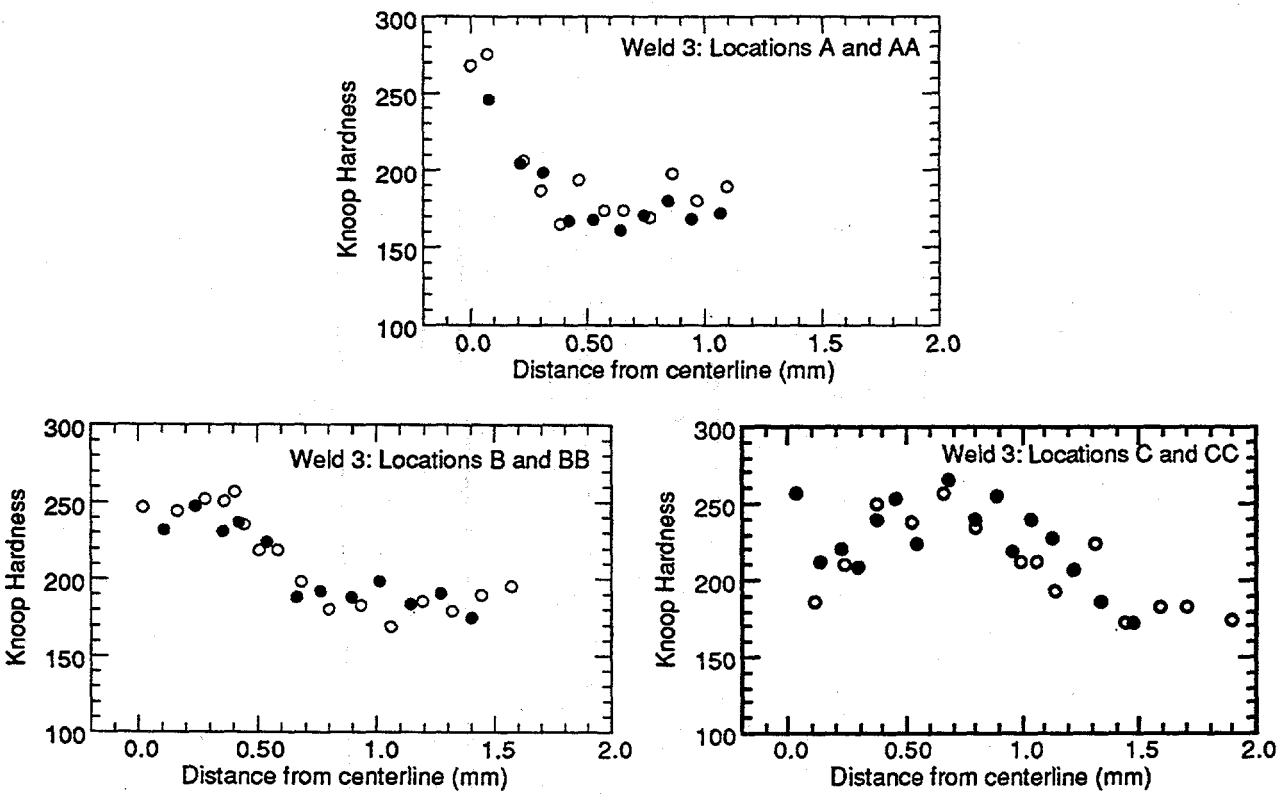

Figure 1. Hardness profiles at elevations indicated in photomicrograph for laser-welded V-4Cr-4Ti specimen in as-welded condition, designated as Weld 3 in Table 1. Open and closed symbols represent hardness values measured on either side of weld centerline.

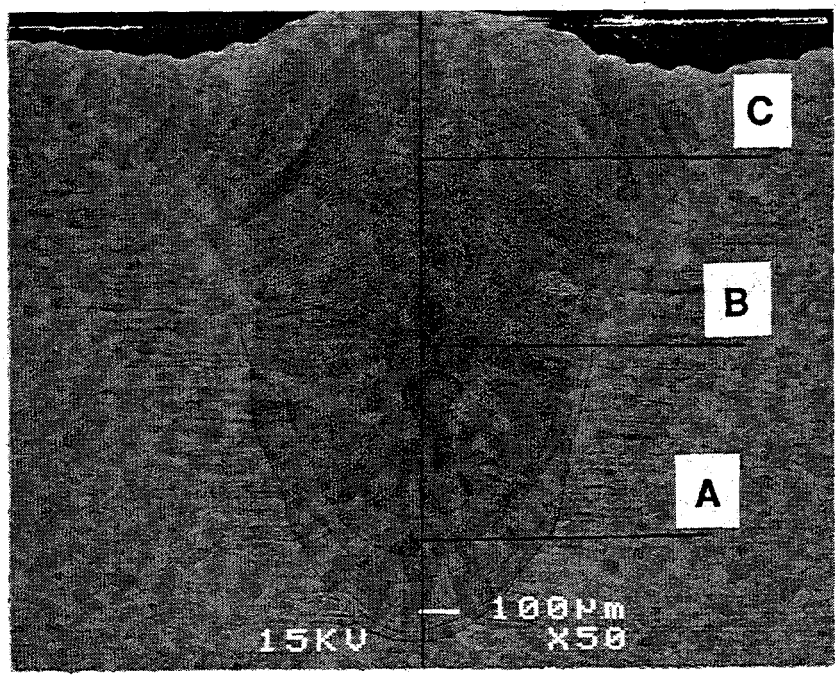

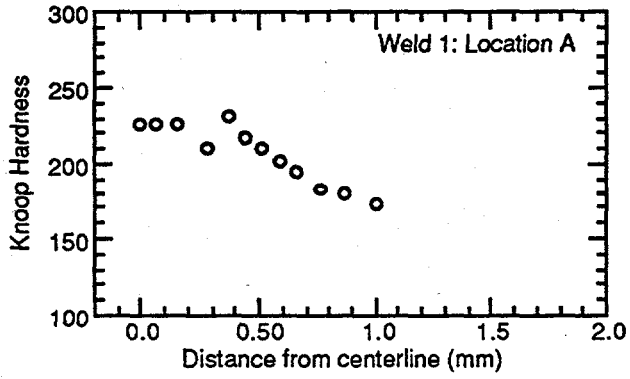

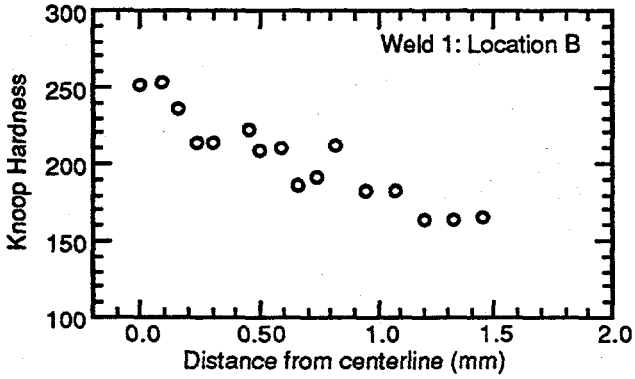

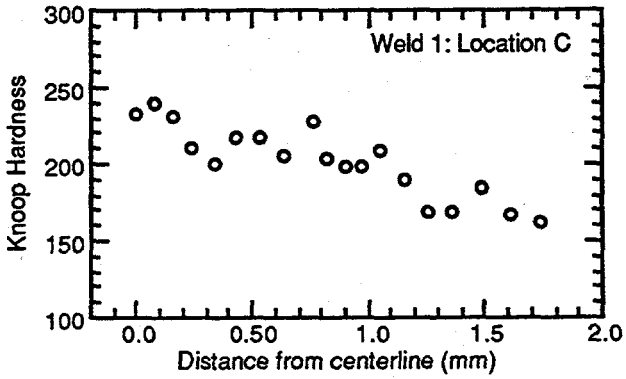

Figure 2. Hardness profiles at several elevations indicated in photomicrograph for laser-welded V-4Cr-4Ti specimen after post-welding treatment, designated as Weld 1 in Table 1.

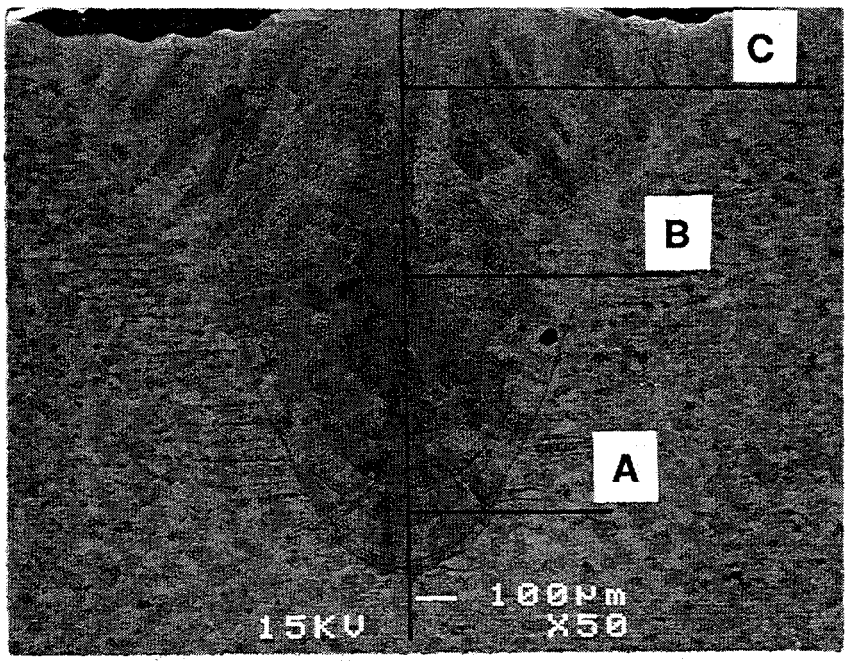

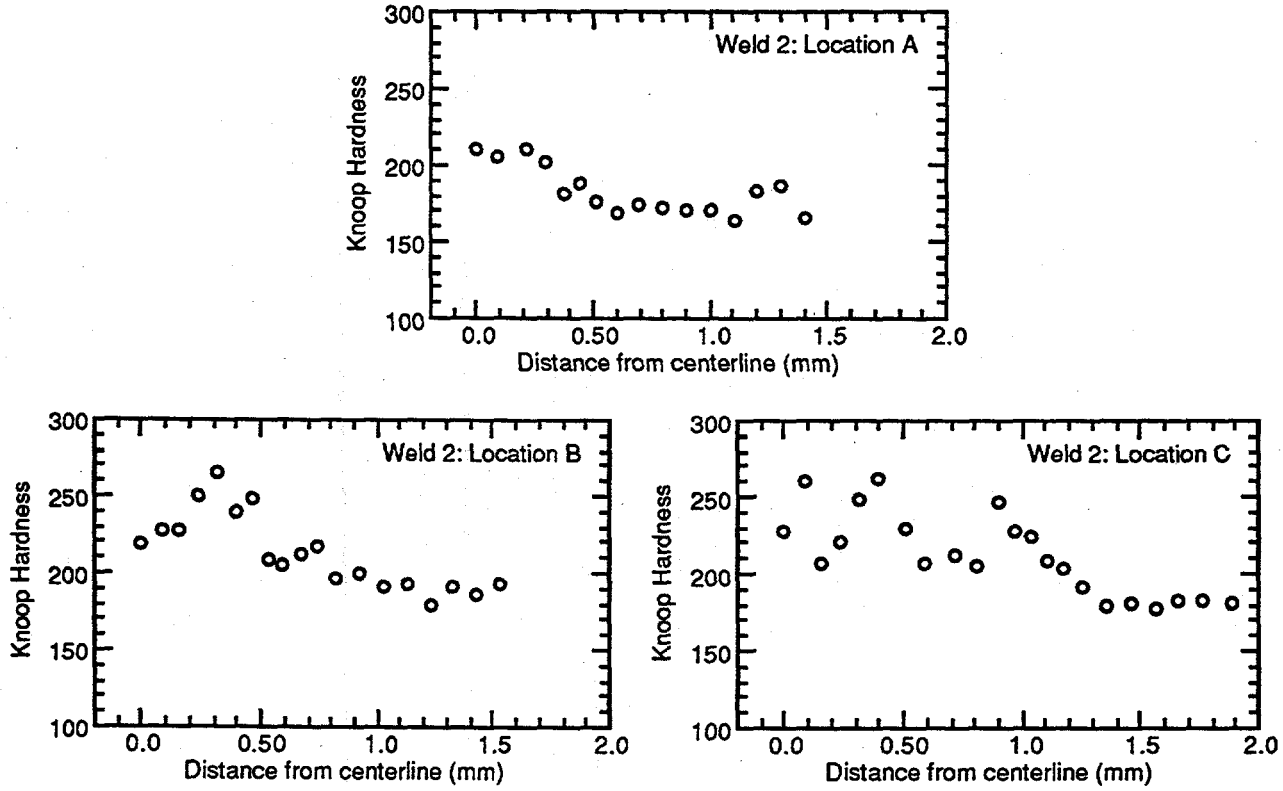

Figure 3. Hardness profiles at several elevations indicated in photomicrograph for laser-welded V-4Cr-4Ti specimen after post-welding treatment, designated as Weld 2 in Table 1.

Performance of V-4Cr-4Ti Material Exposed to the DIII-D Tokamak Environment*

H. Tsai, D. L. Smith, H. M. Chung (Argonne National Laboratory), W. R. Johnson and J. P. Smith (General Atomics), and W. R. Wampler (Sandia National Laboratories)

Summary

A series of tests is being conducted in the DIII-D tokamak to determine the effects of environmental exposure on a V-4Cr-4Ti vanadium alloy. These tests are part of the effort to build and install a water-cooled vanadium V alloy structure in the upgrade of the DIII-D radiative divertor. Data from the test series indicate that the performance of the V-4Cr-4Ti alloy would not be significantly affected by environmental exposure. Interstitial absorption by the material appears to be limited to the surface, and neither the tensile nor the impact properties of the material appear to be affected by the exposure.

Objective

In service, the V-4Cr-4Ti divertor components in the DIII-D will be exposed to a range of temperature and impurity conditions typical of a tokamak. These conditions include alternating- vacuum/low-pressure H plasma operation, thermal cycles and periodic bakeout, glow discharge cleaning with He, periodic B coating, and occasional reexposure to air during vents for maintenance. The objective of the lead tests is to determine the effects of these environmental exposures on the performance of the V alloy material. It is particularly important that we determine whether interstitial impurities (O, H, C, and N) are absorbed in significant quantities to cause material embrittlement.

Introduction

One of the promising features of fusion as an energy source is its potentially low impact on the environment[1]. To reliaze this potential, however, low-activation materials must be used in the construction of fusion systems. In this respect, V-base alloys[2,3] are attractive, because they not only exhibit inherently low neutron-induced activation but they also exhibit the good thermal and mechanical properties that are required for high system performance.

As a first step to demonstrate the viability of V-alloys as a structural material for tokamaks, full-size components made with a newly-procured V-4Cr-4Ti alloy (Heat 832864)[4] will be installed in the radiative divertor of the DIII-D tokamak[5,6]. The objective of the project is to demonstrate both the feasibility of constructing large components with V-base alloys and the satisfactory performance of these components in service. Because the components will be exposed to a wide range of environmental conditions that may affect the properties of the material, tests with coupon-size specimens are being conducted in DIII-D to obtain early performance data. The results from these tests, on specimens made from a comparable V-4Cr-4Ti alloy (Heat 832665)[7], are the subject of this paper.

Experiment and Specimen Description

The test series consisted of four tests. Tests D1 and D2 were designed to study the effects of bakeouts after an air and N vent, respectively. Because of the elevated temperatures and high concentrations of gaseous impurities during the bakeouts, the potential of material degradation would probably be the greatest in these periods. Tests W1 and W2 were designed to study the

* Work supported by U.S. Department of Energy, Office of Fusion Energy Research, under Contract W-31-109-Eng-38.

long-term effects of cumulative events (including bakeouts) during single- and multiple-cycle operations.

Tests D1 and D2 utilized the Divertor Materials Evaluation System (DiMES)[8], a device that is located below the vessel floor and when extended, allows specimens mounted on it to be inserted into the plasma chamber without disturbing the system vacuum. Tests W1 and W2 utilized a fixed mount on the DIII-D chamber wall behind the divertor baffle plate; specimen installation and retrieval were performed with a manned entry during the air vent between cycles. (Each operating cycle is ≈ 8-10 months long.) By design, none of the specimens from the lead tests directly interacted with the plasma.

The D1 Test

The specimen for the D1 test was a polished disk, 33.0 mm in diam. and 3.8 mm thick. Approximately the center one-third of the disk was exposed to the vessel atmosphere via the opening of the graphite retaining ring on the DiMES. The exposure occurred during the bakeouts on April 1, 9, 15 and 16, 1995, following an air vent in March. The exposure conditions, as determined by the DIII-D's infrared camera and the residual gas analyzer (RGA), are summarized in Table 1. In each of the four bakeouts, the duration at temperature was ≈5-10 h. During the experiment, the sample surface was recessed ≈3.8 mm below the DIII-D graphite tile floor.

Table 1. Summary of exposure conditions during the D1 test[a]

Bakeout Date	Temp. (°C)	Pressure (torr)	Impurity Partial Pressure ($\times 10^{-9}$ atm)			
			H_2O	N_2	CO	O_2
4/1/95	250	4.6×10^{-4}	490	0.016	80	3.1
4/9/95	150	1.1×10^{-3}	1400	0.018	30	3.5
4/15/95	325	2.6×10^{-4}	240	0.013	64	2.6
4/16/95	325	6.2×10^{-5}	67	0.013	11	0.63

[a]All values are peak readings.

The D2 Test

In the D2 test, five miniature Charpy specimens were exposed with the DiMES during a single bakeout on June 6, 1995, that following a clean (i.e., N) vent. The vent, for diagnostic repairs, lasted 35 days. Exposure conditions, as determined from temperatures measured in the inner and outer vessel wall and from RGA measurements, are summarized in Table 2. The Charpy specimens were 1/3 size (3.3 x 3.3 x 25.4 mm) and contained a 0.6-mm-deep, 30° blunt notch with a root radius of 0.08 mm. The direction of the crack plane was perpendicular to the rolling direction and through the thickness of the plate from which the specimens were prepared. After machining and before exposure, the specimens were annealed in vacuum at 1000°C for 1.0 h in a pure Ti foil wrap, which acted as an impurity getter.

Table 2. Summary of exposure conditions during the D2 test[a]

Bakeout Date	Temp. (°C)	Pressure (torr)	Impurity Partial Pressure ($x10^{-9}$ atm)			
			H_2O	N_2	Co	O_2
7/13/95	250	5.5×10^{-5}	31	0.33	2.4	0.08

[a]All values are peak readings.

The W1 Test

In the W1 test, five Charpy and five tensile specimens were exposed for an entire DIII-D operation cycle, from February through December 1995. The configuration of the Charpy specimens was the same as in the D2 test. The tensile specimens were 25.4 mm long, with a gauge section that was 7.62 mm long, 1.52 mm wide, and 0.76 mm thick. The long direction of the gauge section was parallel to the final rolling direction of the plate from which the tensile specimens were machined. All specimens were annealed in vacuum at 1000°C for 1.0 h with a Ti foil wrap prior to the test. For the exposure, the specimens were held in a frame mounted on the vessel wall behind the divertor baffle plate. The temperature of the specimens was measured with four thermocouples attached to the ends of the specimens.

During the test, the specimens were exposed for 265 days in a complete range of DIII-D operating conditions, which included air and N vessel vents, elevated temperature bakeouts, H glow discharge cleanings, boronizations[9]of the first wall (graphite tiles), and plasma operations. In their positions behind the divertor baffle plate, the specimens would be most affected only by those DIII-D operations for which the specimens would have been heated to elevated temperatures and at which the greatest interactions with gaseous impurities in the DIII-D environment might be expected. These operations included the elevated-temperature bakeouts and boronizations. Based on the specimen thermocouple data, the temperatures of the specimens tracked with the measured outside vessel wall temperature, and reached values of ≈150-300°C during bakeouts and ≈250 to 280°C during boronizations. Analysis of the RGA monitoring data obtained during the exposure period indicated that, depending on the type of vent, the specimens were exposed to impurity levels generally within the range of the impurities indicated in Tables 1 and 2. A summary of the various vents and bakeouts experienced by the specimens in the W1 test is presented in Table 3.

Table 3. DIII-D environment history (number of events) for the W1 test performed February – December, 1995

Air Vents	Nitrogen Vents	150°C Bakeouts (4-6 h duration)	200-250°C Bakeouts (2-7 h duration)	280-350°C Bakeouts (5-20 h duration)	280°C Boronizations (5.5 h duration)
5	5	2	3	20	2

The W2 Test

The W2 test is still ongoing in the DIII-D at the time of writing. Similar to the W1 test, five Charpy and five tensile specimens are being exposed on a mounted frame behind the divertor baffle plate. The planned exposure is three complete DIII-D operation cycles, from January 1996 through August 1998.

Test Results

The specimens from tests D1, D2, and W1 have been evaluated and the findings indicate that, although there were measurable effects from the exposures, the overall impact of the exposures on the properties of the material was insignificant. The effects of bakeouts after the air vent were studied during the D1 test. Examination of the disk specimen was limited to surface H analysis and microhardness measurements. The geometry of the specimen was not amenable to mechanical testing and none was conducted. The exposed area of the D1 disk exhibited a slight loss of luster. Surface H analyses, by an elastic recoil diffraction technique[10] with a 2.6 MeV ^{4}He beam, showed pronounced surface peaks of ≈25,000 appm for the front (i.e., exposed) side and ≈65,000 appm for the back side. The concentration profiles for both sides, however, decrease rapidly with depth within the first ≈0.1 mm. At a depth of ≈0.45 mm, the limit of beam penetration, the concentrations appear to have reached an asymptote of ≈7,000 appm for both sides. The fact that the H concentration is greater on the back side suggests the high surface readings may be a storage or handling artifact unrelated to the actual DIII-D exposure. Microhardness tests were performed with a light load (10 g) to minimize the depth of indentation (<1 mm). Readings taken at locations of the exposed front surface, the nonexposed front surface (i.e., beneath the graphite retaining ring), and the nonexposed back surface were essentially the same (205±15 KHN) and consistent with nonexposed control data.

The effects of the post-N_2-vent bakeout on the material's impact properties were studied with the Charpy specimens of the D2 test. The energy-vs.-temperature curve from the impact testing of the specimens is shown in Fig. 1 along with nonexposed sibling data[11]. The results indicate that, although there appears to be a slight reduction of the upper shelf energy after the exposure, all of the specimens are still ductile over the test temperature range of -190-150°C. The ductile-to-brittle transition temperature remains very low, <-150°C. The SEM fractograph of the -130°C test specimen, shown in Fig. 2, indicates the fracture mode to be ductile shear.

The composite effect of the exposure to an entire DIII-D operating cycle was studied during the W1 test. This test contained both tensile and Charpy specimens. The postexposure tensile tests were conducted at room temperature in air and at 350°C in high-purity Ar. The strain rate was 1.1 x 10^{-3}/s. The results, summarized in Table 4, indicate that, in spite of the long exposure, there was little change in the strength or ductility when compared with the nonexposed control[12]. The SEM fractograph of the room-temperature tensile specimen (Fig. 3) shows the fracture consisted of ductile dimples and microvoid coalescence. The exposed surface of this tensile specimen away from the gauge section was examined with an electron microprobe to determine the depth profile of interstitial elements O, C, and N. The results, when compared with those of a nonexposed control, show interstitial pickup to be minor and limited to only a thin layer (<0.1 mm thick) of the surface. No discernible differences were detected in the interstitial content beyond that depth. The lack of substantial interstitial uptake corroborates well with the measured tensile data. The postexposure Charpy impact tests were conducted at -190 -150°C; the results are shown in Fig. 4. Similar to those of the D2 test, the effects of the exposure appear to be limited. Although a slight decrease was noted in the upper-shelf energy, the specimens were still ductile, even at temperature as low as -190°C. The SEM fractograph of the -150°C specimen (Fig. 5) confirmed the fracture to be ductile.

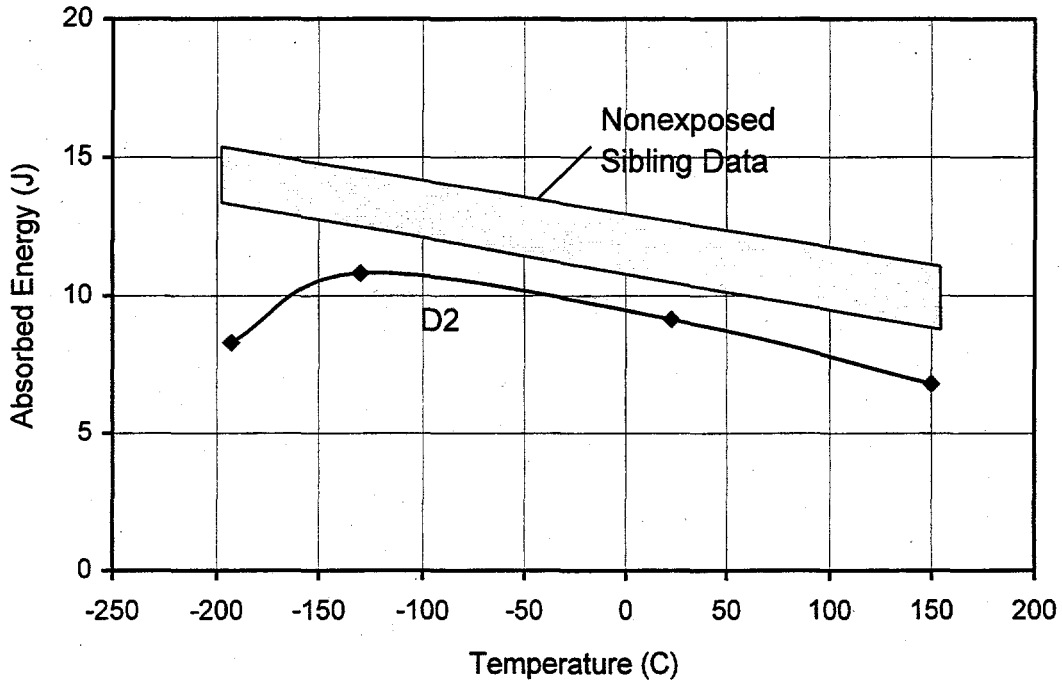

Fig. 1. Charpy impact data for D2 test, showing ductile behavior of exposed specimens even at ≈190°C.

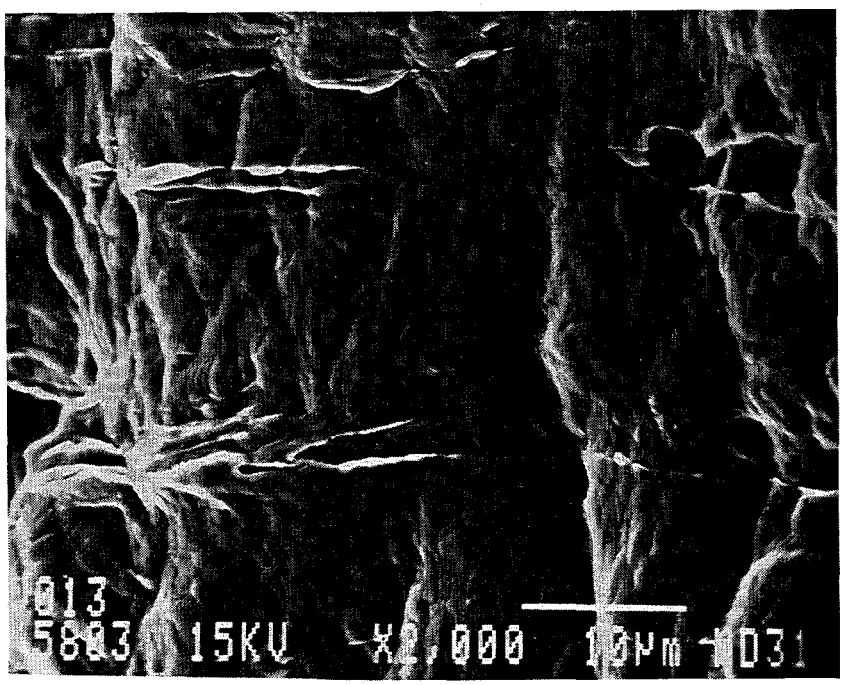

Fig. 2 SEM fractograph of D2 test specimen impact-tested at -130°C. Fracture mode was ductile.

Table 4. Tensile properties of specimens exposed in the W1 test in DIII-D

Tensile Property[a]	Test Temperature			
	25°C		350°C	
	DIII-D	Control	DIII-D	Control[b]
YS (Mpa)	334	357	241	205
UTS (Mpa)	449	428	377	359
UE (%)	19.0	19.1	14.8	17.6
TE (%)	27.0	29.2	22.0	25.4

[a] YS: 0.2% offset yield stress; UTS: ultimate tensile stress; UE: uniform elongation; TE: total elongation.

[b] Conducted at 400°C.

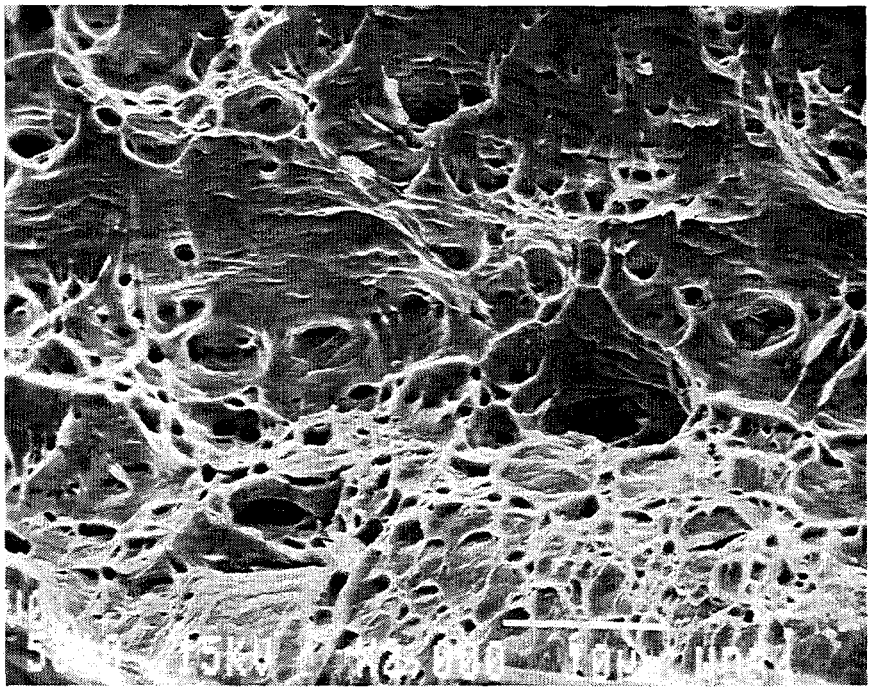

Fig. 3. SEM fractograph of tensile specimen from W1 test. Fracture mode was ductile.

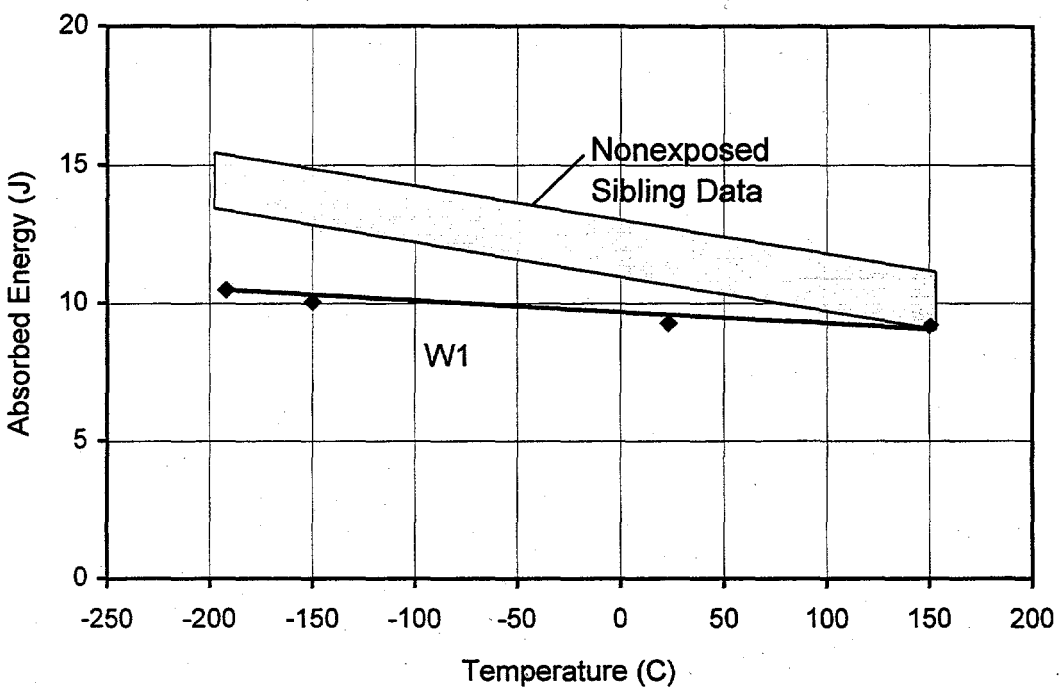

Fig. 4. Charpy impact data for W1 test, showing ductile behavior of specimens after a cycle-long exposure.

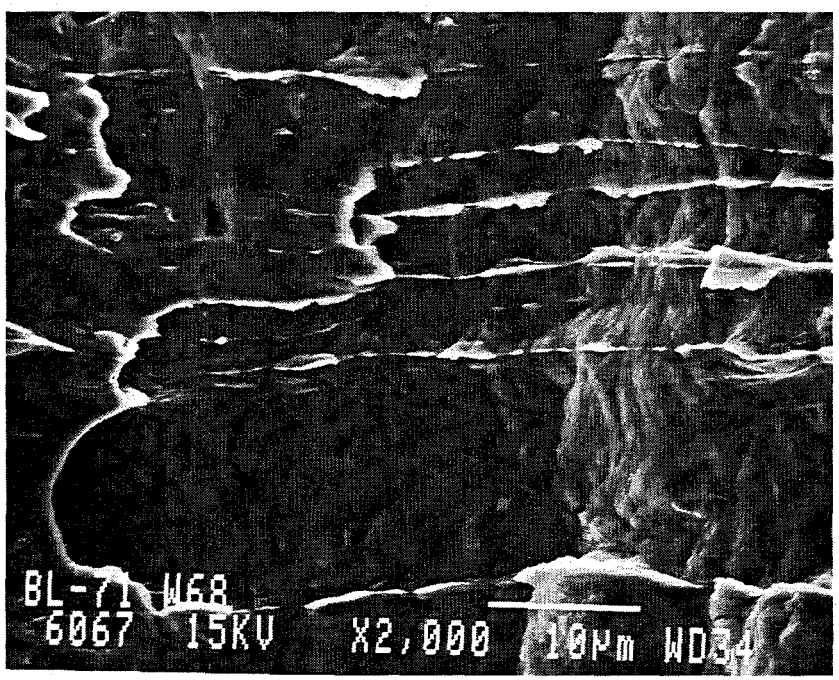

Fig. 5. SEM fractorgraph of W1 test specimen that was impact tested at -150°C. Fracture mode was ductile.

Conclusions

Although the available data from the tests were limited to one cycle of operation, all of the data suggest that the effect of exposing V-4Cr-4Ti divertor components to the DIII-D environment are benign. Interstitial impurity uptake is limited to only the shallow surface and does not alter the bulk material. Neither the tensile nor the impact properties of the V-4Cr-4Ti alloy were significantly affected by a cycle-long exposure. When the three-cycle-exposure specimens from the ongoing W2 test become available, they will be tested and analyzed and hopefully povide confirmation of these positive conclusions.

References

1. E. A. Hoffman et al., "Radioactive Waste Disposal Characteristics of Candidate Tokamak Demonstration Reactors," Fusion Technology, 31 pp. 35-62 (1997).

2. D. L. Smith et al., "Fusion Engineering and Design, 29 p. 399 (1995).

3. D. L. Smith et al., "Reference Vanadium Alloy V-4Cr-4Ti for Fusion Applications," J. of Nuclear Materials, 233-237, pp. 356-363 (1996.

4. W. R. Johnson et al., "Production and Fabrication of Vanadium Alloys for the Radiative Divertor Program of DIII-D," Fusion Reactor Materials Semiannual Progress Report, DOE/ER-0313/20, Oak Ridge National Laboratory, Oak Ridge, TN, pp. 3-10 (1996).

5. "System Design Description of DIII-D," General Atomics Report GA-A19264, Feb. 1989.

6. J. P. Smith et al., "Utilization of Vanadium Alloys in the DIII-D Radiative Divertor Program," J. of Nuclear Materials, 233237, pp. 421-425 (1996).

7. H. M. Chung et al., "Fabrication of 500-kg Heat of V-4Cr-4Ti," Fusion Reactor Materials Semiannual Progress Report, DOE/ER-0313/17, Oak Ridge National Laboratory, Oak Ridge, TN, pp. 5-11 (1995).

8. C. P. C. Wang et al., "Divertor Materials Evaluation System at DIII-D," J. of Nuclear Materials, 196-198, pp-871-875 (1992).

9. G. L. Jackson et al., "Boronization in DIII-D," J. Nuclear Materials, 196-198, p. 236 (1992).

10. J. B. Barbour and B. L. Doyle, "Elastic Recoil Detection: ERD," pp. 83-138 in Handbook of Modern Ion Beam Materials Analysis, eds. J. R. Tesmer and M. Nastasi, Materials Research Society, Pittsburgh, 1995.

11. H. M. Chung et al., "Effects of Annealing on Impact Properties of Production-Scale Heat of V-4Cr-4Ti," Fusion Reactor Materials Semiannual Progress Report, DOE/ER-0313/18, Oak Ridge National Laboratory, Oak Ridge, TN, pp. 273-278 (1995).

12. M. C. Billone et al., "Revision of the Tensile Database for V-Ti and V-Cr-Ti Alloys Tested at ANL," Proc. 8th Conf. on Fusion Reactor Materials (1997), to be published.

Irradiation Creep of Vanadium-Base Alloys* H. Tsai, M. C. Billone, R. V. Strain, and D. L. Smith (Argonne National Laboratory), and H. Matsui (Tohoku University)

Summary

A study of irradiation creep in vanadium-base alloys is underway with experiments in the Advanced Test Reactor (ATR) and the High Flux Isotope Reactor (HFIR) in the United States. Test specimens are thin-wall sealed tubes with internal pressure loading. The results from the initial ATR irradiation at low temperature (200-300°C) to a neutron damage level of 4.7 dpa show creep rates ranging from ≈0 to 1.2 x 10^{-5}/dpa/MPa for a 500-kg heat of V-4Cr-4Ti alloy. These rates were generally lower than reported from a previous experiment in BR-10. Because both the attained neutron damage levels and the creep strains were low in the present study, however, these creep rates should be regarded as only preliminary. Substantially more testing is required before a data base on irradiation creep of vanadium alloys can be developed and used with confidence.

Introduction

Vanadium-base alloys are being developed as candidate materials for fusion first-wall/blanket structures because of their low activation and attractive high-temperature properties[1,2]. While some of these properties have been extensively studied, irradiation creep, however, has not. Knowledge of irradiation creep is important because creep is a principal contributor to deformation and can potentially limit system performance.

Existing data on irradiation creep studies of vanadium base alloy are extremely scarce. In one of the only two tests reported in the open literature, Vitek et al[3]. irradiated pressurized tubes made from a V-20Ti material in the fast reactor EBR-II to study, mainly, the effects of helium implantation on creep deformation. Helium atoms were injected in the middle section of the tubular specimens to 15 appm using a cyclotron before the irradiation, which was conducted at 700°C to a displacement-damage dose of 22 dpa. Postirradiation dimensional measurements were limited to two of the tubes. One tube, at a hoop stress of 34 MPa, showed a creep rate of ≈4 x 10^{-5}/dpa/MPa and no differences in creep rates between the base and helium-implanted materials. The other tube, at 39 MPa, showed a creep rate of ≈7 x 10^{-5}/dpa/MPa for the base material and a rate twice as high for the helium-implanted material. The extent of thermal creep, which could have contributed substantially to total creep because of the high test temperature, could not be discerned from the total creep in this experiment.

More recently, the creep behavior of a V-4Cr-4Ti material was studied in the BR-10 fast reactor at 440°C to a displacement damage of ≈3.0 dpa by Troyanov et al[4]. The test specimen was a thin-wall tube and the applied stress was torsional. Thirteen deformation curves, at specimen stresses ranging from 17 to 164 MPa, were obtained. The results showed a creep rate of 5 x 10^{-6}/dpa/MPa for stresses up to ≈120 MPa, which was approximately one-half of the yield strength measured for the irradiated material. Above 120 MPa, the creep rate increased significantly.

Recognizing the importance of irradiation creep for vanadium-base alloys for fusion application, the U.S./Japan Jupiter collaboration program undertook a study on fusion structural materials. In the first experiment, 10 pressurized-tube creep specimens were irradiated in the ATR-A1 experiment in the Advanced Test Reactor (ATR)[5]. The available results of this experiment are the subjects of this report.

---

* Work Supported by U.S. Department of Energy, Office of Fusion Energy Research, under Contract W-31-Eng-38.

Experimental Procedure

Creep Tube Fabrication

The creep specimens in the ATR-A1 experiments were pressurized tubes with welded end plugs, as shown in Fig. 1. The tubes were prepared from two lots of materials: the 500-kg 832665 heat[6] with a V-4wt.%Cr-4wt.%Ti composition produced in the United States. and the VM9407 laboratory heat with a V-4wt.%Fe-4wt.%Ti-0.1wt.%Si composition produced at Tohoku University in Japan. The 832665-heat tubes were produced by drawing, whereas and VM9407-heat tubes were produced by machining. All specimens had a nominal 4.57 mm outer diameter (OD), 0.25 mm wall thickness, and 25.4 mm length.

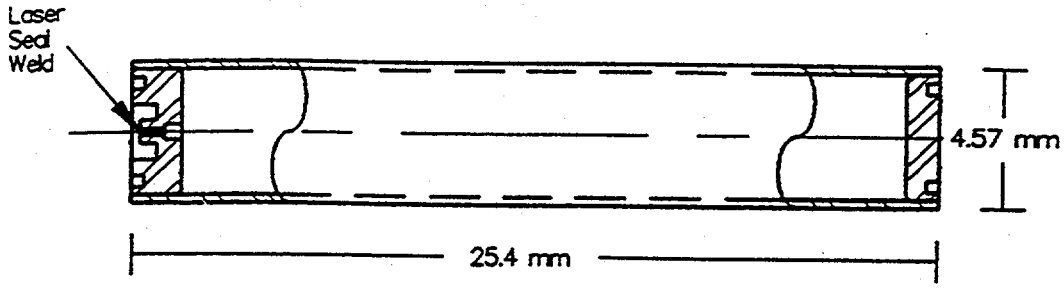

Fig. 1. Configuration of creep specimens.

A U.S. commercial vendor produced the 832665 tubing. The starting material was two 200-mm-long square bars cut from a 28.6-mm-thick warm-rolled plate. The bars, whose long dimensions paralleled the final rolling direction of the plate, were gun-drilled and machined into hollow cylinders with a 19.1-mm inner diameter (ID) and a 27.9-mm OD. Following cleaning and vacuum annealing (≈1025°C for 1 h in a vacuum of ≈7 x 10^{-5} torr), the two cylinders were drawn down at room temperature in three consecutive steps, each producing an areal reduction of ≈12-15%. After a total areal reduction of ≈40-45%, the pieces were cleaned, annealed, and drawn in three steps again. This cleaning/annealing/drawing process was repeated eight times to produce the finished tubing with a nominal 4.57 mm OD, 4.07 mm ID, and ≈45% cold work. To reduce the absorption of interstitial impurities during the vacuum annealing, the tubes were contained inside a pure Ti enclosure, which acted as the impurity getter. A total of ≈12 m of tube sections with various lengths was produced in this manner.

The drawn tubing has a fine grain microstructure with no apparent surface defects, as illustrated in Fig. 2. Sections of the drawn tubing were analyzed for their major alloying elements and interstitial impurity contents. The results indicated that the complex fabrication schedule caused only limited impurity uptake: oxygen content increased from 310 to 560 wppm, carbon from 80 to 300 wppm, and nitrogen from 85 to 95 wppm. These minor increases are not expected to substantially affect the properties of the material.

Because of the tubing's small size and the demanding flaw-detection specification (<0.025 mm flaw size), the drawn tubing could not be satisfactorily inspected with available ultrasonic or eddy current methods. Radiography was the only nondestructive means used to evaluate the internal condition of the tubing. A machined standard defect (0.025-mm-deep longitudinal groove) was included in the radiographs to establish the sensitivity of each exposure. Tube sections with questionable mass densities were excluded.

Before the attachment of the end caps, the 25.4-mm-long tube blanks were measured for their OD, ID, OD roundness, ID roundness, concentricity, and wall thickness with a coordinate measurement machine. The results of these measurements showed the dimensional attributes of the tube blanks to be excellent (all units in mm): ID 4.041 ± 0.002; OD of 4.569 ± 0.001; ID roundness 0.007 ±0.003; OD roundness 0.005 ±0.002; concentricity 0.007 ± 0.003; and wall thickness 0.264 ± 0.001.

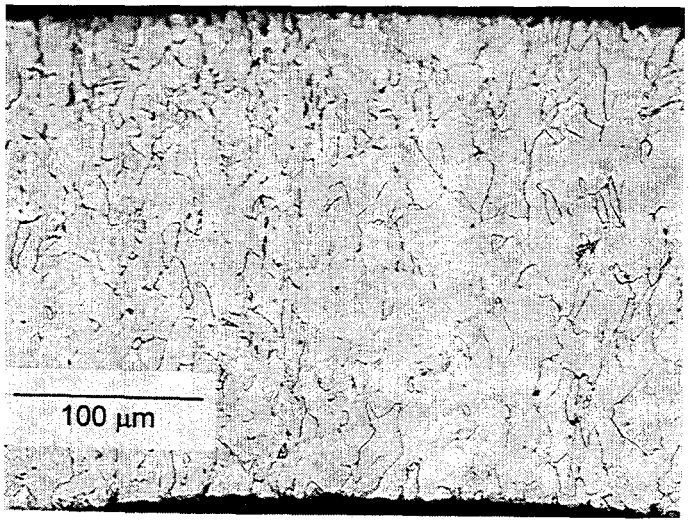

Fig. 2. Microstructure of drawn tube with 832665-heat V-Cr-4Ti material.

Creep Specimen Fabrication

Ten creep specimens, eight with the 832665 heat material and two with the VM9407 heat material, were included in the ATR-A1 experiment. The circumferential plug-to-tube welds were made with an electron-beam welder in vacuum. Figure 3 shows the microstructure of a typical weld. After the end plugs were attached, the assemblies were annealed at 1000°C for 1 h in vacuum while wrapped in a protective Ti getter foil. They were then pressurized to the desired level, through a 0.25-mm-dia. hole in the top end plug, with high-purity helium in a pressure chamber. Two of the 832665 specimens were designated as stress-free swelling controls and were therefore not pressurized. The final closure weld of the 0.25-mm-dia. hole was made with a laser through the quartz window in the pressure chamber. The specified pressure loading was determined with a code that accounted for thermal expansion of the vanadium alloy tubing, compressibility of the helium gas, and anticipated specimen temperature. Following the leak check and visual inspection, the dimensions of the assembled creep specimens were measured with a precision laser profilometer. The measurements were made at 5 axial locations (x/l of 0.1, 0.3, 0.5, 0.7 and 0.9) at every 9° azimuthal interval, and the 19 azimuthal readings were averaged to yield the mean diameter for each axial location.

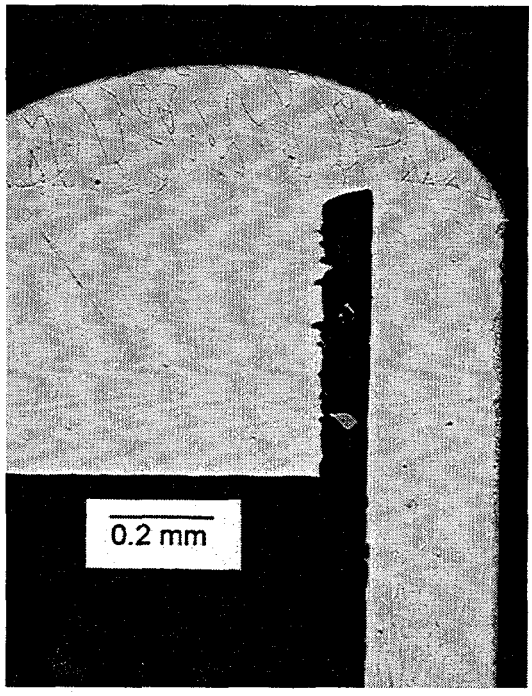

Fig. 3. Optical photomicrograph of specimen closure weld made with electron-beam welder.

Irradiation Conditions

The ATR-A1 experiment consisted of 15 stacked, lithium-bonded subcapsules spanning the 1210 mm core height. The 10 creep specimens were each contained in a subcapsule to preclude interactions should any one rupture unexpectedly. To reduce the atypical transmutation of V into Cr due to the reactor's thermal flux, a neutron filter made of Gd was installed in each subcapsule. The duration of the irradiation was 132.9 effective-full-power days. The experiment had two target temperatures: 200 and 300°C. However, because of the space limitation and axial flux gradient, the achieved displacement damage and specimen temperatures were not uniform, particularly for the nominally 200°C specimens. The calculated dpa, temperature, and stress loading for the specimens are shown in Table 1. For specimens A11 and A3, the calculated effective stress of 172 and 196 MPa were quite high, reaching ≈90 and 97% of the reported yield strength of the nonirradiated material[7].

Experimental Results

The first step in the postirradiation examination was to determine specimen integrity by puncturing the subcapsules containing the specimens and measuring the subcapsule plenum pressure. The results showed no abnormal pressure, implying that all pressurized specimens were intact. This positive finding was later confirmed by visual inspection of the specimens after they were retrieved from the subcapsules.

Diameter measurements have been completed for the eight 832665 specimens with V-4Cr-4Ti material. Measurements for the two VM9407 specimens with V-4Fe-4Ti-0.1Si material have been deferred due to the facility modification required to accommodate the higher gamma activities in these two specimens induced by the irradiation.

Table 1. Efective Stress in ATR-A1 Creep Specimens

Target Temp.(°C)	Specimen No.	Material[a]	Calculated Temp.(°C)	Calculated Damage (dpa)	Effective[b] Stress (MPa)
300	A1	832665	286	4.3	0
	A10	832665	302	4.6	87
	A7	832665	300	4.7	129
	A11	832665	295	4.5	172
	J2	VM9407	300	4.1	163
200	A5	832665	144	0.7	0
	A4	832665	213	1.5	88
	A2	832665	234	3.5	130
	A3	832665	259	3.9	196
	J3	VM9407	212	3.0	165

[a]Heat 832665: nominal composition V-4wt.%Cr-4wt.%Ti; Heat VM9407: nominal composition V-4wt.%Fe-4wt.%Ti-0.1wt.%Si.
[b]Effective von Mises stress.[8]

In calculating the effective strains for the 832665-heat specimens the averaged diameters were determined with the laser profilometer in the same manner as before the irradiation. To preclude end effects, only the three middle-diameter measurements of the specimen were used to calculate the average diametral strain. For the two zero-stress specimens for the 200 and 300°C groups, the diametral strains were small (0.05 and 0.11%), respectively, indicating insignificant density changes under the conditions irradiated. The precision of the profilometry measurements is ≈0.25 mm, or ≈0.05% in strain.) To facilitate a general stress analysis, the specimen's internal pressure loading and the measured diametral strain were converted to the wall-averaged effective von Mises stress and effective strain according to the follow formulas[8].

$$s_e = (0.5)(3)^{0.5}(r_m/t)DP, \text{ and}$$

$$e_e^C = 2\,(3)^{-0.5}(r_o/r_i)(e_{dia}^C),$$

where s_e is the effective stress, r_i, r_m, r_o are the internal, midwall, and external radii, respectively, t is the wall thickness, DP is the difference in internal and external gas pressure at temperature, e_e^C is the effective creep strain, and $e_{dia}^C = (e_{dia}^C - e_e^{stress\text{-}free})$ is the component of the measured OD hoop strain associated with creep. To obtain the creep coefficient (A), the assumed form of the irradiation creep law is

$$e_e^C = A\, s_e D,$$

where D is the neutron damage in dpa. The resultant effective creep strains and creep coefficients are summarized in Table 2.

Table 2. Summary Creep Data for 832665-heat Material in ATR-A1 Experiment

Specimen	Temp. (°C)	Damage (dpa)	Avg. s_e (MPa)	Avg. e_{dia} (%)	Avg. e_e^c (%)	Creep Coef. ($dpa^{-1}MPa^{-1}$)
A1	286	4.3	0	0.11	-	-
A10	302	4.6	87	0.10	≈0	≈0
A7	300	4.7	129	0.28	0.22	3.6×10^{-6}
A11	295	4.5	172	0.79	0.89	11×10^{-6}
A5	144	0.7	0	0.05	-	-
A4	213	1.5	88	0.16	0.14	11.0×10^{-6}
A2	234	3.5	130	0.05	≈0	≈0
A3	259	3.9	196	0.13	0.10	1.4×10^{-6}

Discussion

Vanadium-base alloys have a propensity to absorb interstitial impurities at elevated temperatures and become embrittled. The production of the drawn creep tubing for this study was particularly challenging because of the tubing's large surface-to-volume ratio and the significant number of process steps involved. The successful production of these tubes, by a commercial vendor to a set of tight tolerance specifications, indicates that vanadium-base alloys can be satisfactorily processed if reasonable process control is implemented.

The irradiation creep data from this study, along with the Troyanov et al. data[4] from a 445°C irradiation experiment conducted in BR-10, form a preliminary data set for evaluating the irradiation creep of V-4Cr-4Ti alloy. This data set is shown in Fig. 4. In the present study, because the attained neutron damage levels were low, the measured strains small, and the number of test specimens limited, the uncertainties on strain rates were probably high. These uncertainties are expected to diminish when additional data from tests currently underway or being planned for the HFIR become available. The J2 and J3 specimens from the present study, when evaluated, will provide a performance comparison between the V-4Cr-4Ti and V-4Fe-4Ti-0.1Si materials.

The data from the present study indicate strain rates generally lower than those measured by Troyanov et al., as shown in Fig. 4. The Troyanov et al. data also display a bilinear stress dependence: at stress greater than ≈120 Mpa, which is approximatly one-half of the yield strength of the irradiated alloy, the creep rate increases sharply. This bilinear dependence, however, could not be substantiated in the present study due to the limited data. Troyanov et al. noted that such threshold-type creep acceleration had been observed previously on stainless steel materials in experiments in the BR-10 reactor. But in comparison with the stainless steels, the acceleration threshold for the V-4Cr-4Ti alloy occurs at significantly lower stress with respect to the yield point. Recently, Grossbeck et al[8]. reported similar nonlinear stress dependence for a bcc alloy HT9 (a tempered martensitic steel) at elevated temperatures; they attributed the abrupt rate increase to the domination of a preferred absorption glide mechanism. Determination whether this bilinear behavior exists for vanadium base alloy is an important objective for the future irradiation creep experiments.

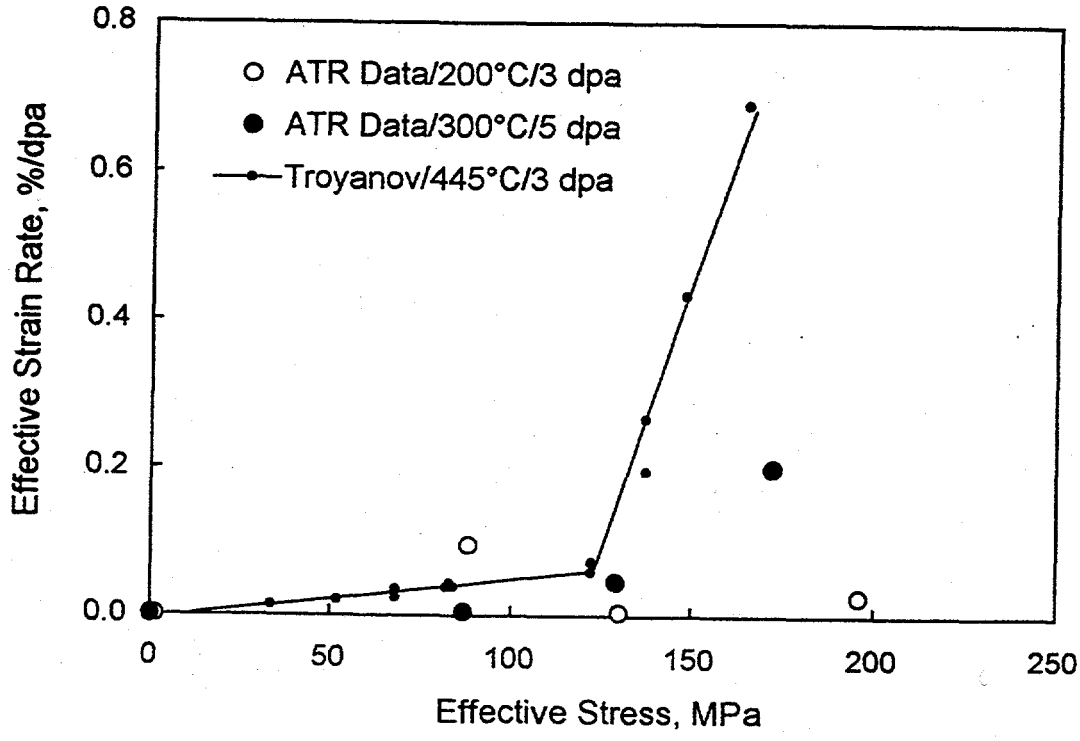

Fig. 4. Data set of effective creep strain rate from ATR experiment and torsional creep tests in BR-10 by Troyanov et al.[4] Correlation given by Troyanov (solid line) shows bilinear stress dependence.

Conclusions

An experiment on irradiation creep of vanadium base alloys with pressurized-tube specimens was recently completed in the ATR at low temperatures (≈200-300°C) to ≈4.7 dpa. Two materials were studied: a V-4Cr-4Ti alloy (Heat 832665) produced in the United States and a V-4wt.%Fe-4wt.%Ti-0.1wt.%Si alloy (Heat VM9407) produced at Tohoku University in Japan. The peak effective stress loading in the specimens was ≈200 MPa. None of the specimens ruptured during the irradiation. The measured strain rates, ranging from 0 to 12 x 10^{-6}/dpa/MPa for the 832665 heat alloy, were generally lower than reported by Troyanov et al. The creep rates for the VM9407 heat specimens have not yet been measured. Within the limitation of the data from the present study, no abrupt acceleration of creep rates at high stress levels, as reported by Troyanov et al., could be substantiated.

References

1. D. L. Smith et al., Fusion Engineering and Design, 29, p.399 (1995).

2. D. L. Smith et al., "Reference Vanadium Alloy V-4Cr-4Ti for Fusion Application," Proc. 7th Int. Conf. on Fusion Reactor Materials, Sept. 25-29, Obninsk, Russia.

3. J. M. Vitek et al., "Effect of Preinjected Helium on the Response of V-20Ti Pressurized Tubes to Neutron Irradiation," Journal of Nuclear Materials, 141-143 (1986), pp. 982-986.

4. V. M. Troyanov et al., "Irradiation Creep of V-Ti-Cr Alloy in BR-10 Reactor Core Instrumented Experiments," Journal of Nuclear Materials, 233-237 (1996), pp. 381-384.

5. J. W. Rogers et al., "Neutron Spectrum Studies in the ATR," 7th ASTM - Euratom Symposium on Reactor Dosimetry, Strasbourg, France (1990).

6. H. M. Chung et al., "Fabrication of 500-kg Heat of V-4Cr-4Ti," Fusion Reactor Materials Semiannual Progress Report, DOE/ER-0313/17, Oak Ridge National Laboratory, Oak Ridge, TN, pp. 5-11 (1995).

7. M. C. Billone, "Revised ANL-Reported Tensile Data for Unirradiated and Irradiated (FFTF, HFIR) V-Ti and V-Cr-Ti Alloys", this report.

8. E. R. Gilbert and L. D. Blackburn, "Creep Deformation of 20 Percent Cold Worked Type 316 Stainless Steel," J. Eng. Mater. & Tech., ASME Trans., pp. 168-180 (1977).

9. M. L. Grossbeck et al., "Irradiation Creep at Temperatures of 400°C and Below for Application to Near-term Fusion Devices," Effects of Radiation on Materials, 18th International Symposium, ASTM STP 1325 (1997).

PROCUREMENT OF V-Cr-Ti ALLOYS TO STUDY MINOR VARIATIONS ON V-4Cr-4Ti — M. L. Grossbeck (Oak Ridge National Laboratory)

OBJECTIVE

The goal of this procurement is to provide commercially prepared alloy product form using minor variations in composition from the candidate alloy, V-4Cr-4Ti.

SUMMARY

The alloys V-6Cr-3Ti, V-4Cr-4Ti-Si, V-6Cr-6Ti, and V-3Cr-3Ti, were prepared by Teledyne Wah Chang Albany Corp. In 1994. Plate and sheet ranging from 0.76 mm to 6.35 mm with residual material being left in 12-20 mm thick bar were fabricated. Although the heats were prepared on a pilot plant scale using different equipment, an effort was made to keep the processing as close to Wah Chang Heat 832665, the reference fusion heat of V-4Cr-4Ti, as possible.

INTRODUCTION

Although work had been done on a number of V-Cr-Ti alloys in the process of developing the V-4Cr-4Ti alloy, minor variations of this specific composition are needed to optimize this alloy composition. This procurement was made to obtain commercially prepared product forms for physical property, mechanical property, irradiation performance, and welding studies in order to optimize the composition of the V-Cr-Ti alloy system.

RESULTS AND DISCUSSION

Four nominally 14 kg vacuum arc remelt heat of the alloys were ordered. Each heat was to be individually melted, extruded, and rolled. The compositions are shown in Table 1, and the product forms are shown in Table 2.

Table 1. Compositions of Vanadium Alloys, wt. %

Element	V-6Cr-3Ti	V-4Cr-4Ti-Si	V-6Cr-6Ti	V-3Cr-3Ti
Cr	6	4	6	3
Ti	3	4	6	3
Si*	400-1000	800-1000	400-1000	400-1000
V	bal	bal	bal	bal

*wt. ppm

Table 2. Product Forms*

Item	Form	Mass, g	Thickness, mm	Approximate Size, mm	No. Pieces
1	Sheet	730	0.76	300 × 500	1
2	Sheet	950	1.02	300 × 500	1
3	Plate	2180	3.81	300 × 300	1
4	Plate	3580	6.35	300 × 190	1
5	Rect. Bar†	bal	12-20	>50	1

Chemical Composition

The maximum impurity concentrations specified in the order appear in Table 3. Also in the table are the compositions of the alloys as determined by the vendor, Teledyne Wah Chang, and the compositions as measured by glow discharge mass spectrometry by an independent laboratory, Charles Evans & Associates. The major elements were specified to be within ±0.5% based on the total alloy. The GDMS technique is very useful for trace elements but less useful for the major

	Table 3. Chemical Compositions of Alloys (wt. ppm except where noted)								
		V-6Cr-3Ti		V-4Cr-4Ti-Si		V-6Cr-6Ti		V-3Cr-3Ti	
		Heat T92		Heat T89		Heat T90		Heat T91	
Element	Specification	Vendor	GDMS	Vendor	GDMS	Vendor	GDMS	Vendor	GDMS
B			3.4		3.5		3.9		3.8
C	200	105	<92	112	<120	104	<120	120	<140
N	200	95	92	79		85		62	
O	400	280		270		250		230	
Al	200	255	300	200	270	235	270	200	240
Si	400-1000*	950	1000	1000	1100	960	1400	940	1200
P	30	<50	22	<50	24	<50	24	<50	26
S	30	10	21	10	23	10	20	10	27
Cl	2		0.11		<0.048		<0.19		<0.15
Ca	10		<0.19		<0.11		<0.12		<0.14
Ti (%)		2.94	3.0	4.1	5.3	5.98		3.02	3.1
V		bal	bal	bal	bal	bal	bal	bal	bal
Cr (%)		5.97	6.2	3.7	4.9	5.74		2.84	3
Mn			1.7		1.9		1.7		1.1
Fe	300	165	140	170	140	195	120	130	110
Co			0.22		0.35		0.19		0.60
Ni			8.3		12		10		7.6
Cu	50	140	130	83	50	55	48	83	79
Zn			4.5		4.7		4.0		5.3
Ga			7.6		5.9		5.0		3.9
As			1.4		2.4		2.0		1.7
Sr			70		<120		<110		<76
Y			6.1		<9.3		8.6		<5.9
Zr			56		<63		<66		<48
Nb	50	<50	50	<50	≤56	<50	<54	<50	≤55
Mo	500		380		360		340		380
Ag			0.091		0.081		0.081		0.076
Cd			0.44		0.45		0.29		0.40
Hf			0.45		1.2		0.82		0.41
Ta			<9.0		<5.2		<98		<9.7
W			32		32		28		32

*800-1000 for V-4Cr-4Ti-Si, range not max.

element compositions. Therefore, for Cr and Ti, the vendor's analysis is likely to be more accurate. Oxygen and nitrogen measured by GDMS were not given because of inconsistencies found previously between this technique and inert gas fusion analysis which is considered to be the method of choice for oxygen and nitrogen.

The minor element specifications were met very well. An exception is copper where measurements were as high as 140 ppm in contrast to the 50 ppm specified. This is not usually a concern in this alloy, and it is not a concern for neutron activation at this level. Measurements of aluminum were often above the specification of 200 ppm. This is a concern for two reasons: aluminum is a limiting element for neutron activation, and aluminum is used to reduce the V_2O_5, so it is a necessary part of the process.

Processing

All of the vacuum arc remelted ingots were machined to a nominal diameter of 117 mm by about 250 mm in length. The ingots were then welded into type 304 stainless steel cans 124 mm in diameter. The billets were then preheated 5 hours to 1149°C and then heated an additional 40 minutes to 1193°C in order to avoid stalling the extrusion press. The V-3Cr-3Ti billet was successfully extruded to 25 × 76 mm in cross section. The V-4Cr-4Ti-Si and the V-6Cr-3Ti were extruded to 35 × 79 mm since they stalled the press at a load of 1500 tons on the first try. The V-6Cr-6Ti was extruded through the same die after remachining and enclosing in a 114 mm diameter steel can. All extrusions were end cropped and sawed into about 300 mm lengths and fully machined to remove the steel cans.

Following the extrusion process, all material was acid pickled and vacuum annealed for two hours at 1075°C. After preheating for 45 minutes at 400°C, all pieces were cross-rolled to 12.7-13.7 mm in thickness. This required three roll passes for the thin extrusion and five passes tor the thicker extrusions. The annealed pieces were preheated for 25 minutes at 400°C and cross-rolled to 6.1-6.6 mm in seven passes. Each piece was reheated 10-30 minutes when about 9.7 mm in thickness. All but one piece of each alloy was pickled and annealed as before. The annealed pieces were then preheated 20 minutes at 400°C and cross-rolled to 3.2-3.4 mm in six passes. The 3.2-3.4 mm pieces were then pickled and vacuum annealed as before. The annealed pieces were cross rolled with no preheat (at ambient temperature) to two different intermediate thicknesses, depending upon the final thickness desired (2 mm for the 1 mm thick sheet and 1.6 mm for the 0.76 mm sheet). The percent reduction per rolling pass for the pieces rolled to 2 mm was within a range of 3% to 5%, and for the pieces rolled to 1.6 mm within a range of 3% to 6%. Based on recrystallization studies performed on a 3 mm plate, the annealing temperature for the 1.6 and 2 mm sheets was lowered to 1060°C for 2 hours. The annealed 2 and 1.6 mm pieces were again cross-rolled at ambient temperature. The rolled thickness was slightly greater to allow for hand conditioning of the final sheets. The reduction per rolling pass was with the range of 3-6%.

All pieces were roller leveled, hand conditioned to remove scratches and other defects and pickled.

CONCLUSIONS

Four heat of variations around the V-4Cr-4Ti composition were prepared. With very minor exceptions, the composition was with specifications. The product forms had excellent surface quality, meeting specifications. The product forms were sheet and plate ranging from 0.76 to 6.35 mm.

2.0 SILICON CARBIDE COMPOSITE MATERIALS

RADIATION RESPONSE OF SIC-BASED FIBERS - G. E. Youngblood and R. H. Jones (Pacific Northwest National Laboratory)*, Akira Kohyama (Institute of Advanced Energy, Kyoto Japan) and L. L. Snead (Oak Ridge National Laboratory)

To be published in the proceedings of the 8th International Conference on Fusion Reactor Materials held in Sendai, Japan, on October 26-31, 1997, in Journal of Nuclear Materials.

EXTENDED ABSTRACT

The radiation response of a base-line silicon carbide composite (SiC/SiC) made with Nicalon™ CG fiber reinforcement was presented for a broad range of dose and irradiation temperatures. Strength loss in this composite and a similar composite made with Tyranno™ fiber was related to shrinkage and a predicted mass loss in the Nicalon CG or Tyranno fibers. In Table 1, measured relative density and length changes ($\Delta p/p_o$ and $\Delta L/L_o$, respectively) for coated and uncoated fibers irradiated at high doses and temperatures (43 dpa-SiC at 1000°C and 80 dpa-SiC at 800°C) are given. Also given are the relative mass loss changes $\Delta m/m_o$, calculated from $\Delta p/p_o$ and $\Delta L/L_o$ by the expression $\Delta m/m_o \approx 3\,\Delta L/L_o + \Delta p/p_o$.

Table 1. Comparison of measured relative density and length changes and calculated mass changes for coated and uncoated SiC fibers irradiated to 43 dpa-SiC at 1000°C and to 80 dpa-SiC at 800°C.

Fiber Type	$\Delta p/p_o$ 43 dpa (%)	$\Delta p/p_o$ 80 dpa (%)	$\Delta L/L_o$ 43 dpa (%)	$\Delta L/L_o$ 80 dpa (%)	$\Delta m/m_o$ 43 dpa (%)	$\Delta m/m_o$ 80 dpa (%)
Tyranno	+11.7	12.6	-5.6	-4.8	-5	-2
Tyranno+PyC[1]	**+12.0**	**+12.5**	**-16.6**	**-32.4**	**-38**	**-84**
Nicalon CG	+9.9	+9.7	-3.4	-3.9	-0.3	-2
Nic CG + BN[1]	+12.4	+9.8	-3.0	-3.4	-3	-0.4
Nic CG+PyC[1]	**+9.9**	**+11.3**	**-7.1**	**-8.9**	**-11**	**-15**
Hi Nicalon	+6.3	+10.2	-4(2)*	-4.1	-6	-2
Dow X	-0.2	+1.6	-1.5	+1(2)*	-5	+5

[1] The boron nitride (BN) and PyC coatings were 150 nm thick.
* Unusually large length uncertainties given in parenthesis.

From this table, it is easy to see that the fiber mass loss, related to a carbothermal reduction of the excess oxygen in the Tyranno and Nicalon CG fibers, is enhanced by the pyrocarbon (PyC) coating. For these irradiation conditions, crystallization and crystal growth also were observed to have taken place at the Nicalon CG and Hi Nicalon fiber surfaces by SEM (see Fig. 1) and in the bulk by XRD.

In Figure 2, the measured densities are given for four categories of SiC-based fibers irradiated over four decades of fluence. The four fiber categories are: (1) "amorphous fibers with excess carbon and oxygen content," represented by Tyranno; (2) "more crystalline fibers than Tyranno,

*Pacific Northwest National Laboratory is operated for the U.S. Department of Energy by Battelle Memorial Institute under Contract DE-AC06-76RLO 1830.

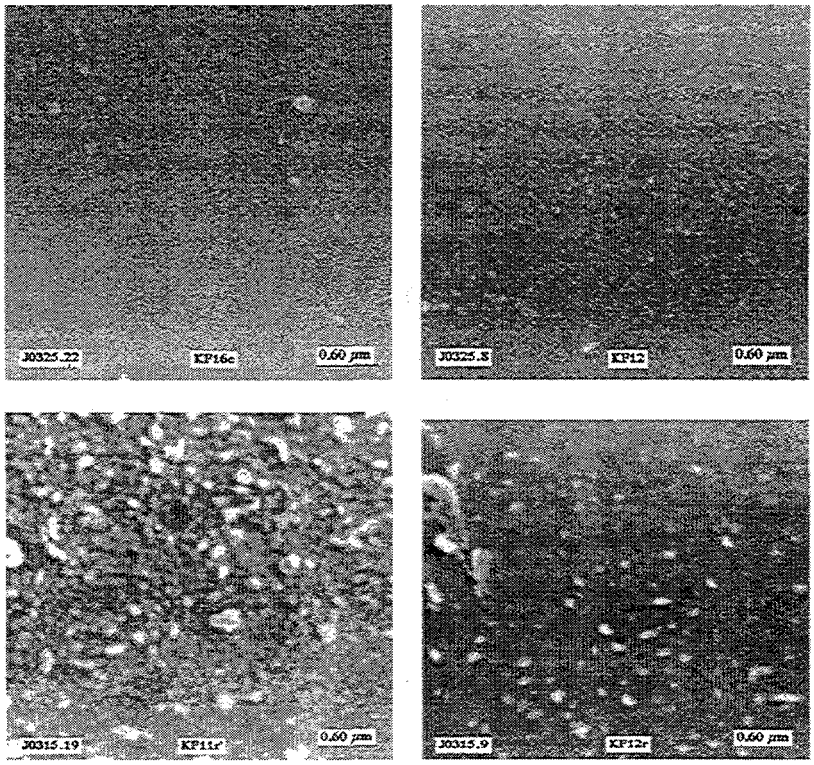

Figure 1. SEM views of unirradiated (upper) and irradiated (lower) fiber surfaces (Nicalon CG, left and Hi Nicalon, right) showing crystallization and crystal growth due to the irradiation conditions.

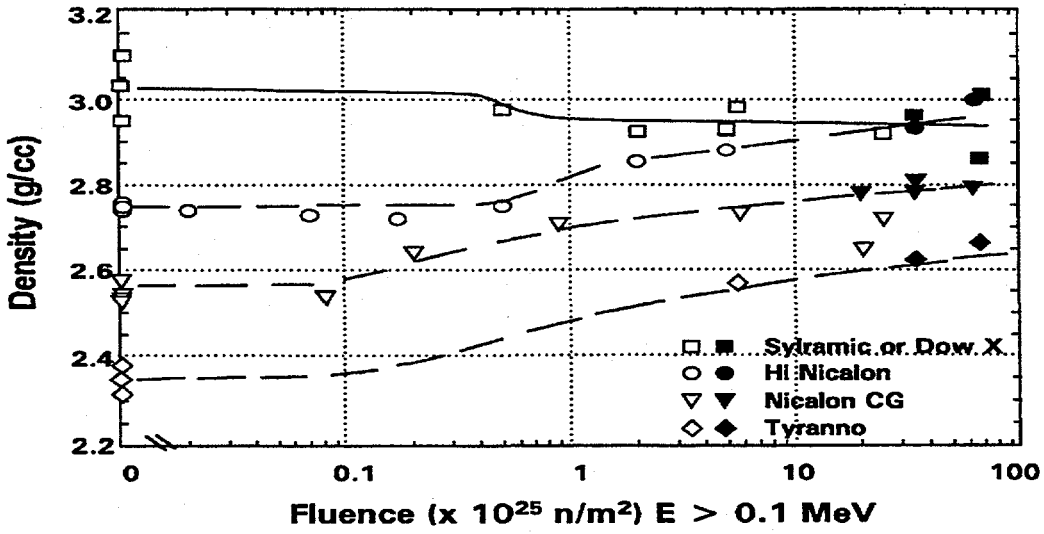

Figure 2. Density as a function of fluence for four categories of irradiated (uncoated) SiC-based fibers. As a rough rule, a fluence of 1 x 10^{25} n/m^2 (E > 0.1 MeV) is equivalent to 1 dpa-SiC dose.

but with excess carbon and oxygen content," represented by Nicalon CG; (3) "relatively all crystalline fiber with low oxygen, but with excess carbon," represented by Hi Nicalon; and (4) "crystalline fibers with essentially stoichiometric SiC compositions," represented by Dow X (an early version of now available Dow Sylramic™ fiber).

The guidance lines in Fig. 2 indicate similar increases in density with fluence up to 69 x 10^{25} n/m^2 (≈80 dpa-SiC) for the three non-stoichiometric SiC fiber categories. In contrast, the Dow X stoichiometric SiC fiber indicates slightly decreasing densities with fluence.

Although the Hi Nicalon fiber exhibited similar dimensional instability when compared to Nicalon CG or Tyranno fibers (Table 1 and Fig. 2) and crystal growth (Fig. 1), it should not be subjected to degradation by internal carbothermal reduction since it does not contain excess oxygen. Nevertheless, long-term degradation of irradiated Hi Nicalon fiber due to crystallization and crystal growth indicates that composite made with this fiber will not exhibit acceptable radiation tolerance. In contrast, a crystalline fiber with stoichiometric SiC composition (Dow X) exhibited only slight swelling, which is similar to that observed for irradiated monolithic SiC. Thus, in a composite, this type of fiber should not exhibit shrinkage and debonding from the matrix. However, the effects of irradiation on strength for these fibers still needs to be examined.

METHODS OF RADIATION EFFECTS EVALUATION OF SIC/SIC COMPOSITE AND SIC FIBERS - G. E. Youngblood and R. H. Jones (Pacific Northwest National Laboratory)*

OBJECTIVE

The objective of this work is to examine current practice for comparing the mechanical and thermal properties of irradiated, continuous SiC fiber/SiC matrix composites (SiC/SiC) and SiC fibers.

SUMMARY

This report covers material presented at the IEA/Jupiter Joint International Workshop on SiC/SiC Composites for Fusion Structural Applications held in conjunction with ICFRM-8, Sendai, Japan, Oct. 23-24, 1997. Several methods for radiation effects evaluation of SiC fibers and fiber-reinforced SiC/SiC composite are presented.

PROGRESS AND STATUS

Fiber Irradiations

Figure 1 illustrates a SiC fiber bundle contained within a SiC tube holder that is ideal for protection of the fiber bundle during high temperature irradiations. The tube holder, 2 mm od x 1 mm id and typically measuring from 30 to 60 mm in length, is made from sintered Hexoloy™ SiC. Placement and arrangement of the small drill hole(s) along the tube holder serve to identify the enclosed fiber bundle type and to allow gas exchange during encapsulation or during irradiation. The sintered SiC tube also can serve as a passive SiC temperature monitor [1].

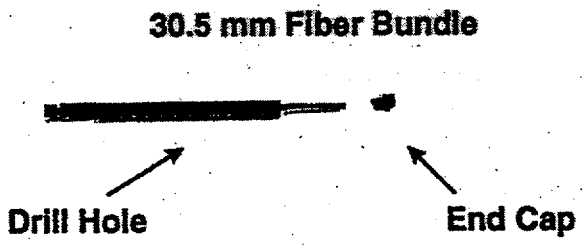

Sintered Hexoloy™ SiC Fiber Tube Holder

Figure 1. A SiC fiber bundle loaded into a capped Hexoloy SiC tube for irradiation tests at high temperature and dose. This holder is 33.5 mm x 2 mm o.d. x 1 mm i.d.

*Pacific Northwest National Laboratory is operated for the U.S. Department of Energy by Battelle Memorial Institute under Contract DE-AC06-76RLO 1830.

Figure 2 illustrates how the length change of an irradiated fiber bundle can be determined. After irradiation, the fiber bundle is carefully pushed out of the SiC tube holder (Fig. 1) with a small diameter rod and laid on top of a graduated scale. Each fiber bundle end together with the reference scale is imaged through a microscope at about x6 magnification with a video camera. Digital images are stored in a video recorder for later analysis. In Fig. 2a, the fiber bundle ends were well-defined and the length was determined to the nearest 0.01 inch. In Fig. 2b, the fiber bundle had shrunk considerably, and the bundle length was determined to the nearest 0.05 inches due to the ill-defined ends.

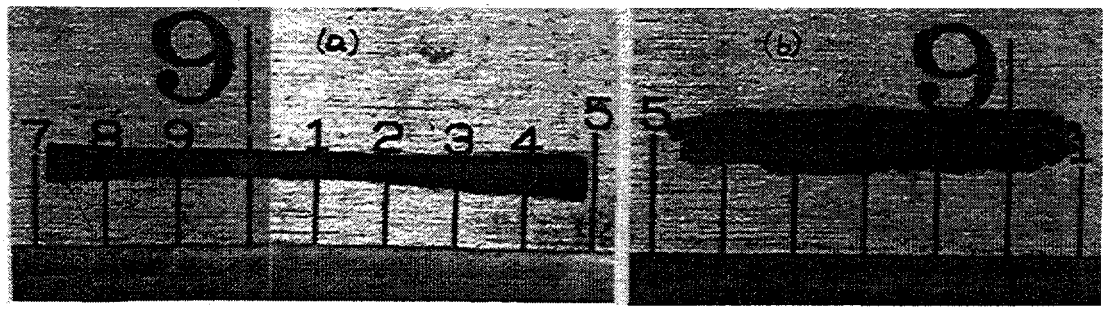

Figure 2. Examples of length change measurements for irradiated fiber bundles. The unirradiated fiber bundle lengths originally were 0.80 ± 0.01 inches; the uncoated Nicalon CG bundle (left) shrunk 3.9 ± 0.3%; the pyrocarbon-coated Tyranno bundle (right) shrunk 32 ± 1%.

Fiber Density

Figure 3 illustrates how the density of a fiber bundle is determined using the liquid gradient column technique. The column is constucted to cover a working range of densities of about 0.4 g/cc by using appropriate mixtures of carbon tetrachloride (1.594 g/cc), bromoform (2.890 g/cc) and methylene iodide (3.325 g/cc). At least five calibrated glass floats are used as density references for each column. The figure shows a typical 1 cm long sample cut from an irradiated fiber bundle suspended at 23.20 ± 0.02 cm and one of the calibration balls at ≈19 cm. For this column, each centimeter is equivalent to a change in density of about 0.003 g/cc, which represents the typical precision for these fiber density measurements.

Using these two techniques, a comparison of relative density and length changes for irradiated coated and uncoated SiC-based fibers is given in Table 1, Reference [2] of this report. From the density and length changes, fiber mass losses were calculated. The mass losses (also given in Table 1) predicted for the irradiated pyrocarbon-coated Tyranno and Nicalon CG fibers were significant, while the uncoated fibers appeared to exhibit no mass loss.

Overall irradiated fiber stability is indicated by examining the fiber density as a function of dose. As an example, the densities for four categories of SiC fibers (uncoated) irradiated up to 70 x 10^{25} n/m^2 (≈80 dpa-SiC) also are given in [2].

Fiber Crystallite Size

Long-term SiC fiber strength degradation occurs primarily due to extensive crystallization and crystal-growth in the fiber during high temperature, high dose irradiations. SEM images of

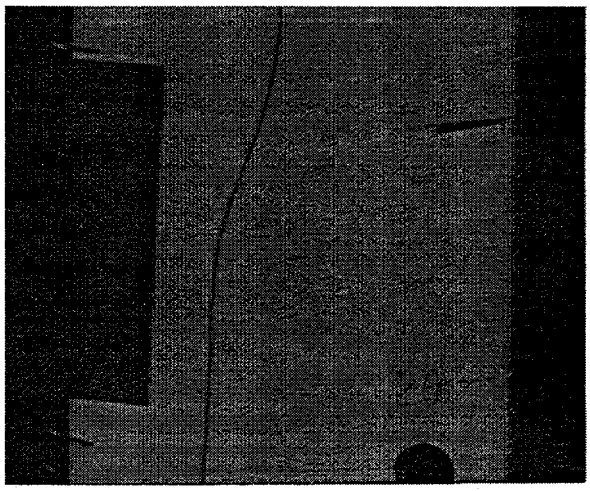

Figure 3. Typical view of a suspended SiC fiber bundle in a liquid density gradient column.

irradiated fiber surfaces depicting crystal growth are given in Figure 1 of Reference 2. Bulk fiber crystallite growth was determined by a modified Scherrer XRD technique. Table 1 presents the procedural changes from the conventional XRD technique necessary to accomodate relatively short (about 2.5 cm) irradiated fiber bundle segments. To achieve acceptable XRD peak resolution from a 5 mg sample, the background signal was reduced by using a silicon wafer substrate, the ground irradiated fibers were contained in 3-in-1 oil, the scan rate was reduced to 0.0002 °/sec, and the 2θ scan was reduced to the 25-50° range to cover only the β-SiC <111> peak and the <200> shoulder.

Table 1. Crystallite size of irradiated SiC fibers by a modified Scherrer XRD technique.

Procedure	**Conventional**	**Irradiated**
Sample Quantity	50 mg (≈25 cm tow)	5 mg (≈2.5 cm tow)
Substrate	Quartz	<100> Silicon
Containment	Colloidon	3-in-1 Oil
Range 2θ	10°-120°	25°-50°
Scan Rate	0.02 °/sec (≈1.5 hr.)	0.0002 °/sec (≈1.5 day)

Using these modified XRD procedures, the crystallite sizes for Hi Nicalon and Nicalon CG fibers were determined to have increased after a 800°C, 80 dpa-SiC irradiation (COBRA 1A2) from 2.7 to 6.1 nm and from 1.6 to 4.0 nm, respectively.

Fiber Creep

In References 3,4 and 5, an experiment developed to examine the creep behavior of irradiated SiC fibers by a bend stress relaxation technique is described, so will not be discussed here.

SiC/SiC Composite Mechanical Properties

To evaluate the radiation effects in SiC/SiC composite, the 4-point flexure test provides an easily reproduced standard method (See Reference 6 for recommended flexure test procedures). It is noted here that simple weighing of bend bars before and after irradiation

provides additional information about the material thermochemical stability, which can be quite different from that observed in a non-irradiation environment. For instance, bend strength degradation was related to a mass-loss mechanism for five types of SiC/SiC composite irradiated in the COBRA 1A2 test series [7].

SiC/SiC Composite Thermal Diffusivity

The measurement of the thermal diffusivity by the laser flash technique is another reproducible standard method used to evaluate irradiation effects in SiC/SiC composite as well as in monolithic SiC. Usually for analysis, the measured thermal diffusivity (α) is converted to thermal conductivity (k) through the relation $k = \alpha\rho c_p$ where ρ and c_p are the bulk density and specific heat capacity at constant pressure, respectively. The bulk density is easily measured before and after irradiation and its temperature dependence is easily estimated. In contrast, because of the difficulty of making accurate heat capacity measuremants especially as a function of temperature, the heat capacity term is not so easily estimated. Generally, the rule of mixtures and handbook values are used to calculate an effective heat capacity. Then, the assumption usually is made that the heat capacity term doesn't change during irradiation. However for fundamental analysis of the effects of irradiation, i.e., defect configurations, concentrations, thermal annealing behavior, etc., it is better to analyze the temperature dependence of α (or $1/\alpha$) rather than k since α is directly proportional to the phonon mean free path (see Fig. 4) and does not depend on a heat capacity estimate [8]. A detailed analyses of irradiation defect configurations and their annealing kinetics is planned for high-purity, Morton CVD β-SiC to be irradiated in the Jupiter P3-4 test series.

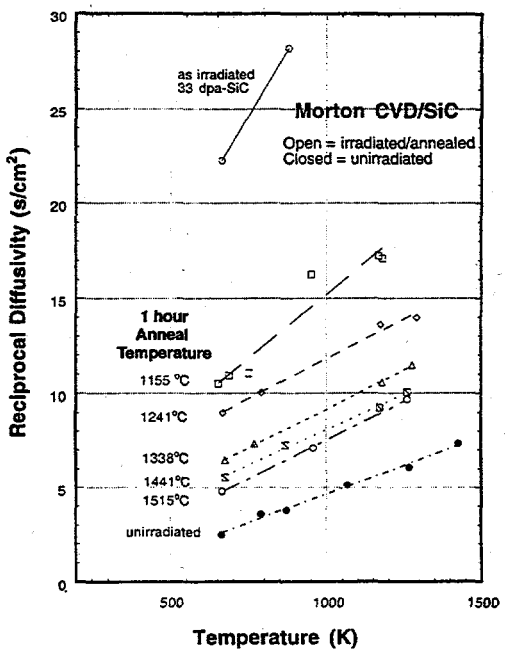

Figure 4. A plot of $1/\alpha$ vs. test temperature is approximately linear for unirradiated and for irradiated and annealed Morton CVD β-SiC. The intercepts are proportional to the residual irradiation defect concentrations after each high temperature anneal, and the approximately constant slopes represent the scattering strengths of the dominant phonon scattering defects, probably vacancies.

Nevertheless, for engineering application it is useful to analyze the temperature dependence of (K_{irr}/K_{unirr}), the ratio of the irradiated to theunirradiated thermal conductivity values, as was reported in [9] for a variety of monolithic and composite SiC structural materials.

REFERENCES

1. G. E. Youngblood, "Passive SiC Irradiation Temperature Monitor," p. 324 in Fusion Materials Semiannual Progress Report for Period Ending December 31, 1995. DOE/ER--0313/19.

2. G. E. Youngblood, R. H. Jones, Akira Kohyama and L. L. Snead, "Radiation Response of SiC-Based Fibers," extended abstract for paper P2-C111 presented at ICFRM-8, Oct. 26-31, 1997, Sendai, Japan (in this report).

3. G. E. Youngblood, M. L. Hamilton and R. H. Jones, "Technique for Measuring Irradiation Creep in Polycrystalline SiC Fibers," p. 146 in Fusion Materials Semiannual Progress Report for Period Ending June 30, 1996. DOE/ER--0313/20.

4. G. E. Youngblood and R. H. Jones, "Creep Behavior for Advanced Polycrystalline SiC Fibers," p. 89 in Fusion Materials Semiannual Progress Report for Period Ending December 31, 1996. DOE/ER--0313/21.

5. G. E. Youngblood, R. H. Jones G. N. Morscher and Akira Kohyama, "Creep Behavior for Advanced Polycrystalline SiC Fibers - II," p. 81 in Fusion Materials Semiannual Progress Report for Period Ending June 30, 1997. DOE/ER--0313/22.

6. G. E. Youngblood and R. H. Jones, "Minimum Bar Size for Flexure Testing on Irradiated SiC/SiC Composite," (in this report).

7. G. E. Youngblood, C. H. Henager and R. H. Jones, "Thermochemical Instability Effects in SiC-Based fibers and SiC/SiC Composites," p. 111 in Fusion Materials Semiannual Progress Report for Period Ending June 30, 1997. DOE/ER--0313/22.

8. G. E. Youngblood and W. Kowbel, "Improvement of the Thermal Conductivity of SiC/SiC Composite," p. 107 in Fusion Materials Semiannual Progress Report for Period Ending December 31, 1995. DOE/ER--0313/19.

9. G. E. Youngblood and D. J. Senor, "Analysis of Neutron Irradiation Effects on Thermal Conductivity of SiC-Based Composites and Monolithic Ceramics," p. 75 in Fusion Materials Semiannual Progress Report for Period Ending June 30, 1997. DOE/ER--0313/22.

FIBER CREEP RATE AND HIGH-TEMPERATURE PROPERTIES OF SiC/SiC COMPOSITES -- C. A. Lewinsohn, R. H. Jones, G. E. Youngblood, and C. H. Henager, Jr., (Pacific Northwest National Laboratory)*

To be published in Journal of Nuclear Materials as Proceedings of the 8th International Conference on Fusion Reactor Materials, Oct. 26-31, 1997, Sendai, Japan.

EXTENDED ABSTRACT

Results of studies aimed at relating the fiber creep rate to the subcritical crack growth rate and fracture properties of SiC/SiC composites have demonstrated that the crack growth rate in a bulk composite is controlled by the fiber creep rate. This result was demonstrated for Nicalon-CG and Hi-Nicalon fiber reinforced material where a 50-75°C shift in the creep strength of the fiber resulted in a similar shift in the crack growth rate of the composite. Irradiation enhanced creep of SiC fibers and matrix must also be considered in the performance assessment of SiC/SiC composites.

The shape of the displacement versus time curve for composites containing Hi-Nicalon fibers were similar to those of the previously tested materials, containing Ceramic-grade fibers, that exhibited subcritical crack growth controlled by time-dependent relaxation of the fiber-bridging stresses due to fiber creep. The crack velocity in the CG-C composites at 1100°C in argon was very close to that of the Hi-C materials at 1150-1175°C, this roughly corresponds to the temperature differential shown by DiCarlo et al. to obtain the same relaxation in 1 hour bend stress relaxation(BSR) tests in the two fibers. This supports the hypothesis that subcritical crack growth in SiC/SiC composites is controlled by fiber creep.

The effective crack velocity of a material containing Ceramic-grade Nicalon fibers and a 150 nm carbon coating was also measured at 1373 K in argon. The crack velocity of this material was faster than the materials containing Ceramic-grade Nicalon fibers with a 1 μm -thick interphase. This is probably due to the stronger clamping stresses, hence higher fiber stresses, that promote fiber creep.

The steady state creep rate, $d\varepsilon_c/dt$, was assumed to be linearly proportional to the product of stress, σ, and flux, ϕ,

$$d\varepsilon_c/dt = K \sigma \phi$$

For a hypothetical stress of 100 MPa and a fluence of 5 dpa, the maximum steady state creep rate, $d\varepsilon_c/dt$, would be 3.98×10^{-12} s^{-1} at 900°C (E>0.18 MeV). The equivalent steady state creep rate of CVD silicon carbide due to thermal effects at the same stress and temperature would be 1.05×10^{-13} s^{-1} according to data published by Carter et al.. Therefore, irradiation may enhance the thermal creep of CVD silicon carbide by an order of magnitude. If irradiation enhanced the creep rate of Nicalon™ fibers by a similar order of magnitude a similar increase in the subcritical crack growth rate in SiC/SiC composites would occur.

*Pacific Northwest National Laboratory is operated for the U.S. Department of Energy by Battelle Memorial Institute under Contract DE-AC06-76RLO 1830.

HIGH THERMAL CONDUCTIVITY SIC/SIC COMPOSITES FOR FUSION APPLICATIONS-II

- W. Kowbel, K. T. Tsou and J. C. Withers (MER Corporation, Tucson AZ) and G. E. Youngblood (Pacific Northwest National Laboratory)*

OBJECTIVE

The objective of this work is to examine SiC composites fabricated by various processing methods designed to improve composite thermal conductivity. Specifically, it is desired to increase the thermal conductivity of these composites to meet requirements for advanced fusion energy systems.

SUMMARY

This report covers material presented at the IEA/Jupiter Joint International Workshop on SiC/SiC Composites for Fusion Structural Applications held in conjunction with ICFRM-8, Sendai, Japan, Oct. 23-24, 1997. An unirradiated SiC/SiC composite made with MER-developed CVR SiC fiber and a hybrid PIP/CVI SiC matrix exhibited room temperature transverse thermal conductivity of 45 W/mK. An unirradiated SiC/SiC composite made from C/C composite totally CVR-converted to a SiC/SiC composite exhibited transverse thermal conductivity values of 75 and 35 W/mK at 25 and 1000°C, respectively. Both types of SiC/SiC composites exhibited non-brittle failure in flexure testing.

PROGRESS AND STATUS

Introduction

This report updates the status of work performed by MER Corporation to develop high thermal conductivity SiC/SiC composites for fusion applications reported initially at the first IEA SiC/SiC Workshop held at Ispra, Italy and in a Fusion Materials Semiannual Progress Report [1,2].

A low-cost, chemical vapor reaction (CVR) process was first developed to directly convert graphite fiber to high-purity, crystalline ß-SiC fiber [3]. Initially Celion 1K, and more recently Amoco T-300 graphite fibers, were used as the precursor graphite fiber. Starting with CVR-converted SiC fiber, two distinct processes (I and II) were developed to fabricate SiC/SiC composite which exhibited high transverse thermal conductivity and non-brittle fracture. Table 1 summarizes the progress-to-date by comparing selected property values for the composites fabricated by the Type I and II processes with those for composites fabricated by the Type I process before it was optimized and by a conventional CVI (chemical vapor infiltration) process using Hi Nicalon™ fiber.

In the hybrid PIP/CVI (Type I) process, the composite matrix was produced by polymer infiltration and pyrolysis (PIP) with a final CVI step. During this reporting period, the Type I process was further optimized to yield composite with increased bulk density (from 2.35 to 2.55 g/cc), increased RT thermal conductivity (from 45 to 55 W/mK in the transverse direction), increased RT 4-pt. flexure strength (from 275 to 320 MPa) and decreased open porosity (from 10 to 8%).

*Pacific Northwest National Laboratory is operated for the U.S. Department of Energy by Battelle Memorial Institute under Contract DE-AC06-76RLO 1830.

In the CVR-CVR (Type II) process, a composite preform made from graphite or partially converted CVR-SiC fiber with a pitch-derived carbon matrix was totally converted to crystalline SiC/SiC composite by a CVR process. An initial fabrication run produced a composite that exhibited a relatively high bulk density (2.65 g/cc), much higher thermal conductivity values (75 and 35 W/mK at RT and 1000°C, respectively) and an acceptable flexure strength (250 MPa).

Table 1. Comparison of selected properties for SiC/SiC composites

Type	Density (g/cc)	Ther. Cond. RT (W/mK)	Ther. Cond. 1000°C (W/mK)	Flex. Strength RT (MPa)	Open Porosity (%)
Hi Nicalon/CVI (Ref.)	2.55	13	10	350	15
Type I - Celion 1K (PIP/CVI hybrid)	2.35	45	nm	275	10
Optimized Type I - T300 (PIP/CVI hybrid)	2.55	55	nm	320	8
Type II - T300 (CVR/CVR)	2.65	75	35	250	15

In common, both Type I and II processes require a final high temperature anneal (≥1600°C) to achieve optimized thermal conductivity values. Such an anneal step is inaccessible with current state-of-the-art CVI- or PIP-produced composite made with Hi Nicalon or Nicalon CG fibers because of the thermochemical instability of the fibers when temperatures exceed about 1200°C [4]. The CVR-produced, high purity β-SiC fiber is thermodynamically stable to temperatures exceeding 1600°C; therefore it is amenable to high temperature treatments [5].

In Figure 1, the RT stress-strain curves for composite made by the optimized hybrid PIP/CVI and the CVR-CVR processes are compared to those for composite made by the CVI process with either Hi Nicalon or Nicalon CG fiber. Although the toughness (area under the curve) and strain-to-failure properties are slightly reduced, the ultimate strengths are comparable and the proportional limit stresses are higher. Thus, the composites produced either by the Type I or II processes with a final high temperature anneal exhibit much improved thermal conductivity values as well as density, strength and toughness values comparable to those for conventional CVI-produced composite.

FUTURE WORK

The irradiation behavior of these newly-developed, high thermal conductivity SiC/SiC composites will be examined after several low dose "rabbit" experiments as well as after a relatively high dose, high temperature (10 dpa-SiC, 800°C) experiment which will be carried out as part of the joint Monbusho/US Jupiter P3-4 SiC/SiC fusion materials test program.

ACKNOWLEDGMENTS

This work is being supported by a DOE- SBIR, Phase II Contract No. DE-FG02-94ER81487.

REFERENCES

1. J. C. Withers, W. Kowbel, R. O. Loutfy, G. E. Youngblood and C. Wong, "High Thermal Conductivity SiC/SiC Composites for Fusion Applications," p. 69 in the Proceedings of the IEA International Workshop on SiC/SiC Ceramic Composites for Fusion Structural Applications, 28-29 October 1996, Ispra, Italy.

2. J. C. Withers, W. Kowbel, R. O. Loutfy, G. E. Youngblood and C. Wong, "High Thermal Conductivity SiC/SiC Composites for Fusion Applications," p. 87 in the Fusion Materials Semiannual Progress Report for Period Ending December 31, 1996. DOE/ER-0313/21.

3. W. Kowbel, J. C. Withers, R. O. Loutfy, C. Bruce and C. Kyriacou, "Silicon Carbide Fibers from Graphite Precursors for Fusion Energy Applications," ?????

4. G. E. Youngblood, R. H. Jones, G. N. Morscher and Akira Kohyama, "Creep Behavior for Advanced Polycrystalline SiC Fibers," p. 89 in the Fusion Materials Semiannual Progress Report for Period Ending December 31, 1996. DOE/ER-0313/21.

5. MER reference on the high temperature stability of the MER fiber.

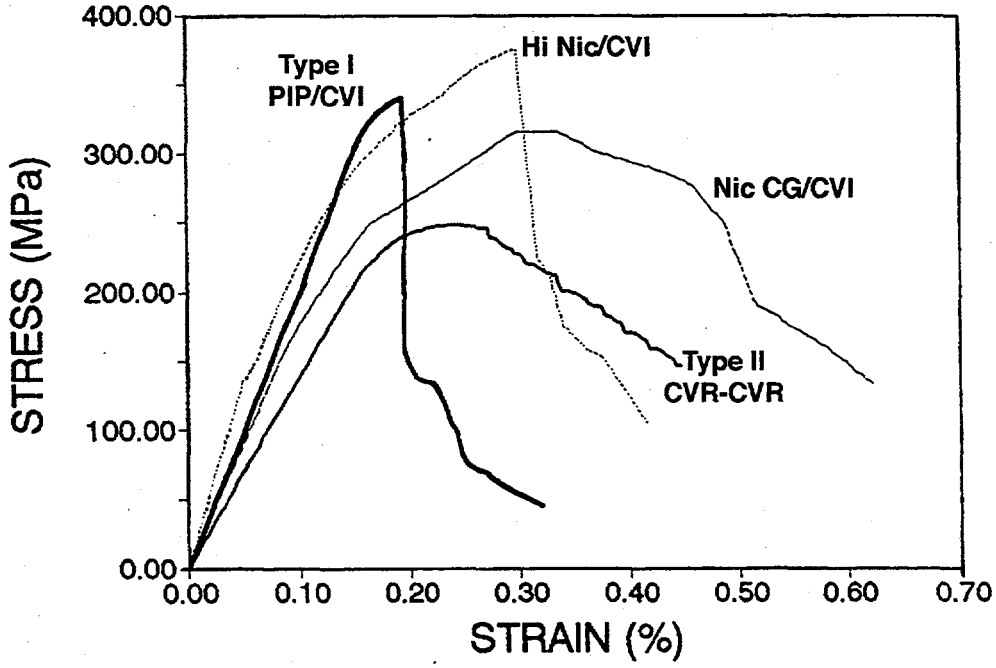

Figure 1. Comparison of 4-point flexure stress-strain curves at RT for SiC/SiC composites

MINIMUM BAR SIZE FOR FLEXURE TESTING OF IRRADIATED SIC/SIC COMPOSITE -
G. E. Youngblood and R. H. Jones (Pacific Northwest National Laboratory)*

OBJECTIVE

The objective of this work is to examine current practice for comparing the mechanical and thermal properties of irradiated, continuous SiC fiber/SiC matrix composites (SiC/SiC) and to recommend consistent and sensible test methodologies within the constraints of limited reactor test volumes.

SUMMARY

This report covers material presented at the IEA/Jupiter Joint International Workshop on SiC/SiC Composites for Fusion Structural Applications held in conjunction with ICFRM-8, Sendai, Japan, Oct. 23-24, 1997. The minimum bar size for 4-point flexure testing of SiC/SiC composite recommended by PNNL for irradiation effects studies is 30 x 6 x 2 mm^3 with a span-to-depth ratio of 10/1 .

PROGRESS AND STATUS

Introduction

This report updates the recommendations and rationale for the minimum bar size for 4-point flexure testing of irradiated SiC/SiC composite previously presented [1]. Because the specimen volume and number likely will be limited in reactor exposures, the minimum conditions recommended by PNNL for SiC/SiC fusion structural material development are less than ASTM recommendations for non-fusion applications. The PNNL and ASTM subcommittee C28.07 recommendations [2] are compared in Table 1.

Table 1. Comparison of conditions for 4-Pt. flexure testing of SiC/SiC.

Category	ASTM Subcommittee C28.07	Fusion PNNL Recommended
No. of Samples	10	5
Minimum Size (Lxbxd mm^3)	45 x 6 x 2	30 x 6 x 2
Span-to-Depth** (S/d)	16/1 to 30 /1	10/1
Bar Width	2 x repeat cell distance	4 bundle widths
Overhang (mm)	5+	5
Surface Finish	Varied	Tensile Surface unfinished
Strain Rate (sec^{-1})	10^{-3}	10^{-3}

** Increase S/d t reduce potential for premature interlaminar shear failure.

* Pacific Northwest National Laboratory is operated for the U. S. Department of Energy by Battelle Memorial Institute under Contract DE-AC06-76RLO 1830.

To reduce irradiated specimen total volume, the ASTM recommended minimum number of samples is reduced from 10 to 5, the bar length from 45 to 30 mm, and the span-to-depth ratio (S/d) from 16/1 to 10/1. For a valid flexure test, the bar must initially fracture at the tensile surface. Since interlaminar shear failures are more likely when the specimen S/d ratio is 10/1, careful examination of the stress-strain curves and the failed bars must be carried out to eliminate invalid tests. To reduce somewhat the potential for shear failure, the minimum bar width and the unstressed overhang are retained at ≈6 mm and 5 mm, respectively. If the bar thickness must be reduced to attain a S/d = 10, the specimen should be machined from the compressive surface only.

As examples of invalid SiC/SiC flexure tests, in Figure 1 several failed bend bars illustrate premature failure by (a) delamination from the ends or (b) at a surface where the reinforcing fibers were preferentially cut through by surface machining along the aligned fabric weave ridges.

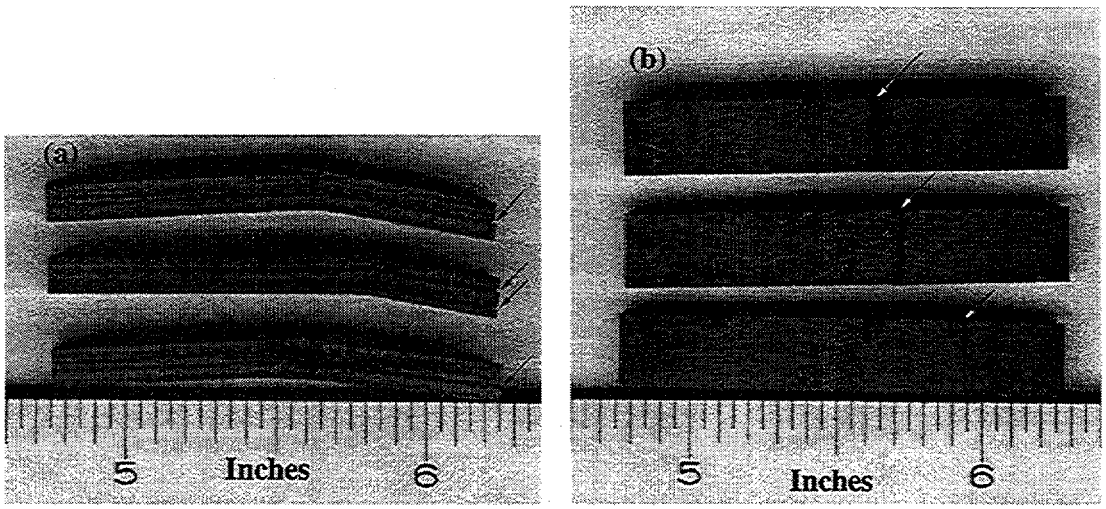

Figure 1. Illustration of invalid SiC/SiC flexure tests. (a) Edge view of bend bars showing delamination from the ends and (b) tensile surface of bend bars showing premature failure due to cutting through aligned woven fibers at the tensile surface.

FUTURE WORK

A size effect analysis for flexure bars (30 x 6 x 2 mm^3) will be carried out on a reference Hi Nicalon SiC/SiC composite scheduled for irradiation as part of the Jupiter P3-4 tests.

REFERENCES

1. G. E. Youngblood, C. H. Henager, Jr., and R. H. Jones, "Specimen Size Effect Considerations for Irradiation Studies of SiC/SiC," Fusion Materials Semiannual Progress Report for Period Ending June 30, 1996. DOE/ER--0313/20.

2. "Standard Test Method for Flexural Properties of Continuous Fiber-Reinforced Advanced Ceramics Composites - ASTM Draft 1.7," 24 February 1996.

3.0 FERRITIC/MARTENSITIC STEELS

RADIATION HARDENING AND DEFORMATION BEHAVIOR OF IRRADIATED FERRITIC-MARTENSITIC STEELS — J. P. Robertson, R. L. Klueh (Oak Ridge National Laboratory), K. Shiba (Japan Atomic Energy Research Institute), and A. F. Rowcliffe (ORNL)

OBJECTIVES

The objectives of this work are to present recently generated tensile data and to review the existing database for ferritic/martensitic steels.

SUMMARY

Tensile data from several 8-12% Cr alloys irradiated in the High Flux Isotope Reactor (HFIR) to doses up to 34 dpa at temperatures ranging from 90 to 600°C are discussed in this paper. One of the critical questions surrounding the use of ferritic-martensitic steels in a fusion environment concerns the loss of uniform elongation after irradiation at low temperatures. Irradiation and testing at temperatures below 200-300°C results in uniform elongations less than 1% and stress-strain curves in which plastic instability immediately follows yielding, implying dislocation channeling and flow localization. Reductions in area and total elongations, however, remain high.

PROGRESS AND STATUS

Introduction

There are four basic goals to this work: (1)present Sandvik HT-9 (12Cr-1MoVW), F82H (8Cr-2WVTa), and modified 9Cr-1Mo (9Cr-1MoVNb) tensile data generated as part of the Collaboration on Fusion Materials between the United States Department of Energy (U.S. DOE) and the Japan Atomic Energy Research Institute (JAERI); (2) review the existing data for these and other ferritic-martensitic steels and to compare the U.S. DOE/JAERI (U.S./J) data with the existing database; (3) develop an understanding of the general dose-temperature regimes where these materials undergo irradiation hardening and loss of uniform elongation; 4) investigate the dose dependencies at various low temperatures. This report summarizes the progress in this effort to date.

Experimental Procedures

The alloy compositions and heat numbers of the ferritic/martensitic steels in the U.S. DOE/JAERI program are given in Table 1. Type SS-3 flat tensile specimens with gage sections 7.6 mm long by 0.76 mm thick were irradiated in either target or removable beryllium (RB) positions in the High Flux Isotope Reactor (HFIR) at ORNL. The irradiation doses ranged from 3 to 31 dpa and the temperatures ranged from 90 to 600°C (see Table 2). Uncertainty limits for the irradiation temperatures are also shown in Table 2. After irradiation, the specimens were tensile tested at the irradiation temperature, in vacuum, at strain rates of 5.6×10^{-4} - 1.1×10^{-3}/s. Comparisons of yield strength data taken from twin specimens from this and other experiments, combined with practical limitations of the testing system, reveal uncertainty limits on yield strength measurements of about ±20 MPa.

Results and Discussions

Representative F82H tensile curves from the U.S. DOE/JAERI program (200-600°C, 3-34 dpa) are shown in Figure 1. For irradiation temperatures less than or equal to 300°C, F82H irradiation hardens and undergoes a severe loss of uniform elongation (E_u) and strain hardening capacity. The maximum increase in yield strength (YS) due to irradiation under these conditions is less than 100%. The E_u is less than 3% for all doses and temperatures in this matrix (200-600°C, 3-34 dpa); the E_u for the same F82H material in the unirradiated condition is less than 5% in this temperature range (200-600°C). Higher dose irradiations at both 400 and 500°C result in slightly higher YS,

Table 1. Alloy Compositions in U.S. DOE/JAERI Program.

	Composition wt. %													
	Fe	Ni	Cr	Mo	Mn	Si	C	N	V	W	Ta	Nb	P	S
F82H (150 kg heat)	Bal	0.05	7.65	---	0.49	0.09	0.093	0.002	0.18	1.98	0.038	---	0.001	0.001
F82H (Heat No. 8091)	Bal	0.01	7.65	tr.	0.49	0.09	0.093	0.0019	0.18	1.98	0.038	---	0.005	0.001
9Cr-1MoVNb (Heat No. C9820)	Bal	0.11	8.62	0.98	0.36	0.08	0.090	0.050	0.209	0.01	---	0.063	0.008	0.004
HT-9 (Heat No.9607-R2)	Bal	0.51	12.1	1.04	0.57	0.17	0.20	0.027	0.28	0.45	---	---	0.016	0.003
HT-9 (Heat No.C9817)	Bal	0.43	11.99	0.93	0.50	0.18	0.21	0.02	0.27	0.54	---	0.018	0.011	0.004

Table 2. U.S. DOE/JAERI Program HFIR Irradiation Conditions.

Capsule	Position	Fast Flux (E>0.1 MeV) $\times 10^{21}$n/cm^2	Thermal Flux (E<0.5 eV) $\times 10^{21}$n/cm^2	Neutron dose, dpa	Temp. ℃	Alloy	Heat Number	Heat Treatment
JP13	target	21	31	15.3	400±30	F82H	150 kg Heat	1040°C/0.5hr/AC+740°C/1.5hr/AC
JP14	target	42	71	31	400±30 500±30	F82H	150 kg Heat	1040°C/0.5hr/AC+740°C/1.5hr/AC
JP17	target	3.7	4.8	2.7	275±25	HT-9	9607R2	1050°C/1hr/AC+780°C/2.5hr/AC
						F82H	150 kg Heat	1040°C/0.5hr/AC+740°C/1hr/AC
JP18	target	3.7	6.4	2.7	90±10	HT-9	9607R2	1050°C/1hr/AC+780°C/2.5hr/AC
JP20	target	10	17	7.4	300±30 500±30 600±30	F82H	8091	1040°C/0.67hr/AC+740°C/2hr/AC
JP22	target	42	71	31	300±30 400±30 500±30 600±30	HT-9 9Cr-1MoVNb	C9817 C9820	1050°C/1hr/AC+780°C/2.5hr/AC 1050°C/0.5hr/AC+700°C/5hr/AC
200J-1	RB 4.2 mm Hf shield	19	3.5	11.4	200±25	F82H	8091	1040°C/0.67hr/AC+740°C/2hr/AC
						HT-9	C9817	1050°C/1hr/AC+780°C/2.5hr/AC
						9Cr-1MoVNb	C9820	1050°C/0.5hr/AC+700°C/5hr/AC
400J-1	RB 4.2 mm Hf shield	19	3.5	11.4	400±25	F82H	8091	1040°C/0.67hr/AC+740°C/2hr/AC
						HT-9	C9817	1050°C/1hr/AC+780°C/2.5hr/AC
						9Cr-1MoVNb	C9820	1050°C/0.5hr/AC+700°C/5hr/AC

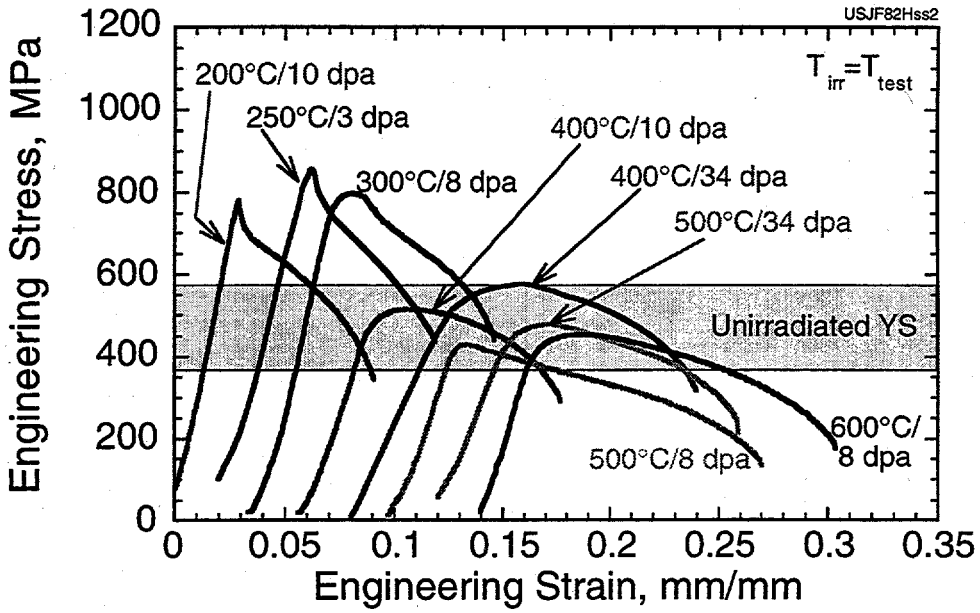

Figure 1. Representative U.S. DOE/JAERI F82H data: 200-600°C, 3-34 dpa.

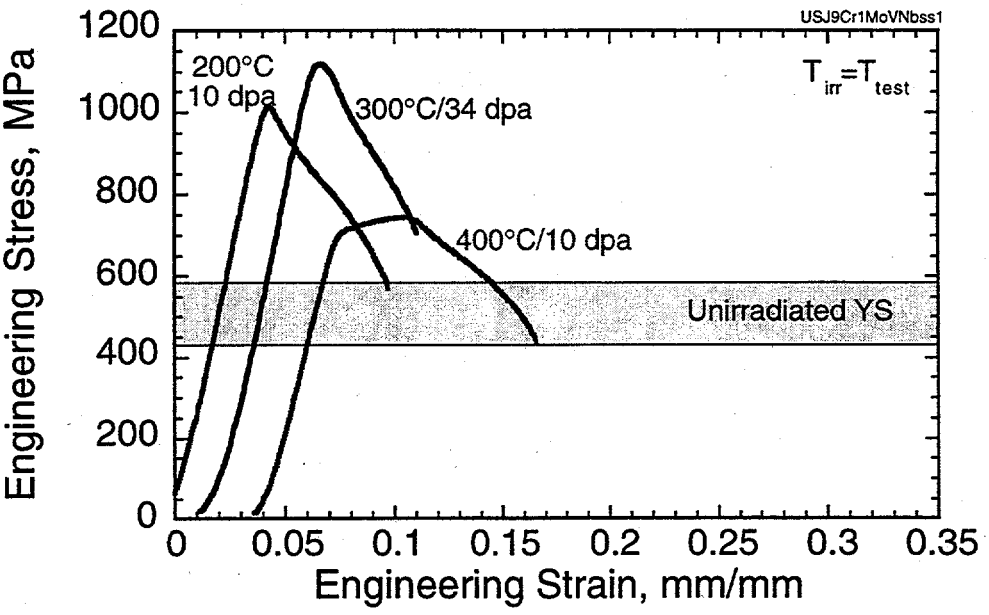

Figure 2. Representative U.S. DOE/JAERI 9Cr-1MoVNb data: 200-400°C, 10-34 dpa.

ultimate tensile strength (UTS), E_u, and total elongation (E_t). The range of unirradiated YS in the temperature range of 200-600°C is shown on the figure.

Representative tensile curves from the 9Cr-1MoVNb alloy tensile tests are given in Figure 2. The 9Cr-1MoVNb irradiation hardens at irradiation temperatures of 200-400°C and undergoes a severe loss of E_u at 200 and 300°C. After irradiation to 10 dpa at 200°C, the 9Cr-1MoVNb has a yield strength about 25% higher than that of F82H. The range of unirradiated YS in the temperature range of 200-400°C is shown on the figure.

Figure 3 shows a set of representative HT-9 tensile curves. Irradiation hardening occurs for all irradiation temperatures in this matrix, 90-400°C, but the increase in YS is less than 100% in each case. The maximum hardening occurs at irradiation temperatures of 200-300°C while the minimum E_u occurs at 90°C. Unlike the F82H alloy, HT-9 retains some strain hardening capacity at irradiation temperatures of 250-400°C. After irradiation to 10 dpa at 200°C, the HT-9 yield strength is almost 40% higher than that for F82H. The range of unirradiated YS in the temperature range of 90-400°C is shown on the figure.

Yield strength data from both the literature [1-25] and the U.S. DOE/JAERI (U.S./J) program are plotted in Figure 4. Examination of the F82H (8Cr) and 9Cr-1MoVNb (9Cr) YS, UTS, E_u, and E_t data as a function of temperature reveals no significant differences between the two alloys and so both the 8 and 9Cr alloys are represented in Fig. 4 by a single symbol after irradiation. (It can be seen in Fig. 4 that the 8-9Cr steel unirradiated tensile data fall in the same band as a function of temperature.) Irradiation increases the yield strength for irradiation temperatures (T_{irr}) less than 400°C, and the radiation hardening is temperature independent up to about 350°C, decreasing sharply in the range 400-450°C. Because of the strong temperature dependence in the range 400-450°C, uncertainties in irradiation temperature result in large differences in irradiated YS in this regime. The U.S. DOE/JAERI F82H data fit in well with the existing data base. The hardening dependence on temperature is clearly visible even with the very large dose range plotted here.

For the 8-9Cr steels, the irradiated E_u is very low (< 1%) for $T_{irr} \leq 300$°C, as shown in Fig. 5. Uniform elongations recover slightly (up to 2-3%) for temperatures above 400°C. Unirradiated 8-9Cr alloys show large scatter in E_t, with no apparent temperature dependence -- E_t values vary from 5 to 30% for T_{irr} from 25 to 700°C. Yield strength is plotted as a function of dose in Fig. 6. For T_{irr} = 500-600°C, there is an initial increase in YS with dose, and then the 8-9Cr steels undergo some softening with increasing dose. For T_{irr} = 430-460°C, there is no significant change in YS with dose up to 94 dpa. For 8-9Cr steels irradiated at temperatures below 300°C, the yield strength approaches saturation at about 5 dpa; the saturation YS value is approximately 1000-1100 MPa.

The HT-9 steel shows moderate irradiation hardening (change in YS less than 100%) for T_{irr} up to and including 400°C (see Fig. 7); hardening then decreases with increasing temperature. The hardening regime extends to higher temperatures (about 50°C higher) compared to the 8-9Cr steels. Radiation hardening is almost independent of temperature up to 400°C and then decreases sharply in the range of 450-500°C. The HT-9 data from the U.S. DOE/JAERI program are consistent with previous data. Unirradiated 8-9Cr and HT-9 yield strengths are the same for T $\leq$ 400°C. For HT-9, the irradiated E_u is very low (<1%) for $T_{irr} \leq 200$°C; it recovers up to 5% at temperatures of 250-400°C (see Fig. 8). The unirradiated E_u of HT-9 is slightly higher than that for F82H and 9Cr-1MoVNb. As observed for the 8-9Cr alloys, the unirradiated HT-9 specimens show large scatter in E_t, with no apparent temperature dependence; E_t values vary from 8 to 25% for T_{irr} from 25 to 600°C. For irradiation temperatures below 365°C, the dose dependence of HT-9 is similar to the 8-9Cr steels.

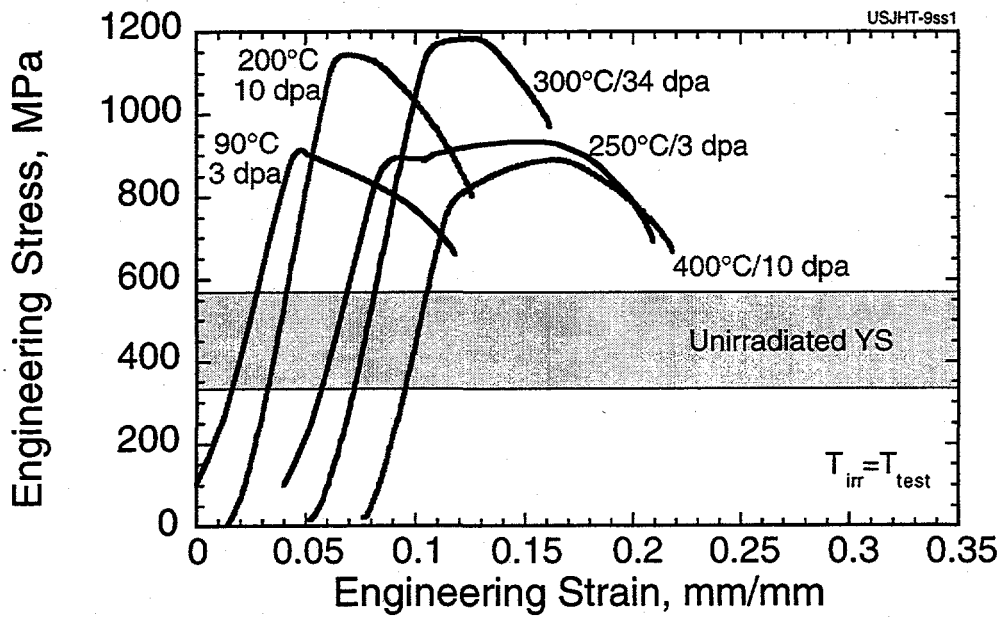

Figure 3. Representative U.S. DOE/JAERI HT-9 data: 90-400°C, 3-34 dpa.

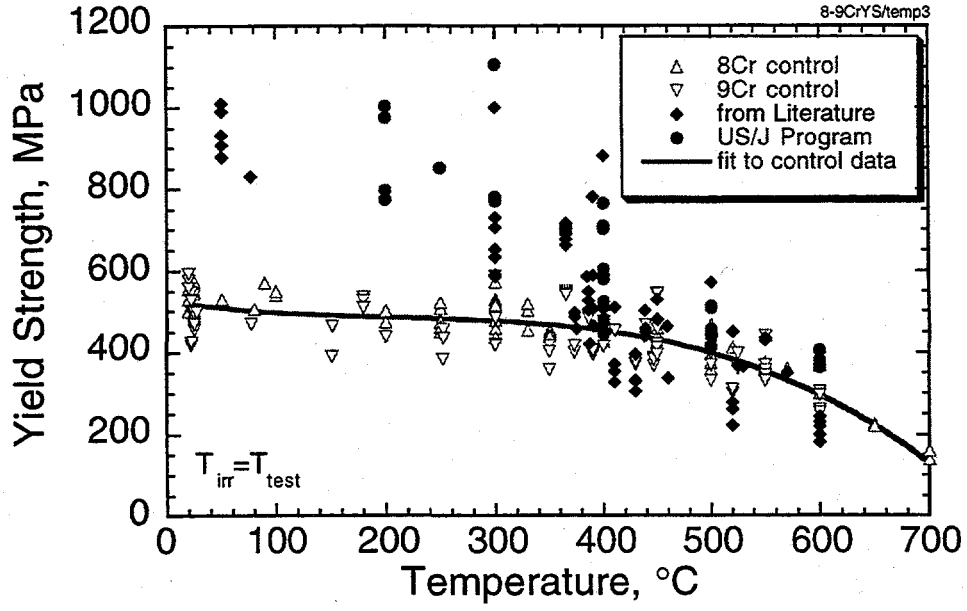

Figure 4. Yield strength as a function of temperature for 8-9Cr steels (0.1-94 dpa) [1-25].

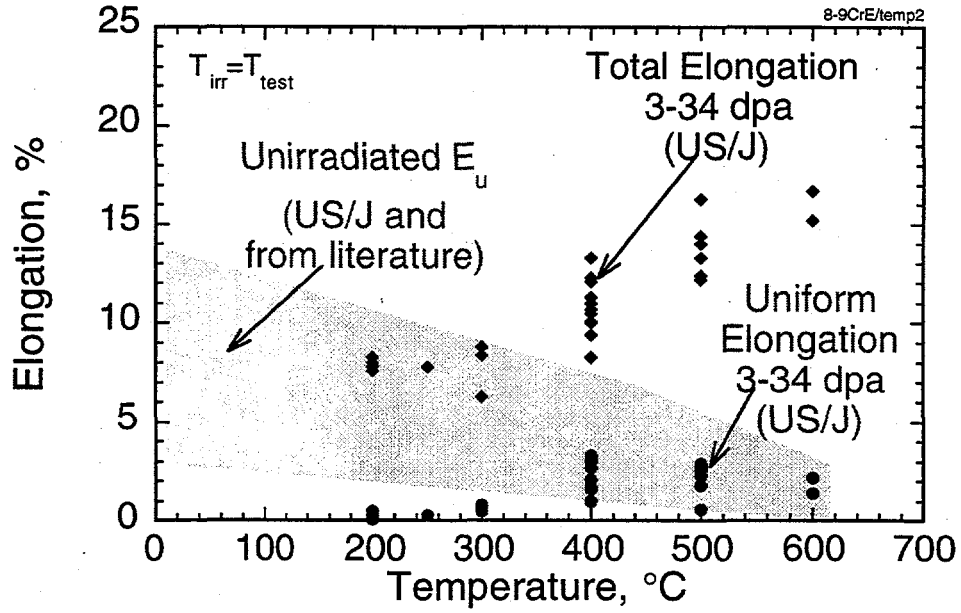

Figure 5. Uniform and total elongation for 8-9Cr steels as a function of temperature [1-26].

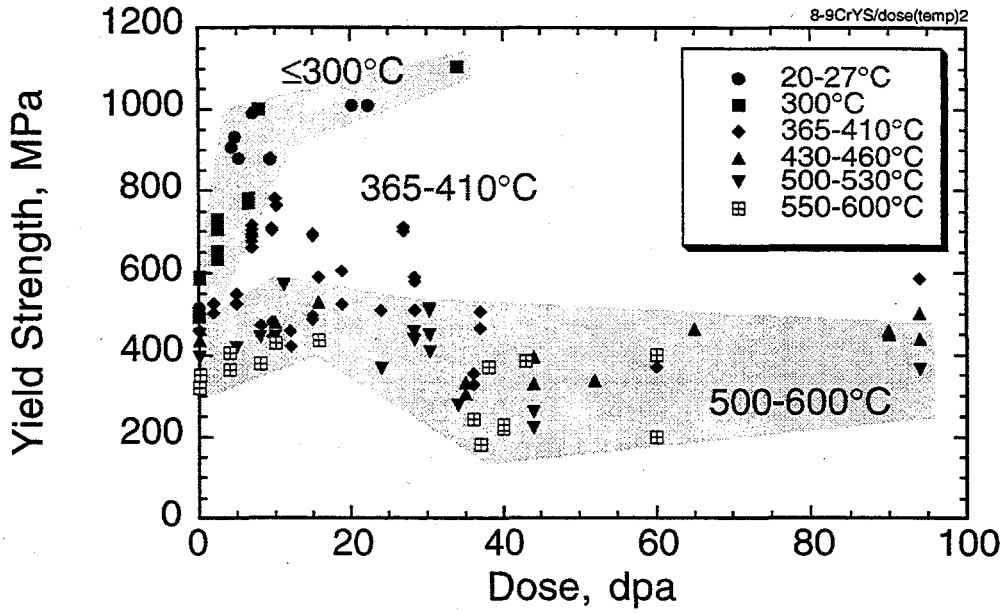

Figure 6. Yield strength as a function of dose and temperature for 8-9Cr steels [1-27].

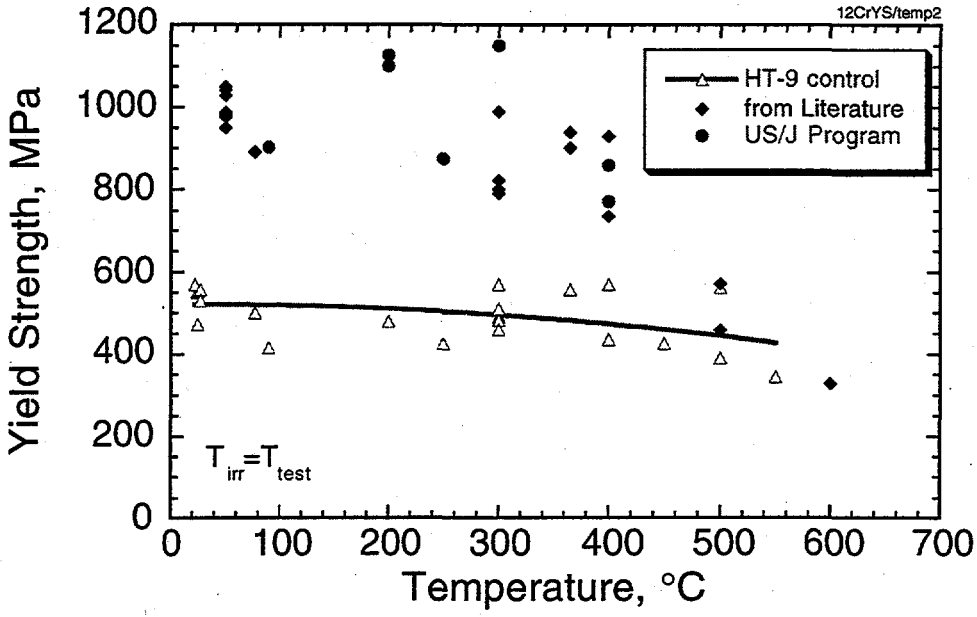

Figure 7. Yield strength as a function of temperature for HT-9 steels [1-27].

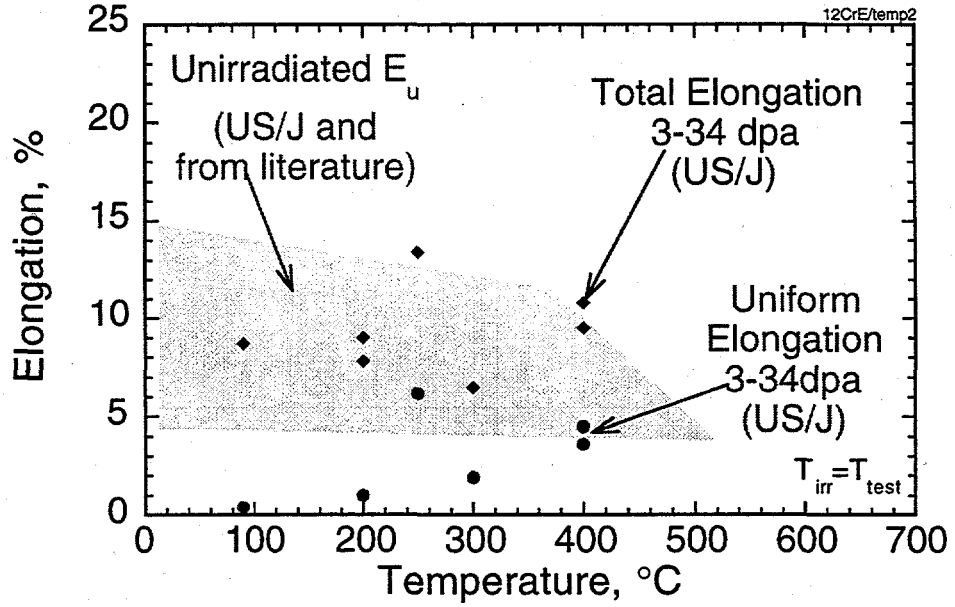

Figure 8. Uniform and total elongation as a function of temperature for HT-9 steels [2, 5, 7, 8, 10, 13, 14, 16, 28].

CONCLUSIONS

The U.S. DOE/JAERI HFIR data for F82H, 9Cr-1MoVNb, and HT-9 fit in well with the existing database; tensile properties for unirradiated 8-9Cr and HT-9 steels fall on the same trend line for $T_{irr} \leq 400°C$. For F82H, irradiation at temperatures less than 400°C results in irradiation hardening and a severe loss of uniform elongation and strain hardening capacity. For T_{irr} = 450-600°C, the irradiated YS are the same as for the unirradiated materials. Radiation hardening is temperature independent up to about 350°C, then decreases sharply at 400-450°C. Because of the strong temperature dependence in the range 400-450°C, uncertainties in irradiation temperature result in large uncertainties in irradiated mechanical properties. For HT-9, irradiation at temperatures less than or equal to 400°C results in irradiation hardening. The hardening regime extends to higher temperatures (about 50°C higher) compared to the 8-9Cr steels. Radiation hardening is almost independent of temperature up to 400°C, then decreases sharply at 450-500°C. The HT-9 retains some strain hardening capacity for T_{irr} = 250-400°C. For 8-9Cr steels irradiated at temperatures below 300°C, the yield strength approaches saturation at about 5 dpa; saturation YS ≈ 1000-1100 MPa. For irradiation temperatures below 365°C, the dose dependence of HT-9 is similar to the 8-9Cr steels.

FUTURE WORK

Future work includes the continued development of the ferritic/martensitic steel database by widening the literature search and testing additional specimens from the U.S./JAERI matrix.

REFERENCES

1. A. Alamo, J. L. Seran, O. Rabouille, J. C. Brachet, A. Maillard, H. Touron, and J. Royer, Effects of Radiation on Materials: 17th International Symposium, ASTM STP 1270, D. S. Gelles, R. K. Nanstad, A. S. Kumar, and E. A. Little, Eds., American Society for Testing and Materials, 1996, p. 761.
2. M. G. Horsten, Proceedings of the IEA Working Group Meeting on Ferritic/Martensitic Steels, Culham, United Kingdom, October 1996, ORNL/M-5674.
3. I. Ioka et al, unpublished data.
4. A. Kimura, T. Morimura, M. Narui, and H. Matsui, J. Nucl. Mater. 233-237 (1996) 319.
5. R. L. Klueh and P. J. Maziasz, J. Nucl. Mater. 187 (1992) 43.
6. R. L. Klueh and J. M. Vitek, J. Nucl. Mater. 132 (1985) 27.
7. R. L. Klueh and J. M. Vitek, J. Nucl. Mater. 150 (1987) 272.
8. R. L. Klueh and J. M. Vitek, J. Nucl. Mater. 161 (1989) 13.
9. R. L. Klueh, P. J. Maziasz and J. M. Vitek, J. Nucl. Mater. 141-143 (1986) 960.
10. R. L. Klueh et al., unpublished data.
11. R. L. Klueh, J. M. Vitek and M. L. Grossbeck, Effects of Radiation on Materials: 11th International Symposium, ASTM STP 782, H. R. Brager and J. S. Perrin, Eds., American Society for Testing and Materials, 1982, p. 648.
12. R. L. Klueh, Proceedings of the IEA Working Group Meeting on Ferritic/Martensitic Steels, Culham, United Kingdom, October 1996, ORNL/M-5674.
13. R. L. Klueh, J. Nucl. Mater. 179-181 (1991) 728.
14. A. Kohyama and Y. Kohno, Proceedings of the IEA Working Group Meeting on Ferritic/Martensitic Steels, Culham, United Kingdom, October 1996, ORNL/M-5674.
15. R. Lindau, Proceedings of the IEA Working Group Meeting on Ferritic/Martensitic Steels, Culham, United Kingdom, October 1996, ORNL/M-5674.
16. A. F. Rowcliffe, J. P. Robertson, R. L. Klueh, K. Shiba, D. J. Alexander, M. L. Grossbeck, and S. Jitsukawa, presented at the 8th International Conference on Fusion Reactor Materials, Sendai, Japan, October 1997, and to be published in the J. Nucl. Mater.
17. J. L. Seran, A. Alamo, A. Maillard, H. Touron, J. C. Brachet, P. Dubuisson, and O. Rabouille, J. Nucl. Mater. 212-215 (1994) 588.

18. J. L. Seran, et al., Effects of Radiation on Materials: 15th International Symposium, ASTM STP 1125, R. E. Stoller, A. S. Kumar, and D. S. Gelles, Eds., American Society for Testing and Materials, 1992, p. 1209.
19. K. Shiba et al., unpublished data.
20. K. Shiba, Proceedings of the IEA Working Group Meeting on Ferritic/Martensitic Steels, Culham, United Kingdom, October 1996, ORNL/M-5674.
21. K. Shiba, M. Suzuki, and A. Hishinuma, J. Nucl. Mater. 233-237 (1996) 309.
22. K. Shiba, M. Suzuki, A. Hishinuma, and J. E. Pawel, Effects of Radiation on Materials: 17th International Symposium, ASTM STP 1270, D. S. Gelles, R. K. Nanstad, A. S. Kumar, and E. A. Little, Eds., American Society for Testing and Materials, 1996, p. 753.
23. M. Victoria, D. Gavillet, P. Spatig, F. Rezai-Aria, and S. Rossman, J. Nucl. Mater. 233-237 (1996) 326.
24. M. Victoria, E. Batawi, Ch. Briguet, D. Gavillet, P. Marmy, J. Peters, and F. Rezai-Aria, Effects of Radiation on Materials: 17th International Symposium, ASTM STP 1270, D. S. Gelles, R. K. Nanstad, A. S. Kumar, and E. A. Little, Eds., American Society for Testing and Materials, 1996, p. 721.
25. N. Yamanouchi, M. Tamura, H. Hayakawa, A. Hishinuma, and T. Kondo, J. Nucl. Mater. 191-194 (1992) 822.
26. K. Shiba et al., unpublished data.
27. A. Koyama and T. Hasegawa, Proceedings of the IEA Working Group Meeting on Ferritic/Martensitic Steels, Culham, United Kingdom, October 1996, ORNL/M-5674.
28. R. L. Klueh, J. M. Vitek, and M. L Grossbeck, J. Nucl. Mater. 103-104 (1981) 887.

A REASSESSMENT OF THE EFFECTS OF HELIUM ON CHARPY IMPACT PROPERTIES OF FERRITIC/MARTENSITIC STEELS - D. S. Gelles and M. L. Hamilton (Pacific Northwest National Laboratory)* and G. L. Hankin (Loughborough University, England)

To be published in the proceedings of the 8th International Conference on Fusion Reactor Materials held in Sendai, Japan, on October 26-31, 1997, in Journal of Nuclear Materials.

EXTENDED ABSTRACT

To test the effect of helium on Charpy impact properties of ferritic/martensitic steels, two approaches are reviewed: quantification of results of tests performed on specimens irradiated in reactors with very different neutron spectra, and isotopic tailoring experiments. Data analysis can show that if the differences in reactor response are indeed due to helium effects, then irradiation in a fusion machine at 400°C to 100 dpa and 1000 appm He will result in a ductile to brittle transition temperature shift of over 500°C. However, the response as a function of dose and helium level is unlikely to be simply due to helium based on physical reasoning. Shear punch tests and microstructural examinations also support this conclusion based on irradiated samples of a series of alloys made by adding various isotopes of nickel in order to vary the production of helium during irradiation in HFIR. The addition of nickel at any isotopic balance to the Fe-12Cr base alloy significantly increased the shear yield and maximum strengths of the alloys. However, helium itself, up to 75 appm at over 7 dpa appears to have little effect on the mechanical properties of the alloys. This behavior is instead understood to result from complex precipitation response. The database for effects of helium on embrittlement based on nickel additions is therefore probably misleading and experiments should be redesigned to avoid nickel precipitation.

*Pacific Northwest National Laboratory is operated for the U.S. Department of Energy by Battelle Memorial Institute under Contract DE-AC06-76RLO 1830.

DEVELOPMENT OF OXIDE DISPERSION STRENGTHENED FERRITIC STEELS FOR FUSION - D.K. Mukhopadhyay (Vista Metals, Inc., McKeesport, PA), F.H. Froes (University of Idaho) and D. S. Gelles (Pacific Northwest National Laboratory)*

To be published in the proceedings of the 8th International Conference on Fusion Reactor Materials held in Sendai, Japan, on October 26-31, 1997, in Journal of Nuclear Materials.

EXTENDED ABSTRACT

An oxide dispersion strengthened (ODS) ferritic steel with high temperature strength has been developed in line with low activation criteria for application in fusion power systems. The composition Fe-13.5Cr-2W-0.5Ti-0.25Y_2O_3 was chosen to provide a minimum chromium content to insure fully delta-ferrite stability. High temperature strength has been demonstrated by measuring creep response of the ODS alloy in uniaxial tension at 650 and 900°C in an inert atmosphere chamber. Results of tests at 900°C demonstrate that this alloy has creep properties similar other alloys of similar design and can be considered for use in high temperature fusion power system designs. The alloy selection process, materials production, microstructural evaluation and creep testing are described.

*Pacific Northwest National Laboratory is operated for the U.S. Department of Energy by Battelle Memorial Institute under Contract DE-AC06-76RLO 1830.

MICROSTRUCTUAL EVOLUTION OF HFIR-IRRADIATED LOW ACTIVATION F82H AND F82H-^{10}B STEELS -- E. Wakai (Japan Atomic Energy Research Institute), N. Hashimoto (Oak Ridge National Laboratory), K. Shiba and T. Sawai (JAERI), and J. P. Robertson and R. L. Klueh (Oak Ridge National Laboratory)

OBJECTIVE

The purpose of the present study is to characterize the microstructure of ferritic-martensitic steels following neutron irradiation in the range 200 - 500^{o}C and explore the relationships between mechanical behavior and microstructure.

SUMMARY

Microstructures of reduced-activation F82H (8Cr-2W-0.2V-0.04Ta) and the F82H steels doped with ^{10}B, irradiated at 250 and 300°C to 3 and 57 dpa in the High Flux Isotope Reactor (HFIR), were examined by TEM. In the F82H irradiated at 250°C to 3 dpa, dislocation loops, small unidentified defect clusters with a high number density, and a few MC precipitates were observed in the matrix. The defect microstructure after 300°C irradiation to 57 dpa is dominated by the loops, and the number density of loops was lower than that of the F82H-^{10}B steel. Cavities were observed in the F82H-^{10}B steels, but the swelling value is insignificant. Small particles of M_6C formed on the $M_{23}C_6$ carbides that were present in both steels before the irradiation at 300°C to 57 dpa. A low number density of MC precipitate particles formed in the matrix during irradiation at 300°C to 57 dpa.

PROGRESS AND STATUS

1. Introduction

Ferritic/martensitic steels are candidate materials for the first wall and blanket structure of fusion reactors. In the D-T fusion reaction, the high-energy neutrons produced induce displacement damage and generate gas atoms in the materials from (n, p) and (n, α) reactions. The presence of these gases could lead to degradation of mechanical properties. The effect of helium atoms generated from the (n, α) reaction can be simulated by using a steel doped with ^{10}B or ^{58}Ni and irradiating in a mixed-spectrum fission reactor, such as the High Flux Isotope Reactor (HFIR).

The effect of neutron irradiation on the tensile deformation of alloy F82H has been reported. Shiba et al. [1,2] described the tensile data following irradiation in HFIR at 200 to 600°C for doses in the range 3-34 dpa. A summary of the tensile data for 9-12Cr ferritic-martensitic steels irradiated under a variety of conditions has been presented by Robertson et al. [3]. Rowcliffe et al. [4] have compared the radiation hardening and deformation behavior of the F82H and HT-9 steels irradiated to low doses at 90 and 250°C. The purpose of the present study is to analyze the radiation-induced microstructural changes occurring in F82H irradiated at temperatures from 90 to 500°C and to identify the distribution of helium produced by doping with ^{10}B. The objective of this work is to identify the defects responsible for the large increases in yield stress and the loss of strain-hardening capacity induced by neutron irradiation at < 400°C.

Table 1. Chemical Compositions of the Specimens used in this Study (wt%)

Alloys	Cr	C	N	P	S	Al	Si	V	Mn	Ta	W	Total B	^{10}B
F82H-std	7.44	0.10	0.002	0.001	0.001	0.019	0.14	0.20	0.49	0.04	2.00	-	-
F82H-^{10}B	7.23	0.10	0.002	0.001	0.001	0.021	0.17	0.22	0.50	0.04	2.10	0.0058	0.0058

2. Experimental Procedure

The chemical compositions of the specimens used in this study are given in Table 1. The standard F82H steel and the F82H steel doped with ^{10}B were prepared to examine the effect of helium generation on the microstructures. The specimens were first austenitized at 1040°C for 30 minutes in a vacuum followed by air-cooling. After that the specimens were tempered at 740°C for 2 hours in a vacuum followed by air-cooling.

Standard 3 mm-diameter disks punched from 0.25 mm-thick sheet stock were irradiated in the HFIR target in the capsules of HFIR-MFE-JP12 and -JP17 as part of the JAERI/U.S. collaborative program. The exposure for JP-12 was 64904 MWd at 85 MW reactor power and achieved a peak fluence of 57 dpa. The exposure for theJP-17 was 3702 MWd, or approximately 43.6 days at 85 MW reactor power, and the capsule achieved a peak fluence of 3 dpa. The complete description and details of the design, construction, and installation of capsules JP12 [5-8] and JP17 [9-11] have been reported. The irradiation temperatures and displacement damage were 250°C and 3 dpa for the JP17 capsule and 300°C and 57 dpa for the JP12 capsule. He generation in the F82H-^{10}B steel was about 320 appm He at 57 dpa. Microstructures were examined using a JEM-2000FX transmission electron microscope with a LaB_6 gun operated at 200 kV. Microstructures of unirradiated control specimens were also examined.

3. Results

A summary of the radiation-induced defect clusters formed in the F82H steels is presented in Table 2.

Table 2 Summary of Radiation-Induced Defect Clusters Formed in the F82H Steels.

Alloy	Dislocation Loop (no. density, mean size)	Unidentified clusters (no. density, mean size)	MC (no. density, mean size)	M_6C (size)	Cavity (no. density, mean size, swelling)	Laths (mean size)
F82H unirradiated			$<1 \times 10^{20}$ m^{-3} 14 nm			440 nm
F82H 3 dpa, 250°C	2×10^{22} m^{-3} 8 nm	4×10^{23} m^{-3} 2.9 nm (1-6 nm)	1×10^{20} m^{-3} 13 nm		0 m^{-3} 0 nm 0%	410 nm
F82H 57 dpa, 300°C	4×10^{22} m^{-3} 8 nm		1×10^{21} m^{-3} 10 nm	3-9 nm	0 m^{-3} 0 nm 0%	450 nm
F82H-^{10}B 57 dpa, 300°C	6×10^{22} m^{-3} 11 nm		1×10^{21} m^{-3} 10 nm	3-9 nm	2×10^{21} m^{-3} 2.5 nm 0.002%	440 nm

3.1 Initial microstructure of the F82H steel

The microstructure after normalizing and tempering was a lath martensitic structure in the F82H-std steel as shown in Fig. 1(a). The dislocation line density was about 1×10^{14} m^{-2}. $M_{23}C_6$ carbides were observed in the matrix and grain boundaries, and the number density and mean size were 6×10^{19} m^{-3} and 73 nm, respectively. Only a few MC carbides were observed in the matrix, and the number density and mean size were $<1 \times 10^{20}$ m^{-3} and 14 nm, respectively. The mean width of the lath structure was about 440 nm.

3.2 Standard F82H steel irradiated at 250°C to 3 dpa

Figures 1(b) and 1(c) show microstructures of the F82H steel at a low and high magnification, respectively, after irradiation at 250°C to 3 dpa. Dislocation loops formed on {111} planes with (**a**/2)<111> Burgers vectors, and many loops were arranged along dislocation lines, as seen in Fig. 1(c). The number density and mean size of the loops were 2×10^{22} m^{-3} and 8.0 nm, respectively. A few MC carbides were observed, and the number density and the mean size were 1×10^{20} m^{-3} and 13 nm, respectively. No cavities were found, but some unidentified defect clusters were observed, as shown in Fig. 2. The unidentified clusters cannot be seen in the bright-field image of Fig. 2(a), but they can be observed in Figs. 2(b) and (c) by weak beam dark-field conditions taken with g or 2g under deviations from the Bragg conditions of 5g excitation. The size of the clusters was 1 - 6 nm (mean size = 2.9 nm), and the number density of the clusters was 4×10^{23} m^{-3}. The clusters were very difficult to observe, even in weak beam dark-field conditions excited with a 5g Bragg reflection. The mean width of the lath structure was about 410 nm.

3.3 Standard F82H steel irradiated at 300°C to 57 dpa

Figure 3 gives a microstructure of the F82H-std steel irradiated at 300°C to 57 dpa. Many dislocation loops and $M_{23}C_6$ and MC carbides are seen. The small black contrast seen inside the $M_{23}C_6$ carbides are M_6C precipitates, which formed during irradiation, and an example of a dark-field image of the M_6C precipitates is shown in Fig. 4. The size of the M_6C particles was 3-9 nm. The mean size and number density of dislocation loops were 11 nm and 4×10^{22} m^{-3}, respectively. The loops formed at 300°C and 57 dpa were larger and of higher number density than those at 250°C and 3 dpa. The mean size and number density of MC carbides were 10 nm and 1×10^{21} m^{-3}, respectively. No cavities or unidentified defect clusters were observed. The mean width of the lath structure was about 450 nm.

3.4 Microstructures of the F82H steels doped with ^{10}B

Figure 5 shows an example of dislocation loops and cavities formed in the F82H steel doped with ^{10}B irradiated at 300°C to 57 dpa. Number densities of dislocation loops in the doped specimens were higher than in the standard F82H alloy, and the mean size and number density of loops for the F82H-^{10}B were 10.5 nm and 6×10^{22} m^{-3}, respectively. Cavities were observed in the matrix and on dislocations. The number density, mean size, and swelling of cavities for the F82H-^{10}B steel were 2.5 nm, 2×1021 m^{-3} and 0.002%, respectively. The unidentified defect clusters were not observed. The mean width of the lath structure was about 440 nm.

4. Discussion

4.1 Microstructural development at 250°C

The tensile properties of F82H steel irradiated at 250°C to 3 dpa were published earlier [1]. In spite of the low dose, a large increase in yield strength occurred (Fig. 6). Yielding was followed by severe flow localization and strain softening. These results imply the presence of a high density of defect clusters and/or precipitates which are assimilated or sheared by mobile dislocations, thus giving rise to dislocation channeling. The number density of dislocation loops formed in the F82H steel irradiated at 250°C to 3 dpa was 2×10^{22} m^{-3}. The dislocation loops are perfect types of **b** = (**a**/2)<111> on {111}; <100> loops were not observed. In pure iron [12-13] and iron chromium alloys [14-19], the types of dislocation loops observed are **b** = (**a**/2)<111> on {111} and/or **b** = **a**<100> on {100}. F82H steel is relatively stable during thermal aging at 250°C [20], and essentially no radiation-induced precipitation occurred during the irradiation to 3 dpa at 250°C. The radiation hardening observed at 250°C is therefore primarily associated with the

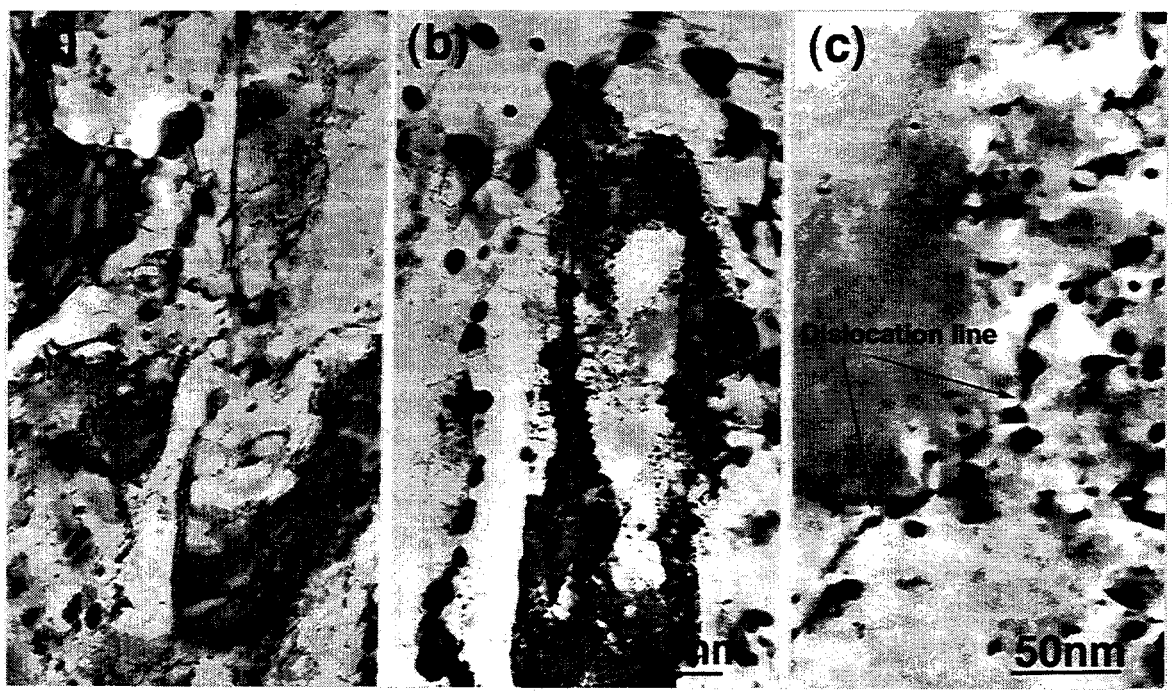

Figure 1. Microstructures of the F82H steel (a) before irradiation, (b), (c) after the 250°C irradiation to 3 dpa, which are at a lower (b)and higher magnification (c), respectively.

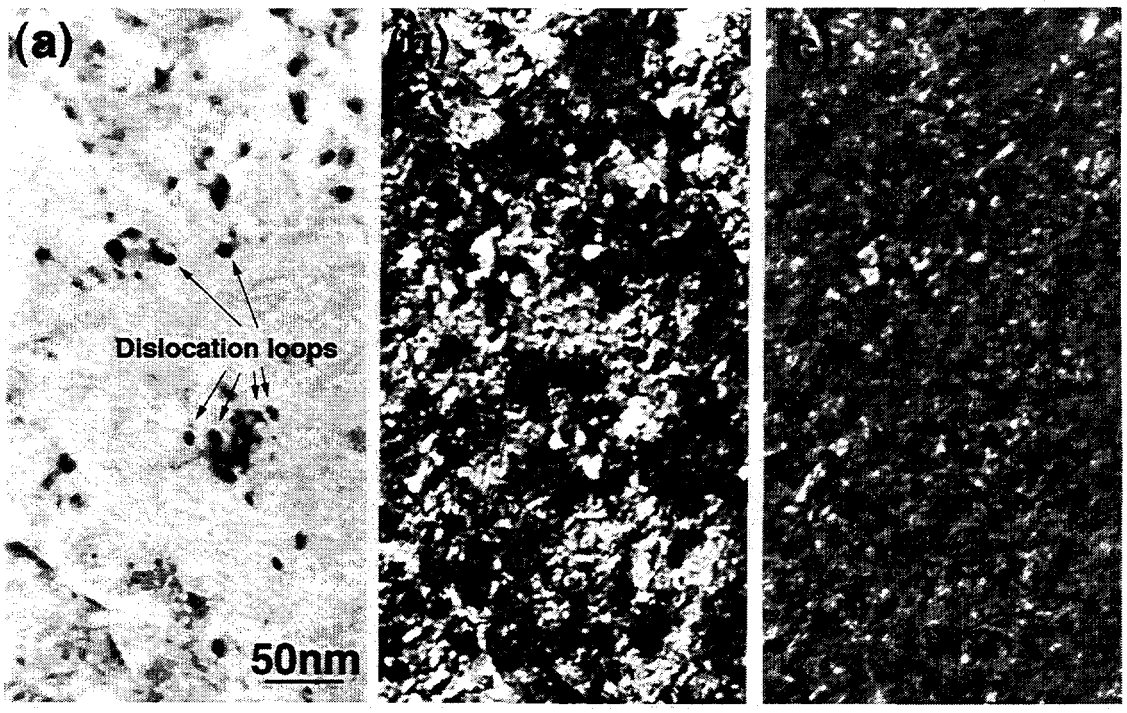

Figure 2. Unidentified defect clusters of the irradiated F82H-std, which are taken by (a) bright-field image, (b) dark-field images of g, and (c) 2g conditions, under s>>0, g=110 near 001. The size of the defect clusters is 1 - 6 nm.

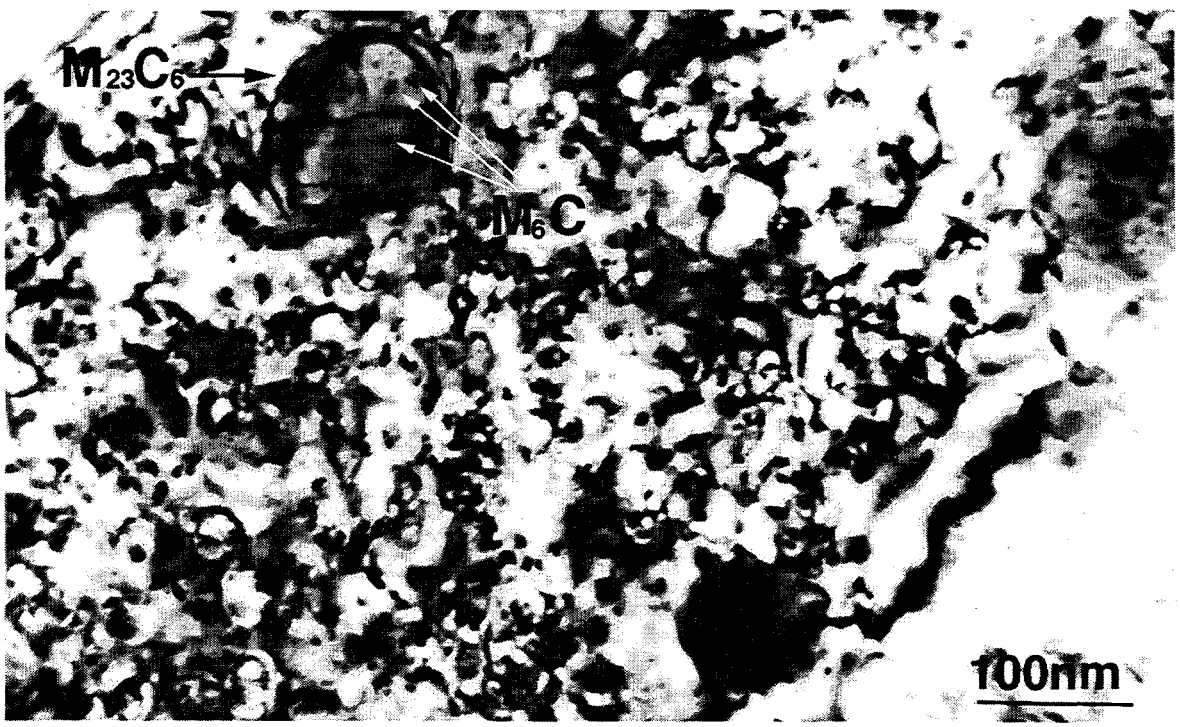

Figure 3. Microstructures in the F82H-std irradiated at 300°C to 57 dpa.

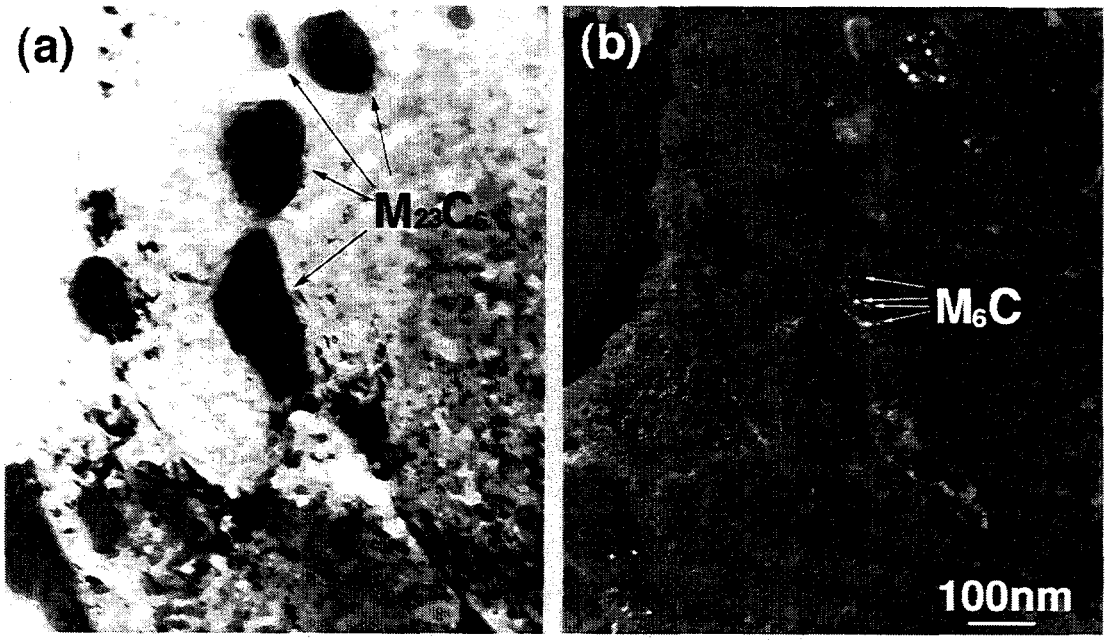

Figure 4. (a) Bright-field image and (b) dark-field image for M_6C precipitates formed on $M_{23}C_6$ carbides in the F82H-std irradiated at 300°C to 57 dpa. The size of M_6C precipitates is 3-9 nm.

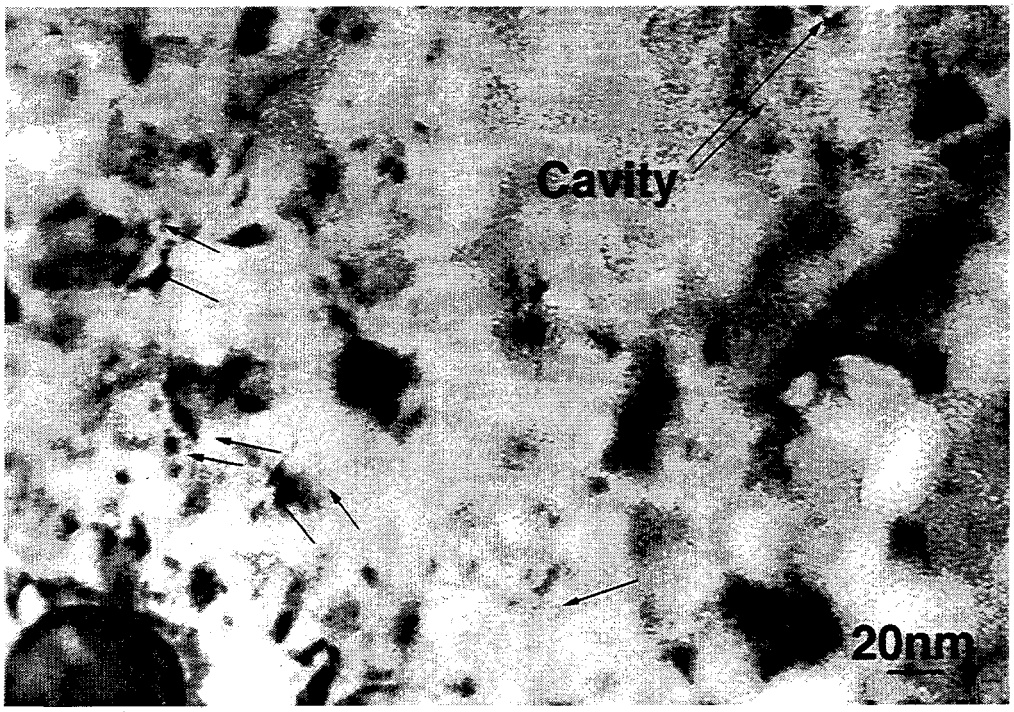

Figure 5. Dislocation loops and cavities formed in the F82H^{10}B steel irradiated at 300°C to 57 dpa.

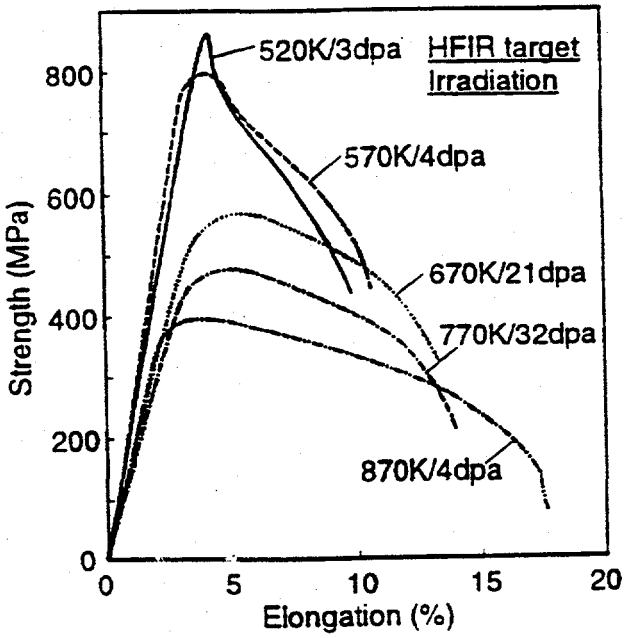

Figure 6. Tensile curves of F82H steel irradiated at temperatures ranging from 250 to 600°C. After ref. [1].

moderate density of <111> loops and the high number density of unidentified small defect clusters.

4.2 Microstructural development at 300°C

The tensile behavior at 300°C following irradiation to 4 dpa is very similar to that observed at 250°C. The yield strength is increased to 800 MPa, and plastic instability occurs after a very limited amount of strain hardening. The defect microstructure after irradiation to 57 dpa was dominated by the loops with a number density of 4×10^{22} m^{-3}. Interestingly, the small unidentified defect clusters which developed at 250°C could not be detected following the 300°C irradiation to 57 dpa.

A small increase in the number of MC carbides was observed in the F82H steel irradiated up to 57 dpa, but the main change was the M_6C precipitate formation on $M_{23}C_6$ carbides. Thermal aging experiments for the F82H steel showed that no formation of M_6C and MC precipitates was observed below 400°C [20]. In previous irradiation experiments of the F82H steel at temperatures above 420°C to 60 dpa in JMTR, large M_6C precipitates formed in matrix [21]. The formation of M_6C precipitates in the matrix was also observed in 9Cr-1MoVNb and 9Cr-1MoVNb-2Ni steels irradiated at 400°C to 37 dpa in the HFIR, but no formation of M_6C precipitates was observed in the alloys irradiated at 300°C [22, 23]. In those studies, no change of $M_{23}C_6$ phase during the irradiation was observed at <500°C [22, 23]. It was mentioned that the M_6C phase was Cr-rich and that Cr supersaturation or segregation during irradiation might play a role for the phase transformation [22, 23]. In another report on several ferritic-martensitic steels (HT9, FV448, and 1.4914), M_6C carbides formed along dislocation lines during irradiation at 460°C to 50 dpa [24]. In the present experiments, M_6C precipitates formed even at 300°C, and the precipitates were not in the matrix, but instead formed on the $M_{23}C_6$ carbides. Judging from these results, M_6C precipitates are likely to form at elevated irradiation temperatures, and the M_6C may be somewhat easier to form in the F82H than in the 9Cr-1MoVNb and the 9Cr-1MoVNb-2Ni steels. The formation mechanism of M_6C precipitates on the $M_{23}C_6$ carbides is not clear, and it may be related to radiation-induced segregation of solute atoms at the surface of $M_{23}C_6$ carbides. Further detailed examination will be necessary to understand it.

4.3 Microstructure of irradiated F82H-^{10}B

The F82H-^{10}B steel has a higher number density of cavities and dislocation loops than those of the standard F82H steel. Because of the preferential helium-vacancy association, vacancy-interstitial recombination is inhibited relative to that in a steel with little or no helium, and interstitial cluster formation is enhanced.

5. Conclusions

Reduced-activation F82H (8Cr-2W-0.2V-0.04Ta) and the F82H steels doped with ^{10}B were irradiated at 250 and 300°C to 3 and 57 dpa in the HFIR. The microstructures were examined by transmission electron microscopy to explore the relationships between mechanical behavior and microstructure. The results can be summarized as follows:

(1) The radiation hardening at 250°C is primarily associated with the moderate density (2×10^{22} m^{-3}) of <111> loops and the high number density (4×10^{23} m^{-3}) of unidentified small defect clusters.(2) The defect microstructure after irradiation to 57 dpa at 300°C is dominated by the loops with a number density of 4×10^{22} m^{-3}. Interestingly, the small unidentified defect clusters which developed at 250°C could not be detected following the 300°C irradiation to 57 dpa.
(3) The formation of M_6C precipitates on $M_{23}C_6$ carbides was observed at 300°C to 57 dpa.

(4) Helium formed from the ^{10}B during irradiation caused an increase in the number of cavities and dislocation loops that formed.

ACKNOWLEDGMENTS

The authors would like to thank Dr. S. J. Zinkle of Oak Ridge National Laboratory for fruitful discussions. The are grateful to Messrs. L. T. Gibson, A. T. Fisher, and J. J. Duff, and members of the hot laboratory of ORNL for technical support.

REFERENCES

1. K. Shiba, I. Ioka, J. P. Robertson, M. Suzuki, and A. Hishinuma, Euromat-**96**(1996), p.265.
2. K. Shiba, unpublished data.
3. J. P. Robertson, R. L. Klueh, K. Shiba, and A. Hishinuma, J. Nucl. Mater., (to be published).
4. A. F. Rowcliffe, J. P. Robertson, K. Shiba, D. J. Alexander, S. Jitsukawa, J. Nucl. Mater., (to be published).
5. R. L. Senn, Fusion Reactor Materials Semiannual Progress Report for Period Ending September 30, 1988, Office of Fusion Energy, DOE/ER-0313/3, p.8.
6. R. L. Senn, Fusion Reactor Materials Semiannual Progress Report for Period Ending March 31, 1988, Office of Fusion Energy, DOE/ER-0313/4, p.7.
7. R. L. Senn, Fusion Reactor Materials Semiannual Progress Report for Period Ending September 30, 1989, Office of Fusion Energy, DOE/ER-0313/5, p.6.
8. J. E. Pawel, K. E. Lenox, A. W. Longest, R. L. Senn, and K. Shiba, Fusion Reactor Materials Semiannual Progress Report for Period Ending September 30, 1994, Office of Fusion Energy, DOE/ER-0313/17, p.3.
9. A. W. Longest, D. W. Heatherly, K. R. Thoms, and J. E. Corum, Fusion Reactor Materials Semiannual Progress Report for Period Ending March 31, 1991, Office of Fusion Energy, DOE/ER-0313/10, p.3.
10. A. W. Longest, D. W. Heatherly, J. E. Wolfe, K. R. Thoms, and J. E. Corum, Fusion Reactor Materials Semiannual Progress Report for Period Ending September 30, 1991, Office of Fusion Energy, DOE/ER-0313/11, p.30.
11. A. W. Longest, D. W. Heatherly, K. R. Thoms, and J. E. Corum, Fusion Reactor Materials Semiannual Progress Report for Period Ending March 31, 1992, Office of Fusion Energy, DOE/ER-0313/12, p.24.
12. A. E. Ward and S. B. Fisher, J. Nucl. Mater., **166**(1989), p.227.
13. E. A. Little, Rad. Effect, **16**(1972), p.135.
14. E. Wakai, A. Hishinuma, Y. Kato, S. Takaki, and K. Abiko, Proc. Ultra High Purity Base Metals, Eds. K. Abiko, K. Hirokawa, and S. Takaki, The Japan Institute of Metals Sendai (Japan), (1994), p.522.
15. E. Wakai, A. Hishinuma, T. Sawai, S. Kato, S. Isozaki, S. Takaki, and K. Abiko, Phys. Stat. Sol. (a), **160** (1997), p.441.
16. Y. Katoh, A. Koyama, and D. S. Gelles, J. Nucl. Mater., **225**(1995), p.154.
17. D. S. Gelles, J. Nucl. Mater., **225**(1995), p.163.
18. S. Ohnuki, H. Takahashi, and T. Takeyama, J. Nucl. Mater., **122&123**(1984), p.317.
19. T. Muroga, A. Yamaguchi, and N. Yoshida, Effects of Radiation on Materials: 14th International Symposium, vol. 1, ASTM STP **1046**(1989), p.396.
20. K. Shiba, unpublished data.
21. T. Shibayama, A. Kimura, and H. Kayano, Euromat-**96**(1996), p.533.
22. P. J. Maziasz: J. Nucl. Mater., **169**(1989), p.95.
23. P. J. Maziasz, R. L. Klueh, and J. M. Vitek, J. Nucl. Mater., **141-143** (1986), p.927.
24. P. Dubuisson, D. Gilbon and J. L. Seran, J. Nucl. Mater., **205**(1993), p.178.

EFFECT OF HEAT TREATMENT AND IRRADIATION TEMPERATURE ON IMPACT BEHAVIOR OF IRRADIATED REDUCED-ACTIVATION FERRITIC STEELS—R. L. Klueh and D. J. Alexander (Oak Ridge National Laboratory)

Objective

The goal of this study is to evaluate the impact behavior of irradiated ferritic steels and relate the changes in properties to the heat treatment of the steel.

SUMMARY

Charpy tests were conducted on eight normalized-and-tempered reduced-activation ferritic steels irradiated in two different normalized conditions. Irradiation was conducted in the Fast Flux Test Facility at 393°C to ≈14 dpa on steels with 2.25, 5, 9, and 12% Cr (0.1% C) with varying amounts of W, V, and Ta. The different normalization treatments involved changing the cooling rate after austenitization. The faster cooling rate produced 100% bainite in the 2.25 Cr steels, compared to duplex structures of bainite and polygonal ferrite for the slower cooling rate. For both cooling rates, martensite formed in the 5 and 9% Cr steels, and martensite with ≈25% δ-ferrite formed in the 12% Cr steel. Irradiation caused an increase in the ductile-brittle transition temperature (DBTT) and a decrease in the upper-shelf energy. The difference in microstructure in the low-chromium steels due to the different heat treatments had little effect on properties. For the high-chromium martensitic steels, only the 5Cr steel was affected by heat treatment. When the results at 393°C were compared with previous results at 365°C, all but a 5Cr and a 9Cr steel showed the expected decrease in the shift in DBTT with increasing temperature.

PROGRESS AND STATUS

Introduction

Reduced-activation or fast induced-radioactivity decay (FIRD) steels for fusion power plant applications are being developed at the Oak Ridge National Laboratory (ORNL) [1]. Eight experimental steels have been studied [2-4]. Nominal compositions of the eight ORNL steels are given in Table 1, along with the designation for each.

TABLE 1—Nominal compositions for reduced-activation steels

Alloy	Nominal Chemical Composition[a] (wt %)				
	Cr	W	V	Ta	C
2.25CrV	2.25		0.25		0.1
2.25Cr-1WV	2.25	1.0	0.25		0.1
2.25Cr-2W	2.25	2.0			0.1
2.25Cr-2WV	2.25	2.0	0.25		0.1
5Cr-2WV	5.0	2.0	0.25		0.1
9Cr-2WV	9.0	2.0	0.25		0.1
9Cr-2WVTa	9.0	2.0	0.25	0.12	0.1
12Cr-2WV	12.0	2.0	0.25		0.1

[a] Balance iron.

Information on microstructure [2], tempering and tensile properties [3], and Charpy impact properties [4] of the eight FIRD steels in the normalized-and-tempered condition has been reported. Results were also published on the tensile properties after irradiation to 6-8 and 25-29 dpa and on the Charpy properties after irradiation at 365°C to 6-8, 15-17, 23-24, and 26-29 dpa in the Fast Flux Test Facility (FFTF) [5]. The results showed that the two 9Cr steels, especially the 9Cr-2WVTa,

compared to the other steels. The 2¼Cr-2WV steel was the strongest of the eight steels [3], but it had relatively poor impact properties, as was true for the impact properties of all of the low-chromium (2¼Cr) steels [4].

For ferritic steels, the heat treatment, which determines the microstructure, includes the cooling rate, which is determined by the cooling medium (i.e., air cool, water quench, etc.) and section size. This paper reports on the effect of irradiation on the Charpy properties of the eight ORNL steels after two different heat treatments: one treatment was the same as that used for previous irradiations [5]; in the other the steels were cooled more rapidly during normalization to produce 100% bainite in the 2¼Cr steels. Observations on Charpy properties after irradiation are useful because neutron irradiation causes an increase in the ductile-brittle transition temperature (DBTT) and a decrease in upper-shelf energy (USE). Such changes generally reflect a degradation in fracture toughness. Developing steels with minimal changes in DBTT and USE is crucial if ferritic steels are to be useful structural materials for fusion.

Experimental Procedure

Details on the processing and chemical composition of the eight steels have been published [2]. The steels were normalized and tempered prior to irradiation. The 2¼Cr-2W steel without vanadium was austenitized at 900°C. The other seven heats contained vanadium and were austenitized at 1050°C; the higher normalizing temperature assured that any vanadium carbide dissolved during austenitization. To determine heat treatment (microstructural) effects, especially for the low-chromium steels, two different geometries were normalized. First, 15.9-mm-thick plates were austenitized 1h and then air cooled. This is the same heat treatment (termed HT1) used in the previous studies [2-6]. In the second heat treatment (HT2), 3.3-mm-square bars (the miniature Charpy specimens) were austenitized 0.5 h in a tube furnace in a helium atmosphere and then pulled into the cold zone of the furnace and cooled in flowing helium. For both HT1 and HT2, the 2¼CrV, 2¼Cr-1WV, and 2¼Cr-2W steel specimens were tempered 1 h at 700°C and the other five heats 1 h at 750°C.

One-third size Charpy specimens were machined from normalized-and-tempered 15.9-mm plates. along the rolling direction with the notch transverse to the rolling direction (L-T orientation). Details on the test procedure for the subsize Charpy specimens have been published [7].

Six Charpy specimens of each heat and each heat treated condition were irradiated in the Materials Open Test Assembly of FFTF at ≈393°C. Specimens were irradiated to ≈2.3×10^{26} n/m^2 (E>0.1 MeV), which produced ≈14 dpa. Helium concentrations were calculated to be less than 1 appm.

Results

Microstructures

Microstructures of the normalized-and-tempered 15.9-mm plates (HT1) were examined [2]. Of the low-chromium steels, all but the 2¼Cr-2W contained a duplex structure of tempered bainite and polygonal ferrite: 2¼CrV contained ≈30% tempered bainite, 70% ferrite; 2¼Cr-1WV contained ≈55% tempered bainite, 45% ferrite; and 2¼Cr-2WV was ≈80% tempered bainite, 20% ferrite. The 2¼Cr-2W steel was 100% tempered bainite. When the 3.3-mm bars were heat treated, the microstructures for all four 2¼Cr steels were 100% bainite.

Microstructures were the same for the high-chromium steels when heat treated in either geometry: the 5Cr-2WV, 9Cr-2WV, and 9Cr-2WVTa steels were 100% tempered martensite, and the 12Cr-2WV steel was tempered martensite with ≈25% δ-ferrite.

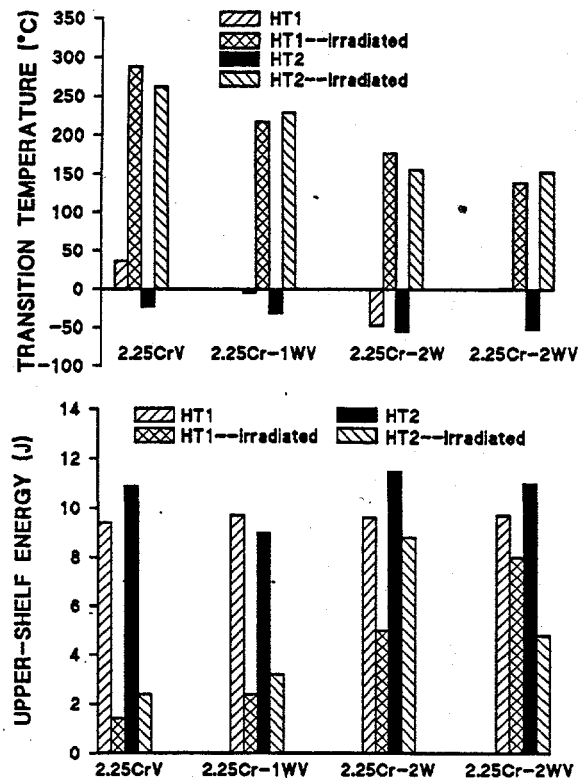

Fig. 1. Transition temperature and upper-shelf energy for low-chromium steels given two different heat treatments (HT1 and HT2) before and after irradiation.

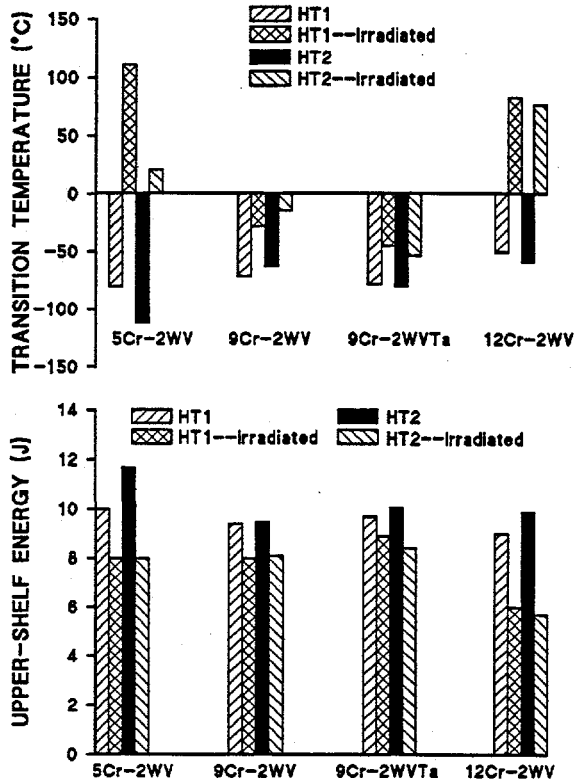

Fig. 2. Transition temperature and upper-shelf energy for high-chromium steels given two different heat treatments (HT1 and HT2) before and after irradiation.

Heat treatment to produce a 100% bainite microstructure (HT2) improved the DBTT of the 2¼Cr steels over those with the duplex structure (HT1) (Table 2 and Fig. 1). However, after irradiation, there was little difference in the DBTT of specimens given the HT1 and HT2 heat treatments and, in some cases, the shift in DBTT (ΔDBTT) was higher after HT2—especially for the 2¼Cr-2WV steel. Likewise, there was no significant difference in the USE after irradiation of the 2¼Cr steels with HT2 than for those with HT1.

Results for the high-chromium steels were somewhat more varied (Table 2 and Fig. 2). For the 5Cr-2WV steel, HT2 caused a significant improvement in the DBTT over that for HT1 (from -70 to -112), which translated into an improved ΔDBTT for the steel given HT2. Heat treatment had relatively little effect on the DBTT of the two 9Cr steels, either before or after irradiation. The DBTT of the 12Cr-2WV steel specimens given HT1 and HT2 heat treatments were quite similar before irradiation and had similar ΔDBTTs after irradiation. Heat treatment also had little effect on the USE of the high-chromium martensitic steels.

Table 2. Charpy impact properties of reduced-activation steels

Steel	Heat	DBTT	ΔDBTT	USE	ΔUSE
2¼CrV	HT1	36		9.4	
	HT1—Irrd	287	251	1.4	-85
	HT2	-24		10.9	
	HT2—Irrd	261	285	2.4	-78
2¼Cr-1WV	HT1	-5		9.7	
	HT1—Irrd	216	221	2.4	-75
	HT2	-32		9.0	
	HT2—Irrd	228	260	3.2	-64
2¼Cr-2W	HT1	-48		9.6	
	HT1—Irrd	176	224	5.0	-48
	HT2	-56		11.5	
	HT2—Irrd	155	211	8.8	-23
2¼ Cr-2WV	HT1	0		9.7	
	HT1—Irrd	138	138	8.0	-18
	HT2	-52		11.0	
	HT2—Irrd	152	204	4.8	-56
5Cr-2WV	HT1	-80		10.0	
	HT1—Irrd	111	191	8.0	-20
	HT2	-112		11.7	
	HT2—Irrd	21	133	8.0	-32
9Cr-2WV	HT1	-71		9.4	
	HT1—Irrd	-28	43	8.0	-15
	HT2	-63		9.5	
	HT2—Irrd	-14	49	8.1	-15
9Cr-2WVTa	HT1	-78		9.7	
	HT1—Irrd	-45	33	8.9	-8
	HT2	-80		10.1	
	HT2—Irrd	-53	27	8.4	-17
12Cr-2WV	HT1	-50		9.0	
	HT1—Irrd	83	133	6.0	-33
	HT2	-59		9.9	
	HT2—Irrd	77	136	5.7	-42

*HT1: normalized and tempered as 15.9-mm plate. HT2: normalized and tempered as 3-mm bar. Irrd: irradiated to ≈15 dpa.

Discussion

This irradiation experiment had two objectives: 1) determine whether the microstructure of the 2¼Cr steels could be changed by heat treatment to favorably affect the Charpy impact properties after irradiation and 2) irradiate the reduced-activation steels in FFTF at a temperature other than 365°C, the temperature of previous irradiations [6]. The different heat treatments were not expected to cause significant changes in the microstructures of the 5-12% Cr steels, since the high hardenability of these steels would be expected to give them the same microstructure for both heat treatments. Specimens irradiated at 393°C in this experiment were expected to have a smaller ΔDBTT than those irradiated at 365°C [6], since the shift is due to irradiation hardening and irradiation hardening decreases with increasing irradiation temperature.

The relatively high DBTT values for the 2¼CrV, 2¼Cr-1WV, and 2¼Cr-2WV steels from the 15.9-mm plate (HT1) before irradiation were tentatively attributed to the ferrite in the mixed ferrite-bainite structures [5]. Only the 2¼Cr-2W steel had a low DBTT, and it was 100% tempered bainite [5]. Subsequent work indicated that heat treatment affected the unirradiated properties of three of the 2¼Cr steels (see Table 2) [7]. The DBTT of the 3.3-mm bar of 2¼Cr-2W steel was relatively unchanged: -48°C when heat treated as 15.9-mm plate (HT1) and -56°C when heat treated as 3.3-mm bar (HT2). For the other three 2¼Cr steels, the specimens given HT2 had considerably lower DBTT values than those given HT1. Thus, it appeared that the conclusion that high DBTT values were caused by the ferrite in the mixed ferrite-bainite microstructure of the unirradiated steels was correct [7].

As expected, there was little difference in the DBTT for HT1 and HT2 for the 9Cr-2WV, 9Cr-2WVTa, and 12Cr-2WV steels (Table 2). Microstructures were unchanged from 100% martensite for the 9Cr steels and 20-25% δ-ferrite , balance martensite for the 12Cr-2WV steel, regardless of the size of specimen heat treated. Although the microstructure of the 5Cr-2WV steel was 100% martensite and the DBTT of this steel was not expected to change, it showed a decrease for HT2 compared to HT1. The reason for this is unclear.

The previous results for the normalized-and-tempered 2¼Cr steels indicated that if it were possible to either use thinner sections, quench instead of normalizing, or improve the hardenability of the steels, it may be possible to lower the DBTT to make these steels attractive for fusion reactor applications [7]. The results of the present experiment indicate that it is somewhat more complicated than that when the steels are irradiated. Despite the decrease in DBTT caused by HT2 compared the HT1, there was no advantage for HT2 after irradiation.

It was previously shown that the bainite that forms in the 2¼Cr steels is not the same in all four steels [7]. Bainite, which is generally defined as a ferrite matrix containing carbides that forms in the temperature range 250-550°C, was originally thought to have only two morphological variations—upper and lower bainite [9]. Classical upper and lower bainite can be differentiated by the appearance of the carbide particles relative to the axis of the bainitic ferrite plate or needle. Upper bainite forms as a collection of ferrite plates or laths with carbides forming on the boundaries between the plates or laths. Lower bainite consists of ferrite plates or needles with carbides forming within the ferrite plates or needles at about a 60° angle to the axis of the plate or needle [9].

There are important variations on the classical bainites, as first shown by Habraken [10]. He found morphological variants in the bainite transformation products that differed from upper and lower bainite, although these products formed in the bainite transformation temperature regime. These "nonclassical" bainites formed more easily during a continuous cool than during isothermal transformation [10,11], where classical bainites are generally formed.

Habraken and Economopoulos contrasted the morphology of the nonclassical structures formed during continuous cooling with classical bainites obtained during isothermal transformation [11].

Classical upper and lower bainites form when the steel is transformed in different temperature regimes of the bainite transformation temperature region, as defined on an isothermal-transformation (IT) diagram [11]. This means that the bainite transformation region of an IT diagram can be divided into two temperature regimes by a horizontal line, above which upper bainite forms and below which lower bainite forms. For the nonclassical bainites, Habraken and Economopoulos [11] showed that a continuous cooling transformation (CCT) diagram could be divided into three vertical regions. Three different nonclassical bainite microstructures form when cooling rates are such as to pass through these different zones. Two of those microstructures are of interest here.

A steel cooled rapidly enough to pass through the first zone produces a "carbide-free acicular" structure, which consists of side-by-side plates or laths [11]. When cooled somewhat more slowly through the second zone, a carbide-free "massive or granular" structure results, generally referred to as granular bainite [11]. Granular bainite consists of a ferrite matrix with a high dislocation density that contains martensite-austenite (M-A) "islands" [11].

Microstructures in the 15.9-mm plates of the 2¼Cr-2W and 2¼Cr-2WV consisted of carbide-free acicular bainite and granular bainite, respectively [7]. During tempering, large globular carbides form in the M-A islands of the granular bainite, whereas elongated carbides form on lath boundaries of acicular bainite [7]. When the 3-mm bars were normalized, carbide-free acicular bainite also formed in the 2¼Cr-2WV steel [7]. Although no TEM was performed on the 2¼CrV and 2¼Cr-1WV, a similar microstructure is expected for these steels.

The results for the 2¼Cr steels in the present experiment indicate that neither the carbide-free acicular structure obtained by heat treating the 3-mm bars nor the granular bainite previously irradiated provides a microstructure that is resistant to irradiation. The large globular carbides that form in granular bainite can provide crack nucleation sites in the normalized-and-tempered - condition, and these carbides grow during irradiation. Likewise, it appears that the interlath carbides in the acicular bainite can also be quite large and provide crack nucleation sites.

Because the 2¼Cr-2WV steel was the strongest of the eight steels in the unirradiated condition and because it is possible to produce a high density of small precipitates in a low-chromium steel that cannot be produced in the high-chromium steel (considering concentrations similar to those in Table 1), it has been suggested that the low-chromium steels may offer some advantages for fusion [3,7]. Results from the present experiment appear to contradict that suggestion—certainly for the compositions and heat treatments used here.

The acicular structures of the 2¼Cr steels irradiated in the present work contained fairly large intra- and inter-lath M_3C and M_7C_3 carbides formed during tempering [3,7]. These carbides can provide crack nucleation sites for fracture, just as the large globular carbides produced during tempering of the granular bainite can. The solution to a more irradiation-resistant steel might be to cool still more rapidly to minimize carbon segregation during cooling that lead to the large carbides when tempered. Alternatively, a vanadium-containing steel should be produced that develops a fine vanadium-rich MC precipitate without the large amounts of M_3C and M_7C_3 that formed in the 2¼Cr steels used here. The latter might be accomplished by using a lower tempering temperature on the acicular bainite or by developing a steel that does not need to be tempered. An alternative to the rapid cooling is to increase the hardenability. This can be done by changing the chemical composition, and a 3Cr-3WV steel has been developed that shows a significant improvement in the Charpy impact properties in the unirradiated condition [12]. This superiority was present even when tempered at 700°C or in the untempered condition. However, the irradiation resistance of this steel still needs to be determined.

Because of the high hardenability of the high-chromium (5-9% Cr) steels, no effect of cooling rate on Charpy properties was expected, and none was observed for the 9Cr and 12Cr steels (Fig. 2).

An effect was observed, however, for the 5Cr-2WV steel (a DBTT of -80°C for the 15.9-mm plate and -112°C for the 3.3-mm bar). All indications were that there was no major difference in the microstructures of the unirradiated plate and bar for the high-chromium steels. Even the grain sizes were similar, although the plate was austenitized 1 h at 1050°C, while the smaller bar was austenitized 0.5 h at 1050°C.

The major difference in the microstructure of the high-chromium steels in the unirradiated condition is the precipitates. The primary precipitate in the 9Cr and 12Cr steels is $M_{23}C_6$; in the 5Cr steel, it is M_7C_3 [3]. Both steels contain vanadium-rich MC, and the 5Cr steel contains a small amount of $M_{23}C_6$. It may be that some M_7C_3 can precipitate in the 5Cr-2WV steel during the slow cool (in the 15.9-mm plate), which could affect the subsequent precipitate morphology during tempering. This is strictly speculation, since no transmission electron microscopy (TEM) has been performed on the steels heat treated as 3.3-mm bar in the normalized-and-tempered condition, and there has been no TEM on the 5Cr-2WV after irradiation. The only change observed for the 9Cr steels after irradiation to 36 dpa at 420°C was the formation of dislocation loops estimated to be 40-100 nm in diameter at a number density of $3 \times 10^{15}/cm^3$ [13].

When the DBTT values obtained previously after irradiation to ≈16 dpa at 365°C are compared to those observed after ≈14 dpa at 393°C in the present experiment, the DBTTs of the 2¼Cr chromium steels (Fig. 3) and the 12Cr-2WV steel (Fig. 4) were higher (larger ΔDBTT) after irradiation at 365°C than after the irradiation at 393°C. This is expected, since the shift in DBTT

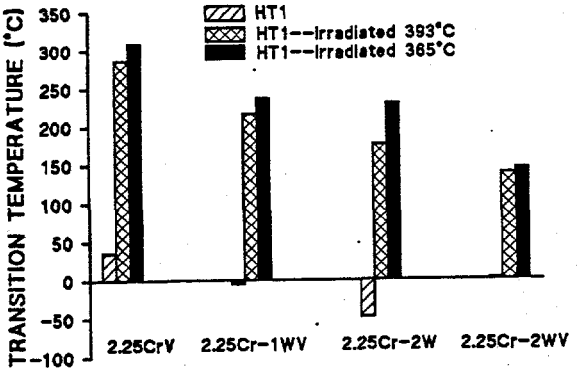

Fig. 5. Transition temperature of the low-chromium steels in HT1 and after irradiation to ≈15 dpa at 365°C and ≈14 dpa at 393°C.

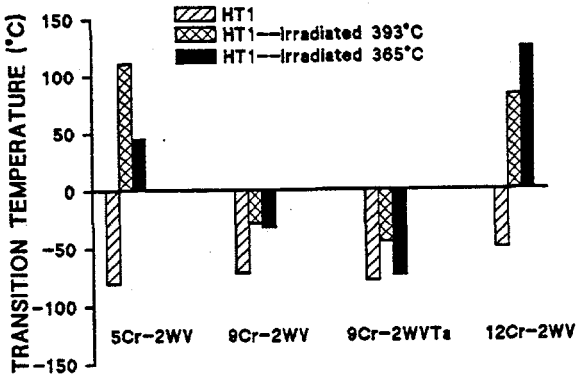

Fig. 6. Transition temperature of the high-chromium steels in HT1 and after irradiation to ≈15 dpa at 365°C and ≈14 dpa at 393°C.

is directly related to irradiation hardening, and irradiation hardening decreases with increasing irradiation temperature. Just the opposite behavior occurred for the 5Cr-2WV and the 9Cr-2WVTa (Fig. 4) with DBTT values of 45°C (16.7 dpa) and 111°C (15 dpa) at 365 and 393°C, respectively, for the 5Cr-2WV steel and -74 °C (15.4 dpa) and -45°C (15 dpa), respectively, for the 9Cr-2WVTa steel. The 9Cr-2WV steel had DBTT values of -32 °C (16.7 dpa) at 365°C and -28°C (15 dpa) at 393°C—a slight increase with increasing temperature (Fig. 4). However, after irradiation at 365°C to 7.7, 23.9, and 27.6 dpa, this steel had DBTT values of 8, -8, and 1°C, respectively, making it appear that the saturation value is higher, around 0°C, and the value at 16.7 dpa is in error. Therefore, it was concluded that the DBTT of the 9Cr-2WV steel at 365°C probably saturates a value somewhat higher than that found after irradiation at 393°C.

As pointed out above, the 5Cr-2WV steel shows a much larger ΔDBTT for HT1 than for HT2 when irradiated at 393°C; it is HT1 that is being compared at the different temperatures. For the two 9Cr

steels, there was little difference for HT1 and HT2, and the difference between the 5Cr-2WV and 9Cr-2WV steels, which only differ in chromium concentration, may be related to the difference in primary precipitates in the 5Cr and 9Cr steel (M_7C_3 in the 5Cr and $M_{23}C_6$ in the 9Cr). The observation of an inverse temperature effect (a larger ΔDBTT at 393°C than 365°C) strengthens the conclusion that precipitates may play a role in the 5Cr-2WV steel. One role of carbide particles during fracture is to act as nucleation sites for the cracks that cause the failure [14,15]. As the size of a brittle precipitate particle increases, so too the size of the initial crack at fracture initiation can increase. Thus a possible reason why the 5Cr steel had a higher DBTT after irradiation at 393°C than at 365°C is that precipitates can grow to a larger size by irradiation-enhanced diffusion at the higher irradiation temperature. It is the larger precipitates that then cause the inverse effect with temperature for this steel. TEM is required to verify this suggestion.

The unexpected results for the 5Cr-2WV steel on the effect of heat treatment and irradiation temperature suggest that the DBTT after irradiation can be improved by decreasing the size of the precipitates. Precipitate size could be decreased by lowering the tempering temperature, and previous work indicated that the 5Cr-2WV steel has excellent Charpy properties even after tempering 1 h at 700°C, as opposed to the 750°C used in the present experiment [5].

The 9Cr-2WVTa steel has the best Charpy properties after irradiation of any of the steels tested here, and in other irradiation experiments it has been shown to have the lowest ΔDBTT for this type of steel ever observed [6,16, 17]. However, it also showed the inverse temperature effect. After 15 dpa at 365°C, the ΔDBTT for HT1 was only 14°C compared to 27°C after 14 dpa at 393°C (Table 2). An inverse temperature effect was noted previously when the steel was irradiated to 0.8 dpa at 250-450°C in the High Flux Reactor (HFR) in Petten, the Netherlands [16]. Figure 5 shows the properties of the 9Cr-2WVTa steel (labeled ORNL) irradiated along with several other reduced-activation steels (F82H, OPTIFER I and OPTIFER II) and conventional Cr-Mo steels (MANET I and II) in the HFR at 250-450°C to 0.8 dpa. The ORNL 9Cr-2WVTa steel had the lowest DBTT below ≈375°C [16]. This superior behavior has now been verified for irradiation to 2.5 dpa in HFR [17]. The inverse temperature effect was displayed by the 9Cr-2WVTa steel in that the DBTT increases above 400°C (Fig. 5), in the temperature regime where hardening is expected to decrease to low values, which should translate to low values of DBTT. Indeed, no such increase was observed for the other steels.

The origin of the superior behavior for the 9Cr-2WVTa has been sought by comparing the behavior of this steel, the 9Cr-2WV steel, which is the same as the 9Cr-2WVTa but without tantalum, and the conventional 9Cr-1MoVNb steel [6]. The 9Cr-2WV and 9Cr-2WVTa steels were irradiated at 365°C in FFTF, with the 9Cr-2WVTa steel showing exceptionally small ΔDBTTs: 4, 14, 21, and 32°C after 6.4, 15.4, 22.5, and 27.6 dpa, respectively (the value after 15.4 dpa is plotted in Fig. 4) [6]. The ΔDBTT for the 9Cr-2WV saturated at ≈60°C, which was reached by ≈8 dpa (the lowest irradiation fluence). This compares with the 9Cr-1MoVNb and irradiated to ≈4 dpa at 365°C in FFTF, which saturated at ≈45°C [6].

When the 9Cr-2WV, 9Cr-2WVTa, and 9Cr-1MoVNb steels with HT1 were compared, it was found that the difference in Charpy properties of these steels before and after irradiation occurred despite there being little difference in the strength of the 9Cr-2WVTa and the other two steels before and after irradiation [6]. Transmission electron microscopy examination of the normalized-and-tempered 9Cr-2WV and 9Cr-2WVTa revealed only minor differences prior to irradiation [3,13]. Likewise, there was no marked difference in microstructure after irradiation, with similar numbers of dislocation loops formed in both steels [13]. Thus, the similarity in strength of these two steels before and after irradiation is not unexpected. However, without any gross differences in the microstructure of the two steels, the only other major difference to account for the difference in Charpy properties is the tantalum in solid solution. Based on the amount of tantalum that appeared to be present in the carbides of the 9Cr-2WVTa steel prior to irradiation, it was estimated that most of the tantalum remained in solid solution [13]. An atom probe analysis of the unirradiated steel

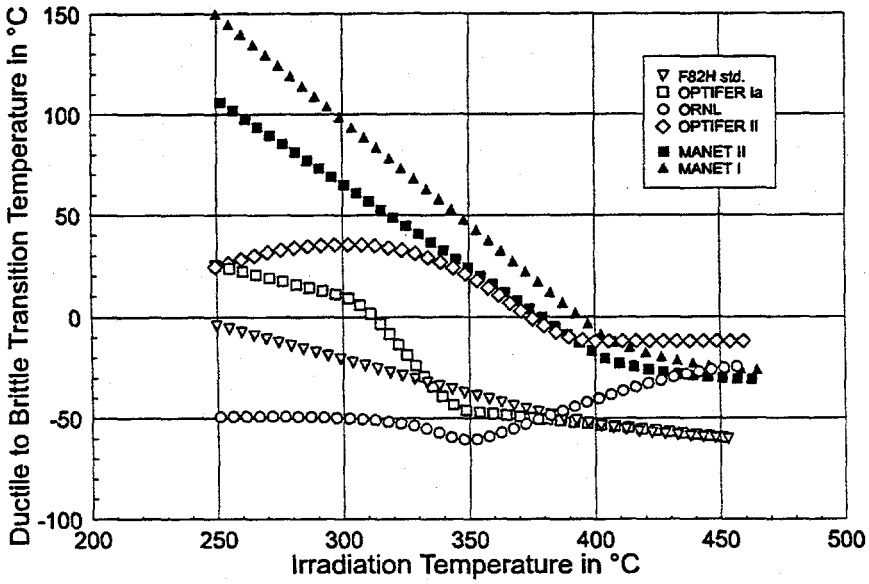

Fig. 5. Transition temperature as a function of temperature for four reduced-activation and two conventional martensitic steels irradiated to 0.8 dpa in the HFR. Taken from Rieth et al. [16].

9Cr-2WVTa steel indicated that >90% of the tantalum was in solution in the normalized-and-tempered condition [18].

Tantalum in solution in the 9Cr-2WVTa can probably account for the smaller prior-austenite grain size in that steel than in the 9Cr-2WV [6]. A smaller lath (subgrain) size might also be expected but was not observed in two studies [3,13], although a smaller lath size was observed in a third examination [18]. The smaller prior-austenite grain size was originally used to explain the difference between the 9Cr-2WV and 9Cr-2WVTa steels [19], since a smaller grain size can lead to a lower DBTT in the normalized-and-tempered condition. However, this explanation was subsequently questioned, because in the normalized-and-tempered condition, the two steels had similar yield stresses, and they also had a yield stress similar to that of the 9Cr-1MoVNb, which had the smallest grain size of the three steels [6]. After saturation, the ΔDBTT of the 9Cr-2WV and 9Cr-1MoVNb were similar, but above the value for the 9Cr-2WVTa [6]. This occurred despite there being only minor differences in the microstructural changes that occurred in the 9Cr-2WVTa and 9Cr-1MoVNb during irradiation, while the microstructural changes in the 9Cr-2WV and 9Cr-2WVTa were similar [13].

These observations led to the conclusion that microstructure (grain size, precipitate type, etc.) does not provide the sole explanation for the observations on mechanical property changes. It appears that tantalum in solution must cause a higher fracture stress for 9Cr-2WVTa than 9Cr-2WV, and the combination of tungsten and tantalum in the 9Cr-2WVTa leads to a higher fracture stress than produced by the combination of molybdenum and niobium in 9Cr-1MoVNb steel [6].

There has been work to determine how alloying elements affect the DBTT, for example, why nickel and platinum decrease the transition temperature of iron alloys and silicon increases it [20,21]. The DBTT can be changed by either decreasing the flow stress or increasing the fracture stress. Since there is little difference in the strength of the steel with and without tantalum, it has been suggested that tantalum increases the fracture stress [19].

To understand the fracture process, Griffith [22,23] considered the balance between the energy released by elastic relaxation and that required for the creation of new surface area during growth of a crack in a brittle material; for a through crack, he found that

$$\sigma_f = \left(\frac{2E\gamma_s}{\pi a(1-\upsilon^2)} \right)^{1/2}, \qquad (1)$$

where σ_f is the stress at fracture, E is Young's modulus, γ_s is the true surface energy, v is Poisson's ratio, and a is the crack half-length. Orowon [24] and Irwin [25] suggested that the true surface energy should be replaced by an effective surface energy, γ_e, which would include the plastic work done during fracture. For an embedded penny-shaped crack, as would result from initiation at a carbide particle or at an inclusion, or from a crack forming within an entire grain or other microstructural unit, this equation becomes [26]

$$\sigma_f = \left(\frac{4E\gamma_p}{D(1-\nu^2)} \right)^{1/2}, \qquad (2)$$

where D is the crack diameter. An additional factor can be included to account for elliptically shaped particles [27].

For a ferritic steel with spherical carbide particles, the diameter of the carbide particle can be used for the crack diameter, D. This could not be used to account for the observations on 9Cr-2WVTa, however, since there appears to be no difference in the amount or morphology of the precipitates in the 9Cr-2WV and 9Cr-2WVTa [3,13].

In the case of a bainitic or martensitic steel, the packet or lath size can be used as the crack size. As stated above, one study found a difference in the lath size of the normalized-and-tempered 9Cr-2WV and 9Cr-2WVTa steels [18], two other studies found no difference [3,13]. More importantly, no difference was observed after irradiation to 36 dpa at 420°C in FFTF [13]. Therefore, lath size does not appear to offer an explanation. If the increase in DBTT with dose and irradiation temperature observed in the 9Cr-2WVTa was due to increasing lath (sub-grain) size during irradiation, then a similar effect might be expected for other ferritic/martensitic steels, which is not the case. That is, other such steels would be expected to show subgrain growth, which would result in increasing DBTT with increasing fluence; instead, most steels show a saturation in the shift in DBTT with increasing fluence. Prior austenite grain size could also be considered as the crack size, but this does not explain the change in DBTT for the same reason lath size does not, as the prior austenite grain size does not change during irradiation.

After eliminating prior austenite grain size, lath size, and carbides, Eq. (2) indicates that the explanation must involve Young's modulus or the effective surface energy. The small amount of tantalum added will have little if any effect on the modulus. Gerberich et al. found effects of nickel and silicon on the effective surface energy for binary iron-based alloys [21], and concluded that a change in fracture stress could explain why nickel caused a decrease and silicon caused an increase in the transition temperature of binary Fe-Ni and Fe-Si alloys. As pointed out in the previous section, the shift in DBTT for 9Cr-2WVTa steel increases with irradiation dose and irradiation temperature. This may be due to the removal of tantalum from solution; this suggestion needs to be confirmed. The effects of microstructural parameters on the transition temperature are complex, as Gerberich et al. [21] have noted; the ductile-brittle transition model for iron and iron-binary alloys that they derived involved 19 flow and fracture parameters.

Thus, microstructural changes (grain size, precipitate type, etc.) cannot provide the sole explanation for the observations on mechanical property changes. It appears that tantalum in solution must change the effective surface energy, which causes a higher fracture stress for 9Cr-2WVTa than 9Cr-2WV, and the combination of tungsten and tantalum in the 9Cr-2WVTa leads to a higher fracture stress than produced by molybdenum and niobium in 9Cr-1MoVNb [6].

The observation that the ΔDBTT of the 9Cr-2WVTa appeared to increase slightly with fluence [6] would follow if tantalum is being removed from solution during irradiation and being incorporated in the existing or new precipitates. This can also explain the increase in DBTT for the 9Cr-2WVTa irradiated above 400°C (Fig. 5). The increase occurs at >400°C, where irradiation-enhanced diffusion, even after only 0.8 dpa, may permit a reduction of tantalum in solution. In the present experiment (Fig. 4), the better properties observed after irradiation to 15 dpa at 365°C than after 14 dpa at 393°C may be the result of more tantalum being removed from solution at the higher irradiation temperature. If this is the case, the ΔDBTT of the 9Cr-2WVTa would be expected to increase with fluence as tantalum is removed from solution, just as is observed at 365°C [6]. Eventually, it might be expected to approach the ΔDBTT for the 9Cr-2WV. Even if that were to happen, however, the 9Cr-2WVTa should still have the lowest DBTT after irradiation because of its lower DBTT before irradiation [6].

5. Summary and Conclusion

Charpy impact properties were determined on eight reduced-activation Cr-W ferritic steels irradiated in FFTF to ≈14 dpa at 393°C. To determine the effect of heat treatment, specimens were taken from normalized-and-tempered 15.9-mm plate and 3.3-mm bar. Chromium concentrations in the steels ranged from 2.25 to 12 wt% (all steels contained 0.1%C). The 2¼Cr steels contained variations of tungsten and vanadium (2¼CrV, 2¼Cr-1WV 2¼Cr-2W) and steels with 2.25, 5, 9, and 12% Cr contained a combination of 2% W and 0.25% V (2¼Cr-2WV, 5Cr-2WV, 9Cr-2WV, and 12Cr-2WV). A 9Cr steel containing 2% W, 0.25% V, and 0.07% Ta (9Cr-2WVTa) was also irradiated. The microstructure of the 2¼Cr steels in the 15.9-mm plate were bainite with various amounts of polygonal ferrite, and they were 100% bainite when heat treated as 3.3-mm bar. The 5Cr steel and the two 9Cr steels were 100% martensite and the 12Cr steel was martensite with ≈25% δ-ferrite after heat treatment in either geometry.

The change in microstructure of the 2¼Cr steels from a duplex structures of bainite plus ferrite to 100% bainite caused by heat treatment resulted in improvement in the Charpy properties before irradiation. After irradiation, however, there was little difference in the properties for the two different heat treatments. As expected, cooling rate had little effect on the high-chromium (9 and 12% Cr) steels. The Charpy properties for the 5Cr-2WV steel were improved by the faster cooling rate of the 3.3-mm bar. The reason for this change is unclear, but it may be caused by the different precipitates present in the 5Cr steel as compared to the other martensitic steels (M_7C_3 is present in the 5Cr-2WV steel but not in the other martensitic steels).

Results from the present irradiation experiment were compared with previous experiments for irradiation at a lower temperature (365°C). The DBTT values of all but the 5Cr-2WV and 9Cr-2WVTa steels were lower after irradiation at 393°C than after irradiation at 365°C, which is the expected behavior. The contrary behavior of the 5Cr steel was tentatively attributed to the M_7C_3 carbides that form in this composition that are not present in the 9Cr and 12Cr steels. The inverse temperature effect in the 9Cr-2WVTa steel was suggested to be due to the loss of tantalum from solution during irradiation at the higher temperature. It was concluded that the tantalum in solution gives the 9Cr-2WVTa steel its advantage over the other steels, and this advantage is decreased by its loss during irradiation..

References

[1] R. L. Klueh, K. Ehrlich, and F. Abe, J. Nucl. Mater. 191-194 (1992) 116.
[2] R. W. Conn et al., Panel Report on Low Activation Materials for Fusion Applications, University of California, Los Angeles, PPG-753, March 1983.
[3] R. L. Klueh and P. J. Maziasz, Met. Trans. 20A (1989) 373.
[4] R. L. Klueh, Met. Trans. 20A (1989) 463.
[5] R. L. Klueh and W. R. Corwin, J. of Mater. Engr. 11 (1989) 169.
[6] R. L. Klueh and D. J. Alexander, in: Effects of Radiation on Materials: 18th International Symposium, ASTM STP 1325, Eds. R. K. Nanstad, M. L. Hamilton, F.A. Garner, and A.S. Kumar (American Society for Testing and Materials, Philadelphia, 1997) to be published.
[7] R. L. Klueh, P. J. Maziasz, and D. J. Alexander, J. Nucl. Mater. 179-181 (1991) 679.
[8] D. J. Alexander, R. K. Nanstad, W. R. Corwin, and J. T. Hutton, in: Applications of Automation Technology to Fatigue and Fracture Testing, ASTM STP 1092, Eds. A. A. Braun, N. E. Ashbaugh, and F. M. Smith (American Society for Testing and Materials, Philadelphia, 1990) p. 83.
[9] R. W. K. Honeycombe, Steels: Microstructures and Properties (Edward Arnold Ltd, London, 1981), p.106.
[10] L. J. Habraken, Proc. 4th Int. Conf. Electron Microscopy, Vol. 1 (Springer-Verlag, Berlin, 1960) p. 621.
[11] L. J. Habraken and M. Economopoulos, Transformation and Hardenability in Steels (Climax-Molybdenum Company, Ann Arbor, MI, 1967) p. 69.
[12] R. L. Klueh, D. J. Alexander, and P. J. Maziasz, Met. Trans. 28A (1997) 335.
[13] J. J. Kai and R. L. Klueh, J. Nucl. Mater. 230 (1996) 116.
[14] R. W. Hertzberg, Deformation and Fracture Mechanics of Engineering Materials, 3rd Edition (John Wiley & Sons, New York, 1989) p. 253.
[15] C. J. McMahon, Jr., Fundamental Phenomena in the Materials Sciences, Vol. 4, L. J. Bonis, J. J. Duga, and J. J. Gilman, Eds. (Plenum Press, New York, 1967) p. 247.
[16] M. Rieth, B. Dafferner, and H. D. Röhrig, J. Nucl. Mater., 233-237 (1996) 351.
[17] K. Ehrlich, Private Communication, October 24, 1996.
[18] R. Jayaram and R. L. Klueh, to be published.
[19] R. L. Klueh and D. J. Alexander, . J. Nucl. Mater., 212-215 (1994) 736.
[20] W. C. Leslie, The Physical Metallurgy of Steels (McGraw-Hill, New York, 1981) 122.
[21] W. W. Gerberich, Y. T. Chen, D. G. Atteridge, and T. Johnson, Acta Met., 29 (1981) 1187.
[22] A. A. Griffith, Phil. Trans. R. Soc. London, 221A (1920) 163.
[23] A. A. Griffith, Proc. 1st Intl. Cong. Appl. Math. (Delft, The Netherlands, 1924) 55.
[24] E. Orowan, Rep. Prog. Phys. 12 (1948-1949) 185.
[25] G. R. Irwin, in: Fracture of Metals (American Society for Metals, Cleveland, OH, 1948) 147.
[26] R. A. Sack, Proc. Phys. Soc. London, 58 (1946) 729.
[27] H. L. Ewalds and R. J. H. Wanhill, Fracture Mechanics (Edward Arnold ltd., London, 1984) 43.

IRRADIATION CREEP OF VARIOUS FERRITIC ALLOYS IRRADIATED AT ~400°C IN THE PFR AND FFTF REACTORS - M. B. Toloczko (Washington State University), F. A. Garner (Pacific Northwest National Laboratory)* and C. R. Eiholzer (Westinghouse Hanford Company)

To be published in Journal of Nuclear Materials as Proceedings of the 8th International Conference on Fusion Materials, Oct. 26-31, 1997, Sendai, Japan.

EXTENDED ABSTRACT

Three ferritic alloys were irradiated in two fast reactors to doses of 50 dpa or more at temperatures near 400°C. One martensitic alloy, HT9, was irradiated in both the FFTF and PFR reactors. PFR is the Prototype Fast Reactor in Dourneay, Scotland, and FFTF is the Fast Flux Test Facility in Richland, WA. D57 is a developmental alloy that was irradiated in PFR only, and MA957 is a Y_2O_3 dispersion-hardened ferritic alloy that was irradiated only in FFTF. These alloys exhibited little or no void swelling at ~400°C.

Depending on the alloy starting condition, these steels develop a variety of non-creep strains early in the irradiation that are associated with phase changes. Each of these alloys creeps at a rate that is significantly lower than that of austenitic steels irradiated in the same experiments. The creep compliance for ferritic alloys in general appears to be ~0.5 x 10^{-6} MPa^{-1} dpa^{-1}, independent of both composition and starting state. The addition of Y_2O_3 as a dispersoid does not appear to change the creep behavior.

*Pacific Northwest National Laboratory is operated for the U.S. Department of Energy by Battelle Memorial Institute under Contract DE-AC06-76RLO 1830.

4.0 COPPER ALLOYS AND HIGH HEAT FLUX MATERIALS

TEMPERATURE AND STRAIN RATE EFFECTS IN HIGH STRENGTH HIGH CONDUCTIVITY COPPER ALLOYS TESTED IN AIR – D.J. Edwards (Pacific Northwest National Laboratory)*

OBJECTIVE

The objective of this work is to investigate the strain rate and temperature dependence of the tensile properties of GlidCop™ Al25 and Hycon 3HP™ CuNiBe tested in air.

SUMMARY

The tensile properties of the three candidate alloys GlidCop™ Al25, CuCrZr, and CuNiBe are known to be sensitive to the testing conditions such as strain rate and test temperature. This study was conducted on GlidCop™ Al25 (2 conditions) and Hycon 3HP™ (3 conditions) to ascertain the effect of test temperature and strain rate when tested in open air. The results show that the yield strength and elongation of the GlidCop™ Al25 alloys exhibit a strain rate dependence that increases with temperature. Both the GlidCop™ and the Hycon 3HP™ exhibited an increase in strength as the strain rate increased, but the GlidCop™ alloys proved to be the most strain rate sensitive. The GlidCop™ failed in a ductile manner irrespective of the test conditions, however, their strength and uniform elongation decreased with increasing test temperature and the uniform elongation also decreased dramatically at the lower strain rates. The Hycon 3HP™ alloys proved to be extremely sensitive to test temperature, rapidly losing their strength and ductility when the temperature increased above 250°C. As the test temperature increased and the strain rate decreased the fracture mode shifted from a ductile transgranular failure to a ductile intergranular failure with very localized ductility. This latter observation is based on the presence of dimples on the grain facets, indicating that some ductile deformation occurred near the grain boundaries. The material failed without any reduction in area at 450°C and 3.9 x 10^{-4} s^{-1}, and in several cases failed prematurely.

PROGRESS AND STATUS

Introduction

The tensile properties of the three candidate copper alloys (GlidCop™ Al25, CuCrZr, and CuNiBe) being considered for use in fusion applications are known to be dependent on test conditions such as strain rate and temperature [1,2]. Solomon and coworkers [1] reported that the tensile properties and the fracture toughness of the GlidCop™ alloys were sensitive to test temperature, with the fracture toughness decreasing as much as 50% when the test temperature was raised from room temperature to 150°C. Their mechanical testing was done in open air for both the tensile and the fracture toughness testing, raising the issue of whether an environmental effect is the source of the drastic decrease in fracture toughness. Zinkle and Eatherly [2] recently demonstrated that the mechanical properties of GlidCop™ are weakly dependent on strain rate below test temperatures of 250°C, but at higher temperatures it can become quite significant. Their tests were conducted under high vacuum over a strain rate range of 4 x 10^{-4} to 6 x 10^{-2} s^{-1} at temperatures ranging from 25 to 500°C. Alexander and coworkers [3] conducted fracture toughness tests on the unirradiated

* Pacific Northwest National Laboratory is operated for the U.S. Department of Energy by Battelle Memorial Institute under Contract DE-AC06-76RLO 1830.

GlidCop™ Al15 in both air and vacuum, and found that testing in air lowered the toughness approximately 50%. The decrease in toughness is therefore thought to be the result of a combination of strain rate sensitivity and possible chemisorption of oxygen to the fracture surface [2-4].

Zinkle and Eatherly also tested Hycon 3HP™ and CuCrZr alloys. Both materials proved to be less sensitive to strain rate than the GlidCop™, but the Hycon 3HP™ alloys were prone to brittle failure when the test temperature exceeded 300°C. The failure mode under these conditions changed from a ductile transgranular mode to a ductile intergranular mode. The behavior of these materials under different strain rates and test conditions suggests fundamental differences in the behavior of these materials that need to be understood.

To compare the effects of testing in air versus vacuum, a series of tensile tests were conducted in air at PNNL on the same materials as those tested by Solomon and coworkers and by Zinkle and Eatherly. The range of strain rates and temperatures were also extended to encompass a broader range of behavior. The tensile yield and ultimate strengths, elongations, and reduction in area are reported, and a brief comparison made with previous work.

Experimental Procedure

Tensile specimens were fabricated from plates of dispersion strengthened GlidCop™ Al25 and Hycon CuNiBe. The compositions of the two materials are given in Table 1. Two types of DS copper plates formed from the same internally oxidized powder were supplied by OMG Americas (formerly SCM Metals). The powder, designated by OMG Americas as LOX-80, was boron deoxidized to remove any free Cu_2O, and the powder was screened to below 80 mesh to narrow the size range of the starting powders. The first plate was in the form of extruded 2.5 cm thick plates that were given a cross-rolling and annealing (CR & Ann) treatment afterwards that corresponds to the designation ITER Grade 0 (IG0). The second GlidCop™ plate was consolidated directly from the powder by hot isostatic pressing, yielding a circular plate approximately 2.5 cm thick. The as-hipped plate was consolidated at ~14:1 reduction ratio at 980°C. No further thermomechanical treatments were given to the plate, simulating the condition of Al25 powder HIP'ped directly to stainless steel, a processing route considered for the ITER first wall. The grain structure of the cross-rolled and annealed material consists of highly elongated grains (1-2 μm in diameter x 10-20 μm in length) in the original extrusion direction, whereas the as-hipped material has a more equiaxed grain structure (20-30 μm diameter) with intergranular aluminum oxide at the grain boundaries.

The CR & Ann Al25 is the result of improved thermomechanical processing that, in conjunction with the LOX-80 starting powder, yields better elongation up to temperatures as high as 350°C [1]. The extruded plate is given an additional warm rolling treatment perpendicular to the original extrusion direction, yielding approximately 60% reduction. The plate is then annealed at 1000°C for 1 hour to stress relieve the plate, producing strength levels closer to that of the as-extruded plate. The final properties of the cross-rolled and annealed plate at room temperature are: σ_{UTS}= 421 MPa, σ_{YS}= 331 MPa, ε_{total} = 27%, and an electrical conductivity 86% IACS. The properties of the as-HIPped plate are almost identical at room temperature.

Four plates of Brush Wellman's Hycon 3HP™ CuNiBe were purchased, two of the plates in the HT condition (fully hardened temper, 69% IACS, hardness R_B= 92) and the second two

Table 1. Composition of materials (wt%)

Al25*	99.65 Cu	.0.25 Al	0.01 Fe	0.01 Pb	0.22 O	~250 ppm B
CuNiBe	99.5 Cu	0.35 Be	1.92 Ni	<0.2 Al	<0.01 Co	-------

*LOX -80 Al25 powder, ITER Grade 0 (IG0)

plates in the AT condition (solution annealed and aged, 65% IACS, R_B= 92). The HT temper involves a solution annealing and quenching step, subsequent cold working, and then ageing to achieve the fully hardened temper, whereas the AT temper does not include the cold working step. While the strengths of both materials are quite high, the lack of cold working in the AT temper yields a reasonably high strength condition with greater ductility. All of these plates were from the same heat (#46546) and originally in the HT temper. The AT plates were made by solution annealing two of the four HT plates and then ageing to achieve the AT temper. Dr. S. Zinkle provided a small piece of Hycon 3HP™ from the same heat (#46546) overaged to produce a higher conductivity condition to include in the testing matrix. The conductivity of this material was 74% IACS, with a σ_{YS}= 633 MPa. Further details on the latter material can be found in the report by Zinkle and Eatherly [2]. The grain structure in the Hycon 3HP™ AT temper is equiaxed with a high density of large beryllides dispersed throughout the matrix, with a grain size of approximately 50-60 μm. The grains in the HT temper are highly elongated as in the CR & Ann Al25, but much larger in size (25 μm dia. x 100 μm long).

The tensile tests were conducted in open air over a strain rate range of 3.9×10^{-4} to 1.5 s^{-1} and covering the temperature range of 25 to 450°C. The testing was conducted on an MTS servo hydraulic frame. The specimens were taken to temperature and then held for 5 minutes to allow the temperature to equilibrate through the entire specimen. Since the tests were conducted in open air, thermal convection was sufficient to help equilibrate the temperature in the short period of time. Oxidation of the specimens did occur during the testing, but from comparison with Zinkle and Eatherly's data [2] the oxide scale does not appear to have affected the tests. The specimen geometry and orientation with respect to the original rolling or extrusion direction is the same as that reported earlier for the STS specimens that were included in a joint RF/US/EU/Japan irradiation experiment in the SM2 reactor in Russia [5]. To aid in gripping and aligning the specimens pin holes were drilled in the center of the specimens grips at each end. Preliminary tests on the high strength Hycon 3HP™ alloys revealed that deformation occurred around the pin holes, leading to an underestimation of the yield strength due to a change in the slope of the tensile curve in the elastic region. This was corrected by increasing the pin hole diameter to 3.2 mm to lower the stress concentration at the pin holes. This problem never occurred in the lower strength GlidCop™ alloys (clamping from the grips was sufficient in itself), and no further problems were found in subsequent tests of the Hycon alloys after switching to the larger pin hole diameter. The 0.2% offset yield, ultimate, uniform and total elongation, and the reduction in area (RA) were measured on selected sets of tested specimens from computerized data. The reduction in area was measured in an optical comparator. Fracture surfaces from selected conditions were examined in an JEOL 840 SEM to analyze the failure mode as a function of strain rate and test temperature.

Results and Discussion

The mechanical properties for all of the tested conditions for the GlidCop™ alloy are listed in Tables 2 and 3. The reduction in area were measured only for the CR & Ann GlidCop™

Table 2. Temperature and strain rate dependence for cross-rolled and annealed GlidCop™ Al25 (IGO).

Strain Rate (s^{-1})	Test Temp. (°C)	YS (MPa)	UTS (MPa)	E_u (%)	e_{tot} (%)	RA (%)
3.9×10^{-4}	25	324	399	13	22.2	54.8
	150	289	333	9.8	29.1	53.6
	250	242	270	6.2	27.6	40.2
	350	184	201	1.8	33.9	36.2
1.5×10^{-3}	25	348	436	14.3	25.0	49.4
	150	304	345	9.0	25.7	55.0
	250	248	286	5.7	32.1	39.2
	350	210	226	2.6	39.5	30.7
	450	155	163	1.0	47.4	36.8
1.5×10^{-1}	25	360	443	14.4	26.5	51.4
	150	315	382	11.5	28.6	55.0
	250	296	333	7.7	28.3	56.3
	350	256	274	6.0	31.8	41.0
	450	218	244	4.9	36.9	54.7
1.5	25	359	454	14.0	25.1	50.5
	150	319	393	10.5	24.3	55.2
	250	304	349	9.9	26.6	60.4
	350	261	303	6.2	27.5	61.7
	450	242	272	5.3	26.5	62.2

Al25. The tensile properties of the dispersion strengthened alloy are generally better in the cross-rolled and annealed condition than in the as-hipped state. The strengths of the two materials are similar throughout the range of conditions tested, but with a noticeable difference in the uniform and total elongation behavior. The uniform elongation decreased in both materials the higher the test temperature, but was higher in the case of the as-hipped material. The total elongation, on the other hand, was higher in all conditions for the cross-rolled and annealed GlidCop™, and increased substantially the higher the test temperature and the lower the strain rate. In contrast, the as-hipped material exhibited lower total elongation as the temperature increased and the strain rate decreased. The reduction in area measured for the CR & Ann Al25 also improved as the strain rate increased but the influence of test temperature was varied. At strain rates of 1.5×10^{-3} s^{-1} and lower the RA tended to decrease as the test temperature increased, but at higher strain rates the RA began to increase with increasing test temperature. The difference in ductility between the CR & Ann and as-hipped Al25 illustrates the effect that the markedly different grain structures have on the behavior of the material. The equiaxed grain structure of the as-hipped material improves the uniform elongation at the higher temperatures and the highest strain rate, yet the as-hipped material fails much sooner.

Figure 1 shows a comparison of the effect of testing in air versus testing in vacuum. The yield strength of the CR & Ann material is plotted as a function of strain rate and the strain rate sensitivity parameter *m* calculated from the equation :

$$\sigma = C\dot{\varepsilon}^m$$

where C is a constant [6]. The data for the tests conducted under vacuum were taken from the work of Zinkle and Eatherly. Below 250°C the sensitivity to strain rate is fairly small, but above 250°C it begins to be more important. In both studies it was found that the strain rate sensitivity increased from 0.01 at room temperature to 0.07 at 300-450°C. Although Zinkle and Eatherly's data suggest that testing in vacuum caused the shift to occur at lower temperatures, the lack of any 300°C data at higher strain rates under vacuum does not allow any conclusions to drawn. Based on the limited results the strain rate sensitivity does not appear to be affected by the testing environment for the CR & Ann Al25. The strain rate sensitivity was also measured for the as-hipped Al25, and it was found that the yield strength in this condition was less sensitive to strain rate, giving a strain rate sensitivity from 0.01 at room temperature to 0.03 at 450°C. Keeping in mind that the as-hipped material failed sooner than the CR & Ann material, the data still indicates that the highly wrought grain structure of the CR & Ann condition strongly influences the behavior of the material. If the properties of the as-hipped material could be improved, it might make a more suitable processing route for the dispersion strengthened material.

The Hycon 3HP™ alloys proved to be more susceptible to the influence of test temperature. The data in Tables 4-6 show that both the uniform and total elongation as well as the

Table 3. Temperature and strain rate dependence for as-hipped GlidCop™ Al25.

Strain Rate (s^{-1})	Test Temp. (°C)	YS (MPa)	UTS (MPa)	e_u (%)	e_{tot} (%)
3.9×10^{-4}	25	281	395	18.8	22.3
	150	252	321	13.0	16.5
	250	221	270	6.4	8.5
	350	187	216	2.7	4.2
1.5×10^{-3}	25	298	417	17.5	27.5
	150	247	323	13.2	18.8
	250	226	277	8.2	9.0
	350	206	232	3.6	4.5
	450	169	183	2.6	3.9
1.5×10^{-1}	25	316	427	16.3	26.3
	150	275	364	13.7	23.8
	250	243	315	12.7	26.1
	350	200	277	12.0	17.6
	450	197	233	7.8	13.0
1.5	25	311	439	17.4	24.1
	150	283	379	14.9	25.9
	250	260	329	12.4	26.7
	350	249	292	11.6	20.7
	450	208	252	10.0	19.7

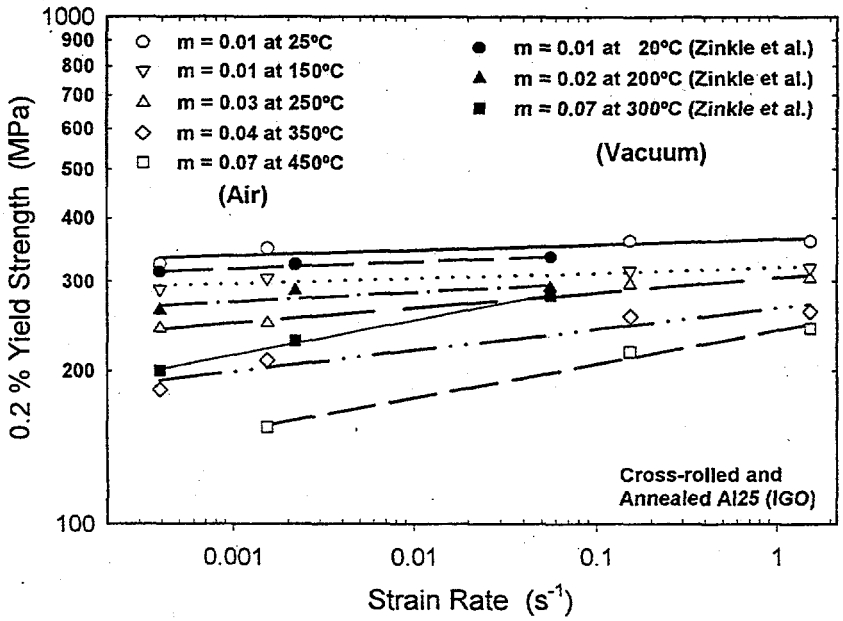

Figure 1. Strain rate dependence of CR & Ann Al25 tested in air and vacuum at different temperatures.

reduction in area (measured for the AT temper only) decrease substantially as the test temperature increases. The Hycon 3HP™ alloys are all susceptible to severe reductions in their ductility as the test temperature increases above 350°C, and the same behavior was observed by Zinkle and Eatherly, though testing under vacuum appears to shift the embrittlement to somewhat higher temperatures. The embrittlement or loss of ductility worsens as the strain rate decreases, suggesting that an environmental effect and/or diffusion controlled mechanism is playing a role. Figure 2 shows a plot of the data from this study and that of Zinkle and Eatherly's work. With the limited data available, the yield strength of the Hycon 3HP™ alloys do not appear to be strain rate sensitive. In all cases the strain rate sensitivity parameter (ignoring those conditions where the specimens failed prematurely) was around 0.01-0.02, irrespective of being tested in air or in vacuum. A change in failure mode was observed at the higher test temperatures and lower strain rates, changing from a ductile transgranular mode to a brittle intergranular with some ductile dimpling present on the grain facets. The reduction in area also decreased drastically, in agreement with the shift to an intergranular failure mode.

None of the three heat treatments offered any real advantage in terms of retention of ductility or strength. One surprising result is that the HT temper, which is nominally in the fully hardened condition, is actually weaker and less ductile than the AT temper. The elongation of the HT temper is closer to that of the higher conductivity heat treatment of heat # 46546. One would expect that the cold working step included in the HT temper would produce a higher strength and lower ductility compared to the AT temper. Since the higher conductivity heat treatment yielded a higher strength than the HT temper processing, it seems likely that the strength of this alloy is very sensitive to prior heat treatments and processing.

CONCLUSIONS

Testing in air versus vacuum does not appear to change the behavior of the strain rate sensitivity of the CR & Ann Al25. Both the CR & Annealed Al25 and the as-hipped Al25 exhibit a decrease in strength as the test temperature is raised, but the as-hipped material is less strain rate sensitive than the CR & Annealed condition. This appears to be related to the difference in the grain size and morphology of the two materials, but there may be other factors such as the presence of aluminum oxide at the grain boundaries in the as-hipped material.

The Hycon 3HP™ alloy suffers from severe loss of strength and ductility whether tested in air or vacuum. The limited data suggests that testing in air shifts the embrittlement to lower temperatures, and certainly testing at lower strain rates causes the material to behave worse. Ignoring the specimens that failed prematurely at the high temperatures, the data shows that the AT temper material is not strain rate sensitive, in agreement with the study of Zinkle and Eatherly.

Table 4. Temperature and strain rate dependence for Hycon 3HP™ CuNiBe AT condition (Heat #46546).

Strain Rate (s^{-1})	Test Temp. (°C)	YS (MPa)	UTS (MPa)	E_u (%)	e_{tot} (%)	RA (%)
3.9×10^{-4}	25	558	727	17.1	19.5	24.5
	150	511	679	13.5	14.7	17.8
	250	508	606	3.2	3.4	6.8
	350	-------	395	------	------	5.5
1.5×10^{-3}	25	578	741	15.9	19.5	25.2
	150	557	689	12.2	15.0	18.9
	250	529	628	3.9	4.8	7.1
	350	477	512	0.42	0.54	4.2
	450	-------	371	------	------	0
1.5×10^{-1}	25	588	744	16.7	20.1	28.1
	150	558	698	14.3	17.5	25.5
	250	538	660	10.2	11.4	14.8
	350	500	597	3.0	4.0	7.3
	450	498	541	0.9	1.03	4.3
1.5	25	597	747	16.1	21.0	27.0
	150	559	703	14.4	18.6	24.9
	250	535	671	11.9	14.2	18.1
	350	545	619	4.9	6.1	7.4
	450	530	547	0.48	0.51	4.3

Table 5. Temperature and strain rate dependence for Hycon 3HP™ CuNiBe HT condition (Heat #46546).

Strain Rate (s^{-1})	Test Temp. (°C)	YS (MPa)	UTS (MPa)	E_u (%)	e_{tot} (%)
3.9×10^{-4}	25	562	675	10.0	15.3
	150	520	608	9.5	14.9
	250	500	562	5.7	6.4
	350	421	498	------	0.75
1.5×10^{-3}	25	563	679	10.9	15.5
	150	538	623	8.6	13.2
	250	513	584	6.1	8.4
	350	499	518	------	0.71
	450	------	370	------	------
1.5×10^{-1}	25	593	694	10.6	16.8
	150	545	646	8.6	14.0
	250	537	610	7.8	12.2
	350	489	555	5.1	6.5
	450	486	505	0.74	0.78
1.5	25	602	694	10.4	16.0
	150	545	630	10.5	16.2
	250	539	612	8.5	12.5
	350	509	565	6.6	10.1
	450	480	532	------	2.1

Table 6. Temperature and strain rate dependence for Hycon 3HP™ CuNiBe high conductivity condition (Heat #46546).

Strain Rate (s^{-1})	Test Temp. (°C)	YS (MPa)	UTS (MPa)	e_u (%)	e_{tot} (%)
1.5×10^{-3}	25	620	703	9.9	15.2
	150	575	657	7.9	12.7
	250	541	598	5.6	7.0
	350				
	450				
1.5×10^{-1}	25	611	704	11.1	17.0
	150	596	677	8.2	12.6
	250	550	623	7.6	13.0
	350				
	450				
1.5	25	627	710	10.8	16.8
	150	601	676	7.9	12.2
	250	565	629	8.3	13.0
	350				
	450				

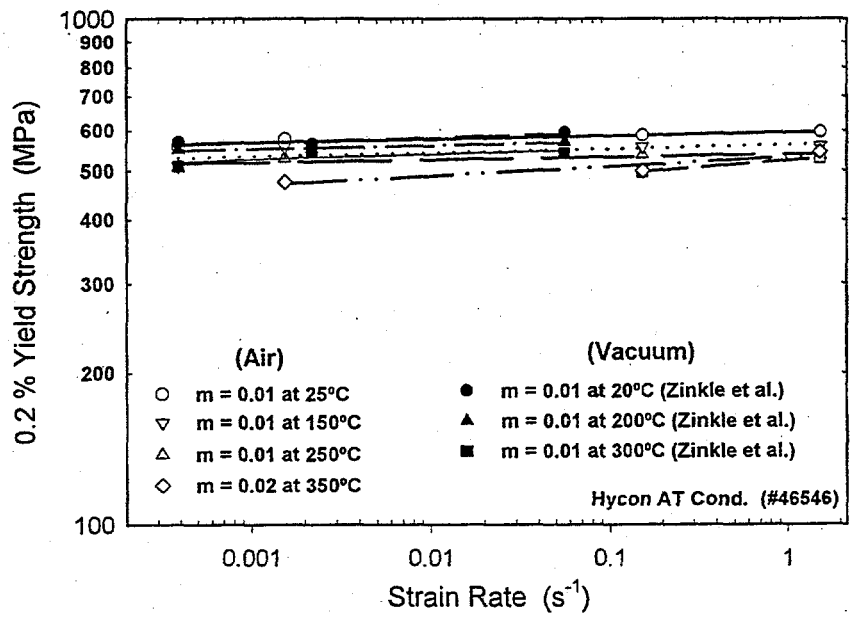

Figure 2. Strain rate dependence of Hycon 3HP™ (AT temper) tested in air and vacuum at different temperatures.

FUTURE WORK

Further measurements on the reduction in area are planned to be made. Specimens from CuCrZr are also planned for testing to compare the results with those obtained from the dispersion strengthened copper and Hycon 3HP™ alloys. Auger analysis will be performed on specimens of all three alloys to provide additional insight into the behavior of the alloys.

ACKNOWLEDGEMENTS

The author would like to express his gratitude to D. Criswell for performing all of the tensile tests and measurements on reduction in area. The high conductivity version of Hycon 3HP™ was supplied by S.J Zinkle at Oak Ridge National Laboratory. This work was supported by the U. S. Department of Energy under Contract DE-AC06-76RLO 1830 with Battelle Memorial Institute.

REFERENCES

1. R.R. Solomon, J.D. Troxell, and A. V. Nadkarni, J. of Nucl. Matls., **233-237**, (1996), p. 542.
2. S.J. Zinkle and W.S. Eatherly, Fusion Materials Semiannual Progress Report for the Period ending December 31, 1996, DOE/ER-0313/21, (Oak Ridge National Laboratory), p. 165.
3. D.J. Alexander, Fusion Materials Semiannual Progress Report for the Period ending June 30, 1996, DOE/ER-0313/20, (Oak Ridge National Laboratory, 1996), p. 217.

4. D.J. Alexander, S.J. Zinkle and A.F. Rowcliffe, Fusion Materials Semiannual Progress Report for the Period ending December 31, 1996, DOE/ER-0313/21, (Oak Ridge National Laboratory, 1996), p. 217.

5. D.J. Edwards et al., Fusion Materials Semiannual Progress Report for the Period ending December 31, 1995, DOE/ER-0313/19, (Oak Ridge National Laboratory), p. 165.

6. G. E. Dieter, Mechanical Metallurgy, 3rd Ed., (McGraw-Hill, New York, 1986) p. 297.

THE EFFECT OF BONDING AND BAKEOUT THERMAL CYCLES ON THE PROPERTIES OF COPPER ALLOYS IRRADIATED AT 100°C - D.J. Edwards (Pacific Northwest National Laboratory)*, B.N. Singh, P. Toft and M. Eldrup (Risø National Laboratory)

To be published in Journal of Nuclear Materials as Proceedings of the 8th International Conference on Fusion Reactor Materials, Oct. 26-31, 1997, Sendai, Japan.

EXTENDED ABSTRACT

This report describes the final irradiation experiment in a series of screening experiments [1,2] aimed at investigating the effects of bonding and bakeout thermal cycles on irradiated copper alloys. Tensile specimens of CuCrZr and CuNiBe alloys were given various heat treatments corresponding to solution anneal, prime-ageing and bonding thermal treatment. [illegible]ged and given a reactor bakeout treatment at 350°C for 100 [illegible] a heat treatment corresponding to a bonding thermal cycle [illegible] irradiated at 100°C to a dose level of ~0.3 dpa in the DR-3 [illegible] tests at 100°C, electrical resistivity, and microstructural examination were performed. Testing and analysis of the unirradiated specimens have been reported earlier [1,2].

The post-irradiation tests at 100°C revealed the greatest loss of ductility occurred in the CuCrZr alloys, irrespective of the pre-irradiation heat treatment, with the uniform elongation dropping to levels of less than 1.5%. The yield and ultimate strengths for all of the individual heat treated samples increased substantially after irradiation. The same trend was observed for the CuNiBe alloys, which overall exhibited a factor of 3 higher uniform elongation after irradiation with almost double the strength. In both alloys irradiation-induced precipitation lead to a large increase in the strength of the solution annealed specimens with a noticeable decrease in uniform elongation. The Al25 alloy also experienced an increase in the overall strength of the alloy after irradiation, accompanied by approximately a 50% decrease in the uniform and total elongation. The additional bakeout treatments given to the CuCrZr and CuNiBe before irradiation served to increase the strength, but in terms of the ductility no improvement or degradation resulted from the additional thermal exposure. The results of this experiment confirm that the Al25 possesses the most resistant microstructure to thermal and irradiation-induced changes, while the competing effects of ballistic dissolution and reprecipitation lead to important changes in the two precipitation strengthened alloys. This study and others have repeatedly shown that these materials can only be used if the very low uniform elongation (1% or less) can be accounted for in the design since pre-irradiation thermal processing cannot mitigate the irradiation embrittlement.

* Pacific Northwest National Laboratory is operated for the U.S. Department of Energy by Battelle Memorial Institute under Contract DE-AC06-76RLO 1830.

Table 1. Tensile results for copper alloys irradiated at 100°C to 0.3 dpa. Tests were conducted at 100°C.

Material	Heat Treatment	$\sigma_{0.05}$ (MPa)	$\sigma_{0.2}$ (MPa)	σ_{max} (MPa)	ε^{p}_{u} (%)	ε_{total} (%)
CuNiBe	Solution annealed	625	663	683	12.5	14.5
CuNiBe	Bonding Cycle	800	880	938	3.4	5.9
CuNiBe	B + Bakeout	880	960	990	3.4	5.4
CuNiBe	Prime Aged	815	885	940	3.3	5.9
CuCrZr	Solution annealed	365	365	370	1.1	4.0
CuCrZr	Bonding Cycle	370	370	373	1.1	4.1
CuCrZr	B + Bakeout	445	450	450	1.3	4.0
CuCrZr	E + Bakeout	440	440	445	1.3	4.0
CuCrZr	Prime Aged	400	405	412	1.2	3.8
Al25*	Annealed	540	544	546	5.5	26.0

* Round specimen, 3 mm diameter gage

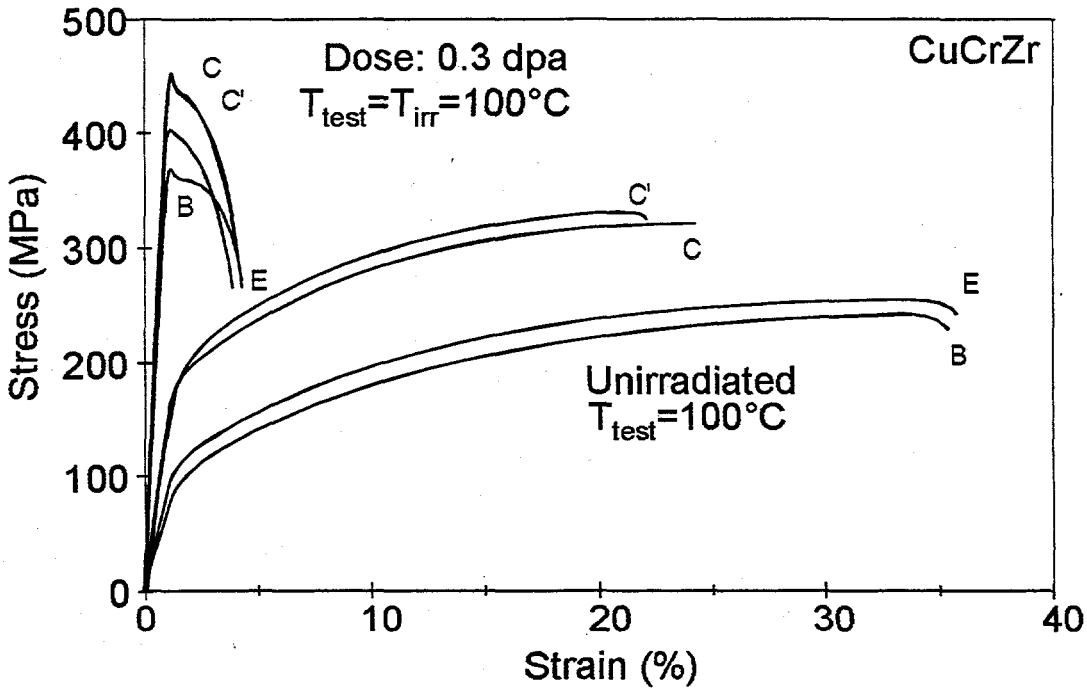

Figure 1. The tensile properties of the various heat treated CuCrZr specimens before and after irradiation. Irradiation leads to a severe loss of uniform and total elongation, and produces an instability upon yielding. The embrittlement is not affected by the pre-irradiation heat treatment.

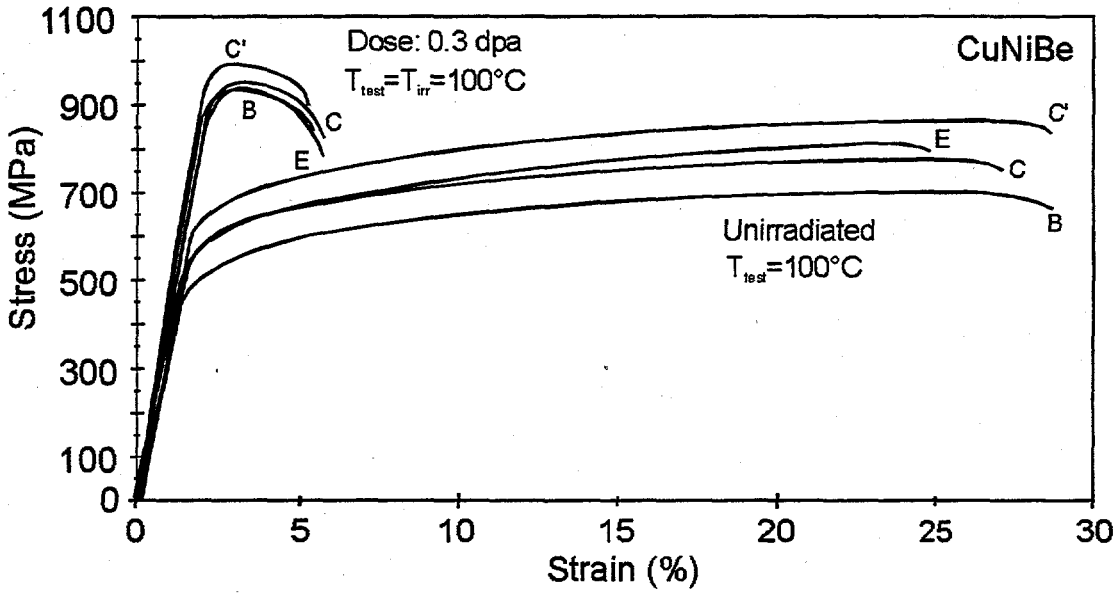

Figure 2. The tensile properties of the various heat treated CuNiBe specimens before and after irradiation. Irradiation produces a significant increase in strength and loss of ductility, but does not lead to the instability shown for the CuCrZr alloys.

REFERENCES

1. B.N. Singh, D.J. Edwards, M. Eldrup, and P. Toft, Pre- and Post-Irradiation Properties of Copper Alloys at 250°C Following Bonding and Bakeout Thermal Cycles, Risø Report R-937, Risø National Laboratory, Roskilde, Denmark, (1997).

2. B.N. Singh, D.J. Edwards, M. Eldrup, and P. Toft, Effect of Bonding and Bakeout Thermal Cycles on the Properties of Copper Alloys Irradiated at 350°C, Risø Report R-971, Risø National Laboratory, Roskilde, Denmark, (1997).

EFFECT OF INITIAL OXYGEN CONTENT ON THE VOID SWELLING BEHAVIOR OF FAST NEUTRON IRRADIATED COPPER — S.J. Zinkle (Oak Ridge National Laboratory) and F.A. Garner (Pacific Northwest National Laboratory)

OBJECTIVE

The objective of this report is to summarize density measurements on oxygen-free and oxygen-doped copper following high dose fast reactor irradiation.

SUMMARY

Density measurements were performed on high purity copper specimens containing ≤10 wt.ppm and ~120 wt.ppm oxygen following irradiation in FFTF MOTA 2B. Significant amounts of swelling were observed in both the oxygen-free and oxygen-doped specimens following irradiation to ~17 dpa at 375°C and ~47 dpa at 430°C. Oxygen doping up to 360 appm (90 wt.ppm) did not significantly affect the void swelling of copper for these irradiation conditions.

PROGRESS AND STATUS

Introduction

It has been recognized for many years that minor concentrations of impurity atoms (particularly gaseous species) can have a significant impact of the defect cluster morphology in quenched [1,2] and ion-irradiated [3-5] face-centered cubic metals. There is also some evidence that high oxygen levels such as that found in electrolytic tough pitch copper may cause significantly higher neutron-induced void swelling than in oxygen-free pure copper specimens [6]. Recent work by Shimomura and coworkers found that vacuum remelted specimens had a factor of 10 lower void density compared to as-received high purity copper at low neutron doses (~0.5 dpa), but in general no appreciable difference in the swelling behavior was observed at doses above ~5 dpa [7-9]. Mixed results were obtained on Cu-Al and Cu-Ni alloys; lower void swelling was observed in vacuum remelted Cu-5%Al specimens whereas no difference was observed for vacuum remelted vs. as-received Cu-5%Ni specimens following fast reactor irradiation to ~40 dpa at temperatures near 400°C [8]. Unfortunately, the concentration of gaseous impurities was not quantified in these neutron irradiation studies [7-9]. The purpose of the present study was to provide further data on the effect of a controlled amount of oxygen on the void swelling behavior of neutron-irradiated copper.

Experimental Procedure

High purity "Puratronic" wrought copper sheet (1 mm thickness) produced by Johnson Matthey Chemicals Ltd. was cold-rolled to a thickness of 0.5 mm and then recrystallized by annealing in helium at 400°C for 1 h. Transmission electron microscopy (TEM) disks of 3 mm diameter were punched from the recrystallized sheet, and several of the disks were annealed in helium containing ≤3 vol.ppm oxygen at a pressure of ~1 atmosphere (0.1 MPa) for 0.5 h at 950°C in order to introduce a controlled amount of oxygen into the matrix [5]. The specimens were mechanically ground to remove punching burrs, with resultant final thicknesses of 0.35 and 0.25 mm for the "low-oxygen" (400°C annealed) and "oxygen-doped" (950°C annealed) disks, respectively. The oxygen contents in the low-oxygen and oxygen-doped samples were measured to be ≤50 and 360 appm, respectively by vacuum fusion techniques. Other measured impurity concentrations were ≤5 wt.ppm N, 3 wt. ppm Fe and 3 wt. ppm Si.

Two TEM disks each of the low-oxygen and oxygen-doped coppers were irradiated in MOTA-2B of the Fast Flux Test Facility to 16.9 dpa at 375°C and 47.3 dpa at 430°C (MOTA-2B packets 7X03 and 7T03, respectively). The TEM disks were laser engraved with a 4-digit ID code at PNNL prior to irradiation, and the irradiation was performed in sealed, helium filled capsules with the specimens separated by thin molybdenum foils to avoid self-welding. Following irradiation, the radiation-induced swelling was measured at PNNL using immersion density techniques.

Results and Discussion

The swelling values for the low-oxygen and oxygen-doped copper specimens are summarized in Table 1, where the swelling levels were calculated based on a pure copper density of 8.9192 g cm^{-3}. Only one of the oxygen-doped specimens was measured for each of the two irradiation conditions. The swelling levels in the specimens irradiated at 375°C exhibited considerable variability, which may be partly due to a flux gradient in the below-core basket of MOTA [10]. It is interesting to note that the oxygen-doped copper exhibited slightly lower swelling than the low-oxygen Cu specimens at both irradiation conditions. The amount of swelling in both the low-oxygen and oxygen-doped Johnson-Matthey copper specimens was significantly lower than the 0.5%/dpa trend line observed for several other grades of high-purity copper in previous fast reactor irradiations at 375 and 423-430°C [10-13].

A previous ion irradiation study performed on the same materials as the present investigation found that void formation did not occur at 375 and 475°C in the low-oxygen copper for doses up to 17 dpa, whereas pronounced void swelling (e.g., 5% at 10 dpa, 475°C) occurred in the oxygen-doped copper [5]. This result is in good agreement with thermodynamic-based calculations [5] which predict that oxygen concentrations of $\geq$50 appm are needed to stabilize void formation in pure copper at 400°C if other gases are not present. In contrast, the present results demonstrate that significant cavity swelling has occurred in both the low-oxygen and oxygen-doped copper specimens during neutron irradiation to doses of 17 and 47 dpa. This difference in behavior between the ion and neutron irradiated specimens can be explained by considering the effects of helium on cavity stability. According to a simple energy-minimization model [4] and atomistic calculations [14,15], small amounts of helium (which would be generated by (n,α) transmutation reactions in neutron-irradiated copper) greatly enhance the stability of void nuclei compared to planar vacancy clusters. The calculated minimum concentration of helium needed to stabilize the cavities nucleated in neutron-irradiated copper is a strong function of temperature, ranging from ~0.1 appm He at 200°C to ~0.001 appm He at 400°C [4]. Using the fast reactor helium generation rate in copper of ~0.1 appm/dpa [16,17], stabilization of the cavity nuclei would be predicted to occur at doses above ~0.01 dpa for neutron irradiation near 400°C. Since the cavity population in the low-oxygen copper specimen would be stabilized by helium during the early stages of the neutron irradiation, no difference in the cavity density or size of low-oxygen vs. oxygen-doped copper would be expected on the basis of the energy-minimization model [4].

Table 1. Summary of swelling measured by immersion density on copper TEM disks

Irradiation condition	Material	% Swelling
16.9 dpa, 375°C	low-oxygen Cu	2.6
"	low-oxygen Cu	4.8
"	oxygen-doped Cu	2.3
47.3 dpa, 430°C	low-oxygen Cu	15.1
"	low-oxygen Cu	14.0
"	oxygen-doped Cu	11.9

The neutron irradiation void swelling data on as-received and vacuum-remelted copper reported by Yamakawa et al. [7] can also be explained by the oxygen [5] and helium [4] cavity stabilization models. In their study, neutron irradiation at ~330°C to a dose of ~0.5 dpa resulted in a factor of 10 higher void density in the as-received copper specimens [7]. According to the helium cavity stabilization model [4], a helium concentration of ~0.01 appm is needed to stabilize the void nuclei under these irradiation conditions. This is comparable to the amount of helium which would have

been generated during the low-dose irradiation (~0.05 appm He), and a reduction in visible cavity density compared to oxygen-bearing specimens is therefore qualitatively consistent with the model predictions. At higher neutron doses and temperatures (2-8 dpa, 390-420°C), comparable levels of void swelling were observed in both as-received and degassed specimens [7]. The predicted amount of helium needed to stabilize cavity formation in neutron-irradiated copper at 400°C is approximately an order of magnitude smaller than at 330°C [4]. Therefore, the cavity density would be predicted to be stabilized in both low-oxygen and oxygen-free copper specimens for doses above ~0.1 dpa at 400°C, and only minor differences in the cavity swelling would be expected at high doses.

At very high oxygen levels, it may be possible to produce a chemisorbed oxygen monolayer on the growing void surfaces. The reduction in surface energy associated with the chemisorbed oxygen [5] would accelerate void growth, and is a possible explanation for the very high swelling (34%) observed in electrolytic tough pitch copper following fast reactor irradiation to 13.5 dpa at 400°C [6]. Since the maximum oxygen content investigated in the present study was 350 appm, further work on oxygen-doped copper specimens with oxygen levels comparable to that found in electrolytic tough pitch copper (800-2000 appm) would be necessary to further investigate the effect of very high oxygen contents on void swelling in neutron-irradiated copper.

REFERENCES

1. L.M. Clarebrough, P. Humble and M.H. Loretto, Acta Metall. 15 (1967) 1007.
2. Y. Shimomura and S. Yoshida, J. Phys. Soc. Jpn. 22 (1967) 319.
3. L.D. Glowinski and C. Fiche, J. Nucl. Mater. 61 (1976) 29.
4. S.J. Zinkle, W.G. Wolfer, G.L. Kulcinski and L.E. Seitzman, Philos. Mag. A 55 (1987) 127.
5. S.J. Zinkle and E.H. Lee, Metall. Trans. A 21 (1990) 1037.
6. O.K. Harling et al., J. Mater. Res. 2 (1987) 568.
7. K. Yamakawa, I. Mukouda and Y. Shimomura, J. Nucl. Mater. 191-194 (1992) 396.
8. Y. Shimomura et al., J. Nucl. Mater. 212-215 (1994) 352.
9. Y. Shimomura, I. Mukouda and K. Sugio, J. Nucl. Mater. 251 (1997) 61.
10. F.A. Garner and B.N. Singh, in Fusion Materials Semiann. Prog. Report for Period ending March 31, 1994, DOE/ER-0313/16 (Oak Ridge National Lab, 1994) p. 364.
11. F.A. Garner, D.J. Edwards, B.N. Singh and H. Watanabe, in Fusion Materials Semiann. Prog. Report for Period ending March 31, 1993, DOE/ER-0313/14 (Oak Ridge National Lab, 1993) p. 345.
12. T. Muroga and N. Yoshida, J. Nucl. Mater. 212-215 (1994) 266.
13. F.A. Garner et al., J. Nucl. Mater. 191-194 (1992) 386.
14. M.I. Baskes, Trans. Am. Nucl. Soc. 27 (1977) 320.
15. Y. Shimomura, M.W. Guinan and T. Diaz de la Rubia, J. Nucl. Mater. 205 (1993) 374.
16. F.A. Garner, H.L. Heinisch, R.L. Simons and F.M. Mann, Radiat. Eff. Def. Solids 113 (1990) 229.
17. D.W. Kneff, L.R. Greenwood, B.M. Oliver and R.P. Skowronski, J. Nucl. Mater. 141-143 (1986) 824.

5.0 AUSTENITIC STAINLESS STEELS

THE DEPENDENCE OF IRRADIATION CREEP IN AUSTENITIC ALLOYS ON DISPLACEMENT RATE AND HELIUM TO DPA RATIO - F. A. Garner (Pacific Northwest National Laboratory)*, M. B. Toloczko (Washington State University) and M. L. Grossbeck (Oak Ridge National Laboratory)

To be published in Journal of Nuclear Materials as Proceedings of the 8th International Conference on Fusion Materials, Oct. 26-31, 1997, Sendai, Japan.

EXTENDED ABSTRACT

Before the parametric dependencies of irradiation creep can be confidently determined, analysis of creep data requires that the various creep and non-creep strains be separated, as well as separating the transient, steady-state, and swelling-driven components of creep. When such separation is attained, it appears that the steady-state creep compliance, B_o, is not a function of displacement rate, as has been previously assumed. It also appears that the formation and growth of helium bubbles under high helium generation conditions can lead to a significant enhancement of the irradiation creep coefficient. This is a transient influence that disappears as void swelling begins to dominate the total strain, but this transient can increase the apparent creep compliance by 100-200% at relatively low ($\leq$20) dpa levels.

*Pacific Northwest National Laboratory is operated for the U.S. Department of Energy by Battelle Memorial Institute under Contract DE-AC06-76RLO 1830.

EXTREME EMBRITTLEMENT OF AUSTENITIC STAINLESS STEEL IRRADIATED TO 75-81 DPA AT 335-360°C - S. I. Porollo, A. N. Vorobjev, Yu. V. Konobeev (Institute of Physics and Power Engineering, Obninsk, Kaluga Region, Russia) and F. A. Garner (Pacific Northwest National Laboratory)*

To be published in Journal of Nuclear Materials as Proceedings of the 8th International Conference on Fusion Materials, Oct. 26-31, 1997, Sendai, Japan.

EXTENDED ABSTRACT

ally accepted that void swelling of austenitic steels ceases below some temperature ge 340-360°C, and exhibits relatively low swelling rates up to ~400°C. This perception be correct at all irradiation conditions, however, since it was largely developed from ained at relatively high displacement rates in fast reactors whose inlet temperatures the range 360-370°C.

s an expectation, however, that the swelling regime can shift to lower temperatures at isplacement rates via the well-known "temperature shift" phenomenon. It is also known swelling rates at the lower end of the swelling regime increase continuously at a sluggish ever approaching the terminal 1%/dpa level within the duration of previous experiments.

This paper presents the results of an experiment conducted in the BN-350 fast reactor in Kazakhstan that involved the irradiation of argon-pressurized thin-walled tubes (0-200 MPa hoop stress) constructed from Fe-16Cr-15Ni-3Mo-Nb stabilized steel in contact with the sodium coolant, which enters the reactor at ~270°C. Tubes in the annealed condition reached 75 dpa at 335°C, and another set in the 20% cold-worked condition reached 81 dpa at 360°C. Upon disassembly all tubes, except those in the stress-free condition, were found to have failed in an extremely brittle fashion. The stress-free tubes exhibited diameter changes that imply swelling levels ranging from 9 to 16%. It is expected that stress-enhancement of swelling induced even larger swelling levels in the stressed tubes.

The embrittlement is explained in terms of the sensitivity of the swelling regime to displacement rate and the large, unprecedented levels of swelling reached at 335-360°C at these high neutron fluences. The failure mechanism appears to be identical to that observed at similar swelling levels in other austenitic steels irradiated in U.S. fast reactors at 400-425°C, whereby stress-concentration between voids and nickel segregation at void surfaces predisposes the steel to an epsilon martensite transformation followed by formation of alpha martensite at crack tips. The very slow strain rate inherent in such creep tests and the relatively high helium levels may also contribute to the failure.

*Pacific Northwest National Laboratory is operated for the U.S. Department of Energy by Battelle Memorial Institute under Contract DE-AC06-76RLO 1830.

SHEAR PUNCH TESTING OF ^{59}Ni ISOTOPICALLY-DOPED MODEL AUSTENITIC ALLOYS AFTER IRRADIATION IN FFTF AT DIFFERENT HE/DPA RATIOS - G. L. Hankin and R. G. Faulkner (I.P.T.M.E., Loughborough University, Leicestershire, LE113UT, UK)
M. L. Hamilton and F.A. Garner (Pacific Northwest National Laboratory)*

To be published in Journal of Nuclear Materials as Proceedings of the 8th International Conference on Fusion Reactor Materials, Oct. 26-31, 1997, Sendai, Japan.

EXTENDED ABSTRACT

A series of three model alloys, Fe-15Cr-25Ni, Fe-15Cr-25Ni-0.04P and Fe-15Cr45Ni were irradiated side-by-side in FFTF-MOTA in both the annealed and the cold worked condition in each of two variants, one using naturally occurring isotopic mixtures, and another doped with ^{59}Ni to generate relatively high helium-to-dpa ratios. Previous papers in this series have addressed the influence of helium on radiation-induced evolution of microstructure, dimensional stability and mechanical properties, the latter using miniature-tensile specimens.

In the final paper of this experimental series, three sets of irradiations conducted at different temperatures and displacement rates were examined by shear punch testing of standard microscopy disks. The results were used to determine the influence of helium generation rate, alloy starting condition, irradiation temperature and total neutron exposure. The results were also compared with the miniature tensile data obtained earlier.

In general, all alloys approached saturation levels of strength and ductility that were relatively independent of He/dpa ratio and starting condition, but were sensitive to the irradiation temperature and total exposure. Some small influence of helium/dpa ratio on the shear strength is visible in the two series that ran at ~490°C, but is not evident at 365°C.

*Pacific Northwest National Laboratory is operated for the U.S. Department of Energy by Battelle Memorial Institute under Contract DE-AC06-76RLO 1830.

DAMAGE STRUCTURE OF AUSTENITIC STAINLESS STEEL 316LN IRRADIATED AT LOW TEMPERATURE IN HFIR - N. Hashimoto (Oak Ridge National Laboratory), E. Wakai (Japan Atomic Energy Research Institute), J. P. Robertson (ORNL), M. L. Grossbeck (ORNL), and A. F. Rowcliffe (ORNL)

OBJECTIVE

The purpose of this work is to investigate the microstructure of austenitic stainless steel 316LN irradiated at low temperatures and to damage levels of about 3 dpa and to relate the microstructure to mechanical behavior.

SUMMARY

TEM disk specimens of austenitic stainless steel 316LN irradiated to damage levels of about 3 dpa at irradiation temperatures of either about 90 °C or 250 °C have been investigated by using transmission electron microscopy. The irradiation at 90 °C and 250 °C induced a dislocation loop density of 3.5×10^{22} m^{-3} and 6.5×10^{22} m^{-3}, a black dot density of 2.2×10^{23} m^{-3} and 1.6×10^{23} m^{-3}, respectively, in the steels, and a high density ($<1 \times 10^{22}$ m^{-3}) of precipitates in matrix. Cavities could be observed in the specimens after the irradiation. It is suggested that the dislocation loops, the black dots, and the precipitates cause irradiation hardening, an increase in the yield strength and a decrease in the uniform elongation, in the 316LN steel irradiated at low temperature .

PROGRESS AND STATUS

1. Introduction

An austenitic stainless steel, 316LN-1G is the structural first wall and shield material for the International Thermonuclear Experimental Reactor (ITER) [1]. The proposed operational temperature range for the structure is from 100 °C to 250 °C, which is below the temperature regimes for void swelling and for grain boundary embrittlement. For austenitic stainless steels, neutron irradiation at low temperature increases the yield strength and decreases the uniform elongation, and fracture toughness. As reported earlier, the magnitudes of these changes are both temperature and dose dependent [2-3].
The objective of this study is to investigate microstructure of 316LN austenitic stainless steel irradiated at low temperatures up to 3 dpa in order to relate the microstructure to the changes in mechanical properties.

2. Experimental Procedure

The chemical composition of the 316LN used in this study falls within the specifications for the ITER reference grade (316LN-1G) as shown in Table 1. Standard 3-mm diameter transmission electron microscopy (TEM) disks were punched from 0.25-mm thick sheet stock, and then these disks were solution annealed. The disks were irradiated in the HFIR in the capsules of HFIR-MFE-JP-17 and -JP-18 to neutron fluences producing 3 dpa. These capsules were designed for irradiation temperatures of either 90 °C (capsule HFIR-MFE-JP18) or 250 °C (HFIR-MFE-JP-17) [4-6]. The helium concentration generated as a result of transmutation of nickel was about 65 appm; this is in the range expected for the ITER first wall blanket and shield structure after a neutron exposure of 3 dpa.

TEM specimens were thinned using an automatic Tenupol electropolishing unit in a shielded glove box. TEM disks were examined using a JEM-2000FX (LaB_6) transmission electron microscope. The foil thickness were measured by thickness fringes in order to quantify defect density values.

Table 1. Chemical compositions of 316LN (wt%)

Steel	Fe	Cr	Ni	Mo	Mn	Si	C	N
316LN	Bal.	17.4	12.3	2.3	1.8	0.46	0.024	0.06
316LN-1G	Bal.	17.0	12.0	2.3	1.6	0.50	0.015	0.06
		18.0	12.5	2.7	2.0		0.030	0.08

3. Results

3.1 Dislocations and dislocation loops

Fig. 1 shows dislocations or dislocation loops in 316LN before and after irradiation up to 3 dpa. The electron micrographs were taken with beam direction **B** close to <110>. Fig. 1(a) is a bright-field image in the unirradiated specimen, and Figs. 1(b) and 1(c) are dark-field images in the specimens irradiated at 90 °C and 250 °C, which are taken using a streak in the diffraction pattern arising from the faulted loops. The loops observed in specimens irradiated at 90 °C or 250 °C were Frank type faulted loops on {111} planes, which were identified by the weak beam dark-field image. The irradiation at 250 °C induced a slightly higher dislocation loop density of 6.5×10^{22} m^{-3} with a slightly smaller mean diameter of 7.0 nm compared with the irradiation at 90 °C. The total dislocation density, which means the total line length of loops per an unit volume, after irradiation at 250 °C is 1.4×10^{15} m^{-3}, which is about twice as high as the loop density observed after the 90 °C irradiation. The irradiation also induced small defect clusters (black dots) in the matrix.

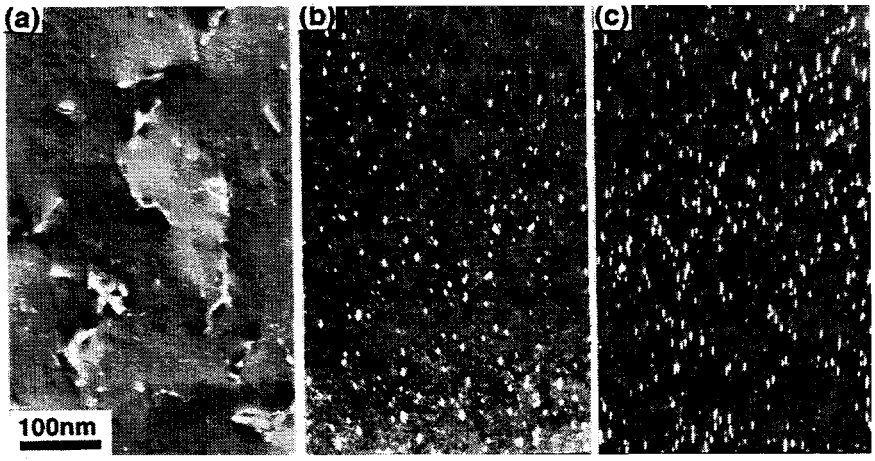

Fig. 1. Dislocations or dislocation loops in 316LN before and after HFIR irradiation up to 3 dpa. Micrograghs were taken with beam direction **B** close to <110>. (a) is a bright-field image in the unirradiated specimen, and (b) and (c) are dark-field images taken using a streak arising from faulted loops in the specimens irradiated at 90 °C and 250 °C

Fig. 2 shows the black dot defect in 316LN after irradiation up to 3 dpa. The number density and the mean diameter of black dots at 90 °C and 250 °C were 2.2×10^{23} m^{-3} and 2 nm, and 1.6×10^{22} m^{-3} and 2 nm, respectively. In the present work, the black dot density and the mean diameter were measured in relatively thick foils (t < 100 nm). The actual black dot number density and mean diameter may be somewhat higher and lower, respectively. The dislocation density in the unirradiated specimen and the dislocation loop density and the black dot density of the irradiated specimens are shown in Table 2.

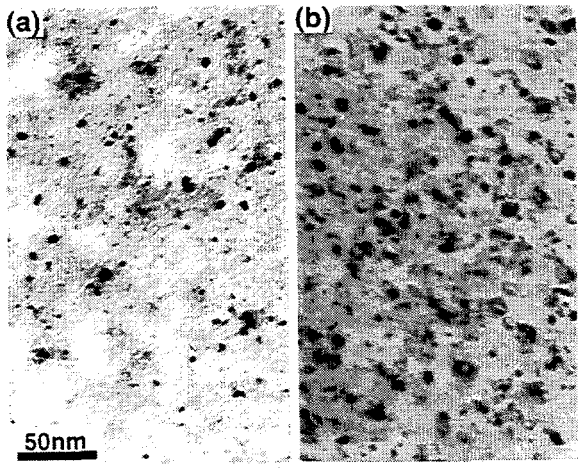

Fig. 2. The black dot in 316LN after HFIR irradiation up to 3 dpa. (a) and (b) are bright-field images in the specimens irradiated at 90 °C and 250 °C. The average thickness is about 100 nm.

Table 2. Summary of dislocation, dislocation loop, and black dot density of 316LN irradiated to 3 dpa. The average thickness of measured area is 100 nm.

Condition	Black Dot		Dislocation or dislocation loop		
	Number density (m^{-3})	Mean diameter (nm)	Number density (m^{-3})	Mean diameter (nm)	Total dislocation density (m^{-2})
Before irradiation	-	-	-	-	1×10^{14}
Irr. at 90 °C	2.2×10^{23}	2	3.5×10^{22}	7.6	8.3×10^{14}
Irr. at 250 °C	1.6×10^{23}	2	6.5×10^{22}	7.0	1.4×10^{15}

Fig. 3 shows another dark-field image in the specimen irradiated at 250 °C, which was obtained from a streak observed in the diffraction pattern. The defects were dislocation loops on {110} planes. The loops on {110} planes were observed only in the specimen irradiated at 250 °C. The number densities and the mean diameter of the loops is 1.2×10^{21} m^{-3} and 10.2 nm, respectively.

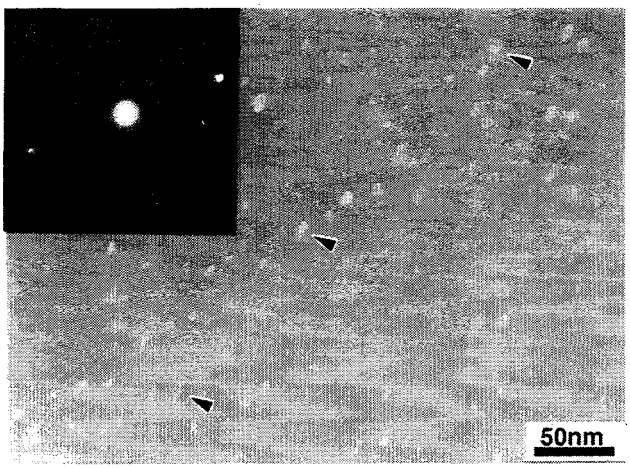

Fig. 3. Dark-field image formed using a streak observed in the diffraction pattern in the specimen irradiated at 250 °C in HFIR. Loops on {110} are observed.

3.2 Precipitate evolution

Fig. 4 shows the microstructures of 316LN before and after irradiation up to 3 dpa. As seen in Fig. 4, the annealed 316LN had no precipitate. The irradiation at both 90 °C and 250 °C induced precipitates, which could be identified as G phase from a spacing of the moiré fringe and the diffraction pattern. The number density and the mean diameter of G formed at 90 °C and 250 °C are 2.0×10^{22} m^{-3} and 5 nm, and 2.0×10^{22} m^{-3} and 7 nm, respectively.
As shown in Fig. 5, the irradiation at 90 °C and 250 °C also induced $M_{23}C_6$ carbide in the matrix but not on grain boundaries; these were identified from the spacing of the moiré fringe. The number density and the mean diameter of $M_{23}C_6$ at 90 °C and 250 °C are nearly equal, and the values are about $<1 \times 10^{19}$ m^{-3} and 14 nm, respectively. There is no clear difference in the precipitate densities between irradiation temperatures. The precipitates observed in the specimens are summarized in Table 3.

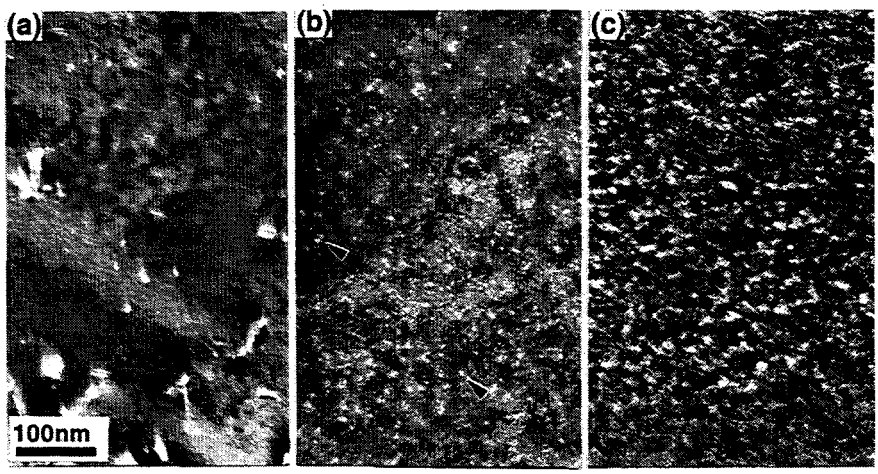

Fig. 4. Microstructure of 316LN before and after irradiation up to 3 dpa. (a) is a dark-field image in the unirradiated specimen, and (b) and (c) are dark-field images in the specimens irradiated at 90 °C and 250 °C. Precipitates are observed with moiré fringes in the specimens irradiated at 90 °C and 250 °C.

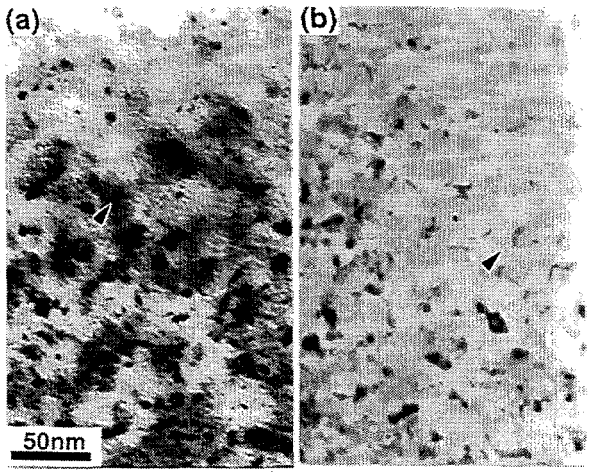

Fig. 5. $M_{23}C_6$ carbide in 316LN after HFIR irradiation up to 3 dpa. (a) and (b) are bright-field images in the specimens irradiated at 90 °C and 250 °C.

Table 3. Precipitate statistics before and after irradiation at 90 and 250 °C up to 3 dpa

Steel	ppt.	Before irradiation		After irradiation (90 °C)		After irradiation (250 °C)	
		Mean diameter (nm)	Number density (m^{-3})	Mean diameter (nm)	Number density (m^{-3})	Mean diameter (nm)	Number density (m^{-3})
316LN	$M_{23}C_6$	-	-	13	$<1x10^{19}$	14	$<1x10^{19}$
	G	-	-	5	$2x10^{22}$	7	$2x10^{22}$

4. Discussion

4.1 Microstructures

HFIR irradiation up to 3 dpa induced the dislocation loop density of about $5x10^{22}$ m^{-3} with mean diameter of 7 nm, as given in Table 2. The dislocation loops formed under irradiation both at 90 °C and 250 °C have been identified as Frank type faulted loops, which are lying on {111} planes with Burgers vectors of type $\boldsymbol{b} = (1/3)\mathbf{a}_o\langle 111\rangle$. The dislocation loop density at 90 °C is slightly higher than that at 250 °C . Previous studies have shown that the both the nature and number density of defects formed in type 316 austenitic stainless steel during neutron irradiation is strongly dependent on irradiation temperature [7-9], Zinkle et. al [7] characterize a low temperature regime as extending from the onset of vacancy motion (annealing Stage 3) up to the temperature where vacancy clusters created in the displacement cascade become thermally unstable (annealing Stage 5). The current study is within this low temperature regime. The number densities of faulted Frank loops reported here are consistent with the values of $\sim 5x10^{22}$ m^{-3} reported by Maziasz for irradiation at 60 °C and by Tanaka for irradiation at 300 °C.

At these low temperatures, the total dislocation density is dominated by faulted loops [10,11], and the total dislocation densities were calculated from the dislocation loop density and the mean diameter as $8.3x10^{14}$ m^{-2} and $1.4x10^{15}$ m^{-2} at 90 °C and 250 °C, respectively. These values are consistent with the results of previous analysis of austenitic stainless steels irradiated in HFIR [12].

At higher irradiation temperatures (> 450 °C), Frank loops tend to unfault to form the lower-energy perfect loop configuration with $\boldsymbol{b} = (1/2)\mathbf{a}_o\langle 110\rangle$ Burgers vectors, which can glide to interact and form network dislocations [7]. In this experiment, however, dislocation loops on {110} planes with mean size of > 10 nm were observed following irradiation at 250 °C. It seems that there is sufficient mobility at 250 °C for the unfaulting reaction, which is triggered by physical impingement of adjoining Frank loops as a result of loop growth [13], to occur for ~2% the Frank loop populations.

The irradiation also induced small defect clusters (black dots) in the matrix. The visibility of very small clusters depend on the foil thickness, the visible cluster density in very thin foils was higher than that found in thick foils [14]. In the present work, the black dot density and the mean diameter were measured in relatively thick foils (t ~ 80 nm). Therefore, the actual black dot number density and mean diameter may be somewhat higher and lower, respectively.

In general, there has been no evidence of fine precipitation in 316 type stainless steels after neutron irradiations at 55-250 °C at doses of >1-2 dpa [14,15]. The HFIR irradiation at 90 °C and 250 °C, however, induced precipitates, identified as G phase and $M_{23}C_6$ from a spacing of the moiré fringe and/or diffraction pattern, in the matrix and not on grain boundaries. G phase is a radiation-induced precipitate, according to ref.15, traces of G phase were also found in JPCA irradiated in HFIR at 300 °C. On the other hand, $M_{23}C_6$ is a radiation-enhanced thermal phase, and is produced more abundantly at lower temperatures during neutron irradiation [16].

4.2 Relation between microstructures and mechanical properties

Load elongation curves for SS-3 tensile specimens of 316LN irradiated and tested at 90 °C and 250 °C are shown in Fig. 6 and the corresponding tensile data are shown in Table 4 [17]. The radiation-induced changes in tensile properties are more severe at 250 °C than at 90 °C.

Table 4. Tensile properties of solution annealed 316LN

Dose dpa	Irr.Temp. °C	Test Temp. °C	YS MPa	UTS MPa	Eu %	Et %
0	-	25	298	582	62.0	68.5
0	-	90	285	516	50.2	57.2
0	-	250	214	451	40.8	51.3
2.9	83-101	90	610	674	37.7	45.0
2.9	83-101	90	605	677	37.0	46.1
3.0	250-300	250	760	764	11.7	18.8
3.0	250-300	250	724	735	12.7	20.8

Irradiation at ~90 °C increased the yield strength from ~285 MPa up to ~600 MPa, and resulted in a modest reduction in both the strain hardening rate and the uniform elongation. A larger increase in yield strength occurred for the irradiation at ~250 °C. Following an initial yield drop, uniform strain exceeded 10 % in spite of a very low rate of strain hardening. These data are plotted in Fig. 6(a) and the corresponding number density data for dislocation loops, black dots and precipitates are shown in Fig. 6(b). While the density of precipitates is nearly constant, the density of dislocation loops and black dots increase and decrease respectively with irradiation temperature.

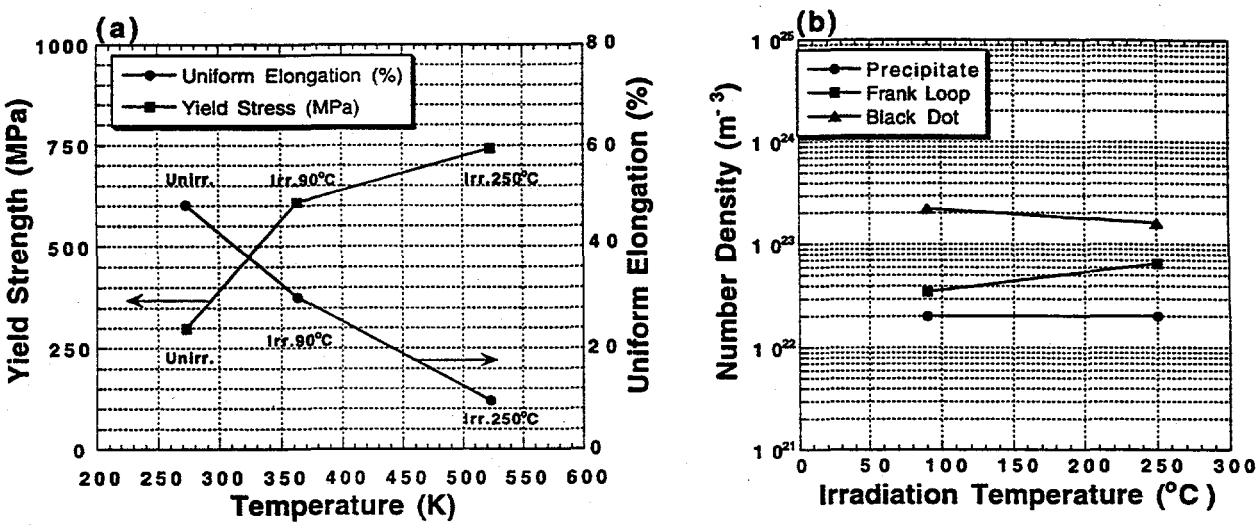

Fig. 6. Dependence of irradiation temperature on the dislocation loop density, the black dot density and the precipitate density; (a) , and the yield strength and the uniform elongation; (b).

According to the theory of hardening [18,19], the yield stress change due to dislocation loops, $\Delta\sigma_y$, is expressed the following equation:

$$\Delta\sigma_y = M\alpha\mu b(Nd)^{1/2},$$

where M, α, μ, b, N and d are the Taylor factor [18], barrier strength of obstacles, shear modulus, Burger's vector, density of dislocation loops and mean diameter of dislocation loops, respectively. The contributions of the Frank loops and black dots are as follows:

$$(\Delta\sigma_y)^{1/2} = (\Delta\sigma_{\text{Frank Loop}})^{1/2} + (\Delta\sigma_{\text{Black Dot}})^{1/2},$$

With the Taylor factor of 3.06 [20], the shear modulus of 58×10^3 MPa and the value of $\alpha_{\text{Black Dot}}$ = 0.146 [21], a value of $\alpha_{\text{Frank Loop}}$ = 0.47 and 0.55 are obtained at 90 °C and at 250 °C, respectively. These values of α = 0.47 and 0.55, which are obtained in the present work, are in good agreement with the data of Odette and Frey [22] and of Garner et al. [23]. Further measurements of the defect densities are in progress using thinner regions of the foil to improve visibility. Although the number densities of defect clusters and Frank loops change only slightly between 90 °C and 250 °C, there is significantly less strain hardening capacity at the higher temperature. This suggests that there is a tendency for dislocation channeling to occur at 250 °C and for deformation to be more homogeneous at 90 °C. Further analysis of these phenomenon is in progress.

ACKNOWLEDGMENTS

This research was supported in part by an appointment to the Oak Ridge National Laboratory Postdoctoral Research Associates Program administered jointly by the Oak Ridge Institute for Science and Education and Oak Ridge National Laboratory.

REFERENCES

1. A.F. Rowcliffe, "ITER Material Assessment Report for Stainless Steels", ITER Doc. G A1 DDD 1 97-12-08 W 0.2, December, 1997.
2. J.E. Pawel, A.F. Rowcliffe, D.J. Alexander, M.L. Grossbeck, and K. Shiba, J. Nucl. Mater., **233-237** (1996) 202-206
3. D.J. Alexander, J.E. Pawel, M.L. Grossbeck, A.F. Rowcliffe, and K. Shiba, "Fracture Toughness of Irradiated Candidate Materials for ITER First Wall/Blanket Structures: Summary Report", Fusion Reactor Materials Semiannual Report for Period Ending December 31, 1995, DOE/ER-0313/19, 1996, p. 204.
4. A.W. Longest, D.W. Heatherly, K.R. Thomas, and J.E. Corum, "Design and Fabrication of HFIR-MFE-JP Target Irradiation Capsules," Fusion Reactor Materials Semiannual Report for Period Ending March 31, 1991, DOE/ER-0313/10, 1991, p. 3.
5. A.W. Longest, D.W. Heatherly, J.E. Wolfer, K.R. Thomas, and J.E. Corum, "Fabrication and Irradiation of HFIR-MFE-JP-17, -18, and -19 Target Irradiation Capsules," Fusion Reactor Materials Semiannual Report for Period Ending September 30, 1991, DOE/ER-0313/11, 1992, p. 30.
6. A.W. Longest, D.W. Heatherly, K.R. Thomas, and J.E. Corum, "Fabrication and Irradiation of HFIR-MFE-JP Target Irradiation Capsules," Fusion Reactor Materials Semiannual Report for Period Ending March 31, 1992, DOE/ER-0313/12, 1992, p. 24.
7. S.J. Zinkle, P.J. Maziasz and R.E. Stoller, J. Nucl. Mater., **206** (1993) 266
8. M. Kiritani, Ultramicroscopy, **39** (1991) 135-159.
9. P.J. Maziasz and C.J. McHargue, Int. Mater. Rev., **32** (1992) 190.
10. H.R. Brager and J.L. Straalsund, J. Nucl. Mater., **46** (1973) 134.
11. P.J. Barton, B.L. Eyre and D.A. Stow, J. Nucl. Mater., **67** (1977) 181.
12. P.J. Maziasz, Effect of He Content on Microstructural Development in Type 316 Stainless Steel under Neutron Irradiation, ORNL-6121, Oak Ridge, TN (1985)
13. P.J. Maziasz and C.J. McHargue, Int. Mater. Rev., **32** (1987) 190.
14. S.J. Zinkle, J. Nucl. Mater., **150** (1987) 140-158.
15. P.J. Maziasz, Am. Nucl. Soc. Trans., **39** (1981) 433.
16. P.J. Maziasz, J. Nucl. Mater., **169** (1989) 95.
17. Brager, F.A. Garner, F.R. Gilbert, J.E. Flinn and W.G. Wolfer, in : Radiation Effects in Breeder Reactor Structural Materials, eds. M.L. Bleiberg and J.W. Bennet (TMS-AIME, New York, 1977) p. 727.
18. U.F. Kocks, Metall. Trans., **1** (1970) 1121.
19. P.M. Kelly, International Metallurgical Reviews, Vol.18 (1973) 31
20. H.R. Higgy and F.H. Hammad, J. Nucl. Mater., **55** (1975) 177.
21. R.L. Sindelar, "Reactor Materials Program - Microstructural and Mechanical Response of Types 304, 304L, and 308 Stainless Steels to low temperature Neutron Irradiation (U)", **WSRC-TR-93-196**, June (1993)
22. G.R. Odette and G. Frey, J. Nucl. Mater., **85-86** (1979) 817
23. F.A. Garner, M. Hamilton, N. Panayotou, G. Johnson, J. Nucl. Mater., **103-104** (1981) 803

6.0 INSULATING CERAMICS AND OPTICAL MATERIALS

No contributions.

7.0 SOLID BREEDING MATERIALS

POSTIRRADIATION EXAMINATION OF BERYLLIUM PEBBLES — D. S. Gelles
(Pacific Northwest National Laboratory)*

OBJECTIVE

The purpose of this work was to determine the effects of irradiation on prototypic beryllium pebbles. Such pebbles are under consideration as the neutron multiplier medium in the European Fusion Technology Program Helium Cooled Pebble Bed (HCPB) Blanket.

SUMMARY

Postirradiation examinations of COBRA-1A beryllium pebbles irradiated in the EBR-II fast reactor at neutron fluences which generated 2700-3700 appm helium have been performed. Measurements included density change, optical microscopy, scanning electron microscopy, and transmission electron microscopy. The major change in microstructure is development of unusually shaped helium bubbles forming as highly non-equiaxed thin platelet-like cavities on the basal plane. Measurement of the swelling due to cavity formation was in good agreement with density change measurements.

PROGRESS AND STATUS

Introduction

A large number of beryllium specimens have been irradiated in U.S. DOE Office of Fusion Energy Sciences (OFES) experiments in the Experimental Breeder Reactor II (EBR-II) in Idaho Falls, ID, and the Fast Flux Test Facility (FFTF) in Hanford, WA. Due to lack of funding, most of those specimens have never been tested, but DOE still retains an interest in the results. With the increased difficulty for performing irradiation experiments, due in part to the shutdown of FFTF and EBR-II and other reactors worldwide, these specimens are becoming very valuable. The German fusion materials development program centered at Forschungszentrum Karlsruhe INR has been concentrating efforts on design of a fusion blanket, using beryllium pellets, an intermediate product in the production of high grade beryllium, as a neutron multiplier. An EBR-II test, called COBRA-1A, included four beryllium pebble product forms, and thereby provides fast neutron irradiated materials for postirradiation testing. Therefore, Forschungszentrum Karlsruhe INR has concluded that it is efficient use of their available funds to invest in the testing of some of these specimens. This report provides results for that testing program.

The program is divided into three phases:

I. Characterization of beryllium pebbles irradiated in the COBRA 1-A experiment, including density change measurement, microstructural examination, helium and tritium release response on heating and neutronic analysis.

II. Removal of beryllium cylindrical specimens with 97 and 100% of theoretical density from capsules irradiated in FFTF experiments and containing lithium as a heat transfer medium.

*Pacific Northwest National Laboratory is operated for the U.S. Department of Energy by Battelle Memorial Institute under Contract DE-AC06-76RLO 1830.

III. Characterization of the FFTF irradiated beryllium specimens. Due to funding limitations, this is to be restricted to density change measurements.

Experimental Procedure

EBR-II

The COBRA-1A vehicle, irradiated in row 2 of EBR-II starting on November 26, 1992 with run 168, contained a number of beryllium specimens in canisters C03 and D03 located in below core positions in capsules B-390 and B-391, respectively. Both capsules were of weeper design, so that reactor coolant was in direct contact with each canister, and canisters were helium filled to provide a heat transfer medium. Experimental details are provided in reference [1]. Capsules B-390 and B-391 were removed from reactor upon removal of the COBRA-1A2 vehicle on September 26, 1994. At that time, EBR-II ceased to operate. Neutron dosimetery and damage calculation for these irradiations are included in reference [2].

Canisters C03 and DO3 contained beryllium in several product forms: 1 mm pebbles, 3 mm pebbles, 5 mm pebbles, 7.6 mm diameter x 20 mm right cylinders and 7.7 mm diameter x 6 mm right cylinders. (The cylinders were of two densities, 100% and 97% and were used for other purposes.) Pebbles were from two sources, Brush Wellman in all sizes and Nippon Gaishi Co. (NGK) at 1 mm. Pebble details, as supplied by the manufacturer are provided in Table 1.

The specimen loading and capsule position within EBR-II were somewhat different for the two capsules. Radiographs of the capsules are provided in Figure 1. In both cases, the bottom of the capsule is at the right and careful observation reveals that in each case the bottom contains a layer of 1 mm pebbles, with the remaining pebbles distributed amongst the cylindrical specimens. The 1 mm pebbles in capsule C03 were from Brush Wellman whereas the 1 mm pebbles in capsule D03 were from NGK. Because reactor neutron flux varied as a function of vertical position, minor differences in dose developed for the 3 mm pebbles in C03 and the 5 mm pebbles in D03. In each capsule, only seven 5 mm pebbles were included whereas about 75 3 mm pebbles and over 150 1 mm pebbles from each manufacturer were irradiated. Accumulated fluences were estimated based on capsule position and information in reference 2, giving 3.77×10^{22} n/cm^2 (E > 0.1 MeV) for Brush Wellman 1 mm pebbles, 3.62×10^{22} n/cm^2 for NGK 1 mm pebbles, 4.31×10^{22} n/cm^2 (E > 0.1 MeV) for Brush Wellman 3 mm pebbles, and 4.88×10^{22} n/cm^2 (E > 0.1 MeV) for Brush Wellman 5 mm pebbles. The operating temperatures are estimated as follows: 379°C for C03 and 378°C for D03. The irradiation temperatures are therefore described as 380°C in the remainder of this report.

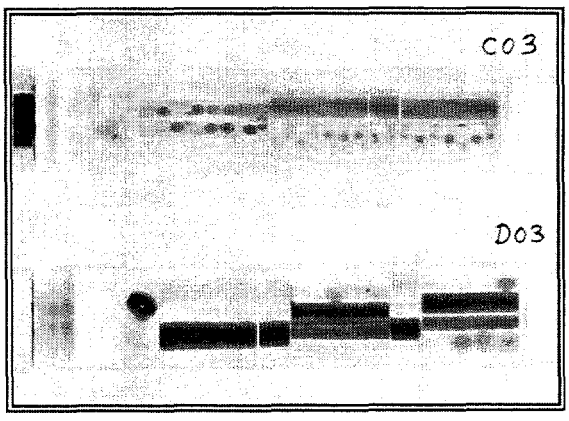

Figure 1. Specimen loading in the COBRA-1A vehicle as shown by neutron radiography with the bottom of the subcapsule filled with 1 mm pebbles located at the right .

In a companion report, [3] the production of ^{4}He and tritium from beryllium in the COBRA-1A2 irradiation based on calculations is provided.

Table 1. Pebble details

Type	Supplier & Batch #	Size	Major Impurities	Minor impurites (in ppm)
1 mm	Brush Wellman 826-64-5	1 ± 0.2 mm -16 +20 mesh	0.094 wt% BeO 0.047 % C 0.06 % O_2	750 Mg, 565 Fe, 380 Si, 365 Al, 110 Cr, 105 Zr, 95 Mn, 90 Ti, 80 Ni, 70 Zn, etc.
3 mm	Brush Wellman 826-64-3	3 mm -6 +7 mesh	0.020 wt% BeO 0.038 % C 0.013 % O_2	2400 Mg, 375 Al, 370 Fe, 250 Si, 105 Zr, 90 Mn, 85 Cr, 85 Zn, 75 Ti, 65 Ni, etc.
5 mm	Brush Wellman 826-64-4	5 mm -3½ +4 mesh	0.094 wt% BeO 0.047 % C 0.06 % O_2	420 Fe, 400 Mg, 390 Al, 230 Si, 95 Mn, 90 Zr, 80 Zn, 75 Cr, 70 Ti, 60 Ni, etc.
1 mm	Nippon Gaishi Co. 4310	1 ± 0.3 mm 0.72 to 1.10 mm	1.51 wt% BeO 0.023 % C	1100 Fe, 780 Al, 300 Si, 170 Mg

FFTF

A description of specimen loadings for all molybdenum alloy (TZM) subcapsules containing beryllium specimens in depleted lithium and progress on disencapsulation and density change measurements on selected specimens are provided in a companion report. [4]

Experimental Results

Optical Microscopy (OM) and Scanning Electron Microscopy (SEM)

In order to gain an understanding of pebble to pebble conformity and determine surface degradation due to irradiation, several specimens were selected for optical examination and one 3 mm pebble of each of the irradiated and unirradiated conditions was then examined by SEM. Figure 2 provides examples of OM; in each case different pebbles are shown with 1 mm pebbles above and 3 mm pebbles below. The figure demonstrates that beryllium pebbles vary significantly in size and many contain surface irregularities, including depressions and seams.

One 3 mm specimen of each of the unirradiated and irradiated pebbles were chosen for SEM examination, and the results are provided in Figure 3 showing an unirradiated pebble above and an irradiated pebble below at several magnification levels. Comparisons between these pebbles reveal that both contain two types of shallow surface depressions, on the order of 100 µm in diameter and on the order of 5 µm in diameter, and specimen #6 has many particles adhered to the surface. The adhered particles are assumed to be dust and dirt accummulated during handling, and therefore both samples contain similar features. Evidence for fine surface porosity

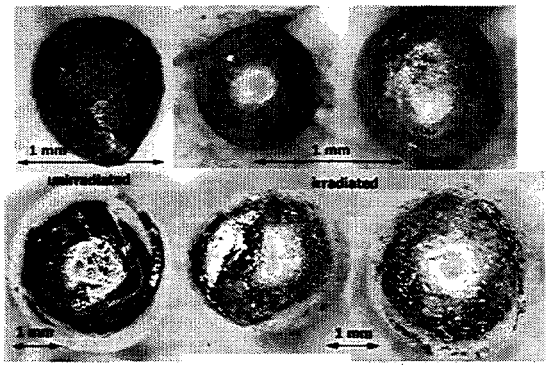

Figure 2. Optical photomicrographs of unirradiated and irradiated beryllium pebbles

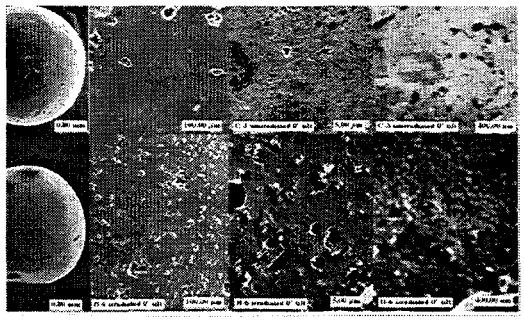

Figure 3. SEM photomicrographs of unirradiated and irradiated 3 mm beryllium pebbles showing the surface features at increasing magnification

due to irradiation was not found.

Swelling in 3 mm pebbles

Four irradiated pebbles from the C03 capsule were selected for density measurement and compared with four unirradiated specimens. Specimens were weighed in air and in water at least three times, until reasonable consistency was obtained because imperfect wetting and air bubble adherence were found to be problems. The results of the measurements are listed in Table 2 so that the density following irradiation (V) was found to be 1.79474 ± 0.01130 and the unirradiated density (V_0) was 1.80969 ± 0.03370. The resultant swelling $(V-V_0)/V_0$ was 1.45%, of the same magnitude as the uncertainty for the unirradiated density (1.86%) but larger than the uncertainty for the irradiated density (0.6%). The large uncertainties may either be due to the surface conditions (bubble adherence) or variations in impurity concentrations within the pebbles. However, given the larger scatter in the unirradiated samples, the latter cause is more likely.

Table 2. Density measurements for 3 mm pebbles

Sample	Condition	density g/cm^2	standard deviation
1	380°C, 4.31x10^{22} n/cm^2	1.78818	± 0.02987
2	"	1.8114	± 0.0096
3	"	1.79206	± 0.02958
4	"	1.7873	± 0.02691
5	unirradiated	1.83124	± 0.02032
6	"	1.77046	± 0.01331
7	"	1.8435	± 0.0152
8	"	1.79354	± 0.00661

Transmission Electron Microscopy (TEM)

Several 3 mm pebbles were ground to disks approximately 0.12 mm thick and thinned by electropolishing in a solution of 75 parts nitric acid, 15 parts sulfuric acid, 15 part hydrochloric acid in 750 parts ethylene glycol at 9 to 13 V with the solution cooled to -20°C. Pitting presumed to be due to internal flaws was found to be a problem, but suitably thin areas were obtained in several specimens prepared for examination following brief repolishing of pitted specimens. Two unirradiated specimens and two irradiated specimens were thinned and polished providing one good specimen and one poor specimen with still another specimen providing sufficient thin area to confirm observations on the other two specimens.

Examinations revealed several noteworthy features. In the irradiated specimens, grain size was found to be large, with a low dislocation density but containing many small features tentatively identified as bubbles lying as plate-like features on the basal plane. Several examples were also found of large regions as big as 5 μm in diameter with amorphous diffraction patterns. Such regions were found to be rich in Si, Al, Mg and Mn, indicating that impurities were non-uniformly distributed and that the impure regions became amorphous due to irradiation. In comparison, the dislocation density was greater in the unirradiated condition, with evidence of subgrain development. Also, a region containing impurity was found. Therefore, irradiation is found to reduce the dislocation density significantly, to form a fine distribution of unusually shaped bubbles and to amorphize large regions of impurity.

Examples of the structure found following irradiation are shown in Figures 4 and 5. The dislocation structure is shown in Figure 4 showing a region in bright field in a) and another region in dislocation dark field contrast in b). The bright field image demonstrates a loose tangle of dislocations, whereas the dark field image also shows a high density of smaller features in weaker contrast. Previously, these weaker features had been identified as c-type dislocations loops. [5] However, when the foil was tilted to bring these weaker features edge-on, they were found to image as cavities. A sequence is provided in Figure 5 using void contrast showing these features

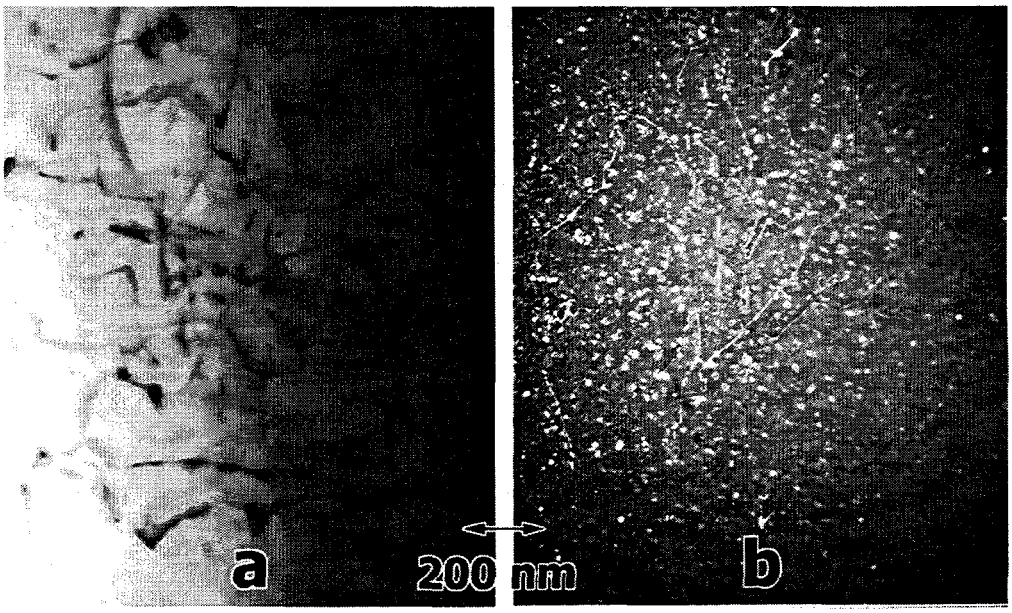

Figure 4. Microstructures in an irradiated 3 mm beryllium pebble showing a) the dislocation structure in (1$\bar{2}$10) bright field contrast and b) (0001) dislocation dark field contrast

edge-on in (a), tilted off 7° in (b) and tilted off 12° in (c). Figure 5d provides the unusual situation where the features are shown in strong contrast with the features tilted edge-on and demonstrates that the features are probably internally stressed. It can therefore be concluded that the weaker features are probably unusually shaped helium bubbles, the planar surfaces of which can be imaged weakly in dislocation contrast.

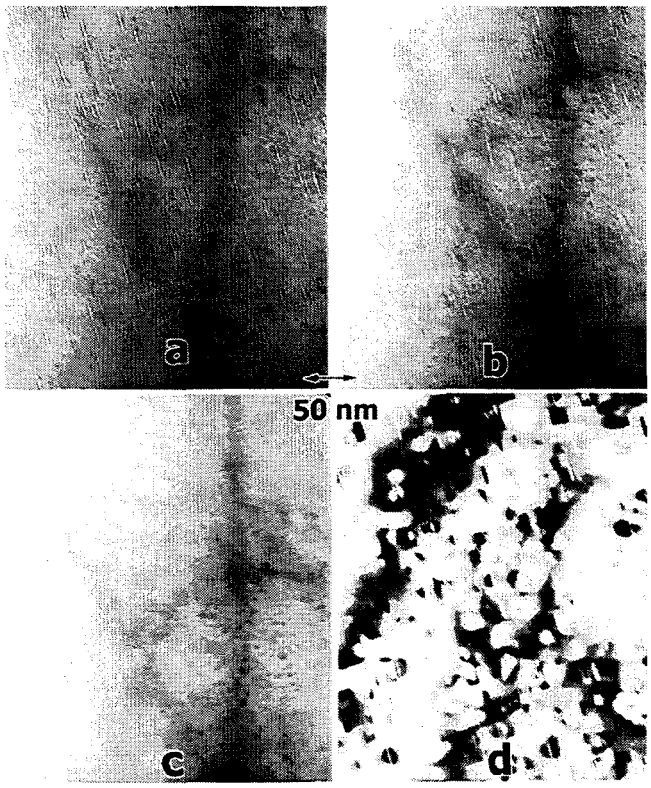

Figure 5. Void swelling in an irradiated 3 mm beryllium pebble tilted parallel to the basal plane so that the voids are edge on in a), tilted off 7° in b), tilted off a further 5° in c) and shown edge on in strong multibeam contrast in d)

Discussion

Effects of Irradiation on Microstructure

It was previously assumed that irradiation would cause microporosity, and c-type loop formation. The added complexity of neutron damage near pebble surfaces was expected to enhance transmutation possibly leading to enhanced surface microporosity. The present SEM examination appears to indicate that surface roughening due to irradiation is negligible to resolutions on the order of 100 nm. TEM did not provide microstructural information regarding cavitation at grain boundaries, but it now appears that swelling in the form of helium bubbles takes on a unusual highly non-equiaxed geometry of thin platelets on the basal plane. Bubbles are approximately 25 nm in diameter and 4 nm in thickness. These features had not been identified previously as bubbles, perhaps because the helium levels were lower, estimated at 80 appm helium following irradiation at 400°C to 8 dpa (1.8×10^{22} n/cm^2) below core in FFTF. In the present experiment, the fluence was approximately 4.3×10^{22} n/cm^2 below core in EBR-II, a similar reactor, and therefore the helium level is expected to be about 3 times larger, and is estimated at 3000 appm. It can be noted that the earlier experiment produced significantly coarser damage structure, possibly because the irradiation temperature was higher. Careful review of the earlier micrographs shows examples of contrast similar to that found in the present experiment. The differences in interpretation may be compatible if it is possible that c-type loops accumulate gases such as helium a tritium, eventually becoming highly anisotropic bubbles.

In the current work, the bubbles were measured to provide diameter, number density and an estimate of swelling. It was found that the bubbles ranged in diameter from 5 to 25 nm, with a mean diameter of 11.9 nm at a number density of 2.0×10^{16} cm^{-3}. If one were to assume spherical voids with these diameters, this corresponded to 2.5% swelling, but as the bubble shape was flattened, with an aspect ratio for thickness to diameter of about 4/25 or .16, the actual swelling can be estimated at about 0.4 of the spherical value or about 1%. Therefore, the measured density change of 1.45% appears to be largely due to the development of internal bubbles estimated at 1% swelling.

Swelling may also originate from the transformation of impurity regions from a crystalline to an amorphous phase. It is difficult to estimate the volume fraction of impurity regions or to estimate the resultant swelling due to phase transformation, so the magnitude of the swelling change cannot be estimated at this time.

If much of the helium and tritium is bound in bubbles, then release of these gases from heated specimens can be expected to occur only after bubble coarsening and therefore will be observed mainly at higher temperatures. Examination of heated specimens may allow verification of such a prediction.

CONCLUSIONS

Post irradiation examinations of COBRA-1A beryllium pebbles irradiated in the EBR-II fast reactor at neutron fluences which generated 2700-3700 appm helium have been performed. Measurements included density change, optical microscopy, scanning electron microscopy, and transmission electron microscopy. The major change in microstructure is development of unusually shaped helium bubbles forming as highly non-equiaxed thin platelet-like cavities on the basal plane. Measurement of the swelling due to cavity formation was in good agreement with density change measurements.

FUTURE WORK

This work is completed.

REFERENCES

1. M. L. Hamilton, R. M. Ermi, and C. R. Eiholzer, DOE/ER-0313/14 (1993) 3.

2. L. R. Greenwood and R. T. Ratner, DOE/ER-0313/21 (1996) 225.

3. L. R. Greenwood, "Production of ^{4}He and Tritium from Be in the COBRA-1A2 Irradiation," in this semiannual report.

4. D. S. Gelles, H. Tsai, and R. M. Ermi, in this semiannual report.

5. D. S. Gelles and H. L. Heinisch, J. Nucl. Mater. V191-4 (1992) 194.

NEUTRON IRRADIATION OF BERYLLIUM PEBBLES — D. S. Gelles, H. Tsai[1], and R. M. Ermi (Pacific Northwest National Laboratory)* and (Argonne National Laboratory)[1]

OBJECTIVE

The purpose of this work was to provide quantitative stepped helium release response from prototypic irradiated beryllium pebbles. Such pebbles are under consideration as the neutron multiplier medium in the European Fusion Technology Program Helium Cooled Pebble Bed (HCPB) Blanket.

SUMMARY

Seven subcapsules from the FFTF/MOTA 2B irradiation experiment containing 97 or 100% dense sintered beryllium cylindrical specimens in depleted lithium have been opened and the specimens retrieved for postirradiation examination. Irradiation conditions included 370°C to 1.6×10^{22} n/cm^2, 425°C to 4.8×10^{22} n/cm^2, and 550°C to 5.0×10^{22} n/cm^2. TEM specimens contained in these capsules were also retrieved, but many were broken. Density measurements of the cylindrical specimens showed as much as 1.59% swelling following irradiation at 500°C in 100% dense beryllium. Beryllium at 97% density generally gave slightly lower swelling values.

PROGRESS AND STATUS

Introduction

Twenty-two subcapsules containing beryllium specimens have been irradiated in U.S. DOE Office of Fusion Energy Sciences (OFS) experiments in the Fast Flux Test Facility (FFTF) in Hanford, WA. With the increased difficulty for performing irradiation experiments, due in part to the shutdown of FFTF and EBR-II and other reactors worldwide, these specimens are becoming very valuable. The German fusion materials development program centered at Forschungszentrum Karlsruhe INR has been concentrating efforts on design of a fusion blanket using beryllium as a neutron multiplier. Therefore, Forschnungszentrum Karlsruhe INR has concluded that it is efficient use of their available funds to invest in the testing of some of these specimens. This report is intended to provide details concerning FFTF experimental design, subcapsule specimen loading, specimen removal operations from seven of the capsules, and density change measurements on selected specimens from those capsules.

Experimental Details

It was possible to obtain permission to include beryllium specimens in the U.S./DOE OFS irradiations of fusion reactor materials in FFTF Materials Open Test Assembly (MOTA) irradiations 2A and 2B performed in 1989 and 1991, respectively. The MOTA design placed specimens or their containers in direct contact with flowing reactor sodium, and therefore it was decided to irradiate the beryllium samples in subcapsules made from the molybdenum alloy TZM and in direct contact with depleted lithium in order to minimize impurity pickup. Two specimen geometries were irradiated: right solid cylinders of pressed and sintered beryllium provided by

*Pacific Northwest National Laboratory is operated for the U.S. Department of Energy by Battelle Memorial Institute under Contract DE-AC06-76RLO 1830.

G.L Longhurst of INEEL, Idaho Falls, ID, and transmission electron microscopy (TEM) disks. The sintered beryllium specimens were prepared at EG&G Rocky Flats with manufacturing details previously described by Beeston etal [1]. Sintered densities were either 80, 85, 97 or 100%. Specimens were all 0.300 inches in diameter by either 0.25, 0.80 or 0.1.20 inches in height. TEM specimens were 3mm (0.125 inch) disks of pure beryllium punched from a sheet 0.010 inches thick made from A65B powder and called PF60 foil from Brush Wellman or of niobium beryllide ($Be_{12}Nb$) obtained from S.M. Bruemmer (PNNL) for subcapsules containing 1.20 inch specimens. Punching was done at room temperature, with the understanding that microcracking might result. Specimen loading details are provided in Table 1 and dosimetery estimates are provided in a companion report beginning on page 64.

It was decided to attempt to open seven of the TZM capsules at Argonne National Laboratory using facilities previously used to open similar TZM capsules containing vanadium alloys in lithium. The seven capsules are defined in Table 2. These capsules were selected because they either contained 97 or 100% dense beryllium cylinders as well as TEM specimens. Note that the TEM disks in V491 are of $Be_{12}Nb$ whereas all other TEM specimens are of sintered beryllium at the same density as the larger specimens in the subcapsule. The disassembly was conducted in an alpha-free air cell. Subcapsule V491 was opened first, as a test case, and then the remaining subcapsules were opened. Capsules were opened with a tube cutter and the contents with subcapsule remnants, in a wire basket, were transferred to a beaker containing liquid ammonia. After dissolution of the lithium, the wire basket was transferred into an alcohol bath for cleaning. After drying, an inventory of the contents of the wire basket was made. Specimens were then placed in vials and transferred to PNNL.

Right cylinder specimens 0.250 inches in height from the capsules describe in Table 2 were selected for density measurements. (Larger specimens were not expected to fit into the density cell.) Density measurements were performed in a cell designed for larger specimens using water as a buoyancy medium. Calibration was based on measurements using laboratory standards.

Results

Specimen retrieval from FFTF subcapsules was very successful. There were two types of specimens in each capsule: cylinders and TEM disks. The condition of the retrieved cylinders appeared to be good, i.e., without obvious cracks or deformation as seen through the hot cell window with a surveyor's telescope. The condition of the TEM disks was mixed: some were intact but some were fractured. The fractures appeared to have occurred during irradiation as the broken disks could be seen immediately after the lithium dissolution before any handling. As many of the broken pieces were collected as possible in case good uses could be found for them. Very small pieces, i.e., less than ≈¼ the size of a full disk, had a tendency to fall through the mesh screen used to contain the specimens. These very small pieces were therefore impossible to retrieve. An inventory of specimens recovered from the capsules is provided in Table 2. Therefore, right cylinders appeared in excellent shape, and at least one whole TEM specimen was obtained from each capsule, with better success retrieving TEM specimens from capsules irradiated at 370°C, indicating that irradiation was probably responsible for TEM specimen degradation.

Results of density measurements on right cylinder specimens 0.250 inches in height are provided in Table 3. The results shown in Table 3 demonstrate that swelling is highest following irradiation at 550°C, with values between 1.23 and 1.59%, the higher value corresponding to the

fully dense condition. Following irradiation at 425, the swelling is found to be lower, between 0.23 and 0.51%, again with the higher value corresponding to the fully dense condition. The lowest swelling observed was for specimens irradiated at 370°C to approximately one third the fluence, where swelling was between 0.13 and 0.29%, but this time the 97% dense specimen showed higher swelling. It can be noted that differences on successive measurements were less than 0.003%.

Table 1. Beryllium containing subcapsules in fusion reactor materials irradiation tests

Irrad. Vehicle	Packet ID	Dimensions (in.)	Contents including Li mass (in gms.)
MOTA 2A	V460	.375 OD x 2.5	2 0.30" Be cylinders & 3 TEMs/Li (.19)
"	V461	.375 OD x 2.5	2 0.30" Be cylinders & 3 TEMs/Li (.19)
"	V462	.375 OD x 2.5	2 0.30" Be cylinders & 3 TEMs/Li (.18)
"	V463	.375 OD x 2.5	2 0.30" Be cylinders & 3 TEMs/Li (.18)
"	V464	.375 OD x 2.5	2 0.30" Be cylinders & 3 TEMs/Li (.19)
"	V458	.375 OD x 1.8	0.30" Be cylinder/Li (.14)
MOTA 2B	V308	.375 OD x 2.5	4 0.30" Be cylinders/Li (.22)
"	V309	.375 OD x 2.5	4 0.30" Be cylinders/Li (.21)
"	V310	.375 OD x 2.5	2 0.30" Be cylinders & 12 TEMs/Li (.21)
"	V311	.375 OD x 2.5	2 0.30" Be cylinders & 7 TEMs/Li (.21)
"	V312	.375 OD x 2.5	0.30" Be cylinder & 7 TEMs/Li (.23)
"	V487	.375 OD x 2.5	4 0.30" Be cylinders/Li (.21)
"	V488	.375 OD x 2.5	4 0.30" Be cylinders/Li (.24)
"	V489	.375 OD x 2.5	2 0.30" Be cylinders & 12 TEMs/Li (.21)
"	V490	.375 OD x 2.5	2 0.30" Be cylinders & 7 TEMs/Li (.21)
"	V491	.375 OD x 2.5	0.30" Be cylinder & 3 TEMs/Li (.24)
"	V566	.375 OD x 2.5	4 0.30" Be cylinders/Li (.23)
"	V567	.375 OD x 2.5	3 0.30" Be cylinders & 2 Discs/Li (.22)
"	V568	.375 OD x 2.5	2 0.30" Be cylinders & 11 TEMs/Li (.23)
"	V569	.375 OD x 2.5	3 0.30" Be cylinders & 6 TEMs/Li (.20)
"	V570	.375 OD x 2.5	0.30" Be cylinder & 3 TEMs/Li (.23)
"	V571	.375 OD x 2.5	0.30" Be cylinder/Li (.24)

Table 2. Inventory of specimens retrieved

Capsule No.	Irradiation Conditions	Loading	Retrieved
V310	370°C, 1.59×10^{22}	2 cylinders (97%) 12 TEM disks	2 cylinders 11 whole TEM disks
V311	370°C, 1.59×10^{22}	2 cylinders (100%) 7 TEM disks	2 cylinders 7 whole TEM disks
V489	425°C, 4.76×10^{22}	2 cylinders (97%) 12 TEM disks	2 cylinders 4 whole TEM disks 3 ≈50% TEM pieces 2 <50% TEM pieces
V490	425°C, 4.76×10^{22}	2 cylinders (100%) 7 TEM disks	2 cylinders 2 whole TEM disks 4 ≈50% TEM pieces 2 <50% TEM pieces
V491	425°C, 4.76×10^{22}	1 cylinder (100%) 3 TEM disks ($Be_{12}Nb$)	1 cylinder 1 whole TEM disk 2 ≈50% TEM pieces
V568	550°C, 4.95×10^{22}	2 cylinders (97%) 11 TEM disks	2 cylinders 6 whole TEM disks 5 ≈70% TEM pieces 1 ≈50% TEM pieces
V569	550°C, 4.95×10^{22}	2 cylinders (100%) 6 TEM disks	2 cylinders 2 whole TEM disks 3 ≈70% TEM pieces 3 <50% TEM pieces

CONCLUSIONS

Seven subcapsules from the FFTF/MOTA 2B irradiation experiment containing 97 or 100% dense sintered beryllium cylindrical specimens in contact with depleted lithium have been opened and the specimens retrieved for post-irradiation examination. Irradiation conditions included 370°C to 1.6×10^{22} n/cm^2, 425°C to 4.8×10^{22} n/cm^2 and 550°C to 5.0×10^{22} n/cm^2.

TEM specimens contained in these capsules were also retrieved, but many were broken. Higher irradiation temperatures resulted in more breakage indicating that irradiation was probably responsible for specimen degradation.

Density measurements of the cylindrical specimens showed as much as 1.59% swelling following irradiation at 550°C in 100% dense beryllium. Beryllium at 97% density generally gave slightly lower swelling values. A limited inventory of irradiated beryllium specimens for microstructural examination is now available, including 97% dense and 100% dense pure beryllium as well as $Be_{12}Nb$.

Table 3. Results of density measurements on 0.200 inch right cylinders either unirradiated or irradiated in selected FFTF/MOTA 2B subcapsules. Results for two successive measurements on the same sample are shown.

Subcapsule	Reactor Conditions (°C, n/cm^2 E>0.1 MeV)	Form	weight in air (mg)	weight in liquid (mg)	Density (gm/cm^3)	Result
Unirr.		100% Be	535.789 535.792	247.62 248.08	1.869674 1.868958	Average 1.869316
Unirr.		97% Be	532.899 532.961	245.019 245.334	1.861462 1.859638	Average 1.86055
V310	370°C, 1.59x10^{22}	97% Be	527.59252 7.548	241.895 241.88	1.857009 1.853378	Swelling 0.29%
V311	370°C, 1.59x10^{22}	100% Be	511.399 511.305	236.164 236.184	1.868426 1.865169	Swelling 0.13%
V489	425°C, 4.76x10^{22}	97% Be	525.949 525.877	241.432 241.172	1.858902 1.853756	Swelling 0.23%
V490	425°C, 4.76x10^{22}	100% Be	531.479 531.192	244.235 244.429	1.860613 1.859051	Swelling 0.51%
V568	550°C, 4.95x10^{22}	97% Be	523.434 523.27	237.339 237.182	1.839821 1.835650	Swelling 1.23%
V569	550°C, 4.95x10^{22}	100% Be	516.718 516.655	234.394 234.663	1.840474 1.838780	Swelling 1.59%

FUTURE WORK

This work will be continued when further funding is available.

ACKNOWLEDGEMENTS

This work was funded by Forschungszentrum Karlsruhe under project 26929 with Battelle Pacific Northwest National Laboratory entitled, "Post-Irradiation Examination of Beryllium". This project was under the direction of Prof. M. Dalle Donne.

REFERENCES

1. J. M. Beeston, G. R. Longhurst and R. S. Wallace, J. Nucl. Mater., 195 (1992) 102.

STEPPED-ANNEAL HELIUM RELEASE IN 1-MM BERYLLIUM PEBBLES FROM COBRA-1A2 - B. M. Oliver (Pacific Northwest National Laboratory)*

OBJECTIVE

The purpose of this work was to provide quantitative stepped helium release response from prototypic irradiated beryllium pebbles. Such pebbles are under consideration as the neutron multiplier medium in the European Fusion Technology Program Helium Cooled Pebble Bed (HCPB) Blanket.

SUMMARY

Stepped-anneal helium release measurements on two sets of fifteen beryllium pebbles irradiated in the Experimental Breeder Reactor - II (EBR-II) at Argonne National Laboratory - West (ANL-W), are reported. The purpose of the measurements was to determine the helium release characteristics of the beryllium using larger sample sizes and longer anneal times relative to earlier measurements. Sequential helium analyses were conducted over a narrower temperature range from approximately 800°C to 1100°C in 100°C increments, but with longer anneal time periods. To allow for overnight and unattended operation, a temperature controller and associated circuitry were added to the experimental setup.

Observed helium release was nonlinear with time at each temperature interval, with each step being generally characterized by an initial release rate followed by a slowing of the rate over time. Sample Be-C03 showed a leveling off in the helium release after approximately 3 hours at a temperature of 890°C. Sample Be-D03, on the other hand, showed a leveling off only after ~12 to 24 hours at a temperature of 1100°C. This trend is consistent with that observed in earlier measurements on single microspheres from the same two beryllium lots. None of the lower temperature steps showed any leveling off of the helium release.

Relative to the total helium concentrations measured earlier, the total helium releases observed here represent approximately 80% and 92% of the estimated total helium in the C03 and D03 samples, respectively.

PROGRESS AND STATUS

Introduction

Beryllium pebbles are being considered for the neutron multiplier medium in the European Fusion Technology Program Helium Cooled Pebble Bed (HCPB) Blanket. That design is also being considered for testing in ITER. The pebbles to be used are an inexpensive form

*Pacific Northwest National Laboratory is operated for the U.S. Department of Energy by Battelle Memorial Institute under Contract DE-AC06-76RLO 1830.

of beryllium produced in an intermediate step of the production of higher purity beryllium. The opportunity to obtain helium release response from prototypic fast neutron irradiated pebbles became possible after pebbles were irradiated in the US/DOE COBRA-1A2 experiment in EBR-II. Experimental details are provided in a companion paper [1]. The helium release measurements were funded by Forschungszentrum Karlsruhe.

Experimental Procedure

Helium Analysis Samples

A total of 30 beryllium pebbles were analyzed in the present study. The materials had been irradiated in the Experimental Breeder Reactor - II (EBR-II) at Argonne National Laboratory - West (ANL-W), as part of the COBRA-1A2 experiment. Fifteen of the samples were from the "C03" assembly, and were fabricated by Brush Wellman. The other fifteen were from the "D03" assembly, and were fabricated by NGK - Japan.

Prior to helium release measurement, the mass of each group of pebbles was determined using a microbalance with calibration traceable to the National Institute of Standards and Technology (NIST). Mass uncertainty is estimated to be ±0.001 mg.

Helium Measurement Procedure

The helium released from the C03 and D03 pebbles was determined by isotope-dilution gas mass spectrometry during heating in resistance-heated graphite crucibles in one of the mass spectrometer system's high-temperature vacuum furnaces [2]. The absolute amount of ^{4}He released was measured relative to known quantities of added ^{3}He "spikes". The ^{3}He spikes were obtained by expanding and partitioning a known quantity of gas through a succession of calibrated volumes [3]. The mass spectrometer was calibrated for mass sensitivity during each series of runs by analyzing known mixtures of ^{3}He and ^{4}He.

For both groups, multiple sequential measurements were conducted while the temperature of the sample crucible was increased in approximately 100°C increments. For this procedure, a ^{3}He spike was first added to the furnace. While still at room temperature (~25°C), a known small fraction (~0.04%), or aliquot of the sample gas was then taken from the furnace to determine the absolute amount of ^{4}He initially present in the furnace. The crucible was then heated to the first temperature step, and additional aliquots taken for ^{4}He measurement. Each temperature was held for a minimum of ~24 hours, or until a leveling off of the ^{4}He was observed. The time period between each measurement was varied from a minimum of about 5 minutes to a maximum of about 2 hours depending on the observed ^{4}He release rate at each temperature.

The fifteen beryllium pebbles were loaded into the central section of one of the system's standard 3/16" (0.48 cm) diameter graphite crucibles. To accommodate the pebbles, the central coaxial hole in the crucible was enlarged to 0.094" (0.24 cm) diameter. Small graphite plugs were placed at each end of the hole to position the samples as close as

possible to the middle of the crucible. A diagram of the setup, showing a section of the high temperature furnace used, is shown in Figure 1. Crucible temperature was measured using a standard K-type (chromel-alumel) thermocouple inserted into the side of the crucible. As indicated in the figure, this thermocouple was also used in conjunction with a separate temperature readout and controller circuit to maintain a constant temperature in the crucible for each temperature step, and to allow for overnight and unattended operation.

Because of the relatively long periods of time the furnace remained isolated, it was decided to pump out the furnace at regular intervals (usually about 24 hours) in order to keep offgas pressure in the furnace to below about 500 microns (67 Pa). Immediately after pumpout, a new ^{3}He spike was added to the furnace, and the measurements continued. Pumpout times were chosen to coincide with periods of slower helium release, usually near the end of each anneal period. Small corrections were made to the total helium release data to account for helium release during the pumpout (about 3 minutes).

All measured helium levels were corrected for background helium buildup in the analysis furnace as a function of time. Background ^{4}He levels generally rise linearly with time due largely to diffusion of helium from the atmosphere through the Pyrex furnace top. Background ^{4}He levels were in the range of 10^{12} to 10^{13} atoms. Uncertainty in the ^{4}He background is estimated to be ~10^{12} atoms. Background ^{3}He levels remained in the 10^{12} atom range, and were negligible compared to the added ^{3}He spike of ~10^{16} atoms.

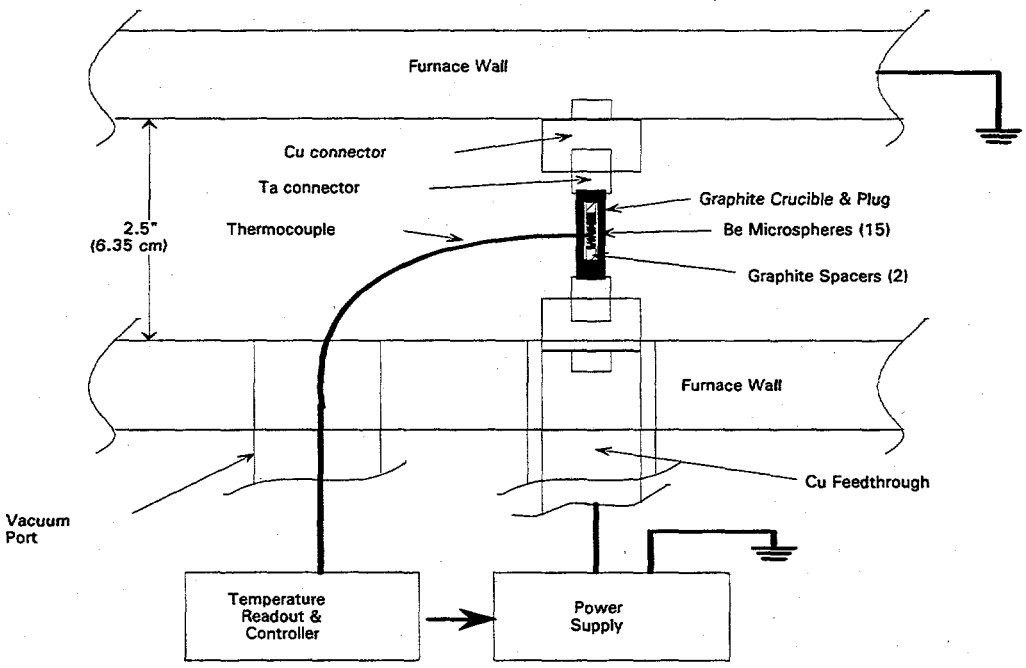

Figure 1. Diagram of sample crucible and temperature control

Results

The results of the helium release measurements are shown graphically in Figures 2 and 3. Separate data tables can be found in the summary report [4]. Each data table gives the anneal time (in hours) from the start of the series, and the time at which each temperature level was started. Temperature increase for each interval took approximately 1 minute. Helium-4 values are given as total atoms released, and as concentrations in atomic parts per million (appm, 10^{-6} atom fraction) with respect to the total number of beryllium atoms in each sample. Conversion from total helium to helium concentration was based on a calculated value of 6.682×10^{22} atoms per gram assuming pure beryllium at 100% of theoretical density. In Figures 2 and 3, the top figure shows the cumulative helium release in atoms, and the bottom figure shows the calculated helium release rate in atoms/second.

After initiation of the measurement series for Sample Be-C03, it was observed that the temperature of the thermocouple was lower than that of the graphite crucible. As a result, additional temperature readings were taken at each temperature step using a separate analog optical pyrometer (the pyrometer data suggested actual crucible temperatures about 100°C higher than indicated by the thermocouple). Later examination verified that the thermocouple had only been pressing against the surface of the crucible, rather than being fully inserted into the interior through the small side hole (see Figure 1). At the conclusion of the Be-C03 run, therefore, this thermocouple was replaced with a second smaller diameter unit which fit completely into the crucible side hole. This second thermocouple was then used to correct the earlier pyrometer readings using identical furnace conditions, and also was used for the subsequent Be-D03 measurements. As a result of the above, the temperature range for the Be-C03 sample was approximately 800 to 1100°C rather than the desired range of 700 to 1000°C.

Absolute uncertainty (1σ) in the individual helium measurement results [4], determined from the cumulative uncertainties in the sample mass, isotope ratio measurement, spike size, and helium background subtractions, is estimated to be approximately 1% to 2% combined with 10^{12} atoms (in quadrature). Indicated uncertainties in the temperature data are estimated based on uncertainties in the measuring equipment, thermocouple calibration, and pyrometer readings (for Be-C03).

Discussion

Consistent with the results obtained earlier for single Be-C03 and Be-D03 pebbles [5], helium release from both sets of pebbles was nonlinear with time at each temperature level. Both samples showed definite "steps" in the helium release at each temperature, with each step being generally characterized by an initial release rate, followed by a slowing of the rate over time. The one exception to the above behavior was the initial helium release in Sample Be-C03 at the first temperature step of 774°C. Here, the release rate initially rises, then falls, then rises again and continues to rise slowly over the remaining anneal period.

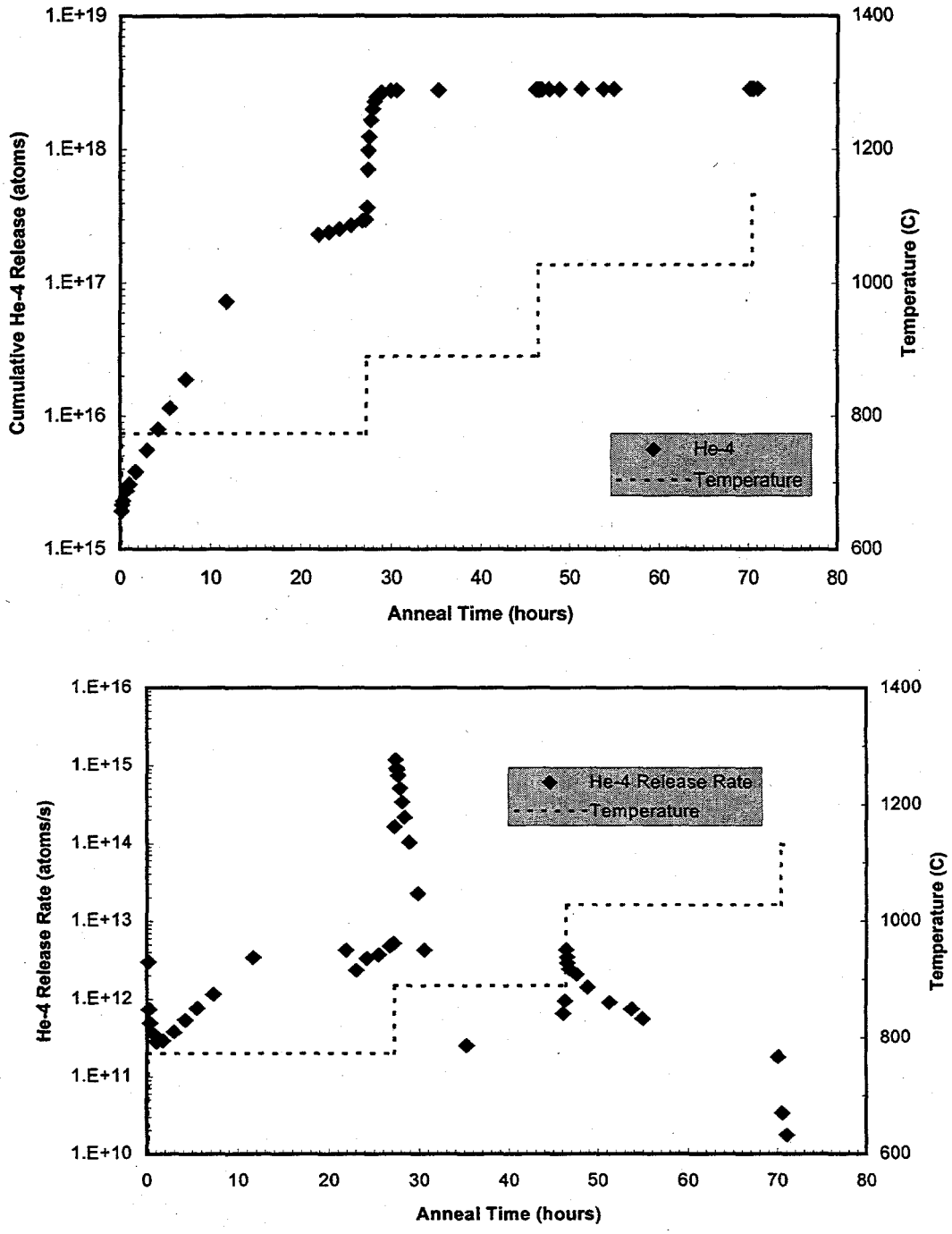

Figure 2. Cumulative helium release and release rate from sample Be-C03

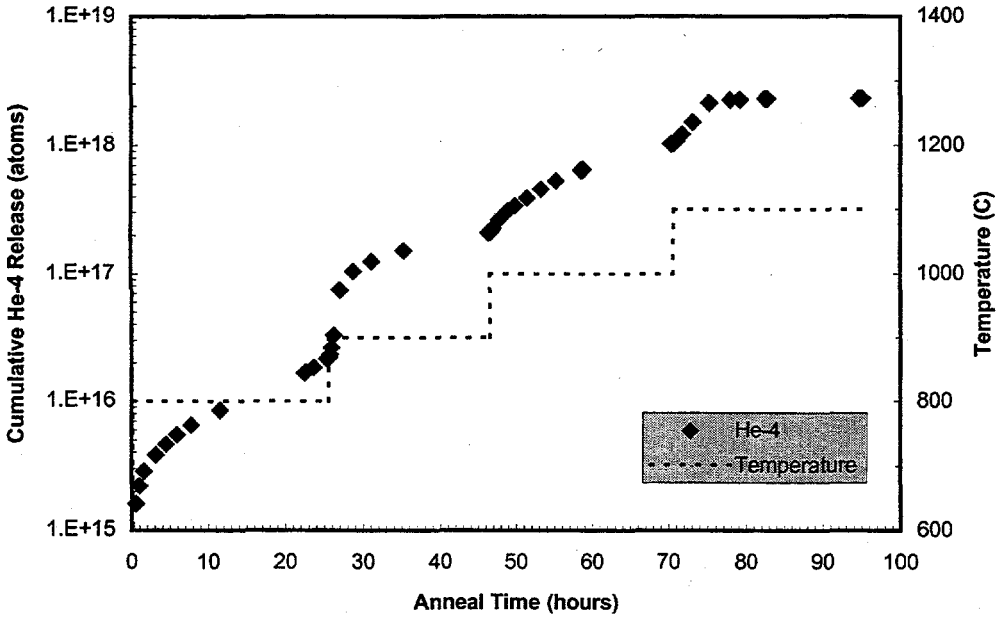

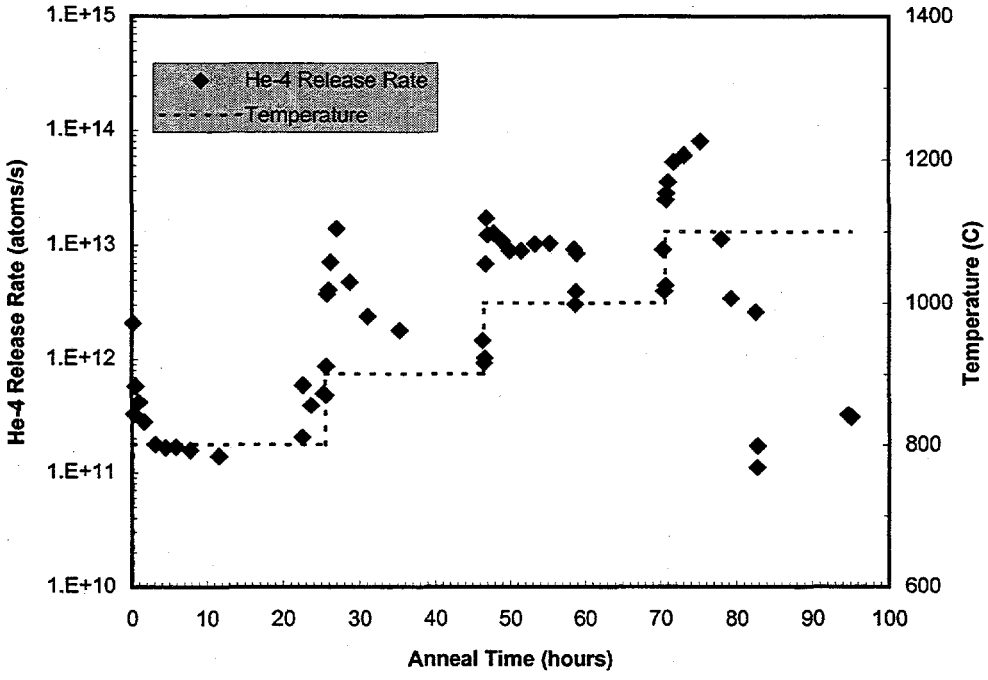

Figure 3. Cumulative helium release and release rate from sample Be-D03

Observed helium release from Sample Be-C03 showed a leveling off at the 890°C temperature step. Additional increases to 1028°C and 1132°C, showed very little extra helium release (<2%). Sample Be-D03, on the other hand, showed a leveling off only at the highest step of 1100°C. Final measured ^{4}He concentrations were 2276 appm for Be-C03 and 2312 appm for Be-D03.

The above trend of lower temperature helium release in the C03 material is consistent with that observed earlier for the single pebble [6], and further supports the conclusion of differences in the helium release characteristics of the two material lots. None of the lower temperature steps showed any leveling off of the helium release, even with increased anneal times of at least 24 hours. The earlier measurements had anneal times of only 1 to 2 hours.

Based on the average helium concentrations measured earlier for the C03 and D03 beryllium (2833 appm for Be-C03-1, and 2517 appm for Be-D03-1), the values observed here represent ~80% and ~92% of the total "expected" helium concentrations. These percentages are in contrast to the previous results which showed virtually complete helium release from Be-C03-1 at 1000°C, but only about 62% release in Be-D03-1 at 1100°C. Additional vaporization helium analyses on the two beryllium sets analyzed here would be required to determine the actual release percentages.

FUTURE WORK

This work is completed.

ACKNOWLEDGEMENTS

Specimens for irradiation were provided by H. Kawamura of JAERI as part of the US/DOE MONBUSHO Fusion Materials Program. The helium release measurements were funded by Forschungszentrum Karlsruhe under project 26919 with Battelle Pacific Northwest Laboratory entitled Post-Irradiation Examination of Beryllium. This project was under the direction of Prof. M. Dalle Donne.

REFERENCES

1. D. S. Gelles, "US/DOE OFES Neutron Irradiation Experiments containing Beryllium," in this semiannual report.
2. H. Farrar and B. M. Oliver, "A Mass Spectrometer System to Determine Very Low Levels of Helium in Small Solid and Liquid Samples," J. Vac. Sci. Technol. **A4**, 1740 (1986).
3. B. M. Oliver, J. G. Bradley, and H. Farrar, "Helium Concentration in the Earth's Lower Atmosphere," Geochim. Cosmochim. Acta **48**, 1759 (1984).

4. D. S. Gelles, L. R. Greenwood, B. M. Oliver, D. L. Baldwin, R. M. Ermi, and H. Tsai, "Post-Irradiation Examination of Beryllium - Project 26929", PNNL-29550 (December 1997)

5. L. R. Greenwood, "Production of ^{4}He and Tritium from Be in the COBRA-1A2 Irradiation", PNNL Report, May 1997.

6. B. M. Oliver, "Helium Analyses of 1-mm Beryllium Microspheres from COBRA-1A2", PNNL Report, May 6, 1997.

THERMAL RAMP TRITIUM RELEASE IN COBRA-1A2 C03 BERYLLIUM PEBBLES -
D. L. Baldwin (Pacific Northwest National Laboratory)*

OBJECTIVE

The purpose of this work was to provide quantitative tritium release response from prototypic irradiated beryllium pebbles. Such pebbles are under consideration as the neutron multiplier medium in the European Fusion Technology Program Helium Cooled Pebble Bed (HCPB) Blanket.

SUMMARY

Tritium release kinetics, using the method of thermal ramp heating at three linear ramp rates, were measured on the COBRA-1A2 C03 1-mm beryllium pebbles. This report includes a brief discussion of the test, and the test data in graph format.

PROGRESS AND STATUS

Introduction

Beryllium pebbles are being considered for the neutron multiplier medium in the European Fusion Technology Program Helium Cooled Pebble Bed (HCPB) Blanket. That design is also being considered for testing ITER. The pebbles to be used are an inexpensive form of beryllium produced in an intermediate step of the production of higher purity beryllium. The opportunity to obtain tritium release response from prototypic fast neutron irradiated pebbles became possible after pebbles were irradiated in the US/DOE COBRA-1A2 experiment in EBR-II. Experimental details are provided in a companion paper [1]. The tritium release measurements were funded by Forschungszentrum Karlsruhe.

Experimental Procedure

The thermal ramp heating method for tritium release kinetics was performed on the C03 1-mm Be pebbles using 15 pebbles for each of three tests. The three tests were conducted over a decade range of ramp rates at 0.5, 2.0, and 5.0°C/min. The temperature range for all tests was 300-900°C. Table 1 shows the ramp rates and sample weights. A ramp maximum temperature of 850°C was initially planned for the tests. However, a scoping test was performed, and the results indicated a T_{max} for this Be of >850°C, therefore, the ramp maximum was increased to 900°C.

Briefly, the sample was heated in a sweep gas of He+0.1%H_2 at 100 SCCM, the released tritium measured in real-time by an ion chamber, then oxidized on copper oxide and collected in a pair of water bubblers, and finally measured by liquid scintillation counting. The ramp rates were preselected as specified. After loading the weighed sample pebbles, the system was purged before heating was begun. After the temperature ramp was completed, the sample temperature was held at the maximum of 900°C for a period of time ranging from 4 to 18 hours, as seen in the plots.

*Pacific Northwest National Laboratory is operated for the U.S. Department of Energy by Battelle Memorial Institute under Contract DE-AC06-76RLO 1830.

Discussion of Results

The plots of the thermal ramp test data for this C03 Be material are shown in Figures 1 through 5. Figure 1 shows the tritium release rate on a log axis versus time in hours, and a temperature ramp of 0.5°C/min. Similarly, Figures 2 and 3 show the analogous curves at ramp rates of 2.0 and 5.0°C/min. Figure 4 shows all three test curves of release rate versus time, with the release rate on linear axis, and with the corresponding temperature profiles, for comparison purposes. The difference in the release curve shapes and peak widths can be

seen clearly in this plot. Figure 5 shows a different view, of all three test curves of release rate versus temperature in °C, again with release rate on linear axis, for comparison purposes.

Table 2 shows release kinetics parameters as determined from this data. The parameter P, in Bq/g, is the "production" rate as measured by the assay test reported earlier, not as calculated from the fluence prediction; R, in Bq/g, is the measured total release from the sample as determined from the bubbler liquid scintillation results; R/P, in percent, is the fractional release at end of test; the temperature, T_{max}, corresponds to the temperature of peak maximum release rate; and DF is the factor by which the release rate decreases, at 900°C in 3 hours.

Table 1. Be pebble sample and test parameters

Sample material	Thermal ramp rate (°C/min)	# of pebbles	Sample weight (g)
C03 Be pebbles (1-mm)	0.5	15	0.0188
	2.0	15	0.0178
	5.0	15	0.0179

Table 2. Tritium release parameters

Material	Ramp rate	P [Bq/g]	R [Bq/g]	R/P [%]	T_{max} [°C]	DF
C03 (1-mm) Be pebbles	0.5°C/min	1.13 E+09	1.04 E+09	92%	882	3.1
	2.0°C/min	1.13 E+09	1.14 E+09	100%	887	8.5
	5.0°C/min	1.13 E+09	1.07 E+09	95%	900	11.4

As can be seen in the table, the fractional release, R/P, is high in these 1-mm pebbles, >92% in all cases. The T_{max} for the three cases shows a slight increase with increasing ramp rate, from 882°C to 900°C, as expected. The DF is consistently low for this material, ranging from 3.1 to 11.4, even at the high hold temperature of 900°C, indicating only gradual continuing release at the hold temperature. These DF numbers are low compared with other studied beryllium specimens.

As has been done previously, the IC cumulative release curve in MBq/g, calculated from the release rate curve in Bq/s, was normalized to the collection bubbler liquid scintillation results in MBq/g. This was done by adjusting the IC baseline and/or IC calibration factor for each

bubbler data point. This method assumes the collection bubbler liquid scintillation results are always reliable and accurate, therefore, the IC curve must be adjusted to obtain agreement. The full data file is also attached, in Excel 4.0 format.

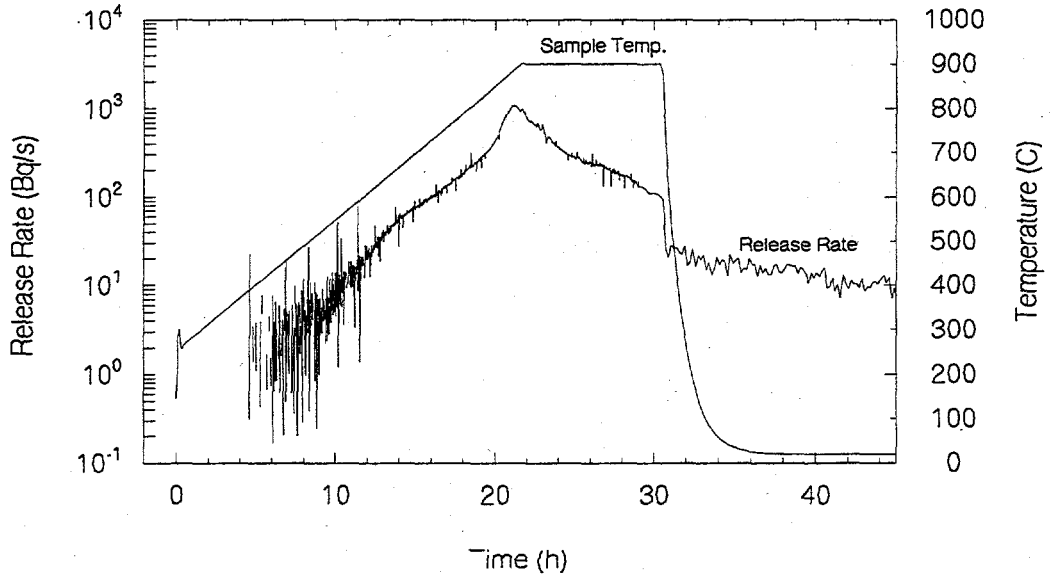

Figure 1. Tritium release kinetics for C03, 1-mm pebbles, thermal ramp test at 0.5°C/min ramp rate.

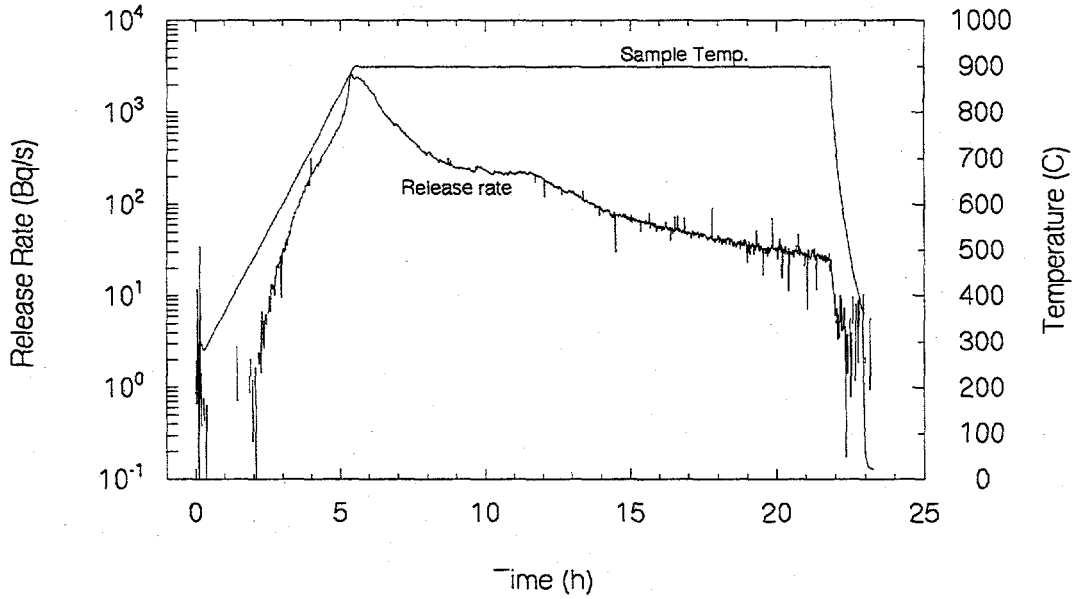

Figure 2. Tritium release kinetics for C03, 1-mm pebbles, thermal ramp test at 2.0°C/min ramp rate.

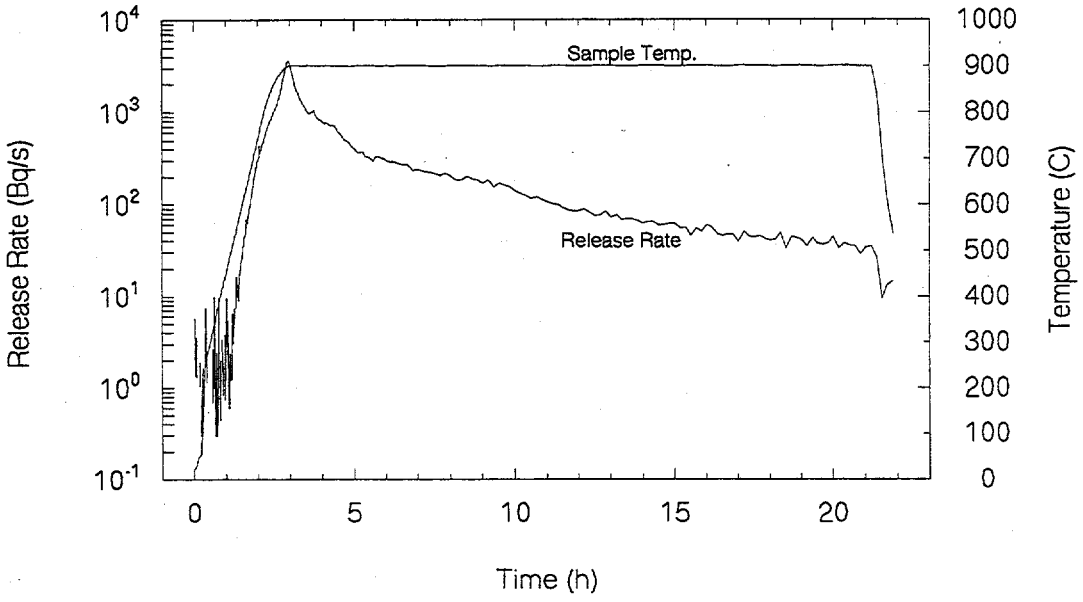

Figure 3. Tritium release kinetics for C03, 1-mm pebbles, thermal ramp test at 5.0°C/min ramp rate.

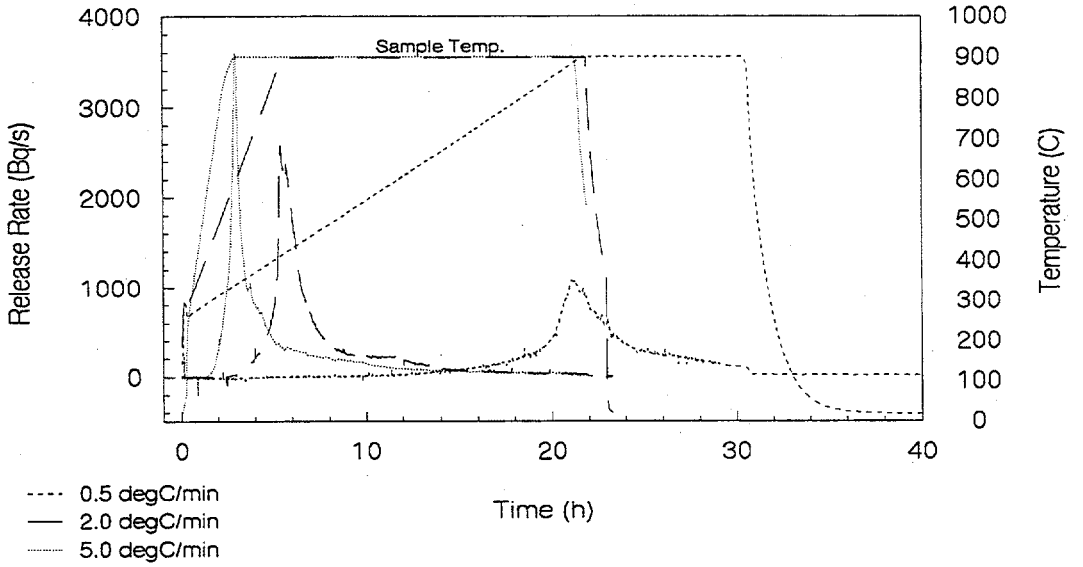

Figure 4. Tritium release kinetics for C03, 1-mm pebbles, thermal ramp tests, showing summary plot of release rate versus time, at 0.5, 2.0, and 5.0°C/min ramp rates, on linear y-axis.

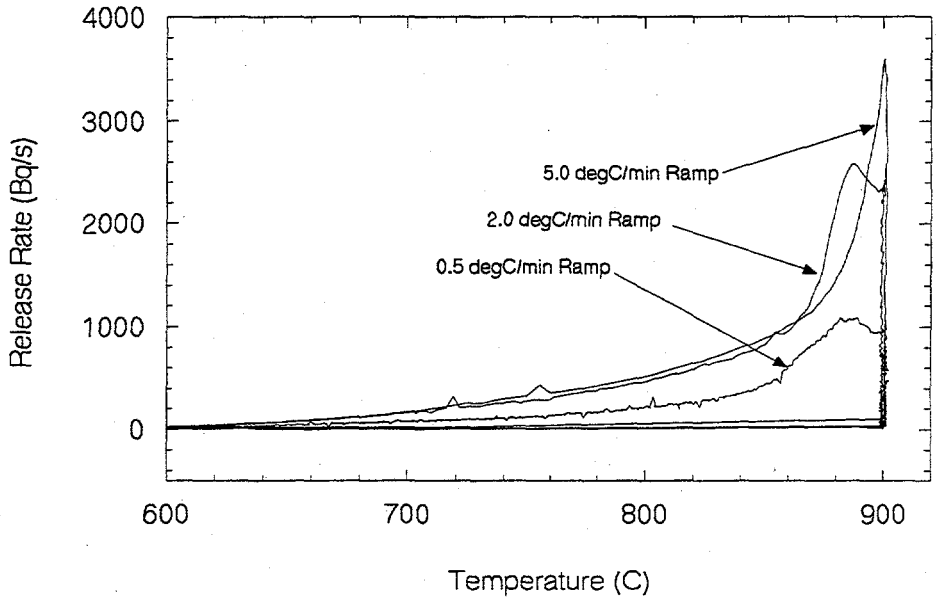

Figure 5. Tritium release kinetics for C03, 1-mm pebbles, thermal ramp tests, showing summary plot of release rate versus temperature, at 0.5, 2.0, and 5.0°C/min ramp rates, on linear y-axis.

FUTURE WORK

This work is completed.

ACKNOWLEDGEMENTS

Specimens for irradiation were provided by H. Kawamura of JAERI as part of the US/DOE MONBUSHO Fusion Materials Program. The tritium release measurements were funded by Forschungszentrum Karlsruhe under project 26919 with Battelle Pacific Northwest Laboratory entitled Post-Irradiation Examination of Beryllium. This project was under the direction of Prof. M. Dalle Donne.

REFERENCES

1. D. S. Gelles, "US/DOE OFES Neutron Irradiation Experiments containing Berylium," in this DOE/ER-0313/23 report.

HELIUM ANALYSES OF 1-MM BERYLLIUM MICROSPHERES FROM COBRA-1A2 –
B. M. Oliver (Pacific Northwest National Laboratory)*

OBJECTIVE

The purpose of this work was to provide quantitative helium release response from prototypic irradiated beryllium pebbles. Such pebbles are under consideration as the neutron multiplier medium in the European Fusion Technology Program Helium Cooled Pebble Bed (HCPB) Blanket.

SUMMARY

Multiple helium analyses on four beryllium microspheres irradiated in the Experimental Breeder Reactor - II (EBR-II) at Argonne National Laboratory - West (ANL-W), are reported. The purpose of the analyses was to determine the total helium content of the beryllium, and to determine the helium release characteristics of the beryllium as a function of time and temperature. For the helium release measurements, sequential helium analyses were conducted on two of the samples over a temperature range from 500°C to 1100°C in 100°C increments. Total helium measurements were conducted separately using our normal analysis method of vaporizing the material in a single analysis run.

Observed helium release in the two beryllium samples was nonlinear with time at each temperature interval, with each step being characterized by a rather rapid initial release rate, followed by a gradual slowing of the rate over time. Sample Be-C03-1 released virtually all of its helium after approximately 30 minutes at 1000°C, reaching a final value of 2722 appm. Sample Be-D03-1, on the other hand, released only about 62% of its helium after about 1 hour at 1100°C, reaching a final value of 1519 appm. Combining these results with subsequent vaporization runs on the two samples, yielded total helium concentrations of 2724 and 2459 appm. Corresponding helium concentrations measured in the two other "C03" and "D03" samples, by vaporization alone, were 2941 and 2574 appm. Both sets of concentrations are in reasonable agreement with predicted values of 2723 and 2662 appm.

Helium-3 levels measured during the latter two vaporization runs were 2.80 appm for Be-C03-2, and 2.62 appm for Be-D03-2. Calculated ^{3}He values are slightly lower at 2.55 and 2.50 appm, respectively, suggesting somewhat higher tritium levels in the beryllium than predicted.

PROGRESS AND STATUS

Introduction

Beryllium pebbles are being considered for the neutron multiplier medium in the European Fusion Technology Program Helium Cooled Pebble Bed (HCPB) Blanket. That design is

*Pacific Northwest National Laboratory is operated for the U.S. Department of Energy by Battelle Memorial Institute under Contract DE-ACO6-76RLO 1830.

also being considered for testing in ITER. The pebbles to be used are an inexpensive form of beryllium produced in an intermediate step of the production of higher purity beryllium. The opportunity to obtained helium release response from prototypic fast neutron irradiated pebbles became possible after pebbles were irradiated in the US/DOE COBRA-1A2 experiment in EBR-II. Experimental details are provided in a companion paper [1]. The helium release measurements were funded by Forschungszentrum Karlsruhe.

Experimental Procedure

Helium Analysis Samples

Four beryllium microspheres were analyzed in the present study. The materials had been irradiated in the Experimental Breeder Reactor - II (EBR-II) at Argonne National Laboratory - West (ANL-W), as part of the COBRA-1A2 experiment [1]. Two of the samples were from the "C03" assembly, and were fabricated by Brush Wellman. The other two were from the "D03" assembly, and were fabricated by NGK - Japan. One of each of the C03 and D03 spheres were analyzed to determine the helium release with time and temperature. These analyses were followed by separate vaporization runs to determine if any remaining helium was in the sample. The two other microspheres (one each for C03 and D03) were analyzed for total helium content by rapid vaporization in a single analysis.

Prior to analysis, the mass of each microsphere was determined using a microbalance with calibration traceable to National Institute of Standards and Technology (NIST). Mass uncertainty is estimated to be ±0.001 mg.

Helium Analysis Procedure

The helium released from each microsphere was determined by isotope-dilution gas mass spectrometry during heating or vaporization in a resistance-heated graphite crucible in one of the mass spectrometer system's high-temperature vacuum furnaces [2]. The absolute amount of ^{4}He released was measured relative to a known quantity of added ^{3}He "spike". The ^{3}He spikes were obtained by expanding and partitioning a known quantity of gas through a succession of calibrated volumes [3]. The mass spectrometer was calibrated for mass sensitivity during each series of runs by analyzing known mixtures of ^{3}He and ^{4}He.

For two of the samples, multiple sequential analyses were conducted while the temperature of the sample crucible was increased in approximately 100°C increments, starting at 500°C and increasing to a maximum of 1100°C. For this procedure, a ^{3}He spike was first added to the furnace. While still at room temperature (~25 °C), a known small fraction (~0.04%), or aliquot of the sample gas was then taken from the furnace to determine the absolute amount of ^{4}He initially present in the furnace. This analysis was done to determine the starting background ^{4}He level. The crucible was then heated to 500°C, and additional aliquots taken for ^{4}He analysis. Each temperature was held until some leveling off of the ^{4}He was observed, at which point the temperature was raised to the next temperature. The time period between each analysis was varied from a minimum of about 5 minutes to a maximum of about 30 minutes depending on the observed ^{4}He release rate at each temperature. Crucible

temperature was measured using a standard chromel-alumel thermocouple in direct contact with the crucible.

All measured helium levels were corrected for background helium buildup in the analysis furnace as a function of time. These background helium levels were determined by separate "control" analyses conducted immediately before or after the sample runs. Background ^{4}He levels generally rise linearly with time due largely to diffusion of helium from the atmosphere through the Pyrex furnace top. Background ^{4}He levels were in the range of 10^{12} to 10^{13} atoms over the 6 to 7 hour time period for each analysis series. Uncertainty in the ^{4}He background is estimated to be approximately 10^{12} atoms. Background ^{3}He levels remained in the 10^{12} atom range, and were negligible compared to the added ^{3}He spike (~10^{16} atoms).

Following the time/temperature measurements, the two microspheres were relocated, in their original crucibles, to different locations in the same furnace for subsequent vaporization analysis along with the other two beryllium samples analyzed as part of the present effort. For the vaporization runs, both ^{3}He and ^{4}He were determined in each sample. This was done by analyzing a first aliquot of the gas released during vaporization prior to the addition of the ^{3}He spike. Because only a small fraction of the gas was taken from the furnace for each analysis, this procedure did not adversely affect the accuracy of the final measured ^{4}He value.

Results

The results of the helium release measurements are shown graphically in Figures 1 and 2. Separate data tables can be found in the summary report [4]. Each data table gives the analysis time (in hours) from the start of the series, and the time at which each temperature level was started. Temperature increase for each interval took approximately 1 minute. Indicated uncertainties in the temperature data are the standard deviations in the observed temperature variations over the temperature interval. Helium-4 values are given as total atoms released, and as concentrations in atomic parts per million (appm, 10^{-6} atom fraction) with respect to the total number of beryllium atoms in each sample. Conversion from total helium to helium concentration was based on a calculated value of 6.682×10^{22} atoms per gram assuming pure beryllium.

Table 1 gives the total helium released after vaporization in the four beryllium microspheres. Results are listed as total atoms of ^{3}He and ^{4}He, and as concentrations, again in atomic parts per million. Also shown in Table 1 are the end results for Be-C03-1 and Be-D03-1 from the helium release measurements [4], and the combined helium release for these two samples from both measurements.

Absolute uncertainty (1σ) in the individual helium analysis results, determined from the cumulative uncertainties in the sample mass, isotope ratio measurement, spike size, and helium background subtractions, is estimated to be approximately 1% combined with 10^{12} atoms in quadrature. For the lowest measured helium levels, therefore, the uncertainty of 10^{12} atoms is the dominant term. For helium levels above about 10^{14} atoms, the uncertainty is approximately 1%.

Table 1. Total helium release from 1-mm beryllium microspheres

Sample	Sample Mass (mg)	Measured Helium (vaporized)[a]				Measured ^{4}He (total) (appm)[b]		
		^{3}He		^{4}He				
		(atoms)	(appm)[b]	(atoms)	(appm)[b]	Heated[c]	Total[d]	Predicted
Be-C03-1	1.419	3.05E13	0.322	1.698E15	1.791	2722	2724	
Be-C03-2	1.633	3.06E14	2.80	3.209E17	2941	--	2941	
						Mean	**2833**	**2723**
						±1σ	**±153**	
Be-D03-1	1.472	1.17E14	1.19	9.249E16	940.3	1519	2459	
Be-D03-2	1.206	2.11E14	2.62	2.074E17	2574	--	2574	
						Mean	**2517**	**2662**
						±1σ	**±81**	

[a]Measured helium from vaporization analysis.
[b]Helium concentration in atomic parts per million (10^{-6} atom fraction) with respect to the total number of beryllium atoms in the sample.
[c]Final ^{4}He from helium release measurements [4].
[d]Total ^{4}He [4].

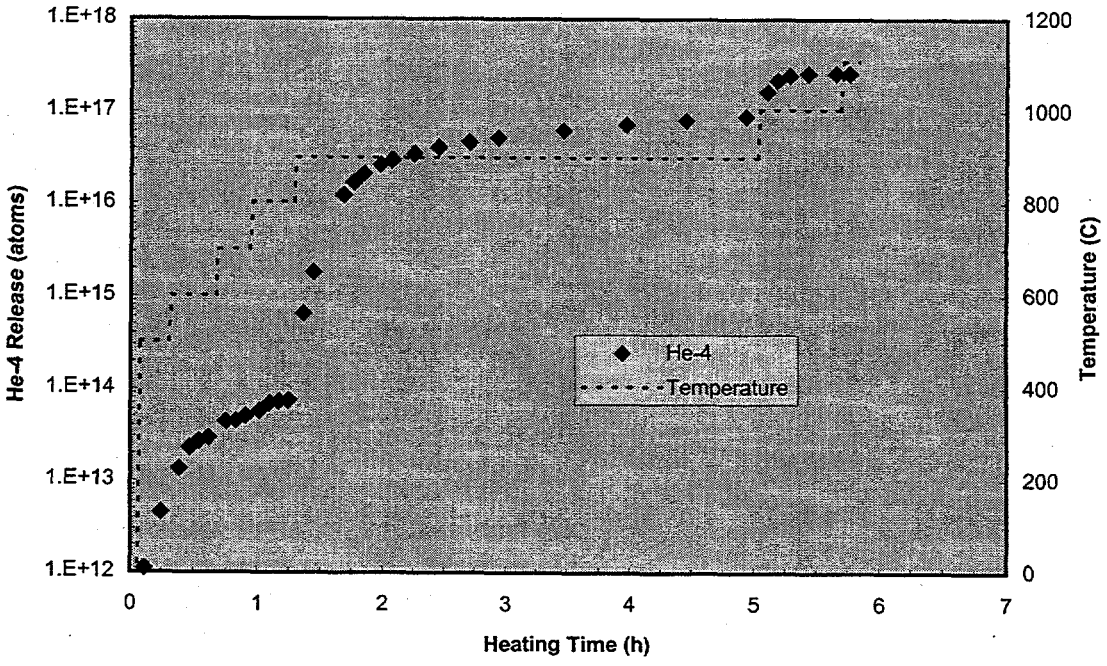

Figure 1. Helium release from sample Be-C03-1

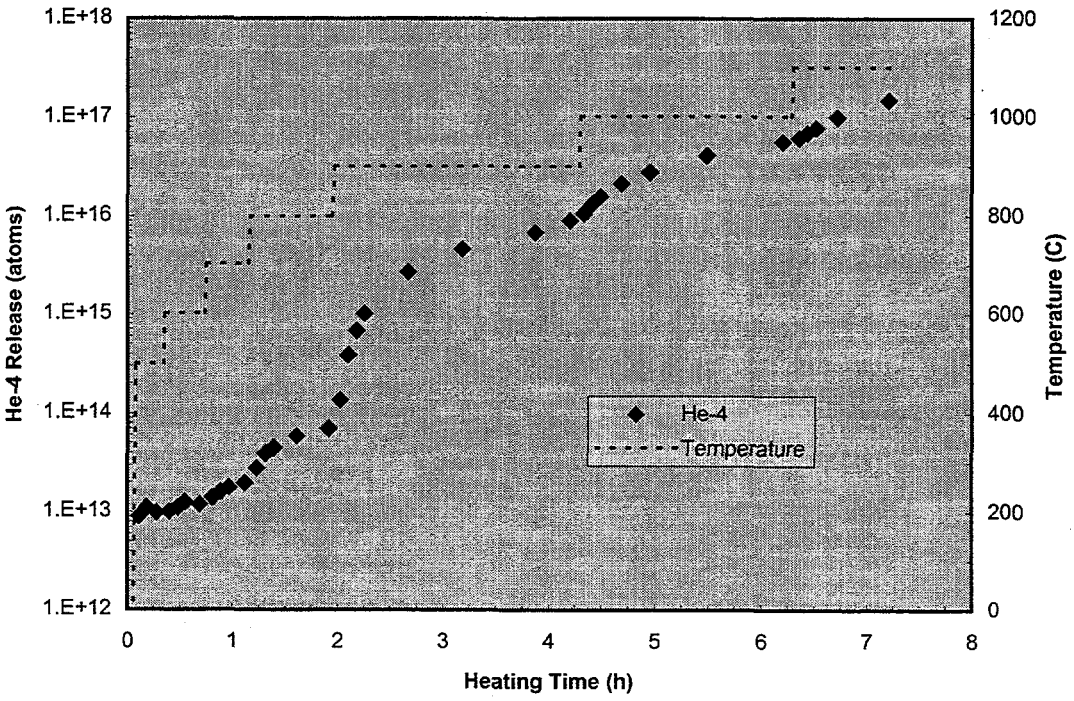

Figure 2. Helium release from sample Be-D03-1

Discussion

Observed helium release from both microspheres was nonlinear with time at each temperature level. As is evident in Figures 1 and 2, both microspheres showed definite "steps" in the helium release at each temperature, with each step being characterized by a rather rapid initial release rate, followed by a gradual slowing of the rate over time. Except for Sample Be-C03-1 at 1000 °C, none of the release steps showed saturation over the 1 to 2 hour time periods the temperatures were held.

Helium release as a fraction of the total helium in the sample was markedly different for the "C03" and "D03" material. Sample Be-C03-1 released virtually all of its helium after approximately 30 minutes at 1000 °C. Sample Be-D03-1, on the other hand, released only about 62% of its helium even after about 1 hour at 1100 °C. Absolute helium release was correspondingly lower for Be-D03-1 at each temperature level. As indicated earlier, the C03 beryllium material was fabricated by Brush Wellman, whereas the D03 material was fabricated by NGK - Japan. The different helium release characteristics suggests some material differences in the two beryllium lots. However, additional analyses would be required to verify any material effects.

Total helium release after vaporization for all four microspheres are given in Table 3. In terms of helium concentration, the totals for Be-C03-1 and -2 are 2724 and 2941 appm, with an average value of 2833 appm. The corresponding totals for Be-D03-1 and -2 are 2459 and 2574 appm, with an average value of 2517 appm. In both cases, the total ^{4}He for the combined heating+vaporization runs is lower than that for the separate vaporization runs alone. This variation amounts to 8% for Be-Co3-1, and 5% for Be-D03-1. Some of this variation may be due to radial gradients in the two irradiation assemblies, although this was not anticipated to be larger than perhaps 5%. Predicted helium concentrations in the C03 and D03 beryllium are 2723 and 2662 appm, respectively [5]. Mean calculated to experimental ratios (C/E's) are 1.04 for Be-C03 and 0.95 for Be-D03.

Helium-3 levels measured during the vaporization runs were 2.80 appm for Be-C03-2, and 2.62 appm for Be-C03-2. Predicted ^{3}He levels, assuming no tritium loss during or after irradiation, are slightly lower at 2.55 and 2.50 appm [3], suggesting somewhat higher levels of tritium in the beryllium than calculated.

FUTURE WORK

The data presented here raise some interesting questions which could be answered by additional work. However, funding has not yet been identified. Suggestions for such additional work are:

1. Perform analyses on replicate samples of the C03 and D03 material to verify any differences related to the helium release characteristics with time and temperature, and to verify any variations in total helium content within the two material lots.
2. Perform more sensitive analyses at lower temperatures to accurately determine the low-temperature release characteristics of the C03 and D03 material.
3. Increase the temperature hold times to determine if the release curves eventually "saturate" at any given temperature.
4. Determine total helium and helium release characteristics of replicate samples of the 3-mm and 5-mm microspheres as outlined above.

AKNOWLEDGEMENTS

Specimens for irradiation were provided by H. Kawamura of JAERI as part of the US/DOE MONBUSHO Fusion Materials Irradiation Program. The helium release measurements were funded by Forschungszentrum Karlsruhe under project 26919 with Battelle Pacific Northwest Laboratory entitled Post-Irradiation Examination of Beryllium. This project was under the direction of Prof. M. Dalle Donne.

REFERENCES

1. D. S. Gelles, "US/DOE OFES Neutron Irradiation Experiments containing Beryllium," in this semiannual report.

2. H. Farrar and B. M. Oliver, "A Mass Spectrometer System to Determine Very Low Levels of Helium in Small Solid and Liquid Samples," J. Vac. Sci. Technol. **A4**, 1740 (1986).

3. B. M. Oliver, J. G. Bradley, and H. Farrar, "Helium Concentration in the Earth's Lower Atmosphere," Geochim. Cosmochim. Acta **48**, 1759 (1984).

4. D. S. Gelles, L. R. Greenwood, B. M. Oliver, D. L. Baldwin, R. M. Ermi and H. Tsai, "Post-Irradiation Examination of Beryllium-Project 26919", PNNL SA-29550 (December 1997).

5. L. R. Greenwood, "Production of ^{4}He and Tritium from Be in the COBRA-1A2 Irradiation", in this semiannual report.

TRITIUM ANALYSES OF COBRA-1A2 BERYLLIUM PEBBLES - D. L. Baldwin (Pacific Northwest National Laboratory)*

OBJECTIVE

The purpose of this work was to provide quantitative tritium analyses for prototypic irradiated beryllium pebbles. Such pebbles are under consideration as the neutron multiplier medium in the European Fusion Technology Program Helium Cooled Pebble Bed (HCPB) Blanket.

SUMMARY

Selected tritium measurements have been completed for the COBRA-1A2 experiment C03 and D03 beryllium pebbles. The completed results, shown in Tables 1, 2, and 3, include the tritium assay results for the 1-mm and 3-mm C03 pebbles, and the 1-mm D03 pebbles, stepped anneal test results for both types of 1-mm pebbles, and the residual analyses for the stepped-anneal specimens. All results have been reported with date-of-count and are not corrected for decay. Stepped-anneal tritium release response is provided in addenda.

PROGRESS AND STATUS

Introduction

Beryllium pebbles are being considered for the neutron multiplier medium in the European Fusion Technology Program Helium Cooled Pebble Bed (HCPB) Blanket. That design is also being considered for testing in ITER. The pebbles to be used are an inexpensive form of beryllium produced in an intermediate step of the production of higher purity beryllium. The opportunity to determine tritium inventories for prototypic fast neutron irradiated pebbles became possible after pebbles were irradiated in the US/DOE COBRA 1A2 experiment in EBR-II. Experimental details are provided in a companion paper. [1] The tritium release measurements were funded by Forschungszentrum Karlsruhe.

Experimental Procedure

The tritium assay and residuals results are been determined by the method of high-temperature sweep gas extraction. The basic method has been described previously [2], but has been modified using sweep gas instead of vacuum. The sweep gas method is used instead of the vacuum method due to much lower method detection limits due to vacuum manifold contamination. The method has an estimated precision and accuracy of 5%. Briefly, the weighed sample is melted, at 1700°C, in a sweep gas of He+0.1% H_2 at 100 SCCM, with the released hydrogen isotopes oxidized on copper oxide, collected in a pair of water bubblers, and measured by liquid scintillation counting, traceable to NIST. Since the extraction takes place in helium, no residual helium measurement in the stepped-anneal Be specimens is possible. See Figure 1 for the schematic.

*Pacific Northwest National Laboratory is operated for the U.S. Department of Energy by Battelle Memorial Institute under Contract DE-AC06-76RLO 1830.

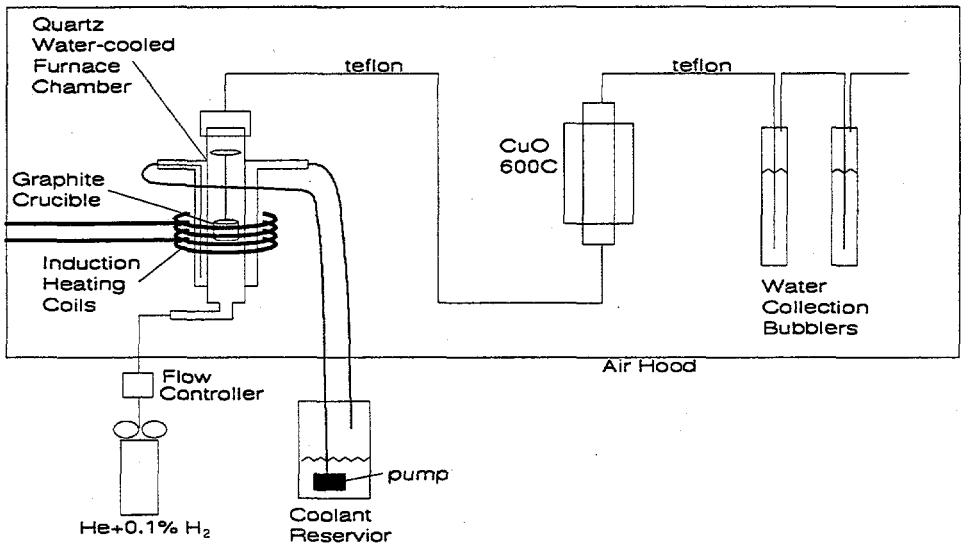

Figure 1. Schematic of method for tritium assay

The stepped-anneal tritium release test method has been described previously [3,4]. The test temperature range is 350-850°C. Briefly, the sample is heated in sweep gas of He+0.1%H_2 at 100 SCCM, the released tritium measured in real-time by ion chamber, oxidized on copper oxide and collected in a pair of water bubblers, and measured by liquid scintillation counting. See Figure 2 for the schematic.

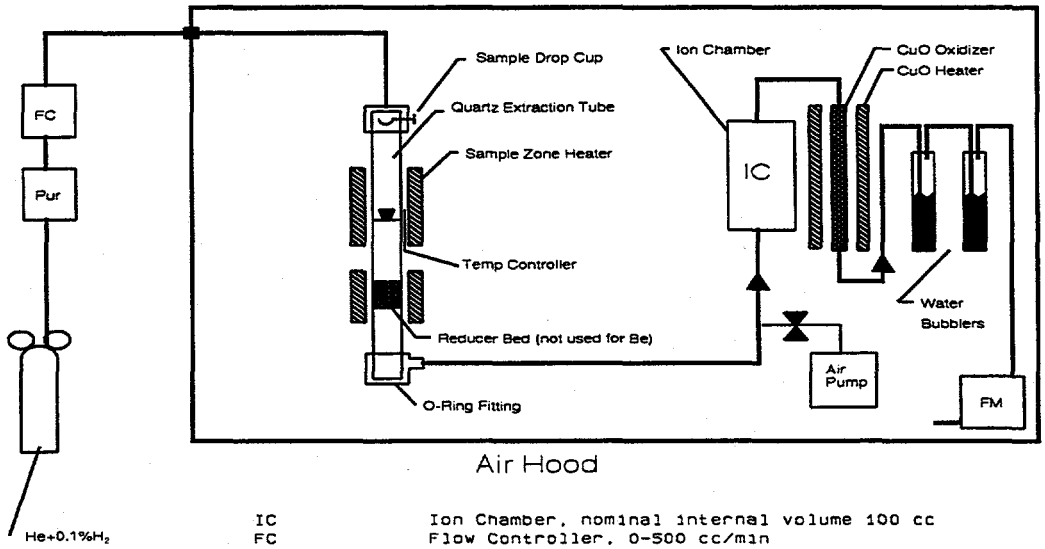

IC	Ion Chamber, nominal internal volume 100 cc
FC	Flow Controller, 0-500 cc/min
FM	Flow Meter, 0-500 cc/min
Pur	Gas Purifier for oxygen and moisture, <50 ppb O_2 + H_2O
Zn	Reducer Bed of Zn
Furnace Tube	Tube with or without reducing bed can be used
Air Pump	Small ambient air pump

Figure 2. Schematic of method for stepped-anneal tritium release

Discussion of Results

The assay results, shown in Table 1, appear to be very self-consistent. Note the 1-mm pebble measured/produced ratios are low, at a consistent 0.73 and 0.71. The 3-mm meas/prod ratio is much higher at 0.93. This apparently indicates the diffusive loss of tritium in-reactor is dependent on pebble diameter. The precision for the C03 pebble duplicate results is 9.8% RPD (Relative Percent Difference) which is surprisingly large, probably due to the use of too-small sample size, 3 pebbles compared to 10 pebbles. The duplicates precision for the 1-mm D03 is much better at 2.6% RPD, and for the 3-mm C03, the precision is 1% RPD. The low RPD for the latter two indicates adequate sample size.

Table 1. Tritium assay results

sample	#of Pebbles	sample weight (g)	Measured (Bq/g)	Meas. (appm)	date of count	Produced (appm)	Avg Meas/ Prod
1-mm C03	3	0.0035	1.187E+09	9.96	21-May-97	13.1	0.73
	10	0.0121	1.076E+09	9.03	21-May-97		
3-mm C03	2	0.0700	1.474E+09	12.38	30-May-97	13.2	0.93
	2	0.0699	1.461E+09	12.26	30-May-97		
1-mm D03	5	0.0043	1.107E+09	9.29	29-May-97	12.9	0.71
	5	0.0055	1.078E+09	9.05	29-May-97		

The stepped anneal tests results are shown in Tables 2 and 3. In the original interest of saving time and funds, some time intervals for selected temperature steps were cut short. In retrospect, this is a limitation in the data set, and longer time intervals for all steps would be useful. For the C03 test, which used 5 pebbles, the 850 step was originally at 7.5 hours. When the cumulative tritium was calculated and determined to be quite low, it was decided to test additional time at 850°C. Therefore, the sample was reheated (it had not been removed from the test apparatus) to 850°C for an additional duration of 25 hours, followed by additional cooldown and purge. This additional step released more tritium, though it was still releasing at 850°C after the total of 33 hours. The total cumulative released at 350-850°C was 75% of the total inventory. The residual remaining tritium, measured by melting the sample at 1700°C, was about 25% of the total inventory, with the totaled cumulative quantities agreeing relatively well with assay result.

For the D03 stepped-anneal test, and learning from the experience of the C03 test, 10 pebbles were used, and generally longer step durations, with the final 850°C step held for 72 hours. This test resulted in much higher cumulative quantities released. From 350-750°C 20% was released and by the end of the 850°C step 94% was released. The residual remaining tritium, of about 6% of the total inventory, brought the total cumulative into excellent agreement with the assay results.

Table 2. 1-mm C03 stepped-anneal tritium release results

Sample	Temp, C	Time (hr)	Bubbler Result (Bq/g)	date of count	Cumulative (Bq/g)	Cumulative (appm)	% of Total
1-mm C03 5 pebbles wt = 0.0066 g He+0.1% H_2 100 SCCM	ambient purge	17.97	2.69E+06	5-May-97	2.69E+06	0.023	0.2
	350	5.88	2.29E+06	5-May-97	4.98E+06	0.042	0.4
	450	18.06	3.85E+06	5-May-97	8.83E+06	0.074	0.7
	550	6.00	7.90E+06	5-May-97	1.67E+07	0.14	1.4
	650	18.38	8.93E+07	5-May-97	1.06E+08	0.89	8.6
	750	23.11	2.40E+08	5-May-97	3.46E+08	2.91	28.0
	850	4.09	2.24E+08	5-May-97	5.70E+08	4.79	46.1
		3.42	1.19E+08	5-May-97	6.89E+08	5.78	55.7
	cool-down	65.4	2.58E+07	5-May-97	7.15E+08	6.00	57.8
	additional 850	24.68	2.10E+08	17-May-97	9.25E+08	7.76	74.8
	cool down	25.00	5.78E+06	17-May-97	9.31E+08	7.81	75.3
	Total Released	---	9.31E+08	17-May-97	9.31E+08	7.81	75.3
Residual Analysis	melted	---	3.06E+08	6-Jun-97	1.24E+09	10.38	100.0
Total released plus residual	—	—	1.24E+09	6-Jun-97	1.24E+09	10.38	100.0

Note for both stepped anneal tests, less than 2% of inventory was released at 350-550°C. A very consistent cumulative about 8.7% was released after 650°C. After 750°C, the cumulative released was 20-28% for both tests. The major difference between the two tests is seen at the 850°C step, though time duration at temperature is definitely a factor.

All tritium data is reported with date-of-count and is not decay-corrected.

Table 3. 1-mm D03 stepped-anneal tritium release results

Sample	Temp, C	Time (hr)	Bubbler Result (Bq/g)	day of count	Cum. (Bq/g)	Cum. (appm)	% of Total
1-mm D03 10 pebbles wt = 0.0098 g He+0.1% H_2 100 SCCM	ambient purge	0.33	1.39E+05	12-May-97	1.39E+05	0.0012	0.01
	350	17.42	3.41E+05	12-May-97	4.80E+05	0.0040	0.04
	450	7.87	1.87E+05	12-May-97	6.67E+05	0.0056	0.06
	550	17.03	6.71E+05	12-May-97	1.34E+06	0.011	0.12
	650	23.75	9.71E+07	12-May-97	9.84E+07	0.826	8.81
	750	22.83	1.27E+08	12-May-97	2.26E+08	1.89	20.2
	850	72.49	8.28E+08	12-May-97	1.05E+09	8.84	94.3
	Total Released	---	1.05E+09	12-May-97	1.05E+09	8.84	94.3
Residual Analysis	melted	---	6.35E+07	6-Jun-97	1.12E+09	9.38	100.0
Total released plus residual	---	---	1.12E+09	6-Jun-97	1.12E+09	9.38	100.0

There were some experimental problems with the ion chamber (IC) resulting in a noisy signal. The IC signal data will be acceptable, but is still being worked on and cleaned up, and prepared for plotting. This data, in plot and digital form, will be sent to you when completed.

FUTURE WORK

This work is completed.

ACKNOWLEDGEMENTS

The laboratory operations of J. D. Matheson and D. L. Bellofatto in the PNNL laboratory are acknowledged. Specimens for irradiation were provided by H. Kawamura of JAERI as part of the US/DOE MONBUSHO Fusion Materials Irradiation Program. The tritium release measurements were funded by Forschungszentrum Karlsruhe under project 26919 with Battelle Pacific Northwest Laboratory entitled Post-Irradiation Examination of Beryllium. This project was under the direction of Prof. M. Dalle Donne.

REFERENCES

1. D. S. Gelles, "US/DOE OFES Neutron Irradiation Experiments containing Beryllium," in this DOE/ER-0313/23 report.

2. D. L. Baldwin and G. W. Hollenberg, J. Nucl. Mater. 141-143 (1986) 305.

3. D. L. Baldwin and M. C. Billone, J. Nucl. Mater. 212-215 (1994) 948-953.

4. D. L. Baldwin, O. D. Slagle, and D. S. Gelles, J. Nucl. Mater. 179-181 (1991) 329-334.

Addendum A:

STEPPED-ANNEAL TRITIUM RELEASE IN COBRA-1A2 C03 BERYLLIUM

SUMMARY

This addendum includes the plot, and data in spreadsheet format, of the tritium stepped-anneal test on the C03 1-mm pebble specimens.

Experimental

The stepped-anneal test for tritium release kinetics was performed on the C03 1-mm pebbles using 5 pebbles with total sample weight of 0.0066g. The test temperature range was 350-850C, in 100C steps. Briefly, the sample was heated in sweep gas of He+0.1%H_2 at 100 SCCM, the released tritium measured in real-time by ion chamber, oxidized on copper oxide and collected in a pair of water bubblers, and then measured by liquid scintillation counting.

Discussion of Results

The plot of the stepped-anneal test data is shown in Figure 1. In the original interest of saving time and funds, some time intervals for selected temperature steps were shortened. In retrospect, this is a limitation in the current data set, and longer time intervals for some steps would have been useful. For this C03 test, using 5 pebbles, the 850C step was originally set at 7.5 hours. When the cumulative tritium was calculated and determined to be quite low, it was decided to test additional time at 850C. Therefore, the sample was reheated (it had not been removed from the test apparatus) to 850C for an additional period of 25 hours, followed by additional cooldown and purge. This additional step released more tritium, and it was still releasing at 850C after the total of 33 hours. The total cumulative released at 350-850C was 75% of the total inventory. The residual tritium, measured by melting the sample at 1700C, was about 25% of the total inventory, with the totaled cumulative quantities agreeing relatively well with assay result.

There were some experimental problems with the ion chamber (IC) resulting in a noisy signal and narrow spikes. The major cause of the noise and spikes is simply the very low range of release rate, at less than 150 Bq/s, with portions of the curve at less than 15 Bq/s.

Numerous single point spikes were manually removed from the data set. As has been done previously, the IC cumulative release curve in MBq/g, calculated from the release rate curve in Bq/s, was normalized to the collection bubbler results in MBq/g, by adjusting the IC baseline and/or IC calibration factor. This method assumes the collection bubbler results are always correct and reliable, therefore, the IC curve must be adjusted to obtain agreement.

Figure 3 below shows the release rate, as measured by the IC in Bq/s on the left axis, with cumulative tritium (both integrated IC signal and collection bubbler results) in MBq/g on the right axis, and temperature in degrees C, also on the right axis.

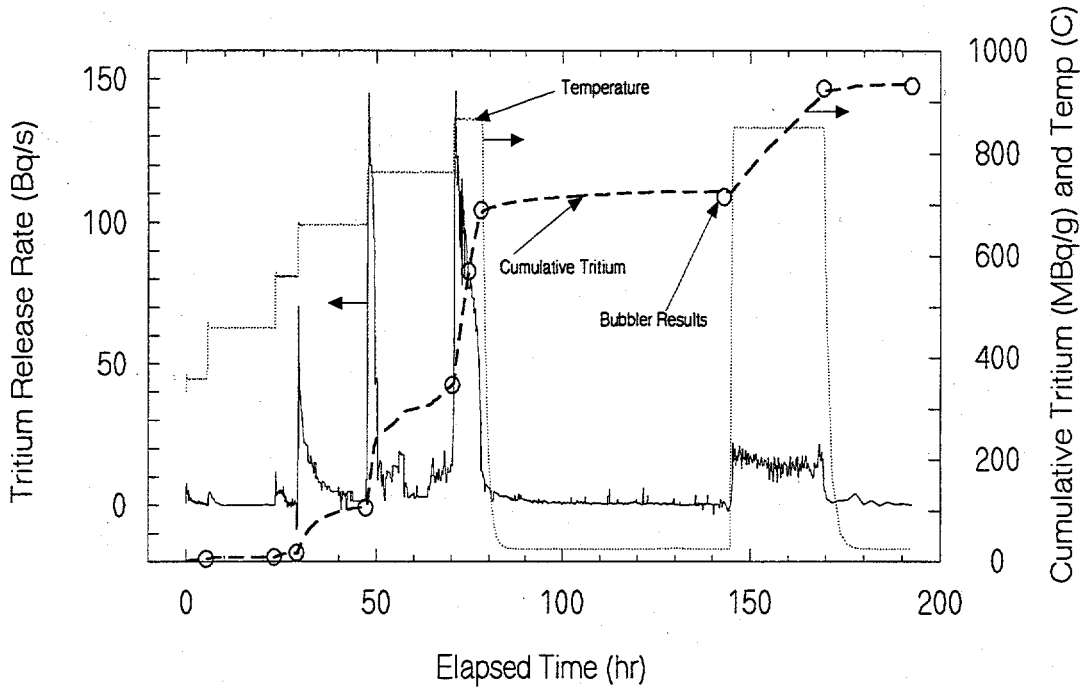

Figure 3. Stepped-anneal tritium release test of C03 (1-mm) beryllium

Addendum B:

STEPPED-ANNEAL TRITIUM RELEASE IN COBRA-1A2 D03 BERYLLIUM

SUMMARY

This addendum B includes a brief discussion of the test, the data shown plotted on both linear and log axes, and the test data in spreadsheet format in an attached file, of the tritium stepped-anneal test on the D03 1-mm pebble beryllium specimens. The tabulated temperatures, time, bubbler results, and assay results, were shown in the first report of June 19, 1997.

Experimental

The stepped-anneal test for tritium release kinetics was performed on the D03 1-mm pebbles using 10 pebbles with total sample weight of 0.0098g. The test temperature range was 350-850°C, in 100°C steps. Briefly, the sample was heated in a sweep gas of He+0.1%H_2 at 100 SCCM, the released tritium measured in real-time by an ion chamber, then oxidized on copper oxide and collected in a pair of water bubblers, and finally measured by liquid scintillation counting.

Discussion of Results

The plots of the stepped-anneal test data are shown in Figures 4 and 5, with Figure 4 showing the release rate on a linear axis and Figure 2 showing the same release rate data on a log axis. This test, compared to the earlier C03 test, used generally longer time intervals as well as a slightly larger sample size (10 pebbles versus 5 pebbles). The total cumulative released tritium at 350-850°C was 1050 MBq/g or 94% of the total inventory of 1120 MBq/g. The final temperature step of 850°C was held for 72 hours, resulting in greater cumulative levels. These compare with 75% of the inventory released for the C03 test. The residual tritium, measured by melting the sample at 1700C, was about 6% of the total inventory, with the totaled cumulative quantities agreeing relatively well with assay result.

A major difference between the C03 and D03 stepped-anneal tests is the release rates at the lower temperatures of 350-550°C. The D03 material showed much lower release rates at these lower temperatures. At the higher temperatures of 650-850°C, the release rates were more comparable between the two sample materials.

Due to the very low release rates (<1 Bq/s) at the lower temperatures of 350-550°C, the IC signal contained a great deal of noise with large narrow spikes, similar to what was seen in the earlier C03 test. The noise and spikes were removed in the data cleanup process. Release rates for the 650 and 750°C steps were larger, but still low at <100 Bq/s. The bulk of the released tritium, 74%, did not come off until 850°C. Due to the still relatively small sample size, the bubbler liquid scintillation results should always be considered the more reliable data, when compared to the IC results.

As has been done previously, the IC cumulative release curve in MBq/g, calculated from the release rate curve in Bq/s, was normalized to the collection bubbler liquid scintillation results in MBq/g. This was done by adjusting the IC baseline and/or IC calibration factor once for each bubbler data point. This method assumes the collection bubbler liquid scintillation results are always reliable and accurate, therefore, the IC curve must be adjusted to obtain agreement.

Figures 4 and 5 below show the release rate, as measured by the IC in Bq/s on the left axis, with cumulative tritium (both integrated IC signal and collection bubbler results) in MBq/g on the right axis, and temperature in degrees C also on the right axis.

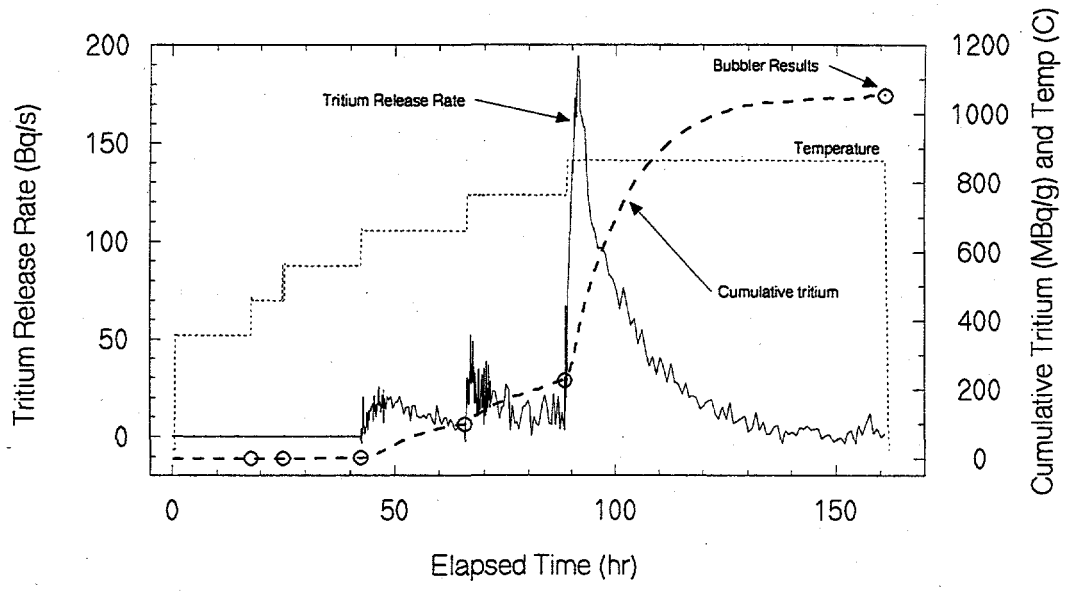

Figure 4. Stepped-anneal tritium release test data, 350-850°C in 100°C steps, for D03 (1-mm) beryllium, 10 pebble sample size.

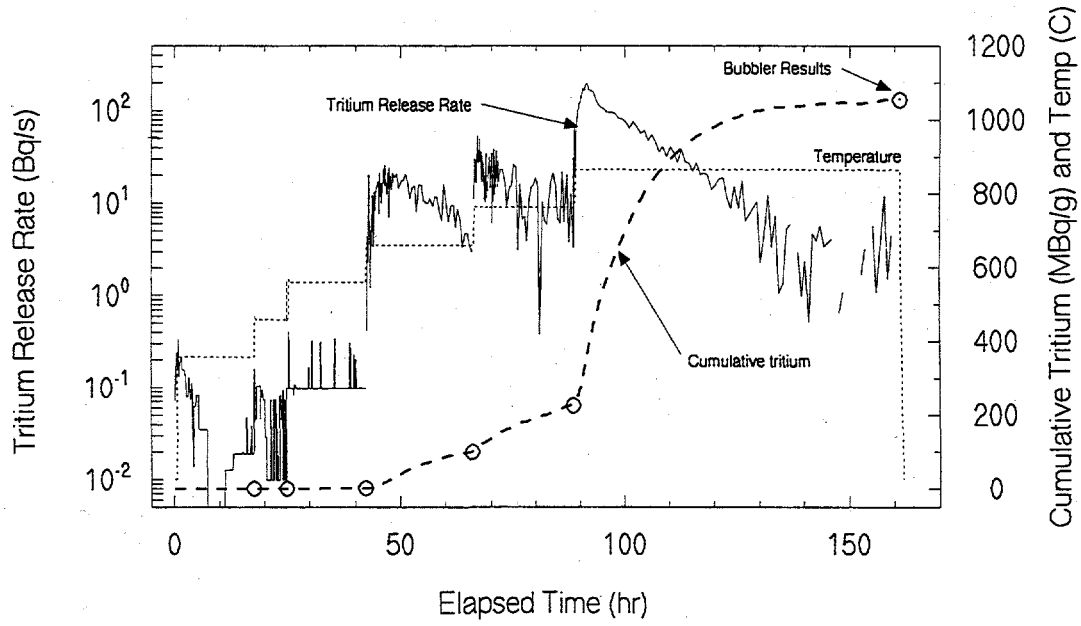

Figure 5. Stepped-anneal tritium release test data for D03 (1-mm) beryllium pebbles. Release rate data are plotted on log-axis to show release rates at lower temperatures.

8.0 RADIATION EFFECTS, MECHANISTIC STUDIES, AND EXPERIMENTAL METHODS

FUNDAMENTAL RADIATION EFFECTS PARAMETERS IN METALS AND CERAMICS* — S. J. Zinkle (Oak Ridge National Laboratory)

Extended Abstract

Useful information on defect production and migration can be obtained from examination of the fluence-dependent defect densities in irradiated materials, particularly when a transition from linear to sublinear accumulation is observed. Analysis of electrical resistivity and TEM data indicates that the fraction of freely migrating interstitials at 300K in 14-MeV neutron irradiated copper is ~10 to 12% of the NRT displacement value. It is interesting to note that similar freely migrating interstitial fractions of ~10% are estimated for neutron-irradiated MgO and Al_2O_3 near 300 K. At temperatures where interstitials are mobile (>50 K in Cu), the defect cluster density in pure copper is initially proportional to the dose and often exhibits a square root dose dependence above ~10^{-4} displacements per atom (dpa). This fluence dependence (determined from electrical resistivity and TEM studies) helps to resolve a long-standing controversy on the fluence dependence of radiation hardening. The activation energy for annealing Stage V (stacking fault tetrahedra evaporation) in copper has been measured to be 0.84 $\pm$0.03 eV. The temperature where recovery stage V is initiated in stainless steel is comparable to that of copper, but further work is needed to determine the stage V activation energy in steel. Void swelling in high-purity copper requires the presence of gas atoms such as oxygen or helium. The helium generated in copper during neutron irradiation is sufficient to stabilize void embryos even at low doses.

Further work is needed on several intriguing reported radiation effects in metals. The supralinear defect cluster accumulation regime in thin foil irradiated metals needs further experimental confirmation, and the physical mechanisms responsible for its presence need to be established. Self-organization of defect clusters occurs readily in commercially available Ni during irradiation. However, it is not clear whether defect cluster alignment can occur in bulk neutron- or ion-irradiated pure copper. The possible roles of impurities and differences in displacement cascade evolution on defect cluster patterning need to be examined.

Radiation hardening and the associated reduction in strain hardening capacity in FCC metals is a serious concern for structural materials. In general, the loss of strain hardening capacity is associated with dislocation channeling, which occurs when a high density of small defect clusters are produced (stainless steel irradiated near room temperature is a notable exception). Detailed investigations of the effect of defect cluster density and other physical parameters such as stacking fault energy on dislocation channeling are needed. Although it is clearly established that radiation hardening depends on the grain size ("radiation-modified Hall-Petch effect"), further work is needed to identify the physical mechanisms. In addition, there is a need for improved hardening superposition models when a range of different obstacle strengths are present.

Due to a lack of information on point defect diffusivities and the increased compexity of radiation effects in ceramics compared to metals, many fundamental radiation effects parameters in ceramics have yet to be determined. Optical spectroscopy data suggest that the oxygen monovacancy and freely migrating interstitial fraction in fission neutron irradiated MgO and Al_2O_3 are ~10% of the NRT displacement value. Ionization induced diffusion can strongly influence microstructural evolution in ceramics. Therefore, fundamental data on ceramics obtained from highly ionizing radiation sources such as electrons must be treated with appropriate caution to determine if it is influenced by ionization induced diffusion effects. $MgAl_2O_4$ is considerably more sensitive to ionization induced diffusion effects than MgO or Al_2O_3. Systematic investigations are needed to determine the sensitivity of a broad range of ceramics to ionization induced diffusion.

*Extended abstract of paper submitted to Rad. Eff. Def. Sol. as part of the proceedings of the Kiritani Symposium on Structural Defects in Advanced Materials, Inuyama, Japan, December 18-20, 1996.

VALIDATION OF THE SHEAR PUNCH-TENSILE CORRELATION TECHNIQUE USING IRRADIATED MATERIALS - G. L. Hankin and R. G. Faulkner (I.P.T.M.E., Loughborough University, Leicestershire, LE11 3UT, UK) M. B. Toloczko (Washington State University) and M. L. Hamilton (Pacific Northwest National Laboratory)*

To be published in Journal of Nuclear Materials as Proceedings of the 8th International Conference on Fusion Reactor Materials, Oct. 26-31, 1997, Sendai, Japan.

EXTENDED ABSTRACT

It was recently demonstrated that tensile data could be successfully related to shear punch data obtained on transmission electron microscopy (TEM) discs for a variety of irradiated alloys exhibiting yield strengths that ranged from 100 to 800 MPa. This implies that the shear punch test might be a viable alternative for obtaining tensile properties using a TEM disk, which is much smaller than even the smallest miniature tensile specimens, especially when irradiated specimens are not available or when they are too radioactive to handle easily.

The majority of the earlier tensile-shear punch correlation work was done using a wide variety of unirradiated materials. The current work extends this correlation effort to irradiated materials and demonstrates that the same relationships that related shear punch tests remain valid for irradiated materials. Shear punch tests were performed on two sets of specimens. In the first group, three simple alloys from the ^{59}Ni isotopic doping series in the solution annealed and cold worked conditions were irradiated at temperatures ranging from 365 to 495°C in the Fast Flux Test Facility. The corresponding tensile data already existed for from tensile specimens fabricated from the same raw materials and irradiated side-by-side with the disks. In the second group, three variants of 316 stainless steel were irradiated in FFTF at 5 temperatures between 400 and 730°C to doses ranging from 12.5 to 88 dpa. The specimens were in the form of both TEM and miniature tensile specimens and were irradiated side-by-side.

*Pacific Northwest National Laboratory is operated for the U.S. Department of Energy by Battelle Memorial Institute under Contract DE-AC06-76RLO 1830.

SUBCASCADE FORMATION IN DISPLACEMENT CASCADE SIMULATIONS: IMPLICATIONS FOR FUSION REACTOR MATERIALS[1] — Roger E. Stoller (Oak Ridge National Laboratory)[2] and Lawrence R. Greenwood (Pacific Northwest National Laboratory)

Extended Abstract

Primary radiation damage formation in iron has been investigated by the method of molecular dynamics (MD) for cascade energies up to 40 keV. The initial energy EMD given to the simulated PKA is approximately equivalent to the damage energy in the standard secondary displacement model by Norgett, Robinson, and Torrens (NRT); hence, EMD is less than the corresponding PKA energy. Using the values of EMD in Table 1, the corresponding EPKA and the NRT defects in iron have been calculated using the procedure described in Ref. 1 with the recommended 40 eV displacement threshold [2]. These values are also listed in Table 1. Note that the difference between the EMD and the PKA energy increases as the PKA energy increases and that the highest simulated PKA energy of 61.3 keV is the average for a collision with a 1.77 MeV neutron. Thus, these simulations have reached well into the fast neutron energy regime. For purposes of comparison, the parameters for the maximum DT neutron energy of 14.1 MeV are also included in Table 1. Although the primary damage parameters derived from the MD cascades exhibited a strong dependence on cascade energy up to 10 keV, this dependence was diminished and slightly reversed between 20 and 40 keV, apparently due to the formation of well-defined subcascades in this energy region. Such an explanation is only qualitative at this time, and additional analysis of the high energy cascades is underway in an attempt to obtain a quantitative measure of the relationship between cascade morphology and defect survival.

The results of the MD simulations have been used in the SPECOMP code to obtain effective, energy-dependent cross sections for two measures of primary damage production: (1) the number of surviving point defects expressed as a fraction of the those predicted by the NRT model, and (2) the fraction of the surviving interstitials contained in clusters. PKA spectra for iron were obtained from the SPECTER code and used to weight the MD-based damage production cross sections in order to obtain spectrum-averaged values for various irradiation environments. The primary results of these calculations are summarized in Fig. 1, where the PKA-spectrum-averaged defect survival fraction is shown in Fig. 1a, and the interstitial clustering fraction in Fig. 1b. Both average cross sections have been divided by the NRT dpa cross section. To provide a broad comparison, results are listed for: the ITER first wall, HFIR PTP and RB* positions, FFTF midcore and below core locations, and the 1/4-thickness position in a commercial reactor pressure vessel.

The average defect survival fraction decreases as the average PKA energy increases. Thus, the lowest defect survival is obtained in the ITER first wall which has the highest average PKA energy as result of the 14.1 MeV neutron source term. However, the differences between the various environments are small. This similarity arises for two reasons. First, the differences between the various fission and fusion PKA spectra are relatively modest in the region below about 10 keV where the energy dependence of the defect survival fraction is strongest. Then, when the PKA spectra become more different at higher energies, the defect survival fraction becomes nearly

---

1. Full paper to be published in Journal of Nuclear Materials, based on a presentation at the Eighth International Conference on Fusion Reactor Materials, October 1997, Sendai, Japan.

2. Research sponsored in part by the Office of Nuclear Regulatory Research, U.S. NRC under inter-agency agreement DOE 1886-8109-8L with the U.S. DOE and by the Division of Materials Sciences, U.S. DOE under contract DE-AC05-96OR22464 with Lockheed Martin Energy Research Corp.

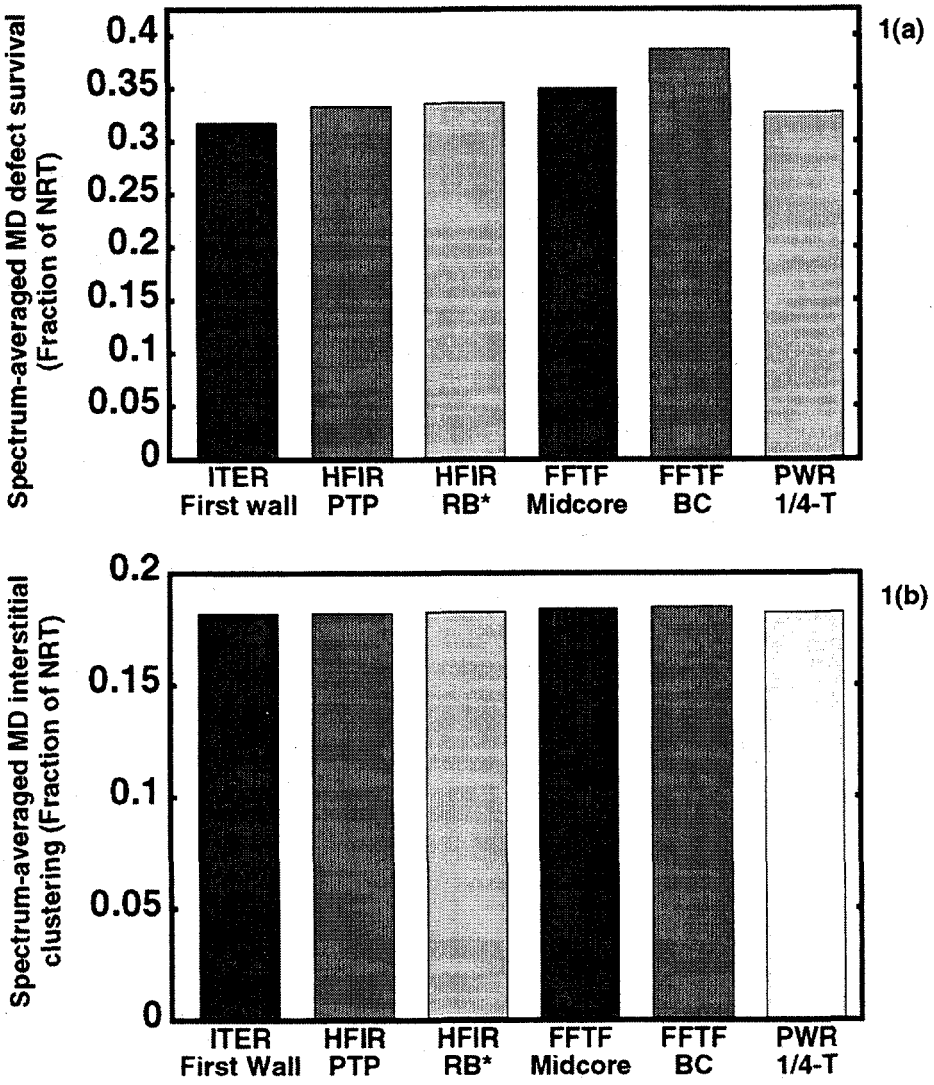

Figure 1. Comparison of spectrally-averaged damage production cross sections (per NRT dpa) for various irradiation environments; point defect survival ratio is shown in (a) and the interstitial clustering fraction is shown in (b).

independent of energy. The average interstitial clustering fraction shown in Fig. 1b is almost independent of the initial neutron energy spectrum.

The spectrum-averaged primary damage parameters shown in Fig. 1 are only weakly dependent on the initial neutron energy spectrum. This result appears unlikely to change significantly if higher energy cascades are included in the analysis. In particular, the extensive subcascade formation observed at 40 keV suggests that the results reported here should be relevant to high-energy neutron sources such as ITER. This conclusion implies that the displacement damage component of radiation damage produced in a DT fusion reactor should be well simulated by irradiation in a fission reactor neutron spectrum, and that differences in nuclear transmutation production may be the primary source of uncertainty in the prediction of material performance at high doses in DT fusion reactors.

Table 1. Typical MD cascade parameters and required atom block sizes

Neutron Energy (MeV)	Average PKA Energy (keV)	Corresponding EMD (keV)	NRT Displacements	Atoms in Simulation
0.00335	0.116	0.1	1	3,456
0.00682	0.236	0.2	2	6,750
0.0175	0.605	0.5	5	6,750
0.0358	1.24	1.0	10	54,000
0.0734	2.54	2.0	20	54,000
0.191	6.6	5.0	50	128,000
0.397	13.7	10.0	100	250,000
0.832	28.8	20.0	200	250,000
1.77	61.3	40.0	400	1,024,000
14.1	487.	220.4	2204	(1)

(1) no simulations done, displacement parameters included for comparison only

References

1. M. J. Norgett, M. T. Robinson, and I. M. Torrens, Nucl. Eng. and Des. 33 (1975) 50-54.
2. ASTM E521, Standard Practice for Neutron Radiation Damage Simulation by Charged-Particle Irradiation, Annual Book of ASTM Standards, Vol. 12.02, American Society of Testing and Materials, Philadelphia.

STOCHASTIC ANNEALING SIMULATION OF COPPER UNDER CONTINUOUS NEUTRON IRRADIATION - H.L. Heinisch (Pacific Northwest National Laboratory)* and B.N. Singh (Risø National Laboratory)

To be published in Journal of Nuclear Materials as Proceedings of the 8th International Conference on Fusion Reactor Materials, Oct. 26-31, 1997, Sendai, Japan.

SUMMARY

This report is a summary of a presentation made at ICFRM-8 on computer simulations of defect accumulation during irradiation of copper to low doses at room temperature. The simulation results are in good agreement with experimental data on defect cluster densities in copper irradiated in RTNS-II.

EXTENDED ABSTRACT

Stochastic annealing simulation provides a bridge between the atomistic and macroscopic scales that enables the direct effects of cascade production on the microstructure to be investigated. We report here on the simulation of damage accumulation under low doses of cascade-producing irradiation in copper at room temperature. The computer simulations were performed using the stochastic annealing code ALSOME, which is described in detail in earlier publications [1,2]. For defect accumulation simulations, the same model for annealing is used as for individual cascades, along with the same defect parameter values. The annealing volume for the accumulation simulations is significantly larger than for individual cascades, and new cascades are introduced into the volume as the annealing progresses to simulate the conditions of an ongoing irradiation. To make the computation tractable with respect to computer time, a relatively small cubic volume 54 nm on edge was chosen, and periodic boundaries were applied. Room temperature irradiation of copper by 14 MeV neutrons, as with RTNS-II, was simulated with a flux of 5, 10, and 25 keV cascades generated in MD simulations by Diaz de la Rubia and Guinan [3] and by Foreman et al. [4]. Fusion neutrons produce recoil atoms with an average energy of about 300 keV, but cascades produced by those high energy recoils are formed as a series of subcascades [5]. Thus, the flux of 5-25 keV MD cascades introduced into the simulation annealing volume should be a reasonable first approximation to the individual subcascades formed in irradiations by 14 MeV neutrons. A dose of slightly more than 0.1 DPA was obtained by introducing approximately 12,000 cascades into the annealing simulation volume. This large set of cascades was produced by repeated use of the 13 available MD cascades. Although periodic boundaries were used, the existence of a finite grain size (or a density of other intrinsic sinks) was simulated by imposing a limit on the number of times a mobile defect could traverse the simulation volume. Defects reaching the equivalent of 380 nm on average are considered to have reached a grain boundary or other intrinsic sink, and they are removed.

Doses up to 0.1 DPA were simulated at various damage rates, and the damage accumulation was observed as a function of dose. Figure 1 shows the defect cluster density as a function of dose for a simulated irradiation at a dose rate of 10^{-10} DPA/s, as in RTNS-II. The simulation results are compared to experimental cluster densities obtained from three different irradiation experiments on annealed copper in RTNS-II [6-8]. The RTNS-II test specimens were irradiated at dose rates varying from about 10^{-11} to 10^{-9} DPA/s. The

*Pacific Northwest National Laboratory is operated for the U.S. Department of Energy by Battelle Memorial Institute under Contract DE-AC06-76RLO 1830.

vacancy and SIA cluster densities are shown separately, as well as their total. The simulated total density of clusters is in very good agreement with the experimentally reported cluster density, being within about a factor of 2 throughout the range of doses.

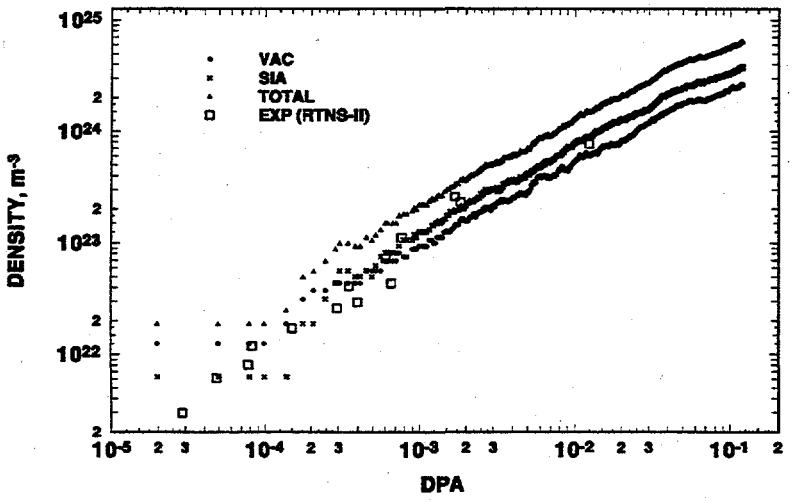

Figure 1. Vacancy, SIA and total cluster densities as a function of accumulated dose for copper irradiated at 300K under cascade-producing irradiation (as by 14 MeV neutrons) at 10^{-10} DPA/s. Simulation results are compared to experimental data from TEM observations of copper irradiated in RTNS-II [6,7,8]

The effects of dose, dose rate, cascade overlap and interstitial cluster mobilities on damage accumulation were investigated in further simulations. The surviving defect fraction is 1-2% of the calculated DPA value, with the vacancy clusters showing the greater variation with dose rate. Other investigations demonstrate the small, but noticeable, effects of cascade overlap at doses up to 0.1 dpa and the considerable sensitivity of defect accumulation to the allowable maximum size of glissile SIA loops in the model. The knowledge of SIA cluster and loop migration and stability are critical to continued development of stochastic annealing simulations of defect accumulation.

REFERENCES

1. H.L. Heinisch and B.N. Singh, J. Nucl. Mater. 232 (1996) 206.

2. H.L. Heinisch and B.N. Singh, J. Nucl. Mater., in press.

3. T.Diaz de la Rubia and M.W. Guinan, Mat Sci. Forum 97-99 (1992) 23.

4. A.J.E. Foreman, W.J. Phythian and C.A. English, Phil. Mag. A 66 (1992) 671.

5. H.L. Heinisch and B.N. Singh, Phil. Mag. A 67 (1993) 407.

6. N. Yoshida, Y. Akashi, K. Kitajima and M. Kiritani, J. Nucl. Mater. 133&134 (1985) 405.

7. S.J. Zinkle, J. Nucl. Mater. 150 (1987) 140.

8. Y. Satoh, I. Ishida, T. Yoshiie and M. Kiritani, J. Nucl. Mater. 155-157 (1988) 443.

CONTRIBUTION TO IRRADIATION CREEP ARISING FROM GAS-DRIVEN BUBBLE GROWTH - C. H. Woo (The Hong Kong Polytechnic University, Kowloon, Hong Kong) and F. A. Garner (Pacific Northwest National Laboratory)*

To be published in Journal of Nuclear Materials as Proceedings of the 8th International Conference on Fusion Materials, Oct. 26-31, 1997, Sendai, Japan.

EXTENDED ABSTRACT

In a previous paper the relationship was defined between void swelling and irradiation creep arising from the interaction of the SIPA and SIG creep-driven deformation and swelling-driven deformation was highly interactive in nature, and that the two contributions could not be independently calculated and then considered as directly additive. This model could be used to explain the recent experimental observation that the creep-swelling coupling coefficient was not a constant as previously assumed, but declined continuously as the swelling rate increased. Such a model thereby explained the "creep-disappearance" and "creep-damping" anomalies observed in conditions where significant void swelling occurred before substantial creep deformation developed.

At lower irradiation temperatures and high helium/hydrogen generation rates, such as found in light water cooled reactors and some fusion concepts, gas-filled cavities that have not yet exceeded the critical radius for bubble-void conversion should also exert an influence on irradiation creep. In this paper the original concept is adapted to include such conditions, and its predictions then compared with available data. It is shown that a measurable increase in the creep rate is expected compared to the rate found in low gas-generating environments. The creep rate is directly related to the gas generation rate and thereby to the neutron flux and spectrum.

*Pacific Northwest National Laboratory is operated for the U.S. Department of Energy by Battelle Memorial Institute under Contract DE-AC06-76RLO 1830.

9.0 DOSIMETRY, DAMAGE PARAMETERS, AND ACTIVATION CALCULATIONS

NEUTRON DOSIMETRY AND DAMAGE CALCULATIONS FOR THE HFIR-JP-9, -12, and -15 IRRADIATIONS - L. R. Greenwood (Pacific Northwest National Laboratory)* and C. A. Baldwin (Oak Ridge National Laboratory)

OBJECTIVE

To provide dosimetry and damage analysis for fusion materials irradiation experiments.

SUMMARY

Neutron fluence measurements and radiation damage calculations are reported for the joint U.S.- Japanese experiments JP-9, -12, and -15. These experiments were conducted in target positions of the High Flux Isotope Reactor (HFIR) at Oak Ridge National Laboratory (ORNL) for a period of nearly four years. The maximum neutron fluence at midplane was 2.6×10^{23} n/cm^2 (7.1×10^{22} n/cm^2 above 0.1 MeV), resulting in about 60 dpa and 3900 appm helium in type 316 stainless steel.

PROGRESS AND STATUS

Introduction

The JP-9, -12, and -15 experiments were irradiated in target positions of HFIR during cycles 289 through 324 starting July 20, 1990, and ending April 1, 1994, for a net exposure of 763.58 effective full- power days at 85 MW. The experiment was a collaborative effort of the U.S. Fusion Materials Program at ORNL and the Japanese Atomic Energy Research Institute (JAERI). The goal of the experiment was to irradiate primarily transmission electron microscope specimens and round bar tensile specimens to very high dose levels. A complete description of the specimen matrices and irradiation assemblies has been published previously [1].

Neutron dosimetry capsules were inserted at six different elevations in each of the three assemblies (JP-9, -12, and –15). The dosimetry capsules consisted of small aluminum tubes measuring about 1.3 mm in diameter and 6.4 mm in length. Each tube contained small monitor wires of Fe, Ni, Ti, Nb, 0.1% Co-Al alloy, and 80.2% Mn-Cu alloy. Following irradiation, the monitors were removed from the assemblies and analyzed for gamma activities at ORNL. Because of our previous experience and the anticipated similarity of the dosimetry monitor results, only 7 of the 18 capsules were analyzed; the remainder of the capsules were stored pending further analyses as necessary.

The measured gamma activities were analyzed at Pacific Northwest National Laboratory. The measured activities were converted to activation rates, as listed in Table 1, by correcting for nuclear burnup, gamma self-absorption, decay during and after irradiation, isotopic abundance, and atomic weight. Burnup corrections are based on an iterative procedure for the thermal/epithermal monitor reactions. The resulting estimates of the thermal/epithermal neutron

*Pacific Northwest National Laboratory is operated for the U.S. Department of Energy by Battelle Memorial Institute under Contract DE-ACO6-76RLO 1830.

fluences were then used to calculate burnup corrections for the threshold fast neutron monitor reactions. Due to the extremely high neutron fluences in these experiments, burnup corrections were quite high for some of the reactions: burnup corrections averaged 40-80% for the thermal/epithermal reactions and 2-70% for the threshold reaction rates. The activation rates listed in Table 1 are normalized to full reactor power of 85 MW and have a net absolute uncertainty of about 5%.

Although the three different irradiations were located in different target positions of HFIR, the activation data all appear to fall on a relatively smooth curve such that flux gradients between the three target positions are less than 10%. Since only 7 of the 18 dosimetry monitors were analyzed, there are insufficient data to determine the small flux gradients between the three assemblies. Consequently, all the data were analyzed together, giving average neutron fluences and damage rates. The activation rates in Table 1 were fit to a polynomial function of form $f(x) = f(0) [1 + a x^2]$, where x is the vertical height from reactor centerline in cm. All of the data are reasonably well fit by the average polynomial (coefficient $a = -9.35 \times 10^{-4}$). Midplane activation rates were then used in the STAY'SL [2] computer code to adjust the neutron flux spectrum determined in previous spectral measurements in the target position in HFIR [3,4]. STAY'SL performs a generalized least-squares adjustment of all measured and calculated values including the measured activities, calculated spectra, and neutron cross sections. Neutron cross sections and their uncertainties were generally taken from the ENDF/B-V [5] evaluation. The resulting neutron fluence values are listed in Table 2. The activation rates and the derived neutron spectra and fluences are in excellent agreement with previous measurements in the target position of HFIR [3,4].

Neutron damage calculations were performed using the SPECTER computer code [6] at the midplane position of HFIR. Midplane dpa and helium (appm) values are also listed in Table 2. The fluence and damage values at other experimental positions can be calculated by the gradient equation given above. Damage parameters for other elements or compounds have been calculated and are readily available on request.

Helium production in nickel and nickel alloys requires a more complicated non-linear calculation [7]. Helium production in stainless steel is thus detailed separately in Table 3.

FUTURE WORK

Additional experiments still in progress in HFIR include MFE-200J-1, MFE-400J-1, and JP20-22.

REFERENCES

1. R. L. Senn, Status of U.S./Japan Collaborative Program Phase II HFIR Target Capsules, Fusion Reactor Materials Semiannual Progress Report, DOE/ER-0313/5, p. 6 (1989).

2. F. G. Perey, Least Squares Dosimetry Unfolding: The Program STAY'SL, ORNL/TM-6062 (1977).

3. L. R. Greenwood, Alloy Development for Irradiation Performance Semiannual Report, DOE/ER-0045/11, pp. 30-37 (1983).

4. L. R. Greenwood and R. T. Ratner, Neutron Dosimetry and Damage Calculations for the HFIR JP-23 Irradiations, Fusion Materials Semiannual Progress Report, DOE/ER-0313/21, p. 229 (1997); L. R. Greenwood and R. T. Ratner, Neutron Dosimetry and Damage Calculations for the JP-10, 11, 13, and 16 Experiments in HFIR, DOE/ER-0313/19, p. 281 (1995); L. R. Greenwood and C. A. Baldwin, Neutron Dosimetry and Damage Calculations for the JP-17, 18, and 19 Experiments in HFIR, p. 286, (1995).

5. Evaluated Nuclear Data File, Part B, Version V, National Nuclear Data Center, Brookhaven National Laboratory.

6. L. R. Greenwood and R. K. Smither, SPECTER: Neutron Damage Calculations for Materials Irradiations, ANL/FPP-TM-197, January 1985.

7. L. R. Greenwood, A New Calculation of Thermal Neutron Damage and Helium Production in Nickel, Journal of Nuclear Materials, Vol. 116, pp. 137-142 (1983).

Table 1. Activation rates (at/at-s) - HFIR JP-9, -12, and -15

Position/ Monitor	Ht,cm	$^{54}Fe(n,p)^{54}Mn$ (E-11)	$^{46}Ti(n,p)^{46}Sc$ (E-12)	$^{55}Mn(n,2n)^{54}Mn$ (E-13)	$^{59}Co(n,\gamma)^{60}Co$ (E-8)	$^{93}Nb(n,\gamma)^{94}Nb$ (E-9)
JP9 - 2	12.0	5.00	6.89	1.31	4.61	2.03
JP9 - 5	-25.3	2.07	2.92	0.63	3.04	1.23
JP12-20	12.6	4.69	6.69	1.34	4.44	2.01
JP12-23	-8.3	5.16	7.43	1.28	4.89	2.20
JP15-38	13.1	4.79	6.63	1.12	4.25	1.88
JP15-37	22.0	2.91	-	0.68	2.82	1.12
JP15-40	0.0	6.07	-	1.37	5.58	2.49

Table 2. Midplane fluence and damage values for HFIR JP-9, 12, and 15

Neutron Fluence, $\times 10^{22}$ n/cm^2		Element	dpa	He,appm
Total	26.3	C	50.4	112.4
Thermal (<.5 eV)	10.9	Al	92.7	43.1
0.5 eV - 0.1 MeV	8.39	V	66.2	1.4
> 0.1 MeV	7.06	Cr	58.5	10.0
> 1 MeV	3.67	Fe	51.8	17.8
		Ni Fast	55.5	242.5
		^{59}Ni	48.2	27349.3
		Total	103.7	27591.8
		Cu	67.1	15.7

Table 3. Dpa and helium values for 316 SS in HFIR JP-9, -12, -15
(includes ^{59}Ni effect)

Ht (cm)	dpa	He (appm)
0	59.6	3601
3	59.2	3573
6	57.8	3488
9	55.4	3345
12	52.1	3140
15	47.7	2869
18	42.2	2525
21	35.8	2102
24	28.3	1593

316SS = Fe(0.645), Ni(0.13), Cr(0.18), Mn(0.019), Mo(0.026) wt%

NEUTRON DOSIMETRY AND DAMAGE CALCULATIONS FOR THE HFIR-JP-20 IRRADIATION - L. R. Greenwood (Pacific Northwest National Laboratory)* and C. A. Baldwin (Oak Ridge National Laboratory)

OBJECTIVE

To provide dosimetry and damage analysis for fusion materials irradiation experiments.

SUMMARY

Neutron fluence measurements and radiation damage calculations are reported for the joint U.S.-Japanese experiment JP-20, which was conducted in a target position of the High Flux Isotope Reactor (HFIR) at Oak Ridge National Laboratory (ORNL). The maximum total neutron fluence at midplane was 4.2×10^{22} n/cm^2 (1.0×10^{22} n/cm^2 above 0.1 MeV), resulting in about 8.4 dpa and 388 appm helium in type 316 stainless steel.

PROGRESS AND STATUS

Introduction

The JP-20 experiment was irradiated in a target position of HFIR during cycles 322 through 326 starting December 16, 1993, and ending June 3, 1994, for a net exposure of 110.20 effective full-power days at 85 MW. The experiment was a collaborative effort cosponsored by the U.S. Fusion Materials Program at ORNL and the Japanese Atomic Energy Research Institute (JAERI). The goal of the experiment was to irradiate primarily transmission electron microscope specimens and flat tensile specimens to moderate dose levels. A complete description of the specimen matrices and irradiation assemblies has been published previously [1].

Neutron dosimetry capsules were inserted at six different elevations in the assembly. The dosimetry capsules consisted of small aluminum tubes measuring about 1.3 mm in diameter and 6.4 mm in length. Each tube contained small monitor wires of Fe, Ni, Ti, Nb, 0.1% Co-Al alloy, and 80.2% Mn-Cu alloy. Following irradiation, the monitors were removed from the assemblies and analyzed for gamma activities at ORNL. Because of our previous experience and the anticipated similarity of the dosimetry monitor results, only 2 of the 6 capsules were analyzed; the remainder of the capsules were stored pending further analyses, as necessary.

The measured gamma activities were analyzed at Pacific Northwest National Laboratory. The measured activities were converted to activation rates, as listed in Table 1, by correcting for nuclear burnup, gamma self-absorption, decay during and after irradiation, isotopic abundance, and atomic weight. Burnup corrections are based on an iterative procedure for the thermal/epithermal monitor reactions. The resulting estimates of the thermal/epithermal neutron fluences were then used to calculate burnup corrections for the threshold fast neutron monitor reactions. Because of the extremely high neutron fluences in these experiments, burnup

*Pacific Northwest National Laboratory is operated for the U.S. Department of Energy by Battelle Memorial Institute under Contract DE-ACO6-76RLO 1830.

corrections were quite high for some of the reactions. Burnup corrections averaged 15-20% for the thermal/epithermal reactions and 0-20% for the threshold reaction rates. The activation rates listed in Table 1 are normalized to full reactor power of 85 MW and have a net absolute uncertainty of about 5%.

The activation rates in Table 1 fit a polynomial function of form $f(x) = f(0) [1 + a x^2]$, where x is the vertical height from reactor centerline in cm. All of the data are reasonably well fit by the average polynomial coefficient $a = -9.35 \times 10^{-4}$, as determined from similar irradiations in HFIR. Midplane activation rates were then used in the STAY'SL [2] computer code to adjust the neutron flux spectrum determined in previous spectral measurements in the target position in HFIR [3,4]. STAY'SL performs a generalized least-squares adjustment of all measured and calculated values including the measured activities, calculated spectra, and neutron cross sections. Neutron cross sections and their uncertainties were generally taken from the ENDF/B-V [5] evaluation. The resultant neutron fluence values are listed in Table 2. The activation rates and the derived neutron spectra and fluences are in excellent agreement with previous measurements in the target position of HFIR [3,4].

Neutron damage calculations were performed using the SPECTER computer code [6] at the midplane position of HFIR. Midplane dpa and helium (appm) values are also listed in Table 2. The fluence and damage values at other experimental positions can be calculated by the gradient equation given above. Damage parameters for other elements or compounds have been calculated and are readily available on request.

Helium production in nickel and nickel alloys requires a more complicated non-linear calculation [7]. Helium production in stainless steel is thus detailed separately in Table 3.

FUTURE WORK

Additional experiments still in progress in HFIR include MFE-200J-1, MFE-400J-1, and JP21-22.

REFERENCES

1. J. E. Pawel, A. W. Longest, R. L. Senn, K. Shiba, D. W. Heatherly, and R. G. Sitterson, Status of U.S./Japan Collaborative Program Phase II HFIR Target and RB* Capsules, Fusion Reactor Materials Semiannual Progress Report, DOE/ER-0313/15, pp. 3-22 (1994).

2. F. G. Perey, Least Squares Dosimetry Unfolding: The Program STAY'SL, ORNL/TM-6062 (1977).

3. L. R. Greenwood, Alloy Development for Irradiation Performance Semiannual Report, DOE/ER-0045/11, pp. 30-37 (1983).

4. L. R. Greenwood and R. T. Ratner, Neutron Dosimetry and Damage Calculations for the HFIR JP-23 Irradiations, Fusion Materials Semiannual Progress Report, DOE/ER-0313/21, p. 229 (1997); L. R. Greenwood and R. T. Ratner, Neutron Dosimetry and Damage Calculations for the JP-10, 11, 13, and 16 Experiments in HFIR, DOE/ER-

0313/19, p. 281 (1995); L. R. Greenwood and C. A. Baldwin, Neutron Dosimetry and Damage Calculations for the JP-17, 18, and 19 Experiments in HFIR, p. 286, (1995).

5. Evaluated Nuclear Data File, Part B, Version V, National Nuclear Data Center, Brookhaven National Laboratory.

6. L. R. Greenwood and R. K. Smither, SPECTER: Neutron Damage Calculations for Materials Irradiations, ANL/FPP-TM-197, January 1985.

7. L. R. Greenwood, A New Calculation of Thermal Neutron Damage and Helium Production in Nickel, Journal of Nuclear Materials, Vol. 116, pp. 137-142 (1983).

Table 1. Activation rates (at/at-s) - HFIR JP-20

Position/ Monitor	Ht,cm	$^{54}Fe(n,p)^{54}Mn$ (E-11)	$^{46}Ti(n,p)^{46}Sc$ (E-12)	$^{55}Mn(n,2n)^{54}Mn$ (E-13)	$^{59}Co(n,\gamma)^{60}Co$ (E-8)	$^{93}Nb(n,\gamma)^{94}Nb$ (E-9)
JP20-16	16.6	3.99	5.83	1.33	4.49	1.94
JP20-38	0.0	5.67	7.94	1.75	6.60	2.85

Table 2. Midplane fluence and damage values for HFIR JP-20

Neutron Fluence, $\times 10^{22}$ n/cm^2	
Total	4.19
Thermal (<.5 eV)	1.84
0.5 eV - 0.1 MeV	1.32
> 0.1 MeV	1.05
> 1 MeV	0.519

Element	dpa	He,appm
C	7.5	17.1
Al	13.5	6.46
V	9.6	0.22
Cr	8.4	1.48
Fe	7.5	2.63
Ni Fast	8.1	34.6
^{59}Ni	5.2	2936.1
Total	13.3	2970.8
Cu	9.7	2.35

Table 3. Dpa and helium values for 316 SS in HFIR JP-20 (includes ^{59}Ni effect)

Ht (cm)	dpa	He (appm)
0	8.38	388
3	8.31	383
6	8.11	368
9	7.75	342
12	7.25	308
15	6.60	265
18	5.81	215
21	4.88	160
24	3.82	104

316SS = Fe(0.645), Ni(0.13), Cr(0.18), Mn(0.019), Mo(0.026) wt%

NEUTRON DOSIMETRY AND RADIATION DAMAGE CALCULATIONS FOR HFBR -
L. R. Greenwood and R. T. Ratner (Pacific Northwest National Laboratory)*

OBJECTIVE

To provide neutron dosimetry and radiation damage analyses for fusion materials irradiations.

SUMMARY

Neutron dosimetry measurements have been conducted for various positions of the High Flux Beam Reactor (HFBR) at Brookhaven National Laboratory (BNL) in order to measure the neutron flux and energy spectra. Neutron dosimetry results and radiation damage calculations are presented for positions V10, V14, and V15.

PROGRESS AND STATUS

Introduction

The HFBR has an enriched fuel core and a heavy water reflector, thus offering a wide range of neutron spectra for irradiation experiments. Researchers from Oak Ridge National Laboratory (ORNL) recently utilized this spectral capability to investigate effects of neutron spectrum on radiation damage in steels. In support of this effort, comprehensive measurements of neutron flux and energy spectra were conducted, as documented in this report.

Irradiation History

The first dosimetry measurements in HFBR were conducted in 1976 in position V15 in support of experiments planned by C. L. Snead (BNL). More recent dosimetry measurements were started in 1989 with two irradiations in positions V10 and V15. Additional planned measurements were delayed by the shutdown of HFBR in the 1990-1991 timeframe. Measurements were resumed in 1994 in V10 and V14. Recently, measurements were conducted in 1996 with several irradiations in positions V10, V14, and V15. Planned additional measurements have been delayed by the present shutdown of the reactor. The irradiation histories for all of these irradiations are summarized in Table 1 below.

The first (V15-S3) and last (V10-5) irradiations included complete spectral sets of dosimeters with both bare and cadmium-covered monitors. The spectral sets consisted of small wires of Fe, 0.1% Co-Al, Al, Ni, Ti, 0.1% Au-Al, 2.2% Lu-Al, Nb, 80% Mn-Cu, and encapsulated oxides of ^{237}Np and ^{238}U. All of the other capsules contained a reduced set of monitors including Fe, 0.1% Co-Al, Al, Ni, and Ti. The irradiations in 1994, denoted as ORNL, were

*Pacific Northwest National Laboratory is operated for the U.S. Department of Energy by Battelle Memorial Institute under Contract DE-ACO6-76RLO 1830.

conducted by C.A. Baldwin at Oak Ridge National Laboratory. Following gamma counting at ORNL, the results were sent to PNNL for analysis. There was one additional irradiation in HFBR denoted as V15-1 that included a full spectral set of monitors and a cadmium cover. The capsules were doubly encapsulated in quartz resulting in very high heating that melted the cadmium; however, most of the monitors were recovered for analysis. The dual irradiations denoted as V10-2 and V10-10 were designed to compare bare and cadmium covered reaction rates; however, due to a miscommunication the two capsules were identical without any cadmium cover.

Table 1. Summary of HFBR dosimetry measurements

Position-Dosimeter	Power (MW)	Height,in.@	Start Date/Time	Stop Date/Time	EFPH*
V15-S3	40	-0.85	4/30/76	4/30/76	#
V15-7	60	0	3/07/89 13:53	3/07/89 17:53	4
V10-3	60	-7.1	3/03/89 13:50	3/07/89 13:53	96
V10-ORNL	30	-7.1	10/21/94 9:55	10/21/94 17:55	8
V14-ORNL	30	-6.1	10/12/94 10:47	10/12/94 18:47	8
V10-2	30	-7.1	4/29/96 14:03	4/30/96 14:03	24
V10-10	30	-7.1	4/29/96 14:03	4/30/96 14:03	24
V10-1	30	-7.1	5/08/96 10:14	5/08/96 15:19	5:08
V14-4	30	-6.1	5/20/96 15:12	5/21/96 15:20	24:13
V10-5	30	-7.1	7/31/96 10:00	7/31/96 17:17	6:17
V15-1	30	0	8/26/96 10:42	8/26/96 15:07	4:25

@Most irradiations were at the bottom of each thimble except for the V15 runs, as noted.
*EFPH = effective full power hours at stated power.
#Details of the 1976 irradiation could not be retrieved from the available records.

Gamma Counting and Data Reduction

L. R. Greenwood analyzed the irradiations in 1976 and 1989 at Argonne National Laboratory. Chuck Baldwin at ORNL conducted the two irradiations in 1994 and the data were analyzed at PNNL. All of the other irradiations were analyzed by the present authors at Pacific Northwest National Laboratory. In all cases, individual monitors retrieved from the dosimetry capsules were gamma-counted using high-resolution Ge spectrometers. The measured activities were then converted to saturated activation rates by correcting for the decay during and after irradiation, gamma self shielding, atomic weight, and fission yield, as appropriate. The resultant activation rates are listed in Tables 2-3 in units of product atom/target atom-second. The values have an estimated accuracy of 2-3%, except as noted. The largest sources of uncertainty are due to the counting statistics and detector calibration. Results measured in 1976 are not listed since these values may contain some small differences in the nuclear decay data and neutron activation cross sections that need to be evaluated.

The cadmium cover and neutron self-shielding corrections are not included for the values listed in Tables 2-3. Since these effects depend on the neutron flux spectrum, we corrected

the energy-dependent neutron activation cross sections so that spectral adjustments, described later, automatically include the proper corrections for these two effects.

Several problems were encountered in the analysis of the activation data for position V10. All of these problems are due to the very thermalized neutron spectrum, which makes it possible for thermal neutron or photon effects to compete with fast neutron reactions. In particular, the $^{27}Al(n,a)^{24}Na$ and $^{46}Ti(n,p)^{46}Sc$ rates are deemed to be unreliable due to competition from (n,γ) reactions with Na and Sc, respectively. The fission rates for ^{237}Np and ^{238}U are also deemed to be unreliable due to photofission effects which were calculated using photon flux calculations provided by Eugene Hu (BNL).

The data for position V10 listed in Table 2 also show an unexplained decrease (about 15%) in the activation rates measured with the full spectral set (V10-5). For the thermal neutron reactions, this decrease might be explained by a flux depression effect caused by the cadmium cover. However, similar effects are seen with the threshold reactions, which are not sensitive to thermal flux depression effects. Another possible cause for the difference may be the reactor power history, which involved a 1 hour unplanned reactor shutdown for this particular irradiation although reactor power history corrections attempted to correct for this effect. Finally, such effects may be caused by differences in the reactor fuel cycle. However, measurements in V10 were deliberately designed to sample different parts of the fuel cycle and the good agreement between the other four experiments would suggest that such effects are quite small. The decreased reaction rates for V10-5 are thus not understood at this time.

Neutron Flux and Spectral Adjustments

The activation rates listed in Tables 2-3 are integral quantities equal to the energy integral of the neutron activation cross section times the neutron flux spectrum. Since the neutron activation cross sections are relatively well known, the set of integral equations represented by the data can be solved by a least-squares technique to determine the neutron flux spectrum that provides the best fit to the data. This spectral adjustment was performed with the STAY'SL computer code [1] which takes into account all known uncertainties.

Eugene Hu (BNL) provided starting neutron flux spectra calculated at a reactor power level of 40 MW. The neutron spectral adjustment results are presented in Table 4 and shown in Figure 1. As can be seen, in general the measured neutron flux values are about 20-40% lower than the calculations. This difference is seen with both the thermal and fast neutron fluxes, which have the lowest uncertainty in the measurements. In the case of V10-5 and V15-S3, full spectral sets were analyzed resulting in reasonably low uncertainties for all neutron energy ranges. However, for the other measurements, the dosimetry reactions used do not result in much sensitivity to neutron energies between 0.5 eV and about 1 MeV; hence, fluxes in this range have a larger uncertainty, as stated in Table 4. Hopefully, additional measurements using full spectral sets will be conducted when HFBR resumes operation.

For position V15, the flux values determined from run V15-7 at 60 MW in 1989 are in good agreement with the more recent results from run V15-1 at 30 MW in 1996. The flux values measured for this position in 1976 agree within 15% except in the epithermal flux region, as

discussed above. The current flux values are believed to be more reliable since they are based on more recent neutronics calculations that better define the flux spectrum.

Radiation Damage Calculations

The adjusted neutron spectra were used to calculate displacements per atom (dpa) values for various elements and compounds using the SPECTER computer code [2]. The results are listed in Table 5. Values are quoted for the specific irradiations that were conducted. Total and fast (> 1 MeV) neutron fluences are also listed and the ratios (dpa/E+22 n/cm^2) are given so that damage rates can be calculated for any length of irradiation. The calculations for SiC were performed using the SPECOMP computer code to calculate the dpa cross sections. Displacement threshold values of 20 eV were assumed for both the Si and C atoms.

Table 2. Activation rates (atom/atom-s) for position V10 of HFBR

Reaction	Run 1	Run 2	Run 5	Run10	ORNL	Run 3	Comments
	30MW	30MW	30MW	30MW	30MW	30MW*	
$^{54}Fe(n,p)^{54}Mn$			7.37E-15				
+Cd			7.16E-15				
$^{58}Fe(n,\gamma)^{59}Fe$	1.80E-10	1.76E-10	1.54E-10	1.75E-10	1.59E-10	1.63E-10	
+Cd			5.06E-12				
$^{59}Co(n,\gamma)^{60}Co$	5.53E-09	5.33E-09	4.59E-09	5.31E-09	4.89E-9	5.06E-09	
+Cd			1.54E-11				
$^{27}Al(n,\alpha)^{24}Na$	5.57E-16	4.19E-16		6.88E-16		4.13E-16	23Na(n,γ)?
$^{58}Ni(n,p)^{58}Co$	1.01E-14	9.23E-15	9.17E-15	8.96E-15	7.72E-15	7.18E-15	
$^{46}Ti(n,p)^{46}Sc$	1.65E-15	1.64E-15	1.29E-15	1.69E-15		1.62E-15	45Sc(n,γ)?
$^{47}Ti(n,p)^{47}Sc$	1.92E-15	2.27E-15		2.20E-15		1.59E-15	
$^{48}Ti(n,p)^{48}Sc$	5.66E-17	6.09E-17		6.32E-17		4.99E-17	
$^{197}Au(n,\gamma)^{198}Au$			1.26E-08				
+Cd			3.54E-10				
$^{176}Lu(n,\gamma)^{177}Lu$			4.73E-07				
+Cd			2.68E-09				
$^{93}Nb(n,\gamma)^{94}Nb$			1.48E-10				
$^{55}Mn(n,2n)^{54}Mn$			7.05E-17				
$^{237}Np(n,\gamma)^{238}Np$ +Cd			4.52E-10				
$^{238}U(n,\gamma)^{239}Np$ +Cd			1.93E-11				
^{238}U(n,fission) +Cd			1.29E-13				Photofission
^{237}Np(n,fission) +Cd			5.32E-13				Photofission

*Rates for run V10-3 were renormalized from 60 MW to 30 MW.

Table 3. Activation rates (atom/atom-s) for positions V14 and V15 in HFBR

Position	V14	V14	V15	V15
Reaction	Run 4	ORNL	Run 1	Run 7
	30 MW	30 MW	30 MW	30 MW*
$^{54}Fe(n,p)^{54}Mn$	2.92E-12	3.19E-12	1.12E-11	1.06E-11
$^{58}Fe(n,\gamma)^{59}Fe$	4.98E-10	4.94E-10	1.78E-10	1.80E-10
$^{59}Co(n,\gamma)^{60}Co$	1.69E-08	1.67E-08	8.06E-9	8.50E-09
$^{93}Nb(n,\gamma)^{94}Nb$			8.36E-10	
$^{27}Al(n,\alpha)^{24}Na$	4.56E-14			8.75E-14
$^{58}Ni(n,p)^{58}Co$	3.06E-12	3.54E-12	1.46E-11	1.38E-11
$^{46}Ti(n,p)^{46}Sc$	4.55E-13			1.50E-12
$^{47}Ti(n,p)^{47}Sc$	7.23E-13			2.51E-12
$^{48}Ti(n,p)^{48}Sc$	1.35E-14			3.78E-14
$^{238}U(n,fission)+Cd$			4.82E-11	
$^{237}Np(n,fission+Cd$			3.06E-10	

*Rates for run V15-7 were renormalized from 60 MW to 30 MW.

Table 4. Comparison of calculated and adjusted neutron fluxes (n/cm^2-s)

V10 (-7.1")

E,MeV	Exp.(PNNL)		Calc.(BNL)	E/C/Norm*
Power	30	+/–%	40	
Th, <0.5 eV	1.57E+14	6	3.48E+14	0.60
0.5 eV-0.1 MeV	2.01E+12	16	1.92E+12	1.40
>0.11 MeV	2.84E+11	22	2.05E+11	1.85
>1.0 MeV	1.03E+11	23	3.91E+10	3.51
Total	1.59E+14	6	3.50E+14	0.61

V14 (-6.1")

E,MeV	Exp.(PNNL)		Calc.(BNL)	E/C/Norm*
Power	30	+/–%	40	
Th, <0.5 eV	4.96E+14	10	8.45E+14	0.78
0.5 eV-0.1 MeV	4.99E+14	20	6.80E+14	0.98
>0.11 MeV	5.99E+13	10	1.24E+14	0.64
>1.0 MeV	2.38E+13	11	5.05E+13	0.63
Total	1.06E+15	8	1.65E+15	0.86

V15 (Midplane) (1996)

E,MeV	Exp.(PNNL)		Calc.(BNL)	E/C/Norm*
Power	30	+/–%	40	
Th, <0.5 eV	1.23E+14	8	2.36E+14	0.69
0.5 eV-0.1 MeV	1.03E+15	15	1.82E+15	0.76
>0.11 MeV	2.64E+14	10	4.89E+14	0.72
>1.0 MeV	1.11E+14	11	1.83E+14	0.81
Total	1.42E+15	8	2.54E+15	0.75

V15 (Midplane) (1989)

E,MeV	Exp.(PNNL)		Calc.(BNL)	E/C/Norm*
Power	60	+/–%	40	
Th, <0.5 eV	2.40E+14	8	2.36E+14	0.68
0.5 eV-0.1 MeV	2.19E+15	15	1.82E+15	0.80
>0.11 MeV	4.80E+14	10	4.89E+14	0.85
>1.0 MeV	1.87E+14	11	1.83E+14	0.68
Total	2.92E+15	8	2.54E+15	0.77

V15 (-0.85") (1976)

E,MeV	Exp.(PNNL)		Calc.(BNL)	E/C/Norm*
Power	40	+/–%	40	
Th, <0.5 eV	1.55E+14	11	2.36E+14	0.66
0.5 eV-0.1 MeV	9.41E+14	12	1.82E+15	0.52
>0.11 MeV	5.84E+14	12	4.89E+14	1.19
>1.0 MeV	1.43E+14	10	1.83E+14	0.78
Total	1.68E+15	6	2.54E+15	0.66

*Ratio of experimental (PNNL) to calculated (BNL) flux normalized to the same reactor power.

Table 5. Radiation damage calculations for HFBR (per day)

Material	dpa	dpa/ 10^{22} n/cm^2
V14 Fluence >1 MeV = 2.05×10^{18} n/cm^2		
Fe	4.00E-3	19.5
Al	6.86E-3	33.5
Cu	5.60E-3	27.3
V	6.39E-3	31.2
SiC	7.82E-3	38.1
V15 Fluence >1 MeV = 9.62×10^{18} n/cm^2		
Fe	1.57E-2	16.3
Al	2.95E-2	30.7
Cu	2.10E-2	21.8
V	2.29E-2	23.8
SiC	3.36E-2	34.9
V10 Total Fluence = 13.8×10^{18} n/cm^2		
Fe	1.23E-4	0.089
Al	5.43E-5	0.039
Cu	2.18E-4	0.159
V	2.64E-4	0.192
SiC	4.41E-5	0.032

FUTURE WORK

At the present time, the HFBR reactor is not operational pending the resolution of regulatory concerns with the State of New York. Further work is planned to study additional positions in the reactor when operations are resumed.

ACKNOWLEDGEMENTS

This work was supported by Contract 19292A with K. Farrell of Oak Ridge National Laboratory, Oak Ridge, TN 37831. The research was sponsored by the Division of Materials Science, US Department of Energy under Contract DE-AC05-96OR22464 with Lockheed Martin Energy Research Corp. The authors would like to acknowledge the extensive support and cooperation of N.E. Holden and J.R. O'Conor of BNL.

REFERENCES

1. F. G. Perey, Least Squares Dosimetry Unfolding: The Program STAY'SL, ORNL/TM-6062 (1977).

2. L. R. Greenwood and R. K. Smither, SPECTER: Neutron Damage Calculations for Materials Irradiations, ANL/FPP-TM-197, January 1985.

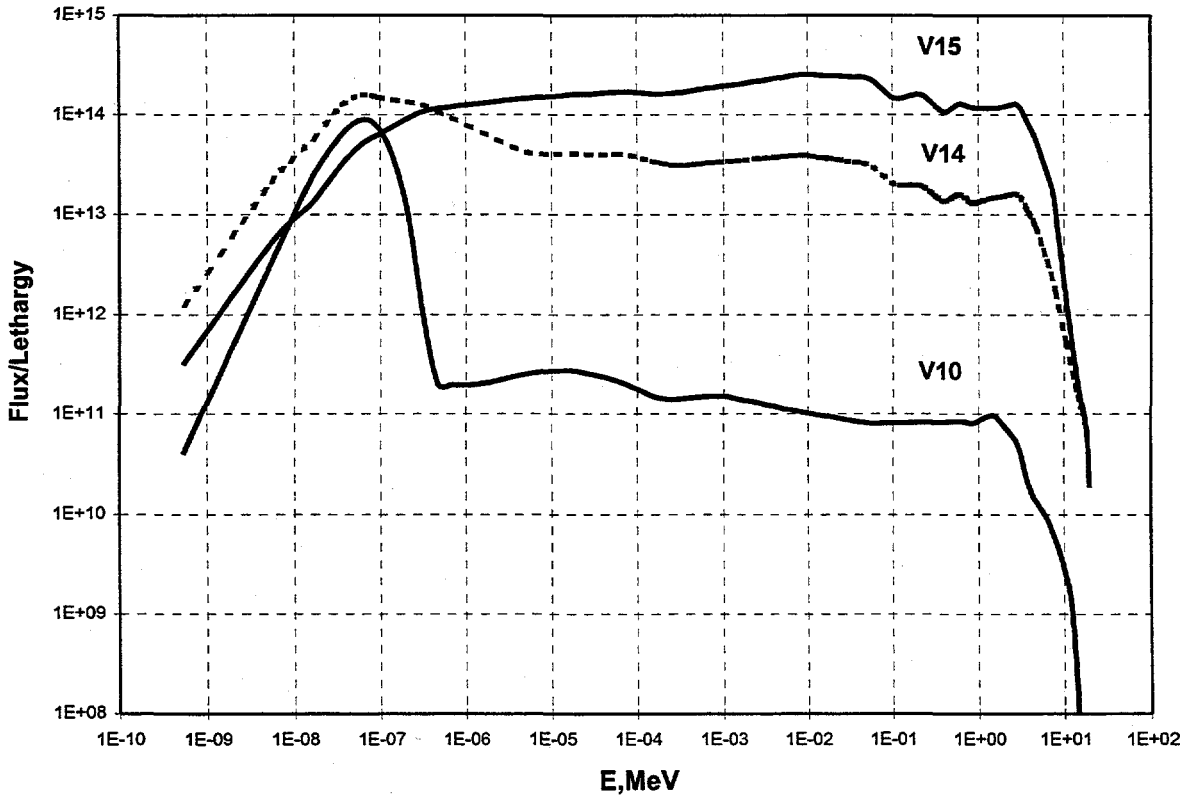

Figure 1. Adjusted neutron spectra for HFBR irradiation positions

PRODUCTION OF ^{4}HE AND TRITIUM FROM BE IN THE COBRA-1A2 IRRADIATION -
L. R. Greenwood (Pacific Northwest National Laboratory)*

OBJECTIVE

The purpose of this work was to predict ^{4}He and tritium production from Be irradiated in the COBRA-1A2 experiment.

SUMMARY

The production of ^{4}He and tritium has been calculated for beryllium irradiated in the COBRA-1A2 experiment in the Experimental Breeder Reactor II. Reaction rates were based on adjusted neutron spectra determined from reactor dosimetry measurements at three different elevations in the region of the beryllium capsules. Equations are given so that gas production can be calculated for any specific capsule elevation.

PROGRESS AND STATUS

Introduction

The irradiation conditions for the COBRA-1A2 experiment are described in a preliminary report by A. M. Ermi [1]. The COBRA subassembly X516 was irradiated in core position 2B1 from November 26, 1992 to September 26, 1994 for a total of 337.26 effective full power days at 62.5 Mwt. Beryllium specimens were irradiated in two different locations including subcapsule C03, spanning -2.29" to -6.10" in capsule B390, and subcapsule D03, spanning -2.46" to -6.27" in capsule B391.

Reactor dosimetry capsules were located above and below both the C03 and the D03 subcapsules. A full report of the neutron dosimetry results has been submitted for publication [2]. For the present calculations, there were three measurements of the neutron fluence spectrum, which cover the elevations of the beryllium capsules. Neutron flux gradient measurements were conducted in the various subcapsules that were located at the same elevations in the reactor. These gradient data indicate that the neutron fluences were virtually identical for the two beryllium assemblies C03 and D03. Hence, the gas production calculations as a function of reactor elevation are the same for both assemblies.

The reactor dosimetry measurements were used to adjust neutron flux spectra at six different heights in the COBRA assembly. Three of these spectral adjustments bound the roughly 9" long beryllium capsules at elevations of -1.2", -6.3", and -11.3". Beryllium reaction rates were thus calculated at these three heights using the dosimetry-adjusted neutron spectra. Table 1 lists the neutron fluences and reaction rates for these three locations.

*Pacific Northwest National Laboratory is operated for the U.S. Department of Energy by Battelle Memorial Institute under Contract DE-ACO6-76RLO 1830.

Table 1. Neutron fluences and dpa for COBRA-1A2

Neutron Energy, MeV	Neutron Fluence, E+22 n/cm^2		
	-1.2"	-6.3"	-11.3"
Total	7.50	6.66	4.19
> 0.1 MeV	5.94	4.95	2.62
> 1 MeV	1.68	1.31	0.330
dpa,Fe	29.3	23.5	10.1
dpa,Be	33.5	28.5	16.4

Gas Production Calculations

The production of tritium and ^{4}He from beryllium is dependent on the following nuclear reaction products:

^{9}Be(n,α)^{6}Li; ^{9}Be(n,2n)2α; ^{9}Be(n,d)2α; Li(n,α)t; ^{9}Be(n,t)^{7}Li

At short irradiation times, only the direct Be reactions are important. However, as ^{6}Li grows in, this reaction can become an increasingly important source of both helium and tritium due to the very high thermal neutron cross section. Two other nuclear processes must also be considered, mainly the decay of tritium to ^{3}He and the ^{3}He(n,p)t reaction which has a very high thermal neutron cross section for converting ^{3}He back into tritium.

Neutron cross sections for these reactions were taken from the ENDF/B-V Gas Production File 533 [3]. This file was specially constructed to sum all sources of a particular gaseous species such as helium. The file thus lists neutron cross section data for the ^{9}Be(n,helium) reaction. This reaction was thus used to determine the direct production of helium from beryllium. Reaction rates calculated from the dosimetry-adjusted neutron spectra at the three elevations spanning the beryllium materials are listed in Table 2.

Table 2. Reaction rates in beryllium for COBRA-1A@ (62.5 MWt)

	Reaction Rate (at/at-day)		
Reaction	-1.2"	-6.3"	-11.3"
^{9}Be(n,helium)	1.22E-5	7.74E-6	1.39E-6
^{9}Be(n,)^{6}Li	2.16E-6	1.51E-6	3.11E-7
^{9}Be(n,t)^{7}Li	1.37E-10	8.85E-11	1.34E-11
^{6}Li(n,)t	1.80E-4	1.79E-4	2.06E-4
^{3}He(n,p)t	1.02E-3	1.02E-3	1.17E-3

The reaction rates listed in Table 2 are given at the full reactor power of 62.5 Mwt. Since tritium decays during irradiation and the resultant ^{3}He can burn back to tritium, it is important to consider the reactor power history for the COBRA-1A2 irradiation. For these calculations, the reaction rates were time-averaged over the entire 669-day irradiation history.

Results and Discussion

The calculations were performed using a Fortran program to numerically integrate the production and burnup of each nuclear species on a daily basis over the 669-day irradiation period. The results are listed in Table 3. The net ^{4}He and tritium values are shown as a function of elevation in the reactor in Figure 1. It is important to note that the net production of both ^{4}He and tritium vary strongly with the elevation in the reactor. The fast neutron fluences and dpa in Be are shown as a function of elevation in the reactor in Figure 2. The trendlines for the calculated values for each reaction as well as neutron fluence and Be dpa are described by polynomials, as shown on Figures 1 and 2. These equations can thus be used to determine the gas production at any height within the C03 and D03 assembly. However, the equations should not be used at higher or lower elevations.

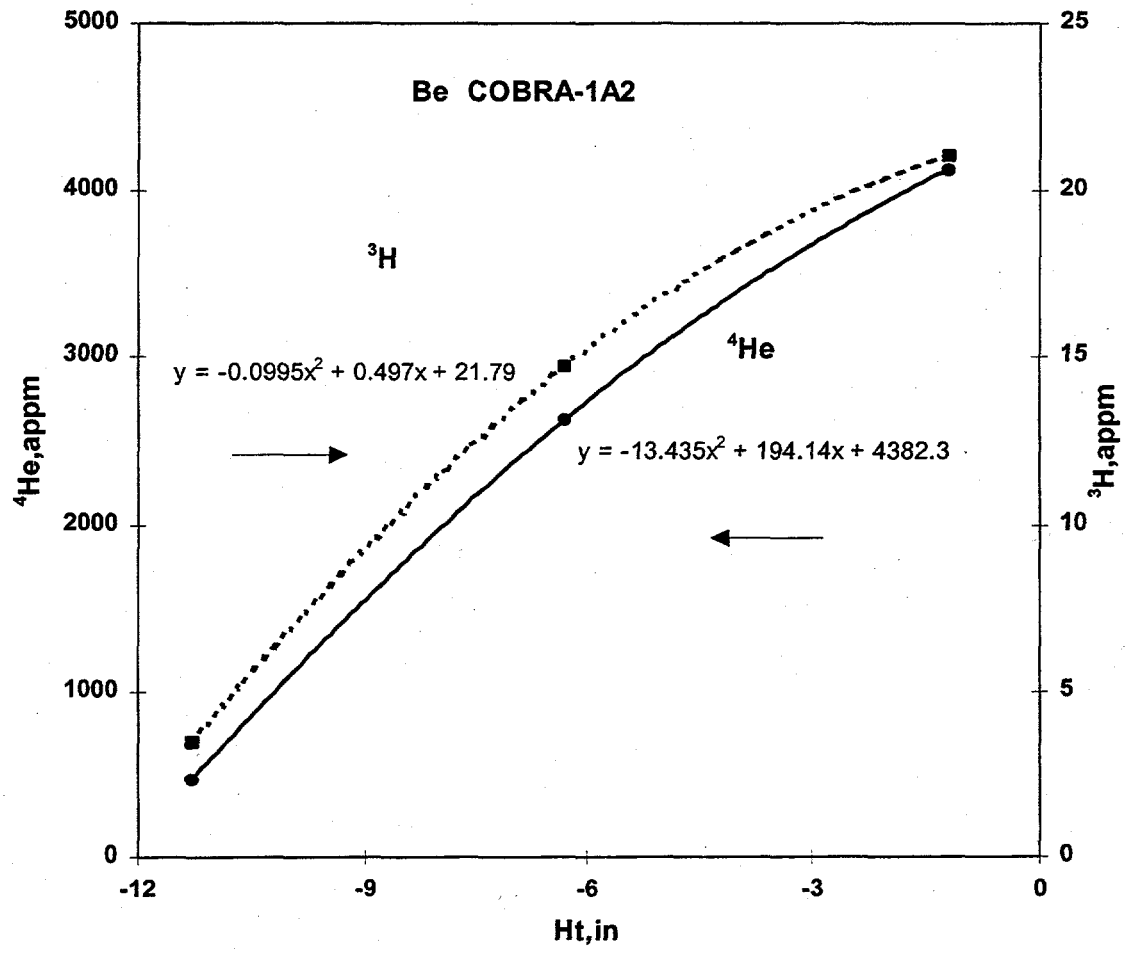

Figure 1. Production of ^{4}He and ^{3}H as a function of reactor elevation

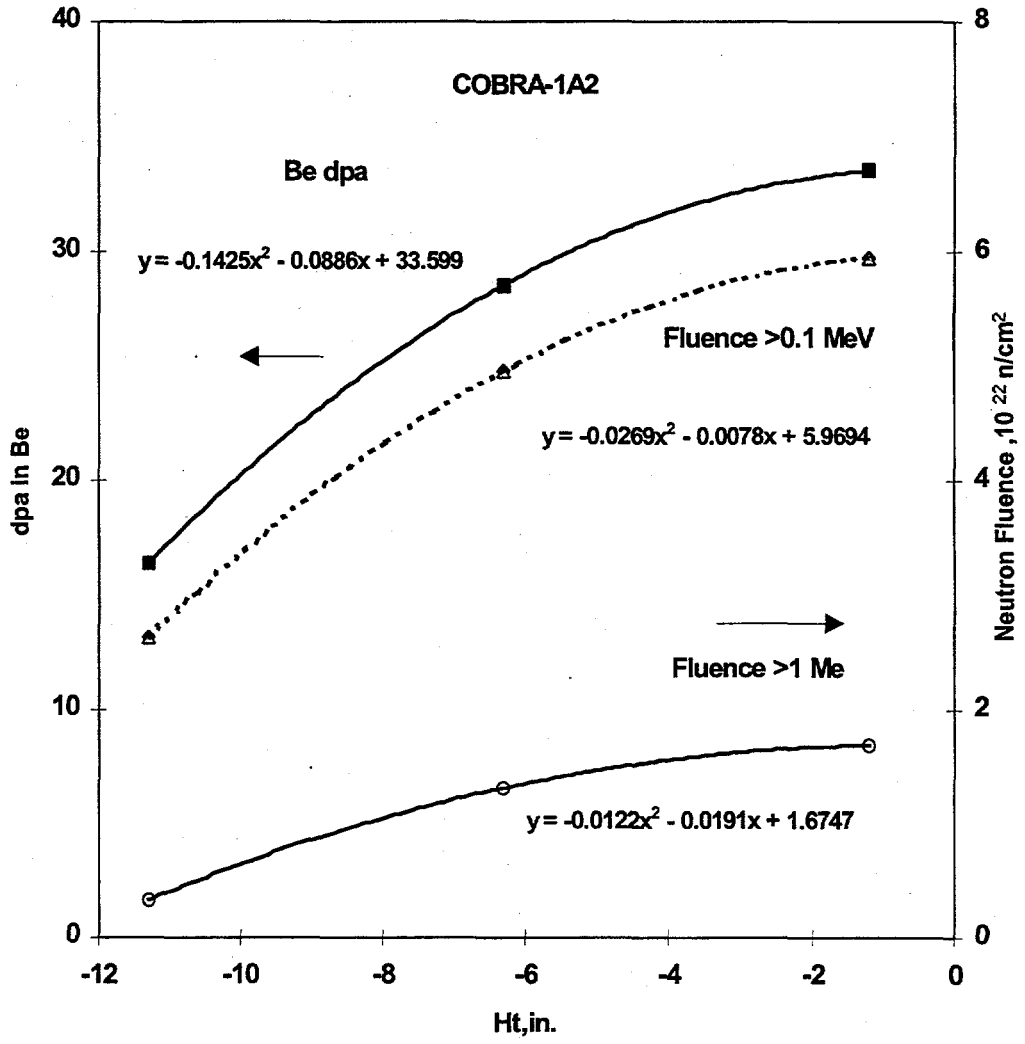

Figure 2. Fast neutron fluence and Be dpa as a function of reactor elevation

The present calculations for the production of ^{4}He and tritium assume that both species remain trapped in the beryllium close to the point of generation. Although this is a good assumption for helium, the tritium may be subject to significant diffusion and possible loss from the beryllium at the irradiation temperatures of 388°C and 395°C for the C03 and D03 subcapsules, respectively. Consequently, comparisons of these calculations with measured tritium evolution from the beryllium must consider the possible diffusion and loss from the subcapsules.

It is also important to note that the calculated values in Table 3 are given at the end of irradiation time, September 26, 1994. Tritium decays with a half-life of 12.32 years, which amounts to 5.5% per year. Table 4 corrects the tritium and ^{3}He values for decay to May 1997.

Table 3. Calculate ^{4}He. ^{3}H, ^{3}He, and ^{6}Li results for COBRA-1A2 (EOI = 9/26/94)

	Production in Be, appm		
	-1.2"	-6.3"	-11.3"
^{4}He	4130	2626	473
^{3}H	21.1	14.7	3.47
^{3}He	0.68	0.47	0.11
^{6}Li	706	495	101

Table 4. Calculated ^{3}H and ^{3}He results for COBRA-1A2 at 5/1/97

	Production in Be, appm		
	-1.2"	-6.3"	-11.3"
^{3}H	18.2	12.7	3.00
^{3}He	3.58	2.47	0.58

The elevations of the 1, 3, and 5 mm beryllium balls were determined using the radiographs shown in Figure 3. The resultant elevation ranges were then used to calculate the ^{4}He and ^{3}H expected for each type of ball in each capsule. There were no 3 mm balls in D03. For the 1 mm balls, the calculated values are given at the estimated center of the ball. For the 3 and 5 mm balls, values are given at the top and bottom of the elevation ranges. It is not possible to determine the exact elevation of each 3 and 5 mm ball; hence, the best we can do is give a range of values. Tables 5 and 6 summarize our best estimates of the ^{4}He and ^{3}H concentrations in each type of Be ball decayed to May 1, 1997.

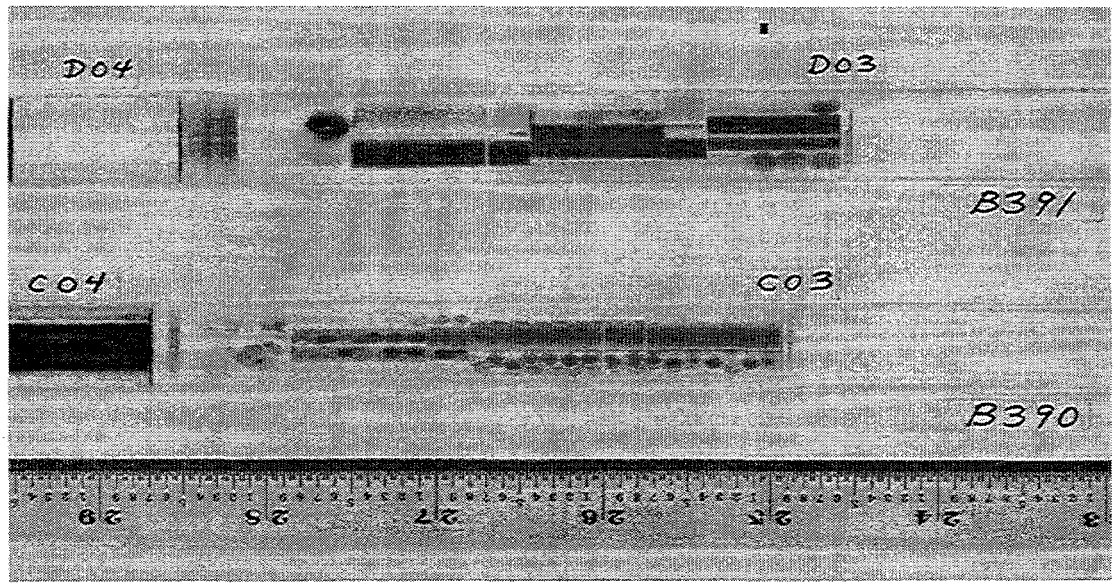

Figure 3. Radiograph of Be capsules in COBRA-1A2

Table 5. Calculations for Be balls in position C03 of COBRA-1A2 at 5/1/97

Be Ball	Ht,in.	^{4}He,appm	^{3}H,appm	Fast Fluence > 1 MeV xE+22 n/cm^2	Fast Fluence >0.1 MeV xE+22 n/cm^2	Be dpa
1 mm	-6.03	2723	13.1	1.35	5.04	29.0
3 mm	-6.0	2734	13.2	1.35	5.05	29.0
3 mm	-3.3	3595	16.5	1.60	5.70	32.3
5 mm	-3.3	3595	16.5	1.60	5.70	32.3
5 mm	-2.8	3733	17.0	1.63	5.78	32.7

Table 6. Calculations for Be balls in position D03 of COBRA-1A2 at 5/1/97

Be Ball	Ht,in.	^{4}He,appm	^{3}H,appm	Fast Fluence > 1 MeV xE+22 n/cm^2	Fast Fluence >0.1 MeV xE+22 n/cm^2	Be dpa
1 mm	-6.20	2662	12.9	1.32	4.98	28.7
5 mm	-6.2	2662	12.9	1.32	4.98	28.7
5 mm	-4.6	3205	15.0	1.50	5.44	31.0

FUTURE WORK

This work is completed.

ACKNOWLEDGEMENTS

This work was funded in part by Forschungszentrum Karlsruhe under project 26919 with Battelle Pacific Northwest Laboratory entitled Post-Irradiation Examination of Beryllium. This project was under the direction of Prof. M. Dalle Donne.

REFERENCES

1. M. L. Hamilton, R. M. Ermi, and C. R. Eiholzer, Fusion Reactor Materials Semiannual Progress Report for Period Ending March 31, 1993, pp. 3-13 (1993).

2. L. R. Greenwood, Neutron Dosimetry and Damage Calculations for the EBRII COBRA-1A Irradiations, Fusion Reactor Materials Semiannual Progress Report, DOE/ER-0313/21, in press.

3. Evaluated Nuclear Data File, Version V, Gas Production File 533, Brookhaven National Laboratory, 1981.

PRODUCTION OF ^{4}HE, ^{3}HE, AND TRITIUM FROM BE IRRADIATED IN FFTF-MOTA-2B -
L. R. Greenwood (Pacific Northwest National Laboratory)*

OBJECTIVE

The purpose of this work was to provide quantitative predictions of ^{4}He, ^{3}He and tritium production from Be irradiated in the FFTF-MOTA-2B experiment.

SUMMARY

The production of ^{4}He, ^{3}He, and tritium has been calculated for beryllium irradiated in the Materials Open Test Assembly (MOTA)-2B experiment in the Fast Flux Test Facility (FFTF). Reaction rates were based on adjusted neutron spectra determined from reactor dosimetry measurements at seven different elevations in the irradiation assembly. Equations are given so that gas production, dpa, and neutron fluences can be calculated for any specific elevation in the MOTA-2B assembly.

PROGRESS AND STATUS

Introduction

The irradiation conditions for the MOTA-2B experiment are described in a report by M. L. Hamilton, et al [1]. The MOTA-2B subassembly was irradiated from May 27, 1991, to March 19, 1992, for a total of 203.3 effective full power days at 291 Mwt. Beryllium specimens were irradiated in four different subcapsules including BCA-1 (–62.19 to –55.84 cm); 4B1 (+23.73 to +30.08 cm); 2B2 (–21.48 to –15.38 cm); and 2B4 (–27.81 to –21.71 cm). Each of these subcapsules contained two cylinders of beryllium measuring 0.635 and 2.03 cm in length. One subcapsule only contained one beryllium cylinder measuring 3.05 cm in length.

Neutron dosimetry capsules were located at seven different locations in the MOTA-2B assembly. A full report of the neutron dosimetry results has been published previously [2]. The dosimetry measurements were used to adjust neutron flux spectra at eight different heights in the assembly. Beryllium reaction rates were then calculated at each of these locations using the dosimetry-adjusted neutron flux spectra. Table 1 lists the neutron fluences and reaction rates for these locations. Figure 1 shows the dependence of the Be dpa and fast neutron fluences on reactor elevation. Trendline equations shown on the figure were used to calculate values at the specific locations of each beryllium cylinder, as shown later in Table 4.

Gas Production Calculations

The production of tritium, ^{3}He, and ^{4}He from beryllium is dependent on the nuclear reactions: ^{9}Be(n,α)^{6}Li, ^{9}Be(n,2n)2α, ^{9}Be(n,d)2α, ^{6}Li(n,α)t, and ^{9}Be(n,t)^{7}Li. At short irradiation times, only the direct Be reactions are important. However, as ^{6}Li grows in, this reaction can become an increasingly important source of both helium and tritium due to the very high

*Pacific Northwest National Laboratory is operated for the U.S. Department of Energy by Battelle Memorial Institute under Contract DE-ACO6-76RLO 1830.

Table 1. Neutron fluences and dpa for MOTA-2B

Neutron Energy, MeV	Neutron Fluence, $\times 10^{22}$ n/cm^2						
Height,cm:	-64.7	-41.2	-27.3	-5.8	0.5	16.8	44.3
Total	3.15	5.63	7.91	8.11	8.73	9.91	4.78
> 0.1 MeV	1.53	3.28	4.91	5.22	5.52	6.36	2.96
> 1 MeV	0.14	0.55	0.81	0.94	1.00	0.94	0.49
dpa,Fe	5.63	13.5	20.1	21.8	23.3	25.0	12.2
dpa,Be	10.3	21.1	30.8	32.0	34.2	39.7	18.5

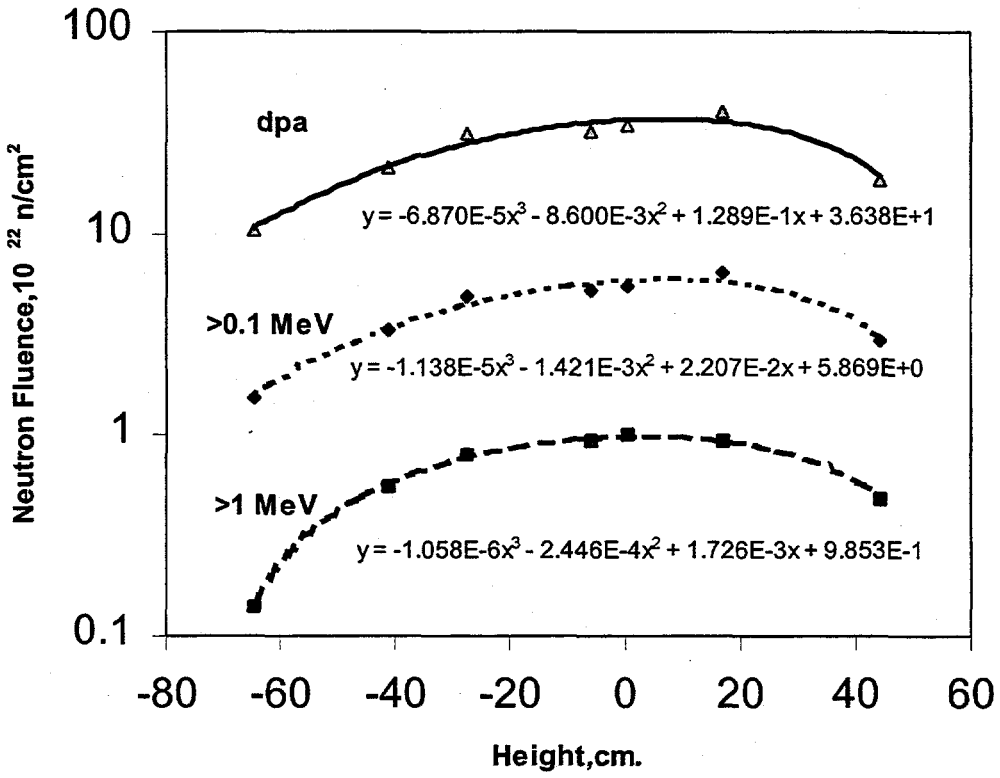

Figure 1. Fast neutron fluence and Be dpa as a function of reactor elevation

thermal neutron cross section. Two other nuclear processes must also be considered, mainly the decay of tritium to ^{3}He and the ^{3}He(n,p)t reaction which has a very high thermal neutron cross section for converting ^{3}He back into tritium.

Neutron cross sections for these reactions were taken from the ENDF/B-V Gas Production File 533 [3]. This file was specially constructed to sum all sources of a particular gaseous species such as helium. The file lists neutron cross section data for the ^{9}Be(n,helium) reaction. This reaction was used to determine the direct production of helium from beryllium. Reaction rates, as calculated from the dosimetry-adjusted neutron spectra, are listed in Table 2 at the elevations spanning the beryllium materials.

Table 2. Reaction rates in beryllium for MOTA-2B (291 MWt)

Reaction	Reaction Rate (at/at-day)						
Height,cm:	-64.7	-41.2	-27.3	-5.8	0.5	16.8	44.3
^{9}Be(n,he) $\times 10^{-6}$	0.458	3.58	5.48	6.40	6.90	6.25	3.05
^{9}Be(n,α)^{6}Li $\times 10^{-6}$	0.124	0.683	1.01	1.20	1.27	1.16	0.580
^{9}Be(n,t)^{7}Li $\times 10^{-11}$	0.604	4.47	7.43	8.43	8.85	8.26	4.02
^{6}Li(n,α)t $\times 10^{-4}$	3.74	2.33	2.79	2.85	3.07	3.57	1.83
^{3}He(n,p)t $\times 10^{-3}$	2.12	1.32	1.58	1.62	1.74	2.02	1.04

The reaction rates listed in Table 2 are given at the full reactor power of 291 Mwt. Since tritium decays during irradiation and the resultant ^{3}He can burn back to tritium, it is important to consider the reactor power history for the MOTA-2B irradiation. For these calculations, the reaction rates were time-averaged over the entire 297-day irradiation history.

Results and Discussion

Gas production calculations were performed using a Fortran computer program to numerically integrate the production and burnup of each nuclear species on a daily basis over the 297 day irradiation period. The results are listed in Table 3 for the seven neutron dosimetry positions. The He and tritium values are shown as a function of elevation in the reactor in Figure 2. It is important to note that the net production of both He and tritium vary strongly with the elevation in the reactor. The trendlines for the calculated values for each reaction, as well as neutron fluence and Be dpa, are described by polynomials, as shown on the figures. These equations were used to determine the gas production at the specific heights of the beryllium cylinders as shown later in Table 4. However, the equations should not be used at higher or lower elevations than shown on the figures since the polynomials are not defined in these regions.

The present calculations for the production of He and tritium assume that both species remain trapped in the beryllium close to the point of generation. Although this is a good assumption for helium, the tritium may be subject to significant diffusion and possible loss from the beryllium at the irradiation temperatures of 370°C (BCA-1), 425°C (4B1), and 550°C (2B2 and 2B4). Consequently, comparisons of these calculations with measured tritium evolution from the beryllium must consider the possible diffusion and loss of tritium from the subcapsules.

Table 3. Calculated ^{4}He. ^{3}H, ^{3}He, and ^{6}Li results for MOTA-2B (EOI = 3/19/92)

	Production in Be, appm						
Height,cm:	-64.7	-41.2	-27.3	-5.8	0.5	16.8	44.3
^{4}He	138	1071	1640	1916	2066	1873	911
^{3}H	1.95	6.79	12.0	14.6	16.5	17.4	4.56
^{3}He	0.026	0.096	0.166	0.201	0.226	0.234	0.065
^{6}Li	34.8	196	287	342	360	326	168

Table 4. Calculations for Be cylinders in MOTA-2B (at 12/1/97)

Sample	Cylinder Length	Ht,cm.	^{4}He appm	^{3}He appm	^{3}H appm	Fluence X10^{22} n/cm^2 > 1 MeV	>0.1 MeV	Be dpa
V310/311	0.25"	-61.7	267	0.91	1.52	0.20	1.77	11.8
	0.80"	-60.4	328	1.00	1.65	0.22	1.86	12.4
V489-490	0.25"	24.2	1734	5.61	9.36	0.87	5.41	33.5
	0.80"	25.5	1697	5.53	9.11	0.85	5.32	32.9
V491	1.20"	25.4	1701	5.58	9.14	0.85	5.33	33.0
V568	0.25"	-21.0	1733	4.91	7.96	0.85	4.88	30.5
	0.80"	-19.7	1762	5.05	8.17	0.86	4.97	31.0
V569	0.25"	-27.3	1574	4.11	6.87	0.78	4.44	27.8
	0.80"	-26.0	1610	4.18	7.10	0.79	4.53	28.4

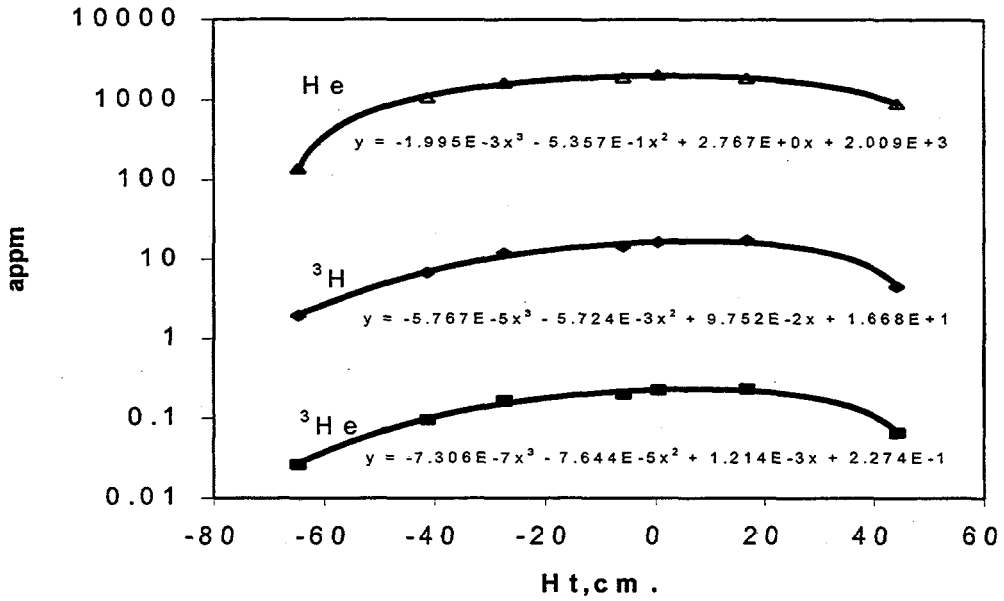

Figure 2. Production of ^{4}He, ^{3}He and ^{3}H as a function of reactor elevation

It is important to note that the calculated values in Table 3 are given at the end of irradiation time, March 19, 1992. Tritium decays with a halflife of 12.32 years, which amounts to 5.5% per year. The tritium and ^{3}He values shown in Table 4 are corrected for decay to December 1, 1997.

FUTURE WORK

Measurements of the tritium and helium content of the beryllium cylinders are planned.

ACKNOWLEDGEMENTS

This work was funded by Forschungszentrum Karlsruhe under project 26919 with Battelle Pacific Northwest National Laboratory entitled "Post-Irradiation Examination of Beryllium". This project was under the direction of Prof. M. Dalle Donne.

REFERENCES

1. M. L. Hamilton, R. M. Ermi, and A. M. Ermi, Fusion Reactor Materials Semiannual Progress Report for Period Ending March 31, 1992, DOE/ER-0313/12, pp. 3-14 (1992).

2. L. R. Greenwood and L. S. Kellogg, Neutron Dosimetry for the MOTA-2B Experiment in FFTF, Fusion Reactor Materials Semiannual Progress Report, DOE/ER-0313/16, pp. 21-27, March 1994.

3. Evaluated Nuclear Data File, Version V, Gas Production File 533, Brookhaven National Laboratory, 1981.

CALCULATION AND MEASUREMENT OF HELIUM GENERATION AND SOLID TRANSMUTANTS IN Cu-Zn-Ni ALLOYS - L. R. Greenwood, B. M. Oliver, and F. A. Garner (Pacific Northwest National Laboratory)* T. Muroga (National Institute of Fusion Science, Nagoya 464-01, Japan)

To be published in Journal of Nuclear Materials as Proceedings of the 8th International Conference on Fusion Reactor Materials, Oct. 26-31, 1997, Sendai, Japan.

EXTENDED ABSTRACT

A method was recently proposed by Garner and Greenwood that would allow the separation of the effects of solid and gaseous transmutation for Cu-Zn-Ni alloys. Pure copper produces zinc and nickel during neutron irradiation. ^{63}Cu transmutes to ^{64}Ni and ^{64}Zn, in about a 2-to-1 ratio, and ^{65}Cu transmutes to ^{66}Zn. The ^{64}Zn further transmutes to ^{65}Zn which has been shown to have a high thermal neutron (n,α) cross-section. Since a three-step reaction sequence is required for natural copper, the amount of helium produced is much smaller than would be produced for the two-step, well-known ^{58}Ni (n,γ) ^{59}Ni (n,α) reaction sequence. The addition of natural Zn and Ni to copper leads to greatly increased helium production in neutron spectra with a significant thermal component. Using a suitable Cu-Zn-Ni alloy matrix and comparative irradiation of thermal neutron-shielded and unshielded specimens, it should be possible to distinguish the separate influences of the solid and gaseous transmutants.

Whereas helium generation rates have been previously measured for natural nickel and copper, they have not been measured for natural Zn or Cu-Ni-Zn alloys. The (n,α) cross section for ^{65}Zn was inferred from helium measurements made with natural copper. By comparing helium production in Cu and Cu-Zn alloys, this cross section can be determined more accurately. In the current study, both the solid and helium transmutants were measured for Cu, Cu-5Ni, Cu-3.5Zn and Cu-5Ni-2Zn, irradiated in each of two positions in the HFIR JP-23 test. Highly accurate helium measurements were performed on these materials by isotope dilution mass spectrometry using a facility that was recently moved from Rockwell International to PNNL.

It is shown that both the helium and solid transmutants for Cu-Zn-Ni alloys can be calculated with reasonable certainty, allowing the development of a transmutation experiment as proposed by Garner and Greenwood.

*Pacific Northwest National Laboratory is operated for the U.S. Department of Energy by Battelle Memorial Institute under Contract DE-AC06-76RLO 1830.

NEUTRON DOSIMETRY AND DAMAGE CALCULATIONS FOR THE HFIR-MFE-200J-1 IRRADIATION - L. R. Greenwood (Pacific Northwest National Laboratory)* and C. A. Baldwin (Oak Ridge National Laboratory)

OBJECTIVE

To provide dosimetry and damage analysis for fusion materials irradiation experiments.

SUMMARY

Neutron fluence measurements and radiation damage calculations are reported for the joint U.S.- Japanese experiment MFE-200-J-, which was conducted in the removable beryllium (RB*) position of the High Flux Isotope Reactor (HFIR) at Oak Ridge National Laboratory (ORNL). The maximum neutron fluence at midplane was 4.1×10^{22} n/cm^2 (1.9×10^{22} n/cm^2 above 0.1 MeV), resulting in about 12 dpa and 28 appm helium in type 316 stainless steel.

PROGRESS AND STATUS

Introduction

The MFE-200-J-1 experiment was irradiated in the RB* position of HFIR during cycles 313 through 332 starting November 21, 1992, and ending January 11, 1995, for a net exposure of 440.59 effective full-power days at 85 MW. The experiment was a collaborative effort of the U.S. Fusion Materials Program at ORNL and the Japanese Atomic Energy Research Institute (JAERI). The goal was to continue spectral tailoring irradiations started in the ORR-MFE-6J and -7J experiments using a 4.2 mm thick Hf liner in the RB* position to limit the further production of helium from the ingrown ^{59}Ni. A complete description of the specimen matrices and irradiation assemblies has been published previously [1].

Neutron dosimetry capsules were inserted at 14 different positions located at relative angles of 0, 90, 180, and 270° in the assembly. The dosimetry capsules consisted of small aluminum tubes measuring about 1.3 mm in diameter and 6.4 mm in length. Each tube contained small monitor wires of Fe, Ni, Ti, Nb, 0.1% Co-Al alloy, and 80.2% Mn-Cu alloy. Following irradiation, the monitors were removed from the assemblies and analyzed for gamma activities at ORNL. Because of our previous experience and the anticipated similarity of the dosimetry monitor results, only 7 of the 14 monitor capsules were analyzed; the remainder of the capsules were stored pending further analyses, as necessary.

The measured gamma activities were subsequently analyzed at Pacific Northwest National Laboratory. The activities were converted to activation rates, as listed in Table 1, by correcting for nuclear burnup, gamma self-absorption, decay during and after irradiation, isotopic abundance, and atomic weight. Burnup corrections were based on an iterative procedure for the thermal/epithermal monitor reactions. The resulting estimates of the thermal/epithermal neutron fluences were then used to calculate burnup corrections for the threshold fast neutron

*Pacific Northwest National Laboratory is operated for the U.S. Department of Energy by Battelle Memorial Institute under Contract DE-ACO6-76RLO 1830.

monitor reactions. Burnup corrections were quite small, averaging 5-10% for the thermal/epithermal reactions and < 6% for the threshold reaction rates. The activation rates listed in Table 1 are normalized to full reactor power of 85 MW and have a net absolute uncertainty of about 3%.

The experimental assembly was initially oriented in the reactor with the 0° side facing the center of the core. The entire assembly was rotated after each reactor cycle (about 22 days) to minimize any potential radial flux gradients caused by the orientation of the assembly. Looking at the data in Table 1, it is apparent that there are some small radial flux effects. Monitors 77 and 81 were both located at the same elevation, +3.01 cm, at 0° and 90°, respectively. However, the data clearly show that the fast flux at the 90° position averages 8.5% higher than at 0°. The thermal flux gradient at 90° averages only 2.5% higher than at 0°. These were the only two monitors at the same elevation. If symmetry around the core centerline is assumed, then we can further compare sets of monitors at symmetric elevations. The activities for the symmetric monitors at 90° at ± 3.0 cm are in excellent agreement. More generally, the ratios of fast neutron activities at 90, 180, and 270° to that at 0° are 1.085, 1.061, and 1.075, respectively; the same ratios for thermal reactions are 1.025, 0.908, and 0.947, respectively. Since complete results for all of the monitors are not available, we decided to simply average the data at the different angles. Consequently, all the data were analyzed together, giving average neutron fluences and damage rates as a function of elevation for the entire assembly. The activation rates in Table 1 were fit to a polynomial function of form $f(x) = f(0) [1 + a x^2]$, where x is the vertical height from reactor centerline in cm. All of the data are reasonably well fit by the average polynomial (coefficient $a = -1.32 \times 10^{-3}$). Radial gradients suggest that the variations from the average fluxes are on the order of 5%.

Midplane activation rates were used in the STAY'SL [2] computer code to adjust the neutron flux spectrum determined in previous spectral measurements in the RB* position in HFIR [3,4]. STAY'SL performs a generalized least-squares adjustment of all measured and calculated values, including the measured activities, calculated spectra, and neutron cross sections. Neutron cross sections and their uncertainties were generally taken from the ENDF/B-V [5] evaluation. The resulting neutron fluence values are listed in Table 2. The activation rates and the derived neutron spectra and fluences are in excellent agreement with previous measurements in the removable beryllium positions of HFIR [3,4].

Neutron damage calculations were performed using the SPECTER computer code [6] at the midplane position of HFIR. Midplane dpa and helium (appm) values are also listed in Table 2. The fluence and damage values at other experimental positions can be calculated by the gradient equation given above. Damage parameters for other elements or compounds have been calculated and are readily available on request.

Helium production in nickel and nickel alloys requires a more complicated non-linear calculation [7]. Helium production in stainless steel is thus detailed separately in Table 3.

It should be noted that the present results consider only the irradiation of specimens in the 200-J-1 irradiation. Specimens that were previously irradiated in ORR-MFE-6J or -7J would have an additional dpa and helium production that needs to be calculated on a case-by-case basis for specified sample locations in the successive experiments.

FUTURE WORK

Additional experiments still in progress include MFE-400-J1 and JP20-22.

REFERENCES

1. A. W. Longest, J. E. Pawel, D. W. Heatherly, R. G. Sitterson, and R. L. Wallace, Fabrication and Operation of HFIR-MFE-RB* Spectrally Tailored Irradiation Capsules, Fusion Reactor Materials Semiannual Progress Report, DOE/ER-0313/14, p. 14 (1993).

2. F. G. Perey, Least Squares Dosimetry Unfolding: The Program STAY'SL, ORNL/TM-6062 (1977).

3. L. R. Greenwood, Alloy Development for Irradiation Performance Semiannual Report, DOE/ER-0045/16, pp. 17-24 (1986).

4. L. R. Greenwood and C. A. Baldwin, Neutron Dosimetry, Damage Calculations, and Helium Measurements for the HFIR-MFE-60J-1 and MFE-330-J-1 Spectral Tailoring Experiments, Fusion Materials Semiannual Progress Report, DOE/ER-0313/17, p. 28 (1995).

5. Evaluated Nuclear Data File, Part B, Version V, National Nuclear Data Center, Brookhaven National Laboratory.

6. L. R. Greenwood and R. K. Smither, SPECTER: Neutron Damage Calculations for Materials Irradiations, ANL/FPP-TM-197, January 1985.

7. L. R. Greenwood, A New Calculation of Thermal Neutron Damage and Helium Production in Nickel, Journal of Nuclear Materials, Vol. 116, pp. 137-142 (1983).

Table 1. Activation rates (atom/atom-s) - HFIR-MFE-200-J-1

Position/ Monitor	Ht,cm	$^{54}Fe(n,p)^{54}Mn$ (E-11)	$^{46}Ti(n,p)^{46}Sc$ (E-12)	$^{55}Mn(n,2n)^{54}Mn$ (E-14)	$^{59}Co(n,\gamma)^{60}Co$ (E-9)	$^{93}Nb(n,\gamma)^{94}Nb$ (E-10)
0°-21	15.1	0.91	1.22	2.86	2.64	2.94
270°-73	9.1	1.26	1.55	3.61	3.46	3.43
0°-77	3.0	1.33	1.65	3.81	3.86	3.76
90°-81	3.0	1.45	1.82	4.05	3.94	3.87
90°-84	-3.0	1.46	1.82	4.03	3.94	3.81
180°-101	-9.1	1.27	1.53	3.49	3.56	3.05
270°-106	-15.1	1.05	1.27	3.02	2.80	2.45

Table 2. Midplane fluence and damage values for HFIR-MFE-200-J-1

Neutron Fluence, $\times 10^{22}$ n/cm^2		Element	dpa	He,appm
Total	4.09	C	14.4	12.1
Thermal (<.5 eV)	3.50	Al	22.7	4.7
0.5 eV - 0.1 MeV	1.81	V	15.0	0.16
> 0.1 MeV	1.94	Cr	12.5	1.2
> 1 MeV	0.705	Fe	11.2	2.1
		Ni Fast	12.4	31.5
		^{59}Ni	0.3	167.5
		Total	12.7	199.0
		Cu	14.9	1.8

Table 3. Dpa and helium values for 316 SS in HFIR-MFE-200-J-1 (includes ^{59}Ni effect)

Ht (cm)	dpa	He (appm)
0	11.6	27.5
3	11.5	27.0
6	11.1	25.4
9	10.5	22.9
12	9.53	19.5
15	8.33	15.5

316SS = Fe(0.645), Ni(0.13), Cr(0.18), Mn(0.019), Mo(0.026) wt%

Neutronics Aspects of a DHCE Experiment* Itacil C. Gomes, Hanchung Tsai, and Dale L. Smith (Argonne National Laboratory)

Summary

The DHCE (Dynamic Helium Charging Experiment) irradiation experiment was conceived to simulate fusion-relevant helium production in a fission reactor irradiation. The main objective is to maintain the Helium-to-DPA ratio at, roughly, the same level as expected in a fusion environment. The problem in fission reactor irradiation is that Helium production is very low, because the fission neutrons, for basically all structural materials relevant for fusion applications, do not have enough energy to trigger the Helium producing reactions. A DHCE experiment involves the decay of Tritium to Helium-3 to produce the required Helium during irradiation. This paper describes an analysis of the most important aspects of a DHCE experiment and compares different types of fission reactors and their suitability for performing such an experiment. It is concluded that DHCE experiments are feasible in a certain class of mixed-spectrum fission reactors, but a careful and detailed evaluation, for each facility and condition, must be performed to ensure the success of the experiment.

Objective

The objective of this work was to analyze and provide data for the design of a DHCE experiment in a mixed-spectrum fission reactor.

Introduction

The DHCE experiment is well suited for vanadium alloys due to the high solubility of tritium in these alloys. High tritium concentrations can be obtained in these alloys without demanding very high pressures to drive the tritium into the samples. This characteristic considerably simplifies the engineering and fabrication of the irradiation capsules. The required tritium is introduced into the capsule in a so-called mother alloy. This alloy sample has a very high tritium concentration while the test samples do not contain any tritium, simplifying their handling and loading into the capsule. The tritium is confined in the mother alloy until the temperature of the capsule is raised upon reactor startup at which time the tritium migrates to the test alloys. As a result helium production in the test samples is initiated at the time that the irradiation capsule is brought up to the desired irradiation temperature.

The first DHCE experiment was performed in the MOTA irradiation vehicle of the FFTF (Fast Flux Test Facility), a fast breeder reactor. This proof-of-principle experiment demonstrated that helium concentrations approaching the desired He/dpa ratio could be obtained. Also, the microstructure of the irradiated vanadium alloys have been shown to be significantly different from similar alloys that have undergone irradiation without enhancing the helium production. The goal for the DHCE MOTA experiment was basically to be "a proof-of-principle experiment", and a large range of parameters was adopted. For example, a range for the tritium distribution coefficient between the lithium thermal bonding (used to homogenize the temperature of the sub-capsule) and the vanadium alloys was assumed to account for variations in the composition

*Work supported by U.S. Department of Energy, Office of Fusion Energy Research, under Contract W-31-109-Eng-38.

of the alloys and irradiation temperatures, different capsules were irradiated at different temperatures and several alloy compositions were irradiated, sometimes, in the same capsule. After irradiation, the samples were analyzed for helium content. All specimens indicated helium concentrations much higher than in conventional irradiation, however, most specimens contained less than the desired 4-5 He/dpa.

Since FFTF and EBR-II fast-breeder reactors were shut down, no other fast-flux irradiation facility is available in US. The feasibility of conducting DHCE experiment in one of the available mixed spectrum reactors in US, mainly ATR (Advanced Test Reactor, LMIT (Lockheed Martin Idaho Technologies Corporation), Idaho Falls) and HFIR (High Flux Irradiation Reactor, ORNL, Oak Ridge), is being evaluated.

This paper presents results of some calculations performed to assess the suitability of the mixed-spectrum reactors for a DHCE experiment. It is shown that it is possible to have DHCE experiments in a mixed-spectrum reactor provided that enough shielding for thermal neutrons is incorporated into the design. Also, a comparison of the performance of different reactors is included with this analysis.

The basic quantities to be controlled in a DHCE experiment

The analysis of a DHCE experiment is complex in nature due to the large number of variables involved. For example, the net increase in the Helium-3 concentration in the sample during irradiation is a function of the tritium concentration in the sample, and of Helium-3 burn-up. The tritium concentration in the sample is a function of the initial tritium load, any tritium generation during irradiation, the tritium leakage through the capsule, and of the distribution coefficient between samples, thermal bonding material, and capsule walls. The Helium-3 burn-up depends on the Helium-3 concentration, on the neutron flux spectrum, and on the neutron flux intensity. Other concerns regarding the tritium solubility in the thermal bonding material and tritium permeation through the capsule wall add to the number of variables to be controlled during the experiment.

From a neutronics point-of-view, the characterization of the thermal and epi-thermal neutron flux is very important because significant ^{3}He burn-up can occur due to very high thermal and epi-thermal cross sections of the ^{3}He(n,p) ^{3}H reaction. Other factors that have to be considered are the Tritium generation in the Lithium bonding and the Tritium leakage.

The relationship between the above parameters can be expressed as follows:

a) Helium generation rate in the vanadium alloy is

$$S_{He}(t) = \lambda_T N_T(t), \quad (1)$$

where, $S_{He}(t)$ is the helium generation rate per cubic centimeter at the time "t" from the decay of tritium, λ_T is tritium decay constant equal to 1.78×10^{-9} sec^{-1}, and $N_T(t)$ is the number of tritium atoms at the time "t" per cubic centimeter.

b) Helium burn-up in the vanadium alloy is

$$D_{He}(t) = N_{He}(t)\, \sigma_{He(n,x)}\, \phi(t), \quad (2)$$

where $D_{He}(t)$ is the rate of disappearance of helium at the time "t" per cubic centimeter due to neutron induced transmutation reaction, $N_{He}(t)$ is the number of ^{3}He atoms at the time "t" per

centimeter-barn, $\sigma_{He(n,x)}$ is the spectrum averaged ^3He transmutation cross section (basically the (n,p) reaction) in barns, and $\phi(t)$ is the energy integrated neutron flux in the sample region at the time "t" in the vanadium alloy.

c) Tritium production in the lithium thermal bonding is

$$P_T(t) = N_{Li}(t)\ \sigma_{Li(n,\alpha)T}\ \phi(t), \quad (3)$$

where, $P_T(t)$ is the tritium production rate at the time "t" per cubic centimeter of lithium, $N_{Li}(t)$ is the number of lithium atoms per centimeter-barn at the time "t" in the lithium region, $\sigma_{Li(n,\alpha)T}$ is the tritium-production cross section for lithium, in barns, averaged over the energy spectrum, and $\phi(t)$ is the energy integrated neutron flux in the lithium region at time "t".

d) Tritium atom distribution coefficient between thermal bonding material and Vanadium alloy is

$$ADC = (N_T / N_{Li})_{Li} / (N_T / N_V)_V, \quad (4)$$

where, ADC is the atom distribution coefficient between lithium and vanadium alloy, $(N_T / N_{Li})_{Li}$ is the tritium atom fraction in lithium thermal bonding with N_T being the number of tritium atoms per cubic centimeter and N_{li} the number of lithium atoms per cubic centimeter, $(N_T / N_V)_V$ is the tritium atom fraction in the vanadium alloy.

e) Tritium Leakage through the capsule walls is

$$dN_T/dt = -L\ N_T(t), \quad (5)$$

where $N_T(t)$ is the number of tritium atoms at the time "t" and L the leakage coefficient. The leakage coefficient can be represented by:

$$L = D^c\ K^c_a\ (\Omega_L/\Omega_c)\ (S/\ dV_L)\ , \quad (6)$$

where D^c is the diffusion coefficient of tritium in the capsule material, K^c_a the distribution coefficient of tritium between the capsule and lithium (in atomic percent), Ω_L the atomic volume of lithium, Ω_c the atomic volume of the capsule material, S the surface area of the capsule, "d" the capsule wall thickness, and V_L the volume of lithium in the capsule. This formulation does not take into account the additional surface-controlled mechanisms. The diffusion coefficient of tritium, for TZM (a molybdenum alloy) capsules, is strongly dependent on the temperature, which makes the leakage coefficient also strongly dependent on the temperature. It is well known that a thin oxide (or other compound) layer can have a notable inhibiting effect in the tritium leakage. Also, desorption of tritium at low pressures was not considered in this formulation. This means that, the leakage coefficient is assumed to be diffusion controlled, without taking credit for the use of surface barrier mechanisms for the tritium or desorption controlled kinetics.

The final relationships obtained from factoring together the above equations are the following:
- Helium concentration variation with the time in the vanadium alloy sample:

$$dN_{He\text{-}3} / dt = S_{He}(t) - D_{he}(t), \quad (7)$$

this equation is dependent on the tritium content in the samples. The variation of the tritium concentration inside the vanadium alloy can be equated by:

$$dN_T / dt = \{N_{li}\ \sigma_{Li(n,\alpha)T}\ \phi - \lambda\ N_T - L\ N_T\}_{Li}\ / \{ADC * (N_{Li} / N_V)\}, \quad (8)$$

The coupled equations (7) and (8) can be either directly integrated or solved by any of the available techniques. In this work the REAC [1] code was slightly modified to solve those equations. The "leakage coefficient" as a function of the temperature was introduced in the decay library of the code in such a way that the leakage is seen as a tritium decay mode which produces the disappearance of the atom. Further, the tritium production from lithium was

simulated through the use of an "equivalent" concentration of lithium, in the vanadium alloy, based on the distribution coefficient of tritium between lithium and vanadium alloy.

Physical constraints to the experiment

The most important physical constraints for the integrity of the irradiation capsules is the pressure build-up inside the capsule, during irradiation due to gas production. The gas pressure build up is largely due to the helium production when lithium is used as the thermal bonding material. Helium is a by-product of the tritium producing reaction Li-6(n,α)^{3}H. This tritium producing reaction has been proposed as a way to increase tritium inventory during irradiation to make-up for the He-3 burn-up and tritium leakage. A higher tritium concentration inside the capsule would allow a higher He-3 burn-up due to the higher He-3 production. Leaving aside the merits of allowing He-3 to be burned, this approach has as the main constraints two points: The first is that a higher tritium concentration creates a more noticeable saw-shaped profile of the Helium to DPA ratio, due to rapid increase in the helium concentration during the shut-down periods followed by the fast burn-up of the excess of He-3 when the reactor resumes the operation (as will be seen in the results presented in the next section). The second limiting constraint is the pressure build up due to associated helium atoms produced by the tritium generating reaction. To define the maximum enrichment that can be used at a given irradiation temperature one can calculate the maximum number of atoms of helium into the plenum (region inside the capsule, fill with inert gas, to accommodate the gases produced during irradiation) of the capsule.

Assuming that the maximum acceptable pressure inside the capsule is 20 atmospheres, and given the volume of the capsule's plenum, one can use the ideal gas law to calculate the number of moles that can be in the plenum for the irradiation temperature. Then, using:

$$PV = nRT, \quad (9)$$

where P is the pressure given in atmospheres, V the volume is given in liters, n the numbers of moles, R the universal gas constant equal to 0.0821 atm.L/(mol.°K), and T the temperature given in degree Kelvin. Now, assuming that the volume of samples plus lithium bonding inside the capsule is roughly the same as the volume of the gas plenum, the maximum number of moles of helium in 1 cm^3 of plenum, as a function of the temperature, is as follows:

$$n = 0.244 / T = N / 6.023 \times 10^{23}. \quad (10)$$

where N is the number of atoms of ^{4}He per cubic centimeter.

The number of ^{4}He atoms produced is a function of the neutron flux, flux averaged ^{6}Li(n,α) cross section, and number of ^{6}Li atoms in the thermal bonding material. The number of helium atoms produced per cm^3 of lithium is as follows:

$$N_{He\text{-}4} = N_{Li\text{-}6} \times \sigma_{Li\text{-}6} \times \phi \times t, \quad (11)$$

where t is total irradiation time, ϕ is the total neutron flux at the position considered, $\sigma_{Li\text{-}6}$ is the spectrum averaged ^{6}Li(n, α) cross section, $N_{Li\text{-}6}$ is the number of atoms of ^{6}Li per cm^3, and $N_{He\text{-}4}$ the number of atoms of ^{4}He produced per cubic centimeter of plenum. Considering that the plenum volume is twice the lithium volume in the capsule, the total number of ^{4}He atoms produced per cubic centimeter of lithium must be divided by 2 to enter in equation (10).

Table 1 presents some values for the flux averaged ^{6}Li(n,α) cross section. The ^{6}Li content considered in these calculation was the natural abundance in Li (7.5%). The reactor positions considered were the ATR-A10 (irradiation position A-10 of the Advanced Test Reactor) with a

neutron thermal filter 3mm thick made of Eu_2O_3 powder 50% dense, the ATR-ITV (Irradiation Test Vehicle of the Advanced Test Reactor) with outside borated aluminum (4.3% weight of ^{10}B) 3mm-thick-thermal filter, the HFIR RB4 (removable beryllium position) with outside Eu_2O_3 thermal filter (50% dense) with the thickness of 4mm and 2 mm, and the MOTA mid-plane (-0.30cm) position of FFTF with no filter.

Table 1. Flux Averaged $^6Li(n,\alpha)$ cross section for different reactor and thermal filter configurations.

ATR		HFIR - RB4 position		MOTA
A10 - 3mm Eu_2O_3 (50% dense)	ITV- 3mm Al with 4.w% ^{10}B	4 mm Eu_2O_3 (50% dense)	2 mm Eu_2O_3 (50% dense)	no filter (mid-plane)
10.2 barns	13.6 barns	56.0 barns	110. barns	1.0 barns

Table 2. Time and associated number of dpa's necessary to reach 20 atm. inside the irradiation capsule (plenum volume equal to samples plus lithium volume) using natural lithium as thermal bonding material.

	ATR				HFIR - RB4 position				MOTA	
Temp (°C)	A10-3mm Eu_2O_3 (50% dense)		ITV- 3mm Al with 4.3w% ^{10}B		4 mm Eu_2O_3 (50% dense)		2 mm Eu_2O_3 (50% dense)		no filter (mid-plane)	
	T(fpd*)	dpa	T(fpd*)	dpa	T(fpd*)	dpa	T(fpd*)	dpa	T(fpd*)	dpa
400°C	185.	7.6	124.	5.1	32.5	0.8	16.5	0.41	160.	24.
500°C	161.	6.6	108.	4.4	28.3	0.7	14.4	0.36	140.	21.
600°C	143.	5.9	95.6	3.9	25.1	0.6	12.7	0.31	124.	19.

* fpd = full power days

The time and the number of dpa's to reach 20 atmospheres pressure inside the capsule is given in Table 2, for the same configurations presented in Table 1. The results presented in Table 2 indicate that for longer irradiation time than calculated, the plenum volume has to be increased by the ratio of the target irradiation time divided by the values presented in the table. This leads us to conclude that the use of lithium as thermal bonding material in HFIR is very difficult due to the high thermal flux and associated ^4He production inside the capsule, unless depleted lithium (1% ^6Li) is used. It is also clear that a higher allowable pressure, or a larger gas plenum, or even a more detailed analysis of the distribution of the produced ^4He between gas phase and that dissolved in lithium phase can make the use of natural or slightly enriched lithium possible in ATR.

Results for MOTA, ATR, and HFIR.

During the course of analyzing DHCE experiments several fission environments were considered. It is worth mentioning that one of the most challenging aspects of designing an experiment such as DHCE is to determine a reliable neutron flux description, mainly for the

thermal and epithermal energy regions. The use of thermal neutron absorbers and their efficiency in removing thermal neutrons and shaping the flux to be compatible with the fusion spectrum is deeply affected by the correct characterization of the neutron flux at the irradiation position.

In this section three different reactors are considered, the FFTF (Fast Flux Test Facility), the ATR (Advanced Test Reactor), and the HFIR (High Flux Irradiation Reactor). The FFTF is not currently in operation, and it is shown here for the sake of comparing fast flux reactor with mixed spectrum reactors, such as ATR and HFIR. The results presented were obtained from neutron flux spectra derived from published data [1, 3], by the introduction of thermal filter material (when applicable) and neutron transport in a simplified MCNP [2] geometric model of the reactor.

Figure 1 presents a comparison of the helium to dpa ratio for different distribution coefficients, keeping constant the temperature (400°C), the tritium concentration in the vanadium alloy (1500 appm) and the lithium thermal bonding enrichment (7.5% ^{6}Li). It can be noted that the lower the distribution coefficient the larger is the helium to dpa ratio. This is due to the larger number of tritium atoms generated in the lithium that can diffuse to the vanadium samples. The distribution coefficient would have a much greater impact if one had maintained the initial tritium charge of the capsule constant but this would mask the only physical effect (migration of tritium atoms) due to different distribution coefficients among different materials.

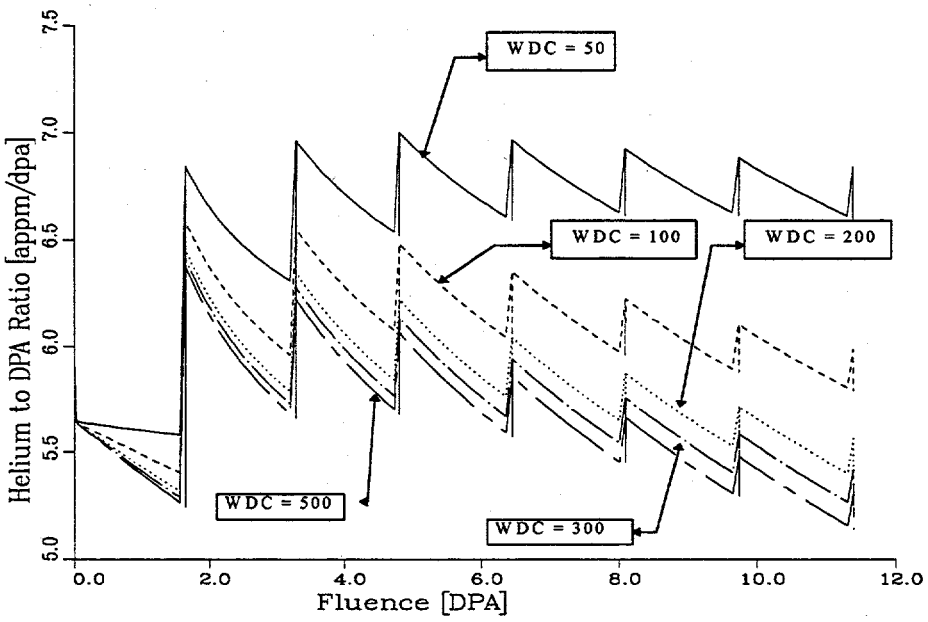

Figure 1. Effect of changing the distribution coefficient on the helium to dpa ratio profile for the ATR A10 position using a 3mm Eu_2O_3 thermal neutron filter.

Figure 2 and 3 show comparisons of the development of the helium to dpa ratio during the irradiation for the three reactors mentioned earlier. The temperature of irradiation in Figure 2 is 400°C and in Figure 3 it is 500°C. In both figures the distribution coefficient was set to 100, the

lithium enrichment to the natural abundance of ^{6}Li (except for HFIR, for which the ^{6}Li enrichment was set to 1%, for the reasons explained in the previous section), and the initial tritium charge equivalent to 1500 appm (for ATR and HFIR) and 5000 appm (for MOTA) of tritium in the vanadium alloy.

It is clear that in ATR it is possible to maintain a relatively flat helium to dpa profile during irradiation for the two temperatures presented, even when using borate aluminum as a filter. HFIR, due to the high thermal flux, can not achieve a flat profile even using a 4mm Eu_2O_3 filter. MOTA as presented in these pictures does not have the same saw-shaped profile as the other reactors because 10 dpa's is about the length of one cycle of the reactor, so the shut down time, which is responsible for the increase in helium concentration, is not shown in the MOTA curve. It is worthwhile mentioning that the tritium leakage term, calculated based on a diffusion driven mechanism, is not large at these temperatures. This makes them very similar to each other. The helium to dpa ratio at the end of the 10 dpa's irradiation campaign is calculated to be for 400°C 6.0 for ATR-A10 with 3mm of Eu_2O_3 filter, 4.1 for ATR-ITV with 3mm of borate (4.3w% 10B) aluminum filter, 0.6 for HFIR-RB with 4mm of Eu_2O_3 filter, 0.7 (at 7.2 dpa's) for HFIR-RB with 2mm of Eu_2O_3 filter, and 4.9 for MOTA mid-plane position. At 500°C the results after 10 dpa's are as follows: 6.0 for ATR-A10, 4 for ATR-ITV, 0.5 for HFIR-4mm, 0.6 for HFIR-2mm (at 7.2 dpa's), and 4.8 for MOTA.

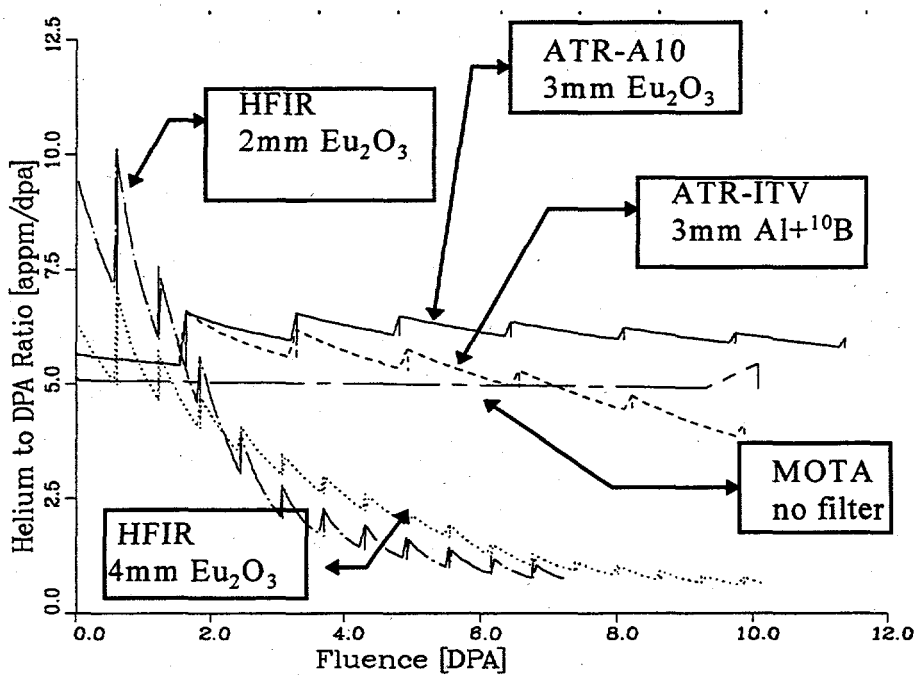

Figure 2. Calculated helium to dpa profile during irradiation for a temperature of 400°C, natural ^{6}Li abundance (except for HFIR which has 1% ^{6}LI), distribution coefficient of 100, and 1500 appm (ATR and HFIR) and 5000 appm (MOTA) tritium concentration in the vanadium alloy.

Figure 4 presents the helium to dpa profile for the same positions and irradiation parameters as the previous two figures except for a irradiation temperature which is set to 600°C in this case.

This figure is included to emphasize the effect of a diffusion driven leakage term for tritium on the helium production. The only barrier to the permeation of tritium out of the capsule is the use of a TZM capsule wall, but as can be seen, the leakage has an important impact on the helium production due to reduction of the tritium inventory inside the capsule.

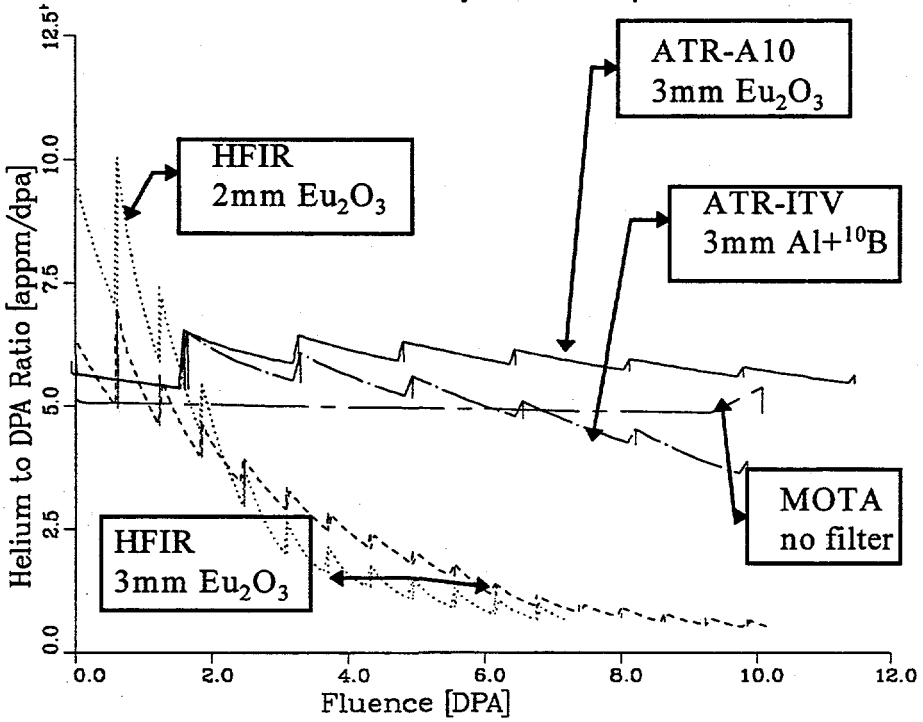

Figure 3. Calculated helium to dpa profile during irradiation for a temperature of 500°C, natural ^{6}Li abundance (except for HFIR which has 1% ^{6}LI), distribution coefficient of 100, and 1500 appm (ATR and HFIR) and 5000 appm (MOTA) tritium concentration in the vanadium alloy.

As it was mentioned earlier, other mechanisms, such as desorption and an oxide layer can significantly reduce the tritium permeation when compared with diffusion controlled leakage. However, the final helium to dpa ratio after 10 dpa's of irradiation are not completely unacceptable for ATR with 3mm Eu_2O_3 (he/dpa=3.3), MOTA (he/dpa=4.7), and ATR-ITV (he/dpa=2.4). On the other hand, the values for HFIR are extremely low, being 0.14 for 4mm of Eu_2O_3 and 0.23 (at 7.2 dpa's) for 2mm Eu_2O_3 filter.

Conclusions

The calculations presented in this paper indicate that the DHCE experiment is possible in mixed-spectrum reactors, and that a significant amount of helium will be produced during irradiation. Furthermore, the results indicate that even for high temperatures, using the most pessimistic assumptions for tritium leakage, it is possible to have fusion relevant helium concentrations in vanadium alloys after an irradiation campaign of 10 dpa's. The amount of helium generated should be enough to demonstrate the influence of helium production in vanadium alloys under intense neutron bombardment.

The calculations also indicate that mixed-spectrum reactors with very high thermal component in the neutron energy spectrum are expected to have a poor performance in this kind of experiment. The case analyzed for the HFIR reactor shows that an external filter in the RB position does not produce good results. As an alternative to reduce the thermal neutron flux inside the neutron thermal filter, it is conceivable to borate the filling material of that position. However the helium production in the filler due to the neutron absorption in the boron may cause serious problems.

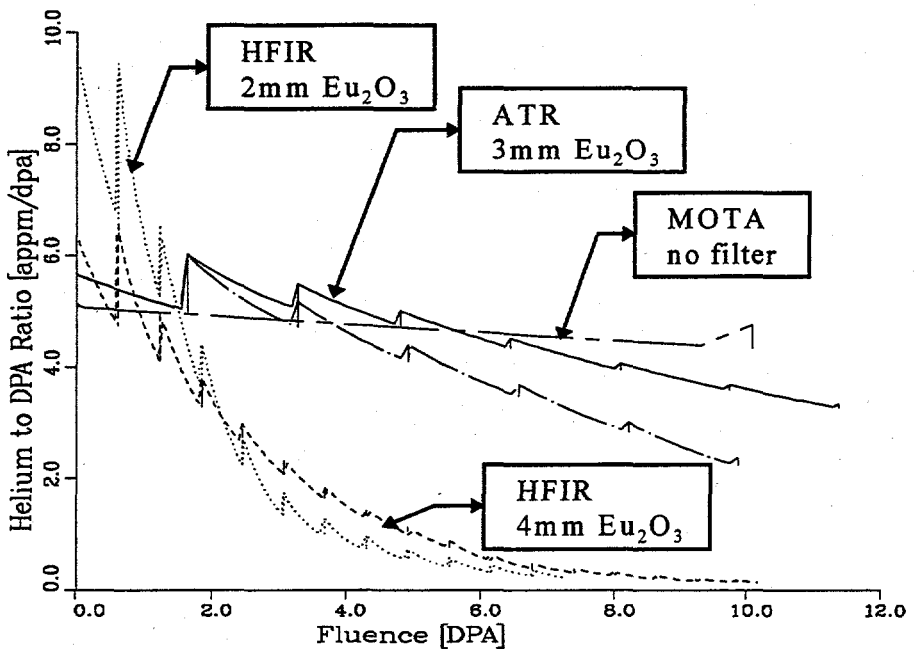

Figure 4. Calculated helium to dpa profile during irradiation for a temperature of 600°C, natural ^{6}Li abundance (except for HFIR which has 1% ^{6}LI), distribution coefficient of 100, and 1500 appm (ATR and HFIR) and 5000 appm (MOTA) tritium concentration in the vanadium alloy.

In the ATR-ITV, despite the relatively good performance, it was recommended to reduce the thermal neutrons to further borate the thermocouple slaves. This would produce a similar performance to the Eu_2O_3 external filter.

Finally, the calculations indicate that with a relatively small margin of uncertainty, it is possible to acquire valuable data from the helium effect on vanadium alloys using the available mixed spectrum reactors.

References

1. F.M. Mann, REAC-3 -- A Computer Code System for Activation and Transmutation, Hanford Engineering Development Laboratory, Report HEDL-TME-81-37 (1993).

2. J.F. Briesmeister, ed., "MCNP -- A General Monte Carlo N-Particle Transport Code, Version 4A", Report LA-12626, Los Alamos National Laboratory, Los Alamos, New Mexico (1993).

3. B. G. Schnitzler, LMIT (Lockheed Martin Idaho Technologies Corporation), Idaho Falls, private communication.

10.0 MATERIALS ENGINEERING AND DESIGN REQUIREMENTS

No contributions.

11.0 IRRADIATION FACILITIES, TEST MATRICES, AND EXPERIMENTAL METHODS

DESCRIPTION AND STATUS OF THE U.S./JAERI HFIR-MFE-RB-10J IRRADIATION CAPSULE -- J. P. Robertson, K. E. Lenox, M. L. Grossbeck, and A. F. Rowcliffe (Oak Ridge National Laboratory), and S. Jitsukawa and K. Shiba (Japan Atomic Energy Research Institute)

SUMMARY

This report describes the HFIR-MFE-RB-10J experiment conducted under the U.S. DOE/Japan Atomic Energy Research Institute Collaborative Testing Program. The irradiation will take place in a Removable Beryllium (RB) position in the High Flux Isotope Reactor (HFIR) for approximately 8 cycles (about 4 dpa in steel). The experiment consists of two distinct parts: the upper region of the capsule will contain vanadium specimens operating at either 420 or 480°C and the lower region will contain austenitic and ferritic/martensitic steel specimens operating at 250°C. The capsule will be surrounded by a Eu_2O_3 shield in order to harden the spectrum and prevent unwanted transmutations.

PROGRESS AND STATUS

Introduction

This report describes the HFIR-MFE-RB-10J experiment conducted under the U.S. DOE/Japan Atomic Energy Research Institute Collaborative Testing Program. Specimens will be provided from both the U.S. and Japanese programs. The irradiation will take place in a Removable Beryllium (RB) position in the High Flux Isotope Reactor (HFIR) for approximately 8 cycles (about 4 dpa in steel). The experiment consists of two distinct parts: the upper region of the capsule will contain vanadium specimens and the lower region will contain austenitic and ferritic steel specimens. The dividing line between the two regions will be at the reactor centerline. The vanadium specimens in the upper region will be contained in two separate lithium-filled subcapsules; one subcapsule will operate at 420°C and the other will operate at 480°C. The steel specimens in the lower region will be contained in a single slotted holder similar to previous RB capsules in this program and will operate at 250°C. The capsule will be surrounded by a Eu_2O_3 shield in order to harden the spectrum and prevent unwanted transmutations.

Vanadium Alloy Experiment

Previous HFBR and EBR-II data have shown that radiation-hardening, loss of strain-hardening capacity, and a propensity for brittle cleavage fracture are characteristics of the V-4Cr-4Ti production heat following irradiation at 385°C and below. The diminished radiation hardening at 525°C suggests that fracture properties might improve rapidly over the range 400 to 500°C. The blunt-notch Charpy data generated to date indicate a significant increase in the DBTT of V-4Cr-4Ti in the hardening regime. A master curve-mechanism approach is proposed for modeling the effects of external parameters on the fracture toughness-temperature behavior of vanadium alloys [1]. This needs to be supported by information on the temperature and strain-rate dependence of radiation-hardening, dislocation/defect structure interactions, strain-hardening, and the micromechanics of crack initiation and propagation. Because of the favorable geometry of the RB-10J experiment, it is possible to accommodate a sufficient variety and number of mechanical property specimens to launch such a program. The existing V-4Cr-4Ti alloy, which has many advantageous unirradiated properties, provides a good material on which to base a study of flow and fracture and to establish a mechanism-based approach to modeling the effects of external parameters on fracture. The fundamental information gained and the modeling of the fracture behavior will provide a sound underpinning for future work on compositionally-modified alloys. In addition, there is sufficient space in the RB-10J to accommodate secondary objectives such as radiation hardening and microstructure of some alternative vanadium alloys and also to conduct additional pressurized tube experiments to complement those currently in RB-11J/12J.

Specimens will be irradiated at either 420 ± 15°C and 480 ± 15°C, which will yield specimens at two different degrees of radiation hardening and fracture resistance. To maximize availability of specimen volume and to simplify design, construction, and disassembly, two subcapsules will be stacked vertically with the higher temperature capsule nearer the center line. With this arrangement, these temperatures can be achieved with a Type 316 austenitic steel holder and a Type 316 housing tube; the interior of the capsule will be lined with vanadium to preclude solute pickup. Assuming a 50/50 volume ratio of lithium and specimens, the volume available for specimens is approximately 20 cm^3 at each temperature.

A proposed specimen distribution, based upon the technical objectives described, is shown in Table 1. Vanadium alloys in the form of miniature DC(T) fracture toughness specimens, pre-cracked bend bars (PCVN), flat SS-3 tensile specimens, transmission electron microscopy (TEM) disks, pressurized creep tube specimens, and sheet specimens are to be included.

Austenitic and Ferritic/Martensitic Steel Experiment

The primary technical objectives of the steel experiment are to derive the constitutive equations for 316LN, which is the structural material to be used in the International Thermonuclear Experimental Reactor (ITER), and for F82H, one of the most promising low activation ferritic/martensitic steels. SS-3 flat tensile specimens tested at various temperatures and strain rates will be used to derive the constitutive equations.

An operating temperature of 250°C was chosen because it is in the range where the microstructure of the 316LN alloy is changing from a low temperature regime dominated by small interstitial clusters (1-2 nm in diameter) to a high temperature regime dominated by Frank loops and small cavities. This transition is reflected in the temperature dependence of the tensile properties, where specimens irradiated 250-350°C undergo an especially large increase in yield strength, a severe decrease in uniform elongation, and a significant loss of strain hardening capacity. In addition, this irradiation temperature is one of vital interest to the ITER design team as 100-250°C represents the proposed ITER PW/SB operating temperature. It is important to understand the

Table 1. Proposed Test Matrix for the Vanadium Alloy Region (Each Temperature)

Specimen Type	Specimen Volume (cm^3)	V-4Cr-4Ti Fracture Experiment	Alloy/ Microstructure Variants	V-4Cr-4Ti Creep Experiment
DCT (12.5 mm dia)	0.56	4	—	—
PCVN	0.28	40	—	—
SS-3	0.06	30	40	—
TEM tube (100 disks ea.)	0.11	1.0	3	—
Creep tube	0.11	—	—	4
Mod. SS-3 tensile	0.08	6	—	—
Volume (cm^3)	—	15.8	2.4	0.4

microstructural and mechanical properties changes in this regime in order to ensure adequate safety margins in the ITER design and to protect against alternate failure modes.

A second goal of this experiment is to address the issues surrounding the loss of strain hardening capacity in austenitic stainless steels and to simultaneously gain fundamental understanding into the post-irradiation properties. The loss of strain hardening capability leads to strain localization and increased notch sensitivity. While most of the ITER PW/SB material will be well below any failure limit, a small region of highly localized strain may develop, especially near a notch or surface scratch. This onset of flow localization and increased notch sensitivity may result in the appearance of alternate failure modes. The possibility of these alternate modes needs to be explored experimentally because additional constraints may need to be placed on the primary membrane plus bending stress limit. Type SS-3 flat as well as notched strip (NS) tensile specimens, will be used to investigate the flow localization in 316LN. Some of the tensile specimens will have offset notches. Transmission electron microscopy (TEM) disks will also be included. The notched strip tensile specimens will be combined with numerical calculations to investigate typical structural discontinuities on deformation and fracture. A few thin strip tensile (TS) specimens (0.25 mm thick × 3 mm wide × 25.4 mm long) will be used to punch TEM disks from center after interim deformation to help characterize flow localization. In addition, miniature CVN specimens will be used in 3-point bending for elastic-plastic fracture toughness measurements.

The proposed matrix for this region of the capsule is given in Table 2.

Capsule Description

The experiment is designed using the idea of monitored double containment due to the presence of lithium. Thus, there are two containment vessels - the outer capsule and an inner containment vessel, and the pressures and temperatures within both containment vessels are monitored. Details of the containment capsules for the experiments are provided in the references [2, 3]; the strength requirements and ASME Pressure Vessel Code compliance are , also addressed in these documents. The irradiation capsule has a Type 316 stainless steel containment tube with a 38.2-mm outer diameter in the in-core region. The capsule does not contain a pressure relief device or rupture tube. The inner containment vessel is also Type 316 stainless steel. The containment design incorporates elements used in previous HFIR-MFE RB capsules. The irradiation capsule is designed for straight access into any of the eight 46-mm diameter reflector positions. The capsule will be surrounded by a Eu_2O_3 liner (with a wall thickness that varies from 1.9 to 4.2 mm due to the variation in flux as a function of distance from

Table 2. Proposed Test Matrix for the Steel Alloy Region

Specimen Type	Total Available	Primary Matrix		Secondary Matrix	
		316LN	JPCA	F82H	316LN (extra)
SS-3 flat tensile	94	30	12	30	22
3-point bend bars	21	21	...	...	...
Notched strip tensile	28	24	...	...	4
Thin strip tensile	6	6	...	...	...
TEM disks (65/packet)	1	25 disks	15 disks	10 disks	15 disks

the reactor centerline). The irradiation length (within the HFIR reflector) is 610 mm. There will be six aluminum flux monitors and twelve thermocouples in the capsule.

The vanadium specimens will be sealed within cylindrical Type 316 stainless steel subcapsules. Each subcapsule is approximately 1 inch in diameter. The presence of lithium is required for several reasons: it will be used to assess and understand the chemical compatibility and complex thermodynamics of lithium-vanadium systems; lithium will control the vanadium absorption of interstitial impurities such as carbon, nitrogen, and oxygen, which can embrittle the vanadium and affect post-irradiation testing results; and the liquid lithium is an excellent heat transfer medium and will help provide temperature uniformity in the specimen region. The two subcapsules will be stacked in a Type 316 stainless steel subcapsule holder in the upper section of the capsule. The subcapsule holder serves as the secondary containment vessel. An annular helium gap between each subcapsule and the subcapsule holder will be sized to obtain the different operating temperatures. The Type 316 subcapsule holder containing the two 316 stainless steel subcapsules is contained within the capsule outer housing tube. The housing tube, which serves as the primary reactor coolant pressure boundary, will be seamless 316 steel. The annular gap between the housing tube and subcapsule holder will be purged with a mixture of helium and neon gas to maintain temperature control. The outer surface of the housing tube is in contact with the reactor coolant.

The lower half of the experiment consists of austenitic and ferritic steel specimens placed into holes and slots cut into in an aluminum alloy block. This design duplicates that found in the RB-11J and -12J capsules. The steel specimens and aluminum alloy holder are inside of the capsule housing tube and directly below the subcapsule holder in the upper half of the experiment. The annular gap between the aluminum alloy holder and the housing tube is filled with the control gas mixture and is sized to produce the desired specimen temperature of 250°C.

The capsule will be irradiated in an RB position of HFIR. It is planned that it be in the reactor for eight (8) cycles and will achieve a peak of approximately 4 dpa in steel.

Three temperature regions are required: 250°C, 420°C, and 480°C. Twelve thermocouples placed throughout the experiment will be used to monitor the internal temperatures. The temperature will be controlled in the capsule by varying the composition of the gas flowing through an annulus surrounding the specimen regions in the capsule. The capsule is designed to require a 50% helium, 50% neon (by volume) gas mixture at the middle of cycle and 85 MW full power operation to maintain desired temperatures. The temperature is adjusted in response to the thermocouples by adjusting the gas mixture in the annulus around the specimen holder. Because helium has a higher thermal conductivity, enriching the mixture in this gas will reduce the temperature of specimens. Enriching in neon, with a lower conductivity, will increase the temperature of the specimens. Several factors make the temperature control in this capsule challenging. These include the use of a single control gas to maintain two different specimen temperatures and the variations of the gamma heating rate over each HFIR fuel cycle.

Status

The engineering drawings for the upper and lower regions are complete, as are those for the outer capsule components. Fabrication of components is in progress. The Eu_2O_3 shield is scheduled to be completed at the end of January 1998. Specimen fabrication is 95% complete and all records are being compiled into a central location. A lithium-fill station has been built and prototype testing is underway. High-purity lithium metal (99.9% Li-7) has been procured in order to mitigate the transmutations to tritium.

REFERENCES

1. G. R. Odette, E. Donahue, G. E. Lucas, and J. W. Sheckherd, Fusion Materials Semiannual Progress Report for the Period Ending June 30, 1996, DOE/ER-0313/20, 1996, p. 11.

2. Martin Marietta Energy Systems Report X-0E-401, February 1988, "Design Calculations for the In-Vessel Portion of the HFIR-MFE RB* Experiment Facility."

3. Lockheed Martin Energy Systems Report X-OE-713, April 1997, "Design Calculations for the HFIR-MFE RB* 10J Multi Temperature Experiment Capsule and the Experiment Facility."

SUMMARY OF THE U.S. SPECIMEN MATRIX FOR THE HFIR 13J VARYING TEMPERATURE IRRADIATION CAPSULE — S. J. Zinkle (Oak Ridge National Laboratory)

OBJECTIVE

The objective of this report is to summarize the U.S. portion of the specimen matrix for the DOE/Monbusho collaborative HFIR 13J varying temperature irradiation capsule.

SUMMARY

The U.S. specimen matrix for the collaborative DOE/Monbusho HFIR 13J varying temperature irradiation capsule contains two ceramics and 29 different metals, including vanadium alloys, ferritic/martensitic steels, pure iron, austenitic stainless steels, nickel alloys, and copper alloys. This experiment is designed to provide fundamental information on the effects of brief low-temperature excursions on the tensile properties and microstructural evolution of a wide range of materials irradiated at nominal temperatures of 350 and 500°C to a dose of ~5 dpa. A total of 340 miniature sheet tensile specimens and 274 TEM disks are included in the U.S.-supplied matrix for the irradiation capsule.

PROGRESS AND STATUS

Introduction

A series of recent neutron irradiation experiments [1-8] have demonstrated that low-temperature excursions at the beginning or during irradiation can have a pronounced effect on the microstructural evolution of face-centered cubic and body-centered cubic metals irradiated at doses up to ~0.2 displacements per atom (dpa). For example a swelling rate of ~10%/dpa was observed in Ti-modified austenitic stainless steel (Fe-16Cr-17Ni-0.25Ti) irradiated at cyclic temperatures of 200/400°C and 300/500°C to a dose of 0.13 dpa [7]. Since temperature transients are likely to occur in fusion reactors (and have routinely occurred in many of the fission reactor irradiation experiments used to establish the current radiation effects data base), there is a pressing need to understand the importance of variations in the irradiation temperature. Unfortunately, the pioneering varying temperature neutron irradiation experiments could not be carried out to doses above ~0.2 dpa due to flux limitations in the RTNS-II and JMTR facilities. Ion [9,10] and electron [11] irradiation experiments suggest that significant effects associated with low-temperature transients may continue to exist at somewhat higher doses of 0.3 to 2 dpa. In order to provide additional neutron irradiation data on this phenomenon at higher doses, the varying temperature experiment was designed to be carried out in the HFIR reactor as part of the DOE/Monbusho JUPITER collaboration.

Information on the capsule design for the HFIR 13J varying temperature experiment has been published in previous semiannual progress reports [12,13]. The capsule utilizes EuO_2-shielding to minimize solid transmutations associated with the high thermal neutron flux in HFIR removable beryllium (RB) position. The capsule consists of four independently controlled temperature zones which are designed for operation at 350, 500, 200/350, and 300/500°C. Electrical heaters are used to maintain a constant temperature during the reactor startup for the 350 and 500°C constant-temperature portions of the capsule. The varying temperature portions of the capsule are designed to operate at the lower temperature (200 and 300°C, respectively) during the first 10% of each reactor cycle. The irradiation will consist of a total of 10 HFIR irradiation cycles, which will produce a dose of ~5 dpa in vanadium alloys, ferritic/martensitic steels, and austenitic alloys and ~7 dpa in copper alloys. The HFIR 13J capsule will be installed in the reactor upon the completion of the HFIR 11J/12J EuO_2-shielded irradiation, which is currently expected to occur in June, 1998.

U.S. Specimen Matrix

A total of 29 different pure metals and alloys and 2 ceramic materials are included in the U.S.-supplied portion of the DOE/Monbusho HFIR 13J varying temperature irradiation capsule. These materials include vanadium alloys, ferritic/martensitic and austenitic steels, nickel alloys, and copper alloys. The U.S. materials were fabricated into miniature sheet tensile specimens and/or transmission electron microscopy (TEM) disks. The U.S. specimen matrix for the HFIR 13J irradiation capsule is summarized in Table 1, along with the researcher who supplied the specimens. The VX-8 heat of V-4Cr-4Ti was supplied to ORNL as thin strips by Dr. V.A. Kazakov, Scientific Research Institute of Atomic Reactors, Dimitrovgrad, Russia. Several of the copper alloys were supplied by Dr. B.N. Singh, Risø National Laboratory, Roskilde, Denmark. The type JP-TN-1 miniature sheet tensile specimens (identified as "SSJ" specimens in Table 1) used in HFIR 13J capsule have an overall length of 16 mm and a thickness of 0.25 mm, with an end tab width of 4 mm. The gage dimensions are 5 mm by 1.2 mm. The thickness of the 3 mm diameter TEM disks was 0.25 mm ($\pm$ 0.01 mm) except for the Cu-Ni specimens (0.16-0.18 mm thick) and the A533B pressure vessel steel specimens which are intended for microhardness measurements (0.76 mm thick). The manufacturer's heat number (where available) and chemical composition of the various materials are listed in Table 2.

REFERENCES

1. M. Kiritani, J. Nucl. Mater. 160 (1988) 135.
2. T. Muroga, Y. Miyamoto, H. Watanabe, and N. Yoshida, J. Nucl. Mater. 155-157 (1988) 810.
3. M. Kiritani et al., J. Nucl. Mater. 174 (1990) 327.
4. M. Kiritani et al., J. Nucl. Mater. 179-181 (1991) 1104.
5. N. Yoshida et al., J. Nucl. Mater. 191-194 (1992) 1114.
6. M. Kiritani et al., J. Nucl. Mater. 212-215 (1994) 241.
7. N. Yoshida et al., J. Nucl. Mater. 212-215 (1994) 471.
8. H. Matsui, K. Kuji, M. Hasegawa, and A. Kimura, J. Nucl. Mater. 212-215 (1994) 784.
9. Q. Xu, H. Watanabe, T. Muroga, and N. Yoshida, J. Nucl. Mater. 212-215 (1994) 258.
10. Q. Xu, H. Watanabe, and N. Yoshida, J. Nucl. Mater. 233-237 (1996) 1057.
11. T. Muroga, Y. Nonaka, and N. Yoshida, J. Nucl. Mater. 233-237 (1996) 1035.
12. A. L. Qualls and T. Muroga, in Fusion Materials Semiann. Prog. Report for Period ending December 31, 1996, DOE/ER-0313/21 (Oak Ridge National Lab, 1996) p. 255.
13. A. L. Qualls, M. T. Hurst, D. G. Raby, and D. W. Sparks, in Fusion Materials Semiann. Prog. Report for Period ending June 30, 1997, DOE/ER-0313/22 (Oak Ridge National Lab, 1997) p. 243.

Table 1. U.S. specimen matrix for the HFIR 13J capsule

Alloy	Number of specimens at each test condition			
	350°C	200/350°C	500°C	300/500°C
Vanadium alloys				
V-4Cr4Ti (832665)[a]	6 SSJ, 3 TEM	6 SSJ, 3 TEM	6 SSJ, 3 TEM	6 SSJ, 3 TEM
V-4Cr4Ti (VX-8)[a]	6 SSJ, 3 TEM	6 SSJ, 3 TEM	6 SSJ, 3 TEM	6 SSJ, 3 TEM
V-4Cr4Ti (VX-8)[a],25%CW	2 SSJ, 2 TEM	2 SSJ, 2 TEM	2 SSJ, 2 TEM	2 SSJ, 2 TEM
V-5Ti-5Ti (T87)[a]	6 SSJ, 3 TEM	6 SSJ, 3 TEM	6 SSJ, 3 TEM	6 SSJ, 3 TEM
V-6Ti-6Ti (T90)[a]	6 SSJ, 3 TEM	6 SSJ, 3 TEM	6 SSJ, 3 TEM	6 SSJ, 3 TEM
V-3Cr-3Ti (T91)[a]	6 SSJ, 3 TEM	6 SSJ, 3 TEM	6 SSJ, 3 TEM	6 SSJ, 3 TEM
V-3Ti-0.5Si (BL-42)[b]	3 SSJ, 3 TEM	—	4 SSJ, 3 TEM	2 SSJ, 1 TEM
V-2.5Ti-1Si (BL-45)[b]	3 SSJ, 3 TEM	—	4 SSJ, 3 TEM	2 SSJ, 1 TEM
V-5Ti (BL-46)[b]	3 SSJ, 3 TEM	—	4 SSJ, 3 TEM	2 SSJ, 1 TEM
Ferritic steels				
9Cr-2WV[c]	4 SSJ, 2 TEM	4 SSJ, 2 TEM	4 SSJ, 2 TEM	4 SSJ, 2 TEM
9Cr-2WVTa[c]	4 SSJ, 2 TEM	4 SSJ, 2 TEM	4 SSJ, 2 TEM	4 SSJ, 2 TEM
9Cr-1MoVNb[c]	4 SSJ, 2 TEM	4 SSJ, 2 TEM	4 SSJ, 2 TEM	4 SSJ, 2 TEM
9Cr-1MoVNb+2Ni[c]	4 SSJ, 2 TEM	4 SSJ, 2 TEM	4 SSJ, 2 TEM	4 SSJ, 2 TEM
5Cr-2WV[c]	4 SSJ, 2 TEM	4 SSJ, 2 TEM	4 SSJ, 2 TEM	4 SSJ, 2 TEM
3Cr-3WV[c]	4 SSJ, 2 TEM	4 SSJ, 2 TEM	4 SSJ, 2 TEM	4 SSJ, 2 TEM
3Cr-3WVTa[c]	4 SSJ, 2 TEM	4 SSJ, 2 TEM	4 SSJ, 2 TEM	4 SSJ, 2 TEM
A533B, plate[d]	2 TEM	2 TEM	2 TEM	2 TEM
A533B, weld[d]	2 TEM	2 TEM	2 TEM	2 TEM
pure Fe[e]	4 SSJ, 1 TEM	3 SSJ, 1 TEM	3 SSJ	3 SSJ, 1 TEM
Stainless steel/Ni alloys	3 TEM	3 TEM	3 TEM	3 TEM
P7, annealed[d]	3 TEM	3 TEM	3 TEM	3 TEM
P7, 20% CW[d]	3 SSJ, 3 TEM	3 SSJ, 3 TEM	3 SSJ, 3 TEM	3 SSJ, 3 TEM
316 SS, solution anneal[f]	3 SSJ, 3 TEM	3 SSJ, 3 TEM	3 SSJ, 3 TEM	3 SSJ, 3 TEM
316 SS, 20% cold work[f]	—	—	9 TEM	—
Fe-15Cr-35Ni[f]	3 TEM	3 TEM	3 TEM	3 TEM
Ni-18Fe-5Cu-1.5Cr[g]	3 TEM	3 TEM	3 TEM	3 TEM
Ni-Be[g]				
Copper alloys				
GlidCop Al25 DS Cu[a]	3 SSJ, 3 TEM	3 SSJ, 3 TEM	—	—
GlidCop Ti/Al_2O_3 DS Cu[e]	3 SSJ, 1 TEM	3 SSJ, 1 TEM	—	1 TEM
CuCrZr (AT temper)[a]	3 SSJ, 3 TEM	3 SSJ, 3 TEM	—	—
99.999% Cu[e]	3 SSJ, 1 TEM	3 SSJ, 1 TEM	—	1 TEM
Cu-1%Ni[e]	3 SSJ, 1 TEM	3 SSJ, 1 TEM	—	1 TEM
Cu-5%Ni[e]	3 SSJ, 1 TEM	3 SSJ, 1 TEM	—	1 TEM
Ceramics				
$MgTiO_3$ [h]	1 TEM	1 TEM		1 TEM
$MgTi_2O_5$ [h]	1 TEM			1 TEM
Totals:	97 SSJ,75 TEM	87 SSJ,65 TEM	81 SSJ,71 TEM	75 SSJ,63 TEM

[a] supplied by S.J. Zinkle (ORNL)
[b] supplied by H.C. Tsai (ANL)
[c] supplied by R.L. Klueh (ORNL)
[d] supplied by R.E. Stoller (ORNL)
[e] supplied by B.N. Singh (Risø)
[f] supplied by J.P. Robertson (ORNL)
[g] supplied by C.W. Allen (ANL)
[h] supplied by K.E. Sickafus (LANL)

Table 2. Chemical composition of U.S. specimens included in the HFIR 13J capsule

Alloy and heat number	Chemical composition (wt% unless otherwise noted)
Vanadium alloys	
V4Cr4Ti(832665,plate R250)	V-3.8Cr-3.8Ti-0.08Si-0.03Mo-0.02Fe-0.02Al (0.03 O-0.008N-0.008C)
V4Cr4Ti (VX-8)	V-3.7Cr-3.9Ti-0.05Si-0.03Mo-0.03Fe-0.11Al-0.13Nb-0.05Co (0.03 O-0.009N-0.01C)
V-5Ti-5Ti (T87, plate D250)	V-4.9Cr-4.9Ti-0.08Si-0.04Mo-0.02Fe-0.02Al (0.03 O-0.009N-0.01C)
V-6Ti-6Ti (T90, plate F150)	V-5.7Cr-6.0Ti-0.12Si-0.03Mo-0.01Fe-0.02Al (0.025 O-0.008N-0.01C)
V-3Cr-3Ti (T91, plate G250)	V-3.0Cr-3.0Ti-0.11Si-0.04Mo-0.01Fe-0.02Al (0.02 O-0.006N-0.01C)
V-3Ti-0.5Si (BL-42)	V-3.1Ti-0.54Si-0.02Fe (0.058 O-0.02N-0.014C)
V-2.5Ti-1Si (BL-45)	V-2.5Ti-0.99Si-0.01Fe (0.034 O-0.012N-0.009C)
V-5Ti (BL-46)	V-4.6Ti-0.016Si-0.04Al (0.03 O-0.005N-0.009C)
Ferritic steels	
9Cr-2WV, heat 3790	Fe-8.95Cr-2.0W-0.24V-0.51Mn-0.23Si-0.03Cu-0.014P-0.02Al--0.12C-0.03N-0.006 O
9Cr-2WVTa,heat 3791	Fe-8.90Cr-2.0W-0.23V-0.44Mn-0.21Si-0.03Cu-0.015P-0.02Al--0.11C-0.02N-0.006 O
9Cr-1MoVNb(#3590)	Fe-8.6Cr-0.98Mo-0.21V-0.063Nb-0.36Mn-0.08Si-0.03Cu-0.01Al--0.09C-0.05N-0.007 O
9Cr-1MoVNb+2Ni(#3591)	Fe-8.6Cr-0.98Mo-0.22V-0.066Nb-0.36Mn-0.08Si-0.04Cu-0.01Al--0.06C-0.05N-0.006 O
5Cr-2WV, heat 3789	Fe-5.0Cr-2.0W-0.24V-0.49Mn-0.23Si-0.03Cu-0.015P-0.01Al--0.12C-0.02N-0.005 O
3Cr-3WV (#10293)	Fe-3.0Cr-2.8W-0.25V-0.50Mn-0.14Si-0.01Ni-0.097C
3Cr-3WVTa (#10294)	Fe-2.9Cr-2.8W-0.25V-0.1Ta-0.50Mn-0.14Si-0.097C
A533B, plate 02	Fe-1.42Mn-0.70Ni-0.50Mo-0.12Cr-0.22Si-0.14Cu-0.02S-0.01P-0.24C
A533B, weld 73W	Fe-1.56Mn-0.60Ni-0.58Mo-0.25Cr-0.45Si-0.31Cu-0.003V-0.005S-0.005P-0.098C
pure Fe (Goodfellow)	99.999 Fe
FeCrNi/Ni alloys	
316 SS, heat P7	Fe-17Cr-16.7Ni--2.5Mo-0.03Mn-0.1Si-0.068W-0.01Ti-0.005C-0.004N-0.028 O
316F SS, JAERI heat	Fe-16.8Cr-14Ni--2.3Mo-0.23Mn-0.04Si-0.002S-0.01Ti-0.038C-0.011N
Fe-15Cr-35Ni (#15.35-130)	Fe-15Cr-34.5Ni--0.01Mn-0.04Cu-0.02Co-0.01Si-0.004S-0.008Al-0.007C-0.004N-0.04 O
Ni-18Fe-5Cu-1.5Cr	Ni-18Fe-5Cu-1.5Cr (at.%)
Berylco Ni-Be (alloy 440)	Ni-1.95Be-0.5Ti
Copper alloys	
GlidCop Al25(IG0) DS Cu (OMG Americas #C-8064)	Cu-0.25Al-0.22 O-0.025B-0.01Fe-0.01Pb-0.025B
GlidCop Ti/Al_2O_3 DS Cu	Cu-2Ti-0.25Al-0.22 O-0.025B (typical analysis)
CuCrZr (Zollern #882)	Cu-0.85Cr-0.09Zr
pure Cu (Trefimetaux)	99.999% Cu (10 wt. ppm Ag, 3 wt. ppm Si)
Cu-1%Ni(Johnson-Matthey)	Cu-1Ni (fabricated from 99.999% purity Cu, Ni metal foils)
Cu-5%Ni(Johnson-Matthey)	Cu-5Ni (fabricated from 99.999% purity Cu, Ni metal foils)
Ceramics	
$MgTiO_3$ (LANL/Alfa Aesar)	65.1TiO_2-34.2MgO-0.28Al_2O_3-0.01BaO-0.07CaO-0.036Fe_2O_3-0.20Na_2O-0.017SO_3-0.09SiO_2
$MgTi_2O_5$ (LANL/Alfa Aesar)	prepared from stoichiometric mix of $MgTiO_3$ and TiO_2 (99.9TiO_2-0.03Al-0.01Si-0.03Zr)

ULE AND STATUS OF IRRADIATION EXPERIMENTS – A. F. Rowcliffe, ossbeck, and J. P. Robertson (Oak Ridge National Laboratory)

:TIVE

ide an updated summary of the status of irradiation experiments for the neutron-interactive materials ı.

ıARY

The current status of reactor irradiation experiments is presented in tables summarizing the experimental objectives, conditions, and schedule.

PROGRESS AND STATUS

Currently, the program has four irradiation experiments in reactor; and five experiments in the design or construction stages. Postirradiation examination and testing is in progress on ten experiments.

Summary of Reactor Irradiation Experiments

Experiment	Lead Lab	Collaborators	Responsible Person	Major Objectives	Materials	Temperature °C	Dose (dpa) or fluence	Irrad. Start	Irrad. Finish	Status
EBR-II, Reactor, ANL, Idaho Falls, ID										
COBRA 1A1	PNL	ORNL, ANL, MONBUSHO	M.L. Hamilton	Tensile and fatigue prop., Charpy impact, fracture toughness, TEM	Austenitic and ferritic steels, Fe-alloys, V, Be, low act. materials, Cu alloys, Ti-Al, SiC, C-C comp.	370, 500, 600	9	Nov-92	Apr-93	
COBRA 1A2	PNL	ORNL, ANL, MONBUSHO	M.L. Hamilton	Tensile and fatigue prop., Charpy impact, fracture toughness, TEM	Austenitic and ferritic steels, Fe-alloys, V, Be, low act. materials, Cu alloys, Ti-Al, SiC, C-C comp.	370, 400, 800	33	Nov-92	Sep-94	
X530	ANL		H. Tsai, H.M. Chung	He-effects, swelling, Charpy impact, fracture toughness, tensile prop.	V alloys	370	5	Aug-94	Sep-94	
High Flux Isotope Reactor, ORNL, Oak Ridge, TN										
HFIR-CTR-60	ORNL		S.J. Zinkle	Flexure bars, TEM, indentation disks	Isotopically tailored ceramics	100-600	2.4E+26 n/m2	Dec-94	Aug-95	
HFIR-CTR-61	ORNL		S.J. Zinkle	Similar to HFIR-CTR-60			7.20E+26	Dec-94	Aug-98	
HFIR-JP-9	ORNL	JAERI	P.J. Maziasz/ J.E. Pawel	He effects by isotopic tailoring, tensile prop., TEM	Austenitic and ferritic steels	300-600	57	Jul-90	Apr-94	
HFIR-JP-10	ORNL	JAERI	P.J. Maziasz/ J.E. Pawel	He effects by isotopic tailoring, tensile prop., TEM	Austenitic and ferritic steels	300-600	17	Jul-90	Sep-91	
HFIR-JP-11	ORNL	JAERI	P.J. Maziasz/ J.E. Pawel	Similar to HFIR-JP-10			17	Jul-90	Sep-91	
HFIR-JP-12	ORNL	JAERI	P.J. Maziasz/ J.E. Pawel	Similar to HFIR-JP-9			57	Jul-90	Apr-94	
HFIR-JP-13	ORNL	JAERI	P.J. Maziasz/ J.E. Pawel	Similar to HFIR-JP-10			17	Jul-90	Sep-91	
HFIR-JP-14	ORNL	JAERI	P.J. Maziasz/ J.E. Pawel	He effects by isotopic tailoring, tensile prop., TEM	Austenitic and ferritic steels	300-600	34	Jul-90	Sep-92	

Summary of Reactor Irradiation Experiments

Experiment	Lead Lab	Collaborators	Responsible Person	Major Objectives	Materials	Temperature °C	Dose (dpa) or fluence	Irrad. Start	Irrad. Finish	Status
HFIR-JP-15	ORNL	JAERI	P.J. Maziasz/ J.E. Pawel	Similar to HFIR-JP-9			57	Jul-90	Apr-94	
HFIR-JP-16	ORNL	JAERI	P.J. Maziasz/ J.E. Pawel	Similar to HFIR-JP-10			17	Jul-90	Sep-91	
HFIR-JP-17	ORNL	JAERI	M.L. Grossbeck/ J.E. Pawel	Fracture toughness, tensile prop. TEM	Austenitic and ferritic steels	250-300	3	Dec-91	Feb-92	
HFIR-JP-18	ORNL	JAERI	M.L. Grossbeck/ J.E. Pawel	Fracture toughness, tensile prop. TEM	Austenitic and ferritic steels	60-125	3	Aug-91	Oct-91	
HFIR-JP-19	ORNL	JAERI	M.L. Grossbeck/ J.E. Pawel	Similar to HFIR-JP-18		60-125	3	Aug-91	Oct-91	
HFIR-JP-20	ORNL	JAERI	J.E. Pawel	Tensile Prop., TEM, He effects by isotopic tailoring	Austenitic and ferritic steels	300-600	8	Dec-93	Jun-94	
HFIR-JP-21	ORNL	JAERI	J.E. Pawel	Similar to HFIR-JP-20			18	Dec-93	Apr-95	
HFIR-JP-22	ORNL	JAERI	J.E. Pawel	Similar to HFIR -JP-20			34	Dec-93	Jan-96	
HFIR-JP-23	PNL	MONBUSHO	D.S. Gelles	TEM	Austenitic and ferritic steels, Cu, Mo, V alloys, TiAl	300-600	8	Dec-93	Jun-94	
HFIR-MFE-60J	ORNL	JAERI	J.L. Scott/ M.L. Grossbeck	Spectrally tailored for fusion He prod. Began in ORR as ORR-MFE-6J (6.9 dpa). TEM, Charpy, irrad. creep, tensile and crack growth prop.	Austenitic and ferritic steels, and Ni alloys	60	19 (total)	Jul-90	Nov-92	
HFIR-MFE-330J	ORNL	JAERI	J.L. Scott/ M.L. Grossbeck	Similar to HFIR-MFE-60J. Began in ORR as ORR-MFE-7J (7.4 dpa)		330	19 (total)	Jul-90	Nov-92	
HFIR-MFE-200J	ORNL	JAERI	M.L. Grossbeck/ J.E. Pawel	Similar to HFIR-MFE-60J. Began in ORR as ORR-MFE-6J (6.9 dpa)		200	17 (total)	Nov-92	Jan-95	
HFIR-MFE-400J	ORNL	JAERI	M.L. Grossbeck/ J.E. Pawel	Similar to HFIR-MFE-60J. Began as ORR-MFE-7J (7.4 dpa)		400	17 (total)	Nov-92	Jan-95	
HFIR-HT-S1, -S7	ORNL		L.L. Snead	Thermal conductivity	Various insulators	80-350	0.01-1.0	Jun-95	Aug-95	
HFIR-HT-F Series	ORNL		L. L. Snead	Fiber tensile	SiC	80-800	0.001-1.0	Jan-95	Mar-96	

Summary of Reactor Irradiation Experiments

Experiment	Lead Lab	Collaborators	Responsible Person	Major Objectives	Materials	Temperature °C	Dose (dpa) or fluence	Irrad. Start	Irrad. Finish	Status
HFIR-TRIST-ER1	ORNL	MONBUSHO/ JAERI	S.J. Zinkle	In-situ electrical conductivity	Al2O3	450	3E+25 n/m2	Apr-96	Jun-96	
HFIR-MFE-RB-10J	ORNL	JAERI	J.E. Pawel	Tensile, fracture	Vanadium, 316LN-1G, J316	200, 500	5	May-98	May-99	
HFIR-MFE-RB-11J	ORNL	MONBUSHO/ JAERI	M. L. Grossbeck	Tensile, fracture, TEM	Low activation ferritics, V alloys, SiC	300	5	Feb-97	May-98	
HFIR-MFE-RB-12J	ORNL	MONBUSHO/ JAERI	M. L. Grossbeck	Tensile, fracture, TEM	Low activation ferritics, V alloys, SiC	500	5	Feb-97	May-98	
HFIR-MFB-RB-13J	ORNL	MONBUSHO/ JAERI	S. J. Zinkle	Varying temp. experiment	Ceramics, Fe-Cr-Ni, V alloys, ferritics, copper	200, 350, 500	5	May-97	May-98	
HFIR-CTR-62	ORNL	JAERI	R.L. Klueh	Charpy impact and He effects	Reduced act. and conventional ferritic steels	300, 400	13	Apr-95	Dec-95	
HFIR-CTR-63	ORNL	JAERI	R.L. Klueh	Charpy impact and tensile, TEM, He effects	Reduced act. and conventional ferritic steels	300, 400	13	Apr-95	Dec-95	
HFIR-JP25	ORNL	JAERI	R.L. Klueh	Tensile, fracture, TEM	Low activation ferritics	300, 500	20	Apr-98	Jun-99	
HFIR-JP27	ORNL	JAERI	L.L. Snead	Fracture, TEM	Intermetallics, SiC	500-800	10	Apr-98	Jul-98	
HFIR-JP28	ORNL	JAERI	L.L. Snead	Fracture, TEM	SiC	500-800	10	Mar-98	Sep-98	
High Flux Beam Reactor, Brookhaven National Laboratory										
HFBR-ISEC-3	ORNL		L.L. Snead	In-situ electrical	WESGO Al2O3	450	1.5	Jul-95	Sep-95	
HFBR-V1	ORNL		L.L. Snead	Tensile, fracture	V-4Cr-4Ti	75, 150, 225	0.4	May-95	Jun-95	
HFBR-V2	ORNL		L.L. Snead	Tensile, fracture	V-4Cr-4Ti	75, 225, 300, 375	0.4	Jul-95	Aug-95	
HFBR-V3	ORNL		L.L. Snead	Tensile, fracture	V-4Cr-4Ti	160, 265, 315, 420	0.4	Aug-96	Sep-96	
HFBR-V4	ORNL		L.L. Snead	Tensile, fracture	V-4Cr-4Ti	105-505	0.1	Aug-96	Sep-96	

Summary of Reactor Irradiation Experiments

Experiment	Lead Lab	Collaborators	Responsible Person	Major Objectives	Materials	Temperature °C	Dose (dpa) or fluence	Irrad. Start	Irrad. Finish	Status
Advanced Test Reactor, Idaho Falls										
ATR-A1	ANL	MONBUSHO	D.L. Smith	Tensile, fracture toughness, TEM, creep	Vanadium alloys	200, 300	5	Dec-95	May-96	
BOR-60 Reactor, RIAR, Dimitrovgrad, Russia										
BOR-60-Fusion-1	ORNL, ANL	RDIPE, RIAR	A.F. Rowcliffe, D.L. Smith	Mechanical and microstructural properties	V alloys	350-380	10	Jul-95	Mar-96	
SM-2 Reactor, RIAR, Dimitrovgrad, Russia										
SM-2.1	ORNL, PNL	RIAR	S.J. Zinkle	Tensile, electrical, microstructural, and creep properties	Cu alloys	100, 200, 330	1, 5	Dec-93	Feb-94	
SM-2.2	PNL	SRIAR	D.J. Edwards	Mechanical behavior of bonded materials	Cu alloys/SS, Cu/Be	120, 300	0.2	Mar-96	May-96	
SM-2.3	PNL	SRIAR	D.J. Edwards	Mechanical behavior of bonded materials	Cu alloys/SS, Cu/Be	100, 250	0.2	Nov-97	May-98	
	Irradiation complete									
	Irradiation in progress									
	Irradiation planned									

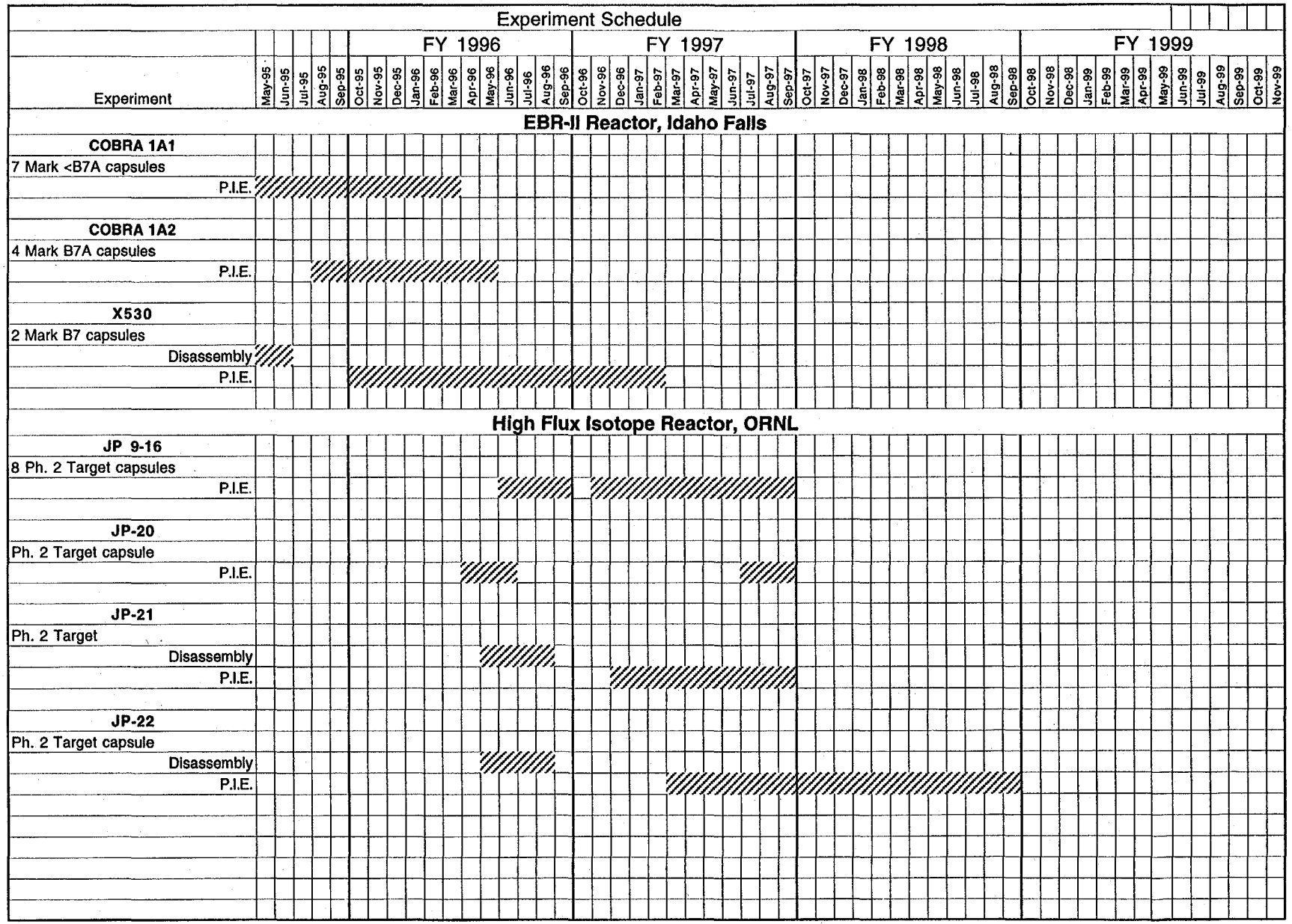
Experiment Schedule
FY 1996
FY 1997
FY 1998
FY 1999
Experiment
May-95 Jun-95 Jul-95 Aug-95 Sep-95 Oct-95 Nov-95 Dec-95 Jan-96 Feb-96 Mar-96 Apr-96 May-96 Jun-96 Jul-96 Aug-96 Sep-96 Oct-96 Nov-96 Dec-96 Jan-97 Feb-97 Mar-97 Apr-97 May-97 Jun-97 Jul-97 Aug-97 Sep-97 Oct-97 Nov-97 Dec-97 Jan-98 Feb-98 Mar-98 Apr-98 May-98 Jun-98 Jul-98 Aug-98 Sep-98 Oct-98 Nov-98 Dec-98 Jan-99 Feb-99 Mar-99 Apr-99 May-99 Jun-99 Jul-99 Aug-99 Sep-99 Oct-99 Nov-99
EBR-II Reactor, Idaho Falls
COBRA 1A1
7 Mark <B7A capsules
P.I.E.
COBRA 1A2
4 Mark B7A capsules
P.I.E.
X530
2 Mark B7 capsules
Disassembly
P.I.E.
High Flux Isotope Reactor, ORNL
JP 9-16
8 Ph. 2 Target capsules
P.I.E.
JP-20
Ph. 2 Target capsule
P.I.E.
JP-21
Ph. 2 Target
Disassembly
P.I.E.
JP-22
Ph. 2 Target capsule
Disassembly
P.I.E.

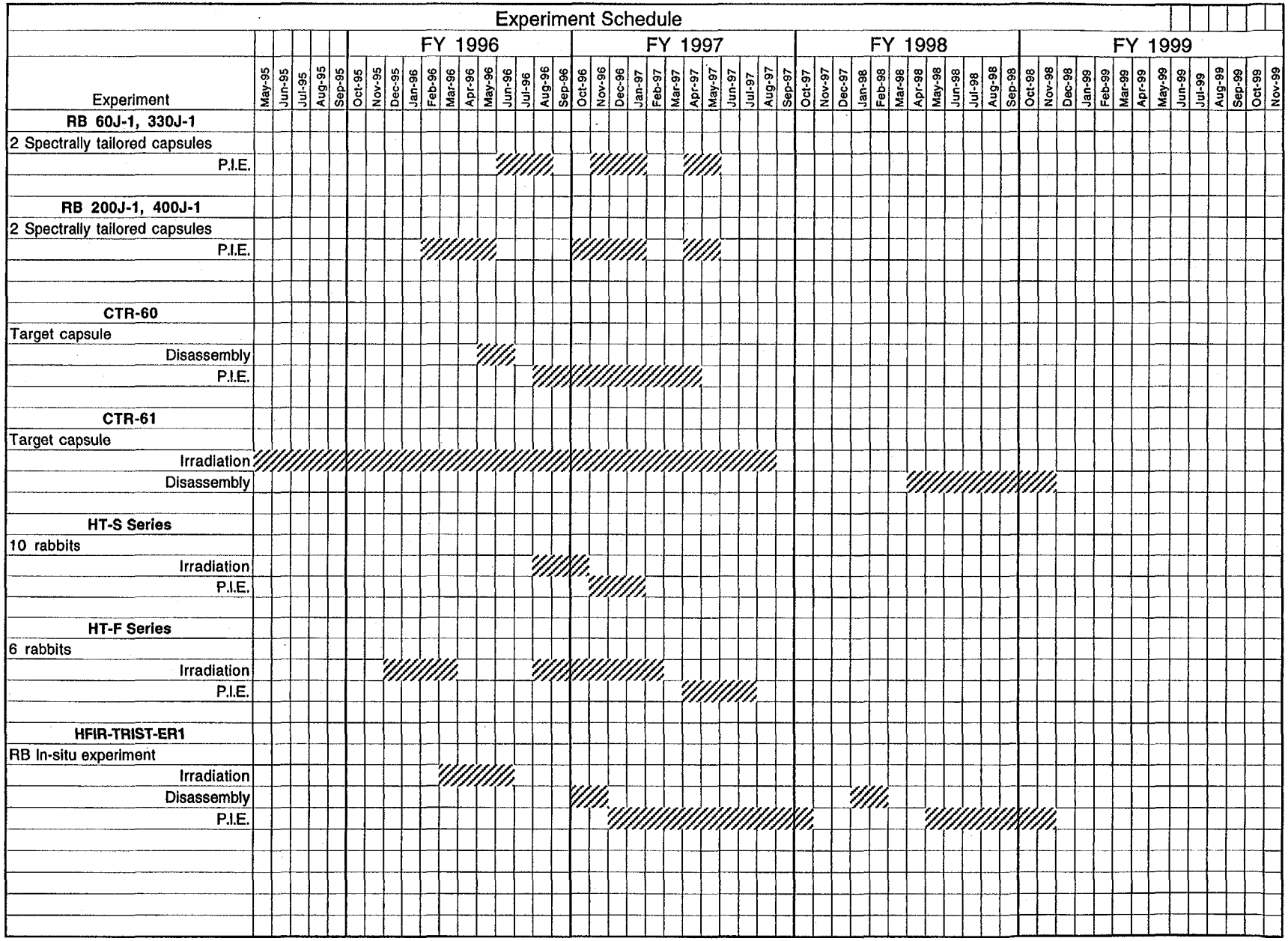
Experiment Schedule
FY 1996
FY 1997
FY 1998
FY 1999
Experiment
May-95
Jun-95
Jul-95
Aug-95
Sep-95
Oct-95
Nov-95
Dec-95
Jan-96
Feb-96
Mar-96
Apr-96
May-96
Jun-96
Jul-96
Aug-96
Sep-96
Oct-96
Nov-96
Dec-96
Jan-97
Feb-97
Mar-97
Apr-97
May-97
Jun-97
Jul-97
Aug-97
Sep-97
Oct-97
Nov-97
Dec-97
Jan-98
Feb-98
Mar-98
Apr-98
May-98
Jun-98
Jul-98
Aug-98
Sep-98
Oct-98
Nov-98
Dec-98
Jan-99
Feb-99
Mar-99
Apr-99
May-99
Jun-99
Jul-99
Aug-99
Sep-99
Oct-99
Nov-99
RB 60J-1, 330J-1
2 Spectrally tailored capsules
P.I.E.
RB 200J-1, 400J-1
2 Spectrally tailored capsules
P.I.E.
CTR-60
Target capsule
Disassembly
P.I.E.
CTR-61
Target capsule
Irradiation
Disassembly
HT-S Series
10 rabbits
Irradiation
P.I.E.
HT-F Series
6 rabbits
Irradiation
P.I.E.
HFIR-TRIST-ER1
RB In-situ experiment
Irradiation
Disassembly
P.I.E.

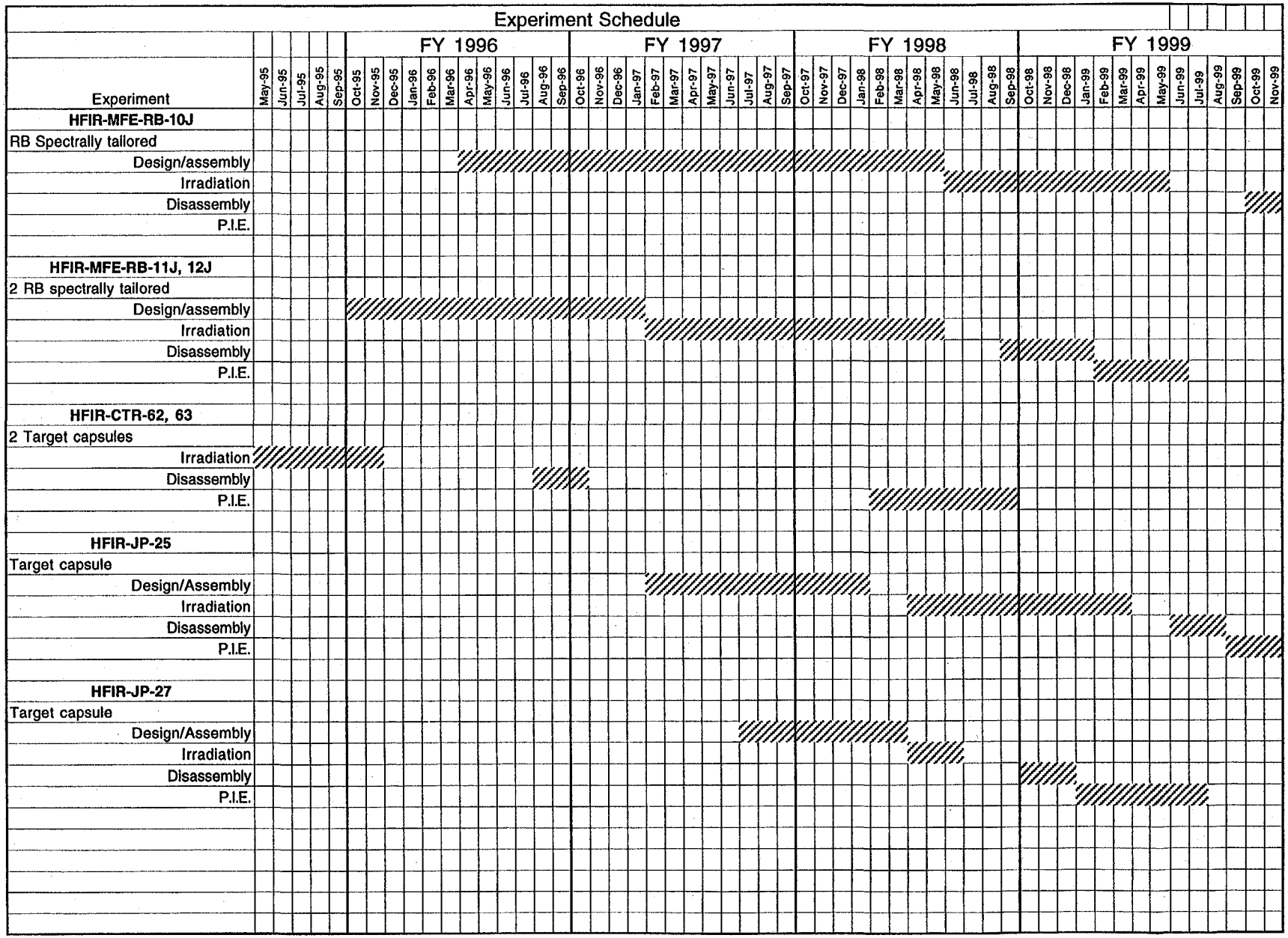
Experiment Schedule
FY 1996
FY 1997
FY 1998
FY 1999
Experiment
May-95
Jun-95
Jul-95
Aug-95
Sep-95
Oct-95
Nov-95
Dec-95
Jan-96
Feb-96
Mar-96
Apr-96
May-96
Jun-96
Jul-96
Aug-96
Sep-96
Oct-96
Nov-96
Dec-96
Jan-97
Feb-97
Mar-97
Apr-97
May-97
Jun-97
Jul-97
Aug-97
Sep-97
Oct-97
Nov-97
Dec-97
Jan-98
Feb-98
Mar-98
Apr-98
May-98
Jun-98
Jul-98
Aug-98
Sep-98
Oct-98
Nov-98
Dec-98
Jan-99
Feb-99
Mar-99
Apr-99
May-99
Jun-99
Jul-99
Aug-99
Sep-99
Oct-99
Nov-99
HFIR-MFE-RB-10J
RB Spectrally tailored
Design/assembly
Irradiation
Disassembly
P.I.E.
HFIR-MFE-RB-11J, 12J
2 RB spectrally tailored
Design/assembly
Irradiation
Disassembly
P.I.E.
HFIR-CTR-62, 63
2 Target capsules
Irradiation
Disassembly
P.I.E.
HFIR-JP-25
Target capsule
Design/Assembly
Irradiation
Disassembly
P.I.E.
HFIR-JP-27
Target capsule
Design/Assembly
Irradiation
Disassembly
P.I.E.

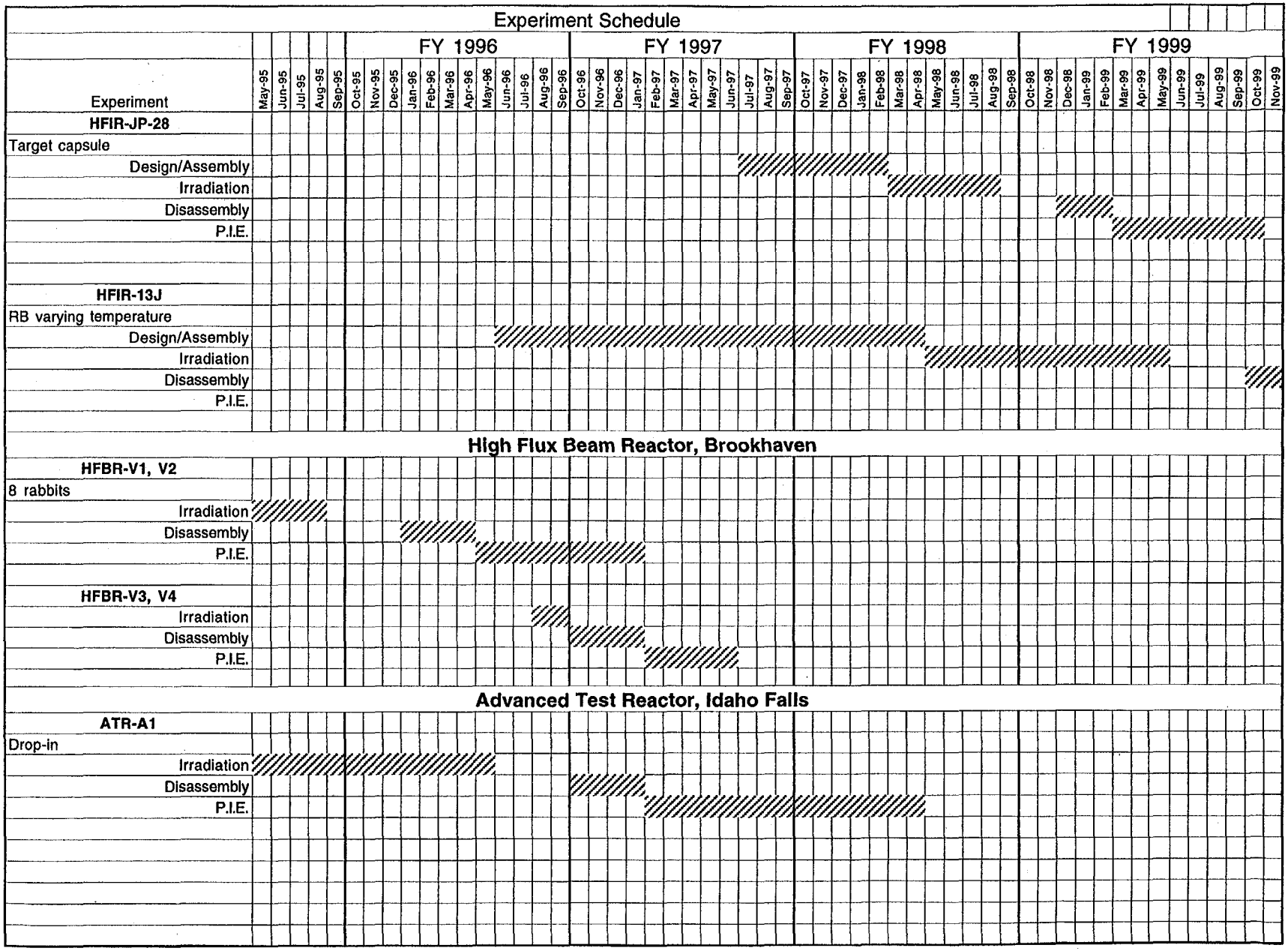
Experiment Schedule
FY 1996
FY 1997
FY 1998
FY 1999
Experiment
May-95 Jun-95 Jul-95 Aug-95 Sep-95 Oct-95 Nov-95 Dec-95 Jan-96 Feb-96 Mar-96 Apr-96 May-96 Jun-96 Jul-96 Aug-96 Sep-96 Oct-96 Nov-96 Dec-96 Jan-97 Feb-97 Mar-97 Apr-97 May-97 Jun-97 Jul-97 Aug-97 Sep-97 Oct-97 Nov-97 Dec-97 Jan-98 Feb-98 Mar-98 Apr-98 May-98 Jun-98 Jul-98 Aug-98 Sep-98 Oct-98 Nov-98 Dec-98 Jan-99 Feb-99 Mar-99 Apr-99 May-99 Jun-99 Jul-99 Aug-99 Sep-99 Oct-99 Nov-99
HFIR-JP-28
Target capsule
Design/Assembly
Irradiation
Disassembly
P.I.E.
HFIR-13J
RB varying temperature
Design/Assembly
Irradiation
Disassembly
P.I.E.
High Flux Beam Reactor, Brookhaven
HFBR-V1, V2
8 rabbits
Irradiation
Disassembly
P.I.E.
HFBR-V3, V4
Irradiation
Disassembly
P.I.E.
Advanced Test Reactor, Idaho Falls
ATR-A1
Drop-in
Irradiation
Disassembly
P.I.E.

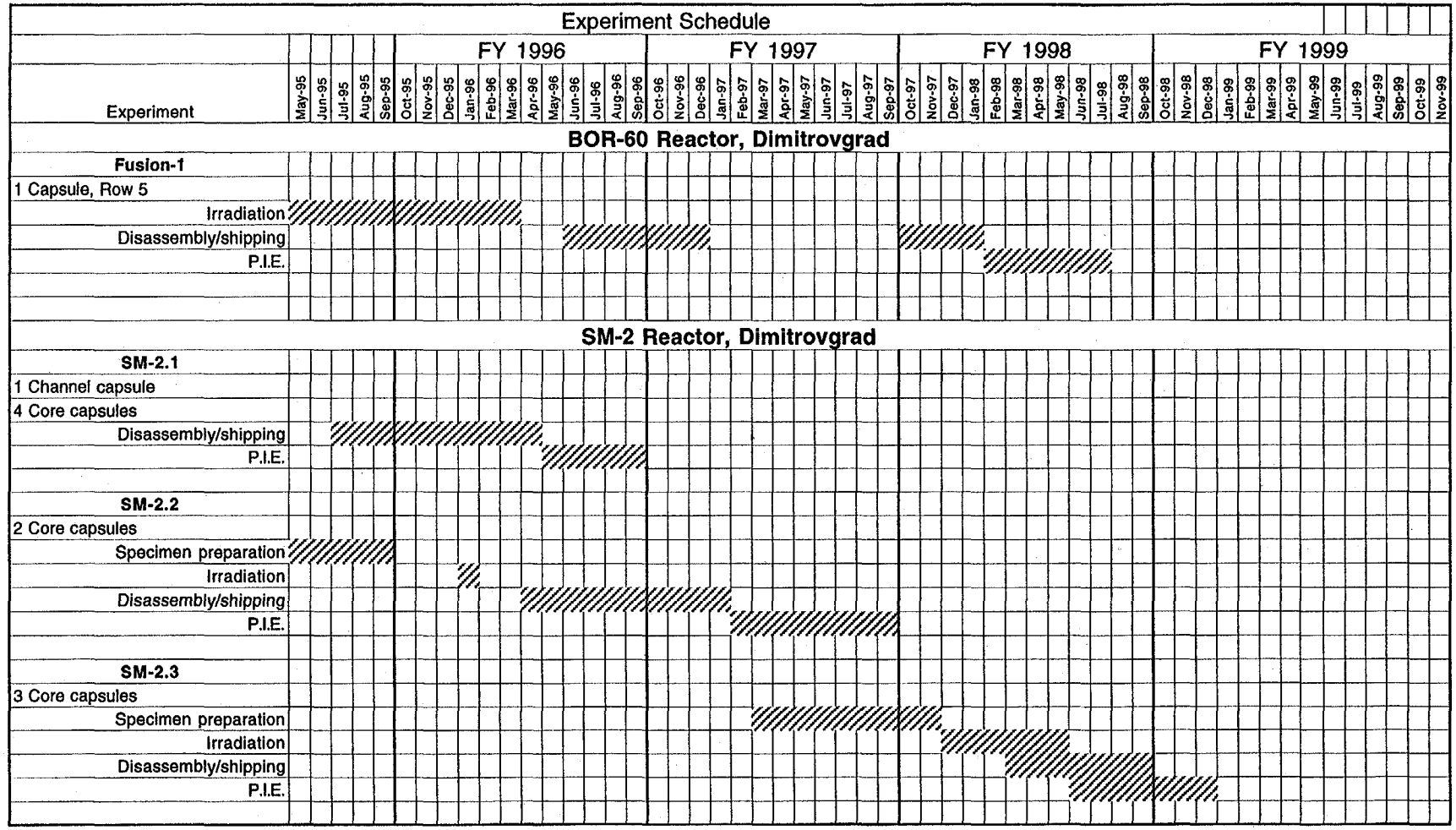
Experiment Schedule
FY 1996
FY 1997
FY 1998
FY 1999
May-95 Jun-95 Jul-95 Aug-95 Sep-95 Oct-95 Nov-95 Dec-95 Jan-96 Feb-96 Mar-96 Apr-96 May-96 Jun-96 Jul-96 Aug-96 Sep-96 Oct-96 Nov-96 Dec-96 Jan-97 Feb-97 Mar-97 Apr-97 May-97 Jun-97 Jul-97 Aug-97 Sep-97 Oct-97 Nov-97 Dec-97 Jan-98 Feb-98 Mar-98 Apr-98 May-98 Jun-98 Jul-98 Aug-98 Sep-98 Oct-98 Nov-98 Dec-98 Jan-99 Feb-99 Mar-99 Apr-99 May-99 Jun-99 Jul-99 Aug-99 Sep-99 Oct-99 Nov-99
Experiment
BOR-60 Reactor, Dimitrovgrad
Fusion-1
1 Capsule, Row 5
Irradiation
Disassembly/shipping
P.I.E.
SM-2 Reactor, Dimitrovgrad
SM-2.1
1 Channel capsule
4 Core capsules
Disassembly/shipping
P.I.E.
SM-2.2
2 Core capsules
Specimen preparation
Irradiation
Disassembly/shipping
P.I.E.
SM-2.3
3 Core capsules
Specimen preparation
Irradiation
Disassembly/shipping
P.I.E.

Distribution

1-16. Argonne National Laboratory, 9700 South Cass Avenue, Argonne, IL 60439

M. C. Billone	C. E. Johnson	J. H. Park
O. K. Chopra	F. Kassner	D. L. Smith
H. M. Chung	J. P. Kopasz	W. Tam
D. R. Diercks	R. F. Mattas	H. C. Tsai
J. Gazda	K. Nateson	
A. B. Hull	L. A. Niemark	

17-18. Argonne National Laboratory, EBR-II Division, P.O. Box 2528, Idaho Falls, ID 83403-2528

H. P. Planchon D. L. Porter

19. Auburn University, Department of Mechanical Engineering, 201 Ross Hall, Auburn, AL 36849

B. A. Chin

20-32. Pacific Northwest National Laboratory, P.O. Box 999, Richland, WA 99352

D. J. Edwards	L. R. Greenwood	G. W. Hollenberg
F. A. Garner (5)	M. L. Hamilton	R. H. Jones
D. S. Gelles	H. L. Heinisch	J. Youngblood

33. Carnegie Institute of Technology, Carnegie-Mellon University, Schenley Park, Pittsburgh, PA 15213

W. M. Garrison, Jr.

34. Commissariat à l'Energie Atomique, Direction des Technologies Advancées, M2R1/DECM Cen-Saclay, Gif Sur Yvette, Cedex, France

F. Tavassoli

35-37. General Atomics, P.O. Box 85608, San Diego, CA 92138

W. R. Johnson K. R. Schultz C. Wong

38. Georgia Institute of Technology, Fusion Research Center, 0225, Atlanta, GA 30332

W. M. Stacey

39. Grand Canyon University, Department of Natural Science, 3300 W. Camelback Rd., Phoenix, AZ 85017

W. A. Coghlan

40-42. Idaho National Engineering Laboratory, Fusion Safety Program, P.O. Box 1625, Idaho Falls, ID 83415-3523

G. Longhurst K. McCarthy D. Petti

43. Knolls Atomic Power Laboratory, P.O. Box 1072, Schenectady, NY 12301

G. Newsome

44-45. Lawrence Livermore National Laboratory, P.O. Box 808, Livermore, CA 94550

E.C.N. Dalder J. Perkins

46-52. Los Alamos National Laboratory, Los Alamos, NM 87545

J. L. Anderson	E. H. Farnum	W. F. Sommer
R. G. Castro	R. E. Siemon	K. E. Sickafus
D. W. Cooke		

53-55. Massachusetts Institute of Technology, Department of Metallurgy and Materials Science, Cambridge, MA 02139
L. W. Hobbs N. J. Grant K. C. Russell

56. Massachusette Institute of Technology, Plasma Fusion Center Headquarters, Cambridge, MA 02139
D. B. Montgomery

57-58. McDonnell-Douglas Corporation, Mail Code 1067220, P.O. Box 516, St. Louis, MO 63166-0516
J. W. Davis G. W. Wille

59. MER Corp., 7960 South Kolb Rd., Tucson, AZ 85706
W. Kowbel

60. Merrimack College, Dept. of Physics, 315 Turnpike Street, North Andover, MA 01845
D. P. White

61. M. J. Schiff & Associates, 1291 N. Indian Hill Blvd., Claremont, CA 91711-3897
G.E.C. Bell

62. NASA Lewis Research Center, MS-106-5, Cleveland, OH 44135
G. Morscher

63-65. National Institute of Standards and Technology, Boulder, CO 80302
F. R. Fickett H. I. McHenry R. P. Reed

66-67. Naval Research Laboratory, Code 6506, Washington, DC 20375
D. L. Gibson J. A. Sprague

68-111. Oak Ridge National Laboratory, P.O. Box 2008, Oak Ridge, TN 37831

Central Research Library	M. L. Grossbeck	A. F. Rowcliffe (10)
Document Reference Section	N. Hashimoto	M. J. Saltmarsh
Laboratory Records Department (2)	J. F. King	J. Sheffield
Laboratory Records-RC	E. A. Kenik	L. L. Snead
Patent Section	R. L. Klueh	R. E. Stoller
D. J. Alexander	E. H. Lee	K. R. Thoms
J. Bentley	L. K. Mansur	P. F. Tortorelli
E. E. Bloom	P. J. Maziasz	R. L. Wallace
T. D. Burchell	L. Qualls	E. Wakai
S. D. Connery	P. M. Rice	S. J. Zinkle
G. M. Goodwin	J. P. Robertson	
R. H. Goulding	T. C. Reuther	

112. Oregon Graduate Institute, Dept. of Materials Science & Engineering, 19600 N.W. Von Neumann Drive, Beaverton, OR 97006
J. M. McCarthy

113-115. Princeton University, Princeton Plasma Physics Laboratory, P.O. Box 451, Princeton, NJ 08540
R. C. Davidson Long-Poe Ku D. M. Meade

116-117. Rensselaer Polytechnic Institute, Troy, NY 12181
D. Duquette D. Steiner

118. Rockwell International Corporation, NA02, Rocketdyne Division, 6633 Canoga Avenue,Canoga Park, CA 91304
D. W. Kneff

119-121. Sandia National Laboratories, Fusion Technology Dept., Dept. No 6531, P.O. Box 5800, Albuquerque, NM 87185-5800
M. J. Davis M. Ulrickson R. D. Watson

122-124. Sandia National Laboratories, Livermore Division 8316, Livermore, CA 94550
W. Bauer K. Wilson W. G. Wolfer

125. San Diego State University, Mechanical Engineering Dept., San Diego, CA 92182-0191
L. D. Thompson

126. Texas A&M University, Box 397, Prairie View, TX 77446
D. Baker

127. TSI Research, 225 Stevens Ave., #110, Solana Beach, CA 92075
E. T. Cheng

128-129. University of California at San Diego, U.S. ITER Project Office, 9500 Gilman Drive, Bldg. 302, La Jolla, CA 92093-0035
C. C. Baker T. R. James

130. University of California at San Diego, Fusion Energy Research Program, 9500 Gilman Drive, MC0417, La Jolla, CA 92093-0417
M. Tillack

131-132. University of California, Dept. of Mechanical and Environmental Engineering, Engineering II, Room 2355, Santa Barbara, CA 93106-5070
G. E. Lucas G. R. Odette

133-135. University of California, Dept. of Chemical, Nuclear, and Thermal Engineering, Los Angeles, CA 90024
M. A. Abdou N. M. Ghoniem S. Sharafat

136. University of Illinois, Dept. of Nuclear Engineering, Urbana, IL 61801
J. Stubbins

137. University of Michigan, Dept. of Nuclear Engineering, Ann Arbor, MI 48109
T. Kammash

138. University of Missouri, Department of Nuclear Engineering, Rolla, MO 65401
A. Kumar

139-140. University of Tennessee, Dept. of Materials Science and Engineering, 427-B Dougherty Bldg., Knoxville, TN 37996-2200
P. K. Liaw C. J. McHargue

141-142. University of Wisconsin, Nuclear Engineering Dept., 1500 Johnson Drive, Madison, WI 53706
J. B. Blanchard G. L. Kulcinski

143-145. Hokkaido University, Faculty of Engineering, Kita 13, Nishi 8, Kita-ku, Sapporo 060, Japan
Heischichiro Takahashi Somei Ohnuki Akira Okada

146-147. Japan Atomic Energy Research Institute, Tokai Research Establishment, Tokai-mura, Naka-gun, Ibaraki-ken 319-11, Japan
Akimichi Hishinuma K. Noda

148-149. Kyoto University, Institute of Advanced Energy, Gokasho, Uji, Kyoto 611, Japan
Yutai Katoh Akira Kohyama

150. Kyushu University, Dept. of Nuclear Engineering, Faculty of Engineering, Kyushu University 36, Hakozaki, Fukuoka 812, Japan
C. Kinoshita

151. Kyushu University, Research Institute for Applied Mechanics, Kasuga, Fukuoka 816, Japan
Naoaki Yoshida

152-153. Muroran Institute of Technology, Dept. of Metallurgical Engineering, 27-1 Mizumoto-cho, Mororan 050, Japan
Toshihei Misawa Akihiko Kimura

154-155. Nagoya University, Dept. of Nuclear Engineering, Furo-Cho, Chikusa-ku, Nagoya 464-01, Japan
Michio Kiritani Tetuo Tanabe

156-159. National Institute for Fusion Science, Furo-cho, Chikusa-ku, Nagoya 464-01, Japan
Osamu Motojima Chusei Namba
Takeo Muroga Nobuaki Noda

160-163. National Research Institute for Metals, Tsukuba Branch, Sengen, Tsukuba-shi, Ibaraki-ken, 305, Japan
Fujio Abe Tetsuji Noda
Josei Nagakawa Haruki Shiraishi

164. PNC Oarai, 4002 Narita, Oarai, Ibaraki 311-13, Japan
Itaru Shibahari

165. Science University of Tokyo, Dept. of Materials Science & Technology, 2641 Yamazaki, Noda City, Chiba Prefecture 278, Japan
Naohira Igata

166. Teikyo University, Otsuka, Hachioji, Tokyo 192-03, Japan
Akira Miyahara

167. Tohoku University, Institute for Materials Research, Katahira 2-2-1, Sendai 980-77, Japan
Hideki Matsui

168-171. Tohoku University, Institute for Materials Research, Oarai Branch, Oarai, Ibaraki 311-13, Japan
Hideo Kayono Tamaki Shibayama
Hiroaki Kurishita Tatsuo Shikama

172-173. Tohoku University, Dept. of Nuclear Engineering, Aoba, Aramaki, Sendai 980-77, Japan
Katsunori Abe Akira Hasegawa

174. Tohoku University, Dept. of Machine Intelligence and Systems Engineering, Aramaki, Aoba-ku, Sendai 980-77, Japan
Tatsuo Kondo

175. Tokai University, Dept. of Nuclear Engineering, 1117 Kitakaname, Hiratsuka-shi, Kanagawa-ken 259-12, Japan
Shiori Ishino

176. University of Tokyo, Dept. of Nuclear Engineering, 3-1, Hongo 7-Chome, Bunkyo-Ku, Tokyo 113, Japan
Naoto Sekimura

177. University of Tokyo, Dept. of Materials Science, 3-1, Hongo 7-Chome, Bunkyo-ku, Tokyo 113, Japan
Yutaka Kohno

178. Commission of European Communities, Directorate-General for Research Science and Education, Fusion Programme RUE De La Loi 200, B-1049 Brussels, Belgium
F. Cozzani

179-180. Chalk River Nuclear Laboratories, Atomic Energy of Canada, Ltd., Chalk River, Ontario KOJ 1J0, Canada
I. J. Hastings D. P. Jackson

181-182. Southwestern Institute of Physics, P.O. Box 432, Chenedu 610041, Sichuan, P.R. China
J. P. Qian Zeng Yu Xu

183. Institute of Atomic Energy, Academia Sinica, P.O. Box 275-51, Beijing, P.R. China
J. Yu

184. Riso National Laboratory, Materials Dept., P.O. Box 49, DK-4000, Roskilde, Denmark
B. N. Singh

185. Centre d'Etudes Nucleaires, Saclay, DLPC/SMCM, Commissariat a l'Energie Atomique, 91191 Gif-Sur-Yvette, Cedex, France
N. Roux

186. Commission for European Communities, Joint Research Centre, I.A.M. Ispra Establishment, 21020 Ispra (Varese), Italy
P. Fenici

187. EURATOM/CIEMAT Fusion Association, Avenida Complutense 22, 28040, Madrid, Spain
E. R. Hodgson

188. Paul Scherrer Institute, CH-5232 Villigen, Wuerenlingen PSI, Switzerland
M. Victoria

189. Harwell Laboratory, B393, Radiation Damage Dept., Oxfordshire, OX11 ORA, United Kingdom
C. A. English

190. Metallurgical and Nuclear Consultant, 9A Cumnor Rise Road, Cumnor Hill, Oxford OX2 9HD, United Kingdom
D. R. Harries

191. Hahn-Mietner-Institut fur Kernforschung Berlin, Postfach 390128, Glienicker Str. 100, D-14109, Germany
H. Wollenberger

192. Institut fur Festkorperforschung Forschungszentrum Jülich, Postfach 1913, D-52425 Jülich, Germany
H. Ullmaier

193-195. ITER Garching Joint Work Site, Max-Planck-Institute für Plasmaphysik, Boltzmannstrasse 2, D-85748 Garching bei München, Germany
V. Barabash G. Kalinin R. Parker

196-197. ITER Naka Joint Work Site, 801-1 Mukouyama, Naka-machi, Naka-gun, Ibaraki-Ken, 311-01, Japan
M. Huguet (2)

198-201. ITER San Diego Joint Work Site, 11025 N. Torrey Pines Road, La Jolla, CA 92037
V. Chuyanov F. Puhn
S. J. Piet P. Smith

202-203. Kernforschungszentrum Karlsruhe, Postfach 3640, 75 Karlsruhe 1, Germany
M. Dalle-Donne (INR) K. Ehrlich (IMF-II)

204. Max-Planck-Institut für Plasmaphysik, Boltzmannstrasse 2, D-85748 Garching bei München, Germany
Patrick Lorenzetto

205. A. A. Baikov Institute of Metallurgy, USSR Academy of Sciences, Leninsky Prospect 49, Moscow, Russia
L. I. Ivanov

206. CRISM "Prometey," Naberezhnava r. Monastyrick 1, 193167, St. Petersburg, Russia
V. V. Rybin

207. D. V. Efremov Institute of Electro-Physical Apparatus, Scientific Technical Center "Sintez,"189631, St. Petersburg, Russia
S. A. Fabritsiev

208. Kharkov Institute of Physics & Technology, Radiation Damage and Materials Dept., Akademicheskaya 1, 310108 Kharkov, Ukraine
I. M. Neckludov

209-211. V. I. Lenin Research Institute of Atomic Reactors, 433510 Dimitrovgrad-10, Ulyanovsk Region, Russia
V. Kazakov A. S. Pokrovsky V. K. Shamardin

212. Korea Advanced Institute of Science and Technology, Department of Nuclear Engineering, DaeDukDanji, Taejon, 305-701, Korea
I-S. Kim

213-214. Korean Atomic Energy Research Institute, P.O. Box 105, Yusung, Taejon, 305-600, Korea
Thak-Sang Byun Jun Hwa Hong

215. Seoul National University, Dept. of Nuclear Engineering, 56-1 Shinrim-Dong, Kwanak-Ku Seoul, 151-742, Korea
K. H. Chung

216. Sung Kyun Kwan University, Dept. of Metallurgical Engineering, 300 Chunchun-dong, Jangan-gu, Suwon, 440-746, Korea
J. G. Han

217. Department of Energy, DOE Oak Ridge Field Office, P.O. Box 2008, Oak Ridge, TN 37831-6269
Assistant Manager for Energy Research and Development

218. Department of Energy, DOE Oak Ridge Field Office, P.O. Box 2008, Oak Ridge, TN 37831-6269
S. D. Frey

219. Department of Energy, Office of Basic Energy Sciences, Washington, D.C. 20585
R. J. Gottschall

220-225. Department of Energy, Office of Fusion Energy, Germantown, MD 20874

S. E. Berk	W. F. Dove	W. Marton
N. A. Davies	R. McKnight	F. W. Wiffen

226. Department of Energy, Richland Operations Office, P.O. Box 550, MS-K850, Richland, WA 99352
J. Turner

227-228. Department of Energy, Office of Scientific and Technical Information, Office of Information Services, P.O. Box 62, Oak Ridge, TN 37831
For distribution by microfiche as shown in DOE/OSTI-4500-R75, Distribution Categories UC-423 (Magnetic Fusion Reactor Materials) and UC-424 (Magnetic Fusion Energy Systems)